Role of adsorption in catalysis: Applications of NMR relaxometry

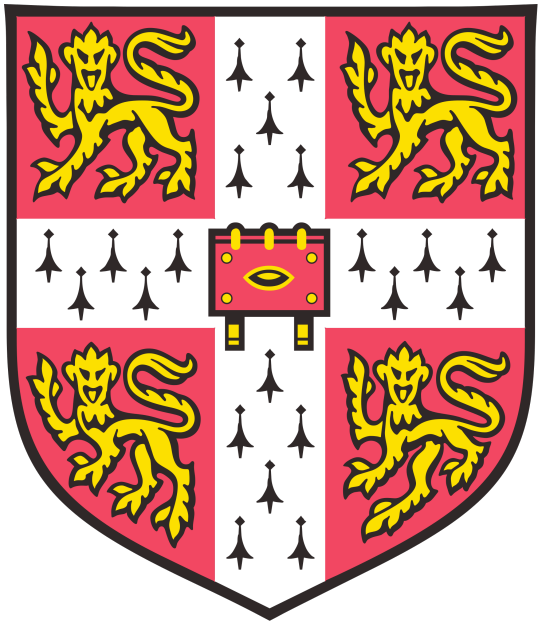

Pablo Arias Vecino
Fitzwilliam College

Department of Chemical Engineering and Biotechnology
University of Cambridge

A dissertation submitted for the degree of Doctor of Philosophy at the University of Cambridge

November 2014

Preface

The work presented in this dissertation was carried out in the Department of Chemical Engineering and Biotechnology, University of Cambridge, between October 2010 and November 2014. This dissertation is all my own work and has not been previously submitted in part, or in whole, for a qualification at any other university. All of the work described in this dissertation is believed to be original, except where explicit reference is made to other authors. The work reported here is part of a large collaborative project (CASTech).

This dissertation does not exceed 150 figures and 65000 words, including abstract, contents, diagrams, references, tables and equations.

Acknowledgements

To my supervisor, Professor Lynn Gladden — Thank you giving me the opportunity to join the Catalysis and Magnetic Resonance Group as well as for all the resources and project scope that I was provided. I will carry with me the experiences and skills gained throughout this programme for many years into my future.

To Dr. James McGregor — Thank you for the constant dedication, support, and guidance that you have provided to me, both while you were at Cambridge and beyond. Thank you also for training me on how to use the TEOM. Working with you has been invaluable and I am extremely grateful for that.

I would also like to thank Dr. Mick Mantle, Dr. Andy Sederman and Dr. Tegan Roberts for introducing me to NMR spectrometers, their continuous help throughout NMR sessions, as well as their advice on data analysis.

I express my gratitude to Dr. Jonathan Mitchell and Mr. Thusara Chandrasekera for instructing me in the use of the regularisation and inversion codes for processing NMR relaxometry raw data. I deeply appreciate the academically robust input of Dr. Kyra Sedransk Campbell on many experimental adsorption techniques - those hours in the lab would have not been the same without your arts and crafts moments.

Thank you to Dr. Evangelia Andreou and Ms. Laura Quintana Gómez for their help with my GC-MS experiments, and Mr. Zlatko Saracevic in acquiring BET and BJH measurements. Special thanks to the Electronics and Workshop teams in the Department — in particular to Ms. Wei-Yao Ma and Mr. Surinder Sall for all their help during the TEOM re-commissioning process.

Furthermore, I would like to acknowledge the collaborators in the CASTech project. In particular, many thanks to Prof. Christopher Hardacre, Dr. Helen Daly and Dr. Haresh Manyar for their insights in citral hydrogenation, Dr. Sam Wilkinson for his input on reaction kinetic modelling and reaction mechanisms, as well as Dr. Nazita Sedaie Bonab for her gas-liquid mass transfer measurements. The overall guidance and advice of Prof. Hugh Stitt and Dr. Andrew York at Johnson Matthey has also greatly been appreciated.

Thank you to the EPSRC and Johnson Matthey Catalysis for the funding of the CASTech project. I am also grateful to the travel bursaries and hardship fund of Fitzwilliam College for the additional financial aid.

Most of all, I want to thank all the dear friends that have been by my side throughout this journey. Finally, I want to thank my family, especially my mother and father who have always been an inspiration. During this time, things have not always been easy, and I could not be more grateful for having their guidance and support. And, needless to say, I want to thank Bonaire. Thanks for everything.

Summary

The work described in this thesis focuses on the effects that adsorption processes on catalysts pose in influencing reaction pathways. In the first phase of this work, Nuclear Magnetic Resonance (NMR) relaxometry methods were implemented and compared with traditional catalytic characterisation methods to study the adsorption of a series of C_5 and C_6 unsaturated hydrocarbons on two different supports, γ- and θ-Al_2O_3. The techniques developed were applied to the study of liquid-phase selective hydrogenation of citral on 5% Pt/SiO_2.

Infrared (IR) spectroscopy, volumetric adsorption isotherms, dynamic adsorption isotherms *via* a Tapered Element Oscillating Microbalance (TEOM), temperature-programmed desorption (TPD) as well as ^{13}C T_1 NMR and ^{1}H 2D T_1-T_2 relaxometry methods have been employed in this work. The particular surface-adsorbate interactions were characterised using IR spectroscopy, occurring predominantly on weak adsorption sites. Energies of adsorption as a function of coverage were obtained *via* adsorption isotherms. For example, 1-pentyne showed the strongest interaction with θ-Al_2O_3 (94 kJ mol^{-1}) while 1-pentene presented a weaker interaction (46 kJ mol^{-1}). Desorption energies obtained from TPD ranged from 85 – 130 kJ mol^{-1}, irrespective of the adsorbate. Evidence of reactivity of the aluminas was observed using TPD, TEOM and NMR relaxometry. ^{13}C T_1 NMR relaxometry is shown to provide atom-specific adsorbate-adsorbent interaction strengths, showing the molecular geometry of adsorption. This method was used to study molecular co-adsorption on θ-Al_2O_3.

The selective hydrogenation of citral as a model α,β-unsaturated aldehyde and the effect of different solvents on the activity and product distribution was studied at 298 and 373 K. A series of polar-protic, polar aprotic and non-polar solvents was investigated. Results showed higher initial reaction rates in non-polar solvents but higher selectivities on polar protic solvents. Solvent used also affected by-product formation. It was observed that the strong variations in reaction rates and selectivities reported correlated with the adsorbate-catalyst and solvent-reactant interactions. For example, adsorption isotherms showed that ethanol notably reduced the adsorption capacity of citral as compared with hexane, and this causes a reduced rate of reaction. ATR-IR measurements indicated solvent-citral interactions were solely present in polar-protic solvents, corresponding to higher yields of geraniol and nerol. Finally, ^{13}C T_1 NMR and ^{1}H 2D T_1-T_2 correlation experiments showed that the geometry of adsorption of citral, which in turn is influenced by the solvent used, affected product selectivity, and that product adsorption affected overall selectivity.

Table of contents

Chapter 1:

Introduction

1 Introduction

The phenomenon of adsorption was discovered by Scheele in 1773 and Fontana in 1777 with the uptake of gases by charcoal, while the first systematic investigations were carried out by Saussure with the adsorption of a variety of gases on several adsorbents (Brunauer, 1943). Adsorption is of great technological importance. For example, sensor development requires the adsorption of species to be detected. Examples of those include competitive adsorption – or preferential adsorption – with albumin proteins for liquid-phase sensing (Wang *et al.*, 2014), or gas-phase detection with metals such as Pd (Oleksenko *et al.*, 2014). Separation processes also require adsorption to occur. Affinity chromatography is widely used in bioprocessing, such as in oligosaccharides separation (Kuhn *et al.*, 2014). Also, gas phase processes exploit adsorption and separation with newly developed materials (Wu *et al.*, 2014), one example of those being metal organic frameworks (Fairen-Jiménez *et al.*, 2012). Purification of water (Mubarak *et al.*, 2014) and gases (Sircar *et al.*, 1996) also requires adsorption of trace impurities. In addition, adsorption phenomena play a vital role in many solid-state reactions and biological mechanisms. Solid catalysts work by adsorbing at least one reactant (Clark, 1970). Further, knowledge of adsorption processes is a crucial step towards understanding catalytic reaction systems.

1.1 Adsorption in catalysis

Catalysis is involved in a very large percentage of processes leading to the production of industrial chemicals, fuels, pharmaceuticals and the removal of environmental pollutants. Modern catalysts are designed in order to reach optimal reaction rates but, most importantly, to allow for high selectivity (Henry, 1998). Catalysts lower the activation barrier of chemical transformations through providing an alternative reaction pathway. As an example, **Figure 1.1** shows the synthesis of ammonia on iron. As can be seen, the reaction on the surface provides a lower activation energy. Very often, catalytic routes can be designed such that raw materials are used efficiently, making them significantly more energy-efficient, environmentally benign, and selective for the desired products. A successful example is the three-way catalyst, which effectively reduces pollution from car engines (Niemantsverdriet, 2000). Other important processes involving heterogeneous catalysts include the Haber-Bosch process for ammonia synthesis or the hydrogenation of fatty acids in foodstuffs. It is estimated that about 20% of all commercial products manufactured in the USA are derived from catalytic processes. Catalysis is believed to contribute to more than 35% of global GDP,

the biggest part coming from high-energy fuels (Armor, 2008). The value of the heterogeneous catalysis market was estimated to be 15 billion USD per year, with the cost of the catalyst of < 0.22% with respect to the total processing costs (Bartholomew and Farrauto, 2006; Boudart *et al.*, 2008).

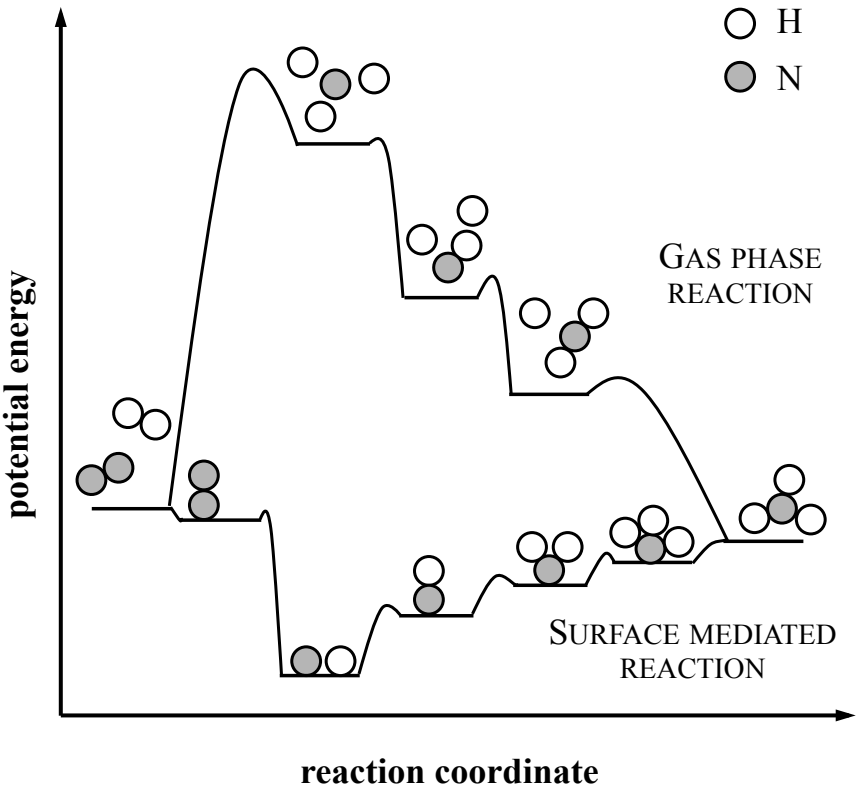

Figure 1.1. Catalysts provide energetically favourable pathways for the desired reaction, in which the activation barriers of all the intermediate steps are low compared to the activation energy of the gas phase reaction. In the scheme, synthesis of ammonia on iron is shown. Adapted from Erlt (1980).

Mechanistically, on a heterogeneous catalyst the reaction starts with the diffusion of the reactant in the bulk fluid and within the pore. Then, the adsorption of the reacting molecules takes place on the surface of the catalyst, where intramolecular bonds are weakened or broken. The adsorbed species then react on the surface and the products desorb from the surface (Niemantsverdriet, 2000). Therefore, understanding the interactions between adsorbates and surfaces is a key area of research in the field of heterogeneous catalysis. Such an understanding is essential to optimise existing processes and to enable the rational design of new catalysts with enhanced properties: higher activity, selectivity, and stability (Christensen and Nørskov, 2008).

Adsorption on solid surfaces is a complex phenomenon, with a broad distribution of sites with different adsorption energies. Additionally, the molecules may be mobile or immobile, with possible interactions between neighbouring molecules. The forces binding the molecules to a surface might be physical – Van der Waals, dipolar or ionic – or equivalent to chemical bonds with molecular orbital overlaps (Clark, 1970). Knowledge of the relative strength of interaction of each adsorbate with the catalytic surface and the influence of each component upon the adsorption of the others is a crucial step towards understanding the catalytic reaction system. Solvents, which act as co-adsorbates, can play a key role in catalytic reactions (Jin *et al.*, 2003). A brief review of the different modes of adsorption, and concepts commonly employed in catalytic systems describing adsorption is shown below.

1.1.1 Physisorption and chemisorption

Atoms in the plane of the surface are subjected to unbalanced forces. Any process that tends to decrease the free surface energy of such surface atoms occurs spontaneously (Brunauer, 1943). Two main processes can occur: physisorption and chemisorption. Physisorption forces are the same as those responsible for the condensation of vapours and the deviations from ideal gas behaviour, whereas chemisorption interactions are essentially responsible for the formation of chemical compounds (Rouquerol *et al.*, 1999). Chemisorption strongly depends on the reactivity of the adsorbent with specific sites on the surface, and is therefore necessarily confined to a monolayer. The opposite is true in physisorption, which is characterised by few specific interactions, allowing multilayer adsorption to occur. The energy of adsorption is a key differential factor: chemisorption usually involves high energies, of the same order of magnitude as a chemical reaction; however, although an exothermic process, physisorption energies are generally < 20 kJ mol^{-1}.

Figure 1.2 shows an example of adsorption of molecule A_2. The first shallow potential energy minimum describes the physical adsorption state. As the molecule approaches the surface, chemical bonding can occur. The potential well of the chemisorption curve is much closer to the surface. In this case, a non-activated dissociative chemisorption process is shown. In some cases, the crossover between the two potential curves can lie above the potential-energy zero line, such energy denoted as the energy of activation of chemisorption. If the adsorbate were to remain intact on the surface then a non-dissociative chemisorption would have occurred.

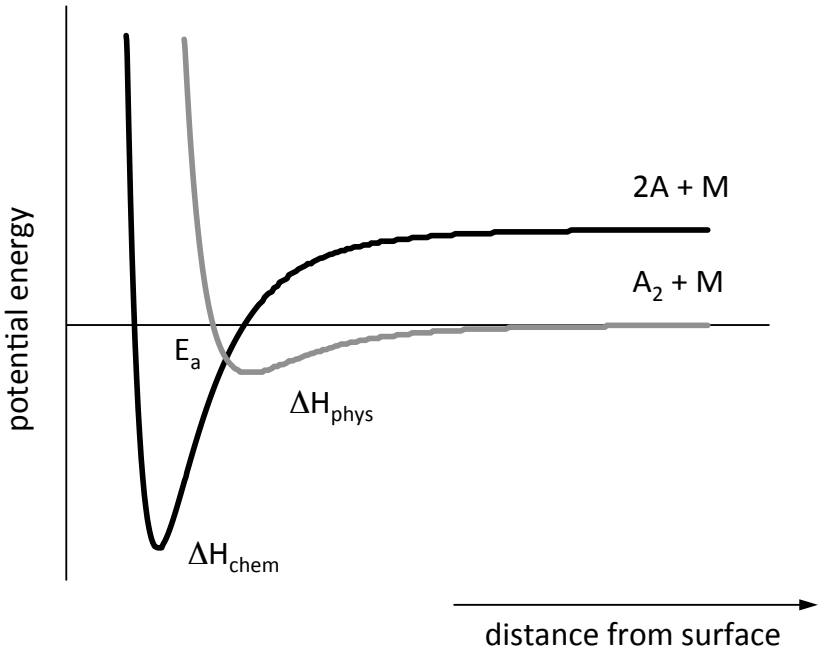

Figure 1.2. Potential energy diagram for the adsorption of A_2. Physisorption and chemisorption processes are shown. A_2 adsorbs dissociatively in a non-activated process.

1.1.2 Adsorption kinetics and adsorption equilibrium

The rate at which molecules adsorb onto a surface is dependent on factors derived from the kinetic theory of gases, such as pressure and temperature. Additionally, only a fraction *s* of molecules will stick to the surface on impact (Thomas and Thomas, 1997). This relationship is established as:

$$r_a = \frac{dN_a}{dt} = s\frac{P}{\sqrt{2\pi mkT}} \tag{1.1}$$

where *s* is the sticking probability, *m* the mass of the adsorbate, *k* is the Boltzmann constant and *T* the temperature in K. Considering that if the adsorbate strikes an empty site, it becomes adsorbed with a sticking probability s_0, whereas if the site is occupied it is reflected, equation 1.1 can be rewritten as:

$$r_a = s_0\frac{P}{\sqrt{2\pi mkT}}(1-\theta) = k_{ads}(1-\theta)P \ . \tag{1.2}$$

As can be seen, equation 1.2 is expressed in terms of the adsorption constant, k_{ads}, and the surface coverage of the adsorbate on the surface, θ.

Similarly, rates of desorption can be expressed as a function of a desorption constant, k_{des}, in the well-known Polanyi-Wigner equation, equation 1.3 (Niemantsverdriet, 2000):

$$r_d = -\frac{d\theta}{dt} = k_{des}\theta^n = A(\theta)\exp\left(-\frac{E_{des}(\theta)}{RT}\right)\theta^n \quad . \tag{1.3}$$

where A is the pre-exponential factor and E_{des} the activation energy for desorption, both potentially dependent on surface coverage.

The equilibrium adsorption of adsorbates describes a dynamic equilibrium situation in which the rate of molecular adsorption onto the catalyst surface is equal to the rate of molecular desorption from the catalyst surface. Following the example shown in **Figure 1.2**, an equation describing the equilibrium adsorption is illustrated below:

$$A_{2(g)} + 2* \rightleftharpoons 2\ A_{(s)}$$

where * represents the adsorption site. This equilibrium adsorption process can be described by equilibrium adsorption isotherms. The most widely used equations, along with their theoretical assumptions are show below.

1.1.2.1 Adsorption isotherms

The simplest interpretation of the adsorbed phase is to consider that at very low surface concentration, the adsorbate molecules are independent of each other. This assumption implies linearity in uptake, v, with increasing pressure, described by Henry's isotherm equation:

$$v = k_H P \quad . \tag{1.4}$$

With increasing temperature, and at higher loading levels for equal increments of pressure, the total uptake becomes smaller. The amount adsorbed becomes proportional to a power of the gas pressure below unity (Brunauer, 1943). The Freundlich adsorption isotherm equation (Freundlich, 1932) describes this behaviour, with an implicit exponential description of the surface energetics:

$$v = k_F P^{1/n} \quad . \tag{1.5}$$

At even higher pressures, a plateau is observed, typical of adsorption with a fixed number of well-defined sites, *i.e.*, typical for chemisorption. The Langmuir isotherm equation describes the adsorption of such systems

$$v = \frac{v_{m,L} k_L P}{1 + k_L P} \quad . \tag{1.6}$$

where $v_{m,L}$ is the monolayer capacity in the Langmuir expression, and k_L is the affinity constant (Chaouati *et al.*, 2013). It considers all sites are energetically equivalent. **Figure 1.3** shows the behaviour of the three equations.

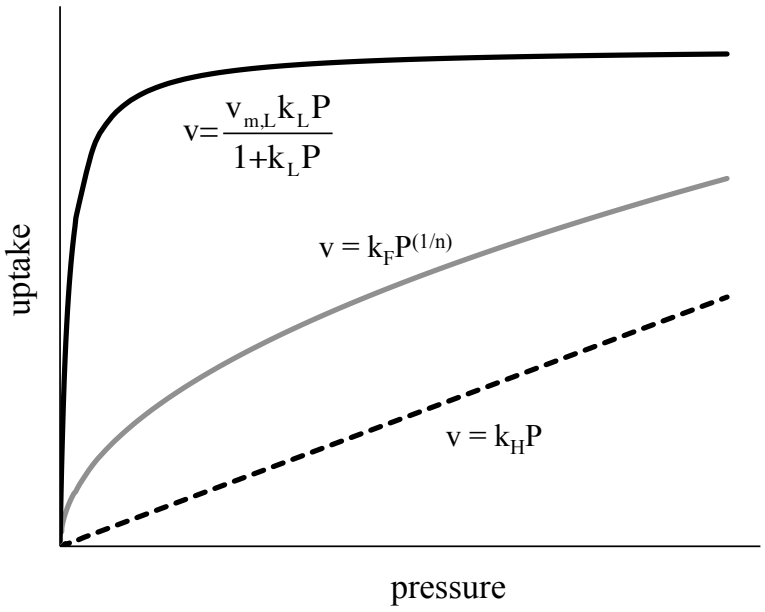

Figure 1.3. Henry (dashed black), Freundlich (grey) and Langmuir (black) adsorption isotherm equations. Values of $k_H = 0.15$, $k_F = 1.4$, $1/n = 0.15$, $v_{m,L} = 12$ and $k_L = 2$ were used.

Additionally, the presence of lateral interactions, interactions between molecules on neighbouring sites, as well as the different surface energetics commonly present in heterogeneous surfaces, result in different adsorption behaviour as that described in previous equations, in particular the Langmuir equation. The Tóth isotherm equation is designed to overcome such limitations (Tedds *et al.*, 2011; Do, 1998):

$$v = \frac{v_{m,T} k_T P}{\left[1 + \left(k_T P\right)^t\right]^{1/t}} \quad . \tag{1.7}$$

In equation 1.7, $v_{m,T}$ is the Tóth saturation coverage, k_T the affinity parameter or adsorption constant and t the Tóth constant of the fitting. When t = 1, the resulting equation is the Langmuir isotherm. The value of t provides an indication of the heterogeneity of interactions; the value of t taking values further from unity as heterogeneity increases (Tóth, 1995).

While previous isotherm equations are used mostly in a chemisorption context, additional adsorption can occur on top of the first layer. The Brunauer-Emmet-Teller (BET) equation is applicable on multilayer adsorption (Brunauer *et al.*, 1938). Additionally, the values of monolayer coverage, as well as an average energy of adsorption for the first layer can be extracted:

$$v = \frac{v_{m,BET} c P}{(P_0 - P)\left[1 + (c-1)(P/P_0)\right]} \quad . \tag{1.8}$$

where

$$c = \exp\left(\frac{E_1 - E_L}{RT}\right) \quad . \tag{1.9}$$

In this equation $v_{m,BET}$ represents the amount of gas adsorbed when a complete unimolecular layer is formed and P_0 is the saturation pressure. E_1 is an average heat of adsorption of the first layer, and E_L is the heat of liquefaction.

1.1.3 Strength of adsorption and competitive adsorption

The strength of interaction of the adsorbate will determine the reaction kinetics observed, as determined in water-gas shift reactions by reactant surface coverage (Liu *et al.*, 2014). Similarly, linear relations between adsorption energies in dissociative adsorption processes and activation energies of the dissociation transition state have been established. They are known as the so-called Brønsted-Evans-Polanyi relations and have been studied in depth in the dissociation of N_2 (Christensen and Nørskov, 2008). A good catalyst should exhibit low N_2 dissociation barriers, as well as a weak N adsorption bond with the surface to allow for reaction to occur and more empty sites to be created. Hence, both adsorption and desorption need to occur and a good catalyst should have the right balance between reactant adsorption and product desorption. Additionally, the simultaneous adsorption of more than one species on the surface of the catalyst could affect the overall reactivity. Such competitive adsorption occurs in many catalytic reactions. For example, the performance of the diesel oxidation

catalyst (DOC) to reduce CO and hydrocarbon emissions is affected by the presence of NO_x from the exhaust engine, due to competitive adsorption (Al-Harbi *et al.*, 2012).

1.1.3.1 Volcano plots

Electronic properties of the surface are also important as they affect the energy of the adsorption bond. In general, the energy of adsorption must be low for reactions to take place, as desorption of products needs to be sufficiently low so they can leave the surface (Clark, 1970). If the adsorption is too weak, the catalyst has little effect and will, for example, be unable to dissociate a bond. If the interaction is too strong, the adsorbates will be unable to desorb from the surface. In both cases, resulting reaction rates are low (Chorkendorff and Niemantsverdriet, 2007). An example of such behaviour was shown in the hydrogenation of citral on SiO_2 supported Group VIII metals (Singh and Vannice, 2001). As shown in **Figure 1.4**, the rates of reaction are plotted against the %*d*-character, defined as the contribution of the *d*-electrons to the *spd* hybrid orbitals in Resonance Band Valence Theory. The figure shows a volcano-shaped plot, indicative of the differences between weak adsorption *vs.* hindered desorption phenomena described.

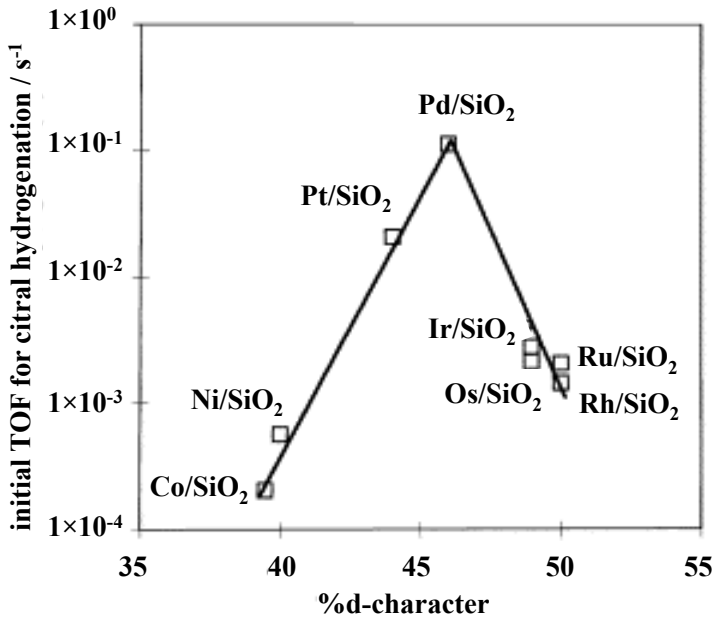

Figure 1.4. Correlation of the initial hydrogenation TOF of 0.06 M citral at 300 K and 1 atm H_2 with the percentage of *d*-band of a series of Group VIII metals. From Singh and Vannice (2001).

1.1.3.2 Role of solvent in adsorption processes

As previously indicated, competitive adsorption has important consequences for the conditions under which reactions are carried out. An example is that of the solvent used in liquid-phase catalytic reactions. For example, previous studies have shown a dependence on the enthalpy of adsorption of alcohols with alkane solvents of increasing chain length over Graphon (Birdi, 1984). Similarly, there are numerous studies reported in liquid-phase catalysis showing important effects of solvent, and attributed to competitive adsorption processes (Bertero *et al.*, 2011; Mounzer *et al.*, 2010; Mukherjee and Vannice, 2006; Takagi *et al.*, 1999).

1.2 Objectives and thesis outline

The overall objectives of this work were to: i) understand adsorption processes on catalytic surfaces as a key step that can affect and control subsequent reaction pathways, ii) establish a coherent interpretation of T_1 and T_2 nuclear magnetic resonance (NMR) relaxation times through correlating nuclear magnetic resonance (NMR) relaxometry data with traditional catalytic measurements, and iii) apply the techniques developed to catalytic systems in order to reveal information about the molecular configuration of adsorbed species, with a particular focus on multicomponent adsorption.

The structure of this thesis describes the work carried out in line with the main objectives previously described. Chapter 2 introduces the experimental techniques used to study adsorption in this dissertation. Particular attention is given to nuclear magnetic resonance (NMR) techniques and relaxometry. In chapter 3, attention is given to the description of the alumina surface in the literature, used in subsequent adsorption studies. Additionally, information on surface adsorption sites is obtained from the adsorption of probe molecules. Chapter 4 reports a detailed study of the adsorption of 1-pentene on γ- and θ-Al_2O_3, establishing a comparison of different characterisation techniques. Chapter 5 extends the study to a series of C_5 and C_6 unsaturated hydrocarbons used and extracts conclusions on the information provided by the different characterisation measurements. An interpretation of the information contained in the nuclear magnetic resonance (NMR) relaxation times T_1 and T_2 with respect to adsorption is presented on the light of those observations.

On the second part of the dissertation, a particular reaction system was selected to expand on the understanding on the importance of adsorption in catalysis. Further, that reaction system

served as a model reaction to apply nuclear magnetic resonance (NMR) relaxometry methods and show the usefulness of these techniques to its full capabilities. Chapter 6 presents a literature review on liquid-phase hydrogenation reactions, with particular attention to multifunctional molecules. The previous reports on solvent effects in the reaction of citral, an α,β-unsaturated carbonyl molecule, are presented and main messages summarised. Chapter 7 presents an extensive study on the hydrogenation of citral in a set of solvents and provides information on reaction rates, selectivities and deactivation. Adsorption and characterisation measurements are performed in chapter 8 in a subset of solvents to provide a cohesive understanding of the influence of solvent on the differences in activity and product distribution observed. A subset of those solvents is selected in chapter 9, where nuclear magnetic resonance (NMR) relaxometry is used to gain a complete understanding on citral results at low and high conversion.

Finally, chapter 10 summarises the principal accomplishments of the work described in this dissertation. Furthermore, this chapter presents a series of recommendations towards extending the contribution of this work.

References

Al-Harbi, M., Hayes, R., Votsmeier, M., Epling, W.S. (2012) Competitive NO, CO and hydrocarbon oxidation reactions over a diesel oxidation catalyst. *Can. J. Chem. Eng.*, 90, 1527 – 1538.

Armor, J.N. (2008) *Explaining what catalysis is*. NACS website (http://nacatsoc.org/above/what-is-catalysis/). Last accessed August 2014.

Bartholomew, C.H., Farrauto, R.J. (2006) *Fundamentals of industrial catalytic processes.* Wiley, New Yersey, pp. 8 – 10.

Bertero, N.M., Trasarti, A.F., Apesteguía, C.R. and Marchi, A.J. (2011) Solvent effect in the liquid-phase hydrogenation of acetophenone over Ni/SiO_2: a comprehensive study of the phenomenon. *Appl. Catal. A-Gen.*, 394, 228 – 238.

Birdi, K.S. (1984) Enthalpy of adsorption on solids from solution. In: Myers, A.L., Belfort, G. (eds.). *Fundamentals of adsorption: proceedings of the Engineering Foundation conference at Schloss Elmau, Bavaria, West Germany, May 6-11, 1983*, The foundation, New York.

Boudart, M., Davis, B.H., Heinemann, H. (2008) *Introduction. The development of industrial heterogeneous catalysis.* In: Ertl, G., Knözinger, H., Weitkamp, J. (eds.). *Handbook of heterogeneous catalysis.* Wiley-VCH, Weinheim, pp. 35 – 36.

Brunauer, S. Emmet, P.H., Teller, E. (1938) Adsorption of gases in multimolecular layers. *J. Am. Chem. Soc.*, 60, 309 – 319.

Brunauer, S. (1943) *The adsorption of gases and vapours*, *vol. 1: physical adsorption*. Princeton University Press, pp. 3 – 6.

Buchbinder, A.M., Weitz, E., Geiger, F.M. (2010) Pentane, hexane, cyclopentane, cyclohexane, 1-hexene, 1-pentene, *cis*-2-pentene, cyclohexene, and cyclopentene at vapor/α-alumina and liquid/α-alumina interfaces studied by broadband sum frequency generation. *J. Phys. Chem. C*, 114, 554 – 566.

Chaouati, N., Soualah, A., Chater, M. (2013) Adsorption of phenol from aqueous solution onto zeolites Y modified by silylation. *C.R. Chimie*, 16, 222 – 228.

Chorkendorff, I. and Niemantsverdriet, J.W. (2007). *Concepts of Modern Catalysis and Kinetics*, Wiley-VCH, Weinheim, pp. 23 – 215.

Christensen, C.H., Nørskov, J.K. (2008) A molecular view on heterogeneous catalysis. *J. Chem. Phys.*,18, 182503.

Clark, A. (1970) *The theory of adsorption and catalysis*, Academic Press, London, pp. 233 – 237.

Do, D.D. (1998) *Adsorption analysis: equilibria and kinetics*. Imperial College Press, London, pp. 49 – 70.

Erlt, G. (1980) Surface science and catalysis – studies on the mechanism of ammonia synthesis: the P.H. Emmett award address. *Catal. Rev. Sci. Eng.*, 21, 201 – 223.

Fairen-Jiménez, D., Colón, Y.J., Fahra, O.K., Bae, Y-S., Hupp, J.T., Snurr, R.Q. (2012) Understanding excess uptake maxima for hydrogen adsorption isotherms in frameworks with rht topology. *Chem. Commun.*, 48, 10496 – 10498.

Freundlich, H. (1932) Of the adsorption of gases. Section II. Kinetics and energetics of gas adsorption. *Trans. Faraday Soc.*, 28, 195 – 201.

Gladys, M.J., Stevens, A.V., Scott, N.R., Jones, G., Batchelor, D., Held, G. (2007) Enantiospecific adsorption of alanine on the chiral Cu{531} surface. *J. Phys. Chem. C*, 111, 8331 – 8336.

Henry, C.R. (1998) Surface studies of supported metal catalyst. *Surf. Sci. Rep.*, 31, 231 – 325.

Jin, G., Ido, T., Goto, S. (2003) Rate enhancement effect of third liquid phase on dibenzyl ether production in solid-liquid-liquid phase transfer catalytic system. *Catal. Today*, 79, 471 – 478.

Kuhn, R.C., Mazutti, M.A., Albertini, L.B., Filho, F.M. (2014) Evaluation of fructooligosaccharides separation using a fixed-bed column packed with activated charcoal. *N. Biotechnol.*, 31, 237 – 241.

Kunkes, E.L., Simonetti, D.A., West, R.M., Serrano-Ruiz, J.C., Gärtner, C.A., Dumesic, J.A. (2008) Catalytic conversion of biomass to monofunctional hydrocarbons and targeted liquid-fuel classes. *Science*, 332, 417 – 421.

Liu, B., Huang, T., Zhang, Z., Wang, Z., Zhang, Y.H., Li, J-L. (2014) The effect of the alkali additive on the highly active Ru/C catalyst for water gas shift reaction. *Catal. Sci. Tech.*, 4, 1286 – 1292.

Mounzer, H.N., Wood, J., Stitt, E.H. (2010) Heterogeneous oxidation of 2-octanol on 5 wt%Pt – 1 wt%Bi/Carbon catalyst. *Chem. Eng. Sci.*, 65, 179 – 185.

Mubarak, N.M., Sahu, J.N., Abdullah, E.C., Jayakumar, N.S. (2014) Removal of heavy metals from wastewater using carbon nanotubes. *Sep. Purif. Rev.*, 43, 311 – 338.

Mukherjee, S., Vannice, M.A. (2006) Solvent effects in liquid-phase reactions I. Activity and selectivity during citral hydrogenation on Pt/SiO_2 and evaluation of mass transfer effects. *J. Catal.* 243, 108 – 130.

Niemantsverdriet, J.W. (2000) *Spectroscopy in catalysis*, Wiley VCH, Weinheim, pp. 9 – 35.

Oleksenko, L.P., Maksymovych, N.P., Sokovykh, E.V., Matushko, I.P., Buvailo, A.I., Dollahon, N. (2014) Study of influence of palladium additives in nanosized tin dioxide on sensitivity of adsorption semiconductor sensors to hydrogen. *Sensor. Actuact. B-Chem.*, 196, 298 – 305.

Rouquerol, F, Rouquerol, J., Sing, K. (1999) *Adsorption by powders and porous solids.* Academic Press, London, pp. 1 – 26.

Singh, U.K., Vannice, M.A. (2001) Kinetics of liquid-phase hydrogenation reactions over supported metal catalysts – a review. *Appl. Catal. A-Gen.*, 213, 1 – 24.

Sircar, S., Golden, T.C., Rao, M.B. (1996) Activated carbon for gas separation and storage. *Carbon*, 34, 1 -12.

Takagi, H., Isoda, T., Kusakabe, K., Morooka, S. (1999) Effects of solvents on the hydrogenation of mono-aromatic compounds using noble-metal catalysts. *Energ. Fuel.*, 13, 1191 – 1196.

Tedds, S., Walton, A., Broom, D.P., Book, D. (2011) Characterisation of porous hydrogen storage materials: carbons, zeolites, MOFs and PIMs. *Faraday Discuss.*, 151, 75 – 94.

Thomas, J.M., Thomas, W.J. (1997) *Principles and practice of heterogeneous catalysis.* Wiley-VCH, Weinheim, pp. 1 – 123.

Tóth, J. (1995) Uniform interpretation of gas/solid adsorption. *Adv. Colloid Interf. Sci.*, 55, 1 – 239.

Wang, R., Wang, W., Ren, H., Chae J. (2014) Detection of copper ions in drinking water using the competitive adsorption of proteins. *Biosens. Bioelectron.*, 57, 179 – 185.

Wu, B., Li, X., An, D., Zhao, S., Wang, Y. (2014) Electro-casting aligned MWCNTs/polystyrene composite membranes for enhanced gas separation performance. *J. Membr. Sci.*, 462, 62 – 68.

Chapter 2:

Techniques to study adsorption

2 Techniques to study adsorption

Several techniques are employed to probe the interaction of adsorbates with catalytic surfaces (Gladys *et al.*, 2007). The range of techniques available will operate at different temperature and pressure conditions. Additionally, some techniques will be preferentially used depending on the type of information acquired, *e.g.*, the structure of adsorbate *vs.* the energy of adsorption. Finally, the systems under study would limit the techniques employed. For example, single crystal surfaces represent well-defined surfaces. Therefore, it is possible to describe adsorption sites in detail. This contrasts with complex catalyst systems, where multiple adsorption sites are present. Section 2.1 presents a summary of well-established adsorption methods. The techniques used in this work, along with some basic theory, will be briefly described in section 2.2.

2.1 General considerations

The principles underlying the techniques that study adsorption are very diverse, limiting its applicability to a subset of conditions. For example, volumetric adsorption methods or mass measurement methods heavily depend on the range of conditions for the adsorbate to remain in the vapour phase. Spectroscopic methods are based on different types of excitation and detection: photons, electrons, neutrons, ions, electromagnetic fields, etc. However, measurements of low-energy electrons, ions and neutrons leaving the catalyst surface need to be carried out *in vacuo.* Of all surface science techniques applied at Ultra High Vacuum (UHV) conditions in single crystals, only a number of them can be directly used in real catalyst conditions at high pressures, namely X-ray techniques, such as X-ray absorption near edge spectroscopy (XANES), or vibrational spectroscopy, infrared (IR) or Raman. In some cases, an important problem is the transfer of scientific results from surface science to applied catalysis due to the so-called “materials gap” and “pressure gap” (Baumer *et al.*, 2007) i.e., the use of single crystals and ultrahigh-vacuum conditions versus a real operating heterogeneous catalyst. A series of commonly used methods to study adsorption is described below. Examples are presented along with the range of operating conditions.

Starting with techniques applied only at UHV, photoemission spectroscopy methods, such as X-ray photoelectron spectroscopy (XPS) and UV photoelectron spectroscopy (UPS) have been used to elucidate adsorbed species formed with different treatments (Hamid and Eric, 2006), or to study adsorption and reaction processes by determining adsorbates formed on metal and metal oxides (Dillard *et al.*, 1984). Both XPS and UPS have been used in the study

of the adsorption of simple molecules, such as CO, O_2, N_2 or N_2O on metal surfaces (Fluggle and Menzel, 1979). Auger electron spectroscopy (AES) is related to these techniques. AES has been used in the analysis of the adsorption of molecules, such as NO, in order to reveal patterns of adsorption (Sasse *et al.*, 1988) or, in surface reactions, to observe the mechanisms involved in the formation of oxides (Patel and Pemble, 1996). XPS and AES are among the most often applied techniques in surface characterisation, despite requiring vacuum conditions (Niemanstverdriet, 2000).

In contrast, other techniques work in conditions more closely related to real operating conditions. For example, vibrational spectroscopies, such as IR, Raman or sum frequency generation (SFG) have also been used to study adsorption processes (Niemanstverdriet, 2000). Direct mass changes upon adsorption have been recorded using a Tapered Element Oscillating Microbalance (TEOM). Equilibrium adsorption isotherms for various alkane systems (Zhu *et al.*, 1998) have been measured, as well as the kinetics of coke formation and its effect on transport and adsorption behaviour (Chen *et al.*, 1996). Thermo gravimetric analysis (TGA) has also been used to study mass changes during desorption of species (Zhu and Ping, 2014). Temperature-programmed techniques (TPx) provide information on energies of desorption or reaction of surface adsorbed species. Calorimetric methods, such as differential scanning calorimetry (DSC) have been used to obtain differential heats of adsorption and to record adsorption isotherms (De Moor *et al.*, 2011). Also, TGA-DSC-MS has been used to study various aspects of heterogeneous reactions such as the energy of steps involved, the strength of adsorption sites, and the products formed during the reaction as a function of temperature (Osorio-Pérez *et al.*, 2008). Other techniques such as electrochemical methods are also useful for characterisation. For example, voltammetry allows for the determination of sites on the catalytic material and the results can be related to the reaction data (Burch *et al.*, 2002).

2.2 Experimental techniques used in this work

In this section, focus will be placed on the adsorption techniques employed in this work. The working principles of volumetric adsorption methods, temperature-programmed techniques, infrared spectroscopy, as well as Tapered Element Oscillating Microbalance (TEOM) are reviewed in section 2.2.1. Particular attention will be given to Nuclear Magnetic Resonance (NMR) techniques. Some NMR basic theory, its use as an adsorption technique and, in particular, the use of NMR relaxometry to study adsorption will be described in section 2.2.2.

2.2.1 Non-NMR techniques

2.2.1.1 Volumetric adsorption isotherms

The use of volumetric methods to study adsorption is well known (Brunauer *et al.*, 1938; Uzio, 2001). Energies of adsorption of different species can be obtained (Ahmed and Teydan, 2014; Yi *et al.*, 2014). Those are important for the study of new materials to characterise adsorption (Fairen-Jiménez *et al.*, 2012), or for high-pressure gas storage (Mitchell *et al.*, 2014). However, multicomponent adsorption with volumetric methods has also been studied to exploit separation strategies (Farzad *et al.*, 2007) or pollutant removal (Ahmed and Teydan, 2014; Duffy *et al.*, 2006; Zhou *et al.*, 2012). Generally, adsorption isotherms are a useful technique to compare results with detailed spectroscopic studies, and are relatively straightforward.

Gas adsorption manometry is the most widely used method, and is considered to be simple and effective (Rouquerol *et al.*, 1999). This method is based on the measurement of the gas pressure in a calibrated, constant volume, at a known temperature. The pressure transducer provides all the information required to determine the adsorption isotherm. After adsorption equilibrium has been established, the amount adsorbed is calculated from the change in pressure. **Figure 2.1** shows a schematic diagram of the experimental apparatus used. It is based on a simple set-up with three valves that delimit a known dosing volume, and a pressure transducer for the range 1 – 1000 mbar (Edwards ASG 1000 mbar). It consists in a glass manifold (Soham Scientific) equipped with a rotary pump (Edwards RV3). Pressure within the lines is monitored with an active pirani pressure gauge (Edwards). A known amount of catalyst is placed in a glass basket (Soham Scientific). The basket is heated with a furnace for sample pre-treatment, and is kept in an isothermal bath during adsorption experiments. Liquid adsorbate is placed in a flask and purified following a series of freeze-thaw-pump cycles. Aliquots of the vapourised adsorbate are admitted into the dosing volume and the change in pressure upon adsorption is recorded. Sufficient time must be allowed for attainment of adsorption. The effective volume occupied by the adsorbent must be assessed so that the remaining dead volume can be determined. Measurements of dead volume are performed at room temperature with a single pressure change measurement using N_2 as an inert gas. Dosing of N_2 is performed through a spare inlet port. Ideal gas behaviour was considered in all cases, as vapour pressure remained below 1 bar in all measurements.

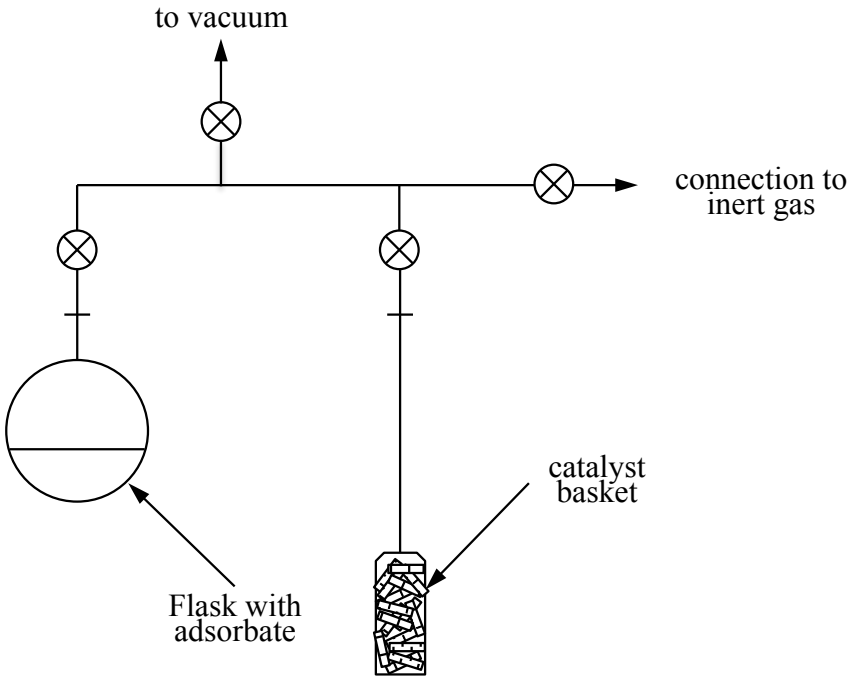

Figure 2.1. Schematic illustration of the experimental apparatus used during volumetric adsorption.

Figure 2.2 shows a typical example of an adsorption measurement performed in the apparatus described, in this case benzene over γ-Al_2O_3. As can be observed, measurements of dead volume are important to determine true adsorption phenomena. The accuracy of the adsorption isotherm is governed by the accuracy of the pressure measurement. Finally, determination of a full adsorption isotherm up to $P/P^{SAT} = 1$ is possible provided that condensation of the vapour does not take place on another part of the assembly, something problematic in the case of liquids with low vapour pressures.

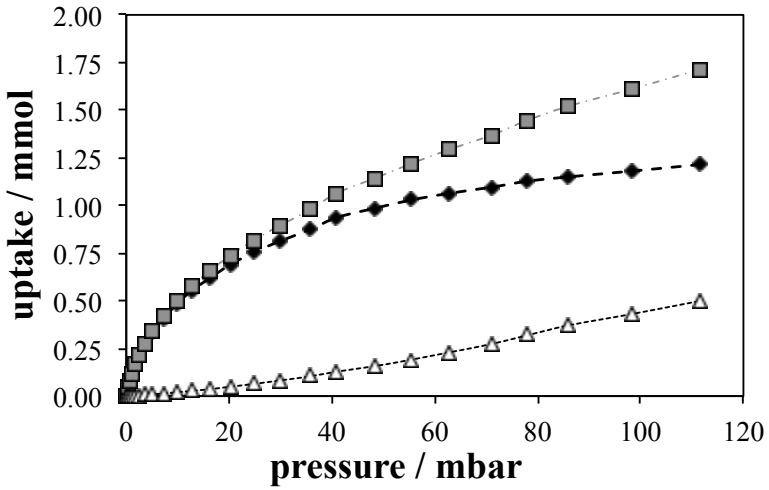

Figure 2.2. Adsorption of benzene on γ-Al_2O_3 at 348 K. Squares show the raw adsorption data, while diamonds show the corrected adsorption considering the dead volume. Triangles show the effect of the dead volume expressed as a mass uptake.

2.2.1.2 Temperature-programmed techniques

Temperature-programmed methods are a valuable source of information on the mechanistic features of catalysed reactions. Depending on the desorption gas used, temperature programmed desorption (TPD) with an inert gas, oxidation (TPO) with oxygen, or reduction (TPH), with hydrogen can be distinguished. Through characterising catalytic materials and correlating with reaction activity (Tittensor *et al.*, 1992), information of desorbed products and adsorption states of different molecules can be obtained (Cornish and Avery, 1990) Additionally, reaction mechanisms by comparing desorption energies from different metal surfaces can be determined (Peck *et al.*, 1998). The adsorption energy gives information on the strength of the adsorbate and substrate bond, allowing recognition of different adsorption conditions of the same molecule. The temperature at which species are desorbed from the surface of a heated solid reflects the strength of surface bond. The relative rate of desorption, defined as the change in adsorbate coverage per unit of time, is given by the Polanyi-Wigner equation (equation 1.3).

TPD records desorption peaks as a function of temperature, often measured using a quadrupole mass spectrometer. TPD-MS experiments are performed in a CATlab microreactor module (Hiden Analytical). Pre-adsorbed catalyst is placed in the microreactor, as seen in **Figure 2.3**, and desorbing species are detected with a QIC-20 quadrupolar mass spectrometer (QMS). A continuous flow of carrier gas is passed through the bed, such that desorbing species can be detected, also limiting re-adsorption. Then a probe dilutes the outlet gas flow before entering the mass spectrometer under vacuum ($P < 1\times10^{-6}$ mbar). An electron ionisation (EI) source generates positive ions of the species transported in the gas flow. The QMS separates the desired ions that reach the detector. Both the Faraday cup and the Secondary Electron Multiplier (SEM) detectors can be used to record the spectra of the desorbed species. However, most of the relevant species were detected with the SEM detector, due to its low detection limit. **Figure 2.4** shows a schematic with the working principle of the SEM detector. In an SEM, positive ions from the analyser are accelerated to a high velocity with a high potential of opposite charge, between 3 to 30 kV. The striking ion causes the emission of several particles, that then are converted to electrons at the first dynode and amplified by a cascade effect to provide the enhanced signal (Hoffmann and Stroobant, 2007).

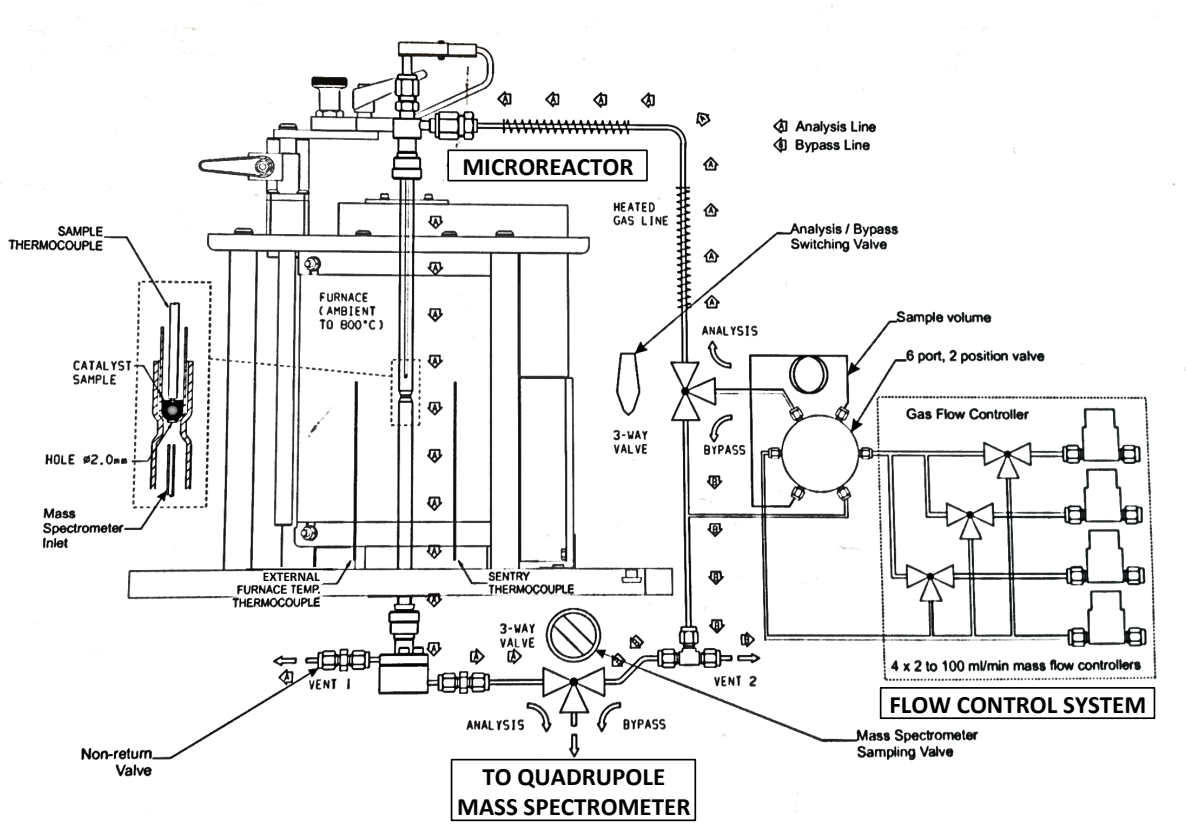

Figure 2.3. Schematic of a CATlab microreactor – QIC analyser. Adapted from Hiden Analytical (www.hidenanalytical.com)

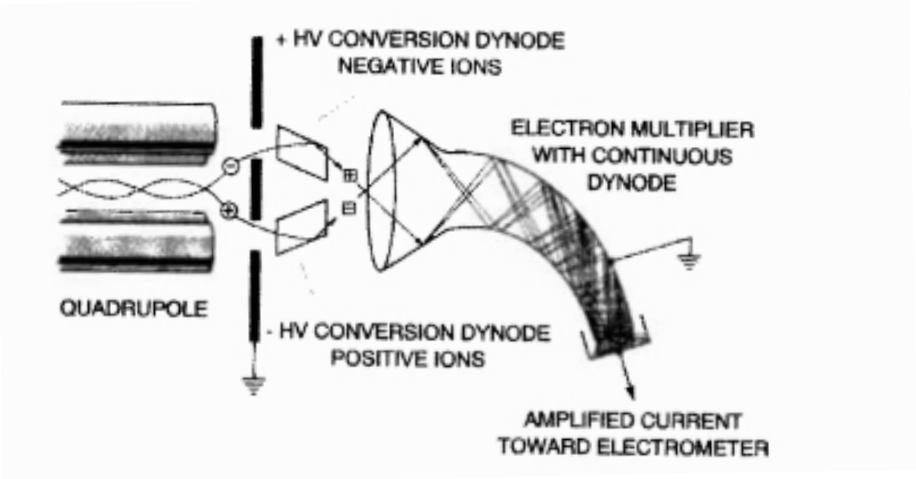

Figure 2.4. Schematic of a secondary electron multiplier (SEM) detector. From Hoffmann and Stroobant (2007).

Figure 2.5 shows the TPD of m/z = 42, corresponding to 1-pentene fragments, from pre-adsorbed 1-pentene on H-ZSM-5. Results are presented in terms of desorbing species (in arbitrary units of pressure) as a function of increasing temperature. Analysis of the energetics of desorption can be performed on these experiments. In this work, calculation of energy distribution curves followed a previously developed methodology (Barrie, 2008; Wilson,

1992). A quadratic programming algorithm was applied using *quadprog* in MATLAB. Both the GCV score function $V_L(\alpha)$ (Wilson, 1992), and the *L*-curve method (Barrie, 2008) were used to determine the correct smoothing parameter.

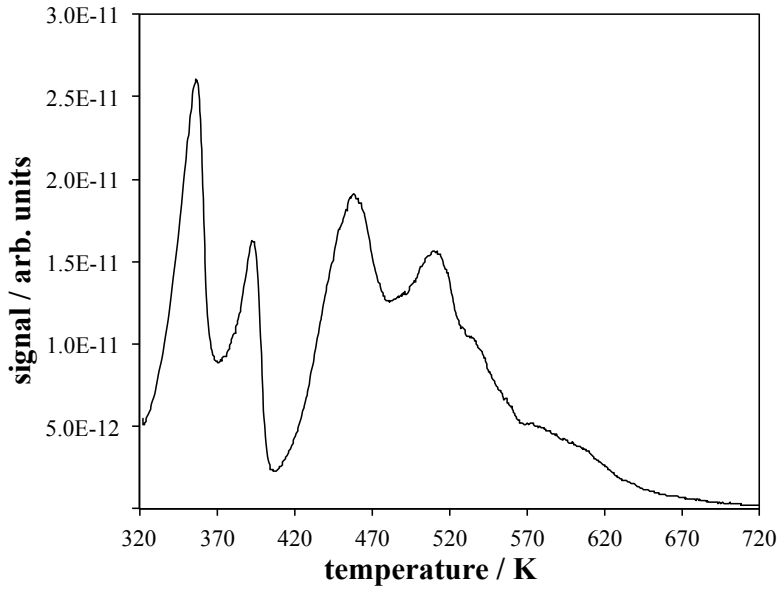

Figure 2.5. Typical example of a TPD experiment using the CATlab microreactor – QIC analyser. Desorption of 1-pentene from H-ZSM-5 followed with m/z = 42, measured in arbitrary units.

2.2.1.3 Infrared spectroscopy

Infrared (IR) spectroscopy is a widely used method for *in situ* characterisation of the surface chemistry of heterogeneous catalysts (Thomas and Thomas, 1997). The resulting observed frequencies provide information on the nature of the adsorption process (Hair, 1967), allowing direct monitoring of the interaction between adsorbed molecules and the catalysts (Riczkowsky, 2001). In turn, IR spectroscopy provides information on the location and orientation of the surface species. Studies have been widely done on adsorption of molecules where it has been possible to determine adsorbed species and their interaction on different surfaces using FTIR (Eischens and Pliskin, 1958). The working principles of IR spectroscopy are described is section 2.2.1.3.1, while a description of the experimental apparatus and methods is shown in section 2.2.1.3.2.

2.2.1.3.1 Principles of IR: Electromagnetic radiation and vibration modes

Infrared spectroscopy is a technique based on the vibrations of the atoms of a molecule. The infrared spectrum is obtained by absorption of a fraction of the infrared radiation passed through a sample. The energy at which any peak in an absorption spectrum appears corresponds to the frequency of a given molecular vibration. The position of an absorption

band in the spectrum is usually expressed in terms of the reciprocal of the wavelength, cm^{-1}. There exist selection rules for a molecule to be infrared-active. The dipole moment of a molecule must change during the normal vibration (Stuart, 2004). Moreover, functional groups present well-defined ranges of vibration frequencies, irrespective of the larger structure to which they belong. This phenomenon is known as the group frequency concept, making the infrared spectrum one of the simplest, most rapid and reliable means for assignment of species (Williams and Fleming, 2008).

The harmonic oscillator is used as a classic description of IR. A molecule can be looked upon as a system of masses joined by bonds with spring-like properties. The atoms in the molecules can move relative to one another, *i.e.*, bond lengths can vary or one atom can move out of its present plane. The stiffness of the bond is characterized by a proportionality constant termed the force constant, k. The equation relating the force constant, the reduced mass of the vibrating atoms, μ, and the frequency of absorption, v, is:

$$v = \frac{1}{2\pi}\sqrt{\frac{k}{\mu}} \tag{2.1}$$

$$\mu = \frac{m_1 m_2}{m_1 + m_2} \tag{2.2}$$

where m_i are the masses of the vibrating atoms. Thus, vibrational frequencies increase with increasing bond strength and with decreasing mass of the vibrating atoms (Niemantsverdriet, 2007). Additional non-fundamental adsorption bands may occur, such as the presence of overtones or harmonics – multiples of the fundamental absorption frequency – or combination bands – result of two fundamental bands absorbing simultaneously, returning a band at the sum of the frequency of each fundamental band.

Figure 2.6 shows the different modes of vibrations. Vibrations can involve either a change in bond length (stretching, v) or bond angle (bending, δ). In addition, some bonds stretch in-phase (symmetrical stretching) or out-of-phase (asymmetric stretching). The latter occurs, for example, if a molecule has different terminal atoms such as HCN, ClCN or ONCl (Stuart, 2004). In-plane (δ) and out-of-plane (γ) bending vibrations can also be distinguished. In-plane bending vibrations can be further divided into rock, twist and wag vibrations. In out-of-plane bending vibrations one atom, usually H, oscillates through a plane defined by at least three neighbouring atoms, usually more rigid parts in a complex molecule. The intensity

of these vibrations depends on multiple factors. Thus, the difference in electronegativity between carbon and oxygen results in a permanently polarized carbonyl group. Therefore, stretching this bond will increase the dipole moment and, hence, ν(C=O) is an intense absorption. The intense ν(C=O) vibration has allowed IR to be extensively applied to understand CO adsorption to metals (Thomas and Thomas, 1997).

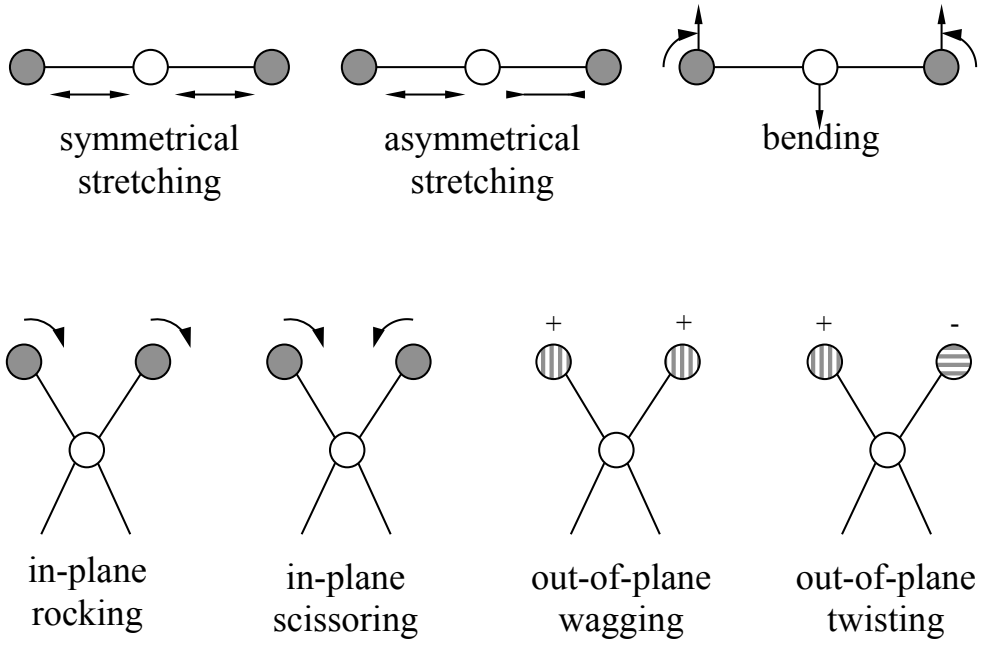

Figure 2.6. Schematic representation of the different vibrational modes within a molecule.

2.2.1.3.2 Instrumentation and experimental methods

The infrared spectral region covers the electromagnetic radiation range from 0.75 μm to 1 mm. This region is subdivided into the near infrared (12500 – 4000 cm^{-1}), mid or fundamental infrared (4000 – 400 cm^{-1}) and far infrared (400 – 10 cm^{-1}). In the mid infrared region molecular vibrations are detected, being the most interesting for adsorption in catalysis (Niemantsverdriet, 2007). Additionally, simpler instrumentation and a greater variety of infrared transparent materials are available in the mid infrared range.

Initially, dispersive instruments were used to obtain infrared spectra. However, Fourier-transform infrared spectrometers are now predominantly used in the mid infrared region, as they have improved the acquisition of infrared spectra dramatically. The spectrometer is based on the idea of the interference of radiation between two beams to yield

an interferogram. **Figure 2.7** shows a schematic of a typical modern spectrometer with a Michelson interferometer. The Michelson interferometer consists of two perpendicularly plane mirrors, one of which can travel in a direction perpendicular to the plane. A semi-reflecting film, the beamsplitter, bisects the planes of these two mirrors. Fifty percent of the beam reflected from the fixed mirror is transmitted through the beamsplitter while 50% is reflected back in the direction of the source. The moving mirror produces an optical path difference between the two arms of the interferometer. The resultant interference pattern, the interferogram, contains all of the spectral information of the radiation falling on the detector. The interferogram is converted back to the original frequency spectrum by the mathematical method of Fourier-transformation. Two detectors are commonly employed for the mid infrared region. The routine detector is a pyroelectric device incorporating deuterium tryglycine sulfate (DTGS) in a temperature-resistant alkali halide window. For more sensitive work, mercury cadmium telluride (MCT) can be used, but this has to be cooled to liquid nitrogen temperatures (Stuart, 2004). The experiments contained in this work have been performed in a Nicolet Avatar 380 (Thermo Scientific), equipped with a KBr-DTGS detector, and a Nicolet Nexus 670 (Thermo Scientific), equipped with an MCT-A detector.

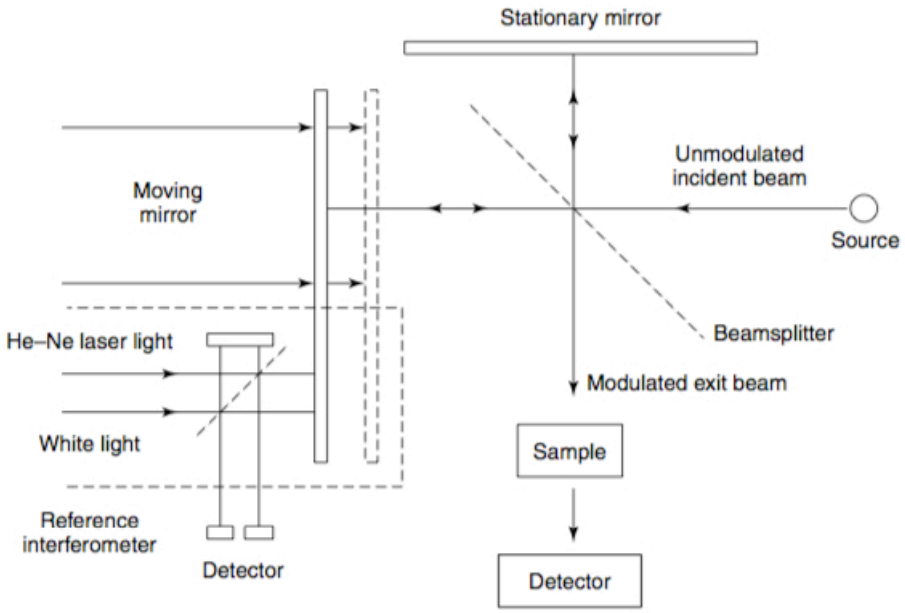

Figure 2.7. Schematic of a Fourier Transform Infrared Spectrometer (FTIR). The moving mirror alters the distribution of IR light that passes through the interferometer. From Stuart (2004).

Figure 2.8 shows the main infrared methods to study adsorbed species in catalysts. Transmission spectroscopy is the oldest and most straightforward infrared method. This technique is based upon the absorption of infrared radiation at specific wavelengths as it passes through a sample. It can be applied if the bulk of the catalyst absorbs weakly, typically in the case of oxide supported catalysts for wavenumbers > 1000 cm^{-1}. Quantitative analysis can be performed by appropriate calibration, as Beer's law applies. Applications for acidity studies with adsorption of pyridine on oxides (Parry, 1963) or zeolites (Benaliouche *et al.*, 2008; Kondo *et al.*, 2010), or adsorption of reactants and products on supported catalysts (Guil *et al.*, 2005; Natesakhawat *et al.*, 2013) have been reported. Reflectance techniques may be used for samples that are difficult to analyse by the conventional transmittance methods. Of the different reflectance methods, attenuated total reflection and diffuse reflectance will be described in more detail for its extended use in catalysis. Both are surface sensitive techniques, *i.e.*, they do not provide information on the bulk of the catalyst but solely on the surface, where adsorption interactions are taking place. Attenuated total reflectance (ATR) spectroscopy utilizes the phenomenon of total internal reflection. The beam penetrates a fraction of a wavelength beyond the reflecting surface. The resultant attenuated radiation gives rise to the absorption spectral characteristics of the sample. Diffuse reflectance infrared Fourier transform spectroscopy (DRIFTS) provides data on the absorption properties of a sample based on the penetration of an incident beam into one or more particles and its diffusion within the sample. Hence, sample preparation issues in transmission mode are avoided. Loose powders can be used in this technique and it is recommended for strongly scattering samples (Armaroli *et al.*, 2004). However, as the information is gathered on the diffusive component on the reflected IR beam, it is not possible to fully quantify the spectral information. Applications include the measurement of Lewis and Brønsted acid sites in a given material *via* adsorption of probe molecules (Eberly, 1968; Parry, 1963). Moreover, DRIFTS has been widely used in the detection of initial adsorbates and species formed during surface reactions (Jacobs *et al.*, 2003). **Figure 2.9** shows a typical example of an infrared spectrum of an adsorbed species on a catalyst. The adsorption of 1-pentene on H-ZSM-5 is manifested by the $\nu(CH_3)$ and $\nu(CH_2)$ bands at 2951 cm^{-1}, 2923 cm^{-1} and 2866 cm^{-1}, noting the presence of a hydrocarbon on the surface. Additionally, the $\nu(=CH_2)$ band at 3067 cm^{-1} and $\nu(C=C)$ band at 1634 cm^{-1}, were indicative of the presence of a double bond. Finally, bands at 1381 cm^{-1}, 1326 cm^{-1}, 1195 cm^{-1}, 554 cm^{-1} and 478 cm^{-1} are indicative of changes in the catalyst, as a result of the interaction with 1-pentene (Karge, 1998).

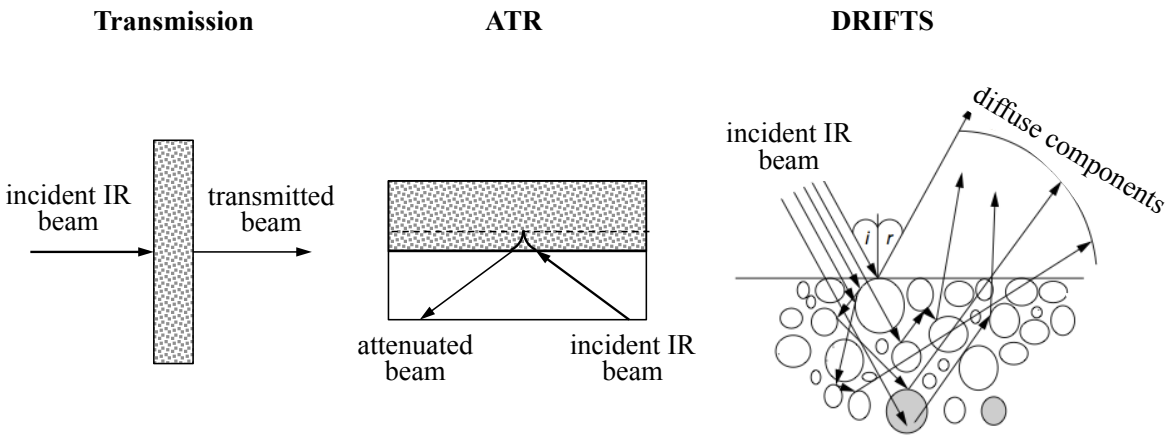

Figure 2.8. Different IR methods used to study adsorption in catalysts.

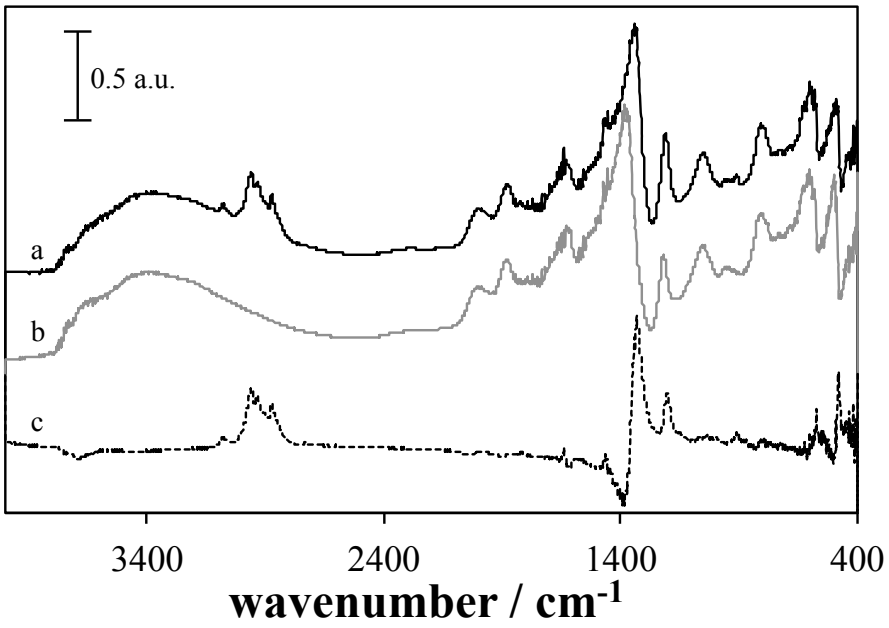

Figure 2.9. DRIFTS spectrum for the adsorption of 1-pentene on H-ZSM-5 using KBr as background. a) 1-pentene on H-ZSM-5, b) H-ZSM-5 before adsorption, c) subtracted spectrum. Typical example of a spectrum obtained with the FTIR spectrometer described.

2.2.1.4 Tapered Element Oscillating Microbalance (TEOM)

A tapered element oscillating microbalance (TEOM) is ideally suited to study small mass changes, of the order of micrograms, with temporal resolution of 0.1 s. Therefore, it is possible to characterise the kinetics of adsorption and desorption, as observed by a number of workers (Gong *et al.*, 2009; McGregor and Gladden, 2008). Adsorption, diffusion, reaction and deactivation in zeolites and similar catalysts have also been studied (Chen *et al.*, 1999; Lee *et al.*, 2004; McMillan *et al.*, 2013).

The TEOM records mass changes by monitoring the change in resonant frequency of a quartz element containing the sample packed within a small cylindrical container (Wang *et al.*, 1980). The TEOM pulse mass analyser principle of operation and governing equation is that of a cantilever beam mass-spring system. As compared to gravimetric microbalances, full contact between feed and sample is established, with similar conditions to a fixed-bed flow reactor (Ilyina *et al.*, 2013; Chen *et al.*, 2007; Zhu *et al.*, 1998). As the mass of the sample holder increases, *i.e.*, as molecules adsorb on to the catalyst, the frequency of the oscillation changes, according to the behaviour of a single harmonic oscillator. Thus, the frequency of the oscillations is converted to a mass change, Δm, through the relationship:

$$\Delta m = \Delta m_a + \Delta m_g = k_0 \left(\frac{1}{f_1^2} - \frac{1}{f_0^2} \right) \tag{2.3}$$

where f_i is the frequency of oscillation (f_0 for the initial conditions of the experiment and f_1 at the selected experimental conditions), Δm_a is the adsorbed mass, Δm_g is the change in the gas density (measured during a blank run) and k_0 is the experimentally determined spring constant. An increase in catalyst mass will be measured as a decrease in the oscillation frequency, f. The spring constant k_0 is unique for each different element and is a measure of the stiffness of the quartz element. A more detailed explanation on the TEOM mass measurement principles has been reported elsewhere (Chen *et al.*, 2007; Chen, 1998; Zhu *et al.*, 1998).

Figure 2.10 shows a diagram of the rig used during TEOM experiments. The TEOM (1500 Pulse Mass Analyser, Rupprecht & Patashnick) is connected to a gas chromatograph (GC) (6890 Hewlett Packard) for adsorbate quantification and TEOM effluent analysis. Three different lines are used: the purge gas, to maintain stability of the element, and avoid dead zones; pre-treatment gas, for catalyst reduction and inert gas flow; and carrier gas, for adsorption experiments. A pneumatic actuated valve (Valco Instruments), AV1, is installed to switch between the adsorbate and the inert gas flow. Flow rates in the lines are controlled *via* mass flow controllers (Tylan FC260 and Unit Instrument Systems Inc. UFC-1100N) and pressure is monitored using pressure transducers (Keller). A saturator is connected to the carrier gas line to vapourise the liquid adsorbate. Temperature within the saturator is controlled with a chiller (Julabo, M32-HC) to obtain the desired partial pressure of vapour. Lines are insulated after the saturator, and a series of heaters and thermocouples (Watlow) are installed to control the temperature of the gases. The automated valves within the GC, GCV1

and GCV2, select and inject the gas to be analysed into the column. Either the stream from AV1 or the outlet of the TEOM can be analysed. A steady pressure in the TEOM (PT4) has to be maintained during pulse experiments, as otherwise the data acquisition will not be reflecting real mass uptake (Lee *et al.*, 2004). In order to ensure pressure stability, manual needle valves NV1 and NV2 are adjusted. Process conditions and data storage are controlled using LabView 8.6 (National Instruments, Inc.). More information on the rig has been described in detail elsewhere (McGregor, 2006). **Figure 2.11** shows a typical example with the adsorption of 1-octene on γ-Al_2O_3. The fast adsorption-desorption dynamics, the equilibrium adsorption value, and the retained mass after desorption are noted.

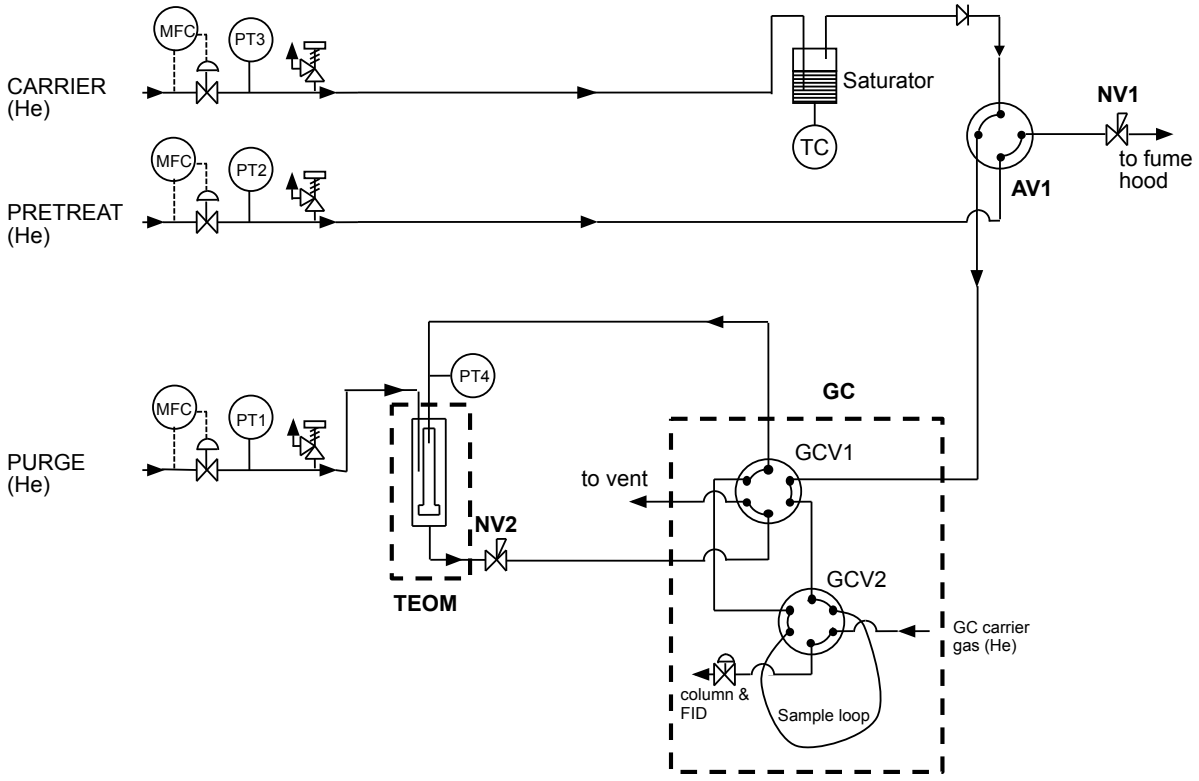

Figure 2.10. Schematic diagram of the Tapered Element Oscillating Microbalance (TEOM) setup.

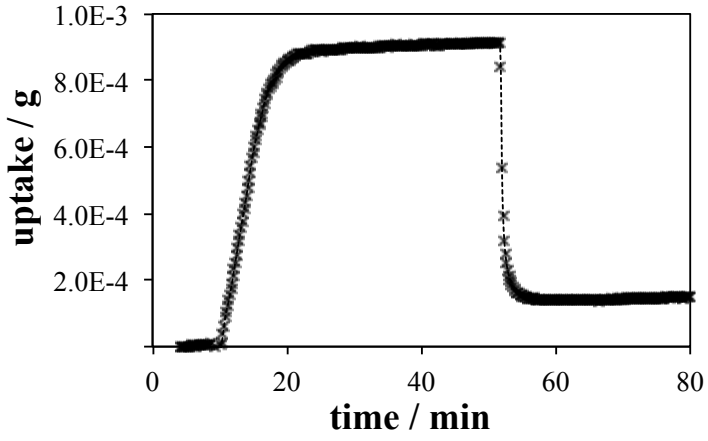

Figure 2.11. Mass uptake measured during pulse adsorption of 1-octene on γ-Al_2O_3 at 323 K by means of a TEOM. The pulse was started at min 10, after pre-treatment of the alumina at 373 K. The symbols indicate the experimental data points obtained every 10 s.

2.2.2 NMR-based techniques

NMR techniques offer the opportunity to study adsorption and surface reactivity without the need for high vacuum conditions and, therefore, can be used as an *in situ* technique. NMR has been applied in the study of adsorption of molecules on the surface of chemically active solids. Traditional ways of obtaining information with NMR involve the use of nuclei chemical shifts, δ, described in section 2.2.2.1.3, and spectral line widths (Rouabah *et al.*, 1991; Yuzawa *et al.*, 2011; Samantaray *et al.*, 2013). Yet poor resolution in solids is an important limitation. Solid-state NMR combined with magic angle spinning (MAS NMR) has allowed moderate resolution in solid samples. Thus, MAS NMR has been applied to the study of adsorbed molecules (Kiricsi *et al.*, 1994), or the investigation of catalyst structure, with the use of appropriate nuclei (De Canio *et al.*, 1993).

The importance of NMR relaxometry in this work as a novel tool to study adsorption in catalysts requires a more detailed background on its working principles. An introduction on the NMR theory is presented in section 2.2.2.1, while a more detailed description on the principles of NMR relaxometry are shown in section 2.2.2.2. The information provided in section 2.2.2.1 has been summarised from Keeler (2005), Hornak (2011) and Callaghan (1991).

2.2.2.1 Principles of NMR

2.2.2.1.1 Nuclear spin and the rotating frame

Nuclear magnetic resonance (NMR) is a direct consequence of the quantum mechanical property known as spin. Nuclei are characterised by a spin quantum number, I, which is either zero or an integral multiple of ½. Only the nuclei with $I \neq 0$ can exhibit a magnetic moment. Elemental isotopes such as ^{1}H, ^{13}C, ^{15}N, ^{19}F or ^{29}Si are NMR active. ^{12}C and ^{16}O possess a quantum number $I = 0$ and are inactive in NMR. The associated motion of the charged nucleus gives rise to a magnetic moment, $\boldsymbol{\mu}$. Although nuclear spin is a quantum phenomenon, a classical mechanical description can be used to explain the motion of an NMR-active nucleus. The motion is described by:

$$\frac{\mathrm{d}\mu}{\mathrm{d}t} = \gamma\mu \times B_0 \qquad (2.4)$$

where γ is the gyromagnetic ratio and is a property of the nucleus, and $\mathbf{B}_0$ is the external magnetic field. The motion traces a circular path around the external field. This movement is analogous to that of a gyroscope and is termed ‘precession’.

In an external magnetic field, nuclei of spin number I can adopt $2I+1$ different orientations, following the Zeeman interaction. Each orientation is specified by the quantum number m, which can take values of $-I, -I+1, \ldots, I$. Both ^{1}H and ^{13}C present ½ spin nuclei, such that they adopt two spin states with $m_I = -½, +½$. These states are referred to α-state (low energy) and β-state (high energy), being parallel and antiparallel to $\mathbf{B}_0$, respectively. At equilibrium, a greater proportion of nuclei will exist in the lower energy state, governed by the Boltzmann distribution:

$$\frac{N_\alpha}{N_\beta} = \exp\left(\Delta E \big/ k_B T\right). \qquad (2.5)$$

The excess of nuclear spins in the α state can be visualised as a number of magnetic moments distributed randomly around the precessional cone, as shown in **Figure 2.12**. Such a distribution gives rise to a net magnetisation parallel to the external magnetic field, aligned to the z-axis in the figure. No net magnetisation results in the transverse or xy plane. Hence, the individual nuclear magnetic moments can be treated as a single bulk magnetisation vector,

$\mathbf{M}_0$, aligned in the *z*-axis. The energy of interaction between the nuclear moment and the magnetic field is described by equation 2.6:

$$E = -\gamma\hbar m_I B_0 \qquad (2.6)$$

where $\hbar = h/2\pi$, with h being Plank´s constant. NMR selection rule only allows transitions with $\Delta m_I = 1$. Hence the energy change of the transition is:

$$\Delta E = -\gamma\hbar B_0 . \qquad (2.7)$$

Following Plank's law, the frequency of the nucleus precessional motion is governed by

$$\nu = \frac{-\gamma B_0}{2\pi} \quad , \quad \omega_0 = -\gamma B_0 \qquad (2.8)$$

where ν is referred to as the Larmor frequency of precession, characteristic of a nucleus in a given external field, $\mathbf{B}_0$. ω_0 corresponds to the respective angular frequency.

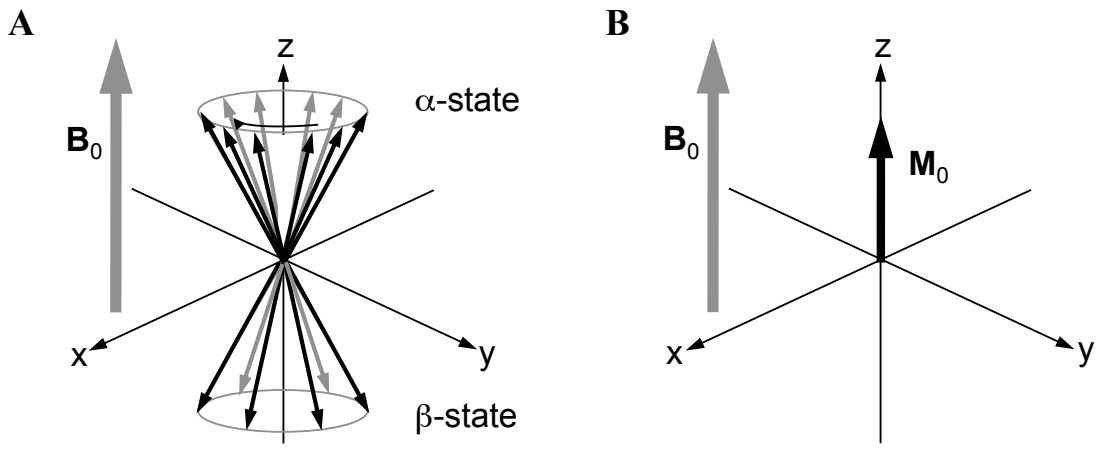

Figure 2.12. Distribution of spin populations in the α- and β-state for a spin ½ nucleus (A), and the Bloch vector model associated (B).

Nuclear magnetic resonance (NMR) arises when a nuclear spin changes spin state to a higher energy level due to adsorption of the requisite quantum of energy. In order to understand the pulse sequences applied for the determination of relaxation times, it is important to note the behaviour of nuclear spins under radiofrequency (r.f.) pulses. The quantum of energy needed for a change in spin state is provided by a time-dependent magnetic field, $\mathbf{B}_1$, oscillating at the Larmor frequency and applied perpendicular to the external field $\mathbf{B}_0$. The nuclei are

spinning about their own magnetic moments and precessing about the static field, $\mathbf{B}_0$, under equilibrium. The interaction between this dynamic system with $\mathbf{B}_1$ is more clearly explained considering a rotating frame of reference. The adoption of a rotating frame simplifies the observation of spin dynamics after excitation, if an appropriate rotation frequency is chosen. In the rotating frame, application of $\mathbf{B}_1$ causes the magnetic moment to precess around an effective magnetic field. Using equation 2.4 with the bulk magnetisation vector, $\mathbf{M}_0$, the following is obtained in the stationary frame:

$$\frac{\mathrm{d}M_0}{\mathrm{d}t} = \gamma M_0 \times B_0 \,. \tag{2.9}$$

The following expression is obtained when related to the rotating frame:

$$\frac{\delta M_0}{\delta t} = \frac{\mathrm{d}M_0}{\mathrm{d}t} - \left(\Omega \times M_0\right) = M_0 \times \gamma\left(B_0 - \frac{\Omega}{\gamma}\right) = M_0 \times \gamma B_{eff} \tag{2.10}$$

where $\mathbf{\Omega}$ is the angular velocity of the rotating frame and $\mathbf{B}_{\mathrm{eff}}$ is the effective field experienced by nuclear spins as observed in the rotating frame. Therefore, if Ω equals the Larmor frequency, then $\Omega/\gamma = B_0$, and the effective applied field is zero; $\delta M/\delta t = 0$, and the magnetisation vector appears stationary in the rotating frame.

The oscillating irradiation field $\mathbf{B}_1$ contributes a transverse component to the effective applied magnetic field. $\mathbf{B}_{\mathrm{eff}}$ becomes, in vector notation:

$$B_{eff} = \left(B_0 - \frac{\Omega}{\gamma}\right)\mathrm{k} + B_1\mathrm{i} \tag{2.11}$$

as observed in **Figure 2.13**. Consequently, for $\Omega = \omega_0$, $\mathbf{M}_0$ will precess around $\mathbf{B}_1$. By applying the rotating frame at the Larmor (resonant) frequency as reference system, only motion derived from the r.f. pulse needs to be considered.

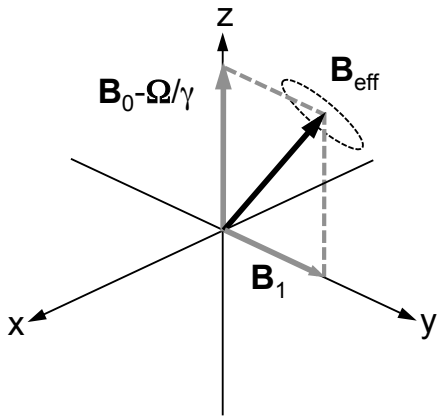

Figure 2.13. Effective field resulting from the application of a r.f. pulse $\mathbf{B}_1$, as seen in the static frame of reference.

2.2.2.1.2 Spin excitation and signal detection

NMR signal is detected by a coil placed around the sample with its axis of symmetry transverse to $\mathbf{B}_0$. The $\mathbf{B}_1$ field applies a torque on nuclear magnetic moments such that $\mathbf{M}_0$ is moved away from the *z*-axis towards the *xy* plane, as shown in **Figure 2.13**. $\mathbf{B}_1$ is applied in pulses, *i.e.*, switched on only for a given period, t_p. The rate of motion and consequently the angle of rotation, in radians, of $\mathbf{M}_0$ are dependent on the strength of $\mathbf{B}_1$, according to:

$$\omega_1 = \gamma B_1 \tag{2.12}$$

$$\theta = \gamma B_1 t_p . \tag{2.13}$$

Most NMR sequences apply 90º and 180º pulses. A 90º pulse rotates the magnetisation vector into the *xy* plane, whereas a 180º pulse inverts the magnetisation towards the negative *z*-axis. In terms of nuclear spin populations, and again considering a spin ½ nucleus, the populations of the α- and β-state are equalised with a 90º pulse, while a surplus of spins in the β-state is generated with an 180º pulse. The pulses and the change in magnetisation vector with respect to the rotation frame are shown in **Figure 2.14**.

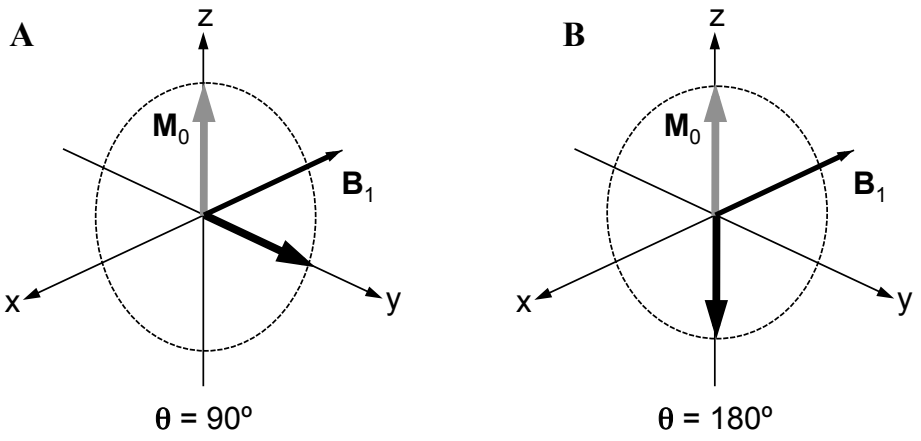

Figure 2.14. Resonant r.f. pulses. Magnetisation precesses around $\mathbf{B}_1$ and moves away from equilibrium along the +*z* axis towards the *xy* plane. In the figure, a 90º pulse (A) and a 180º pulse (B).

The 90º pulse constitutes the basis of signal acquisition, with the simplest "pulse-acquire" sequence. A net polarisation arises in the transverse plane (if $\mathbf{B}_1$ is oriented in the *y* direction, the magnetic moment will be directed towards the *x*-axis and *vice versa*) and precession of transverse magnetisation induces an oscillatory electromagnetic field in the detection coil. This induced field has a frequency equal to the Larmor frequency of precession of the nuclei studied. The signal measured in the time domain is an oscillating and decaying electromagnetic field referred to as a free induction decay (FID). This corresponds to the evolution of the transverse component of the precession of $\mathbf{M}_0$ back to equilibrium aligned with the *z*-axis. **Figure 2.15** shows a typical FID. Fourier transformation of such a time domain signal yields a Lorentzian absorption and a dispersion line-shape in the real and imaginary parts of the frequency domain, respectively.

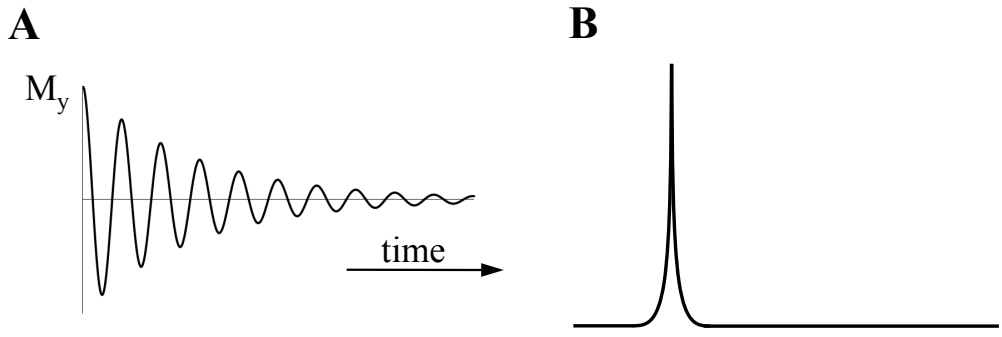

Figure 2.15. Free induction decay (FID) acquired in the time domain (A), and Fourier Transform of the FID, yielding a Lorentzian line shape (B).

The frequencies with which NMR peaks appear in the spectrum are proportional to the strength of B_0. As such, results are reported in terms of a reference frequency – tetramethylsilane (TMS) in the case of ^1H and ^{13}C – following

$$\delta = \frac{\nu - \nu_{ref}}{\nu_{ref}} \times 10^6 . \qquad (2.14)$$

Peak positions are thus identified by a chemical shift value, irrespective of the magnitude of B_0, in parts per million (ppm).

2.2.2.1.3 Chemical shifts and nuclear interactions

Nuclei are surrounded by atomic or molecular electron clouds, which interact with the spin angular momentum. These clouds produce a magnetic shielding effect when an external magnetic field is applied. Such an interaction is characteristic of the local bonding arrangements and provides a chemical fingerprint for a particular chemical species or functional group. It is a useful characterisation technique for molecular structure determination (Williams and Fleming, 2008). This phenomenon causes the Larmor frequency to be slightly and uniquely shifted depending on the chemical environment of the nucleus.

Individual nuclear spins also create a slight polarization of surrounding electrons. A delocalisation of electrons in shared orbitals occurs, which is then transmitted to neighbouring nuclei. This interaction is referred to as *J* or scalar coupling, appearing as binomial multiplets of a given resonance in the NMR spectrum. The signal is thus split between into multiple peaks, characteristic of the chemical bonds of that nucleus. Decoupling methods, such as broadband decoupling, are used to remove the split of a resonance band, thereby increasing the signal in the spectrum. Decoupling is particularly useful in ^{13}C observation, due to the low abundance of that spin. In that case, the entire ^1H resonance region is irradiated with a different field. The rate of transitions between the low- and high-energy spin states is increased, such that only one average magnetic field is experienced by any individual carbon nucleus.

2.2.2.1.4 NMR spectrometer

The experiments conducted in this thesis were performed in a wide bore DMX spectrometer (Bruker) with a vertical bore 7.0 T superconducting magnet, operating at ^{1}H and ^{13}C frequencies of 300 MHz and 75.5 MHz, respectively. A schematic diagram of an NMR spectrometer is shown in **Figure 2.16**. The magnet itself can be distinguished, along with the probe with coils, r.f. transmitter and receiver, digitizer, and computer for control and data processing. Additionally, a magnetic field gradient system is present in spectrometers for spatial resolution and NMR imaging; however this part is not described as relaxometry experiments – with the exception of the saturation-recovery pulses sequence – do not require the use of gradients.

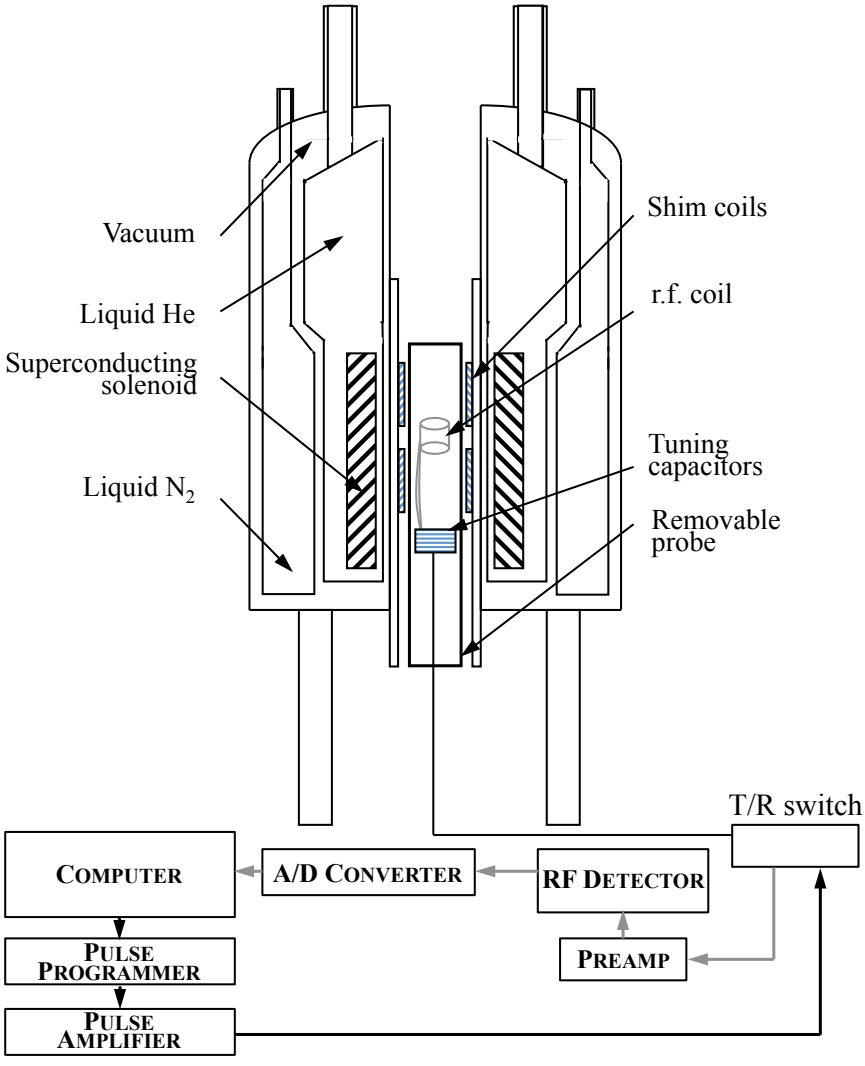

Figure 2.16. Schematic diagram of the NMR spectrometer used.

Magnet

An NMR spectrometer uses superconducting magnets to generate a homogeneous $\mathbf{B}_0$. Copper alloys with niobium or tin are typically used as superconducting materials. Low temperatures of < 6 K are required for null resistance of the alloy. These are maintained with the use of liquid He, a heat shied of liquid N_2 and vacuum. An accessible inner room temperature bore tube is engineered for sample measurements. Inhomogeneities present in the superconducting magnetic field are corrected with the use of a set of shim coils that create local magnetic fields from tunable currents to compensate for such defects.

Probe

A probe is a cylindrical tube inserted into the bore of the magnet. It holds on its top the coil that excites the sample and detects the NMR signal. It needs to be tuned correctly, until it is resonant with the Larmor frequency, in order to optimise sensitivity and power. The tuning of the probe is sensitive to different samples, and the procedure needs to be repeated when a new sample is studied.

Transmitter

The transmitter is the part of the spectrometer that generates the pulse. The pulse is a low level gated signal that needs to be applied for a short time. Therefore an amplifier is used to increase the signal to a high power (in the order of 100 W). An attenuator is included to reduce the power output and protect the coil. The power attenuation is related to the current by the following relationship:

$$\text{power attenuation in dB} = 10\log_{10}\left(\frac{P^{out}}{P^{in}}\right) = 10\log_{10}\left(\frac{i^{out}}{i^{in}}\right)^2 . \qquad (2.15)$$

In order to double $\mathbf{B}_1$ it is necessary to double the current, which requires the power to be multiplied by four: this corresponds to a power ratio of 6 dB.

Receiver

The NMR signal emanating from the probe is low voltage, in the order of μV. The receiver amplifies the signal in a low-noise pre-amplifier. It also mixes the r.f. signal with a reference frequency in a process known as 'heterodyning'. This mixing process gives an output oscillating signal with frequency ~1-10 kHz. Compared to Larmor frequencies of ^{1}H and ^{13}C

of ~300 MHz and ~76 MHz, respectively, a substantial reduction of the frequency range to be digitised is achieved.

ADC

The analogue to digital converter (ADC), transforms the mixed NMR signal voltage from the receiver to a binary number. The accuracy of signal representation can be improved by increasing the number of bits. Additionally, the sampling rate is an important factor. According to the Nyquist theorem, at least two points per wavelength are required to characterise a regularly oscillating signal. The highest frequency that must be sampled will provide a constraint on the minimum sampling rate. This frequency is known as the 'sweep width' (SW), and sampling at twice the sweep width provides the 'dwell time' (DW) between spectrum points:

$$\mathrm{DW} = \frac{1}{2\,\mathrm{SW}}. \qquad (2.16)$$

Any signal with frequency greater than the sweep width will be sampled incorrectly and appear in the spectrum at a lower frequency than its true value.

2.2.2.2 NMR relaxometry

NMR relaxation describes the processes by which the nuclear spin system returns to its equilibrium distribution following excitation by the r.f. pulse. The rates at which this occurs are described by two parameters: T_1 or spin-lattice relaxation time, described in section 2.2.2.2.1, and T_2 or spin-spin relaxation time, explicated in section 2.2.2.2.2. Section 2.2.2.2.3 reports applications of NMR relaxometry in catalytic systems.

2.2.2.2.1 T_1 or longitudinal relaxation

As previously observed, an excitation pulse acts to disturb a spin system from its thermal equilibrium. After a given time, equilibrium is restored *via* spin-lattice or longitudinal relaxation with an exchange of energy with the 'lattice'. Bloch theory (Bloch, 1950) assumes that thermal equilibrium is restored following an exponential behavior. Equation 2.17 describes the return of the longitudinal magnetisation, M_z, with T_1 as the first-order time constant, along the static field, $\mathbf{B}_0$, after a perturbation:

$$\frac{dM_z}{dt} = -\frac{M_z - M_0}{T_1} \tag{2.17}$$

where M_0 is the equilibrium magnetisation. As a general result, and with $M_z(0)$ as the longitudinal magnetization at $t = 0$:

$$M_z = M_z(0)\exp(-t/T_1) + M_0\left(1 - \exp(-t/T_1)\right). \tag{2.18}$$

Immediately after a 90º pulse, there is no longitudinal magnetisation, *i.e.*, $M_z(0) = 0$, and thermal equilibrium is fully re-established at time $t = 5\times T_1$. Hence, NMR experiments require a delay between 4-5$\times T_1$ between scans, *vide supra*.

Different pulse sequences are applied in order to obtain the value of T_1. As NMR signal is detected only in the transverse plane, a 90º pulse needs to be applied to determine the recovery of M_0 along the *z*-axis. Both inversion-recovery and saturation-recovery are shown. The inversion-recovery pulse sequence (**Figure 2.17A**) (Vold *et al.*, 1968) consists on an initial 180º pulse, to invert the equilibrium magnetization and align it along –*z*. The magnetisation recovers towards thermal equilibrium during a time τ_R following an exponential function of the type shown in equation 2.18. A 90º pulse is applied to determine the value of the magnetisation vector. The use of variable recovery times, τ_R, would yield different M_z values to be fitted into the equation to obtain T_1:

$$M_z = M_0\left(1 - 2\exp(-\tau_R/T_1)\right). \tag{2.19}$$

In contrast, saturation-recovery (McDonald and Leigh, 1973) disturbs M_0 thermal equilibrium by applying complete saturation, *i.e.*, the generation of a transverse magnetisation with no coherence. This is achieved by a series of 90º pulses and magnetic field gradients, as shown in **Figure 2.17B**. Thus, $M_z(0) = 0$, and the system is allowed to recover during τ_R. Again, a 90º pulse is applied to transfer the net magnetisation evolved into the transverse plane to be read. A series of different τ_R are used to determine T_1, following the expression:

$$M_z = M_0\left(1 - \exp(-\tau_R/T_1)\right). \tag{2.20}$$

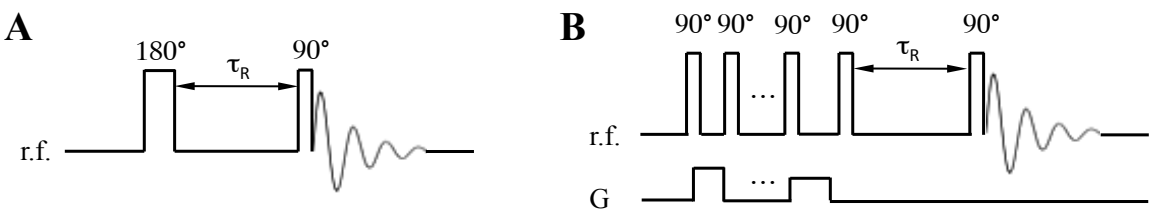

Figure 2.17. T_1 NMR relaxometry pulse sequences: inversion-recovery (A) and saturation-recovery (B) were used to obtain T_1.

2.2.2.2.2 T_2 or transverse relaxation

Following the r.f. excitation, the net magnetisation also loses coherence in the transverse plane. Each spin packet experiences a slightly different local magnetic field, due to inter and intramolecular interactions, and rotates at a slight different Larmor frequency. The time constant describing the dephasing of spins is called the transverse relaxation time, T_2. Retuning to the magnetisation vector description of spins, it is clear the effect in transverse magnetisation with an excitation pulse, as seen in **Figure 2.18**. Also note that it is possible to induce transverse magnetisation with no phase coherence (spins are saturated), as observed for the T_1 saturation-recovery sequence.

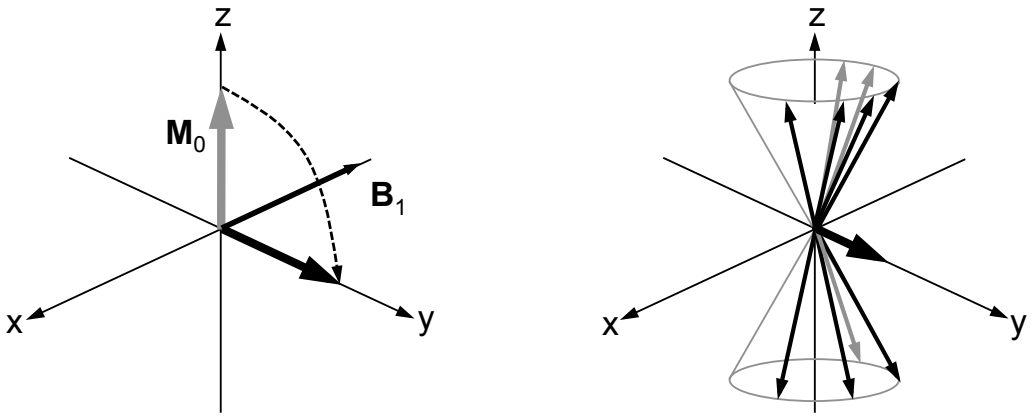

Figure 2.18. Following a decay of the net magnetisation with time. As magnetisation evolves in the transverse plane, slight differences in the individual precession frequencies cause a loss of coherence.

Equation 2.21 describes the decay of the transverse component of the magnetization, M_{xy}, with T_2 as the rate constant:

$$\frac{dM_{xy}}{dt} = -\frac{M_{xy}}{T_2} \tag{2.21}$$

where T_2 is the first order rate constant for the loss of phase coherence. As a general result:

$$M_{xy}(t) = M_{xy}(0)\exp(-t/T_2). \quad (2.22)$$

As noted, when restoring thermal equilibrium, spin-lattice relaxation destroys transverse magnetisation. Therefore, T_2 will always be less than or equal T_1. In addition to the presence of a series of interactions, inhomogeneities in the static field $\mathbf{B}_0$ cause a dephasing in transverse magnetization. However, the dephasing due to inhomogeneities is reversible. Equation 2.23 can be rewritten to account for both phenomena, with the use of T_2^*:

$$\frac{1}{T_2^*} = \frac{1}{T_2} + \frac{1}{T_{2,\Delta B_0}}. \quad (2.23)$$

In the equation $T_{2,\Delta B_0}$ is the relaxation time due to inhomogeneities. T_2^* determines the maximum acquisition time period, as the dephasing process causes a reduction in the NMR signal detected. Further, T_2^* appears in the width of the NMR resonance. The full width at half maximum (FWHM) of the Lorentzian line shape is given by:

$$\Delta\nu_{1/2} = \frac{1}{\pi T_2^*}. \quad (2.24)$$

Hahn (1950) discovered how to recover the dephasing due to magnetic field homogeneities, $T_{2,\Delta B_0}$. After the initial 90º excitation pulse, the FID decay is observed and dephasing occurs. The application of a second pulse after an evolution period τ results in the recovery of the transverse magnetisation after an additional τ delay, forming a spin echo. As dephasing occurs only in the transverse plane, only the transverse components remaining after the second pulse will converge at their precessional rates. Hahn referred to this refocusing pattern as the eight-ball echo. The Carr-Purcell (Carr and Purcell, 1954) spin echo employs an 180º pulse as the second pulse, maintaining all magnetisation in the transverse plane. All the available magnetisation is then refocused. After a period τ_d, the dephasing nuclear spins are rotated into a mirror image with respect to the *xz* plane. The spins continue to precess at the same rate, causing a refocusing of all vectors at time $2\tau_d$, the echo time, τ_E. The pulse sequence is shown in **Figure 2.19A**. T_2 can thus be obtained by fitting the signal intensity in equation 2.22 against different τ_E. In general, if the first pulse has a flip angle α_1 and the second pulse α_2, then the maximum signal intensity of the echo will be smaller than the

Carr-Purcell spin echo by a factor of $\left(\sin\alpha_1\right)\cdot\left(\sin^2\alpha_2/2\right)$. Irreversible dephasing due to spin-spin interactions or the presence of internal gradients cannot be corrected with this sequence.

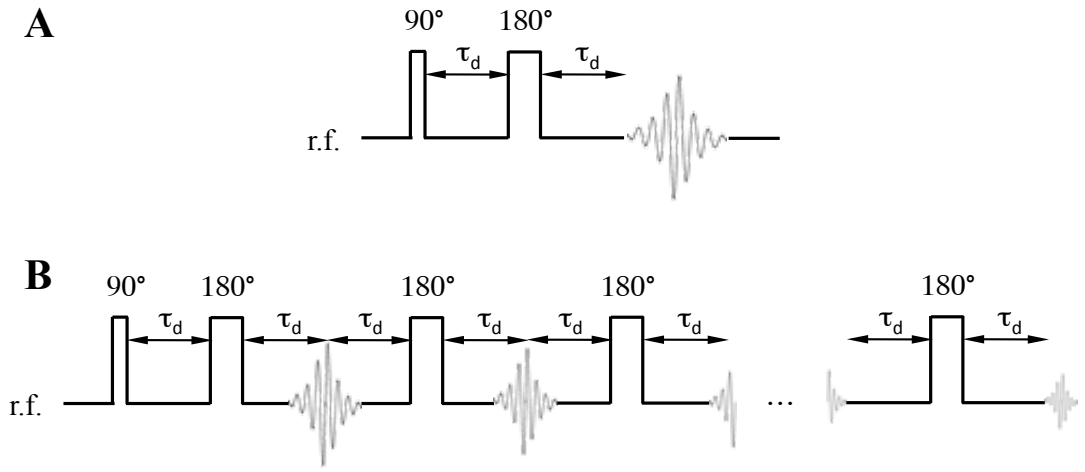

Figure 2.19. Spin echo (top) and CPMG (bottom) pulse sequences to capture T_2.

The spin-echo sequence relies on nuclear spins precessing at the exact rate before and after the refocusing pulse. If significant molecular diffusion occurs during the $2\tau_d$ delay – as is the case for many samples – the refocusing of spins will be incomplete due to nuclei experiencing different local magnetic fields. The effects of diffusion can be minimised by rapidly repeated refocusing using a series of 180º pulses and short τ_d, as shown in **Figure 2.19B**. The resulting sequence, known as the Carr-Purcell-Meiboom-Gill or CPMG (Meiboom and Gill, 1958), is used conventionally to measure T_2, and has been used throughout in this thesis. By varying the number of refocusing pulses n, T_2 can be measured considering $2n\tau_d$ as the echo time.

2.2.2.2.3 Applications in adsorption and catalysis

As previously mentioned, NMR techniques offer the potential for probing adsorbate-adsorbent interactions, *e.g.*, by measuring changes in the chemical shift δ of the NMR spectral line associated with an atom that occur on adsorption. The use of NMR relaxometry represents an alternative tool. NMR relaxation times of liquid molecules on a pore surface can be reduced relative to the bulk liquid relaxation time. The nuclear spin relaxation behaviour of a chemical species adsorbed onto a surface is modified by the strength of that interaction (Kimmich, 1997; Liu *et al.*, 1991; Monduzzi *et al.*, 1987).

Therefore, surface relaxation is a powerful tool in the study of pore surface properties (Mitchell *et al.*, 2005). Two methods are presented below, T_1/T_2 and $T_{1,ads}/T_{1,bulk}$.

^{1}H T_1/T_2 and 2D relaxometry correlations

Reduced T_1 and T_2 relaxation times are observed when liquid molecules adsorb on a solid surface due to a change in the molecular mobility (Liu *et al.*, 1991). In bulk liquids, $T_1 = T_2$, due to free molecular motion. Upon adsorption, enhanced surface interactions will occur for both T_1 and T_2 due to a change in the molecular mobility of the molecules on the surface (Godefroy *et al.*, 2001), as observed in **Figure 2.20**. Molecules adsorbed onto a surface undergo two-dimensional (2D) translational motion governed by the activation energy E_m. The diffusion coefficient associated with this surface motion is:

$$D_m(T) = D_{m0} \exp\left[-\frac{E_m}{RT}\right] \tag{2.25}$$

where D_{m0} is a temperature independent contribution to diffusion, R is the ideal gas constant, and T is the temperature. In liquid-saturated porous materials, the potential binding energy of adsorbed molecules governing the desorption rate is E_s. Therefore, the effective diffusion coefficient D_{eff} (observed) is:

$$D_{eff}(T) = D_{eff0} \exp\left[-\frac{\Delta E}{RT}\right] \tag{2.26}$$

where $\Delta E = E_m - E_s$ is an activation energy for surface diffusion in restricted porous materials. The diffusion coefficient has an associated correlation time τ_m that describes the time for diffusion between surface adsorption sites, such that $D_{eff}(T) \sim \varepsilon^2/(4\tau_m)$, where ε is the thickness of the adsorbed surface layer. Thus, the surface correlation time for surface diffusion is obtained:

$$\tau_m(T) \propto \exp\left[\frac{\Delta E}{RT}\right]. \tag{2.27}$$

There will also be a surface residence time for adsorbed molecules which is similarly defined as:

$$\tau_s(T) \propto \exp\left[\frac{E_s}{RT}\right]. \tag{2.28}$$

However, T_2 is further influenced by translational correlation time associated with surface diffusion. (Mitchell *et al.*, 2013a; Weber *et al.*, 2010). Consequently, when molecules adsorb on surfaces, changes in their translational and rotational dynamics influence T_2 more than T_1, resulting in $T_1 > T_2$ (McDonald *et al.*, 2005). In porous materials with a high surface-to-volume ratio, S/V, the observed relaxation rates are proportional to S/V (Davies and Packer, 1990):

$$\frac{1}{T_{1,2}} = \frac{1}{T_{1,2,\text{bulk}}} + \rho_{1,2}\frac{S}{V} \tag{2.29}$$

where $\rho_{1,2}$ are the surface relaxivity values governing longitudinal and transverse relaxation processes, respectively. Assuming the bulk liquid relaxation times $T_{1,2,\text{bulk}}$ are large compared to the surface relaxation term, the bulk relaxation can be ignored, such that.

$$\frac{1}{T_{1,2}} \approx \rho_{1,2}\frac{S}{V}. \tag{2.30}$$

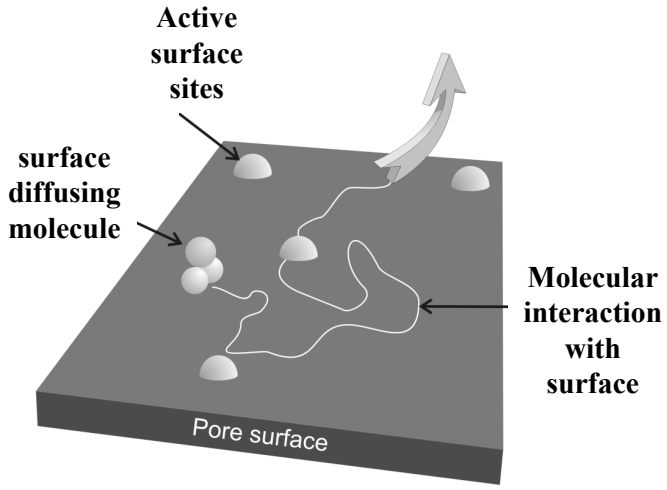

Figure 2.20. Relaxation mechanisms experienced by an adsorbed molecule in a porous material. Extracted from McDonald *et al.* (2005).

Hence, absolute T_1 and T_2 measurements cannot be readily used to compare interactions between materials with differing pore geometries. However, the ratio of relaxation times T_1/T_2 is independent of both pore geometry and the density of surface adsorption sites (D'Agostino *et al.*, 2014). Defining the surface relaxation times in terms of the surface diffusion correlation and residence times (Godefroy *et al.*, 2002), substituting the spectral

density function, and simplifying the resulting expression by assumptions based on expected values of ω_0, τ_m and τ_s (Mitchell *et al.*, 2013a), the following expression for T_1/T_2 is obtained (D'Agostino *et al.*, 2014):

$$\frac{T_1}{T_2} \propto -\frac{1}{\ln(\tau_m)} \propto -\frac{1}{\Delta E} \tag{2.31}$$

Hence, the relaxation time ratio is a qualitative indicator of surface interaction strength: an increase in the activation energy for surface diffusion (i.e., stronger surface adsorption) will result in an increase in the observed T_1/T_2 ratio.

T_2 measurements are known to be influenced by molecular diffusion in magnetic field gradients (Carr and Purcell, 1954). This influence is of particular significance in studies of porous materials because any contrast in magnetic susceptibility between the adsorbent and the adsorbate will induce a perturbation in the uniform field. Such perturbation would result in a distribution of effective internal magnetic field gradients within the pores. The perturbation is more pronounced at high magnetic field strengths, such as the ones used in this work. In the presence of strong internal gradients, an effective transverse relaxation time $T_{2,\text{eff}}$ is observed, governed predominantly by diffusion of the free liquid inside the pores (Mitchell *et al.*, 2010a, 2010b). Fortunately, a method can be used to separate the influence of diffusion and obtain the true T_2 relaxation time, governed by spin interactions of species adsorbed on the pore surface (Mitchell *et al.*, 2013b).

Although previous pulse sequences have shown how to obtain T_1 and T_2 relaxation times, it is possible to record such values in a single experiment with a two-dimensional pulse sequence. The two-dimensional T_1-T_2 pulse sequence comprised a T_1 experiment with a variable recovery delay τ_R, and then a CPMG echo train to encode T_2 (Song *et al.*, 2002). This results in a Fredholm integral of the first kind, as shown in equation 2.32:

$$M(\tau_R,\tau_E) = \iint \left(1-2e^{-\tau_R/T_1}\right) e^{-\tau_E/T_2} \Im(T_1,T_2)\, dT_1\, dT_2 + \varepsilon(\tau_R,\tau_E). \tag{2.32}$$

A fast algorithm for compressing and inverting this type of 2D data sets has been implemented previously (Venkataramanan *et al.*, 2002), allowing T_1/T_2 to be extracted. Previous studies have applied ^{1}H 2D T_1-T_2 NMR relaxation correlation measurements to study liquid adsorption phenomena in porous rocks (Song *et al*., 2002), cements (McDonald et al., 2005), or catalysts to estimate relative strengths of surface interactions (Weber *et al.*,

2009; D'Agostino *et al.*, 2012). **Figure 2.21** shows a typical 2D experiment, for the case of the adsorption of acetonitrile on SiO_2.

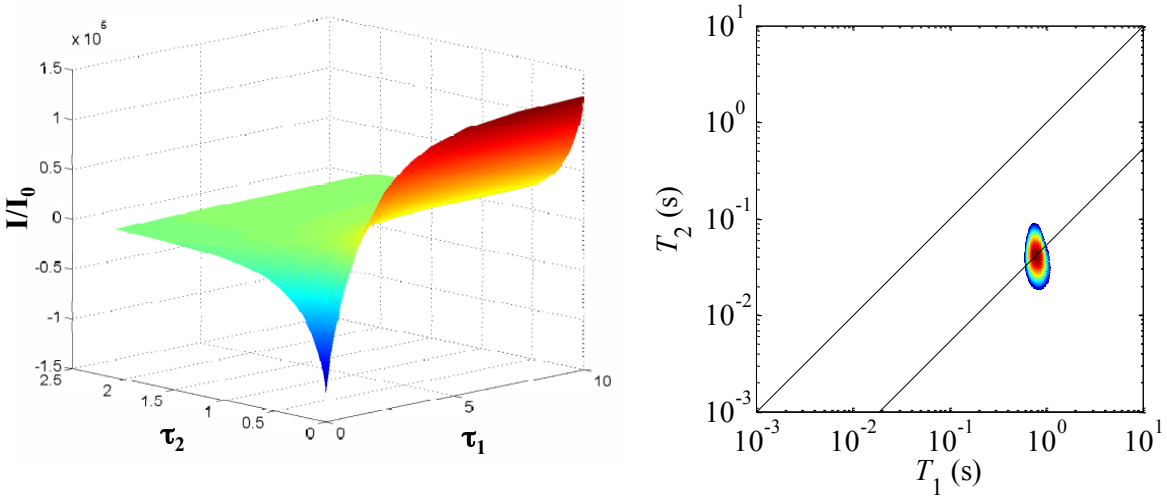

Figure 2.21. ^{1}H T_1-T_2 NMR experiments. On the left, an example of the results from an NMR T_1-T_2 2D experiment: different τ_R and τ_D are used, forming a set of values with respect to τ_1 and τ_2, respectively. On the right, a 2D T_1-T_2 correlation plot for the adsorption of acetonitrile on SiO_2, resulting from the application of the algorithm developed by Venkataramanan *et al.* (2002) to the results on the left. The main diagonal line represents $T_1 = T_2$, corresponding to pure liquid. The diagonal line over the maximum intensity of the peak indicates T_1/T_2 =19, with values of T_1 = 0.78 s and T_2 = 0.041 s.

^{13}C δ-$T_{1,ads}/T_{1,bulk}$

The molecular motion (translation and rotation) of the adsorbate on the surface of the adsorbent is described by the autocorrelation function $G(\tau)$ averaged over the time interval τ. The Fourier-transform of this function is proportional to the longitudinal relaxation time T_1. The autocorrelation function of the molecule will change on adsorption, manifested in a change in T_1 (Kimmich, 1997). In general, energetically stable adsorption conformations (corresponding to reduced mobility of the surface-bound species) are associated with stronger surface interactions. The ratio of T_1 relaxation times for surface adsorbed to free diffusing (bulk) molecules $T_{1,ads}/T_{1,bulk}$ can therefore be used as an indicator of the relative strength of surface interaction. A low $T_{1,ads}/T_{1,bulk}$ ratio is associated with low mobility and hence strong adsorption. It is important to consider this ratio, as different carbon atoms within a molecule can have different T_1 values in the bulk gas or liquid phase and it is the variation of T_1 on adsorption that reveals the relative strength of surface interaction.

The ratio of longitudinal to transverse relaxation times, T_1/T_2, probes the relative strengths of interaction between chemical species in catalysts, *vide supra*. In a fully saturated porous medium, this ratio of relaxation times is preferable as it removes the influence of pore geometry that would be significant in, say, a $T_{1,pore}/T_{1,bulk}$ measurement. The latter ratio is applicable when comparison of the adsorption of different molecules on the same porous material is of interest. However, when considering adsorption of only a monolayer or below monolayer, geometric effects of the pore are not relevant. In those cases, comparison of the relaxation time of the adsorbed liquid molecules to those in the bulk, $T_{1,ads}/T_{1,bulk}$, can be used as an indicator for different adsorbate-adsorbent pairs. The use of the $T_{1,ads}/T_{1,bulk}$ ratio presents clear advantages in heterogeneous materials at submonolayer coverages. Internal gradients are present during relaxometry measurements. It is well known that T_1 relaxation times are independent of such artefacts (Washburn *et al.*, 2008). That does not occur with T_2. The use of T_2 relaxation time measurements is suboptimal, particularly in high-field NMR experiments, employed throughout this work. The magnetic susceptibility differences between the solid and adsorbed liquid and vapour phases prevent accurate interpretation of submonolayer T_1/T_2 results (Mitchell *et al.*, 2010a).

Figure 2.22 shows spectra of 1-pentene aliphatic carbon atoms on the adsorption of 1 ML 1-pentene on θ-Al_2O_3. As can be seen, spectroscopic information is obtained on relaxation times of each spectral resonance, *i.e.*, each different carbon molecular bonding arrangement. The use of chemical shift resolved ^{13}C NMR T_1 measurements probes the adsorption of individual carbon atoms within their parent molecules. These measurements are straightforward to conduct and analyse, and yield direct information on the molecular configuration and relative adsorption strength of adsorbate molecules.

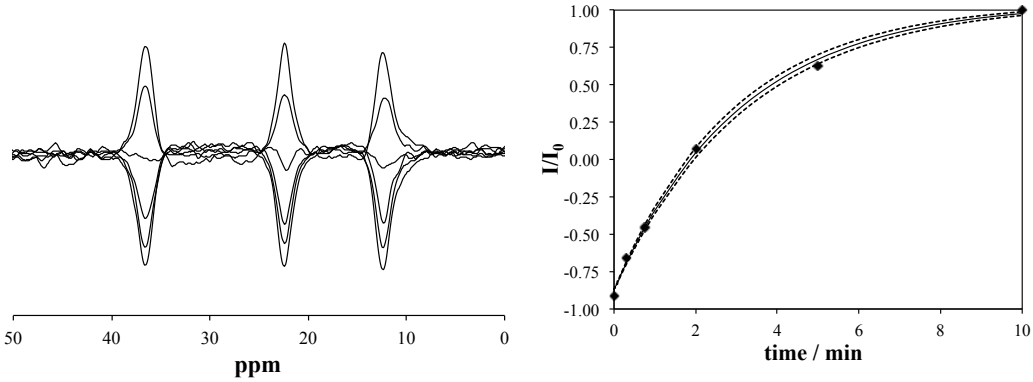

Figure 2.22. ^{13}C NMR T_1 NMR experiments: (left) spectra of 1 ML 1-pentene aliphatic carbons adsorbed on θ-Al_2O_3 for increasing τ_R values during an inversion-recovery experiment; (right) optimum area fitting for aliphatic carbon C4 (δ = 22.3 ppm) from figure in the left. The dashed lines indicate a ± 5% on the T_1 value. An optimum value of T_1 = 3.09 s was obtained.

References

Ahmed, M.J., Theydan, S.K. (2014) Isotherms and thermodynamics studies for binary adsorption of methane and ethane on 4A molecular sieve zeolites. *J. Porous Mater.*, 21, 303 – 310.

Armaroli, T., Bécue, T., Gautier, S. (2004). Diffuse Reflection Infrared Spectroscopy (DRIFTS): Application to the *in situ* analysis of catalysts. *Oil Gas Sci. Technol.*, 59, 215 - 237.

Atkins, P.W. (2001) *Elements of physical chemistry.* Oxford University Press, pp. 424 – 433.

Barrie, P.J. (2008) Analysis of temperature programmed desorption (TPD) data for the characterisation of catalysts containing a distribution of adsorption sites. *Phys. Chem. Chem. Phys.*, 10, 1688 – 1696.

Baumer, M., Libuda, J., Neyman, K.M., Rösch, N.K., Rupprechter, G., Freund, H.-J. (2007) Adsorption and reaction of methanol on supported palladium catalysts: microscopic-level studies from ultrahigh vacuum to ambient pressure conditions. *Phys. Chem. Chem. Phys.*, 9, 3541 – 3558.

Benaliouche, F., Boucheffa, Y., Ayrault, P., Mignard, S., Magnoux, P. (2008) NH_3-TPD and FTIR spectroscopy of pyridine adsorption studies for characterization of Ag- and Cu-exchanged X zeolites. *Micropor. Mesopor. Mat.*, 111, 80 – 88.

Bloch, F. (1950) Nuclear induction. *Phys. Rev.*, 70, 460 – 474.

Bloembergen, N., Purcell, E.M., Pound, R.V. (1948) Relaxation effects in nuclear magnetic resonance absorption, *Phys. Rev.*, 73, 679 – 712.

Buchbinder, A.M., Weitz, E., Geiger, F.M. (2010) Pentane, hexane, cyclopentane, cyclohexane, 1-hexene, 1-pentene, *cis*-2-pentene, cyclohexene, and cyclopentene at vapor/α-alumina and liquid/α-alumina interfaces studied by broadband sum frequency generation. *J. Phys. Chem. C*, 114, 554 – 566.

Burch, R., Attard, G.A., Daniells, S.T., Jenkins, D.J., Breen, J.P., Hu, P. (2002). Low-temperature catalytic decomposition of N2O on platinum and bismuth-modified platinum: identification of active sites. *Chem. Commun.*, 22, 2738 – 2739.

Brunauer, S. Emmet, P.H., Teller, E. (1938) Adsorption of gases in multimolecular layers. *J. Am. Chem. Soc.*, 60, 309 – 319.

Callaghan, P.T. (1991) *Principles of nuclear magnetic resonance microscopy.* Clarendon Press, Oxford, pp. 1 – 75.

Carr, H.Y., Purcell, E.M. (1954). Effects of diffusion on free precession in nuclear magnetic resonance experiments. *Phys. Rev.*, 94, 630 – 638.

Chen, D., Grønvold, A., Rebo, H.P., Moljord, K., Holmen, A. (1996) Catalyst deactivation studied by conventional and oscillating microbalance reactors. *Appl. Catal. A-Gen.*, 137, L1 – L8.

Chen, D. (1998) *Methanol conversion to light olefins over SAPO-34*, A dissertation submitted for the degree of Doctor of Philosophy, NTNU, pp. 91 – 96.

Chen, D., Moljord, K., Fuglerud, T., Holmen, A. (1999) The effect of crystal size of SAPO-34 on the selectivity and deactivation of the MTO reaction. *Micropor. Mesopor. Mat.*, 29, 191 – 203.

Chen, D., Bjorgum, E., Christensen, K.O., Holmen, A., Lodeng, R. (2007) Characterization of catalysts under working conditions with an oscillating microbalance reactor. *Adv. Catal.*, 51, 351 – 382.

Cornish, J.C.L., Avery, N.R. (1990) Adsorption of N_2, O_2, N_2O and NO on Ir(111) by EELS and TPD. *Surf. Sci.*, 235, 209 – 216.

D'Agostino, C., Brett, G.L., Miedziak, P.J., Knights, D.W., Hutchings, G.J., Gladden, L.F., Mantle, M.D. (2012) Understanding the solvent effect on the catalytic oxidation of 1,4-butanediol in methanol over Au/TiO_2 catalyst: NMR diffusion and relaxation studies. *Chem. Eur. J.*, 18, 14426 – 14433.

D'Agostino, C., Mitchell, J., Mantle, M.D., Gladden, L.F. (2014) Interpretation of NMR relaxation as a tool for characterising adsorption strength of liquids inside porous materials. *Chem. Eur. J.*, 20, 13009 – 13015.

Davies, S., Packer, K.J. (1990) Pore-size distributions from nuclear magnetic resonance spin-lattice relaxation measurements of flui-saturated porous solids. I. Theory and simulation. *J. Appl. Phys.*, *67*, 3163-3170.

De Canio, E.C., Bruno, J.W., Nero, V.P., Edwards, J.C. (1993) ^{27}Al NMR, FT-IR and ethanol – ^{18}O TPD characterization of fluorided alumina. *J. Catal.*, 140, 84 – 102.

De Moor, B.A., Reyniers, M.F., Gobin, O.C., Lercher, J.A., Marin, G.B. (2011) Adsorption of C_2-C_8 n-alkanes in zeolites, *J. Phys. Chem. C*, 115, 1204 – 1219.

Dillard, J.G., Moers, H., Klewe-Nebenius, H., Kirch, G., Pfennig, G., Ache, H.J. (1984) An X-ray photoelectron and Auger electron spectroscopic study of the adsorption of molecular iodine on uranium metal and uranium dioxide. *J. Phys. Chem.*, 88, 4104 – 4111.

Duffy, A., Walker, G.M., Allen, S.J. (2006) Investigations on the adsorption of acidic gases using activated dolomite. *Chem. Eng. J.*, 117, 239 – 244.

Eberly, P.E. (1968) High temperature infrared spectroscopy of pyridine adsorbed on faujasites. *J. Phys. Chem.*, 72, 1042 – 1047.

Eischens, R.P., Pliskin, W.A. (1958) The infrared spectra of adsorbed molecules. *Adv. Catalysis*, 10, 1 – 56.

Fairen-Jiménez, D., Colón, Y.J., Fahra, O.K., Bae, Y-S., Hupp, J.T., Snurr, R.Q. (2012) Understanding excess uptake maxima for hydrogen adsorption isotherms in frameworks with rht topology. *Chem. Commun.*, 48, 10496 – 10498

Farzad, S., Taghikhani, V., Ghotbi, C., Aminshahidi, B., Lay, E.N. (2007) Experimental and theoretical study of the effect of moisture on methane adsorption and desorption by activates carbon at 273.5 K. *J. Nat. Gas. Chem.*, 16, 22 – 30.

Fluggle, J.C., Menzel, D. (1979) XPS, UPS and XAES studies of the adsorption of nitrogen, oxygen and nitrogen oxides on W(110) at 300 and 100 K. *Surf. Sci.*, 79, 1 – 25.

Gladys, M.J., Stevens, A.V., Scott, N.R., Jones, G., Batchelor, D., Held, G. (2007) Enantiospecific adsorption of alanine on the chiral Cu{531} surface. *J. Phys. Chem. C*, 111, 8331 – 8336.

Godefroy, S., Korb, J.P., Fleury, M., Bryant, R.G. (2001) Surface nuclear magnetic relaxation and dynamics of water and oil in macroporous media. *Phys. Rev. E*, 64, 021605.

Godefroy, S., Fleury, M., Deflandre, F., Korb, J.P. (2002) Temperature effect on NMR surface relaxation in rocks for well logging applications. *J. Phys. Chem. B*, *106*, 11183 – 11190.

Gong, K., Shi, T., Ramachandran, P.A., Hutchenson, K.W., Subramaniam, B. (2009) Adsorption/desorption studies of 2,2,4-trimethylpentane in β-zeolite and mesoporous materials using a tapered element oscillating microbalance (TEOM). *Ind. Eng. Chem. Res.*, 48, 9490 – 9497.

Guil, J.M., Homs, N., Llorca, L., Ramírez de la Piscina, P. (2005) Microcalorimetric and infrared studies of ethanol and acetaldehyde adsorption to investigate the ethanol steam reforming on supported cobalt catalysts. *J. Phys. Chem. B*, 109, 10813 – 10819.

Hahn, E.L. (1950) Spin echoes. *Phys. Rev.*, 80, 580 – 594.

Hair, M.L. (1967) *Infrared Spectroscopy in Surface Chemistry.* Marcel Dekker, New York, pp. 10 – 63.

Hamid, H.S., Eric, F. (2006) XPS & FTIR study of adsorption characteristics using cationic and anionic collectors on smithsonite. *J. Min. Mat. Char. Eng.*, 5, 21 – 45.

Hoffmann, E., Stroobant, V. (2007) *Mass spectrometry: principles and applications.* Wiley-VCH, Weinheim, pp. 176 – 181.

Hornak, J.P. (1996) *The basics of NMR*. [Online] Available from: http://www.cis.rit.edu/htbooks/nmr/ [Accessed October 2014]

Ilyina, E.V., Mishakov, I.V., Vedyagin, A.A., Bedilo, A., Klabunde, K.J. (2013) Promoting effect of vanadium on CF_2Cl_2 destructive sorption over nanocrystalline mesoporous MgO. *Micropor. Mesopor. Mat.*, 175, 76 – 84.

Jacobs, G., Williams, L., Graham, U., Thomas, G.A., Sparks, D.E., Davis, B.H. (2003) Low temperature water-gas shift: in situ DRIFTS-reaction study of ceria surface area on the evolution of formats on Pt/CeO_2 fuel processing catalysts for fuel cell applications,. *Appl. Catal. A-Gen.*, 252, 107 – 118.

Karge, H.G. (1998) Characterization by infrared spectroscopy. *Micropor. Mesopor. Mat.*, 22, 547 – 549.

Keeler, J. (2005) *Understanding NMR Spectroscopy*. Wiley, Chichester, pp. 23 –296.

Kimmich, R. (1997) *NMR - Tomography, Diffusometry, Relaxometry*. Springer-Verlag, Berlin, pp. 81 – 136.

Kiricsi, I., Flego, C., Pazzuconi, G., Parker, W.O., Millini, R., Perego, C., Bellusi, G. (1994). Progress toward understanding zeolite β acidity: an IR and ^{27}Al NMR spectroscopic study. *J. Phys. Chem.*, 98, 4627 – 4634.

Kondo, J.N., Nishitani, R., Yoda, E., Yokoi, T., Tatsumi, T., Domen, K. (2010) A comparative IR characterization of acidic sites on HY zeolite by pyridine and CO probes with silica-alumina and γ-alumina references. *Phys. Chem. Chem. Phys.*, 12, 11576 – 11586.

Kunkes, E.L., Simonetti, D.A., West, R.M., Serrano-ruiz, J.C., Gärtner, C.A., Dumesic, J.A. (2008) Catalytic conversion of biomass to monofunctional hydrocarbons and targeted liquid-fuel classes. *Science*, 332, 417 – 421.

Lee, C.K., Ashtekar, S., Gladden, L.F., Barrie, P.J. (2004) Adsorption and desorption kinetics of hydrocarbons in FCC catalysts studied using a tapered element oscillating microbalance (TEOM). Part 1: experimental measurements. *Chem. Eng. Sci.*, 59, 1131 – 1138.

Liu, G., Li, Y., Jonas, J. (1991) Confined geometry effects on reorientational dynamics of molecular liquids in porous silica glasses. *J. Chem. Phys.*, 95, 6892 – 6901.

McDonald, G.G., Leigh, J.S. (1973). A new method for measuring longitudinal relaxation times. *J. Magn. Reson.* 9, 358 – 362.

McDonald, P.J., Korb, J.P., Mitchell, J., Monteilhet, L. (2005) Surface relaxation and chemical exchange in hydrating cement pastes: A two-dimensional NMR relaxation study. *Phys. Rev. E*, 72, 011409.

McGregor, J. (2006) *Heterogeneous catalytic hydrogenation and dehydrogenation: catalysts and catalytic processes.* A dissertation submitted for the degree of Doctor of Philosophy, University of Cambridge, pp. 20 – 33.

McGregor, J., Gladden, L.F. (2008) The role of carbon deposits in the hydrogenation of C5 hydrocarbons. *Appl. Catal. A-Gen.*, 345, 51 – 57.

McMillan, L., Lutecki, M., Wang, W., Arias-Vecino, P., McGregor, J., Al-Yassir, N., Al-Khattaf, S., Gladden, L.F. (2013) Toluene alkylation over Metal Organic Frameworks – An evaluation of the role of acidity for catalytic activity and coke deposition. *23rd NAM*, O-M-Fre-6.

Meiboom, S., Gill, D. (1958) Modified spin-echo method for measuring nuclear relaxation times. *Rev. Sci. Instrum.*, 29, 668 – 691

Mitchell, J., Stark, S.C., Strange, J.H. (2005) Probing surface interactions by combining NMR cryoporometry and NMR relaxometry. *J. Phys. D: Appl. Phys.*, 38, 1950 – 1958.

Mitchell, J., Broche, L.M., Chandrasekera, T.C., Lurie, D.J., Gladden, L.F. (2013a) Exploring surface interactions in catalysts using Low-Field Nuclear Magnetic Resonance. *J. Phys. Chem. C*, *117*, 17699-17706.

Mitchell, J., Chandrasekera, T.C., Gladden, L.F. (2013b) A general approach to measurements in the presence of internal gradients. *Micropor. Mesopor. Mat.*, 178, 20 – 22.

Mitchell, J., Chandrasekera, T.C., Johns, M.L., Gladden, L.F. (2010a) Nuclear magnetic resonance relaxation and diffusion in the presence of internal gradients: The effect of magnetic field strength. *Phys. Rev. E*, 81, 026101.

Mitchell, J., Chandrasekera, T.C., Gladden, L.F. (2010b) Obtaining true transverse relaxation time distributions in high-field NMR measurements of saturated porous media: Removing the influence of internal gradients. *J. Chem. Phys.*, 132, 244705.

Mitchell, L.A., Tovar, T.M., LeVan M.D. (2014) High pressure excess isotherms for adsorption of oxygen and argon in a carbon molecular sieve. *Carbon*, 74, 120 – 126.

Monduzzi, M., Monaci, R., Solinas, V. (1987) ^{13}C NMR relaxation study and CNDO/2 calculations of some organic molecules adsorbed on Y-type zeolites. *J. Colloid. Interf. Sci.*, 120, 8 – 14.

Natesakhawat, S., Ohodnicki, P.R., Howard, B.H., Lekse, J.W., Baltrus, J.P., Matranga, C. (2013) Adsorption and deactivation characteristics of Cu/ZnO-based catalysts for methanol synthesis from carbon dioxide. *Top. Catal.*, 56, 1752 – 1763.

Niemantsverdriet, J.W. (2000) *Spectroscopy in Catalysis*. Wiley-VCH, Weinheim, pp. 1 – 35; 201 – 229.

Osorio-Pérez, Y., Palomeque-Forero, L.A., Cristiano-Torres, D.V., Trujillo, C.A. (2008) Brønsted acid site number evaluation using isopropylamine decomposition on Y-zeolite contaminated with vanadium in a simultaneous DSC-TGA analyzer, *Thermoquim. Acta*, 470, 36 – 39.

Parry, E.P. (1963) An infrared study of pyridine adsorbed on acidic solids. Characterization of surface acidity. *J. Catal.*, 2, 371 – 379.

Patel, S.L., Pemble, M.E. (1996) Auger electron spectroscopic (AES) studies of the adsorption and reaction of $SnCl_4$ and H_2O at a silica surface, *Surf. Sci.*, 352 – 354, 534 – 539.

Peck, J.W., Mahon, D.I., Beck, D.E., Koel, B.E. (1998) TPD study of the adsorption and reaction of nitromethane and methyl nitrite on ordered Pt-Sn surface alloys. *Surf. Sci.*, 410, 170 – 188.

Rouabah, D., Benslama, R., Fraissard, J. (1991) ^{1}H NMR study of hydrogen chemisorbed on supported platinum: application to the determination of the metal dispersion. *Chem. Phys. Lett.*, 179, 218 – 222.

Rouquerol, F, Rouquerol, J., Sing, K. (1999) *Adsorption by powders and porous solids.* Academic Press, London, pp. 51 – 92.

Ryczkowski, J. (2001) IR Spectroscopy in Catalysis. *Catal. Today*, 68, 263 - 381.

Samantaray, M.K., Alauzun, J., Gajan, D., Kavitake, S., Mehdi, A., Veyre, L., Lelli, M., Lesage, A., Emsley, L., Copéret, C., Thieleux, C. (2013) Evidence for metal-surface interaction and their role in stabilizing well-defined immobilized Ru-NHC alkene metathesis catalysts. *J. Am. Chem. Soc.*, 135, 3193 – 3199.

Sasse, A.G.B.M., Lakerveld, D.G., Van Silfhout, A. (1988) The adsorption of nitric oxide on a silicon (100) 2x1 surface studied with Auger electron spectroscopy. *Surf. Sci.*, 195, L167 – L172.

Song, Y.Q., Venkataramanan, L., Hürlimann, M.D., Flaum, M., Frulla, P., Straley, C. (2002). T_1–T_2 correlation spectra obtained using a fast two-dimensional Laplace inversion. *J. Magn. Reson.*, 154, 261– 268.

Stuart, B.H. (2004) *Infrared spectroscopy: fundamentals and applications.* Wiley, Chichester, pp. 1 – 44.

Thomas, J.M., Thomas, W.J. (1997) *Principles and Practice of Heterogeneous Catalysis*. VCH, Germany, pp. 161 – 164.

Tittensor, J.G., Gorte, R.J., Chapman, D.M. (1992) Isopropylamine adsorption for the characterisation of acid sites in silica-alumina catalysts. *J. Catal.*, 138, 714 – 720.

Uzio, D. (2001) Textural characterisation of catalysts. In: Lynch J. (ed). *Physico-chemical analysis of industrial catalysts: a practical guide to characterisation*. Editions Technip, Paris, pp. 5 – 18.

Venkataramanan, L., Song, Y. Q., Hürlimann, M. D. (2002) Solving Fredholm integrals of the first kind with tensor product structure in 2 and 2.5 dimensions. *IEEE Trans. Signal Process.*, 50, 1017– 1026.

Vold, R., Waugh, J., Klein, M., Phelps, D. (1968) Measurement of spin relaxation in complex systems. *J. Chem. Phys.* 48, 3831– 3832

Wang, J.C.F., Patashnick, H., Rupprecht, G. (1980) A new real-time isokinetic dust mass monitoring system. *J. Air Pollut. Contr. Assoc.*, 30, 1018 – 1021.

Washburn, K.E., Eccles, C.D., Callaghan, P.T. (2008) The dependence on magnetic field strength of correlated internal gradient relaxation time distributions in heterogeneous materials. *J. Magn. Reson.*, 194, 33 – 40.

Weber, D., Mitchell, J., McGregor, J., Gladden, L.F. (2009) Comparing strengths of surface interactions for reactants and solvents in porous catalysts using two-dimensional NMR relaxation correlations. *J. Phys. Chem. C*, 113, 6610 – 6615.

Weber, D., Sederman, A.J., Mantle, M.D., Mitchell, J., Gladden, L.F. (2010) Surface diffusion in porous catalysts. *Phys. Chem. Chem. Phys.*, 12, 2619 – 2624.

Williams, D., Fleming, I. (2008) *Spectroscopic Methods in Organic Chemistry*. McGraw-Hill, Glasgow, pp. 27 – 79.

Wilson, J.D. (1992) Statistical approach to the solution of first-kind integral equations arising in the study of materials and their properties. *J. Mater Sci.*, 27, 3911 – 3924.

Yi, H., Wang, Z., Liu, H., Tang, X., Ma, D., Zhao, S., Zhang, B., Gao, F., Zuo, Y. (2014) Adsorption of SO_2, NO and CO_2 on activated carbons: equilibrium and thermodynamics. *J. Chem. Eng. Data*, 59, 1556 – 1563.

Yuzawa, H., Aoki, M., Itoh, H., Yoshida, H. (2011) Adsorption and photoadsorption states of benzene derivatives on titanium oxide studied by NMR. *J. Phys. Chem. Lett.*, 2, 1868 – 1873.

Zhou, X., Yi, H., Tang, X., Deng, H., Liu, H. (2012) Thermodynamics for the adsorption of SO_2, NO and CO_2 from flue gas on activated carbon fiber. *Chem. Eng. J.*, 200 – 202, 399 – 404.

Zhu, W., van de Graaf, J.M., van den Broeke, J.P., Kapteijn, F., Moulijn, J.A. (1998) TEOM: A unique technique for measuring adsorption properties. Light alkanes in silicalite-1. *Ind. Eng. Chem. Res.*, 37, 1934 – 1942.

Zhu, X., Ping, W. (2014) Optimization of b-cyclodextrin cros-linked polymer for monitoring of quercetin. *Spectrochim. Acta A-Mol. Biomol. Spectros.*, 132, 38 – 43.

Chapter 3:

Adsorption on aluminas

3 Adsorption on aluminas

In this chapter, a review of the structure of aluminas is presented. Aluminas will be regarded as a model surface for adsorption studies. Many reactions have been shown to occur on aluminas (Knözinger and Ratnasamy, 1978) and it is relevant to explore how adsorption can determine the subsequent steps in such reactions. Furthermore, it is also interesting to determine the influence of adsorption over the aluminas, as they are widely used as supports in catalysis. As such, this chapter is structured as follows: initially, an introductory section on the importance of aluminas as catalytic materials is presented, followed by a description of their structure. Subsequently, initial characterisation studies on the surface properties of the aluminas used in this work, *via* DRIFTS and TPD, revealed the type of adsorption sites present.

3.1 Importance and applications in catalysis

Aluminas have been widely used as adsorbents and catalysts in the past (John and Scurrell, 1977). In industrial catalytic processes, aluminas are mostly used as catalyst supports. One of the most prominent applications of γ-Al_2O_3 as a support is in catalytic converters for pollution control (Schüth and Unger, 2008). Applications of pure aluminas are industrially more limited, with the Claus process to obtain sulphur as a typical example (Piéplu *et al.*, 1998). However, pure aluminas are widely used as catalysts in academic research (Knözinger and Ratnasamy, 1978). Among others, aluminas are used in dimerisation or polymerisation reactions, particularly enhanced with the addition of halogenates (Choudhary, 1977). Thus, the condensation of cyclohexane *via* the aldol condensation mechanism (Chen *et al.*, 2011), the polymerisation of propylene (Holm and Clark, 1963) or cracking reactions (Corma and Fornés, 1990) have been reported. Aluminas are also used as oxidation catalysts, such as in the oxidation of methanol (Cairati and Trifirò, 1983), in dehydrogenation reactions, such as in the case of 1-butanol (Pines and Haag, 1960) or in hydrogenation reactions, such as ethylene hydrogenation (Amenomiya *et al.*, 1967). Other reactions include the conversion of chloromethane to methanol and dimethyl ether (Khaleel *et al.*, 2011). However, isomerisation of olefins has captured the most attention. Thus, ethylene (Amenomiya *et al.*, 1967), butenes (Brouwer, 1962; Cheng and Ponec, 1994; Gerberich and Hall, 1966; Guisnet *et al.*, 1977; Haag and Pines, 1960; Medema, 1974), dimethylbutene (Corado *et al.*, 1975; Haag and Pines, 1960; Pines and Haag, 1960), pentenes and hexenes (Brouwer, 1962) and cyclohexene (Pines and Haag, 1960) have been studied as model adsorbates for isomerisation on aluminas.

There exist a wide variety of aluminas. However, not all aluminas can be used in catalytic or adsorption processes. The reactions described above require the presence of a so-called active alumina. These active aluminas present a particular structure. High surface areas and pore sizes are required for transport and reaction. Additionally, the presence of acid sites on the surface is crucial, as those act as adsorption sites for the reactions mentioned. In order to optimise the adsorption and reaction of the processes described earlier, it is important to know the structure and characterise the surface of the active aluminas. Hence, section 3.2 presents a brief description on the formation and structure of active aluminas. Particular attention will be given to two particular transition aluminas, γ- and θ-Al_2O_3, as they will be used throughout in this dissertation. Section 3.3 shows the initial characterisation studies performed on γ- and θ-Al_2O_3.

3.2 Structure and morphology of transition aluminas

Active aluminas, aluminas used as catalysts and catalyst supports, are aluminium oxide materials formed by thermal dehydration from heating hydroxide ($Al(OH)_x$) or oxy-hydroxide ($Al(OOH)_x$) precursors. Important variables for the adsorptive and catalytic activities such as crystal structure, pore texture and the chemical nature of the surface are largely dependent on the preparation methods and the morphology of the initial hydroxides (Lippens and Steggerda, 1970). In this section, a description of the thermal dehydration process to render the different types of active aluminas is presented.

Heating of hydroxide ($Al(OH)_x$) or oxy-hydroxide ($Al(OOH)_x$) alumina precursors results in dehydration and restructuring of the material. New metastable phases of low crystallinity are formed in this process. These structures are commonly known as transition aluminas. Catalytic aluminas belong to this group of transitional Al_2O_3 phases, metastable in the *ca.* 750-1370 K range. They are characterised by high surface area and open porosity. Eventually, at sufficient high temperatures, corundum, or α-Al_2O_3 is formed. As mentioned, the nature of a transitional alumina strongly depends on its precursor (Pecharromán *et al.*, 1999). **Figure 3.1** shows the different transitional aluminas denoted with Greek characters, and with the approximate temperature range within which they are stable, before thermal decomposition. As can be seen, thermal decomposition of bayerite gives the sequence $\eta \longrightarrow \theta \longrightarrow \alpha$. In contrast, decomposition of bohemite results in $\gamma \longrightarrow \delta \longrightarrow \theta \longrightarrow \alpha$. The overall crystal structure of these transition aluminas should be viewed as a deformed spinel (Zhou and Snyder, 1991). Aluminum precursors and early transition aluminas (η and

γ) present high-energy structures. For example, such high energies are noted on the three-coordinated surface Al atoms in, for example, the η- phase. However, the reduction of surface area with heating and dehydroxylation and the ordering of tetrahedral Al, causes the spinel framework to collapse, settling into θ-Al_2O_3 before transforming into hexagonal corundum. Dehydroxylation reactions preserve the skeleton of the precursor (Lippens and de Boeh, 1964). Thus, in the case of boehmite or bayerite, the fcc arrangement of the oxygen network produces spinel-like materials when heating. The presence of additives, such as La, Na or Ca, generally results in the stabilisation of the transition structure at the expense of the stable α-Al_2O_3 phase (Andersson *et al*., 2005; Chen *et al.*, 2001). Similarly, the structure of Gibbsite presents a hexagonal arrangement (Schoen and Roberson, 1970). Following the diagram in **Figure 3.1**, it is simple to explain why the structures of χ- and κ-Al_2O_3 are also hexagonal (Lippens and Steggerda, 1970; Wolverton and Haas, 2000). Of the transition aluminas, κ-Al_2O_3 and χ-Al_2O_3 are of less industrial interest and applications, related to their mechanical strength and resistance (Paglia *et al.*, 2001).

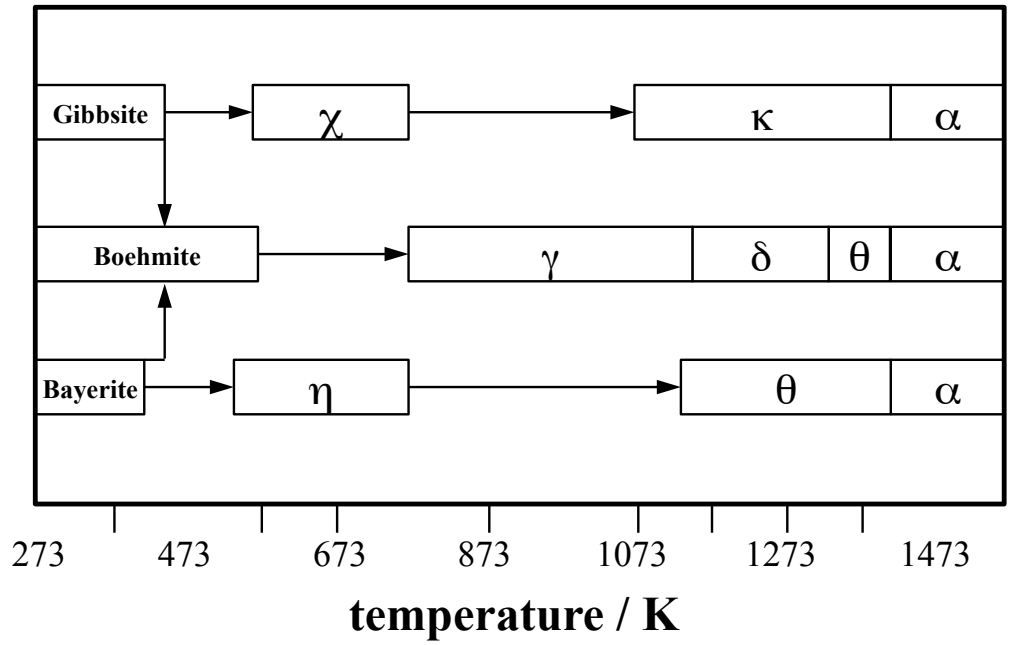

Figure 3.1. Diagram identifying alumina phases. The type of precursor, and calcination temperature strongly affect the form of transition alumina formed

Transition aluminas are divided according to different classifications. Aluminas can be grouped based on crystallographic structure, following the general lines described above. A classification based on the temperature by which the aluminas were obtained divides them amongst the so-called low-temperature transition phases and the high-temperature transition phases. The first group consists of low temperature aluminas obtained by dehydrating at temperatures not exceeding 900 K. With general formula $Al_2O_3 \cdot nH_2O$, in which $0 < n < 0.6$, these include χ-, η- and γ-Al_2O_3, among others. The high-temperature group includes nearly anhydrous alumina, obtained at temperatures between 1200 – 1300 K. To this group belong κ-, θ- and δ-Al_2O_3 (Lippens and Steggerda, 1970). Let us now consider the more catalytically relevant transition aluminas derived from bayerite and boehmite. The structural differences between the two families of aluminas are relatively small as all transition aluminas belong to the cubic system and have the nature of defective spinels. However, in the context of catalysis, the passage from low-temperature to high-temperature transition aluminas is more critical. In fact, the high-temperature transition phases are definitely less active than the low temperature ones (Morterra and Magnacca, 1996). In section 3.2.1, γ- and θ-Al_2O_3 phases will be considered. They represent two characteristic transition aluminas from each group. A brief description of their structures is presented.

3.2.1 Structure of γ- and θ-Al_2O_3: surface active sites

γ- and θ-Al_2O_3 were used during adsorption studies, as they represent two exemplar types of active aluminas. As previously mentioned, they are spinel-like structures, considered defective spinels. The defective nature of the spinel derives from the presence in aluminas of only trivalent cations (the Mg^{2+} in the spinel structure, $MgAl_2O_4$, is replaced by an Al^{3+}). Hence, some of the lattice positions occupied by cations in mixed-oxide spinels must remain empty to guarantee electrical neutrality. The distribution of those vacancies in the precursor and the type of rearrangement occurring with increasing temperature results in the differences between both γ- and θ-Al_2O_3.

Due to its importance as catalyst and catalyst support, γ-Al_2O_3 is the most studied transition alumina (Paglia *et al.*, 2003; Trueba and Trasatti, 2005; Wolverton and Hass, 2000). At the same time, the pseudo-crystalline structure of this transition alumina makes its description somehow complex and under debate. However, there is a general agreement in certain aspects. γ-Al_2O_3 appears at temperatures between 600 and 1200 K and it could be stable to temperatures as high as 1400 K when formed at the higher range of temperatures (Trueba and

Trasatti, 2005). It generally presents surface areas in the range and below 250 $m^2 g^{-1}$. γ-alumina is generally considered a cubic defect spinel. **Figure 3.2** shows the unit cell of γ-alumina. The oxygen lattice is a cubic close-packed stacking of oxygen layers, with Al atoms occupying octahedral and tetrahedral sites in a variable proportion, as well as some non-spinel sites (Paglia *et al.*, 2003). Regarding surface species, removal of OH groups during high temperature treatment creates coordinatively unsaturated Al cations. Tetrahedral (Al^{IV}) and octahedral (Al^{VI}) coordinations are predominant. Additionally, pentahedrally coordinated Al (Al^{V}) has been reported (Digne *et al.*, 2002; 2004; Pencharromán *et al.*, 1999). The presence of such unsaturated cations gives rise to the presence of different Lewis acid sites (Busca, 1999). They can further interact with other hydroxyl groups to form Brønsted acid sites. Details on surface acidity are discussed in section 3.3.2.2.

θ-Al_2O_3 presents a more ordered structure than the previously described γ-Al_2O_3, and more similar to that of the stable α-Al_2O_3. Hence, lower surface areas, of about 100 $m^2 g^{-1}$ are common. However, it presents a similar local coordination to γ-Al_2O_3 (Mo and Ching, 1998). In the case of θ-Al_2O_3, the oxygen network makes up a distorted fcc lattice, but the octahedral and tetrahedral aluminium distribution violates the rotation axis of the spinel space group (Pecharromán *et al.*, 1999). The relative amounts of tetrahedral and octahedral aluminium are 50-50%. **Figure 3.2** shows the structure of θ-alumina when considered as a defect spinel structure. A monoclinic crystal structure has also been proposed to describe the structure (Lippens and Steggerda, 1970; Wolverton and Haas, 2000). This is the highest structure in the bayerite and boehmite series. Transformation from γ-Al_2O_3 occurs at about 1200 – 1300 K, depending on impurities, while this transition occurs earlier in the case of η-Al_2O_3. Similarly to γ-Al_2O_3, heating treatment causes the appearance of uncoordinated ions on the surface. Some of the vacant cationic positions, imposed by the Al_2O_3 stoichiometry, are also present in the surface layer of transition aluminas. In addition to the double coordination presented by Al ions, such vacancies are responsible for the complex surface sites and defects.

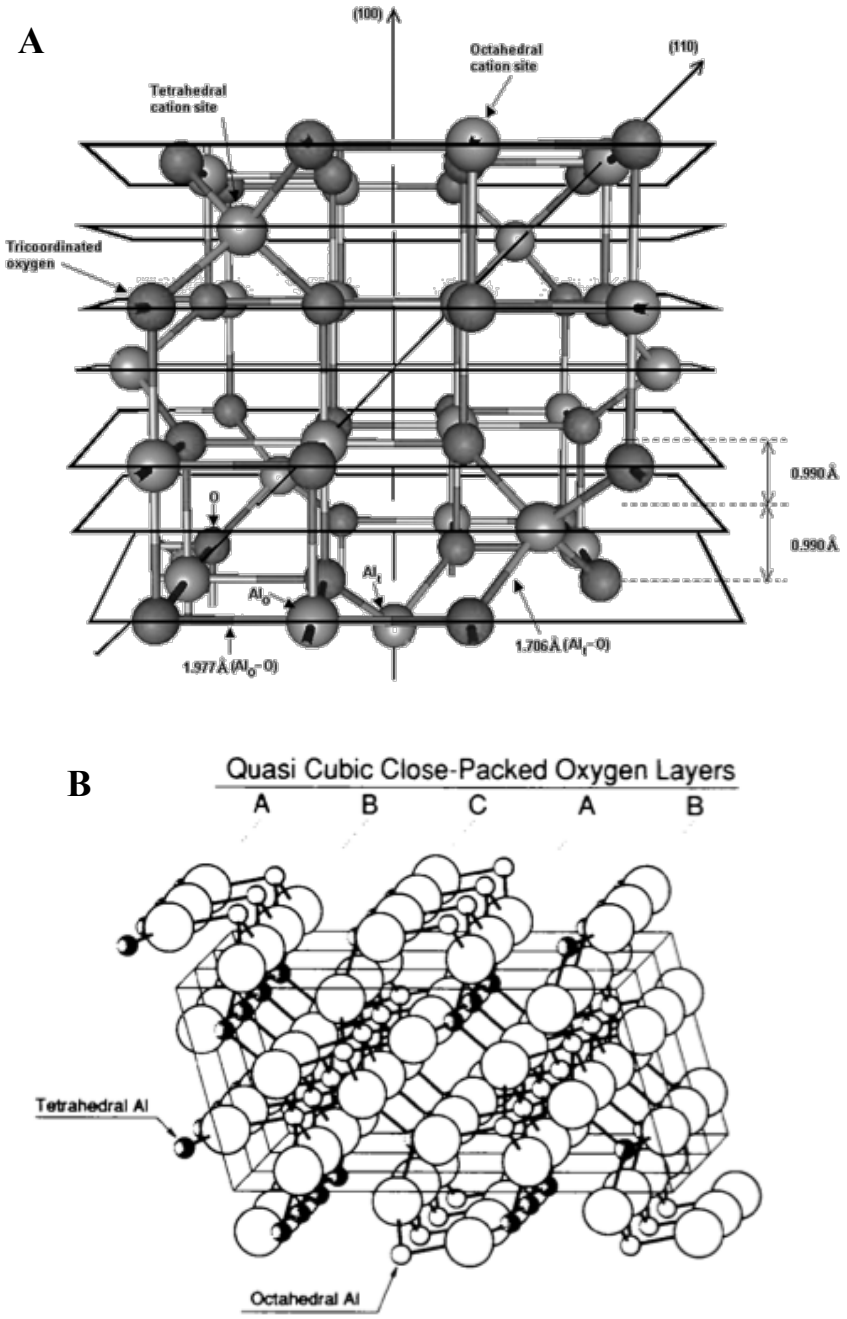

Figure 3.2. Bulk structure of main transition aluminas discussed. Diagram with the proposed structure of γ-Al_2O_3 (A), extracted from Ionescu *et al.* (2002); and proposed structure of θ-Al_2O_3 (B) by Zhou and Snider (1991).

In the following section, the results of the characterisation of the γ- and θ-Al_2O_3 adsorbents used in this dissertation are now reported.

3.3 Characterisation of γ- and θ-Al_2O_3

The importance of surface properties is paramount in catalytic reactions. In order to gain information on the adsorbents used, both aluminas were characterised.

3.3.1 Experimental methods

3.3.1.1 Materials

γ-Al_2O_3 (BET surface area 190 m^2 g^{-1}, BJH pore volume of 0.70 cm^3 g^{-1}) and θ-Al_2O_3 (BET surface area 120 m^2 g^{-1}, BJH pore volume 0.57 cm^3 g^{-1}) were provided by Johnson Matthey as trilobes (diameter = 1 mm, length = 10 ± 2 mm) and crushed to particles of < 150 μm for adsorption experiments, unless stated otherwise. Pyridine (99.8 %, Sigma Aldrich) was used without further purification. He (99.996 %, Air Liquide) was used as pre-treatment and carrier gas during the experiments.

3.3.1.2 Temperature programmed desorption of aluminas

TPD-MS experiments were performed in a CATlab microreactor module (Hiden Analytical) and desorbed species were detected with a QIC-20 quadrupolar mass spectrometer (QMS). Details of the equipment were described in section 2.2.1.2. Approximately 100 mg of θ-Al_2O_3 were heated from 323 K to 673 K with a ramp rate of 10 K min^{-1} at a flow rate of 40 cm^3 min^{-1} of He. Desorption of water was monitored following *m/z* = 18.

3.3.1.3 Infrared spectroscopy

In-situ Diffuse Reflectance Infrared Fourier Transform Spectroscopy (DRIFTS) measurements on the adsorption of pyridine were carried out on a Nicolet Avatar 380 FTIR (Thermo Scientific) equipped with a DTGS-KBr detector. A spectral resolution of 4 cm^{-1} and 256 scans were used. The aluminas were pre-heated at 673 K for 2 h under 40 cm^3 min^{-1} He flow in a reaction chamber (Praying Mantis, Harrick), and then cooled to 298 K. 5.0 ± 0.1 μL of adsorbate were then injected *via* a custom made heated t-port septum sealed. Sample was left to equilibrate until no further changes in the IR spectra were observed. Additionally, the samples were heated to 313 K and 423 K to determine the strength of adsorption of pyridine. KBr was employed as spectral background.

3.3.2 Results and discussion

Active alumina contains, depending upon temperature, from a few tenths to about 5% water. Hence, the surface of the aluminas is saturated with adsorbed water. It is well known that catalytic activity is strongly dependent on dehydroxylation temperatures of the transition aluminas (van Cauwelaert and Hall, 1970). Removal of water and hydroxyl groups results in coordinatively unsaturated oxygen anions being created and exposed Al^{3+} cations. These ions are responsible for chemisorption and catalytic activity (Knözinger and Ratnasamy, 1978). In this section, the characterisation of the adsorption sites of γ- and θ-Al_2O_3 used in this dissertation is reported. The removal of water and adsorbed hydroxyls was followed, with a study on the hydroxyls present on the surface in section 3.3.2.1. Additionally, the acid-base properties of the surface were evaluated in section 3.3.2.2.

3.3.2.1 Pre-treatment of aluminas: removal of water

Desorption of water and hydroxyl groups was followed during pre-treatment of θ-Al_2O_3 by means of temperature programmed desorption. **Figure 3.3** shows the evolution of $m/z = 18$, assigned to water, desorbing from the alumina. As can be observed, significant desorption occurred above 370 K, possibly due to a combination of physisorbed water and weakly adsorbed hydroxyl groups. A significant decay in the rate of desorption was noted after 450 K, followed by a steady rate up to 600 K, when another drop was noted. This behaviour can be related to the hydroxyl concentration at different temperatures reported for a mixture of η- and γ-Al_2O_3 (van Cauwelaert and Hall, 1970). Also, similar authors have reported a sudden change in adsorption sites above 600 K on γ-Al_2O_3 (Lunsford *et al.*, 1975).

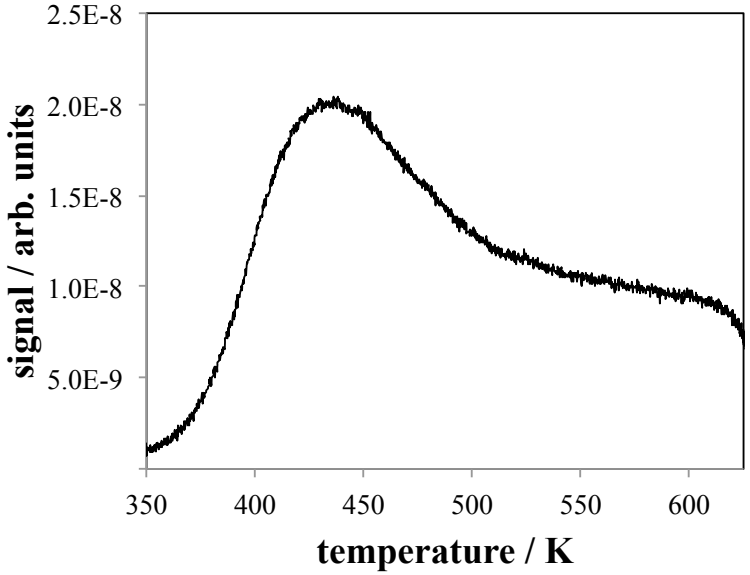

Figure 3.3. TPD of m/z = 18, corresponding to desorbed water from θ-Al_2O_3. 40 cm^3 min^{-1} of He were passed through the sample while heated at a ramp rate of 10 K min^{-1}.

Similarly, it was possible to follow the desorption of hydroxyl groups *via* DRIFTS. Similar conditions to those used during TPD experiments were employed in a reaction chamber within the DRIFTS cell. A sample of θ-Al_2O_3 was heated to 673 K. **Figure 3.4** shows the spectra obtained during heating. As observed, only a band at 3692 cm^{-1} was present at 298 K, with further broad bands observed below 3600 cm^{-1}, corresponding to bulk ν(OH). However, with heating of the alumina, more bands started to appear at higher frequency. Clearly, a band at 3731 cm^{-1} was observed at 373 K, along with the band at 3691 cm^{-1} detected at 298 K. Finally, at 673 K, bands at 3778 cm^{-1}, 3750 cm^{-1}, 3731 cm^{-1}, 3715 cm^{-1} and 3690 cm^{-1} were observed. These bands have been previously reported in transition aluminas (Knözinger and Ratnasamy, 1978; Morterra and Magnacca, 1996; Tsyganenko and Filimonov, 1972), and are associated with surface ν(OH). Precisely, those bands corresponded to three types of hydroxyl groups at the surface of transition aluminas, in addition to differences in charge, following the well-accepted Knözinger model (Knözinger and Ratnasamy, 1978). The different hydroxyls, along with the approximate stretching frequencies, are shown in **Scheme 3.1**. As can be seen, all species were observed in the alumina at 673 K, with the exception of the linear hydroxyl on an octahedral site. Busca and co-workers (1991) and Digne *et al.* (2004) have provided a slightly different assignment, in line with the types of alumina bound to the hydroxyls and the OH coordination on the surface. However, it is usually agreed in all cases that OH stretching is highest for terminal OH groups, intermediate for bridging OH

groups and lowest for triply bridging OH groups (Busca, 1999). During this work, Knözinger's assignment was used throughout. With the identification of the surface groups on the alumina, it is therefore important to determine the adsorption characteristics of these surface groups. The reversible interaction of water with coordinately unsaturated ions can result with these groups potentially showing Brønsted acidity (Busca *et al.*, 1998). In order to determine the type of surface sites present, acidity measurements were performed.

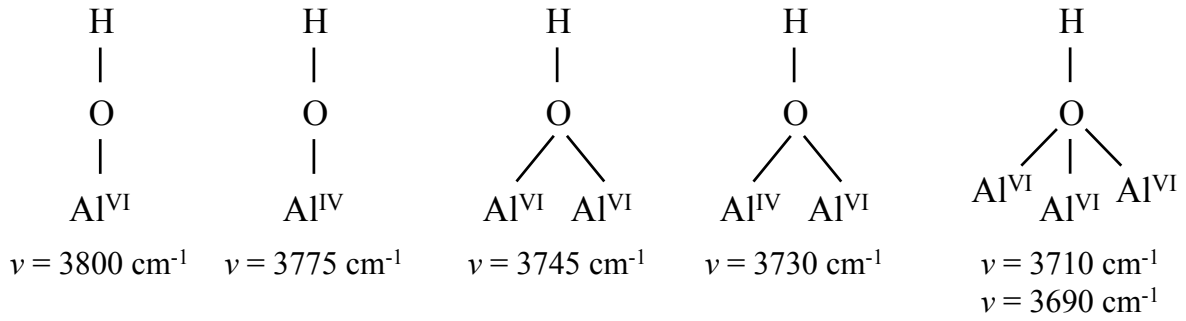

Scheme 3.1. Possible hydroxyl groups present on the surface of pre-treated transition aluminas, and approximate vibration frequencies.

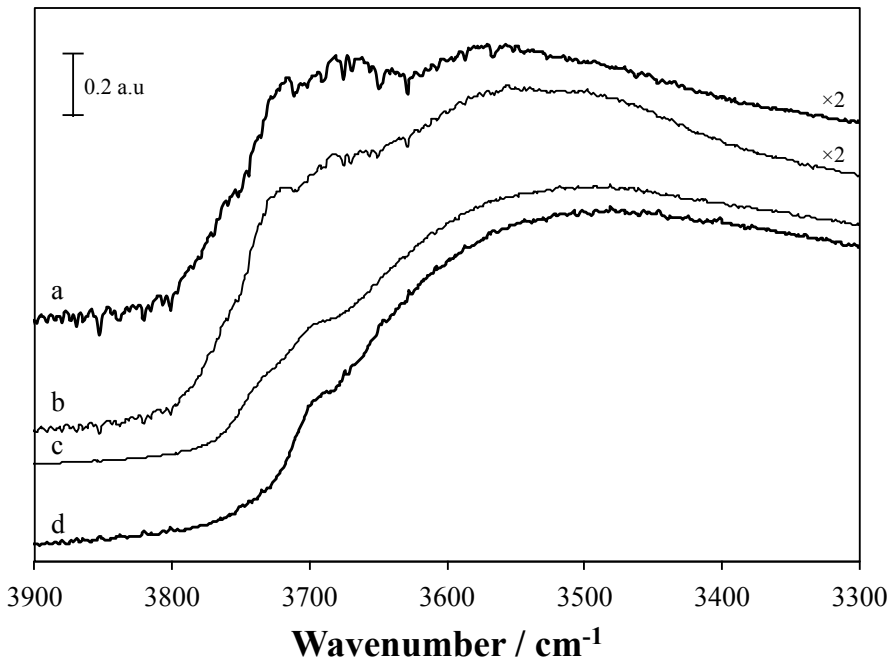

Figure 3.4. DRIFTS spectra of θ-Al_2O_3 at different pre-treatment temperatures: (d) 298 K, (c) 373 K, (b) 573 K and (a) 673 K. Spectra were recorded at the pre-treatment temperature, using KBr as background.

3.3.2.2 Acid-base characterisation

Most of the catalytic reactions described in section 3.1 are acid-base type reactions, or involve the participation of acid sites. Aditionally, dehydroxylation and the type of hydroxyl groups shown in section 3.3.2.1 are indicative of the presence of acid sites on γ-Al_2O_3 and θ-Al_2O_3. Therefore, it would be expected to observe such type of acid-base interactions in any adsorption process occurring on the surface of the alumina. Acidity measurements were performed to determine the types of sites present on the aluminas.

Acidity measurements using DRIFTS were performed with the adsorption of a probe molecule, as mentioned in chapter 2. Pyridine has been widely used as molecule to determine the type and strength of adsorption sites on catalysts (Busca, 1999; Digne *et al.*, 2004; Parry, 1963; Trasarti *et al.*, 2007). The absorption maxima of some ring vibrations of pyridine, in the range 1700 cm^{-1} to 1400 cm^{-1}, are highly sensitive with respect to the form of coordination of pyridine (Lercher *et al.*, 1996). Thus, the presence of Brønsted acid sites on the alumina can be inferred when bands for the pyridinium ion form, *e.g.*, at 1540 cm^{-1}, are present in the IR spectrum. Coordinately bonded pyridine, with characteristic bands at 1450 cm^{-1} or 1600 cm^{-1}, is indicative of Lewis acid sites. Both species are possible to be distinguished *via* IR (Parry, 1963).

Figure 3.5 shows the results of the adsorbed pyridine on γ- and θ-Al_2O_3 pre-treated at 673 K. As can be observed, negative bands appeared at 3736 cm^{-1} and 3696 cm^{-1}, corresponding to the bands described in section 3.3.2.1 for double-bridged and triple-bridged OH groups bound to Al. Hence, pyridine was observed to perturb those hydroxyls, likely to occur by H-bond interactions. These bands disappeared when the samples were heated to 423 K, indicating the weakness of those sites. A weak band was also present at 3060 cm^{-1}, corresponding to $\nu(=CH_2)$ of the benzene ring in pyridine. However, it is most interesting to observe the bands in the spectrum in the range 1400 – 1700 cm^{-1}, as information on the type of acid sites is contained here (Parry, 1963). Bands at 1612 cm^{-1}, 1590 cm^{-1}, 1573 cm^{-1}, 1488 cm^{-1}, 1449 cm^{-1} and 1442 cm^{-1} were noted in both γ- and θ-Al_2O_3. These bands correspond to hydrogen bonded and coordinated bonded pyridine, indicative of Lewis acid sites (Busca, 1999; Flego and Parker, 1999; Parry, 1963). When heated, both bands at 1449 cm^{-1} and 1442 cm^{-1} decayed. However, a more significant decay was observed in the band at 1442 cm^{-1}, indicating two different types of sites with different strength of adsorption. Similar behaviour was observed with the bands at 1612 cm^{-1} and 1590 cm^{-1}. Two kinds of

active sites on alumina have been previously described (Amenomiya *et al.*, 1967). The absence of a band around 1540 cm^{-1} or 1640 cm^{-1} indicated no pyridinium ions were formed, attributed to the lack of Brønsted acid sites on aluminas. It is known that aluminas have Lewis acidity but almost no Brønsted acidity (Flego and Parker, 1999; Knözinger and Ratnasamy, 1978). As can be observed, no major differences were present between the spectra of γ- and θ-Al_2O_3 at low temperature. However, once the sample was heated to 423 K, a more noticeable decay of the bands corresponding to Lewis acid sites on γ-Al_2O_3 as compared to θ-Al_2O_3 was observed. All bands disappeared when the sample was heated above 573 K in both samples.

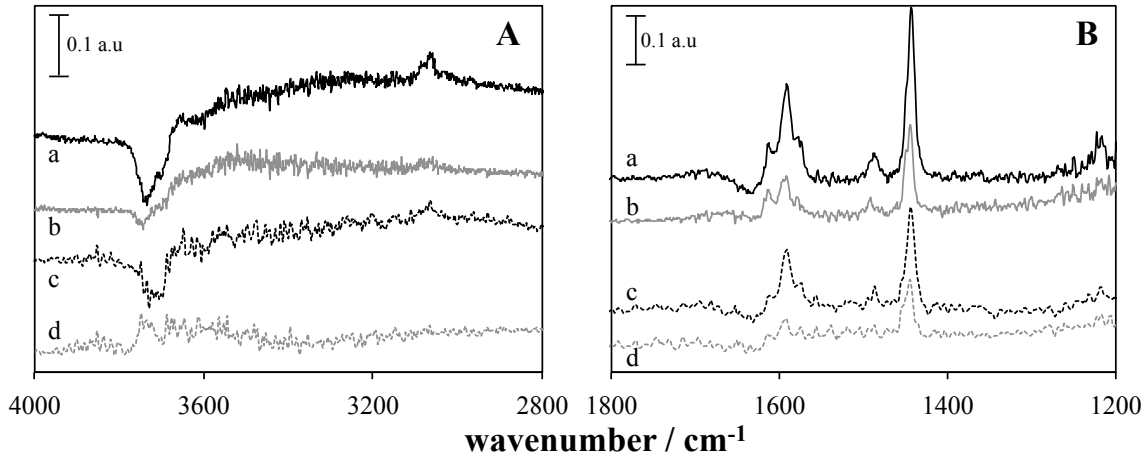

Figure 3.5. DRIFTS spectra of pyridine adsorbed at 313 (a, c) and 373 K (b, d) on pre-treated γ-Al_2O_3 (c, d) and θ-Al_2O_3 (a, b) at 673 K. All spectra were recorder at 298 K, using KBr as background.

The results above indicated the presence of Lewis acid sites on γ- and θ-Al_2O_3. Pyridine adsorption indicated a stronger interaction with θ-Al_2O_3, suggesting stronger acid sites. Considering the surface hydroxyls on the alumina, a perturbation of bridged hydroxyls upon pyridine adsorption was also noted. Additionally, the presence of two different types of acid sites was suggested from DRIFTS results. These results were in agreement with previous literature. The presence of different Lewis acid sites on γ-alumina has been shown by means of CO adsorption (Morterra *et al.*, 1994). The authors showed the presence of three different types of Lewis sites, in relation with the different adsorption bands observed and the coordinatively unsaturated Al species formed upon dehydroxylation. The use of CO has been used to study Lewis acidity in transition aluminas (della Gatta *et al.*, 1976). Morterra and co-workers showed that a reduction on the bridged hydroxyls was correlated with the increase on Lewis sites and enhanced CO adsorption. No Brønsted acid sites were observed

by means of pyridine adsorption. The presence of Brønsted sites was reported on γ-alumina upon NH_3 adsorption (Shen *et al.*, 1994). In that study, both Brønsted and Lewis acid sites were observed before neutralisation with potassium. Busca (1998) has indicated that ammonia is more easily protonated on metal oxide surfaces than pyridine. This might explain the unobserved Brønsted acidity. In turn, these results would indicate the weak nature of such adsorption sites.

3.4 Initial conclusions

Active aluminas are catalytically active material. They participate in multiple reactions, involving isomerisation, hydrogenation, dehydrogenation, oxidation or polymerisation. These active aluminas are formed by dehydroxylation of precursors. High surface areas and porosities are characteristic of those materials. γ- and θ-Al_2O_3 are typical examples of low-temperature activation and high-temperature activation aluminas. Surface properties are dependent on coordinatively unsaturated Al cations and O anions, Surface hydroxylation compensates the high surface energies related to these coordinatively unsaturated ions.

Characterisation of γ- and θ-Al_2O_3 adsorbents used in this work revealed the presence of physisorbed water and a highly hydroxylated surface. Upon heating, different types of surface hydroxyl groups were observed. Coordination of OH groups with unsaturated ions resulted in the presence of weak acid sites. Pyridine adsorption showed the presence of two types of Lewis acid sites. Those sites were postulated to be responsible for the adsorption of molecules. Brønsted acid sites were not shown in acid site measurements. However, the interactions between pyridine and hydroxyl groups suggested the presence of weak Brønsted sites, in line with previous literature for these aluminas

References

Amenomiya, Y., Chenier, J.H.B., Cvetanovic, R.J. (1967) Hydrogenation of olefins on alumina. I. Active sites for hydrogenation of ethylene. *J. Catal.*, 9, 28 – 37.

Andersson, J.M., Wallin, E., Chirita, V., Münger, E.P., Helmersson, U. (2005) *Ab initio* calculations on the effects of additives on alumina phase stability. *Phys. Rev. B*, 71, 014101.

Brouwer, D.M. (1962) The mechanism of double-bond isomerization of olefins on solid acids. *J. Catal.*, 1, 22 – 31.

Busca, G. (1998) Spectroscopic characterization of the acid properties of metal oxide catalysts. *Catal. Today*, 41, 191 – 206.

Busca, G. (1999) The surface acidity of solid oxides and its characterization by IR spectroscopic methods: an attempt at systematization. *Phys. Chem. Chem. Phys.*, 1, 723 – 736.

Cai, S.H., Rashkeev, S.N., Pantelides, S.T., Sohlberg, K. (2003) Phase transformation mechanism between γ- and θ-alumina. *Phys. Rev. B*, 67, 224104.

Cairati, L., Trifirò, F. (1983) SiO_2 and Al_2O_3 as oxidation catalysts of methanol. *J. Catal.*, 80, 25 – 30.

Chen, X., Liu, Y., Niu, G., Yang, Z., Bian, M., He, A. (2001) High temperature thermal stabilization of alumina modified by lanthanum species. *Appl. Catal. A-Gen.*, 205, 159 – 172.

Chen, Y., Yuan, S., Yin, H., Chen, Z., Mao, C. (2011) Kinetics of the reversible dimerization reaction of cyclohexanone over γ-Al_2O_3 catalyst. *Reac. Kinet. Mech. Cat.*, 102, 183 – 194.

Cheng, Z.X., Ponec, V. (1994) Selective isomerization of butene to iso-butene. *J. Catal.*, 148, 607 – 616.

Choudhary, V.R. (1977) Fluorine promoted catalysts: activity and surface properties. *Ind. Eng. Chem., Prod. Res. Dev.*, 16, 12 – 22.

Corado, A., Kiss, A., Knözinger, H., Müller, H.D. (1975) Catalytic isomerization of olefins on alumina. II. Catalyst deactivation and its effects on the mechanism. *J. Catal.*, 37, 68 – 80.

Corma, A., Fornés, V. (1990) Cracking of n-heptane on fluorinated γ-alumina catalysts in the presence of hydrogen. *Appl. Catal.*, 61, 175 – 185.

Della Gatta, G., Fubini, B., Ghiotti, G., Morterra, C. (1976) The chemisorption of carbon monoxide on various transition aluminas. *J. Catal.*, 43, 90 – 98.

Digne, M, Sautet, P., Raybaud, P., Euzen, P., Toulhoat, H. (2002) Hydroxyl groups on γ-alumina surfaces: A DFT study. *J. Catal.*, 211, 1 – 5.

Digne, M., Sautet, P., Raybaud, P., Euzen, P., Toulhoat, H. (2004) Use of DFT to achieve a rational understanding of acid-base properties of γ-alumina surfaces. *J. Catal.*, 226, 54 – 68.

Flego, C., Parker, W.O. (1999) Characterization of γ-alumina and borated alumina catalysts. *Appl. Catal. A-Gen.*, 185, 137 – 152.

Gerberich, H.R., Hall, W.K. (1966) Studies of the hydrogen held by solids. IX. The hydroxyls groups of alumina and silica-alumina as sites for the isomerization of butene. *J. Catal.*, 5, 99 – 110.

Guisnet, M., Lemberton, J.L., Perot, G., Maurel, R. (1977) Catalytic isomerization of ethylenic hydrocarbons. XIV. Effect of drying and reaction temperature on the isomerization of deuterated butenes over alumina. *J. Catal.*, 48, 166 – 176.

Haag, W.O., Pines, H. (1960) Alumina: catalyst and support. III. The kinetics and mechanisms of olefin isomerization. *J. Am. Chem. Soc.*, 82, 2488 – 2494.

Holm, V.C.F., Clark, A. (1963) Catalytic properties of fluorine-promoted alumina. *Ind. Eng. Chem., Prod. Res. Dev.*, 2, 38 – 39.

Ionescu, A., Allouche, A., Aycard, J.P., Rajzmann, M. (2002) Study of γ-Al_2O_3 surface reactivity: adsorption of water and hydrogen sulfide on octahedral aluminum sites. *J. Phys. Chem. B*, 106, 9359 – 9366.

John, C.S., Scurrell, M.S. (1977) Catalytic properties of aluminas for reactions of hydrocarbons and alcohols. In: Kemball, C. (ed.). *Catalysis: volume 1*. Chemical Society, London, pp. 136 – 167.

Khaleel, A., Shehadi, I., Al-Marzouqi, A. (2011) Catalytic conversion of chloromethane to methanol and dimethyl ether over mesoporous γ-Al_2O_3. *Fuel Process. Technol.*, 92, 1783 – 1789.

Knözinger, H., Ratnasamy, P. (1978) Catalytic aluminas: surface models and characterization of surface sites. *Catal. Rev.-Sci. Eng.*, 17, 31 – 70.

Lercher, J.A., Gründling, C., Eder-Mirth, G. (1996) Infrared studies of the surface acidity of oxides and zeolites using adsorbed probe molecules. *Catal. Today*, 27, 353 – 376.

Lippens, B.C., de Boer, J.H. (1964) Study of phase transformations during catalination of aluminum hydroxydes by selected area electron diffraction. *Acta Crystallogr.*, 17, 1312 – 1321.

Lippens, B.C., Steggerda, J.J. (1970) Active alumina. In: *Physical and chemical aspects in adsorption and catalysis.* Linsen, B., Fortuin J.M.H. (Eds), Academic Press, London, 171 – 211.

Lunsford, J.H., Zingery, L.W., Rosynek, M.P. (1975) Exposed aluminum ions as active sites on γ-alumina. *J. Catal.*, 38, 179 – 188.

Medema, J. (1975) Isomerization of butane over alumina. *J. Catal.*, 37, 91 – 100.

Mo, S.D., Ching, W.Y. (1998) Electronic and optical properties of θ-Al_2O_3 and comparison to α-Al_2O_3. *Phys. Rev. B*, 57, 15219 – 15228.

Morterra, C., Magnacca, G. (1996) A case study: surface chemistry and surface structure of catalytic aluminas, as studied by vibrational spectroscopy of adsorbed species. *Catal. Today*, 27, 497 – 532.

Paglia, G, Rohl, A.L., Buckley, C.E., Gale, J.D. (2001) A computational investigation of the structure of κ-alumina using interatomic potentials. *J. Mater. Chem.*, 11, 3310 – 3316.

Paglia, G., Buckley, C.E., Rohl, A.L., Hunter, B.A., Hart, R.D., Hanna, J.V., Byrne, L.T. (2003) Tetragonal structure model for boehmite-derived γ-alumina. *Phys. Rev. B*, 68, 144110.

Parry, E.P. (1963) An infrared study of pyridine adsorbed on acidic solids. Characterization of surface acidity. *J. Catal.*, 2, 371 – 379.

Pecharromán, C., Sobrados, I., Iglesias, J.E., González-Carreño, T., Sanz, J. (1999) Thermal evolution of transitional aluminas followed by NMR and IR spectroscopies. *J. Phys. Chem. B*, 103, 6160 – 6170.

Piéplu, A., Saur, O., Lavalley, J.C., Legendre, O., Nédez, C. (1998) Claus catalysis and H_2S selective oxidation. *Catal. Rev.-Sci. Eng.*, 40, 409 – 450.

Pines, H., Haag, W.O. (1960) Alumina: catalyst and support. I. alumina, its intrinsic acidity and catalytic activity. *J. Am Chem. Soc.*, 82, 2471 – 2483.

Schoen, R., Roberson, C.E. (1970) Structures of aluminum hydroxide and geochemical impications. *Am. Min.*, 55, 43 – 77.

Schüth, F., Unger, K. (2008) Preparation of solid catalysts: precipitation and coprecipitation. In: Ertl, G., Knözinger, H., Weitkamp, J. (eds.). *Handbook of heterogenous catalysis.* Wiley-VCH, Weinheim, pp. 72 – 86.

Shen, J., Cortright, R.D., Chen, Y., Dumesic, J.A. (1994) Microcalorimetric and infrared spectroscopic studies of γ-Al_2O_3 modified by basic metal oxides. *J. Phys. Chem.*, 98, 8067 – 8073.

Trasarti, A.F., Marchi, A.J., Apesteguía, C.R. (2007) Design of catalyst systems for the one-pot synthesis of menthols from citral. *J. Catal.*, 247, 155 – 165.

Trueba, M., Trasatti, S.P. (2005) γ-Al_2O_3 as a support for catalysts: a review of fundamental aspects. *Eur. J. Inorg. Chem.*, 2005, 3393 – 3403.

Tsyganenko, A.A., Filimonov, V.N. (1972) Infrared spectra of surface hydroxyl groups and crystalline structure of oxides. *Spectrosc. Lett.*, 5, 477 – 487.

Van Cauwelaert, F.H., Hall, W.K. (1970) Studies of the hydrogen held by solids. Part 17-The ortho-para H_2 conversion and H_2-D_2 exchange reactions over a transition alumina. *Trans. Faraday Soc.*, 66, 454 – 468.

Wolverton, C., Haas, K.C. (2000) Phase stability and structure of spinel-based transition aluminas. *Phys. Rev. B*, 63, 024102.

Zhou, R., Snyder, R. (1991) Structures and transformation mechanisms of the η, γ and θ transition aluminas. *Acta Cryst.*, B47, 617 – 630.

Chapter 4:

Adsorption of 1-pentene on γ- and θ-Al_2O_3

4 Adsorption of 1-pentene on γ- and θ-Al_2O_3

In this part of the dissertation, detailed studies of the adsorption of a series of C_5 and C_6 unsaturated hydrocarbons on γ- and θ-Al_2O_3 are presented. This chapter focuses on the adsorption of 1-pentene and the use of novel NMR relaxometry techniques. Variables such as coverage, pre-treatment temperature, and co-adsorption with different species, were studied. Chapter 5 will present a more extensive study performed for all hydrocarbons, with a full comparison between adsorption techniques. This chapter will start with a brief introduction to the importance of unsaturated hydrocarbons, such as 1-pentene, in catalysis and the usefulness and choice of this system as a model for new adsorption techniques. NMR relaxometry methods are shown and their use demonstrated in this chapter. ^{13}C T_1 NMR relaxometry measurements were compared with IR spectroscopy and adsorption isotherms. It was possible to quantify the strength of adsorption and the geometry of interaction of 1-pentene, and correlate these findings with results obtained in more conventional techniques. The interactions of 1-pentene with the surface of γ- and θ-Al_2O_3 were related to the surface properties described in chapter 3.

4.1 Selection of adsorbate: Alkene chemistry

Alkenes are a very important class of materials in the chemical industry (Taylor and Gagan, 2002). They are widely used as monomers in polymer synthesis (Kuran, 2001) and are used as starting materials for industrial chemicals such as glycols (antifreeze), ethyl halide and ethyl alcohol. Olefin metathesis has been used on an industrial scale for several decades to convert non-functionalized alkenes into short chain C_3 valuable olefins, or from unsaturated C_5 to unsaturated C_4 and C_6 species (Lwin and Wachs, 2014).

The importance of the double-bond chemistry is paramount. The alkenes ethylene and propylene are the most important chemicals used in the petrochemical industry. About 18 million tonnes of ethylene and 11 million tonnes of propylene are produced annually in the US. These are employed in the production of polyethylene, polypropylene, styrene, ethylbenzene, ethylene dichloride, acrylonitrile and isopropanol (Pinnau and Toy, 1990), or aldehydes, such as butyric aldehyde (Olah and Molnar, 1995). In addition, alkene isomerisation is an atom economical process, useful in chemical transformations in molecules with different functional groups (Larsen and Grotjahn, 2010). Within the olefin family, pentenes are among the lightest, highest vapor pressure components in gasoline (Schmidt *et*

al., 2008). These species fall in between the C_4 and lighter gas phase olefins, and C_6 and heavier liquid gasoline components. Acyclic C_5 molecules provide a proxy for many industrially relevant catalysed reactions, such as hydrogenation or isomerisation (Corado *et al.*, 1975; Guisnet *et al.*, 1977; Hong *et al.*, 1993; Amenomiya *et al.*, 1967), or alkylation (Randolph, 1997; Schmidt *et al.*, 2008). C_5 disproportionation and cracking to ethene or further to produce hydrogen have also been studied (Miyaji *et al.*, 2013).

The choice of catalyst is crucial in the reactions described earlier. Understanding the interactions and adsorption of olefins on different materials is key in order to develop better technologies and improve catalytic processes. Related to reactivity, solid acid catalysts, such as silica-alumina materials or zeolites, play an important role in the hydrocarbon conversion processes in a modern refinery (Rigby and Frash, 1997). Isomerisation of pentenes (MacIver *et al.*, 1964; Oblad *et al*., 1947), butenes (Trombetta *et al.*, 1997) and other olefins (Haag and Pines, 1960) has been reported previously on aluminas. Additionally, separation processes in olefins are also of great importance. For example, olefin/paraffin separation is one of the most important processes in the petrochemical industry and conventional distillation methods are highly energy-intensive. The use of adsorbents, such as π-complexation agents (Son *et al.*, 2004) or zeolites (Narin *et al.*, 2014), has been developed.

Understanding the interactions of alkenes on heterogeneous catalysts is, hence, crucial in order to develop better processes. In the present work, 1-pentene was chosen as an exemplar alkene. Adsorption of 1-pentene was studied on γ- and θ-Al_2O_3 as model acid catalysts. Different pre-treatment temperatures and coverages were used. In addition, co-adsorption was evaluated. The influence of co-adsorption on adsorption states and surface chemical processes was also investigated in order to understand the mechanisms on the surface. The presence of a co-adsorbate allows us to consider how the interaction of the alkene with the active surface sites might be modified during a catalytic reaction where products and solvents are present alongside the reactant. 1-pentene / CO co-adsorbed was used as a model to better understand the mechanisms taking place on 1-pentene adsorption on alumina. For example, in selective hydrogenation of an alkyne/alkene mixture to alkenes, CO is added to increase the selectivity of the catalyst reducing the yield of the alkane (Moses et al., 1983). Reaction of hydrocarbons on solid-state catalysts leads to fast deactivation because of coke formation. One of the major goals of the petrochemical industry is to overcome or to inhibit coking processes (Garbowski and Primet, 1985). The adsorption of cyclohexane and benzene was

considered as a model system for coke studies. Finally, the adsorption of 2-butyne has been chosen to determine the relative strengths of triple *vs.* double-bond interaction, in relation with chemoselective catalytic reactions (Borodziński and Bond, 2006).

4.2 Experimental materials and methods

4.2.1 Materials

γ-Al_2O_3 (BET surface area 190 m^2 g^{-1}, BJH pore volume of 0.70 cm^3 g^{-1}) and θ-Al_2O_3 (BET surface area 120 m^2 g^{-1}, BJH pore volume 0.57 cm^3 g^{-1}) were provided by Johnson Matthey as trilobes (diameter = 1 mm, length = 10 ± 2 mm) and crushed to particles of < 150 μm for adsorption experiments, unless stated otherwise. 1-pentene (98 %), benzene (99 %), 2-butyne (99 %) and cyclohexane (99 %) were used in co-adsorption experiments. All the hydrocarbons were obtained from Sigma-Aldrich at the stated purities. CO (99 %, < 5 ppm H_2O) and He (99.996 %) were supplied from Air Liquide and used without further purification.

4.2.2 ^{13}C T_1 NMR relaxometry

NMR experiments were performed on a Bruker wide bore DMX spectrometer with a vertical bore 7.0 T superconducting magnet operating at ^{13}C frequency of 75.5 MHz. T_1 relaxation properties of both bulk liquid and adsorbed hydrocarbons were measured using the standard inversion-recovery pulse sequence (**Figure 2.17**), with signal acquired in the presence of ^1H broad band decoupling. T_1 values were determined by fitting a single-component exponential recovery function to the data. Due to the limited homogeneity of the applied radio frequency magnetic field, it was necessary to acquire the ^{13}C spectral information in two separate experiments spanning chemical shift ranges of 0 – 100 ppm and 100 – 200 ppm. All experiments were performed at 293 K, unless stated otherwise, and spectra were referenced to tetramethylsilane (TMS). The errors associated with fitting the bulk $T_{1,bulk}$ relaxation times were all within ± 2 %, whilst the errors associated with fitting the adsorbed $T_{1,ads}$ relaxation times were all within ± 5 %. Therefore, the total error on the $T_{1,ads}/T_{1,bulk}$ ratios are considered to be less than ± 7 %. The measurements with 1-pentene were repeated several times on fresh samples and found to be consistent. The repeat data fell within the error bars quoted here.

1-pentene single-component adsorption and co-adsorption onto the aluminas was performed *via* the glass vacuum line (Soham Scientific Ltd.), described in section 2.2.1.1. A glass basket containing approximately 3 g of Al_2O_3 trilobes was attached to the vacuum line and

evacuated to a pressure < 10^{-2} mbar at room temperature, unless stated otherwise. The liquid hydrocarbon was degassed via several freeze-thaw-pump cycles and admitted to the vacuum line in the gas-phase at a known pressure. The sample basket was cooled using liquid nitrogen to condense the hydrocarbon onto the alumina surface. Adsorption was confirmed by a corresponding reduction in pressure in the vacuum line. Subsequent dosing of other species followed in multicomponent experiments, employing the same procedure. When all species were dosed, the basket was then flame sealed. Measurements were also performed on individual liquid species in order to obtain $T_{1,bulk}$. In that case, the hydrocarbons were dosed in empty glass baskets as received. Co-adsorption experiments were performed on θ-Al_2O_3. For cyclohexane and benzene, adsorption of 0.5 ML of 1-pentene was performed after 0.9 ML of the co-adsorbate was dosed on the alumina. In the case of 1-pentene and CO, and 1-pentene and 2-butyne, 0.5 ML of 1-pentene was adsorbed, followed by 0.5 ML of the co-adsorbate, and *vice versa*. A $T_{1,bulk}$ relaxation time for CO in the gas phase could not be measured due to the low ^{13}C density at atmospheric pressure. Consequently, the $T_{1,ads}/T_{1,bulk}$ ratio of the physisorbed CO was not obtained.

4.2.2.1 Surface coverage

Surface coverages were calculated assuming a uniform distribution of the hydrocarbon, estimating the surface area occupied by an individual molecule of 1-pentene (and 2-butyne) from the excluded molecular area of *n*-pentane (4.2×10^{-19} m^2). The excluded area of cyclohexane (4.7×10^{-19} m^2) (Webster *et al.*, 1998) was used to estimate benzene and cyclohexane surface coverages, while data for *n*-pentane was used to estimate 2-butyne behaviour during co-adsorption experiments. For example, 3.5 g of γ-Al_2O_3 has a total surface area of 665 m^2 and can therefore accommodate 1.58×10^{21} molecules of *n*-pentane, equivalent to 2.6×10^{-3} moles. Therefore, in order to obtain a theoretical coverage approximating but not exceeding 1 monolayer (ML), approximately 2×10^{-3} moles of the C_5 species were introduced into the alumina trilobes. Equivalent calculations were performed in order to determine the pressure required for θ-Al_2O_3, for lower surface coverages (Section 4.3.3.1).

4.2.3 Volumetric adsorption isotherms

Adsorption isotherms were obtained using the gas adsorption manometry or volumetric method (Rouquerol *et al.*, 1999) at three different temperatures: 273, 285.5 and 298 K. Only

298 and 313 K were employed during adsorption of cyclohexene due to limited vaporisation of adsorbate. Controlled adsorption measurements were performed in the same glass manifold described in section 2.2.1.1 and used for the ^{13}C NMR sample preparation. Approximately 2 g of alumina trilobes were placed in a glass basket (Soham Scientific). The sample was evacuated to $< 1 \times 10^{-2}$ mbar at 303 K for 1 h. The hydrocarbon was purified following three freeze-thaw-pump cycles. Aliquots of the hydrocarbon were then dosed into the manifold. A known pressure of hydrocarbon was admitted into the glass basket. The pressure drop was recorded until no further change was observed, when equilibrium was assumed to be reached. Successive amounts of hydrocarbon were admitted until saturation. Differential as well as cumulative hydrocarbon adsorption was obtained as a function of increasing equilibrium pressure. Blank experiments were performed with an empty basket. Ideal gas behaviour was assumed in all cases.

4.2.4 FTIR adsorption/desorption

In-situ Diffuse Reflectance Infrared Fourier Transform Spectroscopy (DRIFTS) measurements on the adsorption of 1-pentene at 298 K were carried out on a Nicolet Nexus 670 FTIR (Thermo Scientific) equipped with an MCT detector. A spectral resolution of 2 cm^{-1} and 64 scans were used. The aluminas were pre-heated at 393 and 673 K for 1 h under 40 cm^3 min^{-1} He flow in a reaction chamber (Praying Mantis, Harrick), and then cooled to 298 K. 5.0 ± 0.1 μL of adsorbate were then injected *via* a custom made heated t-port septum sealed. Adsorption-desorption of hydrocarbon was monitored with subsequent spectra every 40 s intervals. KBr was employed as spectral background.

4.3 Results

The adsorption of 1-pentene on γ- and θ-Al_2O_3 was studied by means of infrared spectroscopy, adsorption isotherms and ^{13}C T_1 NMR relaxometry. The type and strength of interaction were examined. Other factors influencing the adsorption of 1-pentene such as the pre-adsorption temperature of the alumina, adsorbate coverage as well as co-adsorption with other molecules were studied with NMR relaxometry.

4.3.1 Infrared spectroscopy

In this section, the adsorption of 1-pentene was studied *via* IR spectroscopy. Interactions of 1-pentene with the surface were examined in terms of the different bands present. The bands

indicated the interactions present between the adsorbate and certain surface sites on the alumina. Additionally, the strength of interaction could be indirectly inferred from the evolution with time of the bands indicative of surface adsorption. **Figure 4.1** shows the infrared difference spectra of the adsorption of 1-pentene at 298 K on θ-Al_2O_3 pre-treated at 393 and 673 K. The spectra have been subtracted from that of the pre-treated alumina to show the peaks only related to adsorption of the hydrocarbons. Interaction bands with their respective assignment are shown in **Table 4.1**. Bands present are indicative of interactions with the surface, and the presence of the olefin group. Thus, in the OH stretching region, negative bands appeared at 3735 cm^{-1}, 3715 cm^{-1}, and 3695 cm^{-1}, and a positive band was observed at 3631 cm^{-1}. These bands were related to the types of hydroxyl groups present on the surface of the alumina, as described in section 3.3.1. According to the assignment of Knözinger and Ratnasamy (1978), these bands have been assigned to double-bridged and tripled bridged hydroxyls bound to Al^{VI}. Hence, adsorption of 1-pentene occurred on double and triple-bridged OH coordinated with Al^{VI}, showing an increase in the presence of bulk OH. The presence of these negative bands has been observed previously in the adsorption of butane isomers at room temperature on γ-Al_2O_3 (Trombetta *et al.*, 1997), or of 1-pentene over zeolites (Föttinger *et al.*, 2003). They were attributed to molecular interactions of the olefins with the surface hydroxyl groups, by hydrogen bonding of the π-orbital of the double bond with the H atoms of the hydroxyl groups. All bands disappeared within 5 min of purging with He, indicative of the reversible adsorption-desorption of the olefin from the surface OH.

Table 4.1. Summary of the observed IR bands for the adsorption of 1-pentene on θ-Al_2O_3. The type of vibration, the position in wavenumbers (cm^{-1}), and the assignment to a corresponding bond are shown.

bond vibration	wavenumber / cm^{-1}	assignment
O-H stretch	3735	double-bridged OH (II)
	3715	triple-bridged OH (II)
	3695	
	3631	bulk OH
C-H stretch	3080	$\nu(=CH_2)_{as}$ [a]
	2967	$\nu(CH_3)$ and $\nu(CH_2)$
	2933	
	2879	
overtone	1830	$2w(CH_2\text{-})$
C-C stretch	1645 [b]	$\nu(C=C)$
	1636	
C-H bend	1456	$\delta(CH_2)$

a Symmetric stretching band at 3000 cm^{-1} not observed, probably embedded in C-H stretching band; b Appearing a shoulder

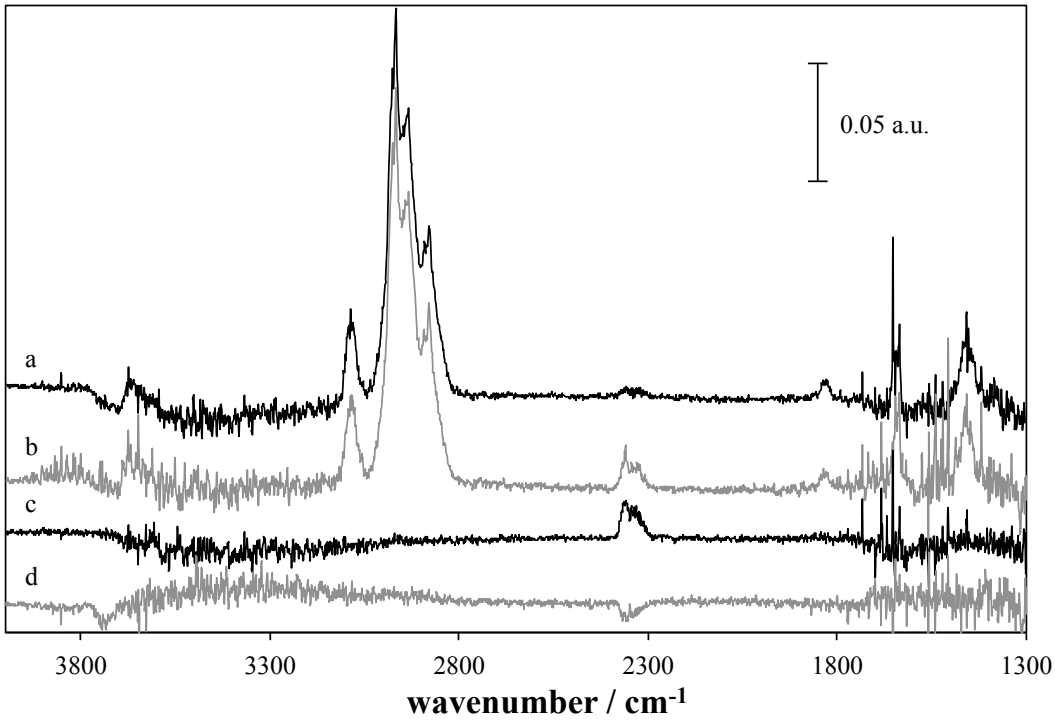

Figure 4.1. DRIFTS difference spectra for the adsorption of 1-pentene on θ-Al_2O_3. Initial desorption after signal saturation (a and b) and after 5 min He flow (c and d). The black lines represent samples pre-treated at 673 K, while the grey lines show the spectra on samples pre-treated at 393 K. Spectra of pre-treated alumina were used for subtraction.

Interaction of the hydrocarbons with the aluminas was also observed through the presence of other bands. C-H stretching bands, corresponding to $\nu(CH_3)$ and $\nu(CH_2)$, appeared at 2967 cm^{-1}, 2933 cm^{-1} and 2879 cm^{-1}during the adsorption of 1-pentene. A band at 3080 cm^{-1}, assigned to $\nu(=CH_2)_{as}$. A weak band around 3000 cm^{-1}, corresponding to $\nu(=CH_2)_s$ was not detected, as it was probably embedded within the $\nu(CH_3)$ band. A small band was observed at 1830 cm^{-1}; this band has been previously assigned to the overtone 2w(CH_2-). The band at 1636 cm^{-1}, with a shoulder at 1645 cm^{-1}, corresponded to ν(C=C). Finally, in the fingerprint region (<1500 cm^{-1}), a band at 1456 cm^{-1}, corresponding to $\delta(CH_2)$ scissors, was present. A slight shift was noted in the spectra for ν(C=C) with respect to the liquid phase spectrum, from 1643 cm^{-1} to 1636 cm^{-1}, respectively (Busca *et al.*, 1996, 1987; Crowder and Guan, 1995; SDBS, 1997). The interaction was too weak to allow breaking of the unsaturation (Busca *et al.*, 1987; Trombetta *et al.*, 1997). Similarly to the bands in the hydroxyl region, a considerable reduction was observed with purging after 5 min. The absence of other bands indicated 1-pentene did not react with the surface, at least to a sufficient extent to be detected *via* IR methods. However, previous studies have manifested the presence of strongly

adsorbed hydrocarbon, as well as yellow discoloration of the alumina after prolonged adsorption of butene isomers (Peri, 1961).

Temporal evolution of bands involved on adsorption was followed. **Figure 4.2** shows integrated areas corresponding to the sum of ν(OH) surface hydroxyl bands – excluding bulk ν(OH) band at 3631 cm^{-1} – as well as ν(C=C) and $\nu(=CH_2)$, for adsorption of 1-pentene on θ-Al_2O_3 pre-treated at 673 K. As can be seen, a strong relationship between the ν(OH) bands was observed with the decay of the ν(C=C) and $\nu(=CH_2)$ bands, as expected. Further analysis of the ν(C=C) band revealed some interesting results. Fitting the integrated area of the IR spectrum with an exponential decay of the type:

$$I = I_0 \exp\left(-t/\tau\right) \qquad (4.1)$$

resulted in the values summarised in **Table 4.2**. As can be seen, the time constant τ was higher for 1-pentene pre-treated at 673 K, as compared to 393 K. Values of $\tau = 2.3 \pm 0.1$ and $\tau = 2.0 \pm 0.1$ min were obtained on θ-Al_2O_3 pre-treated at 673 K and 393 K, respectively. These values might be considered as semi-quantitative, as the experiments were performed using diffuse-reflectance mode. However, the strong correlation between the OH and the C=C decays reinforced that the interaction was taking place through the unsaturation with the Brønsted sites on the aluminas. Additionally, it showed a weak relation with the pre-treatment temperature of the alumina.

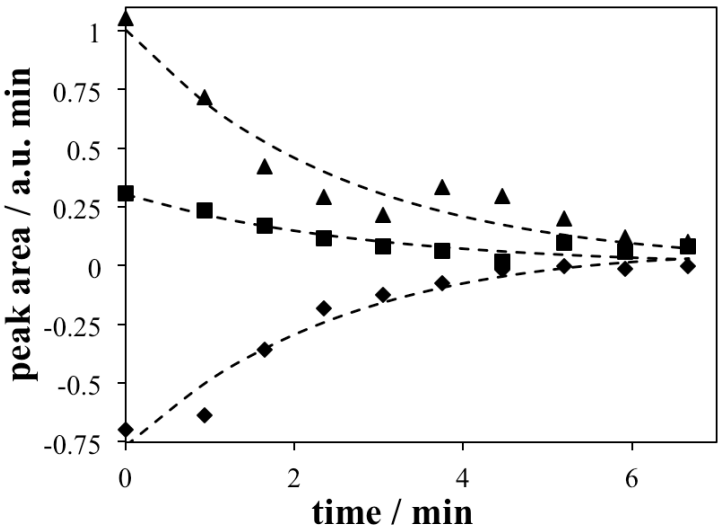

Figure 4.2. Integrated IR bands from desorption of 1-pentene with He at 298 K from pre-treated θ-Al_2O_3 at 673 K. The decay of ν(OH) at 3735-3700 cm^{-1} (diamonds), $\nu(=CH_2)$ at 3080 cm^{-1} (triangles) and ν(C=C) at 1636 cm^{-1} (squares) is shown. The time was considered zero after saturated spectra was reached. The lines show the exponential best fits to the experimental values.

Table 4.2. Parameters resulting from the fitting of an exponential decay to the integrated IR bands for the desorption of 1-pentene on θ-Al_2O_3. I_0 represents the initial peak area, while τ is the time constant for the decay of the signal in equation 4.1.

pre-treatment T / K	I_0 / -	τ / min
673	0.32 ± 0.02	2.3 ± 0.1
393	0.5 ± 0.1	2.0 ± 0.1

4.3.2 Adsorption isotherms

Adsorption isotherm results provide information on the uptake of 1-pentene on the surface on γ- and θ-Al_2O_3. Such information is key, as heats of adsorption dependent on coverage and type of alumina surface can be obtained.

Adsorption experiments were performed at 273, 285.5 and 293 K – unless stated otherwise – for increasing equilibrium pressures. **Figure 4.3** shows a typical adsorption isotherm curve, with the adsorption of 1-pentene on γ-Al_2O_3 at 273 K. As can be seen, a type II isotherm was observed, with an S-shape or sigmoidal curvature. It consisted of a low-pressure region concave to the pressure axis, a convex region at high pressure, and an intermediate linear portion (Brunauer, 1943). **Figure 4.4** shows the results of the adsorption of 1-pentene on γ- and θ-Al_2O_3 pre-treated under vacuum at 303 K. Results are only shown in the region of $P/P^{SAT}(T) < 0.35$, before capillary condensation occurred. The resulting data were fitted to a Tóth isotherm equation (equation 1.7). Here, the value of $v_{m,T}$ is substituted for v_{max}. The value of v_{max} represents the total adsorption capacity at high pressures and should not be misinterpreted with the monolayer coverage (Tóth *et al.*, 1999b). This equation has been applied for gas and liquid-phase adsorption (Tóth, 1962, 1971; Josssens *et al.*, 1978), for type I adsorption (Tóth *et al.*, 1999a, 1999b), but also multilayer adsorption (Khan *et al.*, 1997; Leitao *et al.*, 1992). Both Langmuir (equation 1.6) and Freundlich (equation 1.5) isotherms were fitted to the experimental results, but none of the curves obtained were satisfactory.

$$v = \frac{v_{max} k_T P}{\left[1 + \left(k_T P\right)^t\right]^{1/t}} \quad . \tag{4.2}$$

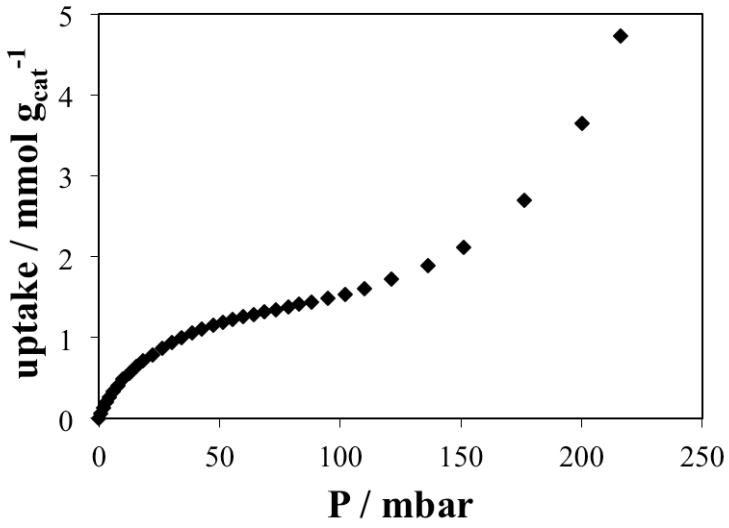

Figure 4.3. Adsorption isotherm of 1-pentene on γ-Al_2O_3 at 273 K.

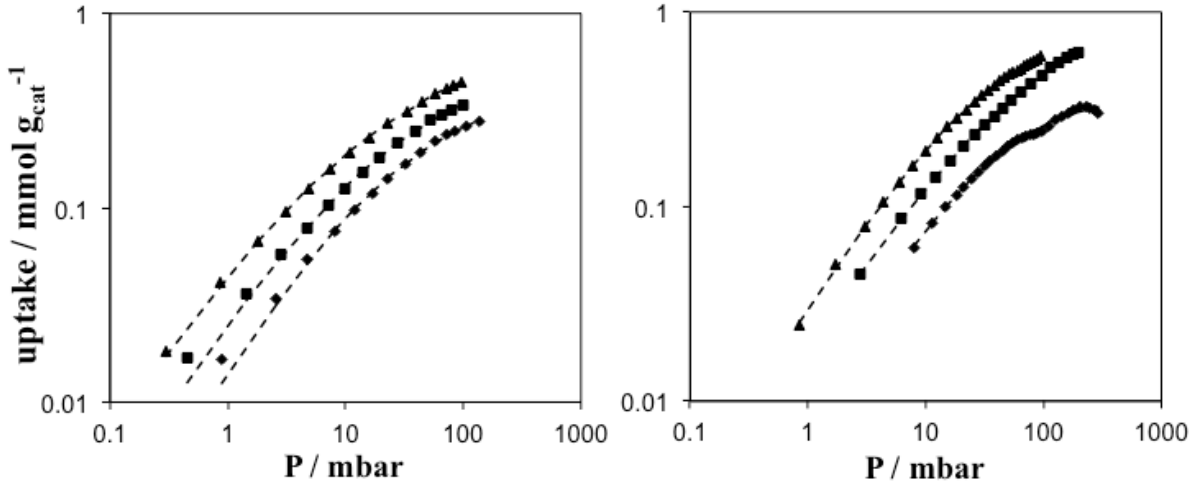

Figure 4.4. Uptake of 1-pentene on θ-Al_2O_3 (left) and γ-Al_2O_3 (right) as a function of equilibrium vapour pressure at 273 (triangles), 285.5 (squares) and 298 K (diamonds). The lines represent the fitted Tóth isotherm equation.

Table 4.3 shows the resulting Tóth isotherm parameters fitted, with their respective R^2 values. In addition, the fits to the experimental isotherms are shown in **Figure 4.4**. The quality of the experimental data and the presence of any outliers were checked following the method proposed by Hinz (2001), whereby v/P values were plotted against P or v. Considering the saturation adsorption values, v_{max}, a clear decreasing trend can be observed with increasing temperature on θ-Al_2O_3. On γ-Al_2O_3, v_{max} increased at the intermediate temperature. The decay in saturation adsorption values could be related to the type of adsorption sites. Saturation adsorption of 1-pentene was reduced at higher temperatures, indicating the energy of adsorption on vacant sites approached physisorption. Dividing the saturation adsorption values, v_{max}, at 273 K in **Table 4.3** by the specific surface area of each

alumina, specific saturation values of $(7.9 \pm 0.4) \times 10^{-6}$ and $(5.1 \pm 0.3) \times 10^{-6}$ mol m^{-2} were obtained on θ-Al_2O_3 and γ-Al_2O_3, respectively. These values indicated preferential adsorption of the hydrocarbon on θ-Al_2O_3.

Table 4.3. Tóth isotherm constants for the adsorption of 1-pentene on pre-treated γ- and θ-Al_2O_3.

surface	T / K	v_{max} / mmol g^{-1}_{cat}	$k_T \times 10^2$ / mbar^{-1}	t / -	R^2
θ-Al_2O_3	273	0.94 ± 0.05	9.4 ± 0.8	0.44 ± 0.02	0.99993
	285.5	0.66 ± 0.03	5.5 ± 0.4	0.53 ± 0.03	0.9997
	298	0.42 ± 0.02	3.8 ± 0.3	0.69 ± 0.03	0.9992
γ-Al_2O_3	273	0.98 ± 0.05	3.4 ± 0.2	0.71 ± 0.04	0.99992
	288	1.40 ± 0.07	1.6 ± 0.1	0.55 ± 0.03	0.9997
	298	0.39 ± 0.02	2.6 ± 0.2	0.89 ± 0.04	0.991

The Tóth constant, t, determines the difference between homogeneous adsorption and adsorption in a heterogeneous surface (Tóth, 1995). Compared with the ideal adsorption behaviour, the Tóth parameter shows that the coverage, θ:

$$\theta_{Tóth} > \theta_{ideal} \; if \; 0 < t < 1 \tag{4.3}$$

$$\theta_{Tóth} < \theta_{ideal} \; if \; t > 1 . \tag{4.4}$$

The parameter t in the Tóth equation also reflects the interactions and mobility/immobility of the molecules adsorbed (Tóth, 1995). Thus, values of $t < 1$ relate to heterogeneous surfaces where the adsorbent-adsorbate interactions are greater than those between the molecules adsorbed. On the contrary, the values $t > 1$ relate to the reverse situation. $t = 1$ can describe isotherms measured on heterogeneous surfaces on the conditions that adsorbent-adsorbate interactions and those between adsorbed molecules are approximately equal. As observed, preferential 1-pentene interactions with the alumina surface are suggested by the Tóth fitting.

4.3.2.1 Heat of adsorption

The fitted values of the adsorption constant k_T revealed important information on the interaction with the aluminas. The values of the adsorption constant k_T decreased with increasing temperature, in a similar fashion to the trends maked by v_{max}. These results have important implications on the description of the adsorption energy of each hydrocarbon on the alumina at infinite dilution. It is possible to obtain the energy of adsorption at zero coverage, $(-\Delta H_{ads})_{zero}$, with the use of the van't Hoff equation (Katz and Gray, 1980; Rouquerol *et al.*, 1999):

$$\left(-\Delta H_{ads}\right)_{zero} = R\frac{d\ln k_H}{d\left(1/T\right)}. \quad (4.5)$$

Knowing that the Tóth equation obeys Henry's equation (equation 1.4) – such that only adsorbate-surface interactions are examined – at low pressures (Foo and Hameed, 2010), it is easy to extract the following relation:

$$k_H = v_{sat}k\,. \quad (4.6)$$

Application of equations 4.5 and 4.6 rendered the results shown in **Table 4.4**. As can be seen, comparing the adsorption of the same molecule on both γ- and θ-Al_2O_3, the interaction strength of 1-pentene was slightly higher on θ-Al_2O_3.

Table 4.4. Isosteric heat of adsorption at zero coverage for 1-pentene adsorbed on γ- and θ-Al_2O_3, obtained after fitting the van't Hoff equation to the Henry adsorption constant values derived from the Tóth model.

surface	$(-\Delta H_{ads})_{zero}$ / kJ mol^{-1}	R^2
θ-Al_2O_3	46 ± 6	0.98
γ-Al_2O_3	31 ± 10	0.91

Considering the dependence of t with temperature, an equation has been proposed to describe this relationship (Do, 1998):

$$t = t_0 + \alpha\left(1 - \frac{T_0}{T}\right) \quad (4.7)$$

where t_0 is the Tóth constant at the reference temperature T_0 and α is a fitting parameter with influence in the calculation of heat of adsorption. If $\alpha > 0$, ($-\Delta H_{ads}$) decreases with increasing coverage, while the opposite is true in the case $\alpha < 0$. The former behaviour would be expected for an adsorption process on a heterogeneous surface, where the strongest sites are occupied first. Considering the increasing trend of t with temperature observed in **Table 4.3**, $\alpha > 0$ is expected for the adsorption of 1-pentene, in line with adsorption on heterogeneous alumina surfaces.

Isosteric heats of adsorption at various coverages were calculated from experimental isotherm data. The isosteric method applies the Clausius-Clapeyron equation, assuming the enthalpy and entropy of adsorption are not dependent on temperature (Clark, 1970; Pan *et al.*, 1998; Rouquerol *et al.*, 1999):

$$q_{st} = \left(-\Delta H_{ads}\right) = -R\left(\frac{\partial \ln P}{\partial\left(1/T\right)}\right)_v . \qquad (4.8)$$

The Tóth fitting parameters were used to interpolate experimental results to obtain values at a given uptake, *v*. **Figure 4.5** shows the isosteric heats of adsorption of 1-pentene on γ- and θ-Al_2O_3, as a function of surface coverage. Surface coverage was estimated from the saturation capacity values, v_{max}, at 273 K. Such selection accounted for most adsorption sites, hence contributing to a better estimation of the excluded area of each molecule. The adsorption strength of 1-pentene on θ-Al_2O_3 presented a somewhat decreasing value of the heat of adsorption up to 15% ML, after which the values start increasing. In contrast, a monotonic increase in the heat of adsorption was observed on γ-Al_2O_3. An increasing heat of adsorption with increasing coverage has been previously observed and attributed to predominant lateral interactions or limited surface interactions (Domínguez *et al.*, 2010; Aguilar-Armenta *et al.*, 2006; Sears, 2001; Siperstein *et al.*, 1999). The effect of temperature on vapour pressure and limited interactions with the surface was not discussed in this work.

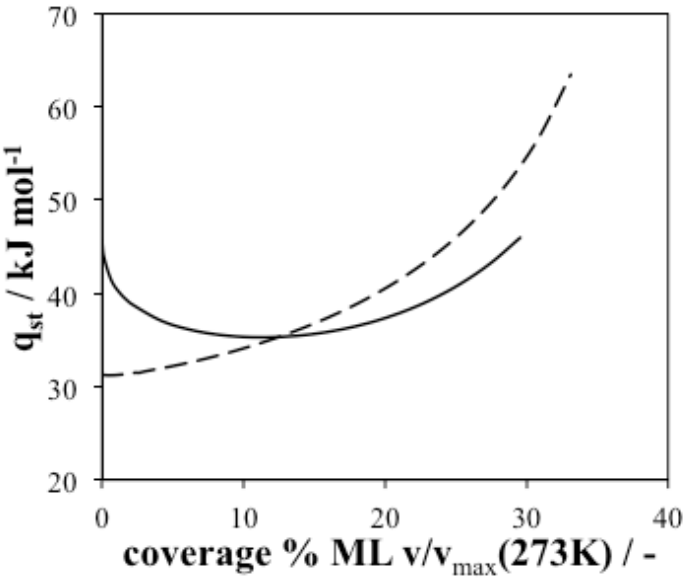

Figure 4.5. Isosteric heats of adsorption as a function of fractional coverage for 1-pentene adsorbed on θ-Al_2O_3 (-) and γ-Al_2O_3 (--) in the range 273 – 298 K obtained from the Tóth full range fit of the volumetric isotherms. The fractional coverage was calculated assuming 1 ML corresponded to the value of v_{max} obtained from fitting the Tóth isotherm to the experimental data 1-pentene at 273 K.

4.3.2.2 Multilayer adsorption

The Brunauer-Emmet-Teller (BET) equation was also used to describe the experimental results (equation 1.8). The usefulness of this equation lays in the possibility of obtaining the values of monolayer coverage in a type II isotherm, as well as an average energy of adsorption for the first layer. The experimental results were fitted in the range of $0.05 < P/P^{SAT}(T) < 0.35$. The upper range is approximate, as capillary condensation is well known to be affected by adsorption temperature (Russo *et al.*, 2008). Stronger adsorption sites would be covered at $P/P^{SAT}(T) < 0.05$, *vide infra*, and capillary condensation would start at $P/P^{SAT}(T) > 0.35$. **Figure 4.6** shows the results of the BET fitting to the adsorption of 1-pentene on γ- and θ-Al_2O_3. As can be observed, the intermediate linear portion of the isotherm was well described by this equation. **Table 4.5** shows the values of the BET model obtained after fitting the adsorption of 1-pentene on θ-Al_2O_3. As can be observed, the values of $v_{m\text{-}BET}$ decreased monotonically with increasing temperature, explained by a thermal expansion on the adsorbed layer. Also, the values of E_1 - E_L increased slightly with increasing temperature in both cases. As E_1 represents the average energy of adsorption for the first layer, the difference E_1 - E_L provided information on the types of adsorption sites. Such a result is in agreement with preferential adsorption on stronger sites, as occupation is relatively unaffected by temperature. Additionally, considering the monolayer coverages at 273 K, it was possible to determine the mean molecular cross-sectional of 1-pentene on both surfaces, summarised in **Table 4.6**. A value of 0.59 nm^2 was observed for 1-pentene on θ-Al_2O_3. This value is in line with the excluded areas of 0.42 nm^2 used during the coverage studies and higher than 0.35 nm^2 predicted for a liquid hexagonal packing of the molecules in the liquid (Russo *et al.*, 2008). The higher excluded area value on γ-Al_2O_3 was indicative of lower uptake, in line with the lower adsorption energies observed.

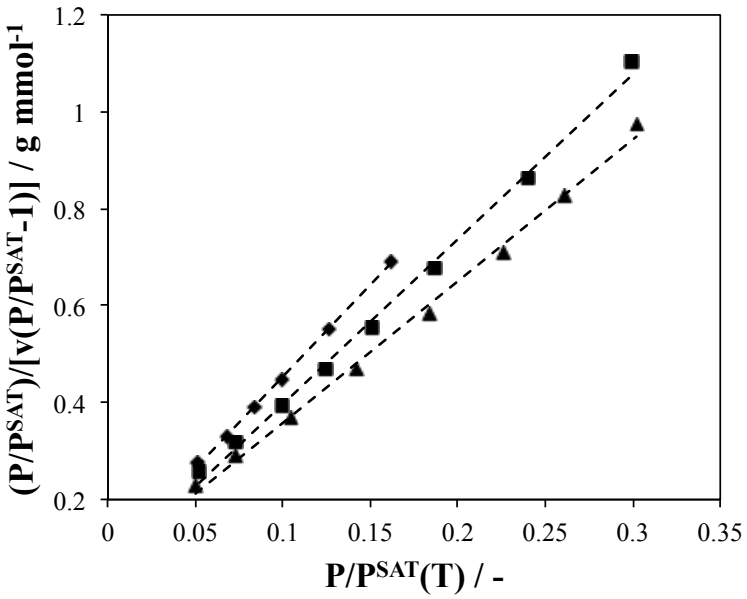

Figure 4.6. 1-pentene uptake as a function of equilibrium vapour pressure on θ-Al_2O_3 at 273 (triangles), 285.5 (squares) and 298 K (diamonds). The lines represent the fitted BET isotherm equation for $0.05 < P/P^{SAT}(T) < 0.3$.

Table 4.5. BET isotherm constants for the adsorption of 1-pentene on pre-treated γ- and θ-Al_2O_3, in the range $0.05 < P/P^{SAT}(T) < 0.30$, approximately.

surface	T / K	$v_{m\text{-}BET}$ / mmol g^{-1}_{cat}	E_1-E_L / kJ mol^{-1}
θ-Al_2O_3	273	0.34 ± 0.02	3.75 ± 0.02
	285.5	0.29 ± 0.02	4.22 ± 0.02
	298	0.26 ± 0.01	4.23 ± 0.01
γ-Al_2O_3	273	0.46 ± 0.01	3.25 ± 0.01
	288	0.47 ± 0.01	3.25 ± 0.02
	298	0.271 ± 0.003	3.900 ± 0.006

Table 4.6. Mean molecular cross sectional area, a_m, heat of liquefaction, E_L, and heat of adsorption for the first layer, E_1, derived from BET monolayer coverage, $v_{m\text{-}BET}$, and values of E_1 - E_L for 1-pentene adsorbed on γ- and θ-Al_2O_3.

surface	a_m / nm^2	E_L (298 K) / kJ mol^{-1}	E_1 (298 K) / kJ mol^{-1}
θ-Al_2O_3	0.59 ± 0.04	25.39	29.62 ± 0.01
γ-Al_2O_3	0.68 ± 0.03	25.39	28.64 ± 0.01

The calculation of a BET monolayer coverage differentiated between adsorption on the first layer, and multilayer adsorption in the adsorption isotherm. Hence, the Tóth equation was applied to the study of the first adsorbed layer (Tóth *et al.*, 1999b; Szekeres *et al.*, 2002). **Figure 4.7** shows the isosteric heats of adsorption after analysis of the experimental uptake values for $P/P^{SAT}(T) < 0.05$ with the Tóth equation and the Clausius-Clapeyron equation (equation 4.6). The general trends resembled those observed with the Tóth fit on the full adsorption range. It was possible to compare the coverage dependent adsorption energy values obtained with the first layer Tóth method (**Figure 4.7**) and E_1 from BET analysis (**Table 4.6**). An average difference of about -15% was observed, indicating a non-uniform energy distribution, assumed on the derivation of the BET equation.

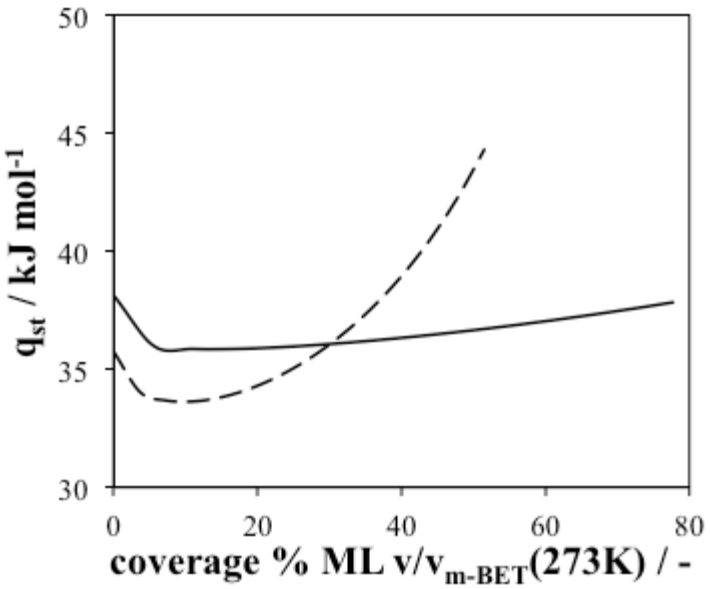

Figure 4.7. Isosteric heat of adsorption as a function of fractional coverage for 1-pentene adsorbed on θ-Al_2O_3 (-) and γ-Al_2O_3 (--) in the range 273 – 298 K, obtained from $P/P^{SAT}(T) < 0.05$ Tóth fit of the volumetric isotherms. The fractional coverage was calculated assuming 1 ML corresponded to the value of v_m obtained from the BET isotherm for each hydrocarbon at 273 K.

4.3.3 ^{13}C T_1 NMR relaxometry

NMR relaxometry was used to gain additional information on the adsorption of 1-pentene. **Figure 4.8** shows a typical NMR spectrum of 1-pentene adsorbed on alumina. In this case, a ^{13}C NMR spectrum of the adsorption of 0.5 ML 1-pentene on θ-Al_2O_3 is shown.

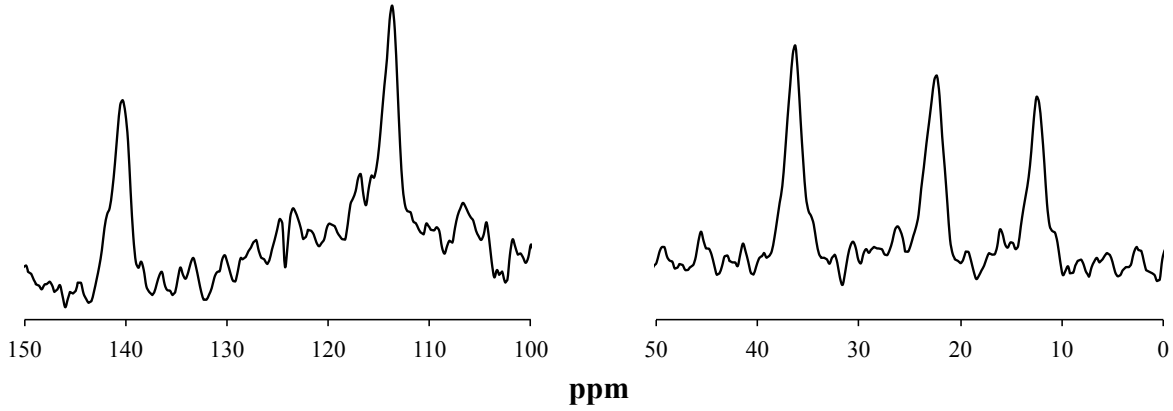

Figure 4.8. ^{13}C NMR spectra of the olefinic (left) and aliphatic (right) carbons of 0.5 ML 1-pentene adsorbed on θ-Al_2O_3. * Spectrum on the left presents a broad peak around 110 ppm, below C1, due to a coil background noise.

The measured $T_{1,ads}/T_{1,bulk}$ ratios for the individual carbon atoms within 1-pentene adsorbed on γ- and θ-Al_2O_3 are shown in **Figure 4.9**. Relative errors of 2% were derived for the calculation of $T_{1,bulk}$, while 5% error was observed for $T_{1,ads}$. Error bars were not included in the figures as they would not be distinguished. Only significant figures are presented in $T_{1,ads}/T_{1,bulk}$ ratios in the text. Carbons were numbered according to IUPAC nomenclature on 1-pentene and were identified on each spectrum according to their chemical shift. In all cases, the $T_{1,ads}/T_{1,bulk}$ ratios associated with olefinic carbons, *i.e.*, those atoms linked by unsaturated carbon-carbon double or triple bonds, are consistently lower than the $T_{1,ads}/T_{1,bulk}$ ratios associated with the aliphatic carbons (those linked by a saturated carbon-carbon single bond) in the same molecule. Consider adsorption on θ-Al_2O_3, (**Figure 4.9**, squares), as an example. The olefinic C1 and C2 carbons exhibit $T_{1,ads}/T_{1,bulk}$ ratios of 6.19×10^{-2} and 5.09×10^{-2}, respectively. These values are lower than for the aliphatic (C3, C4 and C5) carbon atoms where $T_{1,ads}/T_{1,bulk}$ ratios of 9.02×10^{-2}, 9.98×10^{-2}, and 15.89×10^{-2} are observed respectively. It can therefore be concluded that it is the olefinic carbon atoms that interact more strongly with the alumina surface. In contrast, C5 (the terminal aliphatic carbon) shows the weakest interaction. Differences are observed for the same coverages on both alumina surfaces. For example, C2 has a value of $T_{1,ads}/T_{1,b} = 10.53 \times 10^{-2}$ at 0.5 ML on γ-Al_2O_3, whereas for the same coverage the value is $T_{1,ads}/T_{1,b} = 5.09 \times 10^{-2}$ on θ-Al_2O_3. This difference indicates that 1-pentene interacts more strongly with θ-Al_2O_3 than with γ-Al_2O_3.

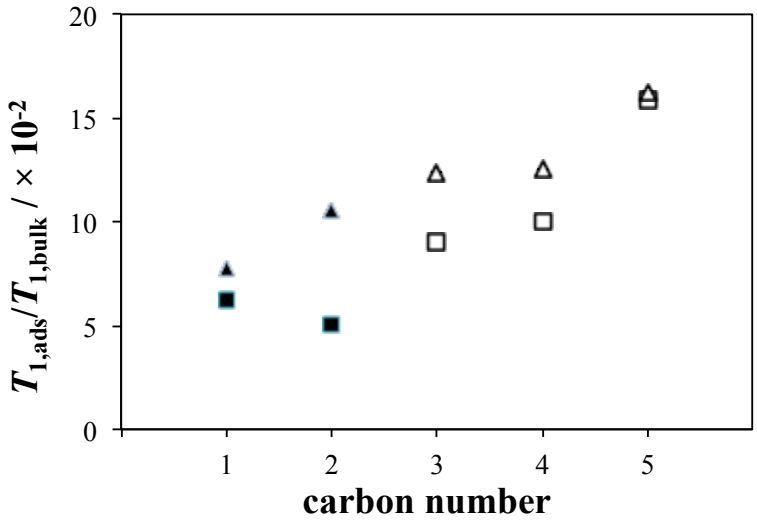

Figure 4.9. The ratio of surface to bulk relaxation times $T_{1,ads}/T_{1,bulk}$ for the individual carbon atoms in 1-pentene adsorbed on γ-Al_2O_3 (triangles) and θ-Al_2O_3 (squares) with a surface coverage of approximately 0.5 ML. In each case the solid symbols represent the olefinic carbons and the open symbols represent the aliphatic carbons.

4.3.3.1 Surface coverage

In order to investigate the influence of surface coverage on molecular configuration, the adsorption of 1-pentene on θ-Al_2O_3 has been further investigated at approximately 1 ML, 0.2 ML and 0.1 ML. **Figure 4.10** shows the $T_{1,ads}/T_{1,bulk}$ ratios determined from these samples. It is apparent that the overall strength of adsorption of 1-pentene decreases with increasing surface coverage. Consider, for instance, C5 where the $T_{1,ads}/T_{1,bulk}$ ratio changes from 7.5×10^{-2} at 0.1 ML to 18.9×10^{-2} at 1 ML. Examining the interacting double-bond in 1-pentene, taking the average of C1 and C2, $T_{1,ads}/T_{1,bulk}$ values of 10.1×10^{-2} at 1 ML, 5.6×10^{-2} at 0.5 ML, 3.8×10^{-2} at 0.2 ML and 3.0×10^{-2} at 0.1 ML are observed. Additional information about the adsorbate-adsorbent interaction is obtained by inspection of the olefinic carbons in **Figure 4.10**. In particular, the $T_{1,ads}/T_{1,bulk}$ ratio of the C2 carbon atom increases significantly as coverage increases from 0.2 ML to 1 ML, while the $T_{1,ads}/T_{1,bulk}$ ratio of C1 decreased gradually from 1 ML to 0.1 ML. This behaviour on C1 and C2 can be explained by the relative interaction of the olefinic bond. Thus, at 0.5 ML, $T_{1,ads}/T_{1,bulk} = 6.2 \times 10^{-2}$ for C1 and $T_{1,ads}/T_{1,bulk} = 5.1 \times 10^{-2}$ for C2, while at 0.1 ML, $T_{1,ads}/T_{1,bulk} = 2.7 \times 10^{-2}$ for C1 and $T_{1,ads}/T_{1,bulk} = 3.2 \times 10^{-2}$ for C2. A shift in the interacting carbon within the olefinic bond is observed with increasing coverage. These changes in interaction affected the overall geometry of the molecule. Overall, these results indicate that the nature of the interaction of

the carbon-carbon double bond with the adsorbent surface is coverage dependent. This decreasing energy with increasing surface coverage has been observed in adsorption of similar alkenes *via* TPD measurements (Miller *et al.*, 2013; Pawela-Crew and Madix, 1995).

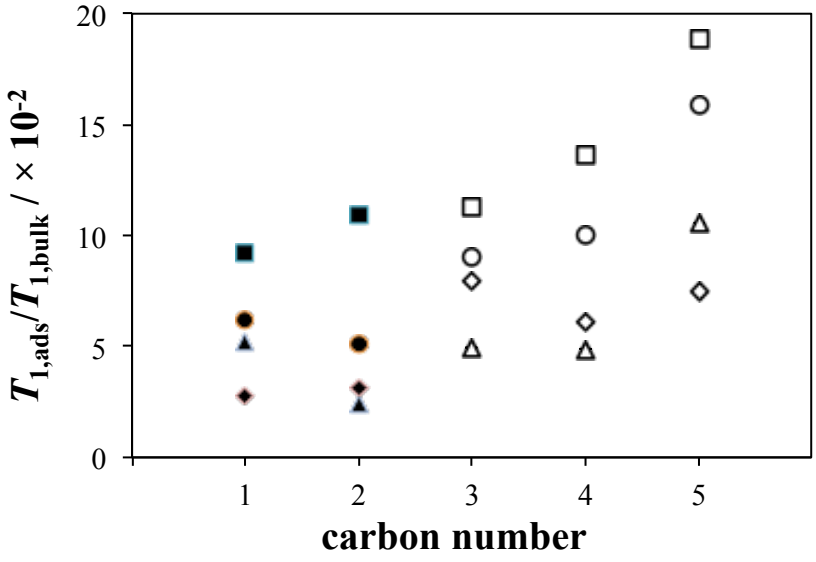

Figure 4.10. The ratio of surface to bulk relaxation times $T_{1,ads}/T_{1,bulk}$ for the individual carbon atoms in 1-pentene adsorbed on θ-Al_2O_3 with a surface coverage of approximately 1 ML (squares), 0.5 ML (circles), 0.2 ML (triangles) and 0.1 ML (diamonds). In each case the solid symbols represent the olefinic carbons and the open symbols represent the aliphatic carbons.

4.3.3.2 Temperature dependence on adsorption

Similarly to the effect of coverage upon adsorption of 1-pentene on θ-Al_2O_3, it is relevant to determine the effect of temperature on interaction strength and geometry of adsorption. **Figure 4.11** shows the NMR relaxometry results of 0.5 ML 1-pentene on θ-Al_2O_3 at 273 K, 283 K and 293 K. An increase in surface interaction can be observed with decreasing temperature. Thus, considering C5, $T_{1,ads}/T_{1,bulk} = 15.9 \times 10^{-2}$ at 293 K decreased to $T_{1,ads}/T_{1,bulk} = 9.9 \times 10^{-2}$ at 283 K and $T_{1,ads}/T_{1,bulk} = 8.4 \times 10^{-2}$ at 273 K. A more significant decrease in $T_{1,ads}/T_{1,bulk}$ values is observed in aliphatic carbons, as compared to the carbons in the olefinic bond. The average $T_{1,ads}/T_{1,bulk}$ values for the aliphatic carbons (C3 to C5) decayed from 11.6×10^{-2} at 293 K to 6.9×10^{-2} at 273 K. If the two olefinic carbons are considered, a reduction in $T_{1,ads}/T_{1,bulk}$ was observed from 5.6×10^{-2} at 293 K to 5.1×10^{-2} at 273 K. Finally, considering the interaction of the carbons within the double-bond, a change in the configuration of 1-pentene is inferred. At 293 K and 283 K, C2 showed the lowest

$T_{1,ads}/T_{1,bulk}$, while C1 showed the lowest $T_{1,ads}/T_{1,bulk}$ value at 273 K. This change in the carbon atom showing the strongest interaction was also observed for the case of single component adsorption at 0.1 ML coverage, in section 4.3.3.1. C1 presented the lowest $T_{1,ads}/T_{1,bulk}$ value for all carbons on θ-Al_2O_3 only at 273 K and 0.5 ML, and at 293 K and 0.1 ML. In summary, the results indicate that 1-pentene adsorption strength *via* the double-bond was only slightly affected by temperature, while the adsorption behaviour of the alkyl chain was significantly more influenced by temperature. These results are in agreement with the strongest interaction taking place *via* the double-bond, and an increase order in the arrangement of 1-pentene on θ-Al_2O_3 with decreasing temperature. These results might be indicative of presence of molecule-to-molecule interactions, as previously observed in adsorption isotherms of propane-propylene mixtures (Aguilar-Armenta *et al.*, 2006).

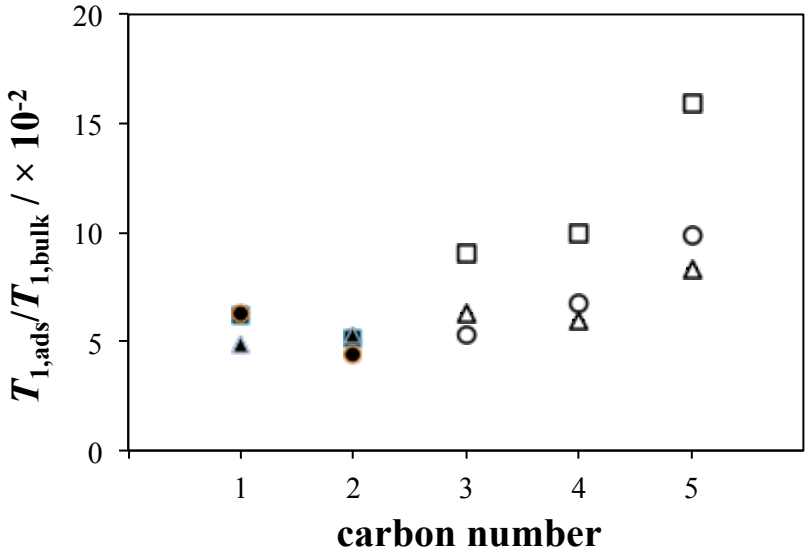

Figure 4.11. The ratio of surface to bulk relaxation times $T_{1,ads}/T_{1,bulk}$ for the individual carbon atoms in 1-pentene adsorbed on θ-Al_2O_3 with a surface coverage of approximately 0.5 ML at 293 K (squares), 283 K (circles), and 273 K (triangles). In each case the solid symbols represent the olefinic carbons and the open symbols represent the aliphatic carbons.

4.3.3.3 Surface pre-treatment

The effect of pre-treatment temperature on alumina surfaces has been widely reported in the literature (Liu and Truitt, 1997; Morterra and Magnacca, 1996; Trombetta *et al.*, 1997). The pre-treatment temperature can then affect adsorption of hydrocarbons on alumina. Hence, adsorption of 0.5 ML of 1-pentene was carried out on pre-treated θ-Al_2O_3 at 673 K under vacuum. **Figure 4.12** shows the ^{13}C NMR spectra of such experiment. As observed, in

addition to 1-pentene, NMR spectral information revealed the presence of *trans*-2-pentene *via* chemical shift analysis of the aliphatic C1 and C4 carbons. **Figure 4.13** shows the ^{13}C NMR spectra of *cis*- and *trans*-2-pentene adsorbed on θ-Al_2O_3 for comparison. **Table 4.7** shows the chemical shifts of the peaks observed in the experiment, and the values for single component *cis*-2-pentene and *trans*-2-pentene. **Figure 4.14** shows the $T_{1,ads}/T_{1,bulk}$ data of the adsorbed species observed in the spectra in **Figure 4.12**. Previous studies have reported isomerisation of *n*-butene to butane isomers on a variety of aluminas (Trombetta *et al*., 1997; Cheng and Ponec, 1994), as well as on 1-pentene and 2-pentenes (Oblad *et al.*, 1947). In this work, an approximate relative proportion 2:1 mol:mol 1-pentene to *trans*-2-pentene is inferred. According to $T_{1,ads}/T_{1,bulk}$ results, a strong adsorption of both molecules occurred. Studying 1-pentene, C2 presented the strongest interaction with the surface, with $T_{1,ads}/T_{1,bulk} = 1.9 \times 10^{-3}$. This value contrasts with the $T_{1,ads}/T_{1,bulk} = 5.1 \times 10^{-2}$ value previously observed for C2 on θ-Al_2O_3 pre-treated at room temperature (section 4.3.3.2). Comparing the $T_{1,ads}/T_{1,bulk}$ ratios of the olefinic region of 1-pentene with pre-treatment temperature of the alumina, $T_{1,ads}/T_{1,bulk} = 6.0 \times 10^{-3}$, at 673 K, and $T_{1,ads}/T_{1,bulk} = 5.6 \times 10^{-2}$, at room temperature, are obtained. Similarly, for the aliphatic chain, $T_{1,ads}/T_{1,bulk} = 1.8 \times 10^{-2}$, at 673 K, *vs*. $T_{1,ads}/T_{1,bulk} = 11.6 \times 10^{-2}$, at room temperature, are determined. Therefore, a considerably stronger interaction is inferred for the case of the pre-heated sample.

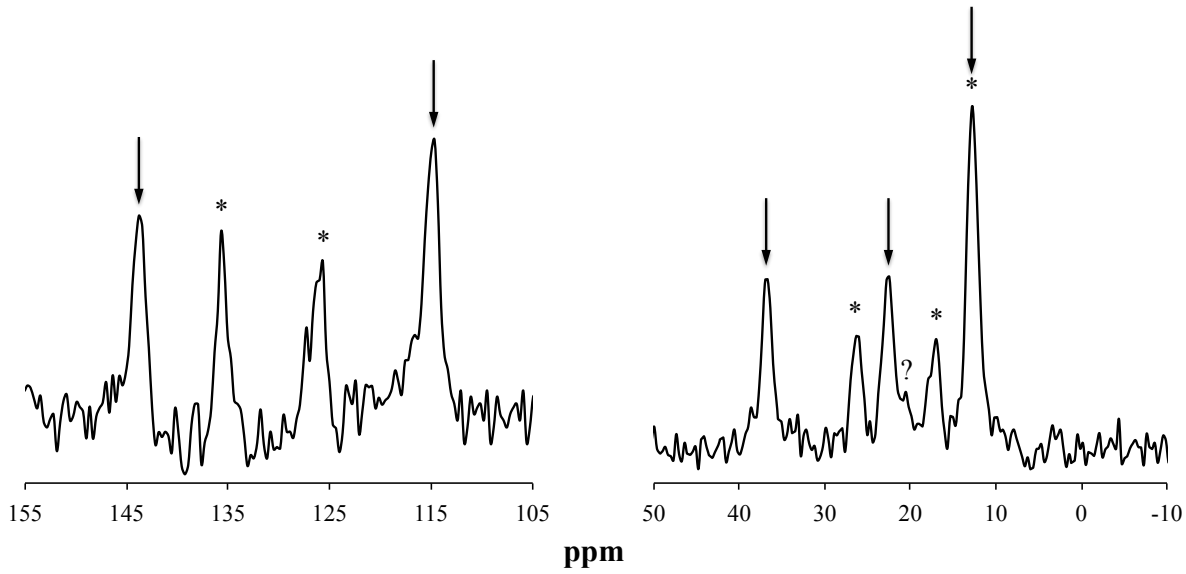

Figure 4.12. ^{13}C NMR spectra of the olefinic (left) and aliphatic (right) carbons present on pre-adsorbed 0.5 ML 1-pentene on θ-Al_2O_3 pre-treated at 673 K. Peaks marked with an arrow indicate the presence of 1-pentene, while peaks marked with an asterisk (*) denoted the presence of *trans*-2-pentene. The only peak of *cis*-2-pentene that would not overlap with the *trans* isomer or 1-pentene (at 20 ppm, denoted with "?") was not observed.

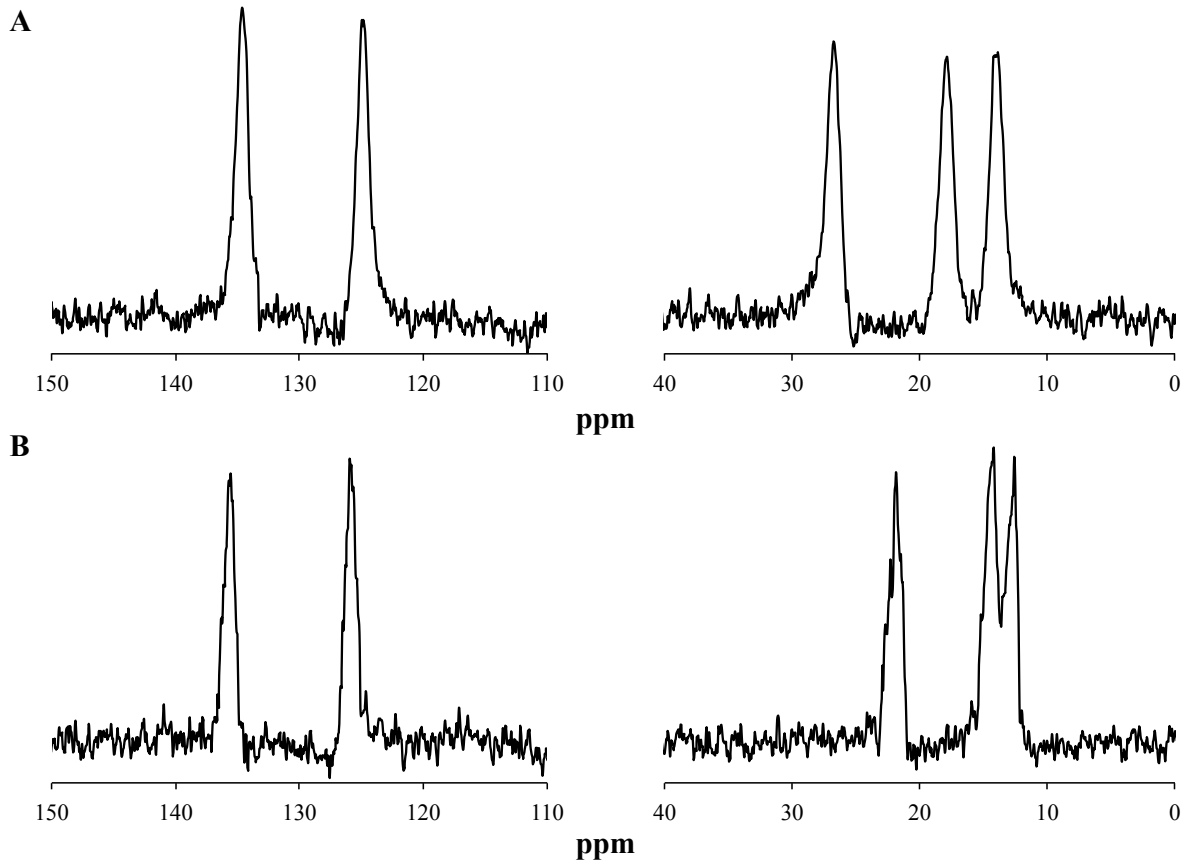

Figure 4.13. ^{13}C NMR spectra of the olefinic (left) and aliphatic (right) carbons of 1 ML coverage (A) *trans*-2-pentene and (B) *cis*-2-pentene adsorbed on θ-Al_2O_3.

Table 4.7. Resonances characteristic of isomerisation to 2-pentenes during adsorption of 1-pentene on θ-Al_2O_3 pre-treated at 673 K. Values on the table (in ppm), are denoted in **Figure 4.12** with an asterisk (*). A comparative with the values for single component *cis*-2-pentene and *trans*-2-pentene adsorption on θ-Al_2O_3 (**Figure 4.13**) is established.

carbon #	δ observed	*cis*-2-pentene	Δδ	*trans*-2-pentene	Δδ
1	17.14	-	-	17.90	0.76
2	126.0	123.13	-2.87	123.75	-2.25
3	135.4	132.57	-2.83	133.35	-2.05
4	26.1	20.25[a]	-5.85	25.80	-0.30
5	12.6	12.59 / 14.16	-0.01 / 1.56	14.02	1.42

[a]The resonance at 20 ppm would have marked inequivocally the presence of *cis*-2-pentene. Such peak was not observed in the ^{13}C NMR spectrum (marked with "?").

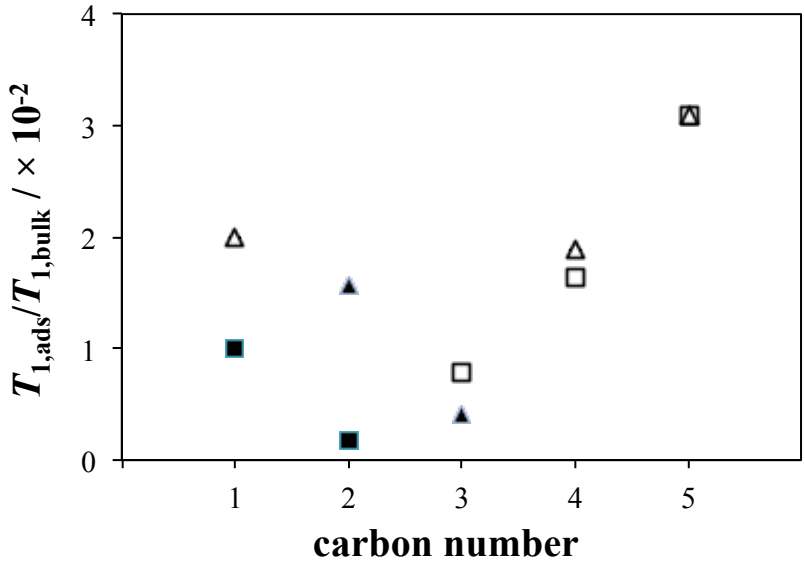

Figure 4.14. The ratio of surface to bulk relaxation times $T_{1,ads}/T_{1,bulk}$ for the individual carbon atoms observed on pre-heated θ-Al_2O_3 at 673 K after the adsorption of 0.5 ML 1-pentene. 1-pentene (squares), and *trans*-2-pentene (triangles) were identified *via* chemical shift. In each case the solid symbols represent the olefinic carbons and the open symbols represent the aliphatic carbons.

Isomerisation of 1-pentene to *trans*-2-pentene (no *cis*-2-pentene was detected) was shown to occur, in agreement with results shown earlier. The presence of exposed acid sites on pre-treated θ-Al_2O_3 at 673 K could be responsible of such reactivity. $T_{1,ads}/T_{1,bulk}$ values of individual carbon atoms in *trans*-2-pentene revealed a stronger interaction of olefinic carbons. In particular, C3 shows the strongest interaction, with $T_{1,ads}/T_{1,bulk} = 4.2 \times 10^{-3}$. Olefinic carbons show on average a $T_{1,ads}/T_{1,bulk} = 9.9 \times 10^{-3}$ *vs*. $T_{1,ads}/T_{1,bulk} = 2.3 \times 10^{-2}$ for aliphatic carbons. The relative strength of interaction can be interpreted as being due to the presence of stronger acid sites having been formed by pre-heating the θ-Al_2O_3 at 673 K. As can be seen, it is possible to describe the interaction strength and geometry of adsorption when co-adsorption occurs. The use of ^{13}C T_1 NMR relaxometry to study adsorption in multicomponent systems will be expanded in section 4.3.3.4.

4.3.3.4 Co-adsorption: binary mixtures

In this section ^{13}C T_1 NMR relaxation time analysis is used to study adsorption in binary systems, showing the sensitivity and versatility of this method to study adsorbate-adsorbent interactions. Here we consider the adsorption of 0.5 ML 1-pentene on θ-Al_2O_3 in the

presence of 2-butyne, CO, cyclohexane and benzene. These molecules are used as model systems to illustrate a series of common multicomponent adsorption systems in heterogeneous catalysis. In addition, the symmetry of most of these molecules resulted in fewer resonance signals appearing in the spectra, minimising any overlap, which facilitated the analysis of the $T_{1,ads}/T_{1,bulk}$ values of 1-pentene. An examination of the changes in the overall strength of adsorption of 1-pentene as compared to single component adsorption is performed. Additionally, the interactions of the co-adsorbate with the surface and with 1-pentene are shown.

4.3.3.4.1 2-butyne

0.5 ML 2-butyne was adsorbed with 0.5 ML 1-pentene on θ-Al_2O_3 to determine the preferential adsorption of unsaturated bonds when a triple bond and a double bond are present in the same system. Results of the $T_{1,ads}/T_{1,bulk}$ values are shown in **Figure 4.15** for three cases studied: (i) 1-pentene adsorbed first, followed by 2-butyne, (ii) 2-butyne adsorbed first, followed by 1-pentene, and (iii) single component 0.5 ML of 1-pentene for comparison. As can be seen, $T_{1,ads}/T_{1,bulk}$ values of the alkyne are always lower than of 1-pentene. This observation reveals that adsorption of the alkyne is always favourable. In this case, olefinic carbons C1 and C2 showed average $T_{1,ads}/T_{1,bulk}$ values of 6.1×10^{-2} in (i) and 7.1×10^{-2} in (ii). As comparison, a $T_{1,ads}/T_{1,bulk}$ value of 5.6×10^{-2} was obtained in (iii), indicating a weakening in the double bond interaction. In all cases, the double-bond has a higher $T_{1,ads}/T_{1,bulk}$ value than 2-butyne, with 5.1×10^{-3} in (i) and 8.4×10^{-3} in (ii). The same $T_{1,ads}/T_{1,bulk}$ ratios for carbons C1 and C4 and for carbons C2 and C3 in 2-butyne are found. This result is based on a single exponential fit to the acetylenic (for C2 and C3) and aliphatic (for C1 and C4) resonances. If the carbons adsorbed to different extents, multiple relaxation times for each resonance line and multiple $T_{1,ads}$ values for the olefinic carbons would be expected. 1-pentene $T_{1,ads}/T_{1,bulk}$ values of C4 and C5 (alkyl chain) show a stronger interaction in (i) than in (iii), where only 1-pentene was adsorbed. This difference in strength of interaction reveals the presence of lateral interactions with excess 2-butyne, similar to the results for adsorption of 1-pentene at low temperature. These interactions are also inferred in (ii), where $T_{1,ads}/T_{1,bulk}$ on 2-butyne C1 and C4 carbons show a weaker interaction with the surface than in (i).

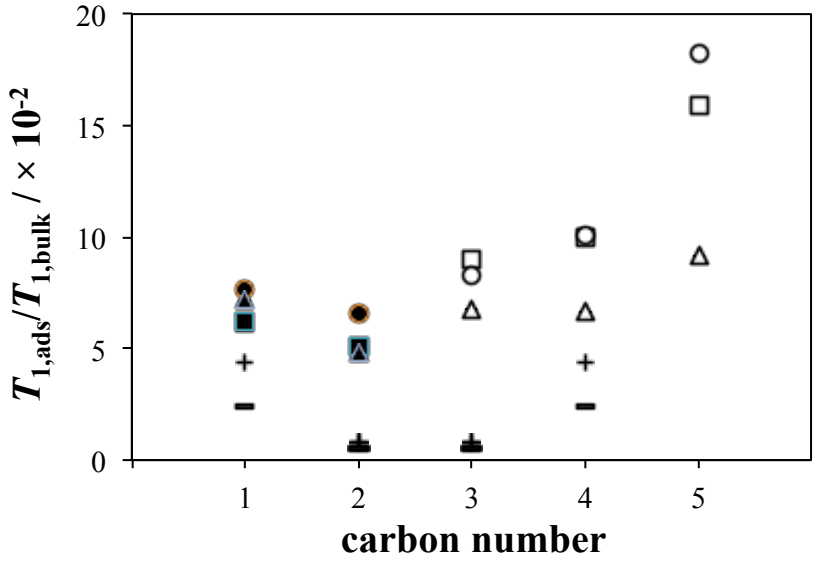

Figure 4.15. The ratio of surface to bulk relaxation times $T_{1,ads}/T_{1,bulk}$ for the individual carbon atoms in 1-pentene co-adsorbed with 2-butyne on θ-Al_2O_3. Data are shown for adsorption of 0.5 ML 1-pentene only (squares), adsorption of 0.5 ML 1-pentene (triangles) followed by 0.5 ML 2-butyne (line), and adsorption of 0.5 ML 2-butyne (cross) followed by 0.5 ML 1-pentene (circles). The solid symbols represent the olefinic carbons and the open symbols represent the aliphatic carbons in 1-pentene.

4.3.3.4.2 CO

Results from the co-adsorption of CO with 0.5 ML 1-pentene are shown in **Figure 4.16**. Similarly to 2-butyne, the $T_{1,ads}/T_{1,bulk}$ ratios are acquired for three cases: (i) 1-pentene adsorbed first, followed by CO, (ii) CO adsorbed first, followed by 1-pentene, and (iii) 0.5 ML of 1-pentene only for comparison. As seen in **Figure 4.16**, the order in which CO and 1-pentene are adsorbed does not have a significant effect on the strength of interaction of 1-pentene with the alumina. Comparing these data with that for 0.5 ML 1-pentene in the absence of CO, we see that relatively little difference is observed for the aliphatic carbons (C3 to C5). In contrast, the presence of CO causes a significant change in the $T_{1,ads}/T_{1,bulk}$ ratio of the olefinic carbons. The influence of CO was observed with IR on the adsorption of benzene on γ-Al_2O_3, although no geometrical information was given (Gordymova *et al.*, 1982). In this work, CO significantly increases the $T_{1,ads}/T_{1,bulk}$ ratio indicating a much weaker interaction. Indeed the $T_{1,ads}/T_{1,bulk}$ values are approximately the same for the olefinic and aliphatic carbons. Additionally, the relative strength of interaction of carbons C1 and C2 reverses, with C1 showing slightly stronger adsorption than C2 in the co-adsorption system. This suggests the adsorption geometry is altered in the presence of CO. The lower values

observed in C3 to C5 in case (ii) are related to a higher proportion of 1-pentene interacting with the first monolayer on θ-Al_2O_3, as obtained by carbon peak area measurements. The presence of lateral interactions between the weakly adsorbed 1-pentene molecules could have created a stabilised configuration, as seen in **Figure 4.16**. For example, TPD studies have shown a stabilisation below 1 ML on weakly binding surfaces due to higher packing density (Roos *et al.*, 2010).

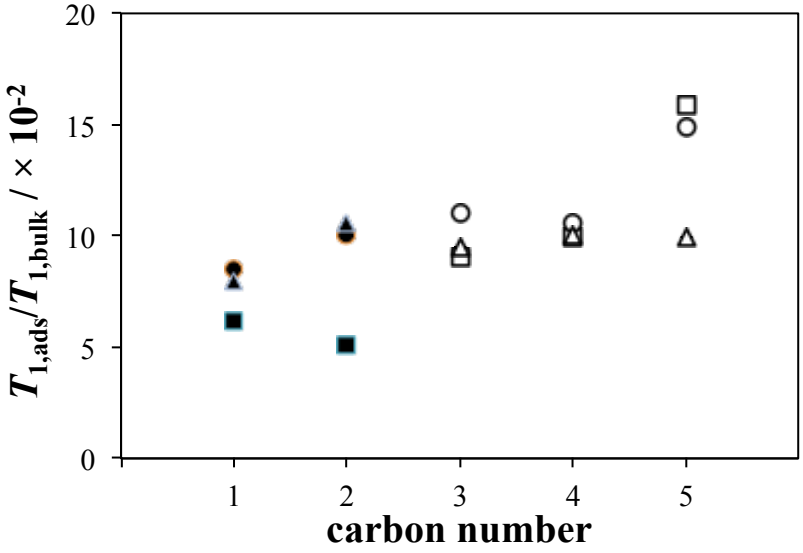

Figure 4.16. The ratio of surface to bulk relaxation times $T_{1,ads}/T_{1,bulk}$ for the individual carbon atoms in 1-pentene co-adsorbed with carbon monoxide on θ-Al_2O_3 Data are shown for adsorption of 0.5 ML 1-pentene only (squares), adsorption of 0.5 ML 1-pentene followed by 0.5 ML CO (circles), and adsorption of 0.5 ML CO followed by 0.5 ML 1-pentene (triangles). In each case the solid symbols represent the olefinic carbons and the open symbols represent the aliphatic carbons.

4.3.3.4.3 Benzene and cyclohexane

Finally, the adsorption of 0.5 ML of 1-pentene on θ-Al_2O_3 is investigated after pre-adsorption of (i) 0.9 ML of cyclohexane, and (ii) 0.9 ML of benzene as model coke compounds at different stages in catalyst deactivation. 0.5 ML 1-pentene adsorption was used for comparison (iii). **Figure 4.17** shows the $T_{1,ads}/T_{1,bulk}$ ratios of 1-pentene in all cases, as well as a single $T_{1,ads}/T_{1,bulk}$ value for each pre-adsorbed molecule (cyclohexane or benzene). As can be seen in **Figure 4.17**, the $T_{1,ads}/T_{1,bulk}$ value of benzene is lower than carbons C1 and C2 of 1-pentene in all cases. Conversely, the $T_{1,ads}/T_{1,bulk}$ ratio of cyclohexane shows a higher value than carbons C1 and C2 of 1-pentene in all cases. These results are in agreement with previous literature in coke formation and catalyst deactivation (Chen *et al.*, 2000; McGregor

et al., 2010). The formation of graphitic deposits avoids the adsorption and subsequent reaction of the desired species. Considering the average C1 and C2 $T_{1,ads}/T_{1,bulk}$ values of the carbon-carbon double-bond in 1-pentene, a value of 6.3×10^{-2} is obtained in (i), while a value of 7.4×10^{-2} is observed in (ii). These values are somewhere between those obtained for single-component 1-pentene adsorbed on θ-Al_2O_3 at increasing coverage. Thus, $T_{1,ads}/T_{1,bulk}$ values of 5.6×10^{-2} at 0.5 ML and 10.1×10^{-2} at 1 ML, represent two boundaries for the pre-adsorption results. Therefore, a weakening of the double-bond interaction upon pre-adsorption of cyclohexane and benzene is inferred, being more significant with benzene.

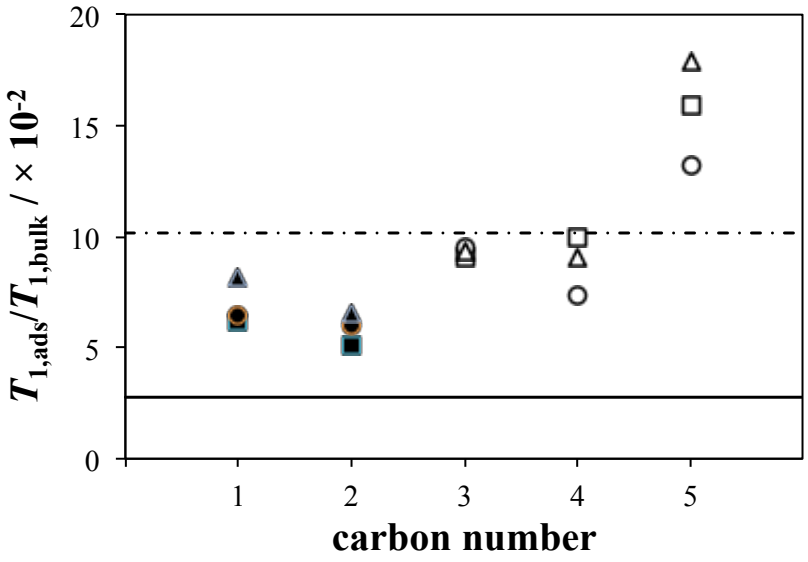

Figure 4.17. The ratio of surface to bulk relaxation times $T_{1,ads}/T_{1,bulk}$ for the individual carbon atoms in 1-pentene co-adsorbed with benzene and cyclohexane on θ-Al_2O_3 Data are shown for adsorption of 0.5 ML 1-pentene only (squares), adsorption of 0.5 ML 1-pentene after 0.9 ML cyclohexane (circles), and adsorption of 0.5 ML 1-pentene after 0.9 ML benzene (triangles). The values of $T_{1,ads}/T_{1,b}$ of benzene (–) and of cyclohexane (-.-) are shown as a continuous line for comparison. In each case the solid symbols represent the olefinic carbons and the open symbols represent the aliphatic carbons.

4.4 Discussion

In this section the results from the adsorption of 1-pentene with different techniques are compared. The influence of surface coverage and the type of interaction between 1-pentene and the aluminas is described. The use of ^{13}C T_1 NMR relaxometry as a novel technique to study adsorption phenomena in catalysis is discussed in comparison with IR and adsorption isotherm results.

4.4.1 The nature of 1-pentene adsorption: interaction with γ- *vs.* θ-Al_2O_3

The results obtained from the different adsorption techniques present a clear picture on the adsorption of 1-pentene on the surface of γ- and θ-Al_2O_3.

IR spectroscopy results showed that the adsorption of 1-pentene on the surface of the alumina was weak in nature. Species only remained on the surface for a limited time. As mentioned in section 3.3, the surface of θ-Al_2O_3 is heterogeneous in nature with a number of different adsorption sites available, including Lewis acid (Al^{3+}) and Brønsted acid (OH) sites (Shen *et al.*, 1994). As observed in **Figure 4.2**, the interaction of the olefin with the surface occurred *via* hydroxyl groups. These hydroxyl groups were identified as weak Brønsted acid sites. Previous infrared studies have shown Brønsted sites participating on the molecular adsorption of C_4 alkenes (Busca *et al.*, 1987). In such study, no reaction was observed over Brønsted acid sites. Other works have shown Brønsted sites have participated on surface reaction, but only in strong acidic surfaces such as zeolites (Föttinger *et al.*, 2003; Yoda *et al.*, 2005), halogenated aluminas (Cheng and Ponec, 1994) or if high adsorption temperatures are involved (Guisnet *et al.*, 1977). In this work, IR spectra did not detect the formation of other species on the surface of the alumina. Hence, reactivity was considered not to be occurring during adsorption-desorption of the alumina on Brønsted acid (OH) sites. Such weak adsorption and lack of reactivity was previously observed with similar olefins (Busca *et al.*, 1987). Furthermore, interaction was taking place through the unsaturated carbon-carbon double-bond, as suggested by IR signal decay. Complementary ^{13}C T_1 NMR relaxometry results were in agreement with these observations, as inferred from the geometrical configuration of 1-pentene upon adsorption on the aluminas. A weak double-bond interaction would be expected on aluminas, as observed on the room temperature adsorption of C_4 olefins (Trombetta *et al.*, 1997). Although previous studies have observed the existence of di-σ bond between alkenes and metal surfaces (de la Cruz and Sheppard, 1991; Shahid and Sheppard, 1994), NMR results reinforced that only a weak molecular interaction was taking place on the aluminas. A di-σ bond would have resulted in the loss of the olefinic lines from the spectrum due to the change in the electron distribution and hence degree of chemical shielding on the ^{13}C nucleus. This was not observed in this system, as exemplified in **Figure 4.8** for 0.5 ML 1-pentene adsorbed on θ-Al_2O_3. Both the NMR chemical shift and DRIFTS data suggest that the dominant interaction is *via* the Brønsted acid sites on the alumina.

Moreover, it was possible to determine the interaction of 1-pentene with both aluminas. Previous literature studies mention a density of sites of 1.9×10^{18} adsorption sites m^{-2}, equivalent to ~0.5 mmol g^{-1} on γ-Al_2O_3 (Roy *et al.*, 2002), and of about ~ 0.31 mmol g^{-1} on θ-Al_2O_3. $v_{m\text{-}BET}$ results in this study (**Table 4.5**) were very similar to the numbers reported on adsorption sites. NMR results in **Figure 4.9** showed that the olefinic carbons (C1 and C2) interacted more strongly with the surface of θ-Al_2O_3, as compared to γ-Al_2O_3. For example, for C2, values of $T_{1,ads}/T_{1,bulk} = 10.53 \times 10^{-2}$ on γ-Al_2O_3 *vs.* $T_{1,ads}/T_{1,bulk} = 5.09 \times 10^{-2}$ on θ-Al_2O_3 were obtained. In terms of strength of interaction, Mándy and Schay (1975) showed the higher specific activity of θ-Al_2O_3 over γ-Al_2O_3 in the isomerization of olefins, which was related with the higher density of acid centres and of Al^{IV} on θ-Al_2O_3 (John and Scurrell, 1977). In this work, adsorption isotherm results presented similar findings on the interactions of hydrocarbon on γ- and θ-Al_2O_3. Values of 46 kJ mol^{-1} *vs.* 31 kJ mol^{-1} for the heat of adsorption at zero coverage were obtained for the adsorption of 1-pentene on θ-Al_2O_3 and γ-Al_2O_3, respectively (**Table 4.4**). These values on aluminas are in agreement with previous literature studies. Typical values for the adsorption of low alkanes and alkenes on activated carbon are around 29 kJ mol^{-1}, while in acid catalysts such as zeolites values in the range 40 – 70 kJ mol^{-1} at 350 – 400 K have been recorded (de Moor *et al.*, 2011). Similarly, heats of adsorption of 46 kJ mol^{-1} for benzene, 40 kJ mol^{-1} for *n*-hexane, and 41 kJ mol^{-1} for methylcyclohexane on γ-Al_2O_3 have been reported from a Freundlich fitting to adsorption isotherms data (Bravo *et al.*, 1986). A heat of adsorption of 40 kJ mol^{-1} for 1-hexene on γ-Al_2O_3 was noted in a similar study (Baumgarten *et al.*, 1977).

Pre-treatment temperature of the alumina had a high influence on the adsorption of 1-pentene. Thus, IR results showed that residence times of 1-pentene on the surface of θ-Al_2O_3 increased with a pre-treatment temperature of 673 K as compared to 393 K (**Table 4.2**). Additionally, ^{13}C T_1 NMR relaxometry results showed a significant reduction in the $T_{1,ads}/T_{1,bulk}$ ratios (section 4.3.3.3). The interaction of the olefinic carbons constituent of the double-bond decreased from $T_{1,ads}/T_{1,bulk} = 5.6 \times 10^{-2}$ to $T_{1,ads}/T_{1,bulk} = 6.0 \times 10^{-3}$ for θ-Al_2O_3 pre-treated at 673 K. Both techniques indicated higher alumina pre-treatment temperature enhanced olefin adsorption. Pre-treatment of the alumina at high temperatures results in the removal of hydroxyl (OH) groups, as noted in section 3.3.2.1. Such dehydroxylation has a signification effect on acid site density and Brønsted to Lewis acid site ratio. DFT simulation models have addressed the effect of hydroxylation/dehydroxylation processes induced by temperature

effects on the acid-base properties of γ-Al_2O_3 (Digne *et al.*, 2002). The pentacoordinated Al, Al^V, hydrates with an energy of 106 kJ mol^{-1} to 66 kJ mol^{-1} for a monolayer OH coverage. The differential energies of hydration for Al^{III} and Al^{IV} sites is 240 kJ mol^{-1} and 87 kJ mol^{-1} for monolayer coverage, respectively. This indicates the strength of the different Al Lewis acid sites present on aluminas. Experimentally, the presence of three different types of Lewis acid sites on γ-alumina has been shown by means of CO adsorption (Morterra *et al.*, 1994). A reduction on the bridged hydroxyls was correlated with the increase on Lewis sites and enhanced CO adsorption. Such Lewis acid sites participated in the reactivity of the alumina, as noted in NMR relaxometry results. Similar results have been observed in isomerisation of butenes on aluminas by Cheng and Ponec (1994), Guisnet *et al.* (1977) and Trombetta and co-workers (1997), or with the effect of Lewis sites in the isomerisation of 1-pentene on zeolites (Föttinger *et al.*, 2003). Therefore, the appearance of Lewis acid sites (Al^{3+}) at higher pre-treatment temperature explained the stronger interaction of 1-pentene *via* the carbon-carbon double-bond. In this work, NMR relaxometry has shown the different reactivity of the pre-treated aluminas and the strength of interaction of both species present. NMR has been used previously to determine the extent of isomerisation and hydrogenation (Mantle *et al.*, 2006; Sederman *et al.*, 2005). Those studies were performed in Pd/Al_2O_3 in the presence of H_2. In this case, evidence of isomerisation was shown for single component adsorption on θ-Al_2O_3.

In summary, it was possible to determine the type of surface active sites present on the adsorption of 1-pentene on both aluminas. A good agreement between the different techniques was shown. In addition, NMR relaxometry results showed a very clear picture, compared to IR or adsorption isotherms, on the type and strength of adsorption and the effect of pre-treatment temperature.

4.4.2 Effect of coverage and co-adsorption

The heterogeneous nature of the surface of the aluminas was manifested in the adsorption of 1-pentene with increasing coverage. Adsorption isotherms (**Figures 4.5** and **4.7**) showed an initial decrease of surface interaction with increasing coverage. Considering the results of the Tóth fit for the first layer (**Figure 4.7**), such a decrease in the heat of adsorption occurred until 10% ML coverage. As already mentioned in section 4.3.2.1, the evolution of the values of t with temperature suggested a decrease in q_{st} with increasing coverage. NMR relaxometry results were also sensitive to surface coverage. Values of $T_{1,ads}/T_{1,bulk}$ for the carbons in

1-pentene increased with increasing coverage, indicating a weaker interaction with the surface. Thus, the average $T_{1,ads}/T_{1,bulk}$ of C1 and C2 (double-bond) increased from 3.0×10^{-2} at 0.1 ML to 5.6×10^{-2} at 0.5 ML and to 10.1×10^{-2} at 1 ML. **Figure 4.10** showed such decrease in the interaction of 1-pentene, on both the olefin carbons and the aliphatic chain. It is expected that the strongest adsorption sites are populated initially, followed by weaker sites. As the coverage increases, it is reasonable to assume that the average strength of adsorption decreases as the alkene molecules are forced to occupy less preferential surface sites. An additional factor may be the disruption of the alkene-alumina interaction through steric effects on approaching saturation of the surface (Shen *et al.*, 1994).

Although not measured directly, the results of adsorption isotherms also noted the presence of strong adsorbate-adsorbate interactions. These were also observed in the adsorption of propane and propene over zirconium phosphates (Aguilar-Armenta *et al.*, 2006), or nitrogen oxides over zeolites (Domínguez *et al.*, 2010). Thus, **Figure 4.7** showed an increase in the isosteric heat of adsorption for coverages higher than 10% ML, particularly noticeable on γ-Al_2O_3. Noticeably, the values of $t < 1$ were indicative of preferential adsorbate-adsorbent interactions. As mentioned above, the overall heat of adsorption was indicative of weak interactions. Thus, adsorbate-adsorbate interactions were likely compensated for by interactions of 1-pentene with strong adsorption sites, present at low coverages. However, in a batch system, both interactions were present. Influence of the latter was eventually manifested. The presence of that transition regime masked the results of the Tóth fitting parameters, fitted for the entire adsorption curve, as previously indicated. There exist multicomponent models to describe adsorption of two adsorbates (Luz *et al.*, 2013). However, they present limitations in studying mixed systems (Wu *et al.*, 2014). On the contrary, ^{13}C NMR relaxometry can provide useful insights on geometry of adsorption, strength of adsorbate-adsorbent interactions, and the presence of adsorbate-adsorbate interactions.

As observed with coverage, the presence of a second species in the adsorption of 1-pentene upon alumina modified the type and strength of interaction. Multicomponent adsorption was studied *via* ^{13}C T_1 NMR relaxometry. Therefore, the adsorption strength, but also adsorption geometry were characterised. 1-pentene co-adsorption on θ-Al_2O_3 with 2-butyne revealed the preferential triple-bond adsorption over the double-bond in unsaturated mixtures (Hoffmann *et al.*, 1966). CO co-adsorption inferred the disruption of the double-bond interaction upon

adsorption of an olefin. Lastly, cyclohexane and benzene show the weakening of the hydrocarbon interaction upon deposition of carbonaceous species. **Table 4.8** shows the $T_{1,ads}/T_{1,bulk}$ values for the individual carbon atoms in 1-pentene adsorbed on θ-Al_2O_3 in co-adsorption experiments. Overall, a modification in the strength of adsorption of 1-pentene is shown, particularly for C1 and C2. This result was in agreement with the preferential double-bond description of individual 1-pentene adsorption on the aluminas. Co-adsorbed hydrocarbons – 2-butyne, cyclohexene and benzene – also showed the preferential adsorption within the different functional groups. The presence of lateral interactions of these molecules with 1-pentene, modified the overall geometry of adsorption. These observations were in agreement with isosteric heats of adsorption of 1-pentene.

Table 4.8. Ratio of surface to bulk relaxation times $T_{1,ads}/T_{1,bulk} \times 10^2$ for the individual carbon atoms in 1-pentene adsorbed on θ-Al_2O_3 in co-adsorption experiments.

carbon #	0.5 ML	cyclohexane	benzene	2-butyne		CO	
dosing	-	-	-	1st	2nd	1st	2nd
1	6.19	6.46	8.20	7.67	7.17	7.94	8.47
2	5.09	6.03	6.58	6.55	4.88	10.61	10.07
3	9.02	9.55	9.37	8.29	6.77	9.48	11.02
4	9.98	7.40	9.04	10.07	6.61	10.04	10.57
5	15.89	13.19	17.83	18.19	9.13	9.95	14.93

CO co-adsorption results were particularly interesting. CO is co-adsorbed with unsaturated hydrocarbons in the industrial process of acetylene selective semi-hydrogenation to ethylene. One of the effects of CO in this process is to weaken the interaction of the alkene with the Pd-based active site on the catalyst thereby limiting further hydrogenation of ethylene to the undesired total hydrogenation product ethane (López *et al.*, 2008; Park and Price, 1991). It is not possible to accurately extrapolate data from adsorption on an alumina surface to that on Pd. However, it is noteworthy that the presence of CO, physisorbed on the surface, induced such weakening of the alkene-alumina interaction in both cases.

4.4.3 Brief comparison between techniques: advantages of NMR relaxometry

A range of techniques was used to study the adsorption of 1-pentene on γ- and θ-Al_2O_3. Positive aspects and limitations of DRIFTS, adsorption isotherms and ^{13}C T_1 NMR relaxometry will be presented. Individual measurements have been performed in very similar

olefin systems on alumina. However, a comparison of these adsorption methods is important, as it indicates what has been extracted from this limited study.

As was discussed previously, the use of IR spectroscopy was employed to study the changes occurring on the surface of the alumina upon adsorption of 1-pentene. Flow-through pulsed 1-pentene experiments determined the influence of hydroxyl groups on the interaction of 1-pentene with Al_2O_3. Additionally, changes in the IR spectra using DRIFTS allowed for changes in adsorption with pre-treatment temperature to be distinguished. Nevertheless, clear limitations were noted on the sensitivity of the method. It was not possible to distinguish the formation of pentene isomers on alumina pre-treated at high temperature, unlike with ^{13}C NMR T_1 relaxometry results (section 4.3.3.3). Short residence times were also characteristic during IR measurements. The heats of adsorption of 35 – 41 kJ mol^{-1} were characteristic of weak adsorption and reversible desorption. IR spectroscopy was performed during dynamic measurements *vs*. batch adsorption of adsorption isotherms and NMR relaxometry. The experimental design would have ideally required a technique with better resolution for low surface density measurements. This would have allowed for strong surface sites to be captured, and for possible reactions to be tracked.

Adsorption isotherms provide a useful method to determine energies of adsorption. Despite the time length of each experimental measurement – equilibrium is required – isotherms contained very interesting information. The type of isotherm curve obtained already revealed information on the adsorption of 1-pentene, and the saturation and condensation pattern (**Figure 4.3**) showed the extent of interaction with the alumina. Still, the most important aspect was the possibility of extracting heats of adsorption as a function of surface coverage. Those values were useful in order to compare with simulation studies or experimental values from similar hydrocarbons or surfaces. A series of assumptions were made in order to obtain such energies. Literature has discussed in detail the validity of those postulates (Pan *et al.*, 1998). Compared to that study, the pressure and temperature ranges allowed for uptake values to be approximated with the ideal gas method and Clausius-Clapeyron equation (equation 4.7). Additionally, comparison between calorimetry results and isosteric heats of adsorption on the adsorption of simple molecules on zeolites showed similar results were obtained (Shen *et al.*, 2000). Nevertheless, the limiting factor in adsorption isotherms is the vapourisation-condensation range of the adsorbate. Further, only macroscopic information was obtained; hence no physically meaningful evidence was gathered on interaction with the adsorbent.

Lastly, chemical shift resolved ^{13}C T_1 NMR relaxometry provided information on relative strength of interaction of 1-pentene individual carbon atoms with the surface of γ- and θ-Al_2O_3. Hence, it was possible to determine the adsorption geometry of 1-pentene interacting with the surface. The technique was sensitive to the alumina type, surface coverage, and dosing temperature, similar to adsorption isotherms. Additionally, it was sensitive to changes in pre-treatment temperature, similarly to IR spectroscopy. Further to this, it was possible to study the adsorption of various hydrocarbons when co-adsorbed on the surface of θ-Al_2O_3. The technique sensitivity, fingerprint for molecular structure and reduced number of assumptions made ^{13}C T_1 NMR relaxometry very versatile. NMR measurements have been demonstrated very useful in the past in order to provide relevant catalytic information (Gladden and Mitchell, 2011; Gladden *et al.*, 2012), including the isomerisation and hydrogenation of alkenes (Mantle *et al.*, 2006). Yet, a comparison with other adsorption techniques or previous results from the literature could be broader. Such wider study will be presented in chapter 5.

As was observed, no single adsorption technique could have fully resolved the interaction of 1-pentene with the surface of aluminas. For example, FTIR is widely used in addition to other techniques, such as Temperature Programmed Desorption (TPD), XPS or solid state NMR. Such a combination has been shown to be useful in providing complementary information on the adsorption sites and interaction energies (Tanaka *et al.*, 1999; DeCanio *et al.*, 1993).

4.5 Conclusions

A comprehensive study on the adsorption of 1-pentene on the surface of γ- and θ-Al_2O_3 was performed. IR spectroscopy, volumetric adsorption isotherms and ^{13}C NMR T_1 relaxometry were used. As observed, a weak adsorption on the aluminas *via* the 1-pentene double-bond was present. 1-pentene bonded weakly to OH groups on the surface of porous alumina. Adsorption was confirmed to be more favourable over θ-Al_2O_3 than over γ-Al_2O_3 as expected. Comparison with infrared spectroscopy provided similar information on strength of interaction. Pre-treatment temperature of the alumina exposed Lewis acid sites responsible for isomerisation, only observed with ^{13}C NMR. Studies of adsorption as a function of surface coverage demonstrated the average interaction strength was greater at lower surface coverage, indicating molecules adsorb preferentially on the strongest adsorption sites. Similarly, the temperature of adsorption showed similar effects. Furthermore, the presence of adsorbate-adsorbate interactions was determined to strongly participate in this system.

Energies of adsorption as a function of coverage were obtained *via* adsorption isotherms and the particular surface-adsorbate interactions were described with IR spectroscopy. Yet, information on atom-specific adsorbate-adsorbent interaction strengths and the molecular conformations of the adsorbates were only inferred with the use of ^{13}C NMR relaxometry. In addition, co-adsorption measurements showed the change in adsorption strength of 1-pentene when in the presence of a second molecule. Important implications were extracted, such as the influence of coke, CO or alkyne in the relative strength of adsorption of olefins. The application of chemical shift resolved ^{13}C NMR T_1 relaxometry to the determination of adsorbate interaction with alumina surfaces is reported. Knowledge of adsorbate geometry and interaction strength is of importance in chemical sensors and heterogeneous catalysis where the interaction of adsorbates with active surface sites influences performance. The results on adsorption of 1-pentene showed that ^{13}C T_1 NMR relaxometry is a useful tool to determine interactions on catalytically-relevant surfaces.

References

Aguilar-Armenta, G., Patiño-Iglesias, M.E., Jiménez-Jiménez, J., Rodríguez-Castellón, E., Jiménez-López, A. (2006) Application of porous phosphate heterostructure materials for gas separation. *Langmuir,* 22, 1260 – 1267.

Amenomiya, Y., Chenier, J.H.B., Cvetanovic, R.J. (1967) Hydrogenation of olefins on alumina. I. Active sites for hydrogenation of ethylene. *J. Catal.*, 9, 28 – 37.

Bardina, I.A., Zhukova, O.S. , Koroleva, N.V., Samadani-Langerudi, N., Lanin, S.N. (2007) Adsorption properties of γ-Al_2O_3 as measured by gas chromatography. *Russ. J. Phys. Chem. A*, 81, 479 – 482.

Baumgarten, E, Weinstrauch, F., Höffkes, H. (1977) Adsorption isotherms of hydrocarbons on γ-alumina. *J. Chromatogr*., 138, 347 – 354.

Borodziński, A., Bond, G.C. (2006) Selective hydrogenation of ethyne in ethene-rich streams on palladium catalysts. Part 1. Effect of changes to the catalyst during reaction. *Catal. Rev.-Sci. Eng.*, 48, 91 – 144.

Bravo, M., Fuertes, A.B., Coca, J. (1986) Adsorption isotherms of several hydrocarbons on γ-Al_2O_3 by gas chromatography. *React. Kinet. Catal. Lett.*, 31, 173 – 179.

Brunauer, S. (1943) *The adsorption of gases and vapors. Volume I. Physical adsorption.* Princeton University Press, pp. 1 – 28.

Busca, G. (1998) Spectroscopic characterization of the acid properties of metal oxide catalysts. *Catal. Today*, 41, 191 – 206.

Busca, G., Finocchio, E., Lorenzelli, V., Trombetta, M., Rossini, S.A. (1996) IR study of alkene allylic activation on magnesium ferrite and alumina catalyst. *J. Chem. Soc., Faraday Trans.,* 92, 4687 – 4693.

Busca, G., Ramis, G., Lorenzelli, V., Janin, A., Lavalley, J-C. (1987) FT-i.r. study of molecular interactions of olefins with oxide surfaces. *Spectrochim. Acta A*, 43, 489 – 496.

Chen, D., Rebo, H.P., Grønvold, A., Moljord, K., Holmen, A. (2000) Methanol conversion to light olefins over SAPO-34: kinetic modelling of coke formation. *Micropor. Mesopor. Mat.*, 35-36, 121 – 135.

Cheng, Z.X., Ponec, V. (1995) Selective isomerisation of butane to iso-butene. *J. Catal.*, 148, 607 – 616.

Clark, A. (1970) *The theory of adsorption and catalysis.* Academic Press, London, pp. 3 – 61.

Corado, A, Kiss, A., Knoezinger, H., Mueller, H.D. (1975) Catalytic isomerisation of olefins on alumina. II. Catalyst deactivation and its effects on the mechanism. *J. Catal.*, 37, 68 – 80.

Crowder, G.A., Guan, H. (1995) 2-methyl-1-pentene: infrared and raman spectra and normal coordinate calculations. *Vib. Spectrosc.*, 10, 3 -11.

De la Cruz, C., Sheppard, N. (1991) The infrared spectrum from hydrogenation of the surface species from ethene chemisorbed on a Pt/SiO_2 catalyst; the surface ethyl group? *J. Mol. Struct.*, 247, 25-30.

De Canio, E.C., Bruno, J.W., Nero, V.P., Edwards, J.C. (1993) ^{27}Al NMR, FT-IR and ethanol - ^{18}O TPD characterization of fluorided alumina. *J. Catal.*, 140, 84 – 102.

De Moor, B.A., Reyniers, M.F., Gobin, O.C., Lercher, J.A., Marin, G.B. (2011) Adsorption of C_2-C_8 *n*-alkanes in zeolites. *J. Phys. Chem. C*, 115, 1204 – 1219.

Digne, M., Sautet, P., Raybaud, P., Euzen, P., Toulhoat, H. (2002) Hydroxyl groups on γ-alumina surfaces: a DFT study. *J. Catal.*, 211, 1 – 5.

Do, D.D. (1998) *Adsorption analysis: equilibria and kinetics*. Imperial College Press, London, pp. 49 – 70.

Domínguez, G., Hernández-Huesca, R., Aguilar-Armenta, G. (2010) Isosteric heats of adsorption of N_2O and NO on natural zeolites. *J. Mex. Chem. Soc.*, 54, 111 – 116.

Foo, K.Y., Hameed, B.H. (2010) Insights into the modelling of adsorption isotherm systems. *Chem. Eng. J.*, 156, 2 – 10.

Föttinger, K., Kinger, G., Vinek, H. (2003) 1-pentene isomerization over zeolites studied by *in situ* IR spectroscopy. *Catal. Lett.*, 85, 117 – 122.

Garbowski, E., Primet, M. (1985) Spectroscopic study of the cokefaction of butene and butane on alumina. *J. Chem. Soc., Faraday Trans.*, 81, 497 – 508.

Gladden, L.F., Mitchell, J. (2011) Measuring adsorption, diffusion and flow in chemical engineering: applications of magnetic resonance to porous media., *New. J. Phys.*, 13, 035001.

Gladden, L.F., Lutecky, M., McGregor, J. (2012) Nuclear magnetic resonance spectroscopy. In: Che, M., Védrine, J.C. (eds.) *Characterization of solid materials and heterogeneous catalysts: from structure to surface reactivity*. Wiley-VCH, Wichester.

Gordymova, T.A., Budneva, A.A., Davydov, A.A. (1982) IR spectra of toluene adsorbed on γ-Al_2O_3. *React. Kinet. Catal. Lett.*, 20, 113 – 117.

Guisnet, M., Lemberton, J.L., Perot, G., Maurel, R. (1977) Catalytic isomerization of ethylenic hydrocarbons. XIV. Effect of drying and reaction temperature on the isomerization of deuterated butenes over alumina. *J. Catal.*, 48, 166 – 176.

Haag, W.O., Pines, H. (1960) Alumina: catalyst and support. III. The kinetics and mechanisms of olefin isomerization. *J. Am. Chem. Soc.*, 82, 2488 – 2494.

Hinz, C. (2001) Description of sorption data with isotherm equations. *Geoderma*, 99, 225 – 243.

Hoffmann, R.L., List, G.R., Evans, C.D. (1966) Gas-solid chromatography of hydrocarbons on activated alumina. II. Alkane, alkene, alkyne separations and subtractive adsorption. *J. Am. Oil Chem. Soc.*, 43, 675 – 677.

Hong, Y., Chen, F.R., Fripiat, J.J. (1993) Structural and textural factors influencing the rate of butene isomerization on aluminas. *Catal. Lett.*, 17, 187 – 195.

John, C.S., Scurrell, M.S. (1977) Catalytic properties of aluminas for reactions of hydrocarbons and alcohols. In: Kemball, C. (ed.). *Catalysis: volume 1*. Chemical Society, London, pp. 136 – 167.

Jossens, L., Prausnitz, J.M., Fritz, W., Schlünder, E.U., Myers, A.L. (1978) Thermodynamics of multi-solute adsoption from filute aqueous solutions. *Chem. Eng. Sci.*, 33, 1097 – 1106.

Katz, S., Gray, D.G. (1980) The adsorption of hydrocarbons on cellophane: I. Zero coverage limit. *J. Colloid Intef. Sci.*, 82, 318 – 325.

Khan, A.R., Ataullah, R., Al-Haddad, A. (1997) Equilibrium adsorption studies of some aromatic pollutants from dilute aqueous solutions on activated carbon at different temperatures. *J. Colloid Interf. Sci.*, 194, 154 – 165.

Knözinger, H., Ratnasamy, P. (1978) Catalytic aluminas: surface models and characterization of surface sites. *Catal. Rev.-Sci. Eng.*, 17, 31 – 70.

Kuran, W. (2001) *Principles of Co-ordination Polymerisation: Homogeneous and Heterogeneous*, Wiley, Chichester.

Larsen, C.R., Grotjahn, D.B. (2010) New insigths on kinetic versus thermodynamic ratios in catalyzed alkene isomerization. *Top. Catal.*, 53, 1015 – 1018.

Leitao, A., da Conceição, E., Santos, R. (1992) Modelling of solid-liquid adsorption: effects of adsorbent loads on model parameters. *Can. J. Chem. Eng.*, 70, 690 – 698.

Liu, X., Truitt, R.E. (1997) DRFT-IR studies of the surface of γ-Al_2O_3. *J. Am. Chem. Soc.*, 119, 9857 – 9860.

López, N., Bridier, B., Pérez-Ramírez, J. (2008) Discriminating Reasons for Selectivity Enhancement of CO in Alkyne Hydrogenation on Palladium. *J. Phys. Chem. C*, **112**, 9346–9350

Luz, A.D., Ulson de Souza, S.M.A.G., da Luz, C., Rezende, R.V.P., Ulson de Souza, A.A. (2013) Multicomponent adsorption and desorption of BTX compounds using coconut shell activated carbon: experiments, mathematical modelling, and numerical simulation. *Ind. Eng. Chem. Res.*, 52, 7896 – 7911.

Lwin, S., Wachs, I.E. (2014) Olefin metathesis by supported metal oxide catalysts. *ACS Catal.*, 4, 2505 – 2520.

MacIver, D.S., Wilmot, W.H., Bridges, J.M. (1964) Catalytic aluminas. II. Catalytic properties of eta and gamma alumina. *J. Catal.*, 3, 502 – 511.

Mándy, T., Schay, Z. (1975) Study on the mechanism of isomerization in olefins on pure aluminas. In: Márta, F., Kalló, D. (eds) *Mechanisms of hydrocarbon reactions: a symposium, 5-7 June, 1973, Siófok, Hungary*, Elsevier, Amsterdam, pp. 321 – 332.

Mantle, M.D., Steiner, P., Gladden, L.F. (2006) Polarisation enhanced ^{13}C magnetic resonance studies of the hydrogenation of pentene over Pd/Al_2O_3 catalysts. *Catal. Today*, 114, 412 – 417.

McGregor, J., Huang, Z., Parrott, E.P.J., Zeitler, J.A., Nguyen, K.L., Rawson, J.M., Carley, A., Hansen, T.W., Tessonnier, J-P., Su, D.S., Teschner, D., Vass, E.M., Knop-Gericke, A., Schlögl, R., Gladden, L.F. (2010) Active coke: carbonaceous materials as catalysts for alkane dehydrogenation. *J. Catal.*, 269, 329 – 339.

Miller, B., Furlong, O., Tysoe, W. (2013) The desorption and reaction of 1-alkenes and 1-alkynes on Cu(111) and copper foils. *Surf. Sci.*, 616, 143 – 148.

Miyaji, A., Sakamoto, Y., Iwase, Y., Yashima, T., Koide, R., Motokura, K., Baba, T. (2013) Selective production of ethylene and propylene *via* monomolecular cracking of pentene over proton-exchanged zeolites: pentene cracking mechanism determined by spatial volume of zeolite cavity. *J. Catal.*, 302, 101 – 114.

Morterra, C., Bolis, V., Magnacca, G. (1994) IR spectroscopic and microcalorimetric characterization of Lewis acid sites on (transition phase) Al_2O_3 using adsorbed CO. *Langmuir*, 10, 1812 – 1824.

Morterra, C., Magnacca, G. (1996) A case study: surface chemistry and surface structure of catalytic aluminas, as studied by vibrational spectroscopy of adsorbed species. *Catal. Today*, 27, 497 – 532.

Moses, J., Weiss, A.H., Matusek, K. and Guczi, L. (1983) The effect of catalyst treatment on the selective hydrogenation of acetylene over Pd/Al_2O_3. *J. Catal.*, 86, 417 – 426.

Narin, G., Martins, V.F.D., Campo, M., Ribeiro, A.M., Ferreira, A., Santos, J.C., Schumman, K., Rodrigues, A.F. (2014) Light olefins/paraffins separation with 13X zeolite binderless beads. *Sep. Purif. Technol.*, 133, 452 – 475.

Oblad, A.G., Messenger, J.U., Brown, H.T. (1947) Isomerisation of 1- and 2-pentenes. *Ind. Eng. Chem.*, 39, 1462 – 1466.

Olah, G.A. and Molnar, Á. (1995) *Hydrocarbon Chemistry*, Wiley, New York.

Pan, H., Ritter, J.A., Balbuena, P.B. (1998) Examination of the approximations used in determining the isosteric heat of adsorption from the Clausius-Clapeyron equation. *Langmuir*, 14, 6323 – 6327.

Park, Y.H., Price, G.L. (1991) Temperature-programmed-reaction study on the effect of carbon monoxide on the acetylene reaction over palladium/alumina. *Ind. Eng. Chem. Res.*, 30, 1693-1699

Pawela-Crew, J., Madix, R. (1995) Lateral interactions in the desorption kinetics of weakly adsorbed species: unexpected differences in the desorption of C_4 alkenes and alkanes from Ag(110) due to oriented π-bonding of the alkenes. *Surf. Sci.*, 339, 8 – 22.

Peri, J.B. (1961) Nature of active sites and of adsorbed hydrocarbon in isomerization of butene on gamma-alumina. *Actes 2ème Congr. Intern. Catalyse, Paris 1960*, 1, 1333 – 1352.

Pinnau, I. and Toy, L.G. (1990) Solid polymer electrolyte composite membranes for olefin/paraffin separation, *J. Membrane Sci.*, 184, 39 – 48.

Randolph, B. B. (1997) *Method for removing amylenes from gasoline and alkylating such amylene and other olefins while minimizing synthetic isopentane production*. U.S. Patent 5629466.

Rigby, A.M., Frash, M.V. (1997) Ab initio calculations on the mechanisms of hydrocarbon conversion in zeolites: skeletal isomerisation and olefin chemisorption. *J. Mol. Catal. A-Chem.*, 126, 61 – 72.

Roos, M., Breitruck, A., Hoster, H.E., Behm, R.J. (2010) Entropic stabilization of large adsorbates on weakly binding substrates – a thermal desorption and scanning tunnelling microscopy study. *Phys. Chem. Chem. Phys.*, 12, 818 – 822.

Rouquerol, F, Rouquerol, J., Sing, K. (1999) *Adsorption by powders and porous solids.* Academic Press, London, pp. 51 – 92.

Roy, S., Mpourmpakis, G, Hong, D.Y., Vlachos, D.G., Bhan, A., Gorte, R.J. (2012) Mechanistic study of alcohol dehydration on γ-Al_2O_3. *ACS Catal*, 2, 1846 – 1853.

Russo, P.A., Ribeiro Carrott, M.M.L., Carrott, P.J.M. (2008) Adsorption of toluene, methylcyclohexane and neopentane on silica MCM-41. *Adsorption*, 14, 367 – 375.

Schmidt, R., Welch, M.B., Randolph, B.B. (2008) Oligomerization of C_5 olefins in light catalytic naphtha. *Energ. Fuel.*, 22, 1148 – 1155.

SDBS (1997) *Spectral database of organic compounds* [Online] Available from: http://sdbs.db.aist.go.jp [Accessed October 2014]

Sears, W.M. (2001) Isosteric heat of adsorption of water vapor on bismuth iron molybdate measured by the method of constant surface conductance. *Langmuir*, 17, 5237 – 5244.

Sederman, A.J., Mantle, M.D., Dunckley, C.P., Huang, Z., Gladden, L.F. (2005) *In situ* MRI study of 1-octene isomerisation and hydrogenation within a trickle-bed reactor. *Catal. Lett.*, 103, 1 – 8.

Shahid, G., Sheppard, N. (1994) IR spectra and the structures of the chemisorbed species resulting from the adsorption of the linear butenes on a Pt/SiO_2 catalyst. Part 2. Spectra of the hydrogenated surface species as a function of temperature. *J. Chem. Soc., Faraday Trans.*, 90, 507-511.

Shen, D., Bülow, M, Siperstein, F., Engelhard, M., Myers, A.L. (2000) Comparison of experimental techniques for measuring isosteric heat of adsorption. *Adsorption*, 6, 275 – 286.

Shen, J., Cortright, R.D., Chen, Y., Dumesic, J.A. (1994) Microcalorimetric and infrared spectroscopic studies of γ-Al_2O_3 modified by basic metal oxides. *J. Phys. Chem.*, 98, 8067 – 8073.

Siperstein, F., Gorte, R.J., Myers, A.L. (1999) - A new calorimeter for simultaneous measurements of loading and heats of adsorption from gaseous mixtures. *Langmuir*, 15, 1570 – 1576.

Son, S.J., Kim, S.W., Choi, D.K., Kim, H.S., Kim, Y.J., Kim, S.H. (2004) Separation of isoprene compounds *via* π-complexation in C_5 mixtures. *Proceedings of the 4th international conference on separation science and technology*, 186 – 191.

Szekeres, M., Tóth, J., Dékány, I. (2002) Specific surface area of Stoeber silica determined by various experimental methods. *Langmuir*, 18, 2678 – 2685.

Tanaka, H., Watanabe, T., Chikazawa, M., Kandori, K., Ishikawa, T. (1999) TPD FTIR and molecular adsorption studies of calcium hydroxyapatite surface modified with hexanoic and decanoic acids. *J. Colloid Interf. Sci.*, 214, 31 – 37.

Taylor, P. and Gagan, M. (2002) Alkenes and Aromatics, RSC, Cambridge, pp. 139 – 160.

Tóth, J. (1995) Uniform interpretation of gas/solid adsorption. *Adv. Colloid Interf. Sci.*, 55, 1 – 239.

Tóth, J., Berger, F., Dékány, I. (1999a) Calculation of the BET compatible surface area from any type I isotherms measured below the critical temperature. *J. Colloid Interf. Sci.*, 212, 402 – 410.

Tóth, J., Berger, F., Dékány, I. (1999b) Calculation of the BET compatible surface area from any type I isotherms measured below the critical temperature. *J. Colloid Interf. Sci.*, 212, 411 – 418.

Trombetta, M., Busca, G., Rossini, S.A., Piccoli, V., Cornaro, U. (1997) FT-IR studies on light olefin skeletal isomerization catalysis. I. The interaction of C4 olefins and alcohols with pure γ-alumina. *J. Catal.*, 168, 334 – 348.

Webster, C.E., Drago, R.S., Zerner, M.C. (1998) Molecular dimensions for adsorptives. *J. Am. Chem. Soc.*, 120, 5509 – 5516.

Wu, C.W., Kothare, M.V., Sircar, S. (2014) Model analysis of equilibrium adsorption isotherms of pure N_2, O_2, and their binary mixtures on LiLSX zeolite. *Ind. Eng. Chem. Res.*, 53, 12428 – 12434.

Yoda, E., Kondo, J.N., Domen, K. (2005) Detailed process of adsorption of alkanes and alkenes on zeolites. *J. Phys. Chem. B*, 109, 1464 – 1472.

Chapter 5:

Adsorption of C_5 and C_6 hydrocarbons on γ- and θ-Al_2O_3

5 Adsorption of C_5 and C_6 hydrocarbons on γ- and θ-Al_2O_3

In this chapter, the adsorption of a series of C_5 and C_6 unsaturated hydrocarbons over γ- and θ-Al_2O_3 was investigated with a wide range of experimental techniques. Specifically, the adsorption of 1-pentene, 1-pentyne, *cis*-2-pentene, *trans*-2-pentene, 1,4-pentadiene and cyclohexene was studied. The presence of different structural isomers, types of unsaturation – double and triple bond – as well as a cyclic molecule, offer different cases to be evaluated. IR spectroscopy, volumetric adsorption isotherms, dynamic adsorption isotherms obtained *via* TEOM as well as temperature-programmed desorption (TPD) techniques are employed in this chapter. Both ^{13}C T_1 and ^{1}H 2D T_1-T_2 NMR relaxometry adsorption techniques are also employed. This section follows on the work described in chapter 4, where the adsorption of 1-pentene was studied with ^{13}C T_1 NMR relaxometry, IR and adsorption isotherms. There, ^{13}C T_1 NMR experiments were shown to provide relevant information on adsorption of 1-pentene. Here, detailed information on the type and strength of interaction for each hydrocarbon will be presented. Additionally, a comparison between the different adsorption techniques used will provide additional information on the different adsorption sites probed, *i.e.*, what is being measured by each technique.

5.1 Experimental materials and methods

A detailed description of the experimental methods used with the different adsorption techniques is shown. Some of the aspects regarding IR and adsorption isotherms have already been described in chapter 4.

5.1.1 Materials

Both γ-Al_2O_3 and θ-Al_2O_3 extrudates were crushed to particles of < 150 μm for adsorption experiments, unless stated otherwise. The adsorbents were described in chapter 3. The adsorbates studied were a series of acyclic C_5 and cyclic C_6 hydrocarbons (of purity): 1-pentene (98 %), 1-pentyne (99 %), *cis*-2-pentene (98 %), *trans*-2-pentene (99 %) 1,4-pentadiene (99 %), and cyclohexene (99 %). All adsorbates were supplied from Aldrich and used as received. He (99.996 %) was supplied from Air Liquide and used without further purification.

5.1.2 TEOM

Mass uptake data were recorded using a Tapered Element Oscillating Microbalance (TEOM) (1500 Pulse Mass Analyser, Rupprecht & Patashnick). Process conditions and data storage were controlled using Labview software (National Instruments). Mass data were acquired every 1 s, and isotherm values were averaged every 10 s. Adsorption of 1-pentene, 1-pentyne and cyclohexene was carried out at 303, 313 and 323 K on pre-heated γ- and θ-Al_2O_3 at 393 or 673 K. Approximately 15 mg of alumina were placed in the oscillating element and pre-heated in 50 $cm^3\,min^{-1}$ of He for 1 h, maintaining an equivalent He purge flow. The adsorbate was vapourised with the use of a saturator using He as carrier gas at a flow rate of 50 $cm^3\ min^{-1}$. The saturator was immersed in an ethylene glycol-ethanol bath at 243 K and temperature was controlled in a chiller (Julabo, M32-HC). Step temperature increments to 253, 263, 268, 273, 278, 283, 288 and 293 K were applied to the bath to increase the hydrocarbon vapour pressure. All stainless steel lines were heated to 333 K to prevent condensation. Adsorption of the hydrocarbon was monitored and temperatures were increased after equilibrium uptake values were reached. The amount of vapourised adsorbate in the feed as well as in the effluent remaining after adsorption was monitored with a GC (6890 Hewlett Packard, splitless mode), as described in section 2.2.1.4. Blank measurements were performed using sand (Sigma Aldrich), and the raw signal was subtracted to remove other effects unrelated with adsorption.

5.1.3 Infrared spectroscopy

In-situ Diffuse Reflectance Infrared Fourier Transform Spectroscopy (DRIFTS) measurements on the adsorption of 1-pentene and 1-pentyne at 298 K over γ- and θ-Al_2O_3 powders were carried out. Procedures were the same as those reported in section 4.2.4. During desorption, spectra were recorded every 15 s.

5.1.4 Volumetric adsorption isotherms

Adsorption isotherms of the hydrocarbons were obtained using the volumetric method at three different temperatures: 273, 285.5 and 298 K. Only 298 and 313 K were employed during adsorption of cyclohexene due to limited vaporisation of adsorbate. Controlled adsorption measurements were performed in a glass manifold, as described in section 4.2.3.

5.1.5 ^{1}H 2D T_1-T_2 NMR relaxometry

Adsorption of 1-pentene, 1-pentyne and cyclohexene on γ- and θ-Al_2O_3 was measured *via* ^{1}H NMR relaxometry. The NMR experiments were performed on a Bruker wide bore DMX spectrometer with a vertical bore 7.0 T superconducting magnet operating at ^{1}H frequency of 300.23 MHz. ^{1}H spectra were recorded for each sample using a standard pulse-acquire sequence, and both 90º and 180º pulses were calibrated for each sample. T_1 experiments were conducted using both inversion-recovery and saturation-recovery pulse sequences for comparison (section 2.2.2.2.1). T_2 experiments were conducted via a Carr-Purcell-Meiboom-Gill (CPMG) sequence (section 2.2.2.2.2). Additionally, two-dimensional T_1-T_2 analysis was performed (section 2.2.2.2.3). The 16 recovery delays varied logarithmically from τ_R = 10 ms to 10 s. In the CPMG echo train, the intensity of n = 1024 echoes were acquired in a single shot with an echo spacing of τ_E = 500 μs. All experiments were performed at 293 K, unless stated otherwise, and spectra were referenced to tetramethylsilane (TMS).

Alumina trilobes were pre-treated at 393 K or 673 K under vacuum for 1 h and fully saturated samples were prepared. The pre-treated alumina was soaked under vacuum in liquid adsorbate for 12 h to ensure pores were completely filled with liquid. Details on final preparation and soaking time have been reported elsewhere (Weber *et al.*, 2009). Samples were then filtered on pre-soaked filter paper and trilobes were transferred into 5 mm NMR tubes (Wilmad), under a saturated atmosphere of adsorbate *via* impregnated cotton on cap, and sealed. A subset of samples were prepared in 5 mm glass tubes (Soham Scientific), dosed 10 monolayer (ML), 1 ML and 0.1 ML of hydrocarbon, following procedure described in section 4.2.2.1, and flame-sealed.

5.1.6 Temperature-programmed desorption (TPD)

TPD-MS experiments were performed in a CATlab microreactor module (Hiden Analytical) and desorbed species were detected with a QIC-20 quadrupolar mass spectrometer (QMS). Details of the equipment were described in section 2.2.1.2. Approximately 100 mg of γ- or θ-Al_2O_3 trilobes were pre-treated at 393 or 673 K, after which the hydrocarbon was adsorbed until saturation. This procedure was either preformed *in situ* with the aid of saturator, or *via* the glass manifold, as detailed in section 5.1.5. In the latter case, the alumina with the pre-adsorbed hydrocarbon was transferred into the reactor gas tube. Desorption of excess

hydrocarbon was achieved at 313 - 323 K under flowing He, at a flow rate of 40 cm^3 min^{-1}, for a duration of 1 h. The samples were then heated from 323 K to 1073 K with a ramp rate of 10 K min^{-1} at a flow rate of 40 cm^3 min^{-1} of He. Desorption of pre-adsorbed hydrocarbon was monitored observing *m/z* = 42 for 1-pentene; *m/z* = 67 for 1-pentyne, 1,4-pentadiene and cyclohexene; and *m/z* = 55 for *cis*- and *trans*-2-pentene. Also, desorption and isomerisation of 2-pentene products to 1-pentene isomer were recorded simultaneously *via* *m*/*z* = 55 and 42. Possible hydrogenation reactions during 1-pentyne desorption were detected following the hydrogenated species up to the alkane, with *m/z* = 43 for *n*-pentane. Finally, the presence of secondary reactions and cracking of the hydrocarbon was monitored *via* a full range scan, set for *m/z* = 2 to 71, during 1-pentene and 1-pentyne desorption.

Calibration of the QMS signal was performed by integration of the respective *m*/*z* following the injection of a known amount of each hydrocarbon, usually 5.0 ± 0.1 μL. Thus, desorption rates were expressed in molecules desorbing by specific surface area of each alumina per unit of time (molec nm^{-2} s^{-1}). The Polanyi-Wigner equation (equation 1.3) was used to determine the energies of desorption. Analysis of the energetics of desorption followed the methods described in section 2.2.1.2.

5.2 Results

The adsorption of C_5 and C_6 unsaturated hydrocarbons was investigated. In addition to IR spectroscopy and adsorption isotherms *via* the volumetric method, other experimental techniques were implemented. TEOM and NMR relaxometry techniques were employed. In the case of TEOM and ^{1}H 2D T_1-T_2 relaxometry correlations, the study was limited to 1-pentene, 1-pentyne and cyclohexene. This allowed for geometric effects as well as double-bond *vs.* triple-bond interactions to be studied.

5.2.1 Infrared spectroscopy

The adsorption of 1-pentyne was studied *via* DRIFTS. The type of interaction with the surface, *via* an adsorbed bond or functional group, was followed. Semi-quantitative information on strength of adsorption was also studied. As shown in section 3.3.1, and as will be evident here, the adsorbed species had only a short residence time on the surface, as shown by IR. Hence, only major differences, such as those between double-bond and triple-bond adsorption were studied.

Figure 5.1 shows the infrared spectrum of the adsorption of 1-pentyne at 298 K on γ- and θ-Al_2O_3 pre-treated at 393 and 673 K. Difference spectra with respect to each pre-treated alumina are shown. **Table 5.1** shows the bands present in the spectra and their assignment. As can be seen, negative bands appeared at 3735 cm^{-1} and 3700 cm^{-1}, and a positive band was observed at 3631 cm^{-1} in the OH stretching region. Similar negative bands have been observed in the adsorption of butene isomers on γ-Al_2O_3 (Trombetta *et al.*, 1997). In the adsorption of 1-pentyne, the bands were related to the types of hydroxyl groups interacting with the hydrocarbons. Thus, the adsorption of 1-pentyne was similar to that of 1-pentene shown in section 4.3.1, whereby double-bridged and triple-bridged OH coordinated to Al^{VI} participated (Morterra and Magnacca, 1996; Knözinger and Ratnasamy, 1978, Tsyganenko and Filimonov, 1972). Comparatively, these bands were more pronounced in the adsorption of 1-pentyne, indicating a stronger interaction with the alumina. All bands decayed after 6 min, indicative of the fast, weak and reversible adsorption-desorption of the alkyne from the surface hydroxyls.

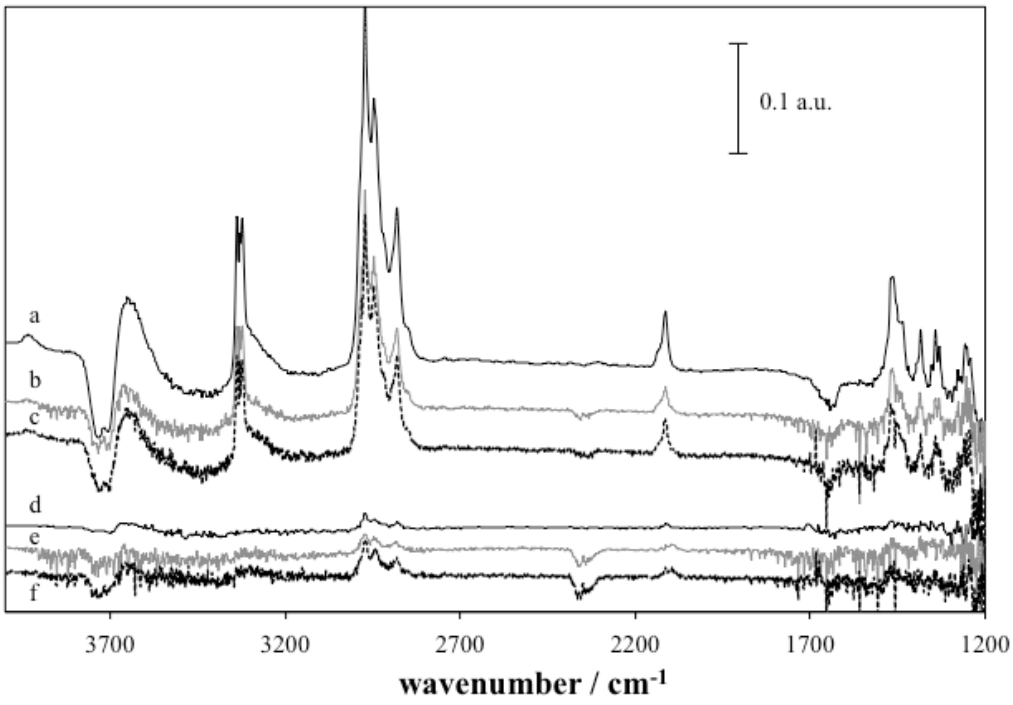

Figure 5.1. DRIFTS spectra for the adsorption of 1-pentyne on γ- (dashed) and θ-Al_2O_3 (continuous). Initial desorption after signal saturation (a, b and c) and after 5 min He flow (d, e and f). The black lines represent samples pre-treated at 673 K, while the grey lines show the spectra on samples pre-treated at 393 K.

Table 5.1. Summary of the observed IR bands for the adsorption of 1-pentyne on γ- and θ-Al_2O_3. The type of vibration, the position in wavenumbers (cm^{-1}), and the assignment to a corresponding bond are shown.

bond vibration	wavenumber / cm^{-1}	assignment
O-H stretch	3730	double-bridged OH (II)
	3716 3700	triple-bridged OH (II)
	3650 - 3630	bulk OH
C-H stretch	3338 3330 3322	ν(≡CH)
	2967 2945 2879	$\nu(CH_3)$ and $\nu(CH_2)$
C-C stretch	2133[a] 2113	ν(C≡C)
C-H bend	1456	$\delta(CH_3)_{as}$
	1440	$\delta(CH_2)_{scissors}$
	1382	$\delta(CH_3)_s$
	1336	$w(CH_2)$[b]

a) Shoulder of main band; b) wagging

Interaction of the hydrocarbons with the aluminas was also shown by the presence of characteristic bands of the hydrocarbon. C-H stretching bands, corresponding to $\nu(CH_3)$ and $\nu(CH_2)$, appeared at 2967 cm^{-1}, 2945 cm^{-1} and 2879 cm^{-1}. Characteristic bands of 1-pentyne unsaturation were noted. Bands at 3330 cm^{-1}, split into a triplet at 3338 cm^{-1}, 3330 cm^{-1} and 3322 cm^{-1}, appeared with the adsorption of 1-pentyne irrespective of the type of alumina or pre-treatment temperature. These bands corresponded to ν(≡CH) from excess vapour and weakly interacting liquid (Crowder and Fick, 1986; Horn *et al.*, 2011), indicative of the weak type of interaction with the surface. Additionally, a weaker band was observed at 2113 cm^{-1}, with a shoulder at 2133 cm^{-1}, corresponding to ν(C≡C) for liquid adsorption and vapour, respectively. Finally, in the fingerprint region (<1500 cm^{-1}), bands appeared at 1456 cm^{-1}, with a shoulder at 1440 cm^{-1}, 1382 cm^{-1} and 1336 cm^{-1}, during the adsorption of 1-pentyne. These bands corresponded to $\delta(CH_3)_{as}$, $\delta(CH_2)$ scissors, $\delta(CH_3)_s$, and $w(CH_2)$ (Crowder and Fick, 1986; SDBS, 1997). Comparing with **Figure 4.1**, bands were more intense for 1-pentyne, indicating more molecules of 1-pentyne were interacting with the alumina, as compared to 1-pentene. In **Figure 5.1** a considerable reduction in these bands with purging was observed after 5 min (spectra c, d and e). Noticeably, a redshift from 2112 cm^{-1} to 2092 cm^{-1} was observed for the ν(C≡C) band after 15 min, indicating a weakening of the

triple bond, in line with interactions of the functional group with the surface OH. No other bands related to products of reactions, such as cracking or hydrogenation, were present, contrary to results from adsorption of butene and butane on aluminas (Garbowski and Primet, 1985). It was inferred that the interaction was too weak to dissociate the molecule (Busca *et al.*, 1987; Trombetta *et al.*, 1997). However, a yellow colouration was observed on the alumina post-adsorption. This is in line with previous studies that have manifested the presence of strongly-adsorbed hydrocarbon. For example, a yellow coloration of the alumina was seen after prolonged adsorption of butane isomers (Peri, 1961).

Fitting the integrated area of the ν(C≡C) band in the IR spectrum with a single exponential decay (equation 4.1) resulted in the values summarised in **Table 5.2**. As can be seen, pre-treatment temperature modified the time constant. Thus, values of $\tau = 3.1 \pm 0.5$ min and $\tau = 2.4 \pm 0.4$ min were obtained for adsorption of 1-pentyne on θ-Al_2O_3 pre-treated at 673 K and 393 K, respectively. Similar values of the time constants were observed for the adsorption of 1-pentyne on γ- and θ-Al_2O_3, indicative of a weak effect on adsorption. Comparison of these time constants with results on the adsorption of 1-pentene in section 4.3.1 (**Table 4.2**) was indicative of stronger interaction of the triple bond. Values of $\tau = 3.1 \pm 0.5$ min and $\tau = 2.3 \pm 0.1$ min were obtained for adsorbed 1-pentyne and 1-pentene, respectively, on θ-Al_2O_3 pre-treated at 673 K. Additionally, I_0 values were higher for 1-pentyne adsorption, in agreement with higher surface density of 1-pentyne molecules interacting with the alumina. These values are semi-quantitative, as the experiments were performed using diffuse-reflectance mode. Overall, IR results were indicative of a weak interaction of the hydrocarbon *via* the unsaturation with surface hydroxyl groups. These adsorption sites can be related with weak Brønsted acid sites on the aluminas. Minor differences in adsorption were observed between both aluminas. Pre-treatment temperatures showed a marked influence on adsorption, which might suggest the participation of Lewis acid sites discussed in section 3.3.2. Differences in the strength of interaction of alkyne *vs*. alkene were noted, following the lower time constant for 1-pentene adsorption.

Table 5.2. Parameters resulting from the fitting of an exponential decay to the integrated IR bands for the desorption of 1-pentyne on γ- and θ-Al_2O_3. Parameters were described in **Table 4.2**

surface	pre-treatment T / K	I_0 / -	τ / min
θ-Al_2O_3	673	0.65 ± 0.07	3.1 ± 0.5
γ-Al_2O_3	673	0.8 ± 0.2	3.0 ± 0.4
θ-Al_2O_3	393	0.6 ± 0.2	2.4 ± 0.4

5.2.2 Batch adsorption isotherms

In this section, the adsorption of hydrocarbons following the gas adsorption manometry method is reported. Results are presented for the adsorption of the hydrocarbons studied, solely on θ-Al_2O_3. Energies of adsorption as well as adsorption in multilayers are discussed, following the structure in section 4.3.2. **Figure 5.2** shows the results of the adsorption of 1-pentyne and *cis*-2-pentene on θ-Al_2O_3 pre-treated under vacuum at 303 K. Adsorption experiments were performed at 273, 285.5 and 298 K for increasing equilibrium pressures, with the exception of cyclohexene, performed only at 298 and 313 K. The selection of such temperatures for cyclohexene and implications on adsorption energies is discussed in section 5.3.2. A type II isotherm was observed experimentally, with an S-shape or sigmoidal curvature. Results are only shown in the region of $P/P^{SAT}(T) < 0.35$, before capillary condensation occurred. The resulting data was fitted to a Tóth isotherm equation. **Table 5.3** shows the parameters resulting from the fitting of the Tóth adsorption equation to the different hydrocarbons on θ-Al_2O_3. The entire isotherm was fitted in the first instance (see section 5.2.2.2). The quality of the data and the presence of any outliers were checked following the method proposed by Hinz (2001), whereby v/P values were plotted against P or v. This analysis was especially useful in the case of adsorption of cyclohexene. The limited range of vapourisation resulted in inaccurate uptake measurements at P < 4 mbar.

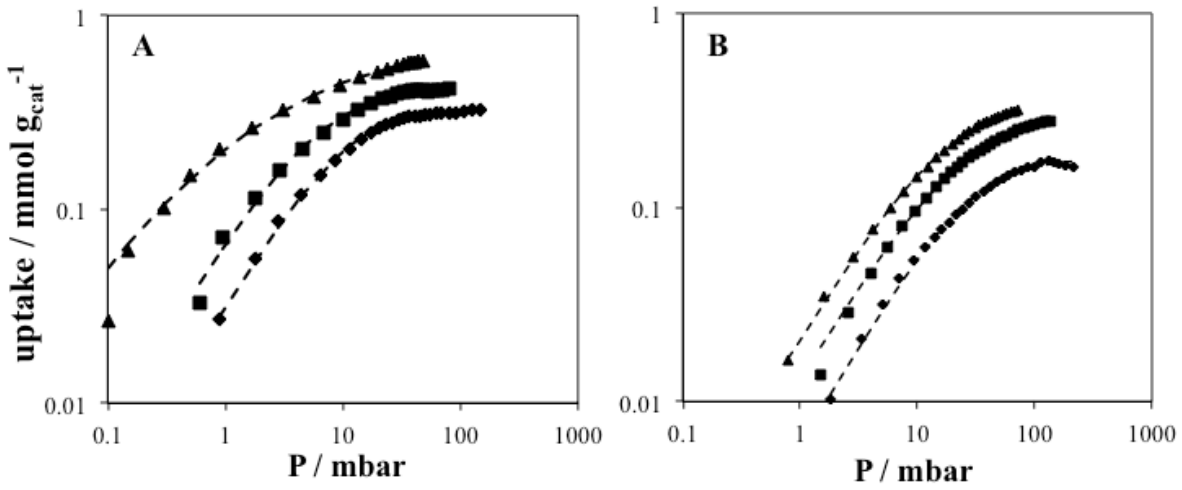

Figure 5.2. Uptake of 1-pentyne (A) and *cis*-2-pentene (B) as a function of equilibrium vapour pressure on θ-Al_2O_3 at 273 (triangles), 285.5 (squares) and 298 K (diamonds). The lines represent the fitted Tóth isotherm equation.

Table 5.3. Tóth isotherm constants for the adsorption of hydrocarbons on pre-treated θ-Al_2O_3.

hydrocarbon	T / K	v_{max} / mmol g^{-1}_{cat}	$k_T \times 10^2$ / $mbar^{-1}$	t / -	R^2
1-pentene	273	0.94 ± 0.05	9.4 ± 0.8	0.44 ± 0.02	0.99993
	285.5	0.66 ± 0.03	5.5 ± 0.4	0.53 ± 0.03	0.9997
	298	0.42 ± 0.02	3.8 ± 0.3	0.69 ± 0.03	0.9992
1-pentyne	273	0.77 ± 0.04	92 ± 9	0.48 ± 0.02	0.998
	285.5	0.44 ± 0.02	12 ± 1	1.15 ± 0.06	0.997
	298	0.33 ± 0.02	7 ± 1	1.40 ± 0.07	0.998
cyclohexene	298	10.95 ± 0.02	0.3 ± 0.2	0.31 ± 0.05	0.99992
	313	2.1 ± 0.2	1.5 ± 0.1	0.39 ± 0.02	0.9994
***cis*-2-pentene**	273	0.38 ± 0.02	5.6 ± 0.4	1.10 ± 0.07	0.9997
	285.5	0.32 ± 0.02	4.1 ± 0.3	1.08 ± 0.06	0.9997
	298	0.18 ± 0.01	3.4 ± 0.2	1.46 ± 0.09	0.995
***trans*-2-pentene**	273	0.46 ± 0.03	8 ± 1	0.78 ± 0.05	0.9995
	285.5	0.23 ± 0.01	3.9 ± 0.6	1.33 ± 0.09	0.997
	298	0.15 ± 0.01	3.3 ± 0.5	1.24 ± 0.09	0.9997
1,4-pentadiene	273	0.30 ± 0.01	6.0 ± 0.6	1.19 ± 0.08	0.9996
	285.5	0.18 ± 0.01	5.5 ± 0.6	1.4 ± 0.1	0.992
	298	0.119 ± 0.006	2.5 ± 0.3	1.4 ± 0.1	0.997

Results indicate various trends in the parameters fitted. Looking at the saturation adsorption values, v_{max}, a clear decreasing trend can be observed with increasing temperature in all cases. Thus, v_{max} values 7.68×10^{-4}, 4.41×10^{-4} and 3.31×10^{-4} mol g^{-1} were observed on adsorption of 1-pentyne at 273, 285.5 and 298 K. This decay in saturation adsorption values indicated that the energy of adsorption was not sufficient to overcome the temperature variation, indicative of weak adsorption. The values of t are quite scattered across adsorbates and temperature. The value of t was the lowest at 273 K in all hydrocarbons, increasing at 298 K (313 K for cyclohexene). The dependence of t with temperature was shown in equation 4.6. Hence, increasing values of t with increasing temperature would be expected for an adsorption process in a heterogeneous surface, where the strongest sites are occupied first. Additionally, the values spread with respect to the ideal Langmuir case ($t = 1$). 1-pentyne and *trans*-2-pentene showed a transition between $t < 1$ and $t > 1$ with increasing temperature. Cyclohexene and 1-pentene showed values $t < 1$, while the opposite was true for *cis*-2-pentene and 1,4-pentadiene. The values of the adsorption constant k revealed important information on the interaction of each hydrocarbon on the aluminas. Similarly to the values taken by v_{max}, the values of the adsorption constant k decreased with increasing temperature, with the only exception on the adsorption of cyclohexene. As can be seen, the highest values

of all the series were obtained on the adsorption of 1-pentyne, as compared, for example, with the values of the adsorption of cis-2-pentene. It was observed that k = 0.924 mbar^{-1} for 1-pentyne, contrasting with k = 0.056 mbar^{-1} for *cis*-2-pentene at 273 K. Cyclohexene showed the lowest values of the series. As can be seen, the adsorption of hydrocarbons on θ-Al_2O_3 was a complex process, where the interactions of the adsorbate with other molecules and the surface varied non-linearly with temperature and adsorbate type.

5.2.2.1 Heats of adsorption

The values of the adsorption constant k_T for the different hydrocarbons have important implications on the description of the adsorption energy. The energy of adsorption at zero coverage, $(-\Delta H_{ads})_{zero}$, is obtained with k_T using the van't Hoff equation as described in section 4.3.2.1. Fitting the adsorption constant k_H at the different temperatures for each molecule resulted in the values shown in **Table 5.4**.

Table 5.4. Isosteric heat of adsorption at zero coverage for the different hydrocarbons adsorbed on θ-Al_2O_3, obtained after fitting the van't Hoff equation to the Henry adsorption constant values derived from the Tóth model.

hydrocarbon	$(-\Delta H_{ads})_{zero}$ / kJ mol^{-1}	R^2
1-pentene	46 ± 6	0.98
1-pentyne	94 ± 12	0.98
cyclohexene	11 ± 8	-
***cis*-2-pentene**	34 ± 6	0.97
***trans*-2-pentene**	54 ± 3	0.996
1,4-pentadiene	48 ± 10	0.95

Isosteric heats of adsorption were also obtained as a function of coverage, as described in section 4.3.2.1. **Figure 5.3** shows the isosteric heats of adsorption of the different hydrocarbons on θ-Al_2O_3, as a function of surface coverage. In order to obtain such coverage, saturation capacity values, v_{max}, at 273 K were used for each molecule (for cyclohexene the value at 298 K was chosen). Such selection accounted for most adsorption sites, as seen by the trends with v_{max} values. 1-pentyne presented a marked adsorption behaviour compared with the rest of hydrocarbons. A decrease in adsorption strength from 94 kJ mol^{-1} to ~ 65 kJ mol^{-1} was observed with increasing coverage up to 30% ML. In contrast, the adsorption strength of the acyclic olefins presented a decreasing value of the heat of adsorption up to 10 - 15% ML, after which the values started increasing. Such an effect has been previously observed and attributed to predominant lateral interactions or limited surface

interactions (Aguilar-Armenta *et al.*, 2006; Domínguez *et al.*, 2010; Sears, 2001; Siperstein *et al.*, 1999). Cyclohexene presented an earlier transition into that regime. The lower value of $(-\Delta H_{ads})_{zero}$ and the limited decrease in q_{st} with increasing coverage, compared with the rest of hydrocarbons, suggested an effect of temperature on vapour pressure.

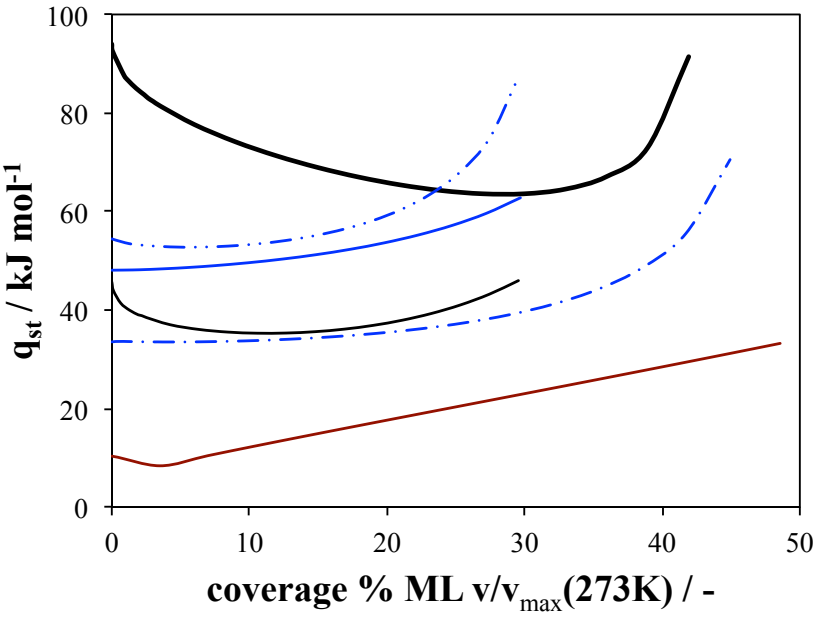

Figure 5.3. Isosteric heats of adsorption as a function of fractional coverage for the different molecules adsorbed on θ-Al_2O_3 in the range 273 – 298 K obtained from the Tóth full range fit of the volumetric isotherms. 1-pentyne (thick black), 1-pentene (thin black), cyclohexene (red), *cis*-2-pentene (blue, -·), *trans*-2-pentene (blue, -··) and 1,4-pentadiene (blue), are shown. The fractional coverage was calculated assuming 1 ML corresponded to the value of v_{max} obtained from fitting the Tóth isotherm to the experimental data for each hydrocarbon at 273 K.

Additionally, adsorption isotherms were analysed using Virial type equations. Previous studies have shown the robustness of this method in the low pressure regime (Tedds *et al.*, 2011; Purewal *et al.*, 2009). The equation used in this study was a subset of the generalised Virial type equation proposed by Czepirski and Jagiełło (1989), as follows:

$$\ln P = \frac{1}{T}\sum_{i=0}^{l} a_i v^i + \sum_{i=0}^{m} b_i v^i + \ln v \,. \qquad (5.1)$$

In this case, l=m=2. Additionally, Henry's law constants were evaluated using this method. Adsorption in the low-pressure region can be accurately modelled with:

$$\ln\left(v/P\right) = K_0 + K_1 v + K_2 v^2 + \cdots \tag{5.2}$$

with equation 5.2 describing Henry's isotherm. Applying this Virial form at zero coverage:

$$\lim_{v\to 0}\left(v/P\right) = k_H = \exp\left(K_0\right). \tag{5.3}$$

Figure 5.4 shows the Virial fitting to the experimental data for the adsorption of 1-pentyne and *cis*-2-pentene on θ-Al_2O_3. **Figure 5.5** shows the calculation of the adsorption energy at zero coverage of 1-pentyne using the Virial method. **Table 5.5** summarises the values of $(-\Delta H_{ads})_{zero}$ for all hydrocarbons obtained with the Virial method. Values at zero coverage calculated with the Virial equation were slightly lower (by about 5 kJ mol^{-1}), with 1-pentyne showing a more significant deviation. These values were used as a constraint in the fitting process for the estimation of the Virial parameters in equation 5.1. Calculation of the heat of adsorption using the Clausius-Clapeyron equation resulted in a polynomial equation:

$$q_{st} = (-\Delta H_{ads}) = -R\sum_{i=0}^{l} a_i v^i \ . \tag{5.4}$$

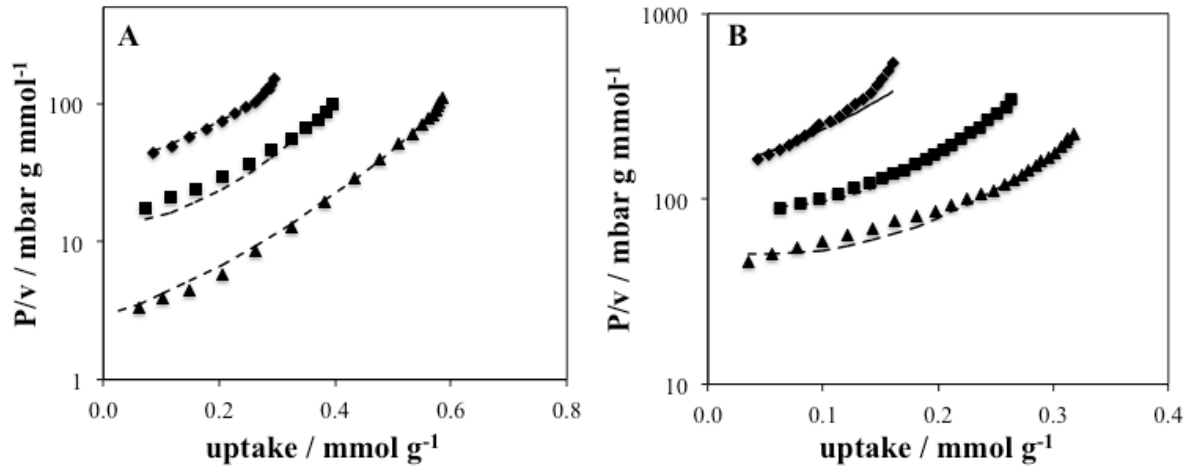

Figure 5.4. Virial form of the uptake of 1-pentyne (A) and *cis*-2-pentene (B) as a function of equilibrium vapour pressure on θ-Al_2O_3 at 273 (triangles), 285.5 (squares) and 298 K (diamonds). The lines represent the fitted Virial equation.

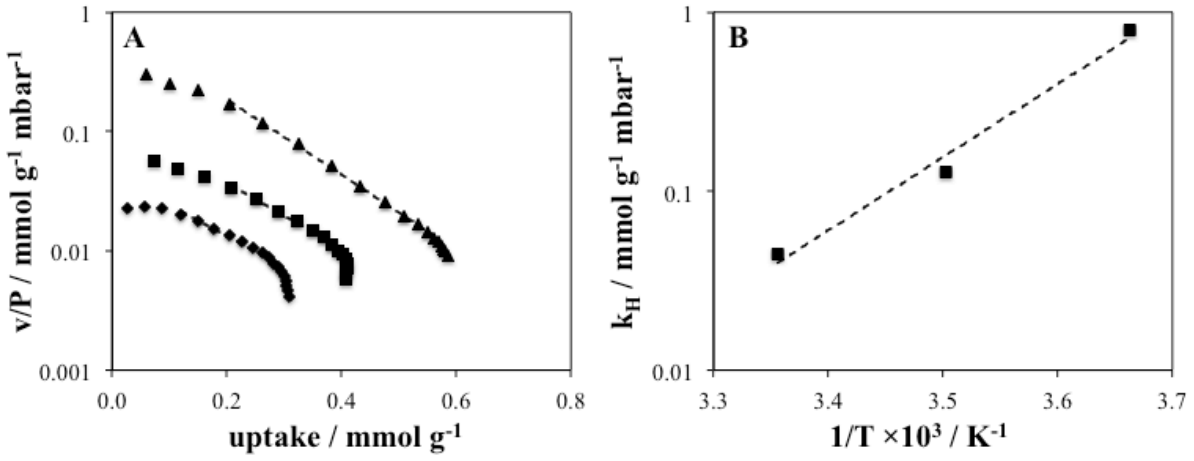

Figure 5.5. Zero coverage analysis: (A) Virial form for the calculation of Henry's constant for 1-pentyne adsorbed on θ-Al_2O_3 at 273 (triangles), 285.5 (squares) and 298 K (diamonds), the lines represent the linear portion of the isotherm, where Henry's model applies; (B) Best fit of the Henry's constant values obtained for the calculation of the heat of adsorption at zero coverage.

Table 5.5. Isosteric heat of adsorption at zero coverage for the different hydrocarbons adsorbed on θ-Al_2O_3, obtained after fitting the van't Hoff equation to the Henry adsorption constant values derived from the Virial equation.

hydrocarbon	$(-\Delta H_{ads})_{zero}$ / kJ mol^{-1}	R^2
1-pentene	32.3 ± 0.7	0.998
1-pentyne	78 ± 14	0.97
cyclohexene	10 ± 8	-
***cis*-2-pentene**	28 ± 2	0.995
***trans*-2-pentene**	50 ± 2	0.996
1,4-pentadiene	43 ± 9	0.96

Figure 5.6 shows the heats of adsorption as a function of coverage for the different hydrocarbons studied calculated using the Virial equation, in comparison with the Tóth fitting. As can be observed, trends remain very similar between both Tóth and Virial equations. Adsorption of 1-pentyne remained the most energetically favoured, followed by the acyclic hydrocarbons. *Trans*-2-pentene and 1,4-pentadiene showed higher adsorption energies than 1-pentene or *cis*-2-pentene. Similarly to the results obtained with the Tóth isotherm, the isosteric heat of adsorption increased with increasing coverage, indicating preferential adsorbate-adsorbate interactions. Overall, both methods pointed towards similar adsorption energies for the hydrocarbons studied on θ-Al_2O_3.

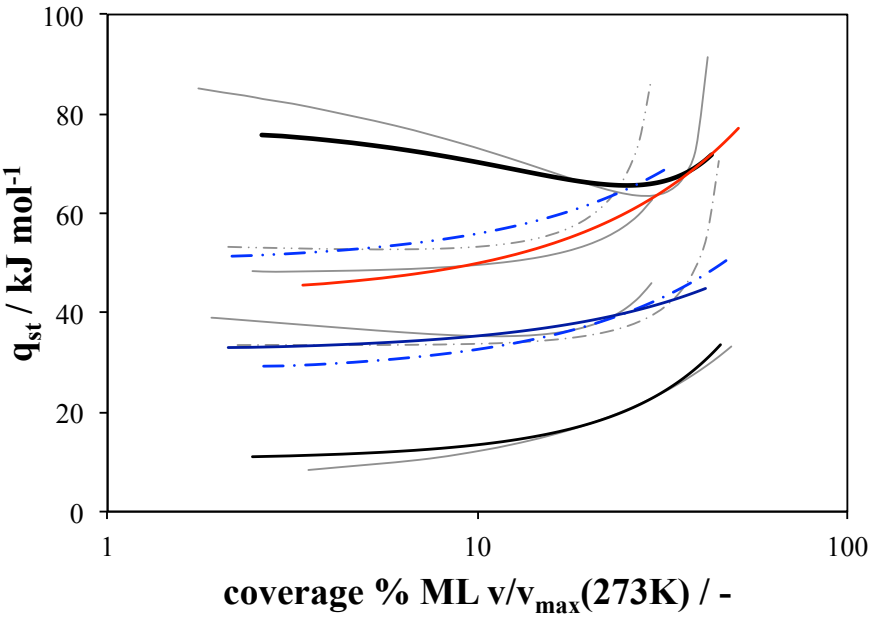

Figure 5.6. Comparison for the isosteric heats of adsorption as a function of fractional coverage for the different molecules adsorbed on θ-Al_2O_3 in the range 273 – 298 K obtained from the Virial (lines in colour) and Tóth full range (lines in grey) fits of the volumetric isotherms. The fractional coverage was calculated assuming 1 ML corresponded to the value of v_{max} obtained from fitting the Tóth isotherm to the experimental data for each hydrocarbon at 273 K in both cases. Refer to **Figure 5.3** for legend.

5.2.2.2 Multilayer adsorption

Finally, the Brunauer-Emmet-Teller (BET) equation was used to describe the experimental results, as described in section 4.3.2.2. **Figure 5.7** shows the results of the BET fitting to the adsorption of 1-pentyne and *cis*-2-pentene on θ-Al_2O_3. As can be observed, the intermediate linear portion of the isotherm was well described by this equation. **Table 5.6** shows the values of the BET model obtained after fitting the adsorption of hydrocarbons on θ-Al_2O_3. The values of $v_{m\text{-}BET}$ decreased monotonically with increasing temperature, explained by a thermal expansion on the adsorbed layer. Also, the values of E_1 - E_L increased slightly with increasing temperature in all cases. This result is in agreement with preferential adsorption on stronger sites, following the reduction in $v_{m\text{-}BET}$ and assuming a constant value of E_L. Results in 1,4-pentadiene represented the only exception to this behaviour. Considering the monolayer coverages at 273 K, $v_{m\text{-}BET}(273)$, it was possible to determine the mean molecular cross-sectional area of each hydrocarbon. **Table 5.7** shows the values for each hydrocarbon, significantly high for 1,4-pentadiene (0.96 nm^2), followed by the 2-pentene isomers. The

lowest value was obtained for 1-pentyne (0.46 nm^2). These values were higher than 0.35 nm^2 predicted for a liquid hexagonal packing of the molecules in the liquid (Russo *et al.*, 2008).

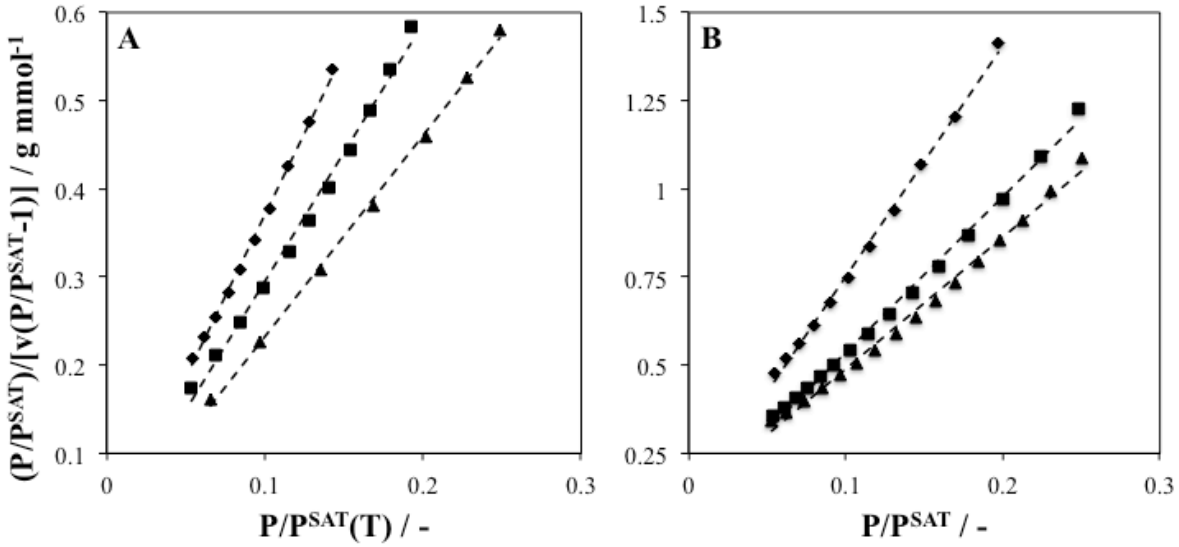

Figure 5.7. 1-pentyne (A) and *cis*-2-pentene (B) uptake as a function of equilibrium vapour pressure on θ-Al_2O_3 at 273 (triangles), 285.5 (squares) and 298 K (diamonds). The lines represent the fitted BET isotherm equation for $0.05 < P/P^{SAT}(T) < 0.3$.

Table 5.6. BET isotherm constants for the adsorption of hydrocarbons on pre-treated θ-Al_2O_3, in the range $0.05 < P/P^{SAT}(T) < 0.30$, approximately.

hydrocarbon	T / K	$v_{m\text{-}BET}$ / mmol g^{-1}_{cat}	E_1-E_L / kJ mol^{-1}
1-pentene	273	0.34 ± 0.01	3.75 ± 0.02
	285.5	0.29 ± 0.01	4.22 ± 0.02
	298	0.26 ± 0.01	4.23 ± 0.02
1-pentyne	273	0.44 ± 0.01	6.19 ± 0.03
	285.5	0.34 ± 0.01	7.12 ± 0.03
	298	0.27 ± 0.01	8.34 ± 0.02
cyclohexene	298	0.354 ± 0.004	2.20 ± 0.01
	313	0.338 ± 0.004	2.79 ± 0.01
***cis*-2-pentene**	273	0.26 ± 0.01	3.45 ± 0.02
	285.5	0.222 ± 0.004	3.98 ± 0.01
	298	0.151 ± 0.003	4.55 ± 0.01
***trans*-2-pentene**	273	0.25 ± 0.02	4.26 ± 0.02
	285.5	0.158 ± 0.003	5.00 ± 0.02
	298	0.104 ± 0.002	5.51 ± 0.02
1,4-pentadiene	273	0.206 ± 0.004	5.45 ± 0.02
	285.5	0.157 ± 0.001	4.54 ± 0.01
	298	0.097 ± 0.003	4.30 ± 0.03

Table 5.7. Mean molecular cross sectional area, a_m, heat of liquefaction, E_L, and heat of adsorption for the first layer, E_1, derived from BET monolayer coverage, v_m, and values of E_1 - E_L for the different hydrocarbons adsorbed on θ-Al_2O_3.

hydrocarbon	a_m / nm^2	E_L (298 K) / kJ mol^{-1}	E_1 (298 K) / kJ mol^{-1}
1-pentene	0.59 ± 0.04	25.39	29.62 ± 0.02
1-pentyne	0.46 ± 0.01	28.17	36.51 ± 0.03
cyclohexene	0.56 ± 0.01	33.41	35.61 ± 0.01
***cis*-2-pentene**	0.77 ± 0.03	26.97	31.52 ± 0.02
***trans*-2-pentene**	0.79 ± 0.06	26.94	31.20 ± 0.02
1,4-pentadiene	0.97 ± 0.02	24.57	28.87 ± 0.02

Additionally, the Tóth equation was applied to the study of the first adsorbed layer on the type II isotherm (Tóth *et al.*, 1999; Szekeres *et al.*, 2002). **Figure 5.8** shows the isosteric heats of adsorption after analysis of the experimental uptake values for $P/P^{SAT}(T) < 0.05$ with the Tóth equation. The general trends resembled those observed with the full Tóth fit. In general, adsorption values are higher (~15%) than the values of E_1 presented in **Table 5.6**. In contrast, 1-pentyne and *trans*-2-pentene showed much higher deviations, of about 80%. Additionally, an unclear distinction between the first layer and subsequent multilayer adsorption was noted for 1,4-pentadiene, with satisfactory BET equation fits below $P/P^{SAT}(T) < 0.05$. This result suggested a different mechanism during adsorption on the first layer. No results are shown for cyclohexene; previous analysis of the low-pressure results revealed limitations in the vapourisation-condensation, mixed with adsorption. Additionally, the use of only two adsorption temperatures could have resulted in higher uncertainty.

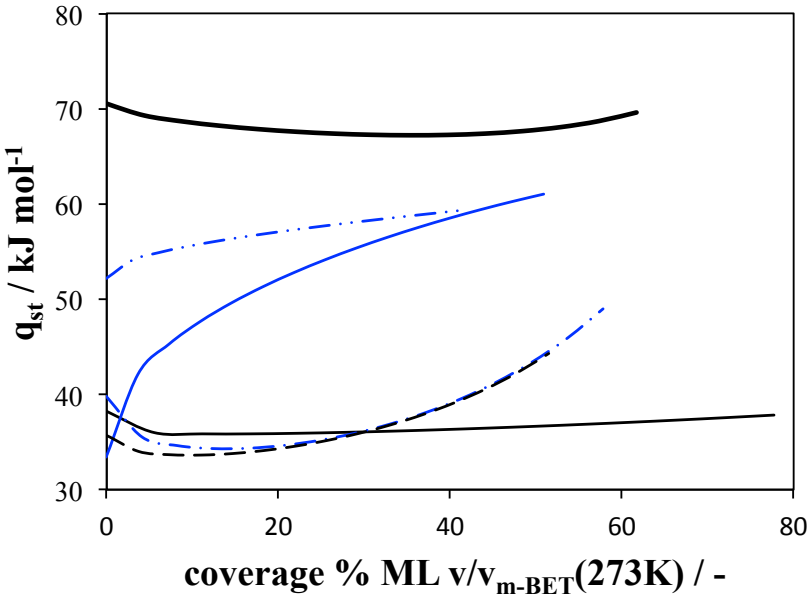

Figure 5.8. Isosteric heat of adsorption as a function of fractional coverage for the different molecules adsorbed on θ-Al_2O_3 in the range 273 – 298 K, obtained from $P/P^{SAT}(T) < 0.05$ Tóth fit of the volumetric isotherms. The fractional coverage was calculated assuming 1 ML corresponded to the value of v_m obtained from the BET isotherm for each hydrocarbon at 273 K. Refer to **Figure 5.3** for legend (cyclohexene not shown, as described in the main text).

5.2.3 TEOM: dynamic adsorption

TEOM provides an ideal experimental setup whereby the adsorbate flows through the pre-treated alumina (Koeken *et al.*, 2012). Similar olefin adsorption experiments were performed over solid acids (Gill *et al.*, 1998). Thus, the total uptake of each hydrocarbon can be determined in flow-through conditions. In this section, uptake results from the adsorption of 1-pentene, 1-pentyne and cyclohexene on γ- and θ-Al_2O_3 are shown. Experiments were performed with the aluminas pre-treated at both 393 and 673 K. For alumina pre-treated at 673 K, adsorption of hydrocarbons was only performed at 303 K. **Figure 5.9** shows the uptake of each hydrocarbon at equilibrium conditions at the three temperatures studied. A typical L ('Langmuir') class isotherm was observed, following the classification of Giles and co-workers (1960). As can be seen, hydrocarbon uptake generally decreased with increasing temperature. Moreover, the total uptake of hydrocarbons was higher on θ-Al_2O_3 compared to γ-Al_2O_3 at all temperatures, for the same equilibrium pressure. Comparing different alumina pre-treatment, it could be noted that the uptake of hydrocarbons at 303 K was higher on γ-Al_2O_3 pre-treated at 673 K than at 393 K. However, the complete opposite behaviour was

seen on θ-Al_2O_3. The uptake of 1-pentyne at 323 K was noticeably higher than at 313 K on both aluminas pre-treated at 393 K. This difference in total uptake of 1-pentyne might indicate a change in mechanism or mode of adsorption at those temperatures.

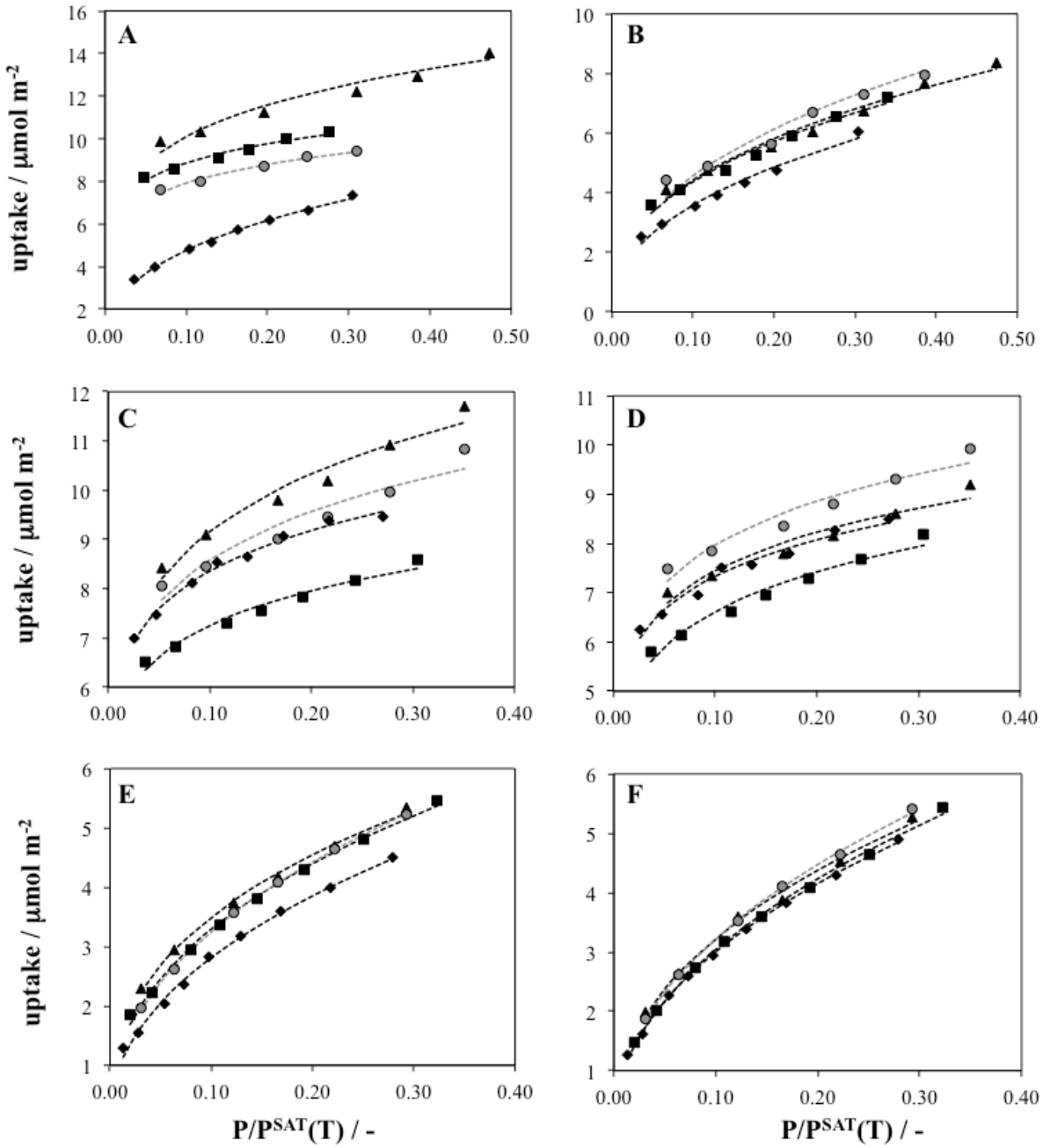

Figure 5.9. Uptake of 1-pentene (A-B), 1-pentyne (C-D) and cyclohexene (E-F) as a function of equilibrium pressure at 303 (triangles), 313 (squares) and 323 K (diamonds) measured by TEOM on θ-Al_2O_3 (A, C, E) and γ- Al_2O_3 (B, D, F). All samples were pre-treated at 393 K, except those shown in grey (circles), adsorbed at 303 K and pre-treated at 673 K.

The Freundlich adsorption isotherm (equation 1.5) was used to further analyse the results. The Freundlich isotherm has been widely used for adsorption of VOCs on various adsorbents (Wu *et al.*, 2012), as well as other hydrocarbons, such as toluene or 2-butanone on a carbon support (Bosnick *et al.*, 2011; Dallos *et al.*, 2002). Uptake values for pressures $P/P^{SAT}(T) > 0.38$ were discarded, for the same reasons as those discussed in section 5.2.2 for volumetric isotherms. **Tables 5.8** and **5.9** summarise the fitted parameters, k_F and $1/n$, of the Freundlich equation for the experiments discussed. k_F values are related with the bonding energy, while $1/n$ values relate with adsorption heterogeneity. Values of $n > 1$ indicate favourable physisorption (Crini *et al.*, 2007). Similar trends in the Freundlich parameters with temperature and type of alumina were observed for adsorption of cyclohexene and 1-pentene on γ- and θ-Al_2O_3. A reduction on k_F and an increase in $1/n$ with increasing temperature was observed, synonym of a reduction in the interactions with the surface. In contrast, fitted values from adsorption on 1-pentyne were lowest at 313 K, and both k_F and n increased at 323 K. These results might indicate the presence of some reactivity during adsorption or a different mechanism of adsorption. Additionally, similar values of $1/n$, lower to those obtained in 1-pentene or cyclohexene, were observed at all temperatures for 1-pentyne, indicative of similar strong and favoured adsorption. Finally, the values obtained on alumina pre-treated at 673 K showed a slight reduction when compared with those for the alumina pre-treated at 393 K. This was opposite to the favoured adsorption of hydrocarbons at 303 K observed on γ-Al_2O_3. These results might suggest a limitation in the formulation of the model in describing the adsorption process, in addition to limitations introduced by an insufficient number and range of data points to constraint the fit adequately.

Overall results showed the favourable adsorption of 1-pentene and cyclohexene at lower temperatures on both aluminas. These results were in agreement with those observed during volumetric adsorption isotherms. In contrast, the adsorption of 1-pentyne showed enhanced adsorption at 323 K. A different mode of adsorption or surface reactivity could explain such a result. Finally, surface pre-treatment enhanced adsorption on γ-Al_2O_3, while it was reduced on θ-Al_2O_3.

Table 5.8. Freundlich isotherm constants for the adsorption of hydrocarbons during TEOM experiments on γ- and θ-Al_2O_3, pre-treated at 393 K.

		θ-Al_2O_3			γ-Al_2O_3		
hydrocarbon	**T / K**	k_F / μmol m^2_{cat} $mbar^{-1/n}$	n^{-1} / -	R^2	k_F / μmol m^2_{cat} $mbar^{-1/n}$	n^{-1} / -	R^2
1-pentene	303	4.9 ± 0.5	0.16 ± 0.02	0.95	0.7 ± 0.1	0.39 ± 0.03	0.96
	313	4.5 ± 0.3	0.14 ± 0.01	0.992	0.7 ± 0.1	0.39 ± 0.03	0.98
	323	0.67 ± 0.04	0.37 ± 0.01	0.995	0.4 ± 0.1	0.44 ± 0.03	0.98
1-pentyne	303	4.4 ± 0.3	0.17 ± 0.02	0.96	4.1 ± 0.3	0.14 ± 0.02	0.93
	313	3.9 ± 0.2	0.13 ± 0.01	0.97	3.1 ± 0.2	0.17 ± 0.01	0.96
	323	4.3 ± 0.1	0.14 ± 0.01	0.992	3.7 ± 0.2	0.14 ± 0.01	0.97
cyclohexene	303	1.19 ± 0.03	0.38 ± 0.01	0.997	0.93 ± 0.04	0.44 ± 0.01	0.994
	313	0.84 ± 0.05	0.42 ± 0.01	0.996	0.63 ± 0.01	0.48 ± 0.01	0.998
	323	0.53 ± 0.04	0.45 ± 0.02	0.996	0.54 ± 0.02	0.47 ± 0.01	0.994

Table 5.9. Freundlich isotherm constants for the adsorption of hydrocarbons at 303 K during TEOM experiments on γ- and θ-Al_2O_3, pre-treated at 673 K.

	θ-Al_2O_3			γ-Al_2O_3		
hydrocarbon	k_F / μmol m^2_{cat} $mbar^{-1/n}$	n^{-1} / -	R^2	k_F / μmol m^2_{cat} $mbar^{-1/n}$	n^{-1} / -	R^2
1-pentene	4.0 ± 0.2	0.15 ± 0.01	0.994	0.7 ± 0.2	0.42 ± 0.04	0.97
1-pentyne	4.4 ± 0.5	0.16 ± 0.02	0.95	4.2 ± 0.4	0.15 ± 0.02	0.97
cyclohexene	0.93 ± 0.02	0.44 ± 0.01	0.9994	0.85 ± 0.01	0.47 ± 0.01	0.9991

5.2.4 Temperature-programmed desorption (TPD)

The temperature at which species are desorbed from the surface of a heated solid reflects the strength of surface bond. In a temperature-programmed desorption (TPD) experiment, the rate of desorption of adsorbed species is obtained. Desorption energies were extracted from the TPD results. A first order overall desorption process was assumed, and readsorption of molecules was considered insignificant. With these assumptions, the parameters A and E_{des} in the Polanyi-Wigner equation (equation 1.3) are independent of coverage (Barrie, 2008). Therefore, the overall rate of desorption is given by:

$$r_d(T) = \int_0^\infty f(E,T) N_0(E) dE \tag{5.7}$$

where f(E,T) is defined as:

$$f(E,T) = A \exp\left(\frac{-E_{des}}{RT}\right) \theta'(E,T) . \tag{5.8}$$

$\theta'(E,T)$ corresponds with the fraction of molecules still adsorbed on sites with activation energy E_{des} at temperature T. $N_0(E)$ is the activation energy distribution, for the adsorbed molecules at the initial adsorption temperature T_0 (Barrie, 2008). As can be seen, the calculation of the energy distribution, $N_0(E)$, required a Fredholm first kind integral to be solved (Kress, 1999; Wazwaz, 2011). Regularisation was used to solve this ill-posed problem. In addition, the Redhead equation was used to calculate the desorption energies of the peaks observed in the TPD curves (Roos *et al.*, 2010; Redhead, 1962), following:

$$\frac{E}{RT_P} = \ln\left(\frac{T_P A}{\beta}\right) - 3.64 . \tag{5.9}$$

In this case, T_P is the temperature of the peak for a first order desorption process, and β is the temperature ramp rate of the TPD experiment.

The selection of an appropriate exponential factor was also considered. Usually, values of $A = 10^{13}$ s^{-1} are used in the desorption of simple molecules, such as CO, H_2, O_2 or Ar (Buatier de Mongeot *et al.*, 1997; Redhead, 1962). This value corresponds to the frequency of a bond vibration for small molecules (Chorkendorff and Niemantsverdriet, 2007; Ulbricht *et al.*, 2006). Therefore such a value would be expected to increase for larger adsorbates. Previous experimental and MD simulation of a series of alkanes and alkenes indicated an increase in

the pre-exponential factor with increasing carbon number (Ulbricht *et al.*, 2006; Fichthorn and Miron, 2002). However, comparing different surfaces, it was observed that the pre-exponential factors of alkanes presented much lower values on oxide surfaces, such as 10^{14} s^{-1} for butane on anatase TiO_2 (Goering *et al.*, 2007), as compared to 10^{16} s^{-1} on Cu(111) or Ag(111) (Miller *et al.*, 2013; Pawela-Crew and Madix, 1995). Additionally, the pre-exponential values on alkenes, compared to the respective alkanes, presented values about one order of magnitude lower compared to the alkane (Pawela-Crew and Madix, 1995). In a previous study, a pre-exponential value of 10^{13} was selected for the analysis of the desorption of C_3 to C_7 saturated and unsaturated acyclic and cyclic hydrocarbons (Teplyakov *et al.*, 1998). Therefore, a value of $A = 10^{13}$ s^{-1} was selected for C_5 and C_6 unsaturated hydrocarbons adsorbed on porous γ- and θ-Al_2O_3.

Figure 5.10 shows a typical TPD plot showing the desorption of pre-adsorbed hydrocarbons and the results obtained after the regularisation method. The rate of desorption for m/z = 55 during the TPD of pre-adsorbed *cis*-2-pentene on θ-Al_2O_3 is shown in **Figure 5.10A**. The experimental rates are expressed in molec nm^{-2} s^{-1}, and surface coverage is shown, after appropriate calibration. A series of desorption peaks are observed, labelled as I, II and III. Temperatures associated with each peak were 390, 482 and 516 K. Additionally, a small peak labelled * was observed, with a temperature of 654 K. This last peak presented very low intensity in most experiments and was believed to be heavily influenced by fragmentation of the hydrocarbon and desorption of hydroxyl groups (Kwal *et al.*, 2011). Simulated desorption rates based on the distribution energy function $N_0(E)$ are also shown. As can be seen, a good agreement between experimental and calculated rates is observed. The distribution energy function resulting from the regularisation procedure is also shown in **Figure 5.10B**. Energy values of 97, 116 and 124 kJ mol^{-1} were extracted, which corresponded with the three main peaks (I, II and III), previously described. Additionally, a series of small peaks between 133 – 157 kJ mol^{-1} were also seen, related with the additional peak (*). Finally, the value of E_{max} is shown, corresponding to the energy values obtained for which 95% of the adsorbed species have desorbed (D'Agostino *et al.*, 2014). This value related to the heterogeneous distribution of the surface and the strength of interaction of the hydrocarbon. The area under the distribution energy function, shown in grey, represents the desorbed fraction.

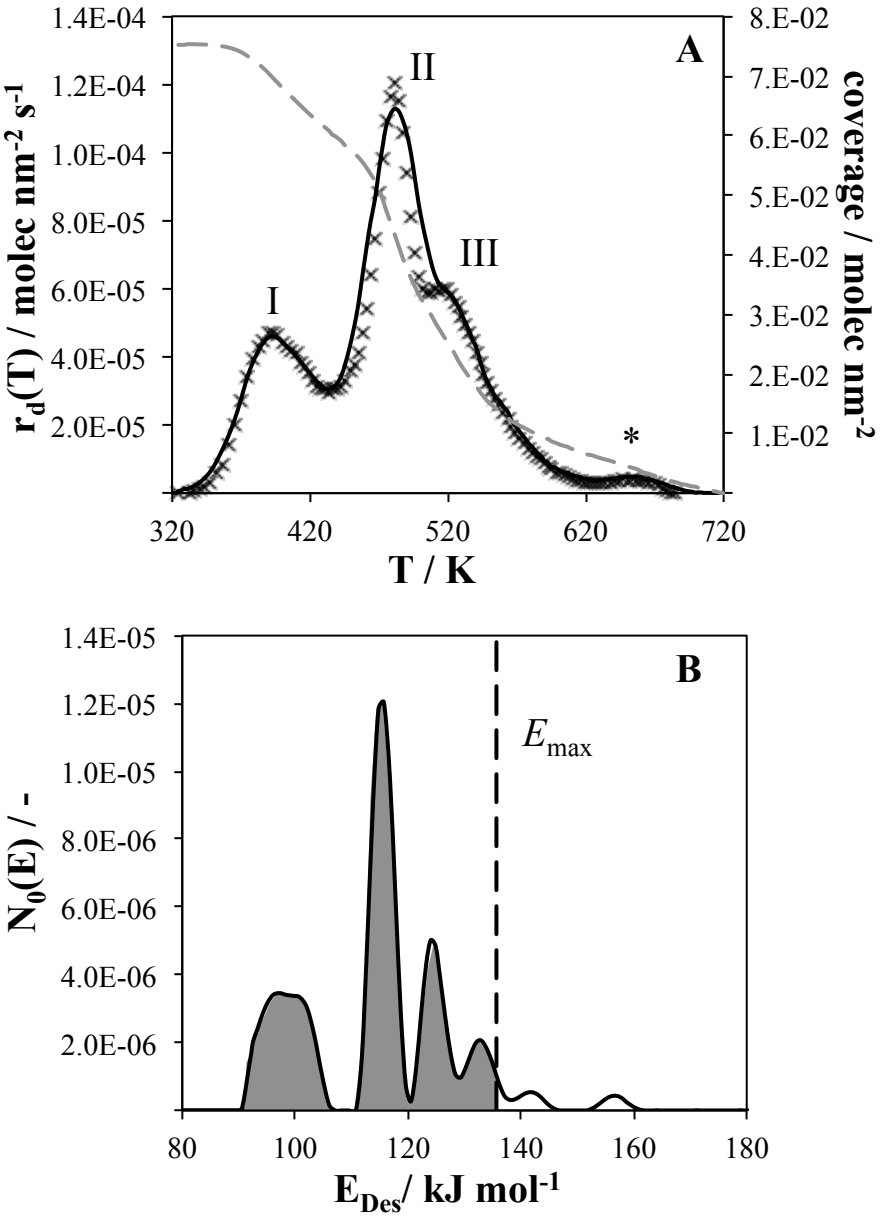

Figure 5.10. TPD-MS of desorption of *cis*-2-pentene on θ-Al_2O_3. (A) Desorption rate obtained for m/z = 55 (x), fitted desorption rate from $N_0(E)$ following equation 5.7 (–), and integrated coverage obtained from the experimental desorption rates. Peaks were numbered as I, II, III and IV with increasing desorption temperature; * indicated a peak likely to be formed from influence of m/z = 18 signal (hydroxyl). (B) $N_0(E)$ distribution obtained after solving the first order Fredholm integral for m/z = 55 in A, and the value of E_{max} derived from it.

Figures 5.11 and **5.12** show the desorption curves and the associated distribution energy functions for pre-adsorbed hydrocarbons on γ- and θ-Al_2O_3. **Table 5.10** shows the results for E_{max}, the energy of desorption at which 95% of the species have desorbed. As can be seen, energy values ranged between 116 kJ mol^{-1} for cyclohexene on θ-Al_2O_3 and 149 kJ mol^{-1} for *cis*-2-pentene on γ-Al_2O_3. Additionally, these values were similar between both aluminas. For

example, E_{max} values of 128 and 130 kJ mol^{-1} were obtained for 1-pentene on γ- and θ-Al_2O_3, respectively. **Table 5.11** shows the temperatures and calculated energies corresponding to the main desorption peaks, using both the $N_0(E)$ function and the Redhead equation, for desorption of hydrocarbons from γ- and θ-Al_2O_3. Generally, three peaks were observed during the desorption of hydrocarbons from the aluminas pre-treated at 393 K. Comparing the energies obtained using the distribution energy, $N_0(E)$, with those obtained using the Redhead equation, it can be seen that the values of the latter method were much higher compared with the former. For example, $N_0(E)$ for peaks I, II and III during the desorption of 1-pentene on γ-Al_2O_3 were 86, 107 and 128 kJ mol^{-1}, respectively, compared with 105, 129 and 144 kJ mol^{-1} with the Redhead equation. $N_0(E)$ varied in the range 86 – 97 kJ mol^{-1} and 89 – 102 kJ mol^{-1} for peak I on γ- and θ-Al_2O_3, respectively; 106 – 110 kJ mol^{-1} and 104 – 116 kJ mol^{-1} for peak II; and 115 – 128 kJ mol^{-1} and 114 – 129 kJ mol^{-1} for peak III. Generally, slightly higher energies were observed for desorption of hydrocarbons from θ-Al_2O_3. As noted, these values represented energies much higher than those obtained during adsorption isotherm experiments. However, initial surface coverage is much lower, with values oscillating from 2.1×10^{-6} mmol g^{-1} on pre-adsorbed cyclohexene on γ-Al_2O_3, and 1.07×10^{-4} mmol g^{-1} on pre-adsorbed *cis*-2-pentene on θ-Al_2O_3. These coverages were at least one order of magnitude lower than initial uptake values in the volumetric method for *cis*-2-pentene.

Table 5.10. Maximum desorption energy (E_{max}) obtained from the distribution energy for each hydrocarbon desorbing from γ- and θ-Al_2O_3.

	E_{max}[a] / kJ mol^{-1}	
hydrocarbon	**γ-Al_2O_3**	**θ-Al_2O_3**
1-pentene	128 ± 3	130 ± 3
1-pentyne	148 ± 4	126 ± 3
cyclohexene	118 ± 3	116 ± 3
***cis*-2-pentene**	139 ± 3 (149 ± 4)[a]	136 ± 3 (137 ± 3)[a]
***trans*-2-pentene**	147 ± 3 (147 ± 4)[a]	144 ± 4 (133 ± 3)[a]
1,4-pentadiene	119 ± 3	128 ± 3

a Values obtained from the distribution of m/z = 42 assigned to 1-pentene

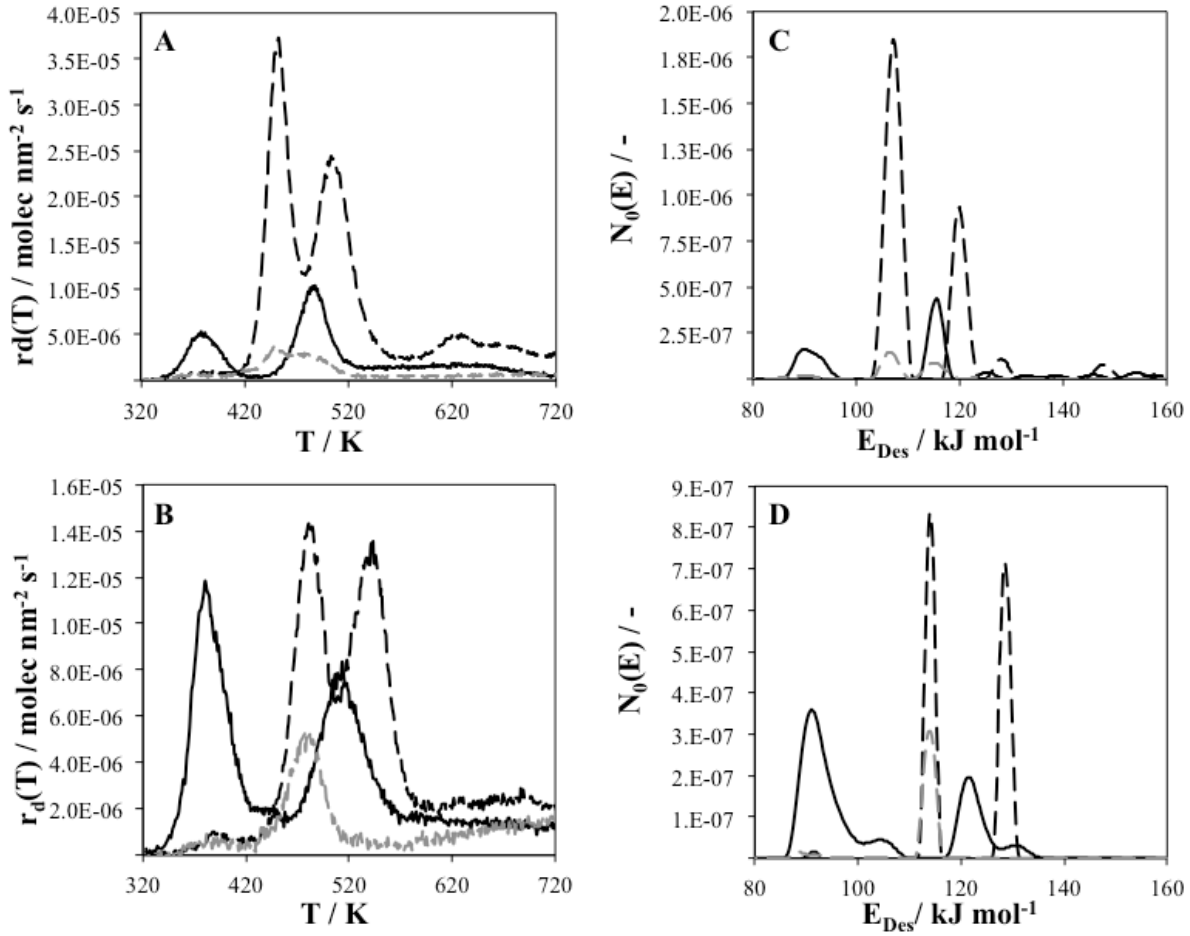

Figure 5.11. TPD-MS desorption rates (A-B) and distribution energy functions $N_0(E)$ (C-D) of the desorption of 1-pentene, 1-pentyne and cyclohexene on γ-Al_2O_3 (A, C) and on θ-Al_2O_3 (B, D). Spectra was set to m/z = 42 for 1 pentene (--); m/z = 67 for 1-pentyne (-), and cyclohexene (--).

Table 5.11. Summary of the desorption peaks obtained from the TPD curves, and the energies associated with each desorption calculated from both the $N_0(E)$ distribution function and the Redhead equation for the desorption of hydrocarbons from γ- and θ-Al_2O_3.

		γ-Al_2O_3			θ-Al_2O_3		
hydrocarbon	**Peak**	**T / K**	E_{Des}[a]	$E(T_P)$[b]	**T / K**	E_{Des}[a]	$E(T_P)$[b]
1-pentene	I	369.8	86	105	388.3	92	110
	II	452.7	107	129	480.8	114	137
	III	503.3	128	144	543.1	129	155
1-pentyne	I	378.0	90	106	380.3	90	107
	II	-	-	-	446.8	104	127
	III	487.9	116	139	513.2	121 (s127)	146
cyclohexene	I	373.2	91	106	381.9	89	108
	II	450.4	106	128	-	-	-
	III	477.6	115	136	479.6	114	136

a Desorption energy obtained from each peak derived from the $N_0(E)$ distribution, kJ mol^{-1}; b Desorption energy calculated with the Redhead equation, kJ mol^{-1}.

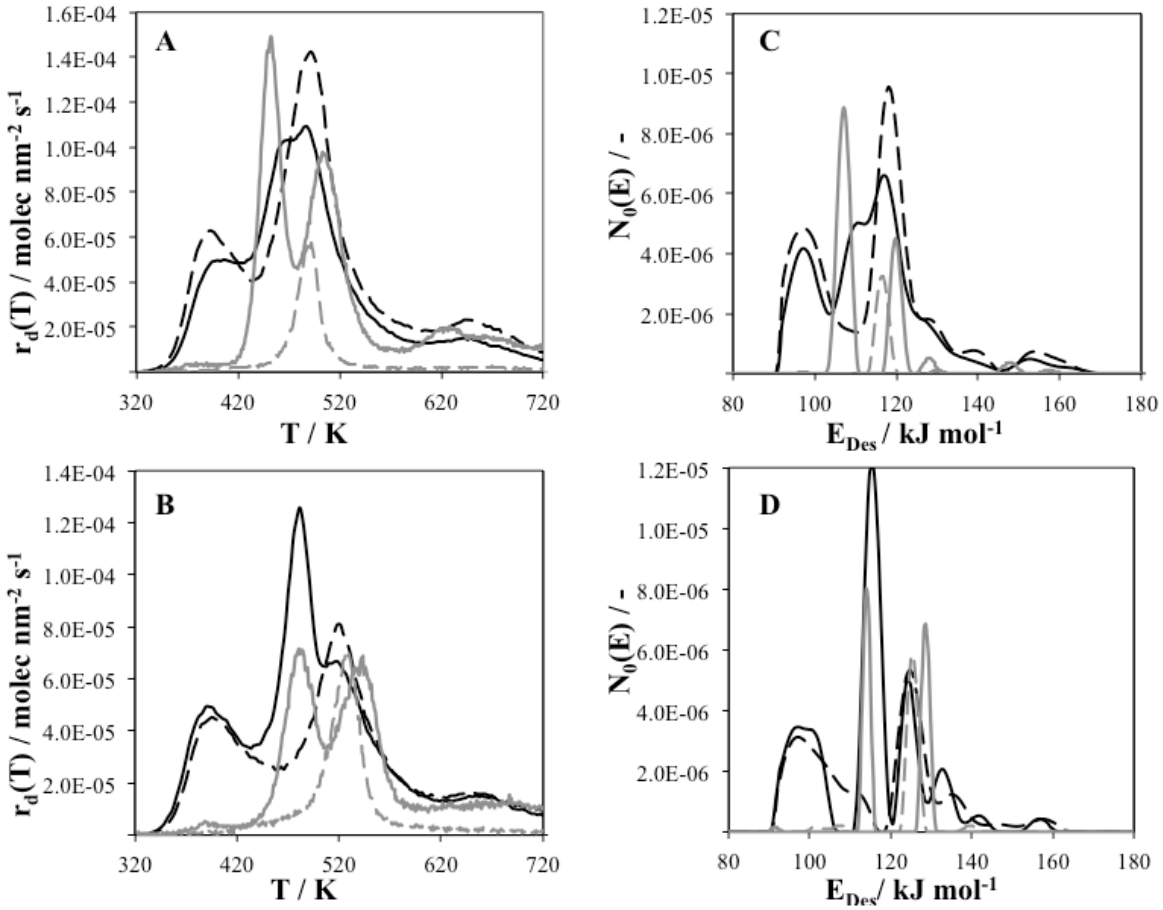

Figure 5.12. TPD-MS desorption rates (A-B) and distribution energy functions $N_0(E)$ (C-D) of the desorption of 1-pentene, *cis*-2-pentene, *trans*-2-pentene and 1,4-pentadiene on γ-Al_2O_3 (A, C), as well as on θ-Al_2O_3 (B, D). Spectra was set to m/z = 42 for 1 pentene (-); m/z = 67 for 1,4-pentadiene (--); and m/z = 55 for *cis*-2-pentene (-) and *trans*-2-pentene (--). 1-pentene and 1,4-pentadiene distribution energy functions were multiplied by 5 and 10 on γ-Al_2O_3 and θ-Al_2O_3 plots, respectively.

Table 5.11. (Continued)

		γ-Al_2O_3			θ-Al_2O_3		
hydrocarbon	**Peak**	**T / K**	E_{Des}[a]	$E(T_P)$[b]	**T / K**	E_{Des}[a]	$E(T_P)$[b]
***cis*-2-pentene**	I	406.1	97	115	389.6	97	110
	II	468.1	110	133	481.5	116	137
	III	485.3	117	138	515.8	124	147
***trans*-2-pentene**	I	393.5	97	111	395.4	97	112
	II	-	-	-	-	-	-
	III	491.9	118	140	521.4	125	149
1,4-pentadiene	I	-	-	-	399.0	102	113
	II	433.1[c]	-	123	435.0	107	124
	III	492.2	117	140	526.3	125	150

a Desorption energy obtained from each peak derived from the $N_0(E)$ distribution, kJ mol^{-1}; b Desorption energy calculated with the Redhead equation, kJ mol^{-1}; c No peak was observed in the $N_0(E)$ distribution at this temperature.

5.2.4.1 Reactivity during desorption

The presence of isomerisation or cracking reactions was also considered at T > 323 K. **Table 5.12** shows the results corresponding to 1-pentene desorption from pre-adsorbed *cis*- and *trans*-2-pentenes on γ- and θ-Al_2O_3. **Figure 5.13** compares the energy distribution functions between 1-pentene (m/z = 42) and 2-pentene isomers (m/z = 55) on both γ- and θ-Al_2O_3. Isomerisation of 2-pentenes to 1-pentene was clearly observed. Significant desorption for peaks I and II with m/z = 42 was present in the TPD and $N_0(E)$ curves. Similar temperatures for peak I were obtained for 1-pentene and both 2-pentene isomers. Peak II showed the most significant differences. Comparison of this peak in 2-pentenes with 1-pentene showed lower desorption temperatures for 1-pentene by about 30 K, representing a difference of 4 to 7 kJ mol^{-1}. The desorption of the remaining pre-adsorbed unreacted 2-pentene isomer occurred at higher temperatures. The difference in desorption temperatures was indicative of isomerisation followed by desorption of the species formed. The weaker interaction of 1-pentene allowed for desorption once it was formed, while the 2-pentene unreacted remained adsorbed. Comparing the TPD curves of the 2-pentene isomers, peak II was absent during desorption of *trans*-2-pentene, unlike during desorption of *cis*-2-pentene. This would indicate that formation of 1-pentene from *trans*-2-pentene was much more favoured. Comparing adsorbents, desorption showed peaks II and III presented higher energies in θ-Al_2O_3 as compared to γ-Al_2O_3, in agreement with previous results.

Table 5.12. Summary of the desorption peaks obtained from the TPD curves for m/z = 42, and the energies associated with each desorption calculated from both the $N_0(E)$ distribution function and the Redhead equation during the desorption of 2-pentene isomers from γ- and θ-Al_2O_3.

		γ-Al_2O_3			θ-Al_2O_3		
hydrocarbon	**Peak**	**T / K**	E_{Des} [a]	$E(T_P)$ [b]	**T / K**	E_{Des} [a]	$E(T_P)$ [b]
***cis*-2-pentene**	I	388.0	92	103	386.0	96	109
	II	430.0	103	122	463.9	112	132
	III	487.9	116	139	524.7	125	150
***trans*-2-pentene**	I	393.5	92	111	388.1	96	110
	II	424.8	102	121	449.7	108	128
	III	475.6	117	135	517.9	126	148

a Desorption energy obtained from each peak derived from the $N_0(E)$ distribution, kJ mol^{-1}; b Desorption energy calculated with the Redhead equation, kJ mol^{-1}.

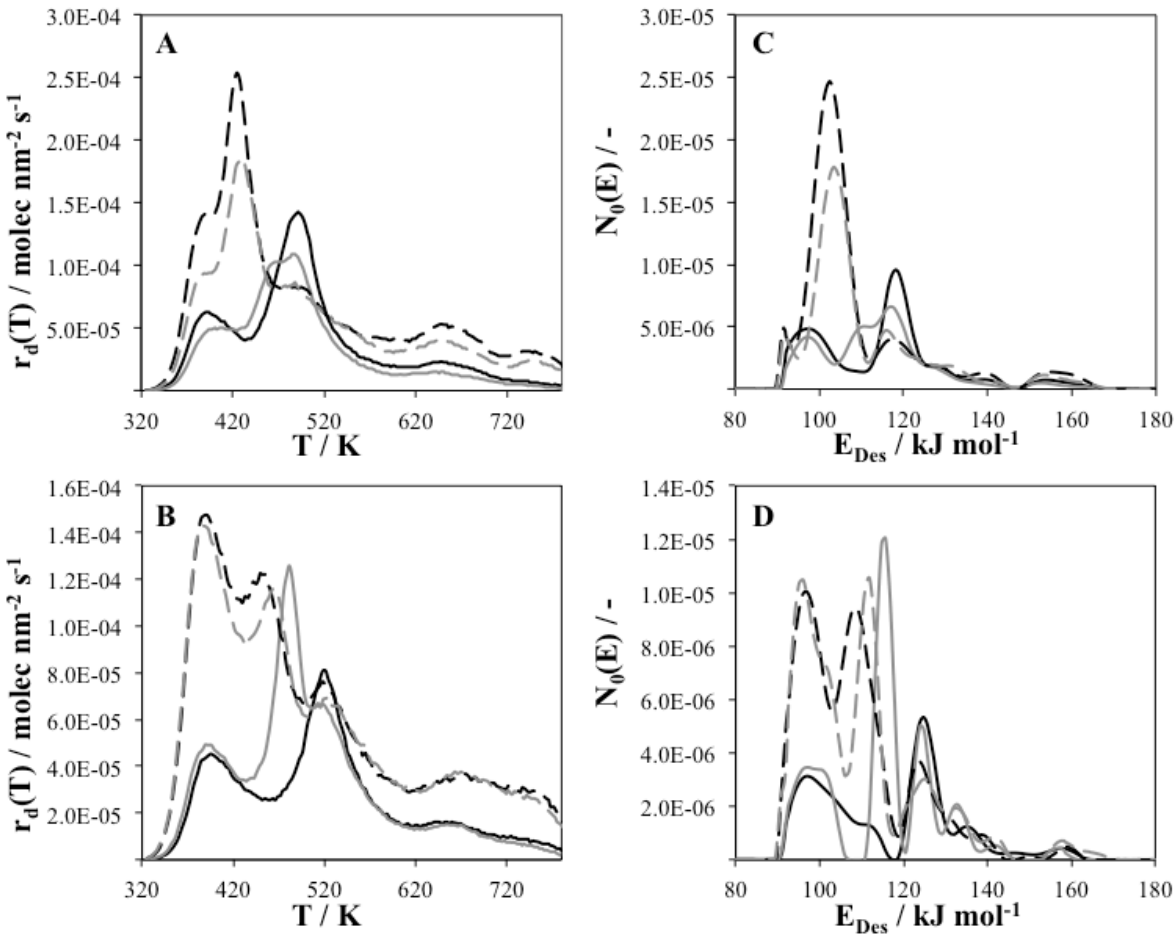

Figure 5.13. TPD-MS desorption rates (A-B) and distribution energy functions $N_0(E)$ (C-D) of the desorption of *trans*-2-pentene (-) and *cis*-2-pentene (-) isomers (m/z = 55), with formation and desorption of 1-pentene (m/z = 42) from each respective sample (dashed, colour coding referred to isomer pre-adsorbed) on γ-Al_2O_3 (A, C) and on θ-Al_2O_3 (B, D).

The effect of pre-treatment temperature of the alumina also revealed interesting information on reactivity during the desorption of 1-pentyne. **Table 5.13** contains the peak temperatures and energies during the desorption of alkane and alkene hydrocarbons from pre-adsorbed 1-pentyne on θ-Al_2O_3 pre-treated by heating at 393 and 673 K. Clearly, reactivity of 1-pentyne was observed, and hydrogenation products were formed. **Figure 5.14** shows the distribution energy functions of the species desorbing from θ-Al_2O_3 at both pre-treatment temperatures. Similar desorption peak temperatures were recorded for all hydrocarbons for a given pre-treatment temperature. The absence of peak I was noted for 1-pentyne on θ-Al_2O_3 pre-treated at 393 K, while no 1-pentyne desorbed from θ-Al_2O_3 pre-treated at 673 K. High desorption temperatures were found for 1-pentene and *n*-pentane, with the presence of a type IV peak on θ-Al_2O_3 pre-treated at 393 K. These values were superior than the highest

desorption energies observed from peak III on θ-Al_2O_3 pre-treated at 673 K. **Table 5.14** presents a summary of these differences with E_{max} values from both pre-treatment temperatures. Furthermore, analysis of desorption peaks for other *m*/*z* revealed the presence of fragmentation products. **Figure 5.15** shows the rates of desorption for three characteristic *m*/*z* values, 15, 39 and 44, corresponding to CH_3^+, $C_3H_3^+$ and $C_3H_8^+$ or CO_2^+, respectively. These species indicated the presence of fragmentation, alkyne products and the formation of coking products. As can be seen, alkyne fragments and methyl groups desorbed from θ-Al_2O_3 at temperatures characteristic of peaks II and III. Additionally, significant amounts of CO_2, as well as methyl fragments desorbed at very high temperatures, > 850 K. Therefore, the pre-treatment of θ-Al_2O_3 at higher temperatures showed increased reactivity and explained the absence of 1-pentyne peaks. Desorption of fragments from pre-adsorbed 1-pentene, also shown in **Figure 5.15**, revealed that reactivity was much more pronounced for species containing an unsaturated triple bond, as compared to those containing a double-bond.

Table 5.13. Summary of the desorption peaks obtained from the TPD curves for *m*/*z* = 67, *m*/*z* = 42 and *m*/*z* = 43, and the energies associated with each desorption calculated from both the $N_0(E)$ distribution function and the Redhead equation during the desorption of 1-pentyne from θ-Al_2O_3 pre-treated at 393 and 673 K.

		393 K			673 K		
m*/*z	**Peak**	**T / K**	E_{Des} [a]	$E(T_P)$ [b]	**T / K**	E_{Des} [a]	$E(T_P)$ [b]
67 (1-pentyne)	II	484.7	115	138	-	-	-
	III	s 552.5	135	158	-	-	-
	IV	689.5	165	198	-	-	-
42 (1-pentene)	I	376.0	95	106	-	-	-
	II	487.0	119	139	460.8	108	131
	III	-	-	-	529.2	119 (s132)	151
	IV	703.0	169	202	-	-	-
43 (pentane)	I	379.6	94	107	-	-	-
	II	446.4	109	127	442.8	106	126
	III	-	-	-	545.1	128	156
	IV	681.1	165	196	-	-	-

a Desorption energy obtained from each peak derived from the $N_0(E)$ distribution, kJ mol^{-1}; b Desorption energy calculated with the Redhead equation, kJ mol^{-1}.

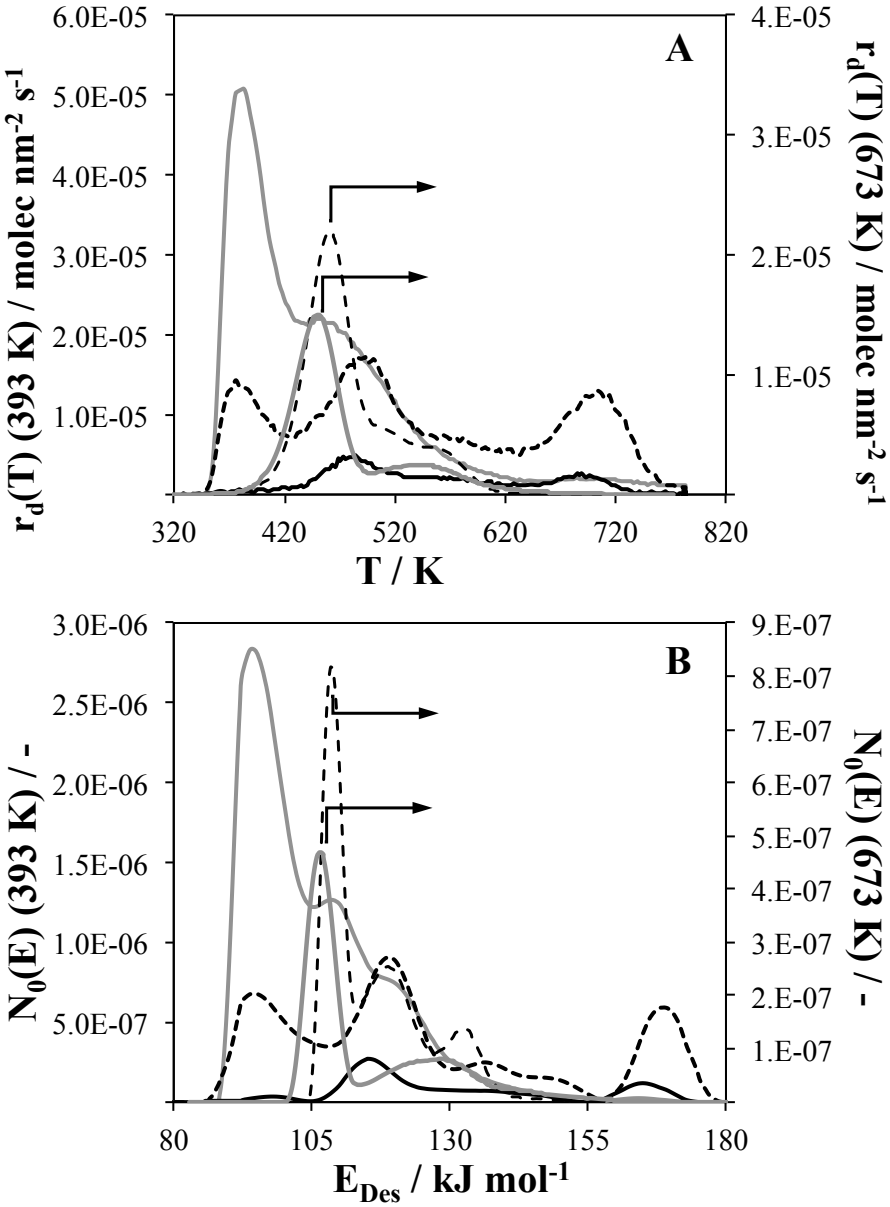

Figure 5.14. TPD-MS of desorption of hydrocarbon species from pre-adsorbed 1-pentyne on θ-Al_2O_3 pre-treated at 393 K and 673 K, respectively. Desorption rates (A) and distribution energy functions $N_0(E)$ (B) for the desorption of reduced products, 1-pentene (m/z = 42, --) and pentane (m/z = 43, -), during desorption of 1-pentyne (m/z = 67, -).

Table 5.14. Maximum desorption energy (E_{max}) obtained from the distribution energy for m/z = 67, m/z = 42 and m/z = 43 during the desorption of 1-pentyne from θ-Al_2O_3 pre-treated at 393 and 673 K.

	E_{max} / kJ mol^{-1}	
m/z	**393 K**	**673 K**
67	168 ± 4	-
42	171 ± 5	135 ± 3
43	129 ± 3	141 ± 4

a Peaks from the desorption of m/z = 42 assigned to 1-pentene

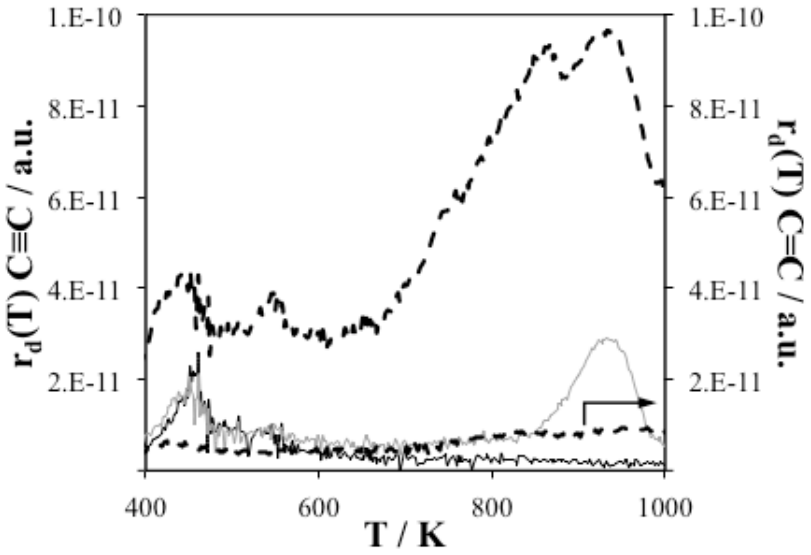

Figure 5.15. TPD-MS rates of desorption of m/z = 39 (-), m/z = 15 (-) and m/z = 44 (--) for pre-adsorbed 1-pentyne (left, C≡C) and 1-pentene (right, C=C) from pre-treated θ-Al_2O_3 at 673 K. Only m/z = 44 is presented for desorption of pre-adsorbed 1-pentene. Desorption rates are presented in arbitrary units.

5.2.5 ^{1}H 2D T_1-T_2 NMR relaxometry correlations

^{1}H 2D T_1-T_2 experiments were performed on 1-pentene, 1-pentyne and cyclohexene adsorbed on both γ- and θ-Al_2O_3. The effect of double bond vs. triple bond adsorption and the interaction of cyclic molecules was evaluated. **Table 5.15** shows the results of the 2D ^{1}H T_1-T_2 relaxometry experiments of 1-pentene, cyclohexene and 1-pentyne saturated on γ- and θ-Al_2O_3 pre-treated at 673 K. These values were extracted from the 2D plots; the T_1/T_2 ratio is obtained by a diagonal line, parallel to $T_1 = T_2$, passing through the maximum intensity of the peak. A lower diagonal line in the plot is indicative of a higher T_1/T_2 ratio, manifesting a stronger interaction. For example, **Figure 5.16** shows T_1/T_2 values of 18 for 1-pentene, 23 for 1-pentyne and 11.5 for cyclohexene, adsorbed on θ-Al_2O_3. T_1/T_2 values indicated that the strength of interaction was cyclohexene < 1-pentene < 1-pentyne on θ-Al_2O_3. Similar trends were observed in the case of γ-Al_2O_3, with higher T_1/T_2 values on γ-Al_2O_3 for the same hydrocarbon. For example, T_1/T_2 = 31 for 1-pentyne on γ-Al_2O_3, as compared to T_1/T_2 = 23 on θ-Al_2O_3. These results indicated an apparent stronger interaction on γ-Al_2O_3 *vs*. θ-Al_2O_3. The effect of pre-treatment temperature was also considered on θ-Al_2O_3. **Table 5.16** and **Figure 5.17** show the 2D ^{1}H T_1-T_2 relaxometry results for 1-pentene, cyclohexene and 1-pentyne saturated on θ-Al_2O_3 pre-treated at 393 K. T_1/T_2 values of 28 for 1-pentene, 27 for

1-pentyne and 7 for cyclohexene were obtained. Thus, the T_1/T_2 values indicated that adsorption followed cyclohexene << 1-pentyne ≈ 1-pentene. Comparing alumina pre-treatment, the T_1/T_2 values increased for both 1-pentene and 1-pentyne at 393 K, while a decay was observed for cyclohexene. The change in T_1/T_2 with pre-treatment temperature was mainly due to an increase in the T_1 component at 393 K. Hence, a stronger interaction of the acyclic hydrocarbons was observed with a lower temperature pre-treatment. 1-pentene and 1-pentyne preferably interacted with hydroxylated θ-Al_2O_3, *via* Brønsted acid sites. The opposite was true for cyclohexene. Additionally, a similar interaction was observed regardless if the unsaturation was double *vs.* triple bond.

Table 5.15. T_1 and T_2 values of saturated 1-pentene, 1-pentyne and cyclohexene adsorbed on γ- and θ-Al_2O_3 pre-treated at 673 K from 2D ^{1}H T_1-T_2 relaxometry correlation results using inversion-recovery to capture T_1.

	θ-Al_2O_3			**γ-Al_2O_3**		
	***T*$_1$ / s**	***T*$_2$ / s**	***T*$_1$/*T*$_2$**	***T*$_1$ / s**	***T*$_2$ / s**	***T*$_1$/*T*$_2$**
1-pentene	0.674	0.038	18 ± 3	0.860	0.033	26 ± 2
1-pentyne	0.784	0.034	23 ± 2	0.890	0.028	31 ± 6
cyclohexene	0.498	0.046	11.5 ± 1.5	-	-	-

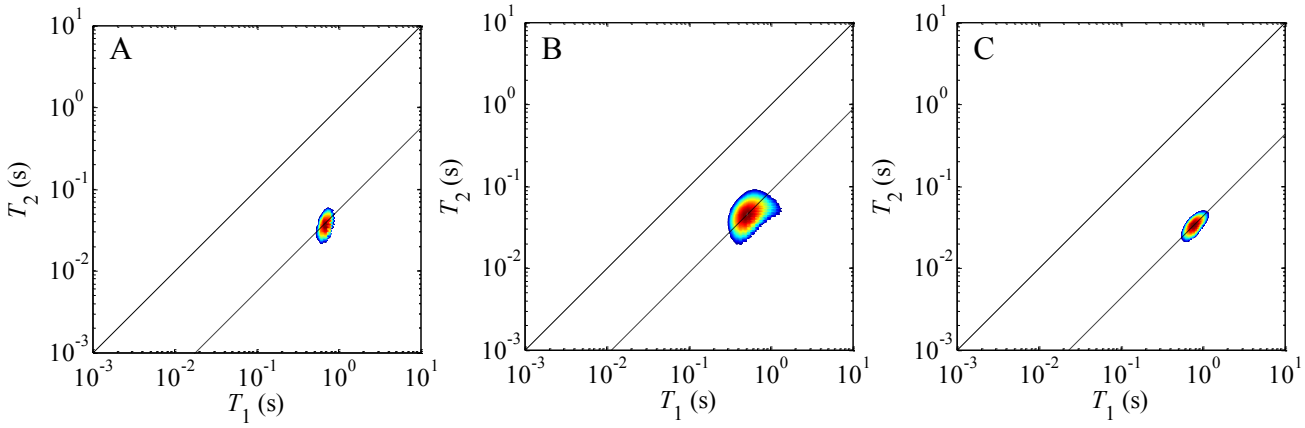

Figure 5.16. 2D ^{1}H T_1-T_2 NMR relaxometry plots for the adsorption of 1-pentene (A), cyclohexene (B) and 1-pentyne (C) soaked on θ-Al_2O_3 after pre-treatment at 673 K. The maximum intensity of the peak shows the T_1/T_2 values, depicted by the diagonal line. The plots indicate $T_1 = 18\ (\pm 3)\ T_2$ in 1-pentene, $T_1 = 11.5\ (\pm 1.5)\ T_2$ in cyclohexene, and $T_1 = 23\ (\pm 2)\ T_2$ in 1-pentyne. The solid diagonal line in all plots show $T_1 = T_2$, for comparison.

Table 5.16. T_1 and T_2 values of saturated 1-pentene, 1-pentyne and cyclohexene adsorbed on θ-Al_2O_3 pre-treated at 393 K from 2D ^{1}H T_1-T_2 relaxometry correlation results using inversion-recovery to capture T_1.

	θ-Al_2O_3		
	T_1 / s	T_2 / s	T_1/T_2
1-pentene	1.173	0.043	28 ± 2
1-pentyne	1.091	0.041	27 ± 3
cyclohexene	0.907	0.128	7 ± 2

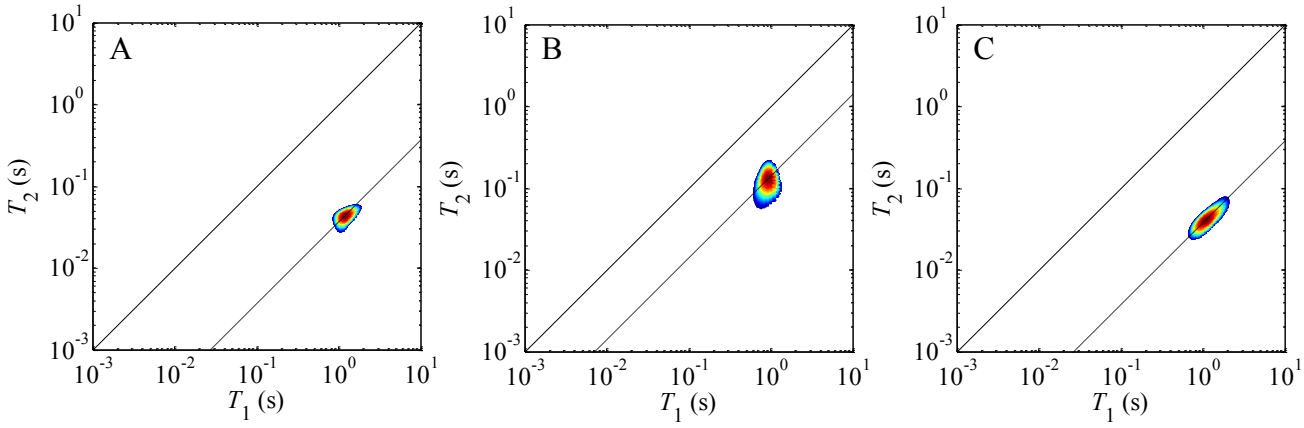

Figure 5.17. 2D ^{1}H T_1-T_2 NMR relaxometry plots for the adsorption of 1-pentene (A), cyclohexene (B) and 1-pentyne (C) soaked on θ-Al_2O_3 after pre-treatment at 393 K. The maximum intensity of the peak shows the T_1/T_2 values, depicted by the diagonal line. The plots indicate $T_1 = 28\ (\pm\ 2)\ T_2$ in 1-pentene, $T_1 = 7\ (\pm\ 2)\ T_2$ in cyclohexene, and $T_1 = 27\ (\pm\ 3)\ T_2$ in 1-pentyne. The solid diagonal line in all plots show $T_1 = T_2$, for comparison.

Although ^{1}H T_1-T_2 experiments are conventionally performed on saturated pores for the reasons discussed in section 2.2.2.2.3, monolayer adsorption was more relevant to this study. Complementary experiments at a controlled loading were performed to provide fractional monolayer coverage. **Table 5.17** and **Figure 5.18** show the results of the 2D ^{1}H T_1-T_2 relaxometry experiments of 1 ML 1-pentene, cyclohexene and 1-pentyne adsorbed on θ-Al_2O_3 pre-treated at 673 K. Values of $T_1/T_2 = 7.8$ for 1-pentene, $T_1/T_2 = 45$ for 1-pentyne, and $T_1/T_2 = 7$ for cyclohexene, were observed. Hence, the strength of interaction of hydrocarbons on θ-Al_2O_3 followed cyclohexene ≈ 1-pentene << 1-pentyne. Comparing with saturated pores, a reduction in T_1/T_2 was seen for 1-pentene and, to a lower extent, for cyclohexene. However, T_1/T_2 for 1-pentyne increased significantly from 23 to 45. Hence, an increase in T_1/T_2 should be expected when decreasing the coverage. Such behaviour was only

observed with 1-pentyne. These results might point to molecule-molecule interactions, or to selective saturation of smaller pores.

Table 5.17. T_1 and T_2 values of 1 ML 1-pentene, 1-pentyne and cyclohexene adsorbed on θ-Al_2O_3 pre-treated at 673 K from 2D ^{1}H T_1-T_2 relaxometry correlation results using inversion-recovery to capture T_1.

	θ-Al_2O_3		
	T_1 / s	T_2 / s	T_1/T_2
1-pentene	0.089	0.012	7.8 ± 0.5
1-pentyne	0.118	0.003	45 ± 8
cyclohexene	0.065	0.009	7 ± 1

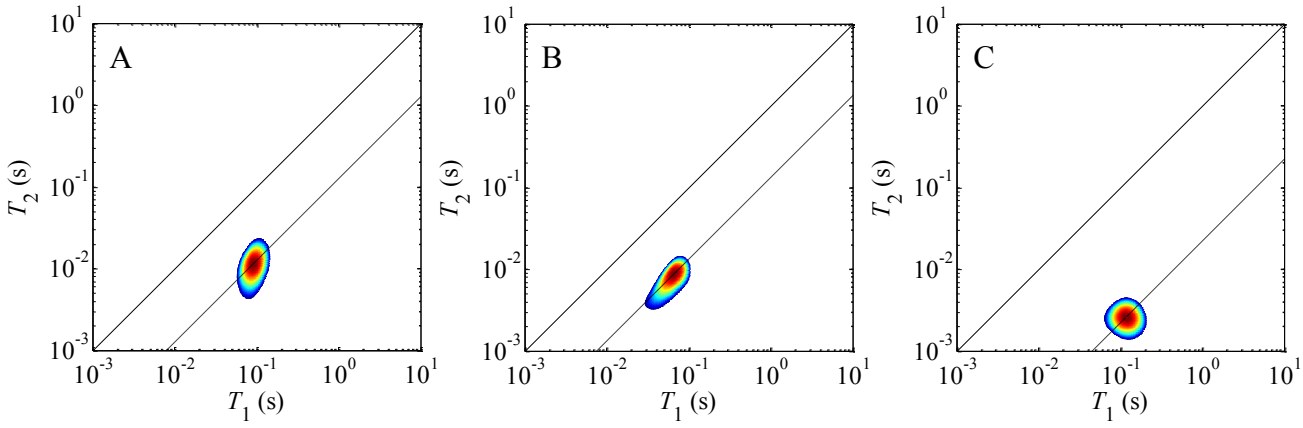

Figure 5.18. 2D ^{1}H T_1-T_2 NMR relaxometry plots for the adsorption of 1 ML 1-pentene (A), cyclohexene (B) and 1-pentyne (C) on θ-Al_2O_3 after pre-treatment at 673 K. The maximum intensity of the peak shows the T_1/T_2 values, depicted by the diagonal line. The plots indicate T_1 = 7.8 (± 0.5) T_2 in 1-pentene, T_1 = 7 (± 1) T_2 in cyclohexene, and T_1 = 45 (± 8) T_2 in 1-pentyne. The solid diagonal line in all plots show $T_1 = T_2$, for comparison.

In order to confirm this observation, and to avoid limitations of ^{1}H T_1/T_2 values affected by pore geometry, ^{1}H $T_{1,ads}/T_{1,bulk}$ was used. Also discussed in section 2.2.2.2.3, $T_{1,ads}/T_{1,bulk}$ provides a better indicator of surface interaction for non-saturated systems, assuming fast diffusion limit applies. **Table 5.18** shows the ^{1}H $T_{1,ads}/T_{1,bulk}$ results for the adsorption of 1-pentene, 1-pentyne and cyclohexene for previously described T_1-T_2 experiments on both aluminas. Resolution between the double-bond unsaturation and the backbone of the molecule was exploited. Unfortunately, 1-pentyne chemical shifts were not effectively resolved upon adsorption. Hence, the interaction of 1-pentene and cyclohexene was studied at 10 ML, 1 ML and 0.1 ML on θ-Al_2O_3 using this NMR relaxometry parameter. As can be

seen in **Tables 5.19** and **5.20** for 1-pentene and cyclohexene, respectively, notable differences were observed on the $T_{1,ads}/T_{1,bulk}$ with variable coverage. A continuous decrease in $T_{1,ads}/T_{1,bulk}$ was observed in 1-pentene, with values of 0.075 for saturated pores, 0.065 for 10 ML, 0.010 for 1 ML and 0.004 for 0.1 ML. These results indicated an average stronger interaction in line with a reduction in coverage. However, considering the double bond *vs.* the hydrocarbon backbone, the trends were different. While the $T_{1,ads}/T_{1,bulk}$ values decreased continuously for the olefinic ^{1}H, a slight increase was observed for the aliphatic ^{1}H from saturated pores to 10 ML. This increase might indicate a stabilisation effect of the hydrocarbon within the pore, disappearing at lower coverages. Similar layer stabilisation phenomena have been previously observed with TPD experiments of weakly adsorbed organic molecules (Roos *et al.*, 2010; Scherwitzl *et al.*, 2014). Additionally, $T_{1,ads}/T_{1,bulk}$ values were always higher in the aliphatic ^{1}H at the same coverages. These results would be in line with a weak interaction of the double bond with the surface. Adsorption of cyclohexene reported similar results. In both cases, these results provided further indication of a stabilisation of the hydrocarbon upon adsorption at multilayer coverage. In summary, an increased interaction of 1-pentene and cyclohexene was observed with decreasing coverage, while a certain stabilisation of the backbone likely *via* dispersive interactions was observed on saturated pores.

Table 5.18. Overall $T_{1,bulk}$ values and $<T_{1,ads}/T_{1,bulk}> \times 10^2$ values for the adsorption of 1-pentene, 1-pentyne and cyclohexene on γ- and θ-Al_2O_3 pre-treated at 393 and 673 K from 1D ^{1}H T_1 inversion-recovery results.

		θ-Al_2O_3			**γ-Al_2O_3**
	$T_{1,bulk}$ / s	**Sat**		**1 ML**	**Sat**
		673 K	**393 K**	**673 K**	**673 K**
1-pentene	8.7 ± 0.2	7.5 ± 0.4	11.2 ± 0.6	1.0 ± 0.1	9.4 ± 0.5
1-pentyne	3.89 ± 0.08	10.2 ± 0.5	13.2 ± 0.7	1.1 ± 0.1	12.1 ± 0.7
cyclohexene	6.8 ± 0.2	12.9 ± 0.7	20 ± 1	1.4 ± 0.1	-

Table 5.19. $T_{1,bulk}$ values and $<T_{1,ads}/T_{1,bulk}> \times 10^2$ values for the aliphatic and olefinic protons on the adsorption of 1-pentene at different coverages, pore saturation, 10 ML, 1 ML and 0.1 ML, on θ-Al_2O_3 pre-treated at 673 K from 1D ^{1}H T_1 inversion-recovery results.

	$T_{1,bulk}$ / s	**Sat**	**10 ML**	**1 ML**	**0.1 ML**
overall	8.7 ± 0.2	7.5 ± 0.4	6.5 ± 0.4	1.0 ± 0.1	0.40 ± 0.05
aliphatic	8.1 ± 0.2	8.6 ± 0.5	9.1 ± 0.5	1.1 ± 0.1	0.47 ± 0.06
olefinic	9.7 ± 0.2	5.8 ± 0.3	3.4 ± 0.2	0.7 ± 0.1	0.24 ± 0.03

Table 5.20. $T_{1,bulk}$ values and $<T_{1,ads}/T_{1,bulk}> \times 10^2$ values for the aliphatic and olefinic protons on the adsorption of cyclohexene at different coverages, pore saturation, 10 ML, 1 ML and 0.1 ML, on θ-Al_2O_3 pre-treated at 673 K from 1D ^{1}H T_1 inversion-recovery results.

	$T_{1,bulk}$ / s	Sat	10 ML	1 ML	0.1 ML
overall	3.89 ± 0.08	12.9 ± 0.7	14.6 ± 0.8	1.4 ± 0.1	0.9 ± 0.1
aliphatic	3.69 ± 0.07	14.8 ± 0.8	17.4 ± 0.9	1.7 ± 0.1	1.0 ± 0.1
olefinic	4.30 ± 0.09	8.9 ± 0.5	8.4 ± 0.5	0.7 ± 0.1	0.47 ± 0.04

5.3 Discussion

Results are analysed in terms of the type of adsorption of the different hydrocarbons on the surface of the aluminas in section 5.3.1. Results indicated different strength of interaction of each hydrocarbon. However, the parameters quantifying the adsorption of each species were different depending on the technique used. Hence, a critical analysis was also performed in section 5.3.2 on the results considering the different adsorption techniques. Complementary ^{13}C T_1 NMR relaxometry results previously presented (Huang, 2008) were included in the analysis.

5.3.1 Adsorption of hydrocarbons on alumina

In this section, the results from the different adsorption techniques will be reviewed, according to the hydrocarbons and conditions studied on each case. In chapter 4 the interaction of the alkene with γ- and θ-Al_2O_3 was already discussed in terms of the adsorption sites of the alumina. Here ^{1}H 2D T_1-T_2 NMR relaxometry correlations, TEOM and TPD were performed for adsorbates on both γ- and θ-Al_2O_3 to complete such observations.

Notable differences in the adsorption strength of the hydrocarbons were noted. These results showed the difference in the adsorption strength of 1-pentyne, with a triple bond, *vs*. the rest of the hydrocarbons, all olefins. Both IR spectroscopy and volumetric adsorption isotherms showed a marked difference in this respect. Taking 1-pentene as an exemplar olefin, the decay in the IR signal corresponding to the olefin presented a value of $\tau = 2.3$ min (**Table 4.2**), as compared to $\tau = 3.1$ min for 1-pentyne on θ-Al_2O_3 pre-treated at 673 K. Adsorption isotherm results also pointed towards enhanced 1-pentyne adsorption. Heats of adsorption at zero coverage, using the Tóth fitting, indicated that for 1-pentyne $(-\Delta H_{ads})_{zero} = 93.8$ kJ mol^{-1} as compared to 45.6 kJ mol^{-1} in the case of 1-pentene. These results were in agreement with previous literature adsorption studies on aluminas (Hoffmann *et al.*, 1966). Energies of

adsorption of an alkyne compared to an alkene have been reported in other catalysts. For example, values of 62 kJ mol^{-1} for the adsorption of acetylene *vs.* 37 kJ mol^{-1} for ethylene were previously reported on hydrogenated silicon surfaces (Takeuchi *et al.*, 2004). Other metals, such as Pt or Pd, have also shown preferential alkyne adsorption 1-hexyne / 1-octene, 1-hexyne / 1-heptene mixtures, which related to preferential hydrogenation (Dobrovolná *et al.*, 1998) Significantly, the selective hydrogenation of alkynes in alkene-alkyne mixtures relies on the preferential adsorption of the alkyne (Teschner *et al.*, 2006). Previous ^{13}C T_1 NMR relaxometry results also revealed important differences between 1-pentyne and the rest of the alkenes (Huang, 2008). Taking 1-pentene again as an example of the olefins, and considering the average $T_{1,ads}/T_{1,bulk}$ value of the carbons constituent of the unsaturation, results were in agreement with previous findings. Thus, the average value for C1 and C2 was $T_{1,ads}/T_{1,bulk} = 6.3 \times 10^{-3}$ for 1-pentyne, while $T_{1,ads}/T_{1,bulk} = 2.64 \times 10^{-2}$ for 1-pentene on θ-Al_2O_3. TPD results did not show such behaviour.

In addition to the differences between double-bond and triple-bond interactions, it was also possible to distinguish adsorption trends within olefins. As shown in **Tables 5.4** and **5.5**, results at zero coverage revealed notable differences within the C_5 molecules and with cyclohexene. Both 1,4-pentadiene and 1-pentene had similar interaction energies, with 1,4-pentadiene showing higher heats of adsorption. These results would be in agreement with an additional interaction provided by the added terminal unsaturation in 1,4-pentadiene. A comparison was also established between the 2-pentene isomers and 1-pentene. A difference of about 10 kJ mol^{-1} in the heats of adsorption of three isomers was observed. The interaction of an internal unsaturation could be expected to present some steric hindrance. The double bond is free of substitution in one carbon in 1-pentene, in contrast to the presence of substituents in both carbons for 2-pentenes. Similar unsaturated systems have shown a reduction in adsorption caused by substitution. However, the higher adsorption energy of *trans*-2-pentene is not well understood. Isomerisation of the *trans* isomer might be occurring in the alumina, with the subsequent additional energy being released. Previous studies have shown the formation of one isomer upon adsorption on aluminas. Adsorption of cyclohexene revealed the lowest heat of adsorption of the series, with a value of 10.5 kJ mol^{-1}.

In contrast to the adsorption isotherm results, desorption energies obtained from TPD were significantly higher than adsorption energies. Energies of desorption were in the range 85 – 130 kJ mol^{-1}, considering peaks I to III, and similar among the different hydrocarbons. These energy values are consistent with previous results reported on energies of desorption of

1-pentene on γ-Al_2O_3 (Clayborne *et al.*, 2004), with a value of 134 kJ mol^{-1}. Similar energies were observed in the energies of activation of alcohol dehydration to alkenes on γ-Al_2O_3. Values of 93.3 kJ mol^{-1} for 1-pentene, 97.9 to 122.2 kJ mol^{-1} for *trans*-2-pentene, 95.4 to 109.6 kJ mol^{-1} for *cis*-2-pentene, or 107.1 kJ mol^{-1} for cyclohexene (Knözinger *et al.*, 1972). In addition, these results were similar to those observed in the formation of isobutylene, with a value of 114 kJ mol^{-1} (Swecker and Datye, 1990). The contrast between such values is discussed in the context of the results from other adsorption methods in section 5.3.2. It was observed that high coverage adsorption was dominated by weak Brønsted adsorption sites, generally of low energy *vs.* Lewis acid sites for TPD, where reactivity is present. As observed, weak adsorption of 1-pentene *via* Brønsted acid sites was considered in section 4.4.1. Here, TPD revealed different adsorption sites. This was shown more clearly in the results of adsorption on high temperature pre-treated aluminas, seen also in IR, TEOM and ^1H T_1/T_2, presented *vide infra*. Previously, different heat of adsorption values have been reported on alumina, *i.e.*, in the σ-coordination of CO onto cus Al^{3+} sites. Calorimetric values ranged between a minimum of 8.5 kJ mol^{-1} and a maximum of 60 kJ mol^{-1}, whereas most calculated isosteric heat values were scattered in the narrow range 20-35 kJ mol^{-1} (Morterra *et al.*, 1994). As shown in chapter 3, no Brønsted acid sites were observed by means of pyridine adsorption, and two types of Lewis acid sites were considered. The presence of various Lewis sites would link with the appearance of peaks I to III during TPD.

Although not measured directly, the presence of adsorbate-adsorbate interactions was noted. Such interactions were present in this system, especially at higher coverages, as observed during adsorption isotherm results, but also during 1-pentene co-adsorption experiments, discussed in section 4.4.2. This interaction was also apparent in the results of the Tóth fitting. The values of the parameter *t* in the Tóth equation were particularly high during the adsorption of 2-pentenes and 1,4-pentadiene, as seen in **Table 5.3**. As can be seen in **Figure 5.3**, those species presented the trends on dominant adsorbate-adsorbate interactions starting at the lowest coverages. These results are in agreement with the description of *t*, previously proposed (Tóth, 1995). ^1H 2D T_1-T_2 relaxometry correlations in 1-pentene and cyclohexene showed in detail the interaction of the double-bond and the aliphatic chain (**Tables 5.19** and **5.20**). The presence of lateral interactions *via* the aliphatic chain was noted.

The pre-treatment of the alumina resulted in an activation process whereby the adsorption sites were modified to stronger acid sites, as discussed in section 4.4.1. While not presented

in the figures, desorption of hydroxyl groups from the alumina was significant. Thus, the rates of desorption for m/z = 18 were of the same order of magnitude compared with m/z = 15, 39 and 44 for pre-adsorbed 1-pentyne on θ-Al_2O_3 pre-treated at 673 K. A difference of over an order of magnitude was seen for m/z = 18 as compared to the fragment species. Analysis of the TPD showed the influence of the hydroxyl groups with the adsorption of the hydrocarbons. A simultaneous desorption of m/z = 18 and m/z = 15, 39 and 44 for peaks II and III was observed. These peaks were also present for m/z = 42 and 43 (1-pentene and *n*-pentane, respectively). The desorption of hydroxyl species could reduce the number of adsorption sites, and induce the desorption of hydrocarbons (Wischert *et al.*, 2012). Infrared results for the adsorption of hydrocarbons on γ- *vs*. θ-Al_2O_3 showed some relation with the removal of OH. Similar findings were obtained with TEOM. These results relate with the findings during TPD desorption of 1-pentyne from alumina pre-treated at 673 K. Similarly, ^{1}H 2D T_1-T_2 relaxometry correlations with T_1/T_2 values of 1-pentyne, 1-pentene and cyclohexene pre-treated at 393 K contrasted with those obtained on pre-treated alumina at 673 K.

The analysis of desorption peaks from TPD was performed considering purely adsorption of the hydrocarbons. However, it is important to note that some reactivity was present in the aluminas. As mentioned in chapter 3, aluminas are widely used as catalyst supports, but have been also used as catalysts in their own right, *e.g.*, in hydrogenation or isomerisation reactions (Knözinger and Ratnasamy, 1978). ^{13}C T_1 NMR results shown during the adsorption of 1-pentene on pre-treated alumina at 673 K (section 4.3.3.3) already indicated reactivity on the alumina surface upon adsorption of these hydrocarbons. However, as discussed in chapter 4 and section 5.2.1, no other species were observed in the IR spectra. An overall weak adsorption of the hydrocarbons was assumed then. Despite IR spectra, results from TPD clearly showed some reactivity on both γ- and θ-Al_2O_3. As presented in section 5.2.4.1, isomerisation of 2-pentenes to 1-pentene, and hydrogenation of 1-pentyne were noted. **Table 5.11** presented the energies of desorption obtained from TPD analysis. As noted, those values were in the range 85 – 130 kJ mol^{-1}, considering peaks I to III, from highest to lowest coverage, respectively. These values are typical for hydrogenation-dehydrogenation processes, and have been previously cited for highly active adsorption sites on alumina surfaces (Digne *et al.*, 2002). It is important to note that the surface coverage was much lower during TPD. For example, an initial coverage of 1-pentyne of $< 1 \times 10^{-5}$ mol g^{-1}, equivalent to < 0.3 % ML or < 1 % of adsorption sites on alumina

resulted in the high energies of desorption obtained. Notwithstanding, these results were also noted during TEOM experiments in the adsorption of 1-pentyne on both aluminas. The increased uptakes with increasing adsorption temperature suggested some reactivity. Again, uptake values were in the line of the initial coverages during TPD experiments. The higher interaction strength of 1-pentyne on the aluminas allowed for TEOM experiments to show the trend observed in **Figure 5.9**.

As observed, the interaction of hydrocarbons on alumina is a complex process. Different strength of adsorption was noted as a function of type of unsaturation. The relative position of the unsaturation also provided different heats of adsorption. Finally, the presence of adsorbate-adsorbate interactions was noted. The heterogeneity of the alumina also played an important role. Thus, while the interaction of C_5 and C_6 hydrocarbons was predominantly a weak adsorption process, reactivity was noted. Isomerisation of 2-pentenes, as well as 1-pentyne hydrogenation was observed. Such processes were considered to be occurring on a small fraction of high energetic adsorption sites.

5.3.2 Comparison of the different adsorption techniques

The use of a varied range of techniques provided information on the type and strength of adsorption of the C_5 and C_6 hydrocarbons adsorbed on γ- and θ-Al_2O_3. As noted, each technique provided different results that did not contradict each observation but were complementary to each other. It is the purpose of this section to clearly describe the type of information presented by each method.

As discussed previously, IR spectroscopy provided information on the relative strength of interaction of 1-pentyne and 1-pentene, with the alumina surface hydroxyl groups. IR was also sensitive to the effect of surface pre-treatment. However, IR did not show evidence of any surface reaction occurring, at least by means of specific absorption bands. As noted in section 4.4.3, DRIFTS experiments were performed under dynamic flow conditions. Here, TEOM experiments were also performed under flowing conditions. The sensitivity of the microbalance was superior to that of the IR method. TEOM provided useful information on adsorption at three different temperatures. Additionally, surface reactivity was inferred from the behaviour of 1-pentyne adsorption measurements. However, no information on the type of interaction with the surface was directly probed with the TEOM.

Results from adsorption isotherms were treated with a series of adsorption isotherm equations. Both Tóth and Virial methods were applied for full range adsorption. Energies were then calculated. As observed in **Figure 5.6**, heats of adsorption were in good agreement, indicating that the information obtained in the adsorption results was consistent. Comparing the adsorption isotherm results between the batch (volumetric) and flow-through (TEOM) methods, **Figure 5.19** shows the uptake values for both techniques at the respective equilibrium pressures. Similar trends were observed across both methods, with TEOM presenting slightly higher uptakes for similar equilibrium pressures, notably over θ-Al_2O_3. Additionally, different trends were noted for 1-pentyne adsorption, with higher uptake values at 343 K compared to 333 K, contrary to results from the volumetric method. Different equilibrium temperatures were used, which might have played a role in subtle adsorption differences. Additionally, the working principle of each method resulted in the measurement of a slightly different quantity. Volumetric adsorption recorded the remaining adsorbate in the vapour phase, indirectly obtaining the uptake, during batch conditions. By contrast, TEOM directly measured the amount adsorbed on the adsorbent in flow-through conditions. Hence, formation of oligomeric by-products in reactive sites would have been recorded only in the TEOM. Therefore, surface reactivity might be a conditioning factor for the subtle uptake differences, particularly noticeable for 1-pentyne, as discussed. A comparison on the heats of adsorption obtained from TEOM isotherms was not performed. The results obtained would have required an extensive extrapolation from the Freundlich isotherms fitted. However, similar isotherm results would be indicative of analogous energetics.

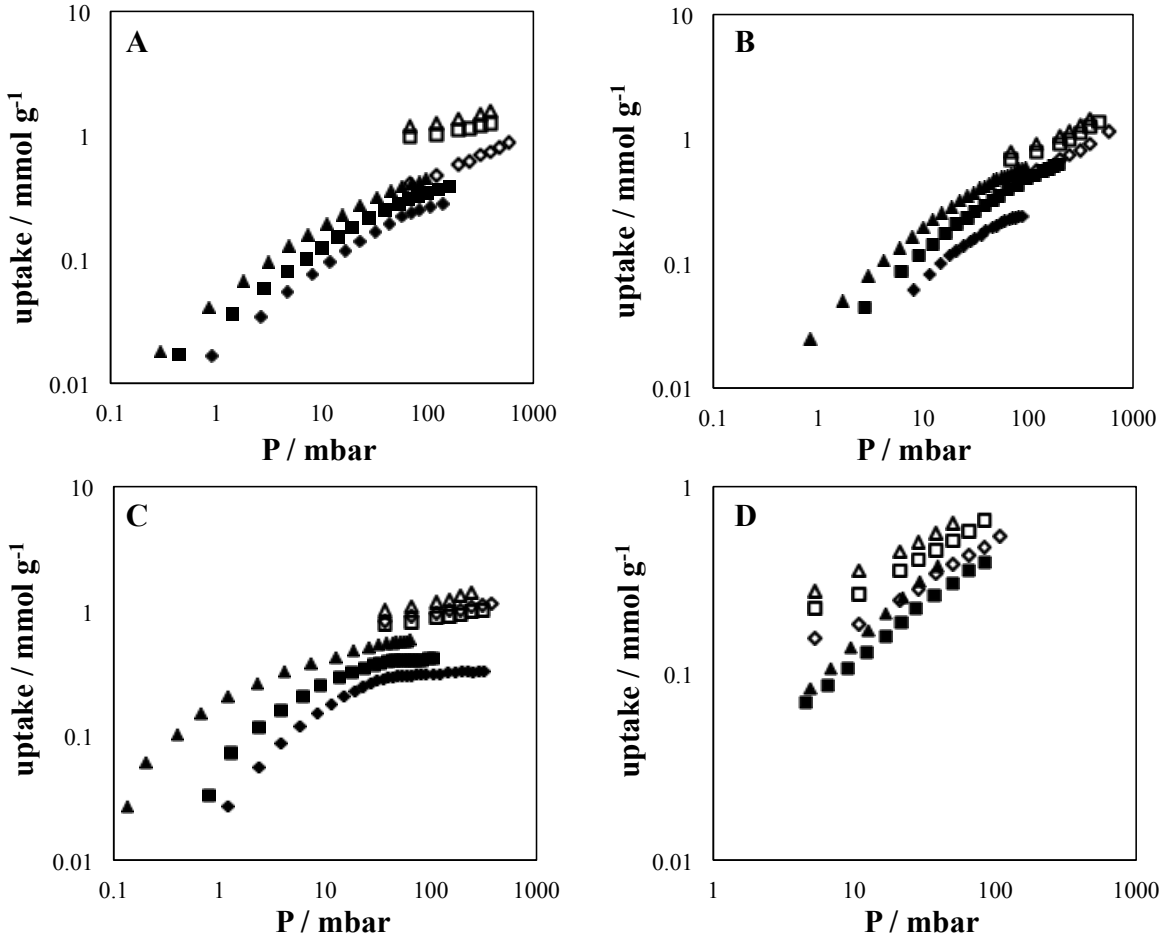

Figure 5.19. Uptake of 1-pentene on θ-Al_2O_3 (A) and on γ-Al_2O_3 (B), 1-pentyne on θ-Al_2O_3 (B), and cyclohexene on θ-Al_2O_3 (D). (Bold symbols) results from the volumetric method at 273 K (triangles), 285.5 K (squares) and 298 K (diamonds); (hollow symbols) results from TEOM experiments at 323 K (triangles), 333 K (squares) and 343 K (diamonds).

Due to the extended adsorption range using the volumetric method, multilayer adsorption was observed to occur (section 5.2.2.2). Hence, BET analysis was performed in order to obtain $v_{\text{m-BET}}$. As noted, the energies of adsorption for the first layer, E_1, were obtained by substitution of condensation enthalpies in E_L (**Table 5.7**); these showed generally lower values to those obtained for the Tóth or Virial fit. Previous studies have shown the limitations of the BET equation in this aspect, attributed to stronger interactions under monolayer, and generally for failing to meet the assumptions considered for its derivation (Sánchez-Montero *et al.*, 2005). Thus, a new Tóth fit was performed, but only for results under monolayer coverage. **Figure 5.8** shows the heats of adsorption for first layer adsorption. These values were useful as they showed similarities with the energies for the full range, being better resolved at lower coverages. However, experimental data at such low adsorption values was limited. For example, no sufficient experiments were performed in cyclohexene (due to

limited vapourisation-condensation behaviour), and energies were not possible to be calculated. Instead, the full adsorption range was considered, as heats of adsorption for both low and high coverages were distinguished. In addition, the reference monolayer uptake value was adopted from the fitted BET parameter, as notable differences were observed between each hydrocarbon.

A comparison between heats of adsorption obtained from volumetric adsorption isotherms, using $v_{m\text{-}BET}$ as the reference for monolayer coverage, and desorption energies from TPD was performed. **Figure 5.20** shows the comparative results for all molecules adsorbed on θ-Al_2O_3. As revealed, two very distinctive energetic regimes were noted: at very low coverages, < 1 - 5 % ML, high energies of > 80 kJ mol^{-1} were obtained, irrespective of the molecular structure or type of unsaturation; on the contrary, at coverages > 2 – 5 % ML, the energies obtained were lower, with values of < 80 kJ mol^{-1}, and dependent on hydrocarbon and coverage. The coverage calculated from TPD experiments was obtained assuming low reactivity of the hydrocarbon. Thus, the integrated signal of the ion followed was indicative of the surface coverage. As can be seen from the results, energies obtained from TPD measurements were representative of low coverages. For example, an initial coverage of 1-pentyne of $< 1 \times 10^{-5}$ mol g^{-1}, equivalent to < 0.3 % ML, was observed. This indicated adsorption of hydrocarbons was taking place on the 1 % strongest and most reactive adsorption sites. It is well known that most reactive sites are occupied first during adsorption. Therefore, such values are characteristic of the reactivity of the aluminas with olefins or alkynes. In contrast, results from adsorption isotherms were heavily influenced by the structure of each unsaturated hydrocarbon, as well as the extent of adsorbate-adsorbate interactions. Hence, adsorption isotherms provided information on the interaction of each hydrocarbon with the alumina, as a function of coverage, while TPD was particularly sensitive to the strongest adsorption sites.

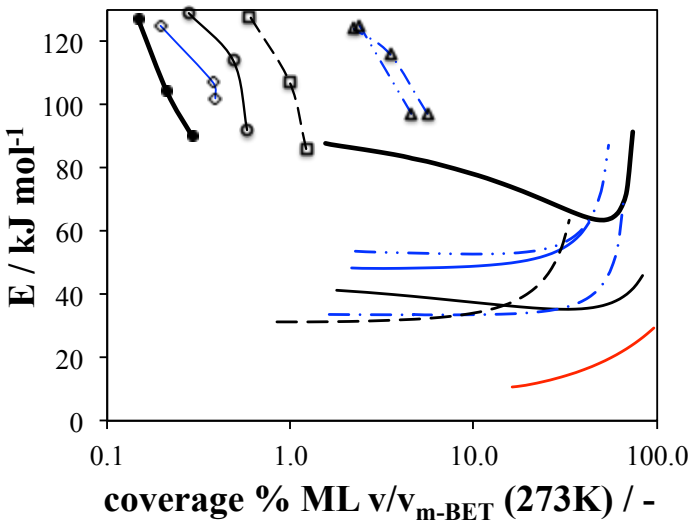

Figure 5.20. Coverage dependent E_{Des} for peaks I, II and III from TPD $N_0(E)$ distribution functions and q_{st} from the full range Tóth isotherms, using the monolayer coverage from the BET equation ($v_{m\text{-}BET}$).

As two different adsorption regimes were observed with TPD and volumetric adsorption isotherms, NMR relaxometry results were compared with energies from each method. As previously mentioned in section 4.4.3, one of the weaknesses of NMR relaxometry is related with the absence of an energy value, in kJ mol^{-1}, for adsorption. ^{13}C T_1 NMR relaxometry results from Huang (2008) were compared with heats of adsorption at 10% ML coverage and E_{max} from TPD. **Figure 5.21** shows the spectra of 1-pentyne adsorbed on on θ-Al_2O_3. (Previously, **Figures 4.8** and **4.13** show the adsorption of 1-pentene and *cis*- and *trans*-2-pentene on θ-Al_2O_3). The interactions of individual carbon atoms of 1-pentyne and the rest of C_5 and C_6 hydrocarbons were obtained, as discussed in section 4.3.3. The comparison with ^{13}C $T_{1,ads}/T_{1,bulk}$ values was established with $(T_{1,ads}/T_{1,bulk})^{-1}$, as this parameter would be proportional with the activation energy for surface diffusion (Huang, 2008). Selection of q_{st}-10%ML_{BET} and E_{max} responded as an overall parameter representative of volumetric adsorption (with reduced lateral interactions) and desorption energies, respectively. **Figure 5.22** shows the comparison for all hydrocarbons adsorbed on θ-Al_2O_3, as well as 1-pentene adsorbed on γ-Al_2O_3. Both the interacting carbon (C*), carbon with lowest $T_{1,ads}/T_{1,bulk}$, and the interacting bond ((C-C)*), average $T_{1,ads}/T_{1,bulk}$ of olefinic carbons, were plotted for comparison. As can be seen, no correlation was observed between TPD (E_{max}) and ^{13}C T_1 NMR relaxometry results. These results indicated that ^{13}C T_1 NMR relaxometry was not probing the 1 % most energetic or reactive sites on the alumina surface. However, a stronger correlation was obtained when NMR relaxometry results were compared against

heats of adsorption. Such information would indicate that ^{13}C T_1 NMR relaxometry results would be sensitive to adsorption of each hydrocarbon on alumina, as a function of coverage, and on the majority of surface sites. This observation would be in agreement with results from 1-pentene adsorbed at variable coverages on θ-Al_2O_3 (section 4.3.3.1). Furthermore, it is interesting to determine the extent of the influence of adsorbate-adsorbate interactions in single component hydrocarbon adsorption. Thus, **Figure 5.23** shows the comparison of q_{st}-10%ML_{BET} with $(-\Delta H_{ads})_{zero}$ and q_{st}-50%ML_{BET}, heavily influenced by lateral interactions. Results showed a stronger correlation between ^{13}C T_1 NMR $(T_{1,ads}/T_{1,bulk})^{-1}$ ((C-C)*) and $(-\Delta H_{ads})_{zero}$, which was weaker with heats of adsorption at higher coverage. Hence, a comparison between $(T_{1,ads}/T_{1,bulk})^{-1}$ ((C-C)*) and $(-\Delta H_{ads})_{zero}$, including error analysis are presented in **Figure 5.24**. In summary, the interacting bond observed by ^{13}C T_1 NMR relaxometry was not influenced by adsorbate-adsorbate interactions. Additionally, it is worth noting that cyclohexene seemed a strong outlier, reinforcing the previous observation on volumetric isotherm limitations. Results presented so far suggest that olefins behaved in a similar way, while 1-pentyne was associated with much stronger interaction.

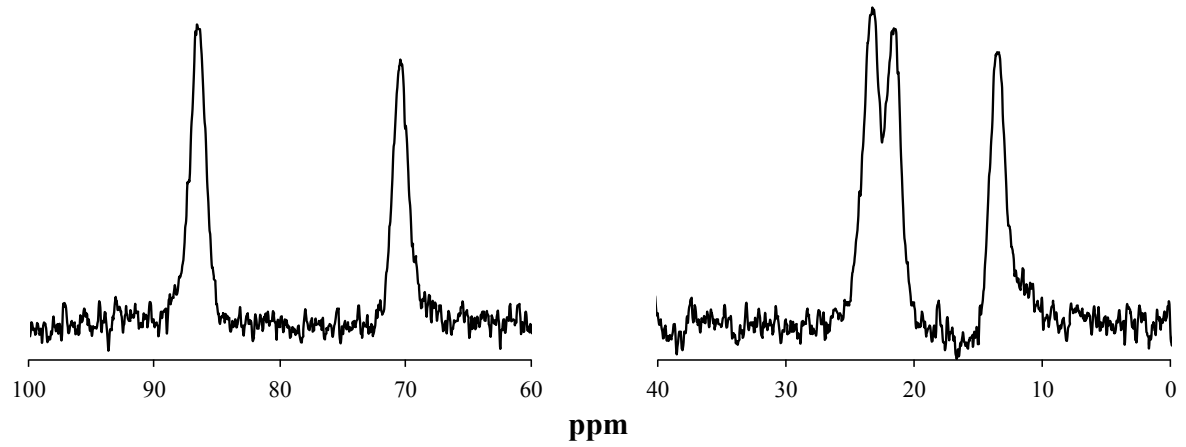

Figure 5.21. ^{13}C NMR spectra of the unsaturated (left) and aliphatic (right) carbons present on 1 ML 1-pentyne adsorbed on θ-Al_2O_3.

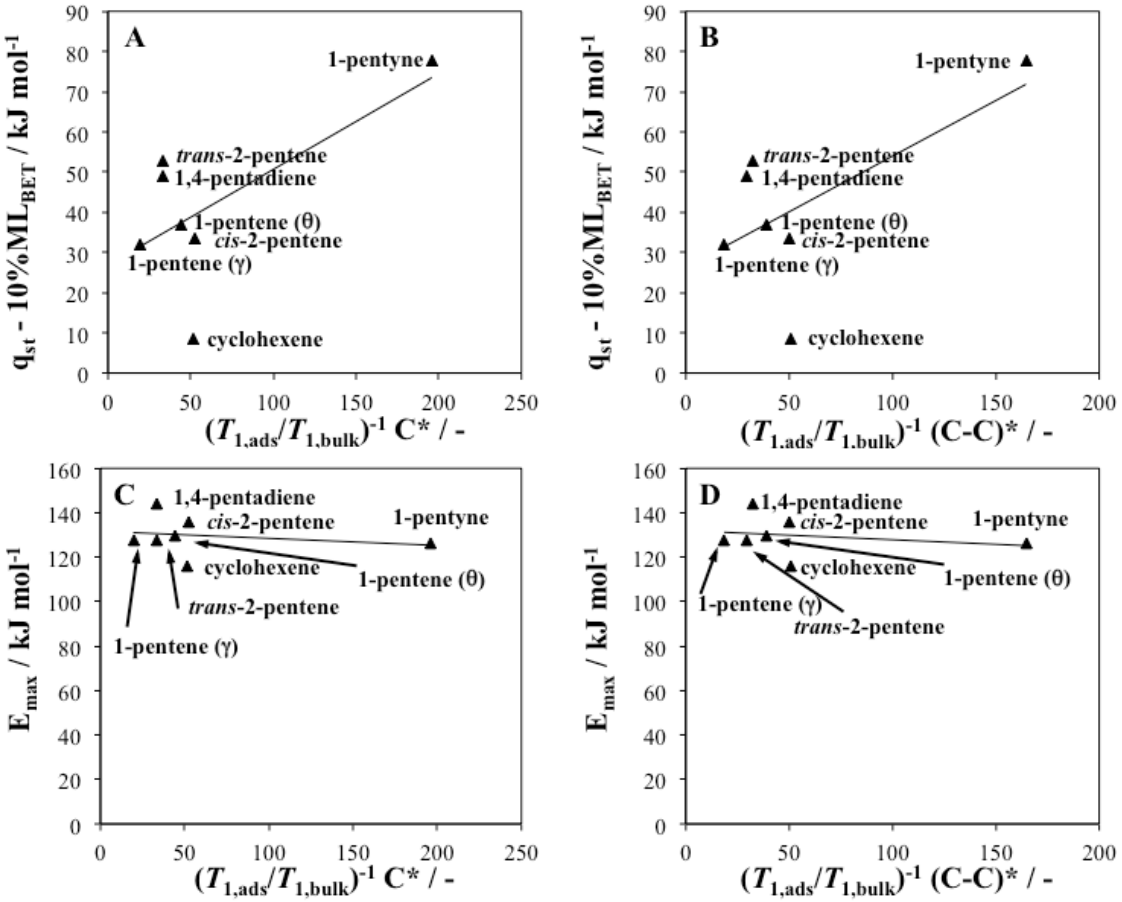

Figure 5.22. Comparison between $(T_{1,ads}/T_{1,bulk})^{-1}$ from ^{13}C T_1 NMR relaxometry results against q_{st} at 10%ML $v/v_{m\text{-}BET}$ using the full Tóth fitting (A-B) and E_{max} from TPD (C-D). Two ^{13}C T_1 NMR relaxometry results were used: (A, C) strongest interacting carbon, C*; (B, D) average value for the interacting unsaturated carbons, (C-C)*. The line represents the best fit in all cases. Error bars are not included for simplicity.

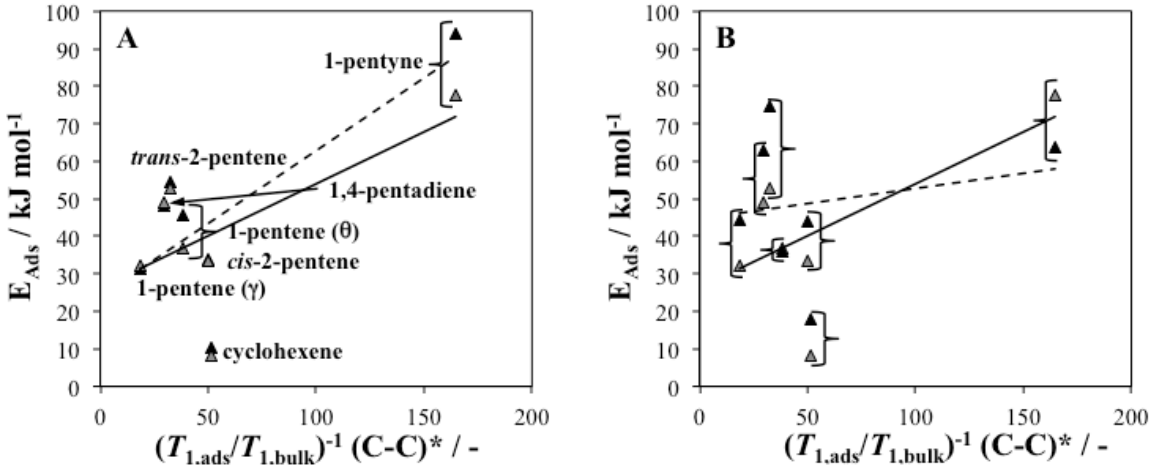

Figure 5.23. Comparison between ^{13}C T_1 NMR relaxometry results against energies of adsorption at different coverages from volumetric isotherms using the full Tóth fitting: (A) 10% ML-BET (as per **Figure 5.22**) (grey) and $(-\Delta H_{ads})_{zero}$; (B) 10% ML-BET (as per **Figure 5.22**) (grey) and 50% ML-BET. Continuous lines represent the best fit on **Figure 5.22**, while dashed lines represent the trendline with the energies for $(-\Delta H_{ads})_{zero}$ (left) and 50% ML-BET (right). Error bars are not included for simplicity.

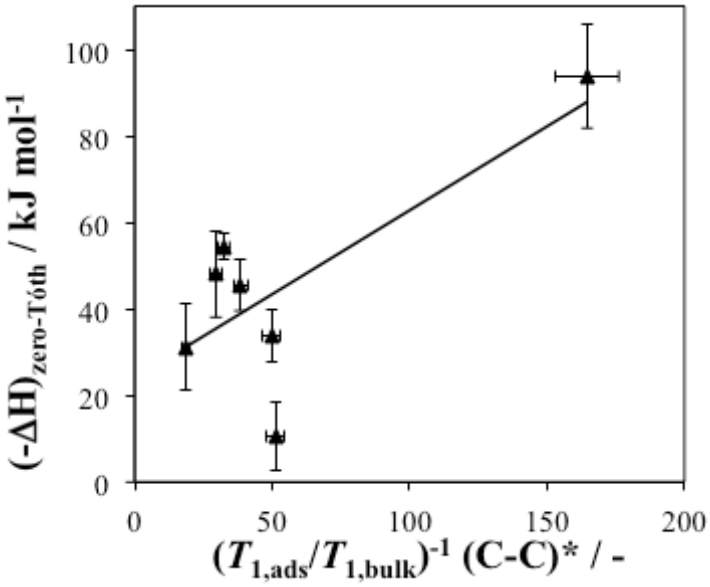

Figure 5.24. Best trend from **Figure 5.23**. Comparison between ^{13}C T_1 NMR relaxometry results against energies of adsorption at zero coverage $(-\Delta H_{ads})_{zero}$, derived from Henry constants using Tóth fitting parameters (**Table 5.4**). Error bars have been included to show the quality of the trend.

Finally, a comparison between ^1H 2D T_1-T_2 NMR relaxometry correlations with the adsorption techniques employed was also made. **Figure 5.25** shows a comparison between the desorption energy value E_{max} from TPD and e_{surf} interaction parameter from T_1/T_2. This parameter has been previously defined by D'Agostino and co-workers (2014), as $e_{surf} = -T_2/T_1$. A successful comparison between both methods was established in that study with the adsorption of water on various metal oxides. In this case, a comparison was established in the case of complex hydrocarbon adsorption. Results were compared with 1-pentene, 1-pentyne and cyclohexene adsorbed on pre-treated alumina at 393 K. As can be seen, results in this case were in line with previous findings. This observation suggested that values from ^1H 2D T_1-T_2 NMR relaxometry correlations were in line with TPD results and representative of strongest and more reactive sites.

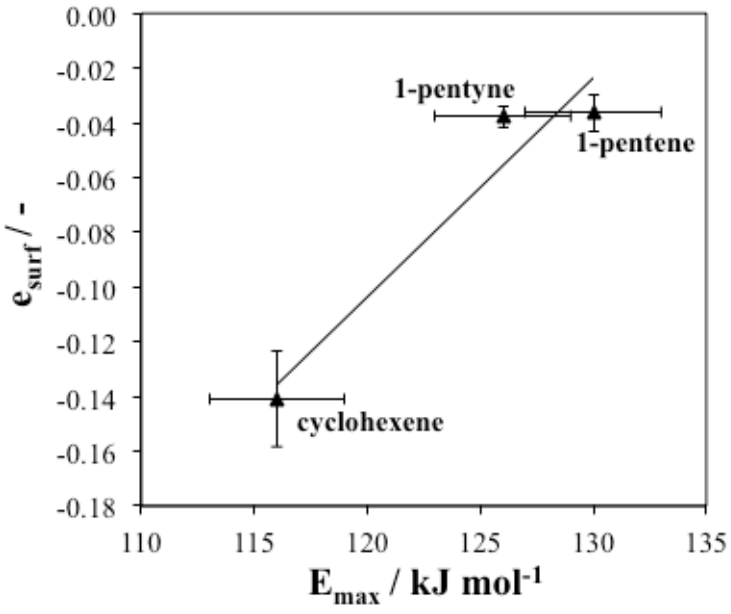

Figure 5.25. Comparison of e_{surf} from ^{1}H 2D T_1-T_2 NMR results against E_{max} from TPD for 1-pentene, 1-pentyne and cyclohexene on θ-Al_2O_3. The diagonal line shows the best fit.

Finally, it is important to reinforce that each adsorption technique presents its limitations, as briefly outlined in section 4.4.3. In this study, the weakness of the volumetric adsorption isotherm method was observed in the case of cyclohexene. Vapour pressure limitations, as well as physical condensation limited the study of cyclohexene adsorption in both the low and the high-pressure regions. Additionally, limitations at low coverage due to the influence of errors have been reported (Purewal, 2010; Russo *et al.*, 2008). Other methods with the use of high affinity chromatography (Katz and Gray, 1981), are used to obtain energies at low coverages. Additionally, calorimetric methods have been tested to overcome such limitations, (Moschetta *et al.*, 2013; Siril and Brown, 2006). Comparison between calorimetry and isotherms has been done, providing similar results (Shen *et al.*, 2000) in a range of coverages. TEOM uptake measurements presented a convenient solution for measurements at high coverage, as flow-through experiments removed any excess physisorbed species. However, as noted in the adsorption of 1-pentyne, reactivity enhanced the uptake values, providing a dissimilar trend when compared with other hydrocarbons. Finally, TPD was used to obtain energies at very low coverages. Although possible to obtain coverage dependent information with TPD (Roos *et al*., 2010), it has been shown to present certain limitations in determining binding energies (Goering *et al.*, 2007). TPD measurements provide an excellent probe for

surface adsorption sites. Multiple studies exploited TPD as a means of determining reaction mechanisms (Pang and Medlin, 2011; Matveev *et al.*, 2004). Compared with the results from this study, IR was able to approximate results on the strength of adsorption for 1-pentyne and 1-pentene, as well as the type of interaction present. However, only information of the weak adsorption sites, which are the most abundant on the surface of the alumina, was provided. Hence, experiments involving low surface density and highly energetic sites should be studied with TPD. In that scenario, 2D ^{1}H T_1-T_2 NMR relaxometry can also provide relevant information. If any reactivity occurs, both TPD and TEOM can provide complementary information on the species formed and the carbonaceous deposits adsorbed on the surface, respectively. Finally, calorimetric or volumetric adsorption studies are suggested for coverage-dependent experiments. ^{13}C T_1 NMR relaxometry is suggested in systems where variable coverage is studied, as well as sensitivity is required to be able to distinguish similar adsorbates.

5.4 Conclusions

The adsorption of a series of C_5 and C_6 hydrocarbons on γ- and θ-Al_2O_3 was studied with various characterisation techniques. IR spectroscopy, volumetric adsorption isotherms, dynamic isotherms *via* TEOM, temperature-programmed desorption (TPD) as well as ^{13}C T_1 NMR and ^{1}H 2D T_1-T_2 relaxometry methods were employed. As was noted, the hydrocarbons interacted with the hydroxyl groups of the aluminas. Heats of adsorption were obtained for each hydrocarbon, reflecting the dependence of adsorption with coverage, adsorption sites and the presence of lateral interactions. 1-pentyne showed the strongest interaction with the alumina (94 kJ mol^{-1}), followed by the acyclic olefins (54 - 34 kJ mol^{-1}) and cyclohexene with the weakest adsorption on θ-Al_2O_3 (11 kJ mol^{-1}). Hence, information was extracted on the preferential triple bond interaction, as well as the relative linear *vs.* cyclic olefin adsorption. Additionally, the relative position of the double-bond in acyclic olefins, 54 kJ mol^{-1} for *trans*-2-pentene *vs*. 34 kJ mol^{-1} for *cis*-2-pentene, showed preferential adsorption behaviour. Finally, the interaction was stronger on θ-Al_2O_3 as compared to γ-Al_2O_3, and pre-treatment temperature influenced adsorption, as noted by TEOM, IR and 2D ^{1}H T_1-T_2 NMR relaxometry results.

The use of a number of adsorption techniques made it possible to establish a comparison on the type of information obtained from each technique. A comparison between dynamic – TEOM – and batch isotherms was established. Results revealed the similar uptake values obtained with both adsorption methods, with the main distinction based on adsorption of reactive products followed with TEOM. Direct flow-through measurements allowed for such distinction. Hence, weak adsorption was predominantly observed with both methods. In contrast, high desorption energies, > 80 kJ mol^{-1}, were obtained with TPD, indicative of a surface characteristic property. Reactivity of the aluminas was captured with TPD and was found to be weakly dependent of the molecule. Hence, two different energetic regimes were found for the adsorption of C_5 and C_6 unsaturated hydrocarbons on aluminas. NMR relaxometry methods probed the two different regimes. While ^{13}C T_1 NMR relaxometry was sensitive to molecule adsorbed, coverage and adsorption geometry, ^{1}H 2D T_1-T_2 showed a good correlation with the 1 % strongest adsorption sites. A good agreement between conventional characterisation techniques and NMR relaxometry methods was found, relative to the characteristics of the adsorbate-adsorbent systems studied. NMR relaxometry was shown to provide relevant information on molecule adsorption, key to understanding catalytic processes. Finally, recommendations on the different techniques to be used in future adsorption experiments were made.

References

Aguilar-Armenta, G., Patiño-Iglesias, M.E., Jiménez-Jiménez, J., Rodríguez-Castellón, E., Jiménez-López, A. (2006) Application of porous phosphate heterostructure materials for gas separation. *Langmuir,* 22, 1260 – 1267.

Barrie, P.J. (2008) Analysis of temperature programmed desorption (TPD) data for the characterisation of catalysts containing a distribution of adsorption sites. *Phys. Chem. Chem. Phys.*, 10, 1688 – 1696.

Bosnick, K., Ban, S., Hiebert, W., Shi, Z., Huang, C., Lister, R., Mleczko, M. (2011) Organic vapor adsorption on *in situ* grown carbon nanotube films. *Carbon*, 49, 3639 – 3644.

Buatier de Mongeot, F., Rocca, M., Valbusa, U. (1997) Isothermal desorption of O_2 from Ag (001). *Surf. Sci.*, 377 – 379, 691 – 695.

Busca, G., Ramis, G., Lorenzelli, V., Janin, A., Lavalley, J-C. (1987) FT-i.r. study of molecular interactions of olefins with oxide surfaces. *Spectrochim. Acta A*, 43, 489 – 496.

Chorkendorff, I., Niemantsverdriet, J.W. (2007) *Concepts of modern catalysis and kinetics.* Wiley VCH, Weinheim, pp. 108 – 111.

Clayborne, P.A., Nelson, T.C., DeVore, T.C. (2004). Temperature programmed desorption-FTIR investigation of C_1-C_5 primary alcohols adsorbed on γ-Al_2O_3. *Appl. Catal.*, 257, 225 – 233.

Crini, G., Peindy, H.N., Gimbert, F., Robert, C. (2007) Removal of C.I. basic green 4 (Malachite green) from aqueous solutions by adsorption using cyclodextrin-based adsorbent: kinetic and equilibrium studies. *Sep. Purif. Technol.*, 53, 97 – 110.

Crowder, G.A., Fick, H. (1986) Vibrational analysis of 1-butyne and 1-pentyne. *J. Mol. Struct.*, 147, 17 – 27.

Czepirski, L., Jagiełło, J. (1989) Virial-type thermal equation of gas-solid adsorption. *Chem. Eng. Sci.*, 44, 797 – 801.

D'Agostino, C., Mitchell, J., Mantle, M.D., Gladden, L.F. (2014) Interpretation of NMR relaxation as a tool for characterising adsorption strength of liquids inside porous materials. *Chem. Eur. J.*, 20, 13009 – 13015.

Dallos, A., Mártha, V.E., Bíró, Sz. (2002) Simultaneous determination of heats, equilibrium and kinetics of adsorption. 1-ethoxyl-2-propanol vapours. *J. Therm. Anal. Cal.*, 69, 353 – 358.

Digne, M., Sautet, P., Raybaud, P., Euzen, P., Toulhoat, H. (2002) Hydroxyl groups on γ-alumina surfaces: a DFT study. *J. Catal.*, 211, 1 – 5.

Domínguez, G., Hernández-Huesca, R., Aguilar-Armenta, G. (2010) Isosteric heats of adsorption of N_2O and NO on natural zeolites. *J. Mex. Chem. Soc.*, 54, 111 – 116.

Dobrovolná, Z., Kačer, P., Červený, L. (1998) Competitive hydrogenation in alkene-alkyne-diene systems with palladium and platinum catalysts. *J. Mol. Catal. A-Chem.*, 130, 279 – 284.

Fichthorn, K.A., Miron, R.A. (2002) Thermal desorption of large molecules from solid surfaces. *Phys. Rev. Lett.*, 89, 196103.

Garbowski, E., Primet, M. (1985) Spectroscopic study on the cokefaction of butene and butane on alumina. *J. Chem. Soc., Faraday Trans.*, 81, 497 – 508.

Giles, C.H., MacEwan, T.H., Nakhwa, S.N., Smith, D. (1960) Studies in adsorption. Part XI. A system of classification of solution adsorption isotherms, and its use in diagnosis of adsorption mechanisms and in measurement of specific surface areas of solids. *J. Chem. Soc.*, 3973 – 3993.

Gill, R., Petkovic, L.M., Larsen, G. (1998) Interaction of isobutene with the surface of different solid acids. *J. Catal.*, 179, 56 – 63.

Goering, J., Kadossov, E., Burghaus, U., Yu, Z.Q., Thevuthasan, S., Saraf, L.V. (2007) Adsorption of iso-/*n*-butane on an anatase thin film: a molecular beam scattering and TDS study. *Catal. Lett.*, 116, 9 – 14.

Hinz, C. (2001) Description of sorption data with isotherm equations. *Geoderma*, 99, 225 – 243.

Hoffmann, R.L., List, G.R., Evans, C.D. (1966) Gas-solid chromatography of hydrocarbons on activated alumina. II. Alkane, alkene, alkyne separations and subtractive adsorption. *J. Am. Oil Chem. Soc.*, 43, 675 – 677.

Horn, A., Hopf, H., Klaeboe, P. (2011) Infrared and Raman spectral data and conformations of 1-pentyne. *J. Mol. Struct.*, 989, 38 – 44.

Huang, Z. (2008) *Magnetic resonance studies of catalysts and catalytic reactors*. A dissertation submitted for the degree of Doctor of Philosophy, University of Cambridge, pp. 179 – 200.

Katz, S., Gray, D.G. (1981) The adsorption of hydrocarbons on cellophane. I. Zero coverage limit. *J. Colloid Interface Sci.*, 82, 318 – 324.

Kim, B.C., Yamamoto, T., Byun, Y.S., Kim, Y.H. (2010) Measurement of adsorption characteristics of alumina and activated carbon using a quartz crystal resonator with *i*-butane. *Korean J. Chem. Eng.*, 27, 328 – 333.

Knozinger, H., Bühl, H., Kochloefl, K. (1972) The dehydration of alcohols on alumina: XIV reactivity and mechanism. *J. Catal.*, 24, 57 – 68.

Knözinger, H., Ratnasamy, P. (1978) Catalytic aluminas: surface models and characterization of surface sites. *Catal. Rev.-Sci. Eng.*, 17, 31 – 70.

Koeken, A.C.J., Torres Glavis, H.M., Davidian, T., Ruitenbeek, M., de Jong, K.P. (2012) Suppression of carbon deposition in the iron-catalyzed production of lower olefins from synthesis gas. *Angew. Chem. Int. Ed.*, 51, 7190 – 7193.

Kress, R. (1999) *Linear Integral Equations*. Springer-Verlag, New York.

Kwal, J.H., Mei, D., Peden, C.H.F., Rousseau, R., Szanyi, J. (2011) (100) facets of γ-Al_2O_3: the active surfaces for alcohol dehydration reactions. *Catal. Lett.*, 141, 649 – 655.

Matveev, A.V., Sametova, A.A., Gorodetskii, V.V. (2004) The study of nitric oxide adsorption and the mechanism of surface "explosions" in the reaction of CO + NO on Pt(100) and Pd (110) single crystal surfaces. *Kinet. Catal.*, 45, 598 – 606.

Miller, B.P., Furlong, O.J., Tysoe, W.T. (2013) The desorption and reaction of 1-alkenes and 1-alkynes on Cu(111) and copper foils. *Surf. Sci.*, 616, 143 – 148.

Morterra, C., Bolis, V., Magnacca, G. (1994) IR spectroscopic and microcalorimetric characterization of Lewis acid sites on (transition phase) Al_2O_3 using adsorbed CO. *Langmuir*, 10, 1812 – 1824.

Morterra, C., Magnacca, G. (1996) A case study: surface chemistry and surface structure of catalytic aluminas, as studied by vibrational spectroscopy of adsorbed species. *Catal. Today*, 27, 497 – 532.

Moschetta, E.G., Gans, K.M., Rioux, R.M. (2013) Characterization of sites of different thermodynamic affinities on the same metal center *via* isothermal titration calorimetry. *J. Catal.*, 302, 1 – 9.

Pawela-Crew, J., Madix, R.J. (1995) Lateral interactions in the desorption kinetics of weakly adsorbed species: unexpected differences in the desorption of C_4 alkenes and alkanes from Ag(110) due to oriented π-bonding of the alkenes. *Surf. Sci.*, 339, 8 – 22.

Pang, S.H., Medlin, W. (2011) Adsorption and reaction of furfural and furfuryl alcohol on Pd(111): unique reaction pathways for multifunctional reagents. *ACS Catal.*, 1, 1272 – 1283.

Purewal, J.J. (2010) *Hydrogen adsorption by alkali metal graphite intercalation compounds*. A dissertation submitted for the degree of Doctor of Philosophy, California Institute of Technology, pp. 40 – 47.

Purewal, J.J., Keith, J.B., Ahn, C.C., Fultz, B. (2009) Adsorption and melting of hydrogen in potassium-intercalated graphite. *Phys. Rev. B*, 79, 054305.

Redhead, P.A. (1962) Thermal desorption of gases. *Vacuum*, 12, 203 – 211.

Roos, M., Breitruck, A., Hoster, H.E., Behm, R.J. (2010) Entropic stabilization of large adsorbates on weakly binding substrates – a thermal desorption and scanning tunnelling microscopy study. *Phys. Chem. Chem. Phys.*, 12, 818 – 822.

Russo, P.A., Ribeiro Carrott, M.M.L., Carrott, P.J.M. (2008) Adsorption of toluene, methylcyclohexane and neopentane on silica MCM-41. *Adsorption*, 14, 367 – 375.

Sánchez-Montero, M.J., Herdes, C., Salvador, F., Vega, L.F. (2005) New insights into the adsorption isotherm interpretation by a coupled molecular simulation-experimental procedure. *Appl. Surf. Sci.*, 252, 519 – 528.

Scherwitzl, B., Resel, R., Winkler, A. (2014) Film growth, adsorption and desorption kinetics of indigo on SiO_2. *J. Chem. Phys.*, 140, 184705.

SDBS (1997) *Spectral database of organic compounds* [Online] Available from: http://sdbs.db.aist.go.jp [Accessed October 2014]

Sears, W.M. (2001) Isosteric heat of adsorption of water vapor on bismuth iron molybdate

measured by the method of constant surface conductance. *Langmuir*, 17, 5237 – 5244.

Shen, D., Bülow, M., Siperstein, F., Engelhard, M., Myers, A.L. (2000) Comparison of experimental techniques for measuring isosteric heat of adsorption. *Adsorption*, 6, 275 – 286.

Siperstein, F., Gorte, R.J., Myers, A.L. (1999) - A new calorimeter for simultaneous measurements of loading and heats of adsorption from gaseous mixtures. *Langmuir*, 15, 1570 – 1576.

Siril, P.F., Brown, D.R. (2006) Acid site accessibility in sulfonated polystyrene acid catalysts: calorimetric study of NH_3 adsorption from flowing gas stream. *J. Mol. Catal. A-Chem.*, 252, 125 – 131.

Swecker, J.L., Datye, A.K. (1990) Alcohol dehydration over model nonporous alumina powder. *J. Catal.*, 121, 196 – 201.

Szekeres, M., Tóth, J., Dékány, I. (2002) Specific surface area of Stoeber silica determined by various experimental methods. *Langmuir*, 18, 2678 – 2685.

Takeuchi, N., Kanai, Y., Selloni, A. (2004) Surface reaction of alkynes and alkenes with H-Si(111): a density functional theory study. *J. Am. Chem. Soc.*, 126, 15890 – 15896.

Tedds, S., Walton, A., Broom, D.P., Book, D. (2011) Characterisation of porous hydrogen storage materials: carbons, zeolites, MOFs and PIMs. *Faraday Discuss.*, 151, 75 – 94.

Teplyakov, A.V., Gurevich, A.B., Yang, M.X., Bent, B.E., Chen, J.G. (1998) NEXAFS and TPD studies of molecular adsorption of hydrocarbons on Cu(100): segmental correlations with the heats of adsorption. *Surf. Sci.*, 396, 340 – 348.

Teschner, D., Vass, E., Hävecker, M., Zafeiratos, S., Schnörch, P., Sauer, H., Knop-Gericke, A., Schlögl, R., Chamam, M., Wootsch, A., Canning, A.S., Gamman, J.J., Jackson, S.D., McGregor, J., Gladden, L.F. (2006) Alkyne hydrogenation over Pd catalysts: A new paradigm. *J. Catal.*, 242, 26 – 37.

Tóth, J., Berger, F., Dékány, I. (1999) Calculation of the BET compatible surface area from any type I isotherms measured below the critical temperature. *J. Colloid Interf. Sci.*, 212, 411 – 418.

Trombetta, M., Busca, G., Rossini, S.A., Piccoli, V., Cornaro, U. (1997) FT-IR studies on light olefin skeletal isomerization catalysis. I. The interaction of C4 olefins and alcohols with pure γ-alumina. *J. Catal.*, 168, 334 – 348.

Tsyganenko, A.A., Filimonov, V.N. (1972) Infrared spectra of surface hydroxyl groups and crystalline structure of oxides. *Spectrosc. Lett.*, 5, 477 – 487.

Ulbricht, H., Zacharia, R., Cindir, N., Hertel, T. (2006) Thermal desorption of gases and solvents from graphite and carbon nanotube surfaces. *Carbon*, 44, 2931 – 2942.

Wazwaz, A-M. (2011) The regularization method for Fredholm integra equations of the first kind. *Comput. Math. Appl.*, 61, 2981 – 2986.

Weber, D., Mitchell, J., McGregor, J., Gladden, L.F. (2009). Comparing strengths of surface

interactions for reactants and solvents in porous catalysts using two-dimensional NMR relaxation correlations. *J. Phys. Chem. C*, 113, 6610 – 6615.

Wischert, R., Laurent, P., Copéret, C., Delbecq, F., Sautet, P. (2012) γ-alumina: The essential and unexpected role of water for the structure, stability, and reactivity of "defect" sites. *J. Am. Chem. Soc.*, 134, 14430 – 14449.

Wu, J., Zhang, L., Long, C., Zhang, Q. (2012) Adsorption characteristics of pentane, hexane, and heptane: comparison of hydrophobic hypercrosslinked polymeric adsorbent with activated carbon. *J. Chem. Eng. Data*, 57, 3426 – 3433.

Chapter 6:

Selective hydrogenation

6 Selective hydrogenation

In this chapter, a brief review of the importance of selectivity in the reaction of complex molecules, with particular attention to solvent effects, is presented. Due to the importance of hydrogenation reactions in catalysis, selectivity during hydrogenation of multifunctional molecules will be the centre of the discussion. Citral is chosen as a model molecule to gain useful insights on the role of solvent in determining the reactivity and selectivity during hydrogenation.

6.1 Importance of selectivity: multifunctional molecules

Many industrially relevant processes require highly selective catalytic routes towards desired products. Selectivity is one of the key drivers in catalysis research: improving selectivity has direct economic and environmental benefits associated with less waste and reduced material and energy inputs (Somorjai and Kliewer, 2009).

Solvents are known to influence reaction rates and selectivities, both in homogeneous catalysis and organic chemistry (Ashworth et al., 2013; Williams, 2013; Zhang and Fang, 2013) as well as in heterogeneous catalysis (Wan *et al.*, 2014; Kishida and Teranishi, 1968; Koopman *et al.*, 1981; Caga *et al.*, 1976). Many heterogeneous catalytic reactions also require the use of a liquid-phase solvent for a number of reasons: i) to dissolve reactants and products, hence allowing key reaction steps (Kunkes *et al.*, 2008), ii) to control reaction rates or extent of reaction and exothermicity (Sedransk *et al.*, 2013) or iii) to remove site blockers from the catalyst (Mukherjee and Vannice, 2006; Singh and Vannice, 2001). Solvent selection in a heterogeneous catalysed liquid-phase reaction remains somewhat empirical despite the fact that it can significantly influence reaction conversion and selectivity (Akpa *et al.*, 2012). Several studies have postulated a number of reasons for the observed changes in reactivity based on physical properties of the solvent, such as solvent polarity (Augustine and Techasauvapak, 1994; Hájek *et al.*, 2004), solubility of gases (Rajadhyaksha and Karwa, 1986) or solvent solvation (Mäki-Arvela *et al.*, 2005). A competitive adsorption role has also been proposed to explain the effect of solvent (Bertero *et al.*, 2011; Mounzer *et al.*, 2010; Mukherjee and Vannice, 2006; Singh *et al.*, 2000; Takagi *et al.*, 1999). The rationalization of solvent effects is very difficult due to the lack of systematic experimental data including different solvents, reactants, reaction conditions, catalysts, adsorption modes of reactant, side reactions, etc. (Mäki-Arvela *et al.*, 2005).

Hydrogenation is by far the largest application of catalysis in chemical transformations (Farrauto and Bartholomew, 2011; Jackson and Monaghan, 2007; McGregor *et al.*, 2010; Nishimura, 2001; Pérez-Cadenas *et al.*, 2007; Ross, 2012), and the selective reduction of one functionality within a multi-functional unsaturated molecule is a subject that receives much attention (Blaser *et al.*, 2003). A small set of studies has also considered low temperature oxidation reactions (D'Agostino *et al.*, 2012) or alkylation of aromatics (McMillan *et al.*, 2013). In such liquid-phase reactions, using a suitable solvent towards tailoring high selectivities is desirable. **Table 6.1** summarises important findings from the literature, mostly from hydrogenation reactions, depicting the importance of solvent effects on selective chemical reactions. Important applications relate to selective hydrogenation reactions towards the valorisation of biomass raw materials (Trasarti *et al.*, 2012, Delhomme *et al.*, 2013), such as the selective hydrogenation of glucose derivatives (Gallezot, 2007). Hydrogenation of terpenes for the fine chemical industry as i) intermediates for vitamins or drugs, and ii) constituents for flavours and fragrances has also been exploited (Swift, 2004). Recently, reduction of unsaturated nitriles (McGregor *et al.*, 2010; Kukula *et al.*, 2007; Kukula and Koprivova, 2005) towards amines as intermediates for pharmaceuticals, textile additives, disinfectants, corrosion inhibitions or detergents among others has been investigated (Gómez *et al.*, 2002). In all these processes, the challenge is to react the functionality that is thermodynamically less favourable with the use of different catalysts or reaction conditions. Of particular interest are the hydrogenation of α,β-unsaturated aldehydes (Mäki-Arvela *et al*., 2005). For example, in the case of the hydrogenation of α,β-unsaturated aldehydes, the hydrogenation of the C=C bond is favoured thermodynamically (Loffreda *et* al., 2006, Gallezot and Richard, 1998). Therefore, interest is placed in the selective hydrogenation of the C=O moiety in a variety of molecules, such as acrolein (Wei *et al.*, 2013, Bailie *et al*., 1997), crotonaldehyde (Englisch *et al.*, 1997, Consonni *et al.*, 1998), cinnamaldehyde (Hájek *et al.*, 2004, Ide *et al.*, 2012) or citral (Stolle *et al.*, 2013). The structure of these α,β-unsaturated aldehydes is shown in **Figure 6.1**. In summary, literature on the hydrogenation of multifunctional molecules reveals the presence of multiple effects related with changes in selectivity. **Table 6.2** summarises the most relevant effects. As can be seen, a number of those factors are dependent on the choice of solvent.

Table 6.1. Summary of important findings from the literature in selective chemical transformations: solvent effects are described in detail; other parameters, such as reaction temperature or catalyst characterisation are also noted.

study	molecule	catalyst	solvent(s)	remarks
Abdul-Wahab and Jackson (2013)	3-nitroacetophenone	Rh/SiO_2	2-propanol	Consecutive reaction. Reaction rates enhanced by increased temperature, metal dispersion and pore size of support. Dehydration reactions were also observed.
Akpa *et al*. (2012)	2-butanone	Ru/SiO_2	2-propanol heptane methanol water	Solvent was shown to affect reaction rates by altering the preferred reaction mechanism.
Augustine and Techasauvapak (1994)	4-methyl-1-cyclohexene	Pt/SiO_2	ethyl acetate ethanol heptane tetrahydrofuran	Solvent polarity strongly influenced the extent of interaction of the solvent with the catalyst. Such interaction decreased the hydrogenation rate of the substrate
Bertero *et al*. (2011)	acetophenone	Ni/SiO_2	1-propanol 2-propanol γ-butyrolactone acetonitrile benzene cyclohexane ethanol methanol tetrahydrofuran toluene	Solvent had a strong influence in reaction rates, higher in C_1-C_3 alcohol solvents, while it did not modify selectivity towards phenylethanol. Comprehensive study: i) rates were affected by polarity, particularly related with H-bond formation, ii) solvent-reactant interactions were weak in apolar solvents, with the hydrogenation rate dependent on solvent-catalyst interactions, iii) strength of solvent adsorption on catalyst determined hydrogenation rate.
Breen *et al*. (2004)	cinnamaldehyde	Ir/C	2-propanol	Adsorption of the unsaturated alcohol (cinnamyl alcohol) resulted in an inhibition of the hydrogenation of the C=C bond due to steric effects
D'Agostino *et al*. (2012)	1,4-butanediol	Au/TiO_2	methanol water	The addition of water limited the adsorption of reactant, decreasing the oxidation rate. NMR relaxometry methods were employed to determine such effect.
Englisch *et al*. (1997)	crotonaldehyde	Pt/SiO_2	2-propanol chloroform cyclohexane ethanol methanol	Polar protic solvents favoured higher unsaturated alcohol selectivity. Selectivity towards unsaturated alcohols increased with Pt particle size. Deactivation was observed *via* decarbonylation of catalyst

Table 6.1. (Continued)

Háyek *et al*. (2004)	cinnamaldehyde	Ru/Y	2-butanol 2-pentanol 2-propanol 3-pentanol acetone cyclohexane cyclohexanol ethylacetate isooctane *t*-butanol tetrahydrofuran toluene triethylamine xylene	Highest reactivity was noted in alcohols, showing a good correlation with solvent polarity. Selectivity towards unsaturated alcohol was highest in polar aprotic solvents, reasonable selectivity was noted in alcohols. Condensation reactions were observed when short chain alcohols were used. Substrate to catalyst ratio (reactant concentration) had a negative effect at low concentrations of reactant, suppressing the selectivity towards unsaturated alcohols.
Hronec *et al*. (2012)	2-methylfuran furfural furfuryl alcohol	Ni Pt/Al_2O_3 (Pt, Pd, Ru)/C Pt/MgO Pt-Ru/C Ru/TiO_2	water 2-propanol *n*-decanol	The distribution of reaction products was shown to be influenced by furfural concentration and acid-base properties of solvent and supported metal catalyst
Ide *et al*. (2012)	benzalacetone cinnamaldehyde crotonaldehyde methyl vinyl ketone	Au/C Au/Fe_2O_3 Au/TiO_2 Pd/C Pt/C Ru/C	ethanol water	Unsaturated alcohols were obtained from unsaturated aldehydes, but not from unsaturated ketones. DFT calculations showed lower activation barriers for the hydrogenation steps over Pt compared to Ru.
Koopman *et al*. (1981)	acetone benzene cyclohexanone cyclohexene phenol	Ru Ru/C Ru/SiO_2	1-propanol cyclohexane water (and mixtures)	Influence of support in combination with solvent to determine selectivity. Importance of hydrophilic and hydrophobic supports, solvent-support interactions and partition of reactant between bulk and adsorbed solvent
Kukula *et al*. (2007)	1-cyclohexenyl-acetonitrile 3,3-dimethyl-acrylonitrile cinnamonitrile *cis*-2-pentenenitrile geranylnitrile *trans*-3-pentenenitrile	CoB CoBCr NiB NiBCr	methanol	Ni preferentially hydrogenated C=C bond, while Co was selective towards C≡N hydrogenation. The addition of a Cr dopant increased the performance of the catalyst.

Table 6.1. (Continued)

Mercadante *et al*. (1996)	cinnamaldehyde citral	Ru/Al_2O_3	ethanol	The adsorption mode of the reactant was shown to have an important effect on selectivity. Metal particle size influenced the selectivity of cinnamaldehyde hydrogenation.
Mounzer *et al*. (2010)	2-octanol	Pt-Bi/C	dioxane DMSO heptane *p*-xylene	Product adsorption was shown to have an important effect on reaction rates and deactivation. Solvent favoured product desorption, enhancing catalytic activity.
Poltarzewski *et al*. (1986)	acrolein cinnamaldehyde,	Pt/C Pt/Nylon Pt-Sn/Nylon	ethanol	Pt on its own preferentially resulted in the hydrogenation of the C=C bond, forming saturated aldehydes (specially in the case of acrolein). Addition of Sn increased the selectivity towards unsaturated alcohols in both substrates.
Rajadhyaksha and Karwa (1986)	*o*-nitrotoluene	Pd/C	2-propanol benzene cyclohexane cyclohexanol hexane *i*-butanol methanol	Solvent-reactant interactions were shown to depend on the extent of solvent polarity, which can be measured using activity coefficient values. Solubility of H_2 on each solvent, as well as solvent competitive adsorption were noted to be an important factor determining hydrogenation rates.
Rojas *et al*. (2012)	benzalacetone cinnamaldehyde	Au/SiO_2 Ir/SiO_2	ethanol	Particle size effects were shown to have an influence in selectivity towards unsaturated alcohols in cinnamaldehyde hydrogenation.
Shirai *et al.* (2001)	cinnamaldehyde	Pt/SiO_2	2-propanol cyclohexane ethanol methanol	Higher rates were observed in short chain alcohols, following methanol > ethanol > 2-propanol > cyclohexane. Selectivity towards unsaturated alcohols decreased with increasing hydrogen pressure, but increased with higher initial cinnamaldehyde concentration (in ethanol). Higher concentrations of reactant were believed to affect its geometry of adsorption.

Table 6.1. (Continued)

Takagi *et al*. (1999)	benzoic acid benzyl alcohol phenol toluene	Pt/Al_2O_3 Ru/Al_2O_3	1-propanol 1,4-dioxane 2-propanol acetic acid acetone benzene butyric acid diethyl ether dimethyl sulfoxide methanol ethanol formic acid hexane heptane lauric acid N,N-dimethyl formamide N-methyl-2-pyrrolidone tetrahydrofuran	A relation between solvent polarity (permittivity) and reaction rate was established. Competitive adsorption between substrate and solvent, as well as deactivation of the catalyst by solvents that contain sulphur or nitrogen was also shown to be key affecting hydrogenation rates.
Trasarti *et al*. (2014)	acetophenone	Co/SiO_2 Cu/SiO_2 Ni/SiO_2	2-propanol benzene cyclohexane toluene	Selectivity towards 1-phenylethanol followed Cu > Co > Ni. 2-propanol contributed *via* C=O activation with polarisation. Toluene and benzene effectively blocked the surface active sites, due to strong solvent adsorption. Solvent effects also depended on the type of metal used.
Von Arx *et al*. (1999)	ketoisophorone	Pd/Al_2O_3 Pt/Al_2O_3	acetic acid hexane methanol tetrahydrofuran	Pd favoured C=C reduction as compared to Pt. Higher solvent polarity increased reaction rates in Pd.
Wan *et al*. (2014)	2-butanone 2-pentanone phenol	Ru/C	γ-butyrolactone acetonitrile cyclohexane ethanol methanol *n*-butanol *n*-heptane *n*-propanol tetrahydrofuran water	2-butanone hydrogenation rates were high in polar protic solvents, while they decreased dramatically for non-polar and polar aprotic solvents. Solvent-substrate and solvent-catalyst interactions were weak, allowing for certain hydrogenation rates. Additionally, solvent-reactant interactions were observed for polar protic solvents by means of FTIR.

Table 6.2. Main factors affecting selectivity during the hydrogenation of α,β-unsaturated aldehydes.

effect	reactant	references
solvent polarity	acetophenone cinnamaldehyde	Bertero *et al.* (2011) Hájek *et al.* (2004)
solvent-catalyst interaction	acetophenone crotonaldehyde	Bertero *et al.* (2011) Englisch *et al.* (1997) Mäki-Arvela *et al.* (2006)
solvent-reactant interaction	acetophenone citral citronellal	Bertero *et al.* (2011) Fuentes *et al.* (1989) Mäki-Arvela *et al.* (2002)
temperature	citral cinnamaldehyde crotonaldehyde cyclohexenone	Breen *et al.* (2004) Englisch *et al.* (1997) Mäki-Arvela *et al.* (2006) Ronzón and del Ángel (1999) Singh and Vannice (2000a)
pressure	acetophenone cinnamaldehyde crotonaldehyde furfural	Bergault *et al.* (1998) Englisch *et al.* (1997) Mäki-Arvela *et al.* (2005) Shirai *et al.* (2001) Vaidya and Mahajani (2003)
metal	citral crotonaldehyde methyl vinyl ketone oxopromegestone	Ide *et al.* (2012) Ryndin *et al.* (2000) Singh and Vannice (2001)
support/acidity	citral citronellal	Chuah *et al.* (2001) Ekou *et al.* (2012) Mäki-Arvela *et al.* (2005)
initial reactant concentration	2-cyclohexenone acetophenone cinnamaldehyde citralcyclohexenone furfural	Bergault *et al*. (1998) Breen *et al.* (2004) Geneste *et al.* (1980) Hájek *et al.* (2004) Reyes *et al.* (2003) Ronzón and del Ángel (1999) Shirai *et al.* (2001) Singh and Vannice (2000b) Vaidya and Mahajani (2003)
reactant steric effects	2-methylbenzaldehyde acetophenone benzaldehyde	Delbecq and Sautet (1995) Mäki-Arvela *et al.* (2005) Marinelli *et al.* (1995)

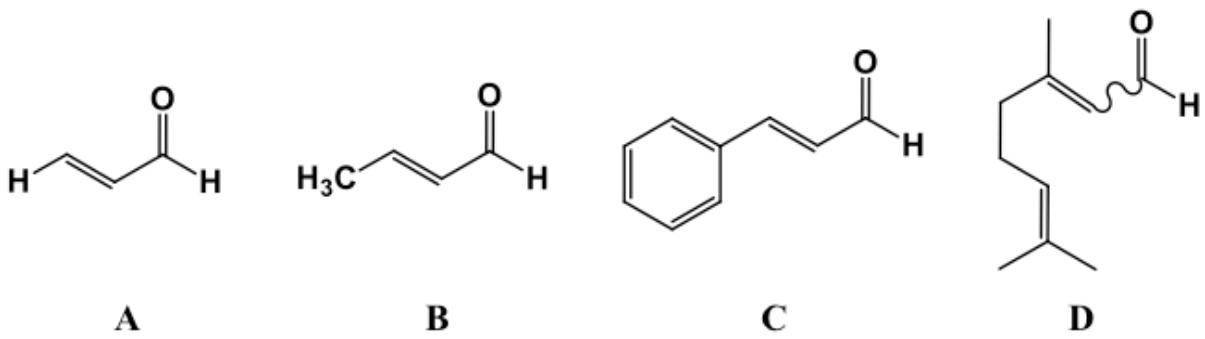

Figure 6.1. Structure of acrolein (A), crotonaldehyde (B), cinnamaldehyde (C) and citral (D).

6.2 Hydrogenation of citral: model system

In this work, the hydrogenation of citral (3,7-dimethyl-2,6-octadienal) has been chosen as a model molecule to understand the effect of solvent in the selectivity of competitive reaction pathways. This serves as a model molecule for selective hydrogenation on a multifunctional species. Implications on biomass transformations and fine chemical processes can then be extrapolated.

Hydrogenation of citral has been extensively studied over different metal supported catalysts under a variety of reaction conditions (Ĉervený and Růžička, 1988; Stolle *et al.*, 2013). **Scheme 6.1** shows the reaction network of the hydrogenation of citral. The two isomers of citral can undergo hydrogenation of the conjugated C=O functionality to yield the unsaturated alcohol *cis* and *trans* isomers nerol and geraniol (UALC), respectively. Alternatively, the conjugated C=C bond of citral can react to yield citronellal (CAL); or the isolated C=C bond can react to yield the *cis* and *trans* isomers of 3,7-dimethyl-2-octenal (ENALS). Subsequent hydrogenation of primary products results in the formation of citronellol (COL), dihydrocitronellal (DHCAL), 3,7-dimethyl-2-octen-1-ol isomers (ENOLS) and the final hydrogenated product 3,7-dimethyl-2-octanol (37OH). Formation of isopulegols (IP), menthols (IPH) and acetals can also occur in this system. Recent efforts have explored a selective enhancement in the hydrogenation of citral towards unsaturated alcohols geraniol, nerol and citronellol by means of newly design catalysts. The use of a wide range of metals such as Pt or Pd (Singh and Vannice, 2001), but also Ru (Álvarez-Rodríguez *et al.*, 2012), Au (Milone *et al.*, 2002) or Ir (Bernas *et al.*, 2012), has been investigated. Bimetallics of Pt and Pd (Bertero *et al.*, 2009; Reyes and Rojas, 2006; Stassi *et al.*, 2013; Vicente *et al.*, 2011; Yang *et al.*, 2014) have also been researched. In addition, the use of different supports (Milone *et al.*, 1999; Santiago-Pedro *et al.*, 2013) such as silica (Mäki-Arvela *et al.*, 2004),

zirconia (Chuah *et al.*, 2001), but also zeolites (Álvarez-Rodríguez *et al.*, 2011; Concepción *et al.*, 2013) or carbon nanotubes (CNTs) (Stassi *et al.*, 2013; Zgolicz *et al*., 2012) was also studied. Temperature (Mäki-Arvela *et al.*, 2006; Singh and Vannice, 2000a, 2000b), metal particle size (Teddy *et al.*, 2011; Zgolicz *et al.*, 2012), or initial citral concentration (Mukherjee and Vannice, 2006; Reyes *et al.*, 2003; Singh and Vannice, 2000a, 2000b) are reported to modify selectivity. In most of these studies, either alkanes, such as hexane or cyclohexane, or alcohols, such as ethanol or 2-propanol were used as solvents. The selection of solvents was discussed in a reduced number of those studies, and the objective was solely focused on reducing the selectivity towards side reactions (Mäki-Arvela *et al.*, 2002; Stassi *et al.*, 2013). **Table 6.3** highlights important findings from the literature regarding solvent effects in the hydrogenation of citral and main reaction intermediates.

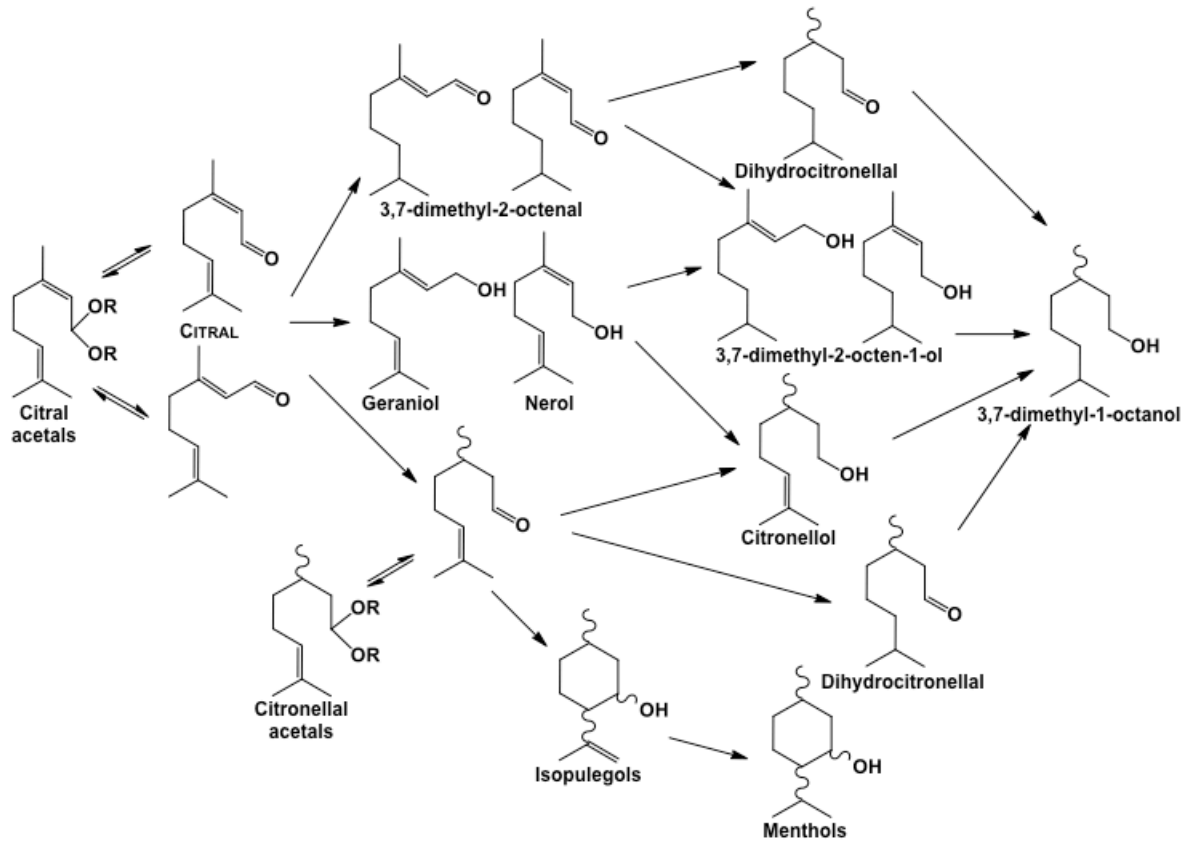

Scheme 6.1. Citral hydrogenation reaction network. Reaction species have been abbreviated in some instances following the acronym in brackets: nerol and geraniol (UALC), citronellal (CAL), 3,7-dimethyl-2-octenal isomers (ENALS), citronellol (COL), dihydrocitronellal (DHCAL), 3,7-dimethyl-2-octen-1-ol isomers (ENOLS), 3,7-dimethyl-2-octanol (37OH), isopulegols (IP), menthols (IPH).

Table 6.3. Summary of important findings in the selective hydrogenation of citral.

study	catalyst	solvent(s)	remarks
Aramendía *et al.* (1997)	$Pd/SiO_2/AlPO_4$	cyclohexane dioxane methanol tetrahydrofuran	Solvent was believed to impact the reduction of the catalyst. Alcohol solvents resulted in the formation of acetal, reducing hydrogenation rates. Faster rates were observed in non-polar solvents (cyclohexane and dioxane).
Bernas *et al.* (2012)	Ir/C	2-propanol	Hhydrogenation rate increased with increasing metal particle size (up to 6 nm). Etherification of products was observed.
Burgener *et al.* (2004)	Pd/Al_2O_3	hexane $scCO_2$	Catalyst deactivation and formation of hydrocarbons was observed *via* ATR measurements. Pd catalyst selectively hydrogenated C=C bond.
Chatterjee *et al.* (2004)	Pd/Al_2O_3 Pd-MCM-48 Pd/SiO_2	benzene hexane methanol $scCO_2$	Selectivity of the reaction was determined by adsorption geometry of the reactant, which was influenced by solvent polarity.
Depboylu *et al.* (2011)	Pt/SiO_2	2-pentanol ethanol	Product distribution and reaction rates were influenced by the length of the alcohol chain. A reduction in the formation of acetals was noted in 2-pentanol.
Hubaut (1992)	$CuCrO_x$	decalin	Hydrogen pressure was shown to affect the relative C=C *vs*. C=O hydrogenation. Isomerisation citronellal - geraniol/nerol was observed to occur on Cr sites.
Jiang *et al.* (2012)	Ru/AlO(OH)	2-propanol 1,4-dioxane ethanol *n*-hexane water	The addition of water was shown to enhance catalytic activity and selectivity. The formation of a hydrophilic adlayer was believed to contribute towards preferential C=O adsorption and limit C=C hydrogenation.
Mäki-Arvela *et al.* (2002)	Ni Ni/Al_2O_3 Ni/SiO_2 Rh/Al_2O_3 Ru/C	2-methyl-2-propanol 2-pentanol 2-propanol ethanol	Formation of acetals was reduced when using long chain alcohols. Formation of cyclic by-products increased with solvent hydrophobicity
Mäki-Arvela *et al.* (2004)[a]	Pt/H-MCM-41 Pt/H-Y Pt/SiO_2	2-pentanol	Formation of dehydroxylated products correlated with the concentration of Brønsted acid sites of the support
Mäki-Arvela *et al.* (2006)	Pt/Al_2O_3	2-pentanol cyclohexane	Decarbonylation was shown to cause deactivation. A maximum hydrogenation rate in 2-pentanol at 323 K was observed in the 298 K - 373 K temperature range.
Mukherjee and Vannice (2006)	Pt/SiO_2	cyclohexane cyclohexanol ethanol ethyl acetate *n*-amyl acetate *n*-hexane *p*-dioxane tetrahydrofuran	Comprehensive study: i) solvent did not influence product distribution at 30% conversion, ii) deactivation of about 1-2 order of magnitude was observed after 24 h of reaction, possibly caused by decarbonylation and CO adsorption, iii) variation in TOF did not correlate with solvent polarity (dielectric constant or dipole moment).

Table 6.3. (Continued)

Singh and Vannice (2000a,b)	Pt/SiO_2 Pt/TiO_2	hexane	Temperature affected reaction rates, showing a minimum value at 373 K. Decabonylation was believed to cause deactivation, as well as geraniol/nerol decomposition. Selectivity towards unsaturated alcohols increased with increasing reaction temperature (from 298 K to 423 K)
Singh and Vannice (2001)	$Me(VIII)/SiO_2$	hexane	A volcano plot dependence of the hydrogenation rate (in TOF) with %d-character of the metal was demonstrated. Ni, Pd, and Rh showed high citronellal and isopulegol selectivity, as opposed to Co, Os, and Ru. Selectivity was related with d-band width and stabilisation of two-electron *vs*. four-electron interactions
Singh *et at.* (2000)[a]	Pt/SiO_2	hexane	Competitive hydrogenation of citral with either geraniol or citronellal was observed. Activation of the C=O bond occurred at higher temperature (373 K)
Stassi et al. (2013)	PtFe/CNT PtSn/CNT	2-propanol	Addition of a second metal enhanced selectivity towards unsaturated alcohols, although particular optimal loadings depended on the different promotion mechanism. Pre-treatment of the support influenced metal particle size dispersion and the formation of the bimetallic phase.
Trasarti et al. (2007)	Al-MCM-41 CsHPA H-ZSM-5 H-BEA (Ir, Pt, Pd, Co, Ni, Cu)/SiO_2 SiO_2-Al_2O_3 ZnO_2/SiO_2 (combinations)	2-propanol toluene	Only Pd and Ni favoured C=C hydrogenation of citral. Formation of cyclic products was favoured on catalysts containing Lewis/Brønsted acid sites.

a These studies refer to the hydrogenation of main citral reaction intermediates

However, the use of a solvent to tailor the reactivity of the carbonyl bond in detriment of the double-bond conversion has not been exploited extensively. Some literature has been dedicated to understanding the role solvent might play in the hydrogenation of citral towards the production of unsaturated alcohols on Pt/Al_2O_3 (Mäki-Arvela *et al.*, 2006) as well as on Pt/SiO_2 (Mukherjee and Vannice, 2006; Singh and Vannice, 2000a, 2000b, 2001; Singh *et al.*, 2000). In the case of 5% Pt/Al_2O_3, Mäki-Arvella *et al.* (2006) have reported results for the hydrogenation of citral (0.1 M) at 373 K with two different solvents, cyclohexane and 2-pentanol showing similar hydrogenation rates, with higher selectivity towards geraniol and nerol in the case of 2-pentanol (31%) *vs.* cyclohexane (15%). The use of alcohols as solvents has been of particular interest. Increasing the length of the alcohol chain – from ethanol to

2-pentanol – showed a reduction in selectivity towards unsaturated alcohols during the hydrogenation of citral (Depboylu *et al.*, 2011). Similar results were observed in the series ethanol, 2-propanol, 2-methyl-2-propanol and 2-pentanol on Ni/Al_2O_3, Ru/C, Rh/Al_2O_3 and Ni/SiO_2 (Mäki-Arvela *et al.*, 2002). Mukherjee and Vannice (2006) reported reaction rates and selectivities on 3.15% Pt/SiO_2 with a range of solvents. Temperature had a big impact in selectivity. However, no solvent effect was observed with regards to selectivity. This result contrasts with similar α,β-unsaturated systems. For example, solvent effects are reported in the hydrogenation of crotonaldehyde at 298 K on Pt/SiO_2 (Englisch *et al.*, 1997). Chloroform and cyclohexane showed low conversions to unsaturated alcohol crotylalcohol, as compared to ethanol. Similarly, high selectivity towards unsaturated alcohols followed the trend: methanol > ethanol > 2-propanol > cyclohexane in the hydrogenation of cinnamaldehyde on 1% Pt/SiO_2 at 323 K (Shirai *et al.*, 2001).

In this context, a complete understanding of the effect of solvent on the observed reaction rates and selectivity trends remains unknown. It seems clear that the optimal solvent selection needs a more detailed knowledge on the relationship between the chemical nature of the solvents and the interactions taking place in the gas-liquid-solid catalytic systems (Bertero *et al.*, 2011): competitive adsorption between solvent and reactant (Takagi *et al.*, 1999), competitive adsorption between different reaction species, as well as interactions between solvent and reaction species need to be considered. Such work will be presented in the following chapters.

References

Abdul-Wahab, M.I., Jackson, S.D. (2013) Hydrogenation of 3-nitroacetophenone over rhodium/silica catalysts: effect of metal dispersion and catalyst support. *Appl. Catal. A-Gen.*, 462-463, 121 – 128.

Akpa, B.S., D'Agostino, D., Gladden, L.F., Hindle, K., Manyar, H., McGregor, J., Li, R., Neurock, M., Sinha, N., Stitt, E.H., Weber, D., Zeitler, J.A., Rooney, D.W. (2012) Solvent effects in the hydrogenation of 2-butanone. *J. Catal.*, 289, 30 – 41.

Álvarez-Rodríguez, J.; Rodríguez-Ramos, I.; Guerrero-Ruiz, A.; Arcoya, A. (2011) Selective hydrogenation of citral over Pt/KL type catalysts doped with Sr, La, Nd and Sm. *Appl. Catal. A-Chem.*, 401, 56 – 64.

Álvarez-Rodríguez, J.; Rodríguez-Ramos, I.; Guerrero-Ruiz, A.; Gallegos-Suárez, E.; Arcoya, A. (2012) Influence of the nature of support on Ru-supported catalysts for selective hydrogenation of citral. *Chem. Eng. J.*, 204 – 206, 169 – 178.

Aramendía, M.A., Borau, V., Jiménez, C., Marinas, J.M., Porras, A., Urbano, F.J. (1997) Selective liquid-phase hydrogenation of citral over supported palladium. *J. Catal.*, 172, 46 – 54.

Ashworth, I.W., Nelson, D.J., Percy, J.M. (2013) Solvent effects on Grubbs pre-catalyst initiation rates. *Dalton Trans.*, 42, 4110 – 4113.

Augustine, R.L., Techasauvapak, P. (1994) Heterogeneous catalysis in organic synthesis. Part 9. Speific site solvent effects in catalytic hydrogenations. *J. Mol. Catal.*, 87, 95 – 105.

Bailie, J.E., Rochester, C.H., Hutchings, G.J. (1997) IR study of acrolein hydrogenation over Co/SiO_2 catalysts. *J. Chem. Soc., Faraday Trans.*, 93, 4389 – 4394.

Bergault, I., Fouilloux, P., Joly-Vuillemin, C., Delmas, H. (1998) Kinetics and intraparticle diffusion modelling of a complex multistep reaction: hydrogenation of acetophenone over a rhodium catalyst. *J. Catal.*, 175, 328 – 337.

Bernas, H.; Simakova, I.; Prosvirin, I.P.; Mäki-Arvela, P.; Leino, R.; Murzin, D.Y. (2012) Hydrogenation of citral over carbon supported iridium catalysts. *Catal. Lett.*, 142, 690 – 697.

Bertero, N.M.; Trasarti, A.F.; Moraweck, B.; Borgna, A.; Marchi, A.J. (2009) Selective liquid-phase hydrogenation of citral over supported bimetallic Pt-Co catalysts. *Appl. Catal. A-Gen.*, 358, 32 – 41.

Bertero, N.M., Trasarti, A.F., Apesteguía, C.R. and Marchi, A.J. (2011) Solvent effect in the liquid-phase hydrogenation of acetophenone over Ni/SiO_2: a comprehensive study of the phenomenon. *Appl. Catal. A-Gen.*, 394, 228 – 238.

Blaser, H-S., Malan, C., Pugin, B., Spindler, F., Steiner, H., Studer, M. (2003) Selective hydrogenation for fine chemicals: recent trends and new developments. *Adv. Synth. Catal.*, 345, 103 -151.

Breen, J.P., Burch, R., Gómez-López, J., Griffin, K., Hayes, M. (2004) Steric effects in the selective hydrogenation of cinnamaldehyde to cinnamyl alcohol isung an Ir/C catalyst. *Appl. Catal. A-Gen.*, 268, 267 – 274.

Burgener, M., Wirz, R., Mallat, T., Baiker, A. (2004b) Nature of catalyst deactivation during citral hydrogenation: a catalytic and ATR-IR study. *J. Catal.*, 228, 152 – 161.

Caga, I.T., Shutt, E., Winterbottom, J.M. (1976) The composition of reduced palladium oxide and its behaviour as a catalyst for liquid phase hydrogenation. *J. Catal.*, 44, 271 – 280.

Ĉervený, L., Růžička, V. (1988) Catalytic hydrogenation of dehydrolinalool and citral. *SÖFW*, 114, 605 – 609.

Chatterjee, M., Chatterjee, A., Ikushima, Y. (2004) Pd-catalyzed completely selective hydrogenation of conjugated and isolated C=C of citral (3,7-dimethyl-2,6-octadienal) in supercritical carbon dioxide. *Green Chem.*, 6, 114 – 118.

Chuah, G.K., Liu, S.H., Jaenicke, S., Harrison, L.J. (2001) Cyclisation of citronellal to isopulegol catalysed by hydrous zirconia and other solid acids. *J. Catal.*, 200, 352 – 359.

Concepción, P.; Pérez, Y.; Hernández-Garrido, J.C.; Fajardo, M.; Calvino, J.J.; Corma, A. (2013) The promotional effect of Sn-beta zeolites on platinum for the selective hydrogenation of α,β-unsaturated aldehydes. *Phys. Chem. Chem. Phys.*, 15, 12048 – 12055.

Consonni, M., Touroude., R., Murzin, D.Y. (1998) Deactivation and selectivity pattern in crotonaldehyde hydrogenation. *Chem. Eng. Technol.*, 21, 605 – 609.

D'Agostino, C., Brett, G.L., Miedziak, P.J., Knights, D.W., Hutchings, G.J., Gladden, L.F., Mantle, M.D. (2012) Understanding the solvent effect on the catalytic oxidation of 1,4-butanediol in methanol over Au/TiO_2 catalyst: NMR diffusion and relaxation studies. *Chem. Eur. J.*, 18, 14426 – 14433.

Delhomme, C., Schaper, L-A., Zhang-Preβe, M., Raudaschl-Sieber, G., Weuster-Botz, D., Kühn, F.E. (2013) Catalytic hydrogenation of levulinic acid in aqueous phase. *J. Organomet. Chem.*, 724, 297 – 299.

Depboylu, C.O.; Yilmaz, S.; Akkurt, S. (2011) Effects of catalyst precursor type and preparation conditions, and solvent type on activity and selectivity of Pt/SiO_2 catalyst in citral hydrogenation. *Int. J. Chem. React. Eng.*, 9, 15.

Englisch, M., Ranade, V.S., Lercher, J.A. (1997) Liquid phase hydrogenation of crotonaldehyde over Pt/SiO_2 catalysts. *Appl. Catal. A-Gen.*, 163, 111 – 122.

Farrauto, R.J., Bartholomew, C.H. (2011) *Fundamentals of industrial catalytic processes*, Wiley, pp. 650 – 700.

Fuentes, M., Magraner, J., de las Pozas, C., Roque-Malherbe, R., Pérez Pariente, J., Corma, A. (1989) Cyclization of citronellal to isopulegol by zeolite catálisis. *Appl. Catal.*, 47, 367 – 374.Gallezot, P. (2007) Catalytic routes from renewables to fine chemicals. *Catal. Today*, 121, 76 – 91.

Gallezot, P., Richard, D. (1998) Selective hydrogenation of α,β-unsaturated aldehydes. *Catal. Rev.-Sci. Eng.*, 40, 81 – 126.

Geneste, P., Bonnet, M., Frouin, C. (1980) Influence of a second reducible function on the mechanism of the hydrogenation of an ethylenic double bond. *J. Catal.*, 64, 371 – 380.

Gómez, S., Peters, J.A., Maschmeyer, T. (2002) The reductive amination of aldehydes and ketones and the hydrogenation of nitriles: mechanistic aspects and selectivity control. *Adv. Synth. Catal.*, 344, 1037 – 1057.

Hájek, J., Kumar, N., Mäki-Arvela, P., Salmi, T. and Murzin, D.Y. (2004) Selective hydrogenation of cinnamaldehyde over Ru/Y zeolite. *J. Mol. Catal. A-Chem.*, 217, 145 – 154.

Hronec, M., Fulajtarová, K., Liptaj, T. (2012) Effect of catalyst and solvent on the furan ring rearrangement to cyclopentanone. *Appl. Catal. Gen-A*, 437 – 438, 104 – 111.

Hubaut, R. (1992) Study of the competitive reactions between an α,β-unsaturated aldehyde and allylic alcohol on a copper chromite catalyst. *React. Kinet. Catal. Lett.*, 46, 25 – 32.

Jackson, S.D., Monaghan, A. (2007) Hydrogenation of unsaturated hydrocarbons – 40 years on: hydrogenation of 1,3-pentadiene over Pd/alumina. *Catal. Today*, 128, 47 – 51.

Jiang, H-J., Jian, H-B., Zhu, D-M., Zheng, X-L., Fu, H-Y., Chen, H., Li, R-X. (2012) Cooperation between the surface hydroxyl groups of the support and organic additives in the highly selective hydrogenation of citral. *Appl. Catal. A-Gen.*, 445 – 446, 351 – 358.

Kishida, S., Teranishi, S. (1968) Kinetics of liquid-phase hydrogenation of acetone of over Raney nickel catalyst. *J. Catal.*, 12, 90 – 96.

Koopman, P.G.J., Buurmans, H.M.A., Kieboom, A.P.G., van Bekkum, H. (1981) Solvent-reactant-support interactions in liquid phase hydrogenation. *Recl. Trav. Chim. Pays-Bas*, 100, 156 – 161.

Kukula, P., Koprivova, K. (2005) Structure-selectivity relationship in the chemoselective hydrogenation of unsaturated nitriles. *J. Catal.*, 234, 161 – 171.

Kukula, P., Gabova, V., Koprivova, K., Trtik, P. (2007) Selective hydrogenation of unsaturated nitriles to unsaturated amines over amorphous CoB and NiB alloys doped with chromium. *Catal. Today*, 121, 27 – 38.

Kunkes, E.L., Simonetti, D.A., West, R.M., Serrano-Ruiz, J.C., Gärtner, C.A., Dumesic, J.A. (2008) Catalytic conversion of biomass to monofunctional hydrocarbons and targeted liquid-fuel classes. *Science*, 332, 417 – 421.

Loffreda, D., Delbecq, F., Vigné, F., Sautet, P. (2006) Chemo-regioselectivity in heterogeneous catalysis: competitive routes for C=O and C=C hydrogenations from a theoretical approach. *J. Am. Chem. Soc.*, 128, 1316 – 1323.

Mäki-Arvela, P., Hájek, J., Salmi, T., Murzin, D.Y. (2005) Chemoselective hydrogenation of carbonyl compounds over heterogeneous catalysts. *Appl. Catal. A-Gen.*, 292, 1 -49.

Mäki-Arvela, P, Kumar, N., Eränen, K., Salmi, T., Murzin, D.Y. (2006) Inverse temperatura dependence due to catalyst deactivation in liquid-phase citral hydrogenation over Pt/Al_2O_3. *Chem. Eng. J.*, 122, 127 – 134

Mäki-Arvela, P., Kumar, N., Paseka, I., Salmi, T., Murzin, D.Y. (2004) Support effects in nerol hydrogenation over Pt/SiO_2, Pt/H-Y and Pt/H-MCM-41 catalysts. *Catal. Lett.*, 98, 173 - 179.

Mäki-Arvela, P., Tiainen, L-P., Neyestanaki, A.K., Sjöholm, R., Rantakyla, T-K., Laine, E., Salmi, T., Murzin, D.Y. (2002) Liquid phase hydrogenation of citral: suppression of side reactions. *Appl. Catal. A-Gen*., 237, 181 – 200.

McGregor, J., Canning, A.S., Mitchell, S., Jackson, S.D., Gladden, L.F. (2010) The influence of carbon laydown on selectivity in the hydrogenation of pentenenitriles over supported-nickel catalysts. *Appl. Catal. A-Gen.*, 384, 192 – 200.

McMillan, L., Lutecki, M., Wang, W., Arias-Vecino, P., McGregor, J., Al-Yassir, N., Al-Khattaf, S., Gladden, L.F. (2013) Toluene alkylation over Metal Organic Frameworks – An evaluation of the role of acidity for catalytic activity and coke deposition. *23rd NAM*, O-M-Fre-6.

Mercadante, L., Neri, G., Milone, C., Donato, A., Galvagno, S. (1996) Hydrogenation of α,β-unsaturated aldehydes over Ru/Al2O3 catalysts. *J. Mol. Catal. A-Chem*, 105, 93 – 101.

Milone, C.; Gangemi, C.; Ingoglia, R.; Neri, G.; Galvagno, S. (1999) Role of the support in the hydrogenation of citronellal on ruthenium catalysts. *Appl. Catal. A-Gen.*, 184, 89 – 94.

Milone, C.; Tropeano, M.L.; Gulino, G.; Neri, G.; Ingoglia, R.; Galvagno, S. (2002) Selective liquid phase hydrogenation of citral on Au/Fe_2O_3 catalysts. *Chem. Comm.*, 8, 868 – 869.

Mounzer, H.N., Wood, J., Stitt, E.H. (2010) Heterogeneous oxidation of 2-octanol on 5 wt%Pt-1 wt%Bi/Carbon catalyst. *Chem. Eng. Sci.*, 65, 179 – 185.

Mukherjee, S., Vannice, M.A. (2006) Solvent effects in liquid-phase reactions I. Activiy and selectivity during citral hydrogenation on Pt/SiO_2 and evaluation of mass transfer effects. *J. Catal.* 243, 108 – 130.

Nishimura, S. (2001) *Handbook of heterogeneous catalytic hydrogenation for organic synthesis*, Wiley, Chichester, pp. 10 – 80.

Pérez-Cadenas, A.F., Kapteijn, F., Zieverink, M.P., Moulijn, J.A. (2007) Selective hydrogenation of fatty acid methyl esters over palladium on carbon-based monoliths: structural control of activity and selectivity. *Catal. Today*, 128, 13 – 17.

Poltarzewski, Z., Galvagno, S., Pietropaolo, R., Staiti, P. (1986) Hydrogenation of α,β-unsaturated aldehydes over Pt-Sn/Nylon, *J. Catal.*, 102, 190 – 198.

Rajadhyaksha, R.A., Karwa, S.L. (1986) Solvent effects in catalytic hydrogenation. *Chem. Eng. Sci.*, 41, 1765 – 1770.

Reyes, P., Rojas, H., Fierro, J.L.G. (2003) Kinetic study of liquid-phase hydrogenation of citral over Ir/TiO_2 catalysts. *Appl. Catal. A-Gen.*, 248, 59 – 65.

Reyes, P.; Rojas, H. (2006) Hydrogenation of citral over Pt and $Pt-Fe/SiO_2$ catalysts. *React. Kinet. Catal. L.* 88, 363 – 369.

Rojas, H.; Díaz, G.; Martínez, J.J.; Castañeda, C.; Gómez-Cortés, A.; Arenas-Alatorre, J. (2012) Hydrogenation of α,β-unsaturated carbonyl compounds over Au and Ir supported on SiO_2. *J. Mol. Catal. A-Chem.*, 363 – 364, 122 – 128.

Ronzón, E., del Ángel, G. (1999) Effect of rhodium precursor and thermal treatment on the hydrogenation of 2-cyclohexenone on Rh/SiO_2 catalyst. *J. Mol. Catal. A-Gen.*, 148, 105 – 115.

Ross, J.R.H. (2012) *Heterogeneous catalysis: fundamentals and applications*, Elsevier, London, pp. 20 – 38.

Ryndin, Y.A., Santini, C.C., Prat, D., Basset, J.M. (2000) Chemo-, regio-, and diasteroselectivity hydrogenation of oxopromegestone into trimegestone over supported platinoids: effect of the transition metal, support nature, tin additives and modifiers. *J. Catal.*, 190, 364 – 373.

Santiago-Pedro, S.; Tamayo-Galván, V.; Viveros-García, T. (2013) Effect of the acid-base properties of the support on the performance on Pt catalysts in the partial hydrogenation of citral. *Catal. Today*, 213, 101 – 108.

Sedransk, K.L., McGregor, J., Mitchell, J., Moggridge, G. (2013) Towards tailored porous polymers using solvent effects in catalytic degradation. *Macromol. Mater. Eng.*, 298, 1344 – 1349.

Shirai, M., Tanaka, T., Arai, M. (2001) Selective hydrogenation of α,β-unsaturated aldehyde to unsaturated alcohol with supported platinum catalysts at high pressures of hydrogen. *J. Mol. Catal. A-Chem.*, 168, 99 – 103.

Singh, U.K., Vannice, M.A. (2000a) Liquid-phase hydrogenation of citral over Pt/SiO_2 catalysts. I. Temperature effects on activity and selectivity. *J. Catal.*, 191, 165 – 180.

Singh, U.K., Vannice, M.A. (2000b) Influence of metal-support interactions on the kinetics of liquid-phase citral hydrogenation. *J. Mol. Catal. A-Gen.*, 163, 233 – 250.

Singh, U.K., Sysak, M.N., Vannice, M.A. (2000) Liquid-phase hydrogenation of citral over Pt/SiO_2 catalysts. II. Hydrogenation of reaction intermediate compounds. *J. Catal.*, 191, 181 – 191.

Singh, U.K., Vannice, M.A. (2001) Kinetics of liquid-phase hydrogenation reactions over supported metal catalysts – a review. *Appl. Catal. A-Gen.*, 213, 1 – 24.

Somorjai, G.A., Kliewer, J. (2009) Reaction selectivity in heterogeneous catalysis. *React. Kinet. Catal. Lett.*, 96, 191 – 208.

Stassi, J.P.; Zgolicz, P.D.; de Miguel, S.R.; Scelza, O.A. (2013) Formation of different promoted metallic phases in PtFe and PtSn catalysts supported on carbonaceous materials used for selective hydrogenation. *J. Catal.*, 306, 11 – 29.

Stolle, A., Gallert, T., Schmöger, C., Ondruschka, B. (2013) Hydrogenation of citral: a wide-spread model reaction for selective reduction of α,β-unsaturated aldehydes. *RSC Advances*, 3, 2112 – 2153.

Swift, K.A.D. (2004) Catalytic transformations of the major terpene feedstocks. *Top. Catal.*, 27, 143 – 155.

Takagi, H., Isoda, T., Kusakabe, K., Morooka, S. (1999) Effects of solvents on the hydrogenation of mono-aromatic compounds using noble-metal catalysts. *Energ. Fuel.*, 13, 1191 – 1196.

Teddy, J., Falqui, A., Corrias, A., Carta, D., Lecante, P., Gerber, I. (2011) Influence of particles alloying on the performances of Pt-Ru/CNT catalysts for selective hydrogenation. *J. Catal.*, 278, 59 – 70.

Trasarti, A.F., Bertero, N.M., Apesteguía, C.R., Marchi, A.J. (2014) Liquid-phase hydrogenation of acetophenone over silica-supported Ni, Co and Cu catalysts: influence of metal and solvent. *Appl. Catal. A-Chem.*, 474, 282 – 291.

Trasarti, A.F., Marchi, A.J., Apesteguía, C.R. (2007) Design of catalyst systems for the one-pot synthesis of menthols from citral. *J. Catal.*, 247, 155 – 165.

Trasarti, A.F., Segobia, D.J., Apesteguía, C.R., Santoro, F., Zaccheria, F., Ravasio, N. (2012) Selective hydrogenation of soybean oil on copper catalysts as a tool towards improved bioproducts. *J. Am. Oil. Chem. Soc.*, 89, 2245 – 2252.

Vaidya, P.D., Mahajani, V.V. (2003) Kinetics of liquid-phase hydrogenation of furfuraldehylde to furfuryl alcohol over a Pt/C catalyst. *Ind. Eng. Chem. Res.*, 42, 3881 – 3885.

Vicente, A.; Lafaye, W.; Especel, C.; Marécot, P.; Williams, C.T. (2011) The relationship between the structural properties of bimetallic Pd-Sn/SiO2 catalysts and their performance for selective citral hydrogenation. *J. Catal.*, 283, 133 – 142.

Von Arx, M.V., Mallat, T., Baiker, A. (1999) Unprecedent selectivity behaviour in the hydrogenation of an α,β-unsaturated ketone: hydrogenation of ketoisophorone over alumina-supported Pt and Pd. *J. Mol. Catal. A-Chem.*, 148, 275 – 283.

Wan, H., Vitter, A., Chaudhari, B.V., Subramaniam, B. (2014) Kinetic investigations of unusual solvent effects during Ru/C catalyzed hydrogenation of model oxygenates. *J. Catal.*, 309, 174 – 184.

Wei, H., Gómez, C., Liu, J., Guo, N., Wu., T., Lobo-Lapidus, R., Marshall, C.L., Miller, J.T., Meyer, R.J. (2013) Selective hydrogenation of acrolein on supported silver catalysts: a kinetics study of particle size effects. *J. Catal.*, 298, 18 – 26.

Williams, C. (2013) Exploiting solvent effects in drug design and optimization. *Abstracts of papers of the American Chemical Society*. 246, 246-COM.

Yang, L., Jiang, Z., Fan, G., Li, F. (2014) The promotional effect of ZnO addition to supported Ni nanocatalysts from layered double hydroxide precursors on selective hydrogenation of citral. *Catal. Sci. Technol.*, 4, 1123 – 1131.

Zhang, L., Fang, D.C. (2013) Catalytic C-H activation/C-C coupling reaction: DFT studies on the mechanism, solvent effect and role of additive. *J. Org. Chem.*, 78, 2405 – 2412.

Zgolicz, P.D.; Stassi, J.P.; Yañez, M.J.; Scelza, O.A., de Miguel, S.R. (2012) Influence of the support and the preparation methods on the performance in citral hydrogenation of Pt-based catalysts supported on carbon nanotubes. *J. Catal.*, 290, 37 – 54.

Chapter 7:

Solvent effects in the selective hydrogenation of citral over 5% Pt/SiO_2

7 Solvent effects in the selective hydrogenation of citral over 5% Pt/SiO_2

Following the summary of literature in chapter 6, a more detailed knowledge on the relationship between the chemical nature of the solvents and the interactions taking place in the gas-liquid-solid catalytic systems need to be considered. In this chapter, a detailed study on the liquid-phase hydrogenation of citral has been performed using a range of solvents on 5% Pt/SiO_2 at two temperatures, 298 and 373 K, under the same reaction conditions. A series of non-polar, polar aprotic and polar protic solvents with different molecular structure were used. General trends with regards to activity, selectivity and deactivation were established as a function of type of solvent used. Those results were compared with literature trends. The findings obtained here will be used in chapters 8 and 9 to gain better information on the nature of solvent effects.

7.1 Experimental materials and methods

In this section, in addition to the materials (section 7.1.1) used during the hydrogenation of citral, a detailed description of the reactor setup and analytical methods is also presented (section 7.1.2).

7.1.1 Materials

The catalyst, 5 wt% Pt/SiO_2 (metal surface area 7.0 $m^2\ g^{-1}$, BET surface area 239 $m^2\ g^{-1}$, BJH pore volume 1.0 $cm^3\ g^{-1}$ and 16 nm pore diameter) was provided by Johnson Matthey and used as received. Assuming the spherical shape approximation of Spenadel and Boudart (1960), a 10% Pt metal dispersion was determined *via* CO chemisorption, giving an average particle size of 18 nm. Reaction rate values, expressed in terms of turnover frequency (TOF), were calculated considering 10% Pt dispersion. Elemental analysis of the SiO_2 support used for the preparation of the catalyst was also conducted. Inductively coupled plasma (ICP) analysis performed at Johnson Matthey revealed the presence of 90 ppm Fe (< 0.01 wt.%). Iron impurities have been shown to increase C=O hydrogenation in the hydrogenation of citral (Houzvicka *et al.*, 1995; Nonneman *et al.*, 1990). < 0.06 wt.% Fe content on 1% Pt/SiO_2 (Siani *et al.*, 2009) showed an increase in C=O selectivity from 5% to 25%, while < 0.35 wt.% Fe in 5%Pt/CNTs also showed a promoting effect in C=O selectivity (Stassi *et al.*, 2013). The Fe content in the catalyst was lower compared to previous studies. Any contribution towards C=O selectivity was assumed to be minimal and irrespective of solvent.

Citral (63%:34% E/Z mixture, 95%), 3,7-dimethyl-1-octanol (> 98%), citral diethyl acetal (> 93%), decalin (mixture of cis and trans, 98%) and 2-pentanol (98%) were obtained from Sigma-Aldrich, while geraniol (97%,), nerol (97%), citronellal (+/-, 96%), citronellol (95%), and isopulegol (mixture of isomers, 97%) were obtained from Alfa Aesar. They were used as received for catalytic reactions and calibration standards for gas chromatography. 2-propanol (99.5 %), acetone (99%), cyclohexane (98%), dichloromethane (DCM, 99%), diethyl ether (99%), ethanol (99%) and hexane (≈ 95%) were purchased from Fisher Scientific. H_2 (99.993%), N_2 (99.998%) and O_2 (99.5%), all from Air Liquide, were used without further purification. A wide range of acyclic and cyclic solvents of different molecular weights was chosen for this study. They were grouped according to their polarity (Hájek *et al.*, 2004): hexane, cyclohexane and decalin as apolar molecules; acetone, dichloromethane (DCM) and diethyl ether as polar aprotic solvents; and ethanol, 2-propanol and 2-pentanol as polar protic species. This also allowed a range of functional groups to be studied: primary and secondary alcohols, ethers or halogenates were considered. This selection permitted varied catalyst-solvent-reactant interactions to be present.

7.1.2 Reaction studies

7.1.2.1 Reactor setup

Figure 7.1 shows a schematic representation of the reactor setup used during citral hydrogenation experiments. A 300 ml pressurised reactor (Parr Instrument Co.) equipped with a gas entrainment impeller and baffles was employed. The instrument was equipped with a pressure gauge (Edwards) and a temperature controller to follow reaction conditions and control the reaction temperature. Reactant was injected into the reactor with a syringe (10in, Sigma-Aldrich) through a septum in order to prevent air from entering the vessel after catalyst pre-treatment. Solvent was added *via* a syringe pump (LC 5000, Isco). H_2 and N_2 lines contained a non-return valve (Swagelok) for adequate reactor containment. Samples were withdrawn after passing a 15 μm filter, ensuring no catalyst left the reactor. The outlet line was back-flushed to ensure fresh samples were withdrawn each time, based on a similar setup from Singh and Vannice (1999).

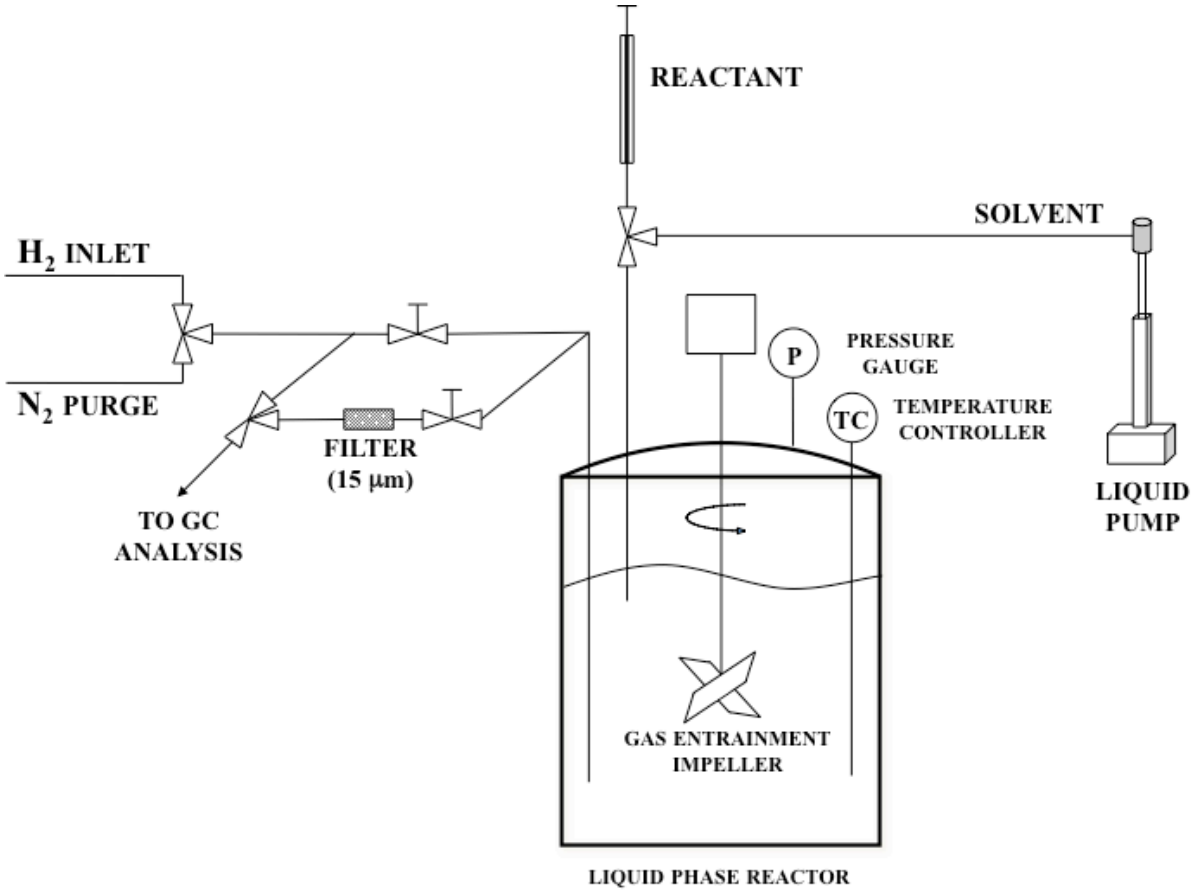

Figure 7.1. Schematic representation of the liquid-phase reactor setup used during citral hydrogenation experiments.

7.1.2.2 Gas chromatography (GC) analysis

Gas chromatography (GC) is employed to separate and analyse the species formed during the hydrogenation reaction, after vapourisation at the inlet. All GC data have been acquired employing the same set up, including column and detector. A DB-1 column (dimethylpolysiloxane, 60 m x 250 μm x 0.5 μm, J&W) was used in constant pressure mode with a split ratio 50:1. Injector temperature was set to 523 K and detector was at 623 K. The method used involved a constant temperature of 413 K for 18.5 min, an initial ramp rate of 20 K min^{-1} to 503 K and a final ramp rate of 30 K min^{-1} to 593 K, held for 6 min. The interaction of molecules with the stationary dimethylpolysiloxane phase affects the amount of time the compounds take to pass through the column. This, along with the variations in the oven temperature, determines when molecules reach the detector, and their presence, recorded. A flame ionisation detector (FID) has been used, which is sensitive to organic compounds but is not capable of detecting materials such as water or dissolved hydrogen. An

FID detector operates in the following way. At the outlet from the chromatography column the vapour under analysis is mixed with hydrogen and air, and is burned in a flame. This results in the production of conducting ions and electrons. A potential is applied at the burner tip, while a collector electrode is located above the flame. The current resulting from the burning of organic materials can then be measured, giving a measure of the quantity of material leaving the column as a function of time. Different molecules are then distinguished by their retention times. Response factors for main products were obtained *via* calibration with a set of prepared solutions of individual species by serial dilutions. The amount of solvent on each injection was used as internal standard for each reaction. **Figure 7.2** shows a typical example of a chromatogram from a citral hydrogenation reaction in hexane.

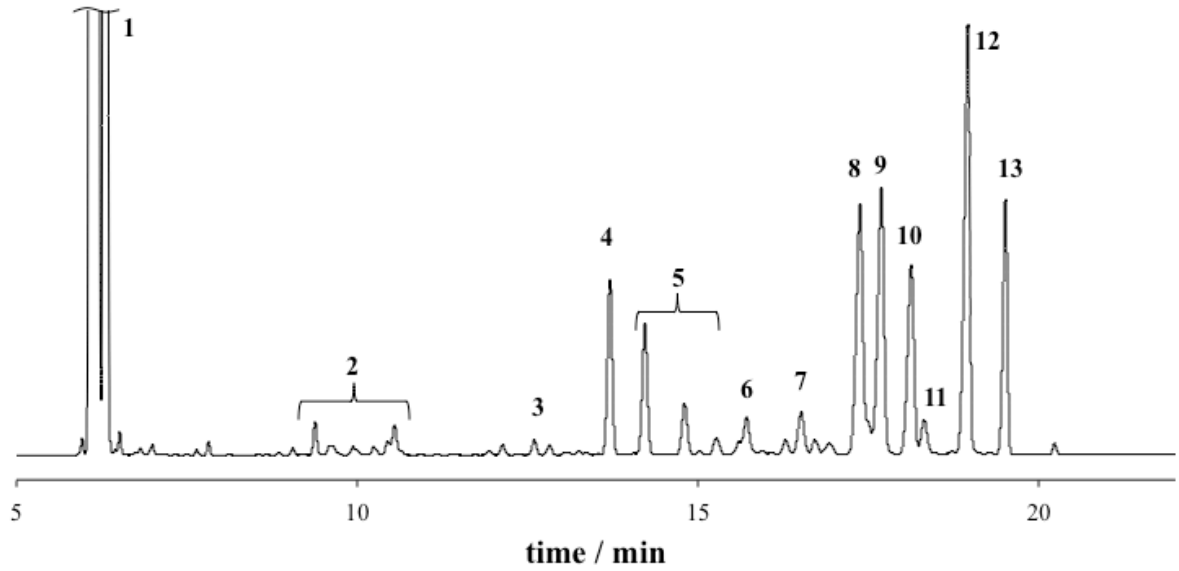

Figure 7.2. Chromatogram showing the product distribution of citral hydrogenation (c_0 = 0.13 M) on 5% Pt/SiO_2 in hexane at 373 K at 1680 min of reaction. Species shown include (1) hexane, (2) fragments, (3) dihydrocitronellal, (4) citronellal, (5) isopulegol isomers, (6) 3,7-dimethyl-1-octanol, (7) 3,7-dimethyl-2-octen-1-ol (ENOL), (8) citronellol, (9) nerol, (10) citral Z, (11) 3,7-dimethyl-2-octenal (ENAL), (12) geraniol, (13) citral E. *Note not all species are shown: citral acetals and citral dimer appeared at longer retention times (> 25 min), only in certain alcohol solvents.

7.1.2.3 Hydrogenation of citral

Hydrogenation of citral was performed in a 300 ml pressurised reactor (section 7.1.2.1) at a stirring rate of 700 rpm. 300 mg of 5% Pt/SiO_2 catalyst were used. Pre-treatment of the catalyst was carried out *in situ* at 423 K for 1 h under flowing H_2. The reactor was then cooled down to room temperature and purged with N_2. 0.02 mol of citral and 150 ml of

solvent (c_0 = 0.13 M) were added. The reactor was then heated to the reaction temperature. Reaction was started with addition of H_2 at reaction conditions. A small subset of reactions was performed with a higher concentration, c_0 = 0.33 M, maintaining the same reactant to catalyst ratio. Two temperatures were studied: 298 K and 373 K at a total pressure of 10 bar(g). Conversion was determined from the decay in the liquid reactant concentration.

Samples (0.5 ml) from the reactor were collected at defined time intervals and analysis of the reaction products was carried out with the GC described above. Analysis of unknown products was identified *via* GC-MS (QP2010 SE, Shimadzu). Mass balances during the reaction were 95% ± 5%. Reaction data are presented in the following way: calculation of reaction rates did not consider the formation of citral acetals, so as to provide information solely based on hydrogenation. However, selectivity data considered the formation of such by-products, so as to determine the extent of acetalysation depending on the solvent used. In addition, the formation of C_9 and C_{10} decarbonylated/hydrodeoxygenated products has been grouped in "fragments", considering the response factor of these species equivalent to that of *n*-octane. Product selectivity was calculated as follows for all species *i*, including acetals:

$$S_i = \frac{concentration\ of\ i}{\sum_{\text{Products}} concentration\ of\ i}. \qquad (7.1)$$

7.2 Results

Hydrogenation rates and selectivities were studied for a range of solvents for the hydrogenation of citral on 5% Pt/SiO_2. The impact of solvent on rate (section 7.2.1), selectivity (section 7.2.2), and deactivation (section 7.2.3) is shown.

7.2.1 Reaction rates

Figure 7.3 shows the initial reaction rates expressed in TOF for the hydrogenation of citral on each solvent at both 298 and 373 K. As can be seen, hydrogenation of citral at 298 K occurred faster in non-polar solvents, particularly hexane, with a value of 0.023 s^{-1}. In contrast, hydrogenation occurred more slowly in polar protic solvents, *e.g.*, ethanol, with a rate of 0.0015 s^{-1}. The only exception in the series was cyclohexane, with a hydrogenation rate of 0.0047 s^{-1}, similar to 2-propanol. A marked trend was seen per solvent group. Non-polar solvents exhibited higher hydrogenation rates in the order hexane > decalin > cyclohexane. Rates in polar protic solvents followed 2-pentanol > 2-propanol > ethanol.

Acetone presented a rate between 2-pentanol and decalin. Thus, reaction within the same solvent group occurred faster as polarity decreased. No reaction was observed when diethyl ether and DCM were used as solvents. Reaction rates at 373 K increased with a decrease in polarity within the same solvent type. Thus, reaction with hexane was 0.012 s^{-1} *vs.* a rate of 0.0012 s^{-1} in the case of ethanol. The TOF value in hexane was very similar to 0.0148 s^{-1}, reported by Singh *et al.* (2000) at the same conditions. Initial reaction rates at 373 K increased in the following order per solvent group: ethanol < 2-propanol < 2-pentanol (polar protic solvents); acetone < diethyl ether < DCM (polar aprotic series); decalin < cyclohexane < hexane (non-polar solvents). As can be seen, reaction rates followed a trend with polarity within solvent type at both reaction temperatures.

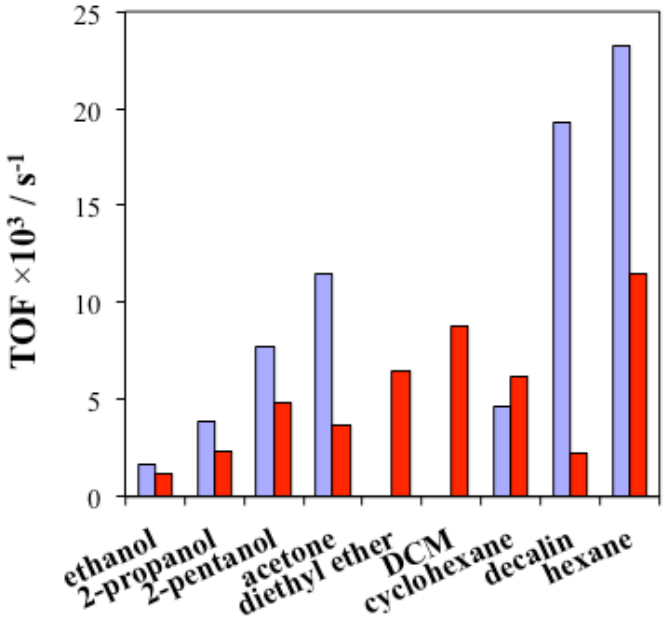

Figure 7.3. Initial reaction rate, in TOF, for the hydrogenation of citral at 298 K (blue) and 373 K (red) with different solvents on 5 % Pt/SiO_2. Reaction conditions: 0.3 g 5% Pt/SiO_2, 150 cm^3 solvent, 10 bar(g), c_0 = 0.13 M.

Considering the effect of temperature, a decrease on initial hydrogenation rates was observed at 373 K. For example, reaction with hexane at 373 K was about ½ of the reaction at 298 K. Only in ethanol rates remained similar at both temperatures, with a value of about 0.0012 s^{-1}. Important rate changes were also observed in non-polar solvents at 373 K, especially with decalin and cyclohexane, as compared with results at 298 K. Additionally, results in polar aprotic solvents showed a strong change with temperature, with reactions observed in DCM

and diethyl ether at 373 K. Overall, lower initial rates were observed when the reaction was performed at 373 K. Trends between reaction rates and polarity of solvent remained similar at both 298 K and 373 K within each solvent type. The particular behaviour of solvent as a function of polarity and temperature with rates will be discussed later in sections 7.3.1.

7.2.2 Selectivities

Tables 7.1 and **7.2**, and **Figure 7.4** show the product distribution as a function of solvents used at both 10% and 70% conversion. Both conjugated C=C and C=O bond hydrogenation were significant across solvents. Citronellal and geraniol/nerol were the major hydrogenation products formed at 298 K, accounting for 74% and 42% of the hydrogenated products formed in hexane at 10% and 70% conversion, respectively, or 67% and 73% of the hydrogenated products in 2-propanol at similar conversions, respectively. These results were in agreement with previous literature on citral hydrogenation at low temperatures (Rojas *et al.*, 2008; Singh and Vannice, 2000a, 2000b; Mercadante *et al.*, 1996; Galvagno *et al.*, 1993). The relative selectivity of citronellal relative to geraniol and nerol, as well as the formation of other products were also dependent on the solvent used. Higher selectivity towards citronellal was observed in apolar solvents and longer chain alcohols. In contrast, selectivity towards geraniol and nerol was higher in polar protic solvents. Cyclohexane and 2-pentanol represented the extreme scenarios on each solvent group. Acetone presented an intermediate behaviour between both solvent types, with significant conversion towards citronellal and geraniol and nerol. These selectivity trends remained similar at high conversion. Coupled with a decrease in reaction rates, a different selectivity was also observed at higher temperature. Selectivity to unsaturated alcohols, geraniol and nerol, was more favoured at 373 K, excluding DCM (see later in this section). This effect of temperature in the selectivity towards geraniol and nerol has been reported previously (Singh and Vannice, 2000a). Selectivity towards C=O hydrogenation increased significantly in non-polar solvents, while it remained similar in polar protic solvents. Conversely, selectivity towards citronellal decreased in non-polar solvents, although, hydrogenation of conjugated C=C was still more favoured in non-polar solvents, especially decalin, when compared with polar protic solvents such as 2-pentanol. In summary, higher selectivity towards C=O hydrogenation was observed in polar protic solvents, decreasing with increasing chain length, as compared to non-polar solvents.

Table 7.1. Initial reaction rates and product distribution at 10%, and rates after 24 h and product distribution at 70% conversion, respectively, during the hydrogenation of citral at 298 K. Reaction conditions: 0.3 g 5% Pt/SiO_2, 150 cm^3 solvent, 10 bar(g), c_0 = 0.13 M. For abbreviations of the reaction species, refer to **Scheme 6.1**.

Solvent	TOF[a] $\times 10^3$/ s^{-1}	CAL	nerol	geraniol	IP	COL	37OH	ENALS	ENOLS	DHCAL	citral acetal	prod acetal	fragm.	dimer
decalin	19.3	64	4.2	4.9	9.1	18	3.9	-	4.2	0.3	-	-	-	-
hexane	23.2	49	2.1	2.5	7.4	18	3.7	8.8	-	3.7	-	-	5.4	-
cyclohexane	4.7	25	13	13	26	9.7	4.3	-	2.6	5.9	-	-	1.7	-
acetone[b]	11.5	20	19	31	4.6	7.1	-	-	-	2.7	-	15	1.4	-
diethyl ether[c]	-	-	-	-	-	-	-	-	-	-	-	-	-	-
DCM[c]	-	-	-	-	-	-	-	-	-	-	-	-	-	-
2-pentanol	7.7	64	6.9	10.9	10.6	7.6	-	-	-	-	-	-	-	-
2-propanol	3.9	12	22	32	2.7	7.6	-	-	-	1.2	1.8	0.8	1.2	18.5
ethanol	1.6	4.0	14	22	5.2	0.8	0.7	0.8	-	1.0	13	4.2	0.7	34.3

Solvent	TOF[d] $\times 10^3$/ s^{-1}	CAL	nerol	geraniol	IP	IPH	COL	37OH	ENALS	ENOLS	DHCAL	fragm.	dimer	heavy
decalin[e]	0.01	-	-	-	-	-	-	-	-	-	-	-	-	-
hexane	0.50	37	2.7	2.1	1.9	-	17	15	10.2	0.5	11.1	2.2	-	-
cyclohexane[e]	-	-	-	-	-	-	-	-	-	-	-	-	-	-
acetone[e]	0.12	-	-	-	-	-	-	-	-	-	-	-	-	-
diethyl ether[c]	-	-	-	-	-	-	-	-	-	-	-	-	-	-
DCM[c]	-	-	-	-	-	-	-	-	-	-	-	-	-	-
2-pentanol	0.14	30	7.7	10	1.1	0.5	31	13	-	1.6	4.9	-	-	0.3
2-propanol	0.07	4.9	32	37	1.2	-	14	1.2	0.8	-	0.5	1.1	7.8	-
ethanol[e]	0.03	-	-	-	-	-	-	-	-	-	-	-	-	-

a: TOF values calculated for initial 60 min of reaction, product distribution at 10% conversion; b: ethers of geraniol and nerol are listed as product acetals; c: no reaction observed; d: TOF values calculated for 24 h of reaction, product distribution at 70% conversion; e: reaction did not proceed to 70% conversion.

Table 7.2. . Initial reaction rates and product distribution at 10%, and rates after 24 h and product distribution at 70% conversion, respectively, during the hydrogenation of citral at 373 K. Reaction conditions: 0.3 g 5% Pt/SiO_2, 150 cm^3 solvent, 10 bar(g), c_0 = 0.13 M. For abbreviations of the reaction species, refer to **Scheme 6.1**.

solvent	TOF[a] $\times 10^3$/ s^{-1}	CAL	nerol	geraniol	IP	IPH	COL	37OH	ENALS	ENOLS	DHCAL	citral acetal	prod acetal	fragm.	heavy
decalin	2.2	33	16	24	19	-	6.5	1.5	-	-	-	-	-	-	-
hexane	11.5	26	13	17	23	-	4.5	-	-	13	-	-	-	3.8	-
cyclohexane	6.2	8.8	31	36	14	1.1	1.8	1.8	-	1.0	2.8	-	-	1.2	-
acetone[b]	3.7	15	15	22	0	-	-	-	-	-	4.6	-	33	11	-
diethyl ether	6.4	28	24	31	9.0	-	6.5	-	-	-	0.8	-	-	-	-
DCM	8.7	9.5	14	14	17	7.1	3.7	5.9	-	2.6	3.6	-	-	23	-
2-pentanol	4.9	9.9	22	30	14	-	3.2	-	-	-	4.1	5.5	7.7	-	3.94
2-propanol	2.3	18	21	34	6.5	-	5.6	1.2	1.9	-	1.4	6.9	1.7	2.1	-
ethanol	1.2	1.7	11	22	-	-	-	-	-	-	0.6	49	14	0.8	-

solvent	TOF[c] $\times 10^3$/ s^{-1}	CAL	nerol	geraniol	IP	IPH	COL	37OH	ENALS	ENOLS	DHCAL	citral acetal	prod acetal	fragm.	heavy
decalin	0.33	8.7	30	40	1.7	0.9	12	5.2	-	-	-	-	-	1.0	-
hexane	1.42	8.5	22	27	9.9	2.0	18	2.8	1.1	4.5	0.7	-	-	3.5	-
cyclohexane	0.59	1.5	29	37	1.6	2.2	4.6	0.9	-	0.4	0.6	-	-	15	7.01
acetone	0.24	7.4	34	41	-	-	11	-	1.1	-	-	-	-	4.6	-
diethyl ether	0.53	6.1	38	42	0.5	-	13	0.9	-	-	-	-	-	0.2	-
DCM	1.06	1.4	2.4	6.6	5.0	0.4	1.9	1.4	-	1.3	0.3	-	-	75	4.44
2-pentanol	0.74	6.6	31	40	1.6	-	13	0.6	-	0.5	0.4	0.6	1.3	-	4.03
2-propanol	0.37	4.5	31	50	0.7	-	8.2	0.3	1.3	-	0.3	2.5	-	1.4	-
ethanol	0.66	0.6	29	52	-	-	2.0	-	-	-	0.4	10	2.8	2.5	-

a: TOF values calculated for initial 60 min of reaction, product distribution at 10% conversion; b: ethers of geraniol and nerol are listed as product acetals; c: TOF values calculated for 24 h of reaction, product distribution at 70% conversion.

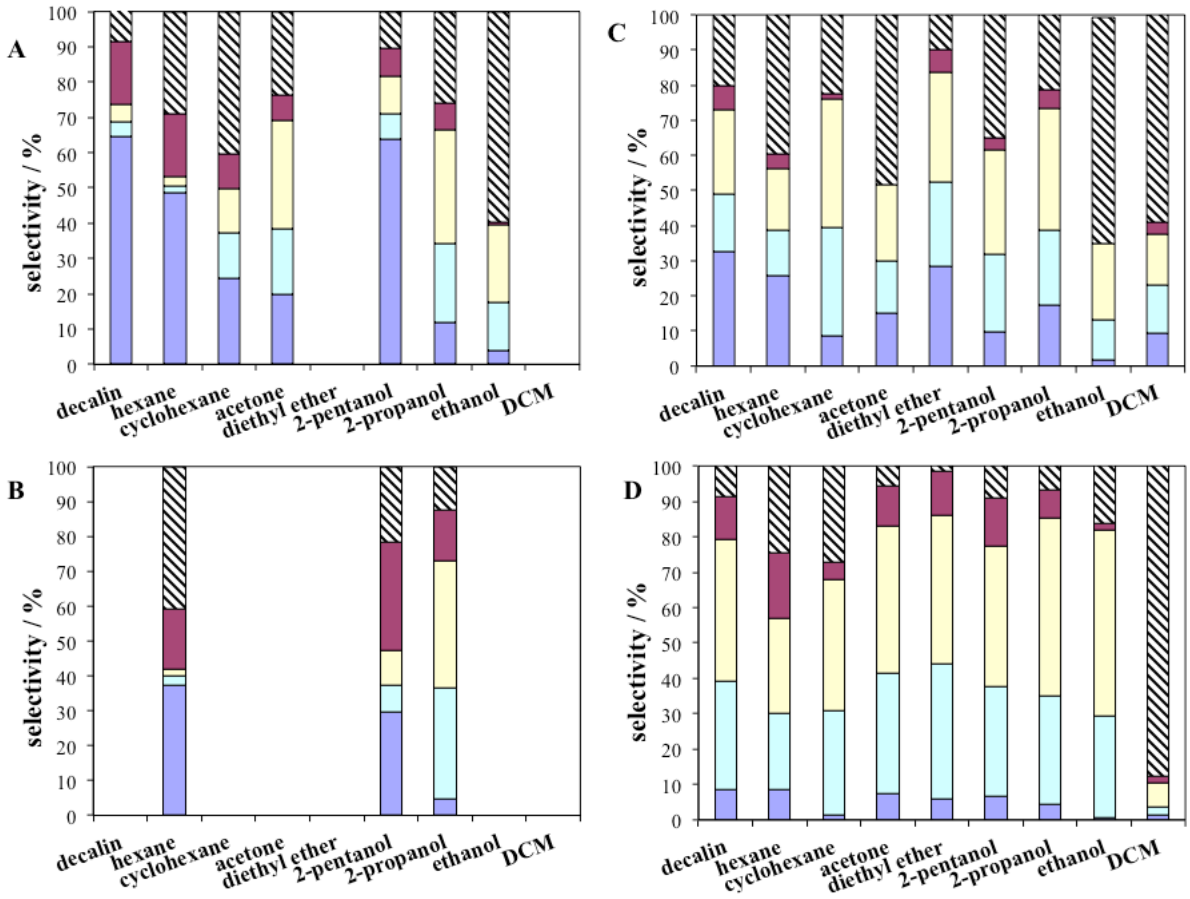

Figure 7.4. Selectivity: Product distributions of citral hydrogenation at 298 K (A) at 10 % and (B) at 70 % conversion; and 373 K (A) at 10 % and (B) at 70 % conversion. Citronellal (dark blue), nerol (light blue), geraniol (yellow), citronellol (dark red) and others (dashed black), are shown. Reaction conditions: 0.3 g 5% Pt/SiO_2, 150 cm^3 solvent, 10 bar(g), c_0 = 0.13 M.

Formation of other species shown in **Scheme 6.1** was also noted, particularly at high conversion. The products of subsequent hydrogenated reactions, citronellol and 3,7-dimethyl-1-octanol, were formed in all solvents at 70% conversion. Significant amounts of 3,7-dimethyl-1-octanol were formed at 373 K in non-polar solvents cyclohexane, decalin and hexane. Products resulting from the reduction of the isolated citral double bond were observed at 70%, with <2% selectivity. This poor reactivity was consistent with previous work (Mukherjee and Vannice, 2006; Zgolicz *et al.*, 2012). By-products from different side reactions were preferentially formed depending on the solvent used. Thus, in the case of alcohols, the formation of a heavy product, ascribed to a citral dimer, was observed at 298 K. In addition, acetals of citral, citronellal and dihydrocitronellal were also formed in alcohol solvents. The formation of citral and product acetals was more significant in shorter chain alcohols, as noted in **Table 7.3** Furthermore, GC-MS results showed the presence of

isopropyl ethers of geraniol and nerol in acetone. Cyclisation products from citronellal were also formed selectively in non-polar solvents, in agreement with literature (Mäki-Arvela *et al.*, 2002; Fuentes *et al.*, 1989; Wismeijer *et al.* 1986). The formation of more than one isopulegol isomer was noted and assignment from a similar column (Siedenburg *et al.*, 2012), revealed a distribution of 10:65:25 on isopulegol:neo-isopulegol:neoiso-isopulegol, regardless of solvent. For simplicity, all isomers were grouped together. Formation of menthols in hexane and cyclohexane at 373 K reinforced the observed preferential cyclisation in non-polar solvents. Lastly, the formation of hydrocarbon fragments from decarbonylation or hydrodeoxygenation was noted. C_9 species – 2,6-dimethyl-2-heptene and 2,6-dimethylheptane – and C_{10} products – 3,7-dimethyl-2,6-octadiene isomers and 2,6-dimethyl-2-octene – were identified by GC-MS. Significant selectivity towards fragments was noted at 373 K in non-polar solvents at 70% conversion. Also acetone showed high proportion towards fragments. In contrast, alcohols showed lower selectivity towards fragment products.

Table 7.3. Citral:citral acetal ratios during the hydrogenation of citral in polar protic solvents. Reaction conditions: 0.3 g 5% Pt/SiO_2, 150 cm^3 solvent, 10 bar(g), c_0 = 0.13 M.

T / K	ethanol	2-propanol	2-pentanol
298	23:1	270:1	-
373	2:1	51:1	266:1

Reaction in DCM showed a significant difference in the product distribution when compared to the other solvents. As seen in **Table 7.2**, significant amounts of cyclisation products, isopulegols and menthols, were formed, in addition to a range of fragments. These trends increased at high conversion. Formation of fragments accounted for 87.5% of the products. GC-MS results revealed the formation of significant amounts of limonene isomers, menthanes, terpinenes and *p*-cymene, shown in **Figure 7.5**. **Table 7.4** summarises the contribution of each species in the fragments fraction. In addition, the presence of a series of molecules of high carbon number, grouped as heavy species, represented a selectivity of 4.4% of the total products formed. These heavy products were identified with isopulegol ethers, reported elsewhere (Fuentes *et al.*, 1989; Nagai, 1974). DCM was believed to direct selectivity towards the formation of cyclic products *via* formation of hydrogen chloride. As such, the hydrogenation of citral was performed in hexane, to which 5 ml $HCl_{(ac)}$ (32% vol.) were added after 3 h of reaction. Results in **Figure 7.6** showed a significant shift in the product distribution towards dehydroxylated cyclic products after the injection of HCl. **Table**

7.5 summarises the comparative results before and after injection in comparison with reactions in hexane and DCM. As can be seen, the addition of HCl to the reaction in hexane resulted in a modification of the product distribution towards results observed when DCM was used.

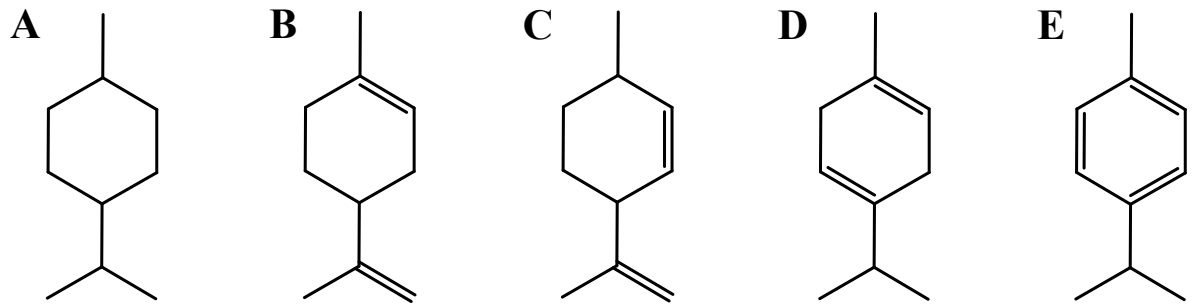

Figure 7.5. Cyclic dehydroxylated reaction species formed during the hydrogenation of citral in DCM at 373 K detected with the use of GC-MS: (A) fully saturated *p*-menthane, (B) limonene, (C) unsaturated endo-exocyclic menthadiene isomers, (D) unsaturated exocyclic terpinenes, and (E) *p*-cymene.

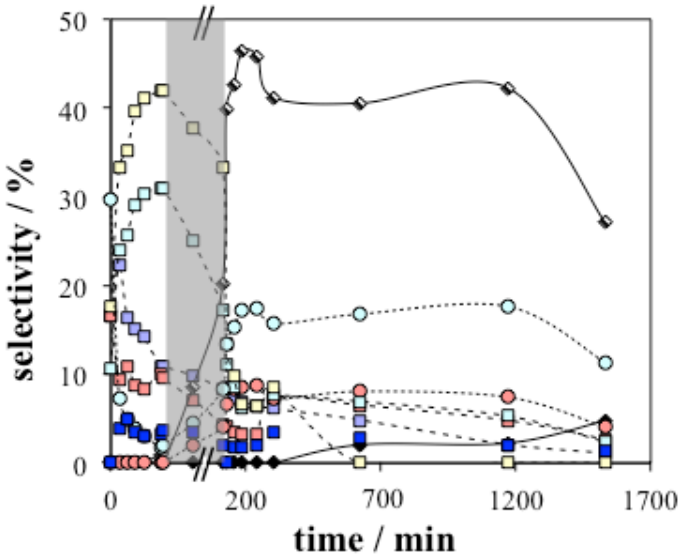

Figure 7.6. Selectivity: Product distribution during hydrogenation of citral at 373 K in hexane spiked with HCl after 3 hours of reaction (30% citral conversion). Reaction conditions: 0.3 g 5% Pt/SiO_2, 150 cm^3 solvent, 10 bar(g), c_0 = 0.13 M. Citronellal, citronellol, geraniol, nerol and 37OH (dark blue) are shown in squares with the same colours as in **Figure 7.4**. Isopulegols (light blue) and menthols (light red) are shown in circles. Fragments (dashed) and heavy species (bulk) are shown in diamonds. Grey area has been enhanced ×10 to reflect the effect of the injection of HCl.

Table 7.4. Product distribution of the fragments obtained during hydrogenation of citral in DCM, identified *via* GC-MS. Reaction conditions: 0.3 g 5% Pt/SiO_2, 150 cm^3 solvent, 373 K, 10 bar(g), c_0 = 0.13 M.

species	%
C_9 + menthanes	0.7
***p*-cymene**	3.2
limonene	74
$C_{10}^{=}$	15
terpinenes	1.6
menthadiene	5.7

Table 7.5. Product distribution during the hydrogenation of citral in hexane, DCM and pulse experiment with HCl. Reaction conditions: 0.3 g 5% Pt/SiO_2, 150 cm^3 solvent, 10 bar(g), c_0 = 0.13 M.

	selectivity / %			
products	**hexane (30% conv)**	**before HCl (30% conv)**	**after HCl (55% conv)**	**DCM (55% conv)**
citronellal	16	10.9	7.3	1.8
nerol	28	31	8.5	3.9
geraniol	33	42	9.9	9.4
isopulegols	6.2	1.9	15.4	6.9
menthols	-	-	8.3	0.8
citronellol	14	10.0	3.4	2.0
37OH	1.4	-	1.8	1.4
ENALS	-	-	-	-
ENOLS	-	-	-	1.5
DHCAL	1.3	-	2.9	1.0
fragments	-	1.0	43	71
C_9 + menthanes	-	-	1.5	16
***p*-cymene**	-	-	5.1	12
limonene	-	-	20	28
$C_{10}^{=}$	-	1.0	3.6	8.7
terpinenes	-	-	6.8	1.8
menthadienes	-	-	5.3	3.6
heavy	-	-	-	0.7

7.2.3 Deactivation

TOF values were obtained for the hydrogenation of citral on the different solvents after 24 h of reaction. As observed in **Figure 7.7** and **Tables 7.1** and **7.2**, rates decreased dramatically with time. Reduction to values < 2% of the initial rates was observed at 298 K, while in average a decay to 17% of the initial rates was seen at 373 K. This reduction has been previously shown to occur in this reaction system (Mukherjee and Vannice, 2006; Singh and Vannice, 2000a, 2000b). A reduction of two orders of magnitude with respect to the initial TOF at 298 K contrasted with the more sustained hydrogenation rates at 373 K. These results might suggest a slower deactivation process within the catalyst at high temperatures that allowed for higher conversions to be obtained. Catalyst blockage by poisoning of the active sites has been previously reported to explain such deactivation (Mäki-Arvela *et al.*, 2006; Burgener *et al.*, 2004b). Decarbonylation reactions have been considered a relevant step towards deactivation. A limited adsorption of by-products and site blockers at high temperatures would be expected, in contrast to reaction at 298 K. Such effect of temperature in deactivation and the effect of solvent will be described in more detail in chapter 8.

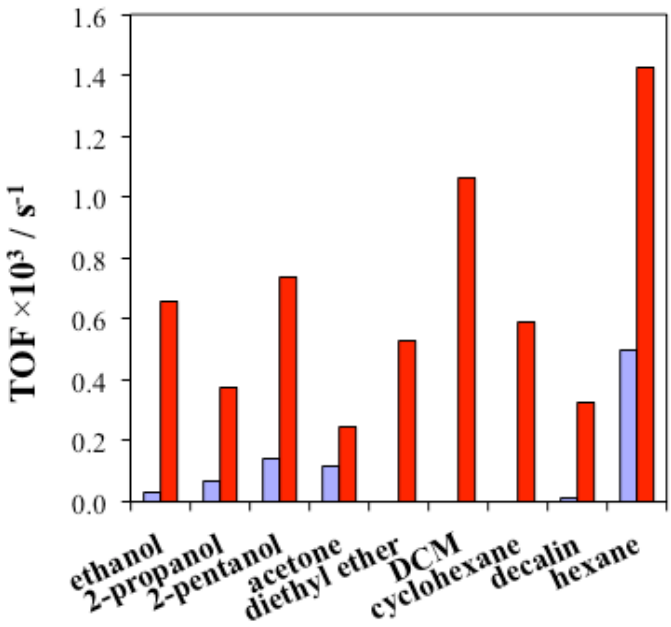

Figure 7.7. Reaction rate after 24h, in TOF, for the hydrogenation of citral at 298 K (blue) and 373 K (red) with different solvents on 5 % Pt/SiO_2. Reaction conditions: 0.3 g 5% Pt/SiO_2, 150 cm^3 solvent, 10 bar(g), c_0 = 0.13 M.

7.3 Discussion

In this section, a detailed analysis of the effect of solvent on reaction rates, selectivity, and deactivation will be shown. A discussion of the observed results in citral hydrogenation will be considered in terms of solvent used, and reaction temperature.

7.3.1 Effect of solvent on reaction rates

A clear difference in reaction rates was observed in the hydrogenation of citral depending on the solvent used, as seen in **Figure 7.3**. In order to study the effects that solvents might present on the overall activity of the catalyst, firstly, H_2 pressure, H_2 solubility and effective mass transfer were considered. Analysis of the mass transfer coefficient *via* the physical absorption method (Dietrich *et al.*, 1992) revealed values of k_La between 0.35 and 0.47 s^{-1}, in line with other reaction systems (Hichri *et al.*, 1992). Hence, overall external H_2 transfer was not considered a limitation of the reaction.

Variations in hydrogen pressure in the reactor were dependent on solvent vapour pressures (Perry and Green, 1999). Such variations in solvent volatility led to minor differences in H_2 pressure in the reactor at 298 K, as seen in **Table 7.6**, but to significant differences at 373 K. For example, H_2 pressures were 9.80 and 7.56 bar(g) at 298 K and 373 K, respectively, in hexane. Despite H_2 pressure been shown to affect the reduction rates of citral and similar α,β-unsaturated carbonyl molecules (Aramendía *et al.*, 1997; Bergault *et al.*, 1998; Mukherjee and Vannice, 2006; Poltarzewski *et al.*, 1986), the reduction in H_2 pressure in this work had no relation with the changes observed in reactivity. Notably, hydrogenation rate increased in cyclohexane at 373 K as compared to 298 K, when H_2 pressure decayed over 16%. Hydrogenation occurred at 373 K in diethyl ether or DCM, while no apparent reaction was seen at 298 K, opposite to trends on hydrogen pressure. Since reaction takes place in the liquid-phase, it was also important to consider the effective concentration of H_2 in the liquid phase. Solubility of H_2 in the different solvents was also considered, and values shown in **Table 7.7** were obtained considering the H_2 pressures present in the reactor. Results revealed no relation between solubility and initial reaction rates, in some cases opposite, such as in cyclohexane or ethanol. Similar conclusions had been found elsewhere (Bertero *et al.*, 2011). The pressure and solubility of H_2 were discarded as major factors affecting reaction rates during the hydrogenation of citral. Therefore the changes observed were directly related to the solvents employed.

Table 7.6. H_2 pressure during the hydrogenation of citral in the solvents studied for a total pressure in the reactor of 10 bar(g). Solvent vapour pressures were calculated using Antoine's equation using tabulated constants (Perry and Green, 1999). Values coincided with the experimental measurements of reactor pressure before H_2 addition.

	H_2 pressure / bar	
solvent	**298 K**	**373 K**
decalin	9.92	7.77
hexane	9.94	8.06
cyclohexane	9.99	9.51
acetone	9.69	6.29
diethyl ether	9.29	3.51
DCM	9.43	4.08
2-pentanol	9.87	8.26
2-propanol	10.00	9.93
ethanol	9.80	7.57

Table 7.7. Solubility of H_2 in the solvents studied. Values extracted from Young *et al.* (1981)*, unless specified otherwise.

	solubility, $x_2 \times 10^2$ / -	
solvent	**298 K**	**373 K**
decalin	0.37	0.10
hexane[a]	0.78	0.64
cyclohexane	0.41	0.34[b]
acetone[a]	0.28	0.14
diethyl ether	0.57	-
DCM	0.16[1]	-
2-pentanol	0.26[2]	0.48[2]
2-propanol	0.27[c]	0.25[b]
ethanol	0.20[c]	0.25[d]

[a]Brunner (1985); [b]Considered Henry's constant at 363 K extracted from Bertero *et al.* (2011); [c]Katayama and Nitta (1976); [d]Extrapolated from 298-353 K Henry's constant values reported in Gupta *et al.* (1973).

*[1]Value obtained after extrapolation of results from tetrachloromethane and chloroform; [2]Henry's constant obtained from solubility in 1-pentanol.

Solvents can influence reaction rate in a number of ways, *e.g.* through solvent-catalyst interactions or solvent-reactant interactions. Reaction rates of citral increased in polar protic solvents in the order ethanol < 2-propanol < 2-pentanol; in polar aprotic solvents they followed acetone < diethyl ether < DCM; and in non-polar solvents, cyclohexane < decalin < hexane at 298 K and decalin < cyclohexane < hexane at 373 K. Rate in decalin at 373 K was shown to be very low. The use of a bulk solvent parameter of polarity provided a first

indication of such reactivity-polarity relationship. **Table 7.8** shows the $E_T(30)$ solvent polarity parameter (Reichardt, 1994), for all solvents used in this study. A higher $E_T(30)$ value indicates higher solvent polarity. As can be seen, results at 298 K showed a clear trend with polarity for both polar protic and aprotic solvents. A reduction in polarity coincided with an increase in reaction rates. In addition, a clear correlation existed on polar protic solvents at both temperatures. Also, an increasing rate corresponded with a reduced polarity for polar aprotic solvents – excluding DCM. An agreement between solvent polarities with reaction rates was reported for polar solvents (Bertero *et al.*, 2011). A similar observation was obtained in the hydrogenation of 2-butanone in 1% Ru/C (Wan *et al.*, 2014). Polar aprotic solvents and polar protic solvents were discussed to increase the solvation of the reactant, H-bonding being the major mode of interaction in protic solvents (Bertero *et al.*, 2011; Hájek *et al.*, 2004). However, no correlation was established between reaction rate and solvent polarity when non-polar solvents were included. Similar $E_T(30)$ polarity parameters contrasted with the notable changes in reaction rates within solvents in this group. Additionally, the absence of reaction in DCM or diethyl ether at 298 K could indicate different effects from polarity are also relevant determining rates. Overall, the results observed for non-polar and polar aprotic solvents might be indicative of the presence of relevant solvent-reactant-catalyst interactions, discussed in section 7.3.2.

Table 7.8. $E_T(30)$ polarity parameters for solvents used in the hydrogenation of citral.

solvent	$E_T(30)$ / kcal mol^{-1}
hexane	31
cyclohexane	30.9
decalin	31.2
DCM	40.7
diethyl ether	34.5
acetone	42.2
2-pentanol	46.5
2-propanol	48.4
ethanol	51.9

The possibility of transfer hydrogenation (Dayan *et al.*, 2013; Ohtaka *et al.*, 2012) of α,β-unsaturated aldehydes in some solvents, particularly in 2-propanol, was considered (Alonso *et al.*, 2008; Baig and Varma, 2013; Battilocchio *et al.*, 2013; Gliński and Ulkowska, 2011; Mizugaki *et al.*, 1998; Szöllösi and Bartók, 1999). Results obtained from a test reaction

performed in 2-propanol in N_2 (not shown), however, revealed the absence of such reaction mechanism. Such observation was in agreement with findings from Liu *et al.* (2013) and Trasarti *et al.* (2014).

7.3.2 Effect of solvent on selectivity

In this section, selectivity trends will be assessed in terms of solvent. The influence of solvent in the preferential hydrogenation pathway, *i.e.*, hydrogenation of C=O towards geraniol and nerol *vs.* hydrogenation of C=C towards citronellal, is shown in section 7.3.2.1. The effect of solvent in the extended reaction network and by-products formed, including the effect that DCM showed in the product distribution, will be reviewed in section 7.3.2.2.

7.3.2.1 Influence of solvent on the reaction pathway: C=C *vs.* C=O

The use of solvent tailored the hydrogenation towards unsaturated alcohols and citronellal. Isomerisation between citronellal and geraniol/nerol was unseen previously in a number of studies (Mäki-Arvela *et al.*, 2006; Singh and Vannice, 2000a; Singh *et al.*, 2000). However, formation of citronellal from geraniol/nerol was observed to a low extent (Mäki-Arvela *et al.*, 2005a) with solvent influencing the extent of isomerisation.

Figure 7.8 shows the yield towards the production of unsaturated alcohols geraniol and nerol as a function of conversion in the different solvents studied at 298 and 373 K. Yield *vs.* conversion plots were used to remove the effect of deactivation. Considering the reaction at 298 K, non-polar solvents, with the exception of cyclohexane, presented low selectivity towards geraniol and nerol. Polar protic solvents revealed a decreasing selectivity with increasing chain length, already observed in the hydrogenation of 2-butanone (Wan *et al.*, 2014) or acetophenone (Bertero *et al.*, 2011). Thus, reaction in 2-pentanol returned yields towards geraniol and nerol similar to non-polar solvents, while ethanol and 2-propanol showed high yields. For polar aprotic solvents, results in acetone showed similar values to those observed with ethanol and 2-propanol. Hence, a selective hydrogenation process towards unsaturated alcohols was enhanced by the presence of short chain polar protic solvents. Cyclohexane could be affecting the reaction mechanism at low temperature. Previously, the hydrogenation of cinnamaldehyde in cyclohexane, toluene and *p*-xylene showed similar conversion and selectivity trends (Bertero *et al.*, 2011). The cyclic C_6 structure of the solvents could be increasing C=O selectivity. Deuterium exchange experiments in *cis*-2-pentenenitrile showed that gas-phase hydrogenation proceeded *via* a

cyclic intermediate (McGregor *et al.*, 2010). A modification in the flat adsorption mode of citral with both C=C and C=O bonds interacting with Pt, previously described for α,β-unsaturated carbonyls (Delbecq and Sautet, 1995; Haubrich *et al.*, 2009), could lead to an increased C=O selectivity. Yield towards geraniol and nerol at 373 K showed a very similar trend in all solvents up to 60% conversion, with the exception of the aforementioned DCM. Subsequent hydrogenation was observed in hexane and a reduction in the yield towards unsaturated alcohols was noted in non-polar solvents, particularly hexane and cyclohexane. These results indicated adsorption had a weaker influence in selectivity at higher temperatures.

Further to this, stereoselectivity of the conjugated carbon-carbon double-bond reaction of the E and Z citral isomers, and relative geraniol to nerol formation provided additional insights on the reaction pathway. As can be observed in **Figure 7.9**, citral E isomer concentration decayed faster than isomer Z (E/Z < 1) at 298 K, in agreement with results from crotonaldehyde hydrogenation (Englisch *et al.*, 1997b). Higher isomer reactivity was generally more significant in alcohols as compared to non-polar solvents. C=O hydrogenation was also stereospecific towards the E isomer, geraniol *vs.* the Z isomer, nerol, as seen by C_{Ger}/C_{Ner} values. $C_{Ger}/C_{Ner} > 1.7$ in polar protic and aprotic solvents, while $C_{Ger}/C_{Ner} = 0.75$ in hexane. At 373 K, DCM showed the highest citral E/Z ratio with $C_{Ger}/C_{Ner} > 2.7$. These values are in line with preferential limonene formation *via* nerol (Cruz-Costa *et al.*, 1998). Reactions in polar protic solvents showed a greater preference for the hydrogenation of isomer Z, while polar aprotic and non-polar solvents, with the exception of diethyl ether, showed no initial hydrogenation preference. Formation of geraniol *vs.* nerol was favoured in all solvents, being more significant in polar protic solvents. Subsequent hydrogenation in hexane led to $C_{Ger}/C_{Ner} < 0.3$ at 90% conversion. Hydrogenation of both citral isomers occurred at different rates. For example, reaction at 298 K of isomer Z was 11.1×10^{-3}, isomer E was 12.1×10^{-3} and the rate ratio was 1.1 in hexane, while in ethanol those values were 0.3×10^{-3}, 0.6×10^{-3} and 2.31, respectively. In all cases, polar protic solvents marked the extreme concentration ratio at both temperatures.

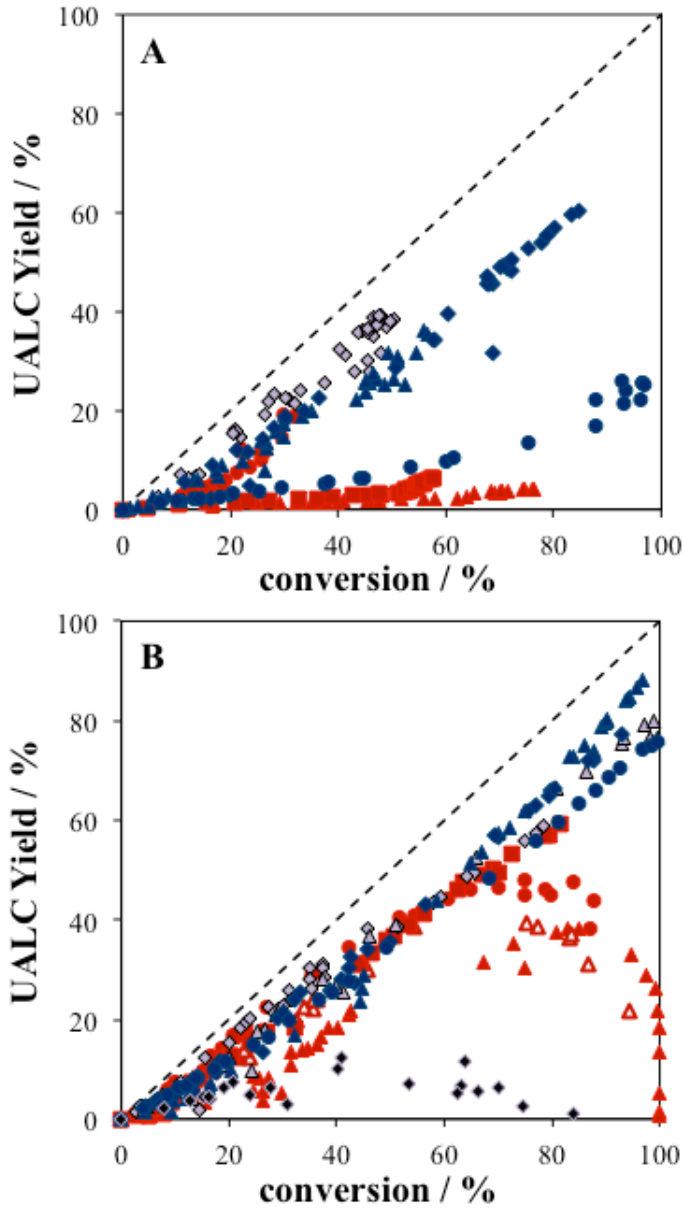

Figure 7.8. Yield towards unsaturated alcohols (UALC), geraniol and nerol, during the hydrogenation of citral at 298 K (A) and 373 K (B) with different solvents on 5% Pt/SiO_2. Reaction conditions: 0.3 g 5% Pt/SiO_2, 150 cm^3 solvent, 10 bar(g), $c_0 = 0.13$ M. Non-polar solvents are shown in red, polar protic solvents in blue, and polar aprotic solvents in grey. DCM is shown in black to remark its distinct behaviour. 2-propanol and acetone (diamonds), 2-pentanol and cyclohexane (circles), decalin (squares), diethyl ether, ethanol and hexane (triangles), are shown.

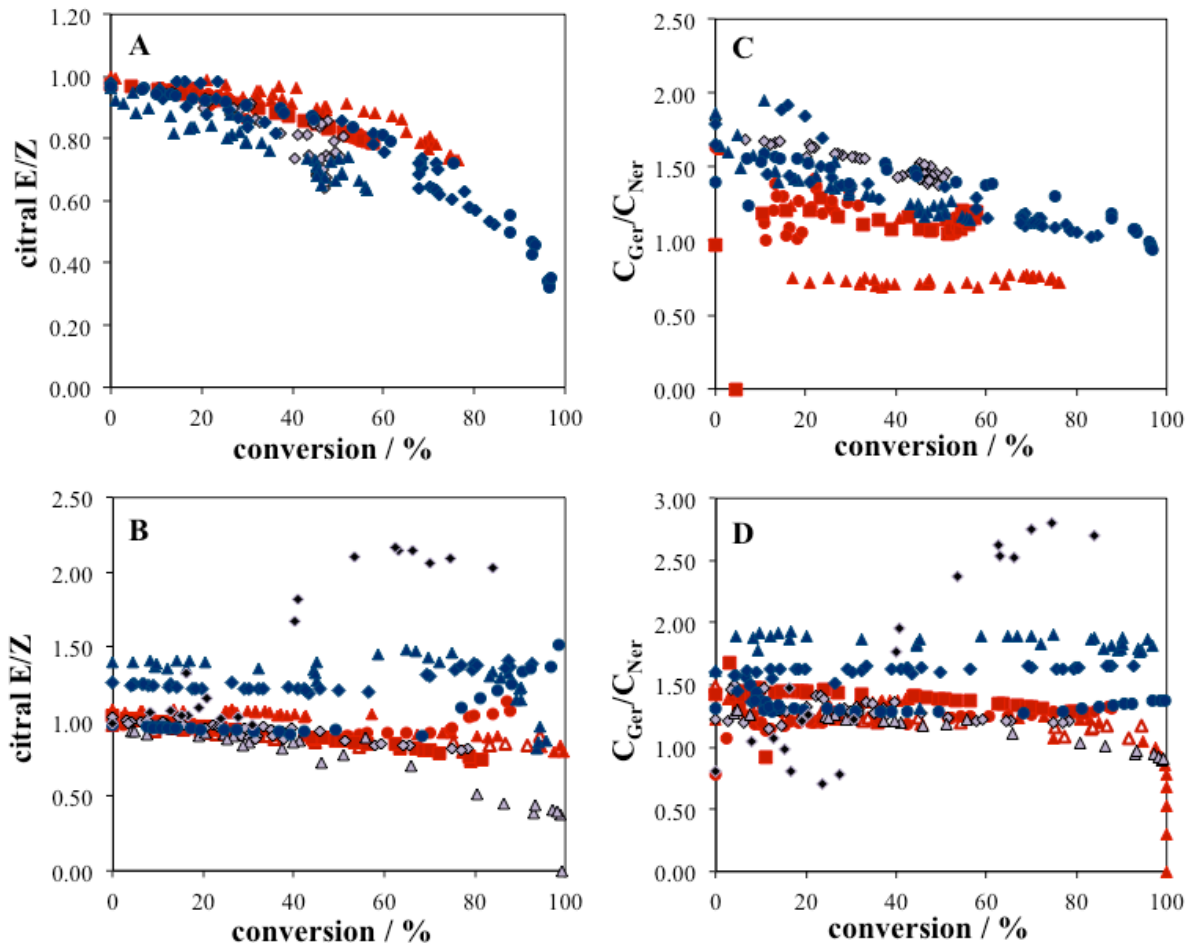

Figure 7.9. E/Z stereoselectivity ratios of citral isomers (A and B) and geraniol/nerol ratio (C and D) as a function of conversion in different solvents during the hydrogenation of citral at 298 K (top) and 373 K (bottom) on 5 % Pt/SiO_2. The ratio of citral E/Z takes as reference (value of 1) the relative proportion of isomers before the start of reaction. Reaction conditions: 0.3 g 5% Pt/SiO_2, 150 cm^3 solvent, 10 bar(g), c_0 = 0.13 M. The legend of the different solvents is the same as shown in **Figure 7.8.**

7.3.2.2 Effect of solvent on the extended reaction network

Solvent effects were also observed in the formation of i) secondary hydrogenation products, *i.e.*, species formed by hydrogenation of the primary products citronellal, geraniol and nerol, and ii) by-products in the citral reaction network, **Scheme 6.1**. Understanding the extent of those reactions as a function of solvent could increase the yield towards desired products.

Formation of citronellol was observed during the reaction. Higher citronellol yields were observed in non-polar and polar protic solvents. These results indicated there was a relation between formation of citronellal and hydrogenation to citronellol, in agreement with previous reaction results in hexane (Singh and Vannice, 2000b). Within alcohols, higher yields were

observed in 2-pentanol as compared to 2-propanol or ethanol, in agreement with previous observations (Mäki-Arvela, 2002). Selectivity towards the final hydrogenation product, 3,7-dimethyl-1-octanol, was low in line with results from Singh and Vannice (2000a), and varied with temperature and solvent. Results at high conversion indicated relatively high selectivities in non-polar solvents, DCM and longer chain alcohols. A decrease in the selectivity at 373 K for the same solvent was observed, in agreement with results in 2-pentanol on Ru/Al_2O_3 (Mäki-Arvela *et al.*, 2005b). Therefore polar protic solvents tended to solely favour hydrogenation towards geraniol and nerol avoiding the formation of subsequent hydrogenation products. The hydrogenation of isolated C=C in citral towards 3,7-dimethyl-2-octenal isomers (ENALS) and 3,7-dimethyl-2-octen-1-ol alcohols (ENOLS) is usually not favoured (Mäki-Arvela *et al.*, 2004; Mukherjee and Vannice, 2006; Zgolicz *et al.*, 2012). Formation of such species was predominantly observed in non-polar solvents, especially in hexane at 298 K. The formation of dihydrocitronellal (DHCAL) was also low in all solvents. Non-polar solvents have been proposed to favour isolated bond hydrogenation by means of molecular conformation upon adsorption (Chatterjee *et al.*, 2004).

The formation of C_9 and C_{10} unsaturated and saturated hydrocarbon fragments was observed during citral hydrogenation. These products have been reported previously in the hydrogenation of citral (Hubaut, 1992; Singh and Vannice, 2000a) and similar α,β-unsaturated carbonyl molecules (English *et al.*, 1997a, 1997b; Neri *et al.*, 1997; Rojas *et al.* 2012). Yield towards fragments was shown to increase at higher temperature (Mäki-Arvela *et al.*, 2005b), and comparing solvents at 373 K, cyclohexane showed the highest selectivity to fragments, followed by acetone and hexane, while 2-propanol and ethanol showed low selectivities. Hence, fragments were formed to a greater extent in non-polar solvents. These results were in agreement with previous results from Mäki-Arvela *et al.* (2006) in cyclohexane and 2-propanol on Pt/Al_2O_3.

The influence of solvent in cyclisation has not been reported in detail in the literature. The presence of acid supports is required for cyclisation reactions (Chuah *et al.*, 2001; Kropp *et al.*, 1995) sometimes related to the use of Cl^- catalyst precursors (Mäki-Arvela *et al.*, 2006; Milone *et al.*, 1999; Vandichel *et al.*, 2013; Wismeijer, *et al.*, 1986). Results showed that formation of isopulegols was greater in non-polar solvents and DCM, in line with findings by Fuentes *et al.* (1989). Lower yields in alcohols were obtained, increasing in those with a longer alkyl chain, in agreement with results from Mäki-Arvela *et al.* (2002) over a 5% Ru/C catalyst. The production of menthol was also noted. Menthols were observed in hexane,

cyclohexane and DCM, in agreement with solvents with higher yields of isopulegols. Menthol formation during citral hydrogenation has been previously reported when acid catalysts are used (Trasarti *et al.*, 2013; 2007; Álvarez-Rodríguez *et al.*, 2011).

Acetalisation reactions are acid catalysed processes (Vaidya and Mahajani, 2003), *e.g.*, with Si-OH groups present in silica, as shown by Englisch *et al.* (1997b). The formation of acetals (and hemiacetals) requires the presence of an alcohol and a carbonyl (Englisch *et al.*, 1997b; Hájek *et al.*, 2004; Poltarzewski *et al.*, 1986). Also the use of Cl^- precursors has been related to their formation (Kouachi *et al.*, 2008; Mukherjee and Vannice, 2006). In this study, acetals of citral and citronellal were observed predominantly in ethanol and 2-propanol, with some traces present in 2-pentanol. Such observation is in agreement with a previous study by Mäki-Arvela *et al.* (2002). In this work, in addition, it was noted the reversibility of the acetalisation at high conversion. No acetals were present at 298 K in all solvents, and < 10% selectivity was noted at 373 K at 70% conversion. Moreover, the formation of isopropyl ethers of geraniol and nerol was observed in this work in acetone *via* reaction with the unsaturated alcohols. A similar mechanism to acetalisation was believed to participate in etherification. In summary, formation of acetals occurred only in polar protic solvents, and within this group, shorter chain alcohols favoured acetal formation.

Formation of ethers, typically acidic catalysed products (Markus *et al.*, 2007; Ruppert *et al.*, 2009), was observed in short chain alcohols. Ethers of geraniol and nerol were observed in ethanol at 373 K, in agreement with previous observations in 2-propanol (Bernas *et al.*, 2012). Additionally, the formation of a condensed product from citral at <10% conversion was noted at 298 K in the presence of ethanol and 2-propanol. GC-MS results indicated the formation of a series of C_{18}-C_{22} products. A citral dimer species was hypothesised to be formed. The formation of this product has been little discussed in the context of heterogeneous catalytic reactions, however it has been described in homogeneous catalytic and non-catalytic studies (Peña *et al.*, 2012; De Andrade *et al.*, 1996). Additionally, dimerisation was reported during hydrogenation of other α,β-unsaturated aldehydes (Englisch *et al.*, 1997b; Keresszegi *et al.*, 2002; Santori *et al.*, 2002). However, condensation of citral with hydrogenation products *via* aldol condensation (Bailie *et al.*, 1997; Burgener *et al.*, 2004a; Englisch *et al.*, 1997a; Luo and Falconer, 1999), or the formation of condensation products from alcohols (Bertero *et al.*, 2013; Bertero *et al.*, 2008) cannot be discarded.

The yield to geraniol and nerol at 373 K followed 2-pentanol > 2-propanol > ethanol. This trend was opposite to that observed in acetal, ether and dimer formation. An appropriate choice of solvent, in line with a non-acidic support, has previously led to the elimination of acetalisation products (Mäki-Arvela *et al.*, 2002; Stassi *et al.*, 2013). However, acetal formation was believed to prevent cyclisation (Gallezot and Richard, 1998). This cyclisation-acetalisation behaviour was similar to results reported in this work in polar protic solvents. As observed in this work, longer chain alcohols and non-polar solvents reduced the formation of acetals and dimer, at the expense of cyclisation and decarbonylation products. Acetalisation of citral in polar protic solvents was reversible, contributing towards formation of geraniol and nerol. However, acetalisation of citronellal and formation of dimer and ethers contributed negatively to high geraniol and nerol yields. Herein, results reinforced the importance of the right solvent selection to render the desired products.

7.3.2.3 The use of DCM as solvent

DCM has been shown to provide an entirely different product distribution to the citral reaction network shown in **Scheme 6.1**. As noted, DCM was believed to direct selectivity towards the formation of cyclic products *via* formation of hydrogen chloride. Previous studies have shown the likelihood of this hypothesis. Thus, the formation of HCl from DCM and chloroform has been previously reported on Pt/C and Pd/γ-Al_2O_3 at similar conditions to those of citral hydrogenation (Álvarez-Montero *et al.*, 2010; Malinowski *et al.*, 1998). In addition, C-Cl activation has been reported to occur at temperatures as low as 150 K (Lee *et al.*, 2004). Results after the injection of HCl in the hydrogenation of citral in hexane, shown in **Figure 7.6**, confirmed such hypothesis.

Different pathways for the formation of dehydroxylated cyclic products, formed during the hydrogenation of citral in DCM, can be indicated. Solvent-free dehydration of geraniol and nerol to limonene and other cyclic products has been previously reported in γ-alumina or zirconias (Cruz-Costa *et al.*, 1998). Dehydration of isopulegols to *p*-menthadiene products (Abdul-Wahab and Jackson, 2013; Chuah *et al.*, 2001) and subsequent isomerisation to limonene (Filippenko *et al.*, 1985) can occur. Formation of menthane isomers, terpinenes and *p*-cymene could have occurred *via* disproportionation reactions, or by subsequent hydrogenation, as previously shown (Grau *et al.*, 1999; Hunter and Brodgen, 1963; Lesage *et al.*, 1996). Reaction on DCM seemed to proceed *via* acid cyclisation and dehydration from

HCl formed from the solvent towards the formation of limonene, with subsequent secondary reactions.

7.3.3 Influence of solvent on deactivation

Deactivation occurred in all reaction systems as observed with the TOF after 24 h (**Tables 7.1** and **7.2**, **Figure 7.7**). **Figure 7.10** showed the conversion of citral as a function of time. Reaction at 298 K resulted in overall lower conversions and significant deactivation, whereas hydrogenation at 373 K progressed to higher conversion. The solvent determined the extent of reaction at 298 K. Conversion increased with solvent in the order cyclohexane << acetone ≈ ethanol < decalin < 2-propanol ≈ hexane < 2-pentanol. In particular, cyclohexane showed only about 30% citral conversion. These differences in reaction at 298 and 373 K have been seen previously (Singh and Vannice, 2000a). Deactivation was previously explained *via* CO adsorption-desorption processes (Englisch *et al.*, 1997b; Mäki-Arvela *et al.*, 2006; Mukherjee and Vannice, 2006). Additionally, the adsorption strength of citral and products of reaction on the catalyst in the presence of a given solvent influenced deactivation, especially at 298 K. The strong influence of solvent on product blockage was shown in 2-octanol oxidation (Mounzer *et al.*, 2010). Cyclohexane (<30%), followed by acetone (<50%), presented low conversions, while DCM and diethyl ether showed no reaction. Product blockage of unsaturated alcohols was suggested by Singh *et al.* (2000) during citral hydrogenation in hexane. Hence, solvent can also be considered to play a key role in deactivation. Such effect will be extensively studied in chapters 8 and 9.

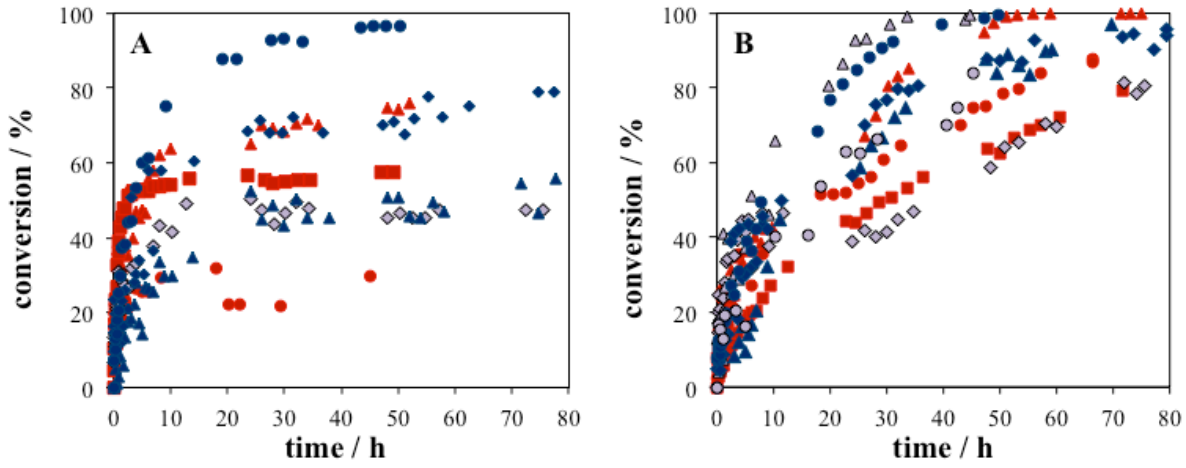

Figure 7.10. Conversion of citral (excluding citral acetals) at 298 K (A) and 373 K (B) with different solvents on 5% Pt/SiO_2. Reaction conditions: 0.3 g 5% Pt/SiO_2, 150 cm^3 solvent, 10 bar(g), c_0 = 0.13 M. The legend of the different solvents is the same as shown in **Figure 7.8**.

7.4 Conclusions

The hydrogenation of citral on 5% Pt/SiO_2 was studied in a range of solvents to provide information on the effect they present in reaction rates and selectivities. The complex reaction network of citral served as an exemplary system for other reactions of multifunctional molecules important in the energy and fine chemical sectors. Polar protic solvents, ethanol, 2-propanol and 2-pentanol; polar aprotic solvents, diethyl ether, DCM and acetone; and non-polar solvents, hexane, cyclohexane and decalin, were used. Results showed that solvent polarity influenced reaction rates and selectivities in the hydrogenation of citral. However, solely H_2 solubility in the different solvents was not able to explain hydrogenation rates. Higher rates were observed in non-polar solvents at 298 K, while polar protic solvents showed lower initial hydrogenation rates. In contrast, polar protic solvents showed higher yields of geraniol and nerol. In the extreme, diethyl ether and DCM inhibited reaction completely at 298 K. Reaction temperatures also had a strong influence in citral hydrogenation. Increasing the temperature to 373 K decreased initial reaction rates, affecting predominantly non-polar solvents, while it also reduced deactivation. Selectivity towards unsaturated alcohols geraniol and nerol increased with temperature, predominantly in non-polar solvents, while it remained similar in polar protic solvents. Deactivation of the catalyst was observed to occur in all solvents, and was considered to be strongly affected by by-product adsorption and decarbonylation. Deactivation was more pronounced at 298 K as opposite to higher conversions at 373 K. A number of side reactions were also observed. Overall, cyclisation and decarbonylation were favoured in non-polar solvents, while acetals were reversibly formed in polar protic solvents. Finally, the hydrogenation of citral in DCM resulted in cyclisation reactions that led to the formation of hydrogenated dehydrated products, such as limonenes and menthanes.

References

Abdul-Wahab, M.I., Jackson, S.D. (2013) Hydrogenation of 3-nitroacetophenone over rhodium/silica catalysts: effect of metal dispersion and catalyst support. *Appl. Catal. A-Gen.*, 462-463, 121 – 128.

Alonso, F.; Riente, P.; Rodríguez-Reinoso, F.; Ruiz-Martínez, J.; Sepúlveda-Escribano, A; Yus, M. (2008) Platinum nanoparticles supported on titania as an efficient hydrogen-transfer catalyst. *J. Catal.*, 260, 113 – 118.

Álvarez-Montero, M.A., Gómez-Sainero, L.M., Juan-Juan, J., Linares-Solano, A., Rodriguez, J.J. (2010) Gas-phase hydrodechlorination of dichloromethane with activated carbon-supported metallic catalysts. *Chem. Eng. J.*, 162, 599 – 608.

Álvarez-Rodríguez, J.; Rodríguez-Ramos, I.; Guerrero-Ruiz, A.; Arcoya, A. (2011) Selective hydrogenation of citral over Pt/KL type catalysts doped with Sr, La, Nd and Sm. *Appl. Catal. A-Chem.*, 401, 56 – 64.

Aramendía, M.A., Borau, V., Jiménez, C., Marinas, J.M., Porras, A., Urbano, F.J. (1997) Selective liquid-phase hydrogenation of citral over supported palladium. *J. Catal.*, 172, 46 – 54.

Bailie, J.E., Rochester, C.H., Hutchings, G.J. (1997) IR study of acrolein hydrogenation over Co/SiO_2 catalysts. *J. Chem. Soc., Faraday Trans.*, 93, 4389 – 4394.

Battilocchio, C.; Mawkins, J.M.; Ley, S.V. (2013) A mild and efficient flow procedure for the transfer hydrogenation of ketones and aldehydes using hydrous zirconia. *Org. Lett.*, 15, 2278 – 2281.

Bergault, I., Fouilloux, P., Joly-Viullemin, C., Delmas, H. (1998) Kinetics and intraparticle diffusion modelling of a complex multistep reaction: hydrogenation of acetophenone over a rhodium catalyst. *J. Catal.*, 175, 328 – 337.

Bernas, H.; Simakova, I.; Prosvirin, I.P.; Mäki-Arvela, P.; Leino, R.; Murzin, D.Y. (2012) Hydrogenation of citral over carbon supported iridium catalysts. *Catal. Lett.*, 142, 690 – 697.

Bertero, N.M., Trasarti, A.F., Apesteguía, C.R. and Marchi, A.J. (2013) Liquid-phase dehydration of 1-phenylethanol on solid acids: Influence of catalyst acidity and pore structure. *Appl. Catal. A-Gen.*, 458, 28 – 38.

Bertero, N.M., Trasarti, A.F., Apesteguía, C.R. and Marchi, A.J. (2011) Solvent effect in the liquid-phase hydrogenation of acetophenone over Ni/SiO_2: a comprehensive study of the phenomenon. *Appl. Catal. A-Gen.*, 394, 228 – 238.

Bertero, N.M., Apesteguía, C.R., Marchi, A.J. (2008) Liquid-phase dehydration of 1-phenylethanol over mordenite-like zeolite: influence of Si/Al ratio. *Catal. Commun.*, 10, 261 – 265.

Burgener, M., Furrer, R., Mallat, T., Baiker, A. (2004a) Hydrogenation of citral over Pd/alumina: comparison of "supercritical" CO_2 and conventional solvents in continuous and batch reactors. *Appl. Catal. A-Gen.*, 268, 1 – 8.

Burgener, M., Wirz, R., Mallat, T., Baiker, A. (2004b) Nature of catalyst deactivation during citral hydrogenation: a catalytic and ATR-IR study. *J. Catal.*, 228, 152 – 161.

Chatterjee, M., Chatterjee, A., Ikushima, Y. (2004) Pd-catalyzed completely selective hydrogenation of conjugated and isolated C=C of citral (3,7-dimethyl-2,6-octadienal) in supercritical carbon dioxide. *Green Chem.*, 6, 114 – 118.

Chuah, G.K., Liu, S.H., Jaenicke, S., Harrison, L.J. (2001) Cyclisation of citronellal to isopulegol catalysed by hydrous zirconia and other solid acids. *J. Catal.*, 200, 352 – 359.

Cruz-Costa, M.C., Johnstone, R.A.W., Whittaker, D. (1998) Catalysis of terpene rearrangements by zirconium phosphates and zirconium organo-substituted phosphonates. *J. Mol. Catal. A-Chem.*, 129, 79 – 89.

Dayan, S., Kayaci, N., Kalaycioglu, N.O., Dayan, O., Öztürk, E.C. (2013) Synthesis of ruthenium(II) complexes derived from reduced imine ligands: as catalysts for transfer hydrogenation of ketones. *Inor. Chim. Acta.*, 401, 107 – 113.

De Andrade, A.R., Romero, J.R., Boodts, J.F.C. (1996) Competitive pathways in the electrochemical reduction of citral. *J. Electrochem. Soc.*, 143, 2452 – 2457.

Delbecq, F., Sautet, P. (1995) Competitive C=C and C=O adsorption of α,β-unsaturated aldehydes on Pt and Pd surfaces in relation with the selectivity of hydrogenation reactions: a theoretical approach. *J. Catal.*, 152, 217 – 236.

Dietrich, E., Mathieu, C., Delmas, H., Jenck, J. (1992) Raney-nickel catalysed hydrogenations: gas-liquid mass transfer in gas-induced stirred slurry reactors. *Chem. Eng. Sci.*, 47, 3597 – 3604.

Englisch, M., Jentys, A., Lercher, J.A. (1997a) Structure sensitivity of the hydrogenation of crotonaldehyde over Pt/SiO_2 and Pt/TiO_2. *J. Catal.*, 166, 25 – 35.

Englisch, M., Ranade, V.S., Lercher, J.A. (1997b) Liquid phase hydrogenation of crotonaldehyde over Pt/SiO_2 catalysts. *Appl. Catal. A-Gen.*, 163, 111 – 122.

Filippenko, Z.A., Baranov, O.M., Roganov, G.N., Kabo, G.Y. (1985) Isomerization equilibrium of the *p*-menthadienes in the vapor phase. *Chem. Nat. Compd.*, 21, 47 – 51.

Fuentes, M., Magraner, J., De las Pozas, C., Roque-Malherbe, R.; Pérez-Pariente, J., Corma, A. (1989) Cyclization of citronellal to isopulegol by zeolite catalysis. *Appl. Catal.*, 47, 367 – 374.

Gallezot, P., Richard, D. (1998) Selective hydrogenation of α,β-unsaturated aldehydes. *Catal. Rev.*, 40, 81 – 126.

Galvagno, S., Milone, C., Donato, A., Neri, G., Pietropaolo, R. (1993) Influence of metal particle size in the hydrogenation of citral over Ru/C. *Catal. Lett.*, 18, 349 – 355.

Gliński, M.; Ulkowska, U. (2011) Reactivity of alcohols in chemoselective transfer hydrogenation of acrolein over magnesium oxide as the catalyst. *Catal. Lett.*, 141, 293 – 299.

Grau, R.J., Zgolicz, P.D., Gutiérrez, C., Taher, H.A. (1999) Liquid phase hydrogenation, isomerisation and dehydrogenation of limonene and derivatives with supported palladium catalysts. *J. Mol. Catal. A-Chem.*, 148, 203 – 214.

Gupta, S.K., Lesslie, R.D., King, A.D. (1973) Solubility of alcohols in compressed gases. A comparison of vapour-phase interactions of alcohols and homomorphic compounds with various gases. I. ethanol in compressed helium, hydrogen, argon, methane, ethylene, ethane, carbon dioxide, and nitrous oxide. *J. Phys. Chem.*, 77, 2011 – 2015.

Hájek, J., Kumar, N., Mäki-Arvela, P., Salmi, T. and Murzin, D.Y. (2004) Selective hydrogenation of cinnamaldehyde over Ru/Y zeolite. *J. Mol. Catal. A-Chem.*, 217, 145 – 154.

Haubrich, J., Loffreda, D., Delbecq, F., Sautet, P., Krupski, A., Becker, C., Wandet, K. (2009) Adsorption of α,β-unsaturated aldehydes on Pt(111) and Pt-Sn alloys: II. Crotonaldehyde. *J. Phys. Chem. C*, 113, 13947 – 13967.

Hichri, H., Accary, A., Puaux, J.P., Andrieu, J. (1992) Gas-liquid mass-transfer coefficients in a slurry batch reactor equipped with a self-gas-inducing agitator. *Ind. Eng. Chem. Res.*, 31, 1864 – 1867.

Houzvicka, J., Pestman, R., Ponec, V. (1995) The role of carbonaceous deposits and support impurities in the selective hydrogenation of ethyne. *Catal. Lett.*, 30, 289 – 296.

Hubaut, R. (1992) Study of the competitive reactions between an α,β-unsaturated aldehyde and allylic alcohol on a copper chromite catalyst. *React. Kinet. Catal. Lett.*, 46, 25 – 32.

Hunter, G.L.K., Brodgen, W.B. (1963) Isomerization and disproportionation of *d*-limonene on silica gel. *J. Org. Chem.*, 28, 1679 – 1682.

Katayama, T., Nitta, T. (1976) Solubilities of hydrogen and nitrogen in alcohols and *n*-hexane. *J. Chem. Eng. Data*, 21, 194 – 196.

Keresszegi, C., Bürgi, T., Mallat, T., Baiker, A. (2002) On the role of oxygen in the liquid-phase aerobic oxidation of alcohols on palladium. *J. Catal.*, 211, 244 – 251.

Kouachi, K., Lafaye, G., Especel, C., Cherifi, O., Marécot, P. (2008) Effects of support and metal loading on the characteristics of Co based catalysts for selective hydrogenation of citral. *J. Mol. Catal. A-Chem.*, 280, 52 – 60.

Kropp, P.J., Breton, G.W., Craig, S.L., Crawford, S.D., Durland, W.F., Jones, J.E., Raleigh, J.S. (1995) Surface-mediated reactions. 6. Effects of silica gel and alumina on acid-catalyzed reactions. *J. Org. Chem.*, 60, 4146 – 4152.

Lesage, P., Candy, J.P., Hirigoyen, C., Humblot, F., Basset, J.M. (1996) Selective dehydrogenation of dipentene (R-(+)-limonene into paracymene on silica supported palladium assisted by α-olefins as hydrogen acceptor. *J. Mol. Catal. A-Chem.*, 112, 431 – 435.

Liu, R., Wang, Y., Cheng, H., Yu, Y., Zhao, F., Arai, M. (2013) Reduction of citral in water under typical transfer hydrogenation conditions-Reaction mechanisms with evolution of and hydrogenation by molecular hydrogen. *J. Mol. Catal. A-Chem.*, 366, 315 – 320.

Luo, S., Falconer, J.L. (1999) Aldol condensation of acetaldehyde to form high molecular weight compounds on TiO2. *Catal. Lett.*, 57, 89 – 93.

Mäki-Arvela, P., Hájek, J., Salmi, T., Murzin, D.Y. (2005a) Chemoselective hydrogenation of carbonyl compounds over heterogeneous catalysts. *Appl. Catal. A-Gen.*, 292, 1 -49.

Mäki-Arvela, P, Kumar, N., Eränen, K., Salmi, T., Murzin, D.Y. (2006) Inverse temperatura dependence due to catalyst deactivation in liquid-phase citral hydrogenation over Pt/Al_2O_3. *Chem. Eng. J.*, 122, 127 – 134

Mäki-Arvela, P., Kumar, Nasir, A., Salmi, T., Murzin, D.Y. (2005b) Selectivity enhancement by catalyst deactivation in three-phase hydrogenation of nerol. *Ing. Eng. Chem. Res.*, 44, 9376 – 9383.

Mäki-Arvela, P., Kumar, N., Paseka, I., Salmi, T., Murzin, D.Y. (2004) Support effects in nerol hydrogenation over Pt/SiO_2, Pt/H-Y and Pt/H-MCM-41 catalysts. *Catal. Lett.*, 98, 173 - 179.

Mäki-Arvela, P., Tiainen, L-P., Neyestanaki, A.K., Sjöholm, R., Rantakyla, T-K., Laine, E., Salmi, T., Murzin, D.Y. (2002) Liquid phase hydrogenation of citral: suppression of side reactions. *Appl. Catal. A-Gen*., 237, 181 – 200.

Malinowski, A., Łomot, D., Karpiński, Z. (1998) Hydrodechlorination of CH_2Cl_2 over Pd/γ-Al_2O_3. Correlation with the hydrodechlorination of CCl_2F_2 (CFC-12). *Appl. Catal. B-Environ.*, 19, L79 – L86.

Markus, H., Plomp, A.J., Mäki-Arvela, P., Bitter, J.H., Murzin, D.Y. (2007) The influence of acidity of carbon nanofibre-supported palladium catalysts in the hydrogenolysis of hydroxylmatairesinol. *Catal. Lett.*, 113, 141 – 146.

McGregor, J., Canning, A.S., Mitchell, S., Jackson, S.D., Gladden, L.F. (2010) The influence of carbon laydown on selectivity in the hydrogenation of pentenenitriles over supported-nickel catalysts. *Appl. Catal. A-Gen.*, 384, 192 – 200.

Mercadante, L., Neri, G., Milone, C., Donato, A., Galvagno, S. (1996) Hydrogenation of α,β-unsaturated aldehydes over Ru/Al2O3 catalysts. *J. Mol. Catal. A-Chem*, 105, 93 – 101.

Milone, C.; Gangemi, C.; Ingoglia, R.; Neri, G.; Galvagno, S. (1999) Role of the support in the hydrogenation of citronellal on ruthenium catalysts. *Appl. Catal. A-Gen.*, 184, 89 – 94.

Mizugaki, T.; Kanayama, Y.; Ebitani, K.; Kaneda, K. (1998) Chemoselective transfer hydrogenation of α,β-unsaturated aldehydes to allylic alcohols using formic acid catalysed by polymer-bound Rh carbonyl clusters. *J. Org. Chem.*, 63, 2378 – 2381.

Mounzer, H.N., Wood, J., Stitt, E.H. (2010) Heterogeneous oxidation of 2-octanol on 5 wt%Pt – 1 wt%Bi/Carbon catalyst. *Chem. Eng. Sci.*, 65, 179 – 185.

Mukherjee, S., Vannice, M.A. (2006) Solvent effects in liquid-phase reactions I. Activiy and selectivity during citral hydrogenation on Pt/SiO_2 and evaluation of mass transfer effects. *J. Catal.* 243, 108 – 130.

Nagai, K. (1974) Ether formation from l-Isopulegol in the presence of boron trifluoride etherate. *J. Sci. Hiroshima. Univ. A*., 38, 141 – 150.

Neri, G., Bonaccorsi, L., Mercadante, L., Galvagno, S. (1997) Kinetic analysis of cinnamaldehyde hydrogenation over alumina-supported ruthenium catalysts. *Ind. Eng. Chem. Res.*, 36, 3554 – 3562.

Nonneman, L.E.Y.; Bastein, A.G.T.M.; Ponec, V. (1990) Role of impurities in the enhancement of C_2-oxygenates activity. *Appl. Catal.*, 62, L23 – L28.

Ohtaka, A., Kono, Y., Inui, S., Yamamoto, S., Ushiyama, S., Ushiyama, T., Shimomura, O., Nomura, R. (2012) Linear polystyrene-stabilized Pt nanoparticles for aerobic alcohol oxidation and hydrogen transfer reduction in aqueous media. *J. Mol. Catal. A-Chem.*, 360, 48 – 53.

Peña, J., Moro, R.F., Basabe, P., Marcos, I.S., Díez, D. (2012) Solvent free L-proline-catalysed domino Knoevenagel/6π-electrocyclization for the synthesis of highly functionalised 2*H*-pyrans, *RSC Adv.*, 2, 8041 – 8049.

Perry, R.H., Green, D.W. (1999) *Perry's Chemical Engineers' Handbook*. McGraw-Hill, pp. 121 – 130.

Poltarzewski, Z., Galvagno, S., Pietropaolo, R., Staiti, P. (1986) Hydrogenation of α,β-unsaturated aldehydes over Pt-Sn/Nylon, *J. Catal.*, 102, 190 – 198.

Reichardt, C. (1994) Solvatochromic dyes as solvent polarity indicators. *Chem. Rev.*, 94, 2319 – 2358.

Rojas, H.; Borda, G.; Martínez, J.J.; Valencia, J.; Reyes, P. (2008) Liquid-phase hydrogenation of citral and intermediaries $Ir/TiO_2/SiO_2$. *J. Mol. Catal. A-Chem.*, 286, 70 – 78.

Rojas, H.; Díaz, G.; Martínez, J.J.; Castañeda, C.; Gómez-Cortés, A.; Arenas-Alatorre, J. (2012) Hydrogenation of α,β-unsaturated carbonyl compounds over Au and Ir supported on SiO_2. *J. Mol. Catal. A-Chem.*, 363 – 364, 122 – 128.

Ruppert, A.M., Parvulesco, A.N., Arias, M., Hausoul, P.J.C., Bruijnincx, P.C.A., Klein Gebbink, R.J.M., Weckhuysen, B.M. (2009) Synthesis of long alkyl chain ethers through direct etherification of biomass-based alcohols with 1-octene over heterogeneous acid catalysts. *J. Catal.*, 268, 251 – 259.

Santori, G.F., Casella, M.L., Ferretti, O.A. (2002) Hydrogenation of carbonyl compounds using tin-modified platinum-based catalysts prepared *via* surface organometallic chemistry on metals (SOMC/M). *J. Mol. Catal. A-Chem.*, 186, 223 – 239.

Siani, A., Alexeev, O.S., Lafaye, G., Amiridis, M.D. (2009) The effect of Fe on SiO_2-supported Pt catalysts: structure, chemisorptive, and catalytic properties. *J. Catal.*, 266, 26 – 38.

Siedenburg, G., Jendrossek, D., Breuer, M., Juhl, B., Pleiss, J., Seitz, M., Klebensberger, J., Hauer, B. (2012) Activation-independent cyclization of monoterpenoids. *Appl. Environ. Microbiol.*, 78, 1055 – 1062.

Singh, U.K., Vannice, M.A. (1999) Kinetic and thermodynamic analysis of liquid-phase benzene hydrogenation. *AIChE Journal*, 45, 1059 – 1071.

Singh, U.K., Sysak, M.N., Vannice, M.A. (2000) Liquid-phase hydrogenation of citral over Pt/SiO_2 catalysts. II. Hydrogenation of reaction intermediate compounds. *J. Catal.*, 191, 181 – 191.

Singh, U.K., Vannice, M.A. (2000a) Liquid-phase hydrogenation of citral over Pt/SiO_2 catalysts. I. Temperature effects on activity and selectivity. *J. Catal.*, 191, 165 – 180.

Singh, U.K., Vannice, M.A. (2000b) Influence of metal-support interactions on the kinetics of liquid-phase citral hydrogenation. *J. Mol. Catal. A-Gen.*, 163, 233 – 250.

Spenadel, L., Boudart, M. (1960) Dispersion of platinum on supported catalysts. *J. Phys. Chem.*, 64, 204 – 207.

Stassi, J.P.; Zgolicz, P.D.; de Miguel, S.R.; Scelza, O.A. (2013) Formation of different promoted metallic phases in PtFe and PtSn catalysts supported on carbonaceous materials used for selective hydrogenation. *J. Catal.*, 306, 11 – 29.

Szöllösi, G., Bartók, M. (1999) Catalytic transfer hydrogenation of 2-butanone on MgO. New active surface sites generated by treatment with chloroform. *Catal. Lett.*, 59, 179 – 185.

Trasarti, A.F., Bertero, N.M., Apesteguía, C.R., Marchi, A.J. (2014) Liquid-phase hydrogenation of acetophenone over silica-supported Ni, Co and Cu catalysts: influence of metal and solvent. *Appl. Catal. A-Chem.*, 474, 282 – 291.

Trasarti, A.F., Marchi, A.J., Apesteguía, C.R. (2007) Design of catalyst systems for the one-pot synthesis of menthols from citral. *J. Catal.*, 247, 155 – 165.

Trasarti, A.F., Marchi, A.J., Apesteguía, C.R. (2013) Synthesis of menthols from citral on Ni/SiO_2-Al_2O_3 catalysts. *Catal. Comm.*, 32, 62 – 66.

Vaidya, P.D., Mahajani, V.V. (2003) Kinetics of liquid-phase hydrogenation of furfuraldehyde to furfuryl alcohol over a Pt/C catalyst. *Ind. Eng. Chem. Res.*, 42, 3881 – 3885.

Vandichel, M., Vermoortele, F., Cottenie, S., De Vis, D.E., Waroquier, M., Van Speybroeck, V. (2013) Insight in the activity and diastereoselectivity of various Lewis acid catalysts for the citronellal cyclization. *J. Catal.*, 305, 118 – 129.

Wan, H., Vitter, A., Chaudhari, B.V., Subramaniam, B. (2014) Kinetic investigations of unusual solvent effects during Ru/C catalyzed hydrogenation of model oxygenates. *J. Catal.*, 309, 174 – 184.

Wismeijer, A., Kieboom, A., Van Bekkum, H. (1986) Selective hydrogenation of citronellal over Ru/TiO_2 as compared to Ru/SiO_2. *Appl. Catal.*, 25, 181 – 189.

Young, C.L. (ed.), Battino, R., Clever, L., Wiesenburg, D.A., Cargill, R.W., Cramer, A.L., Derrick, M.E., Gjaldbaek, J.C., Johnson, S.A., Long, P.L., Thomsen, E.S., Thornhill, D.G.T., Wilhelm, E. (1981) *Hydrogen and deuterium*. Solubility data series, vol. 3. Oxford. Pergamon Press.

Zgolicz, P.D.; Stassi, J.P.; Yañez, M.J.; Scelza, O.A., de Miguel, S.R. (2012) Influence of the support and the preparation methods on the performance in citral hydrogenation of Pt-based catalysts supported on carbon nanotubes. *J. Catal.*, 290, 37 – 54.

Chapter 8:

Characterisation of solvent effects in the selective hydrogenation of citral

8 Characterisation of solvent effects in the selective hydrogenation of citral

In chapter 7, a detailed study on the liquid-phase hydrogenation of citral was performed using a range of solvents on 5% Pt/SiO_2 at two temperatures, 298 and 373 K, under the same reaction conditions. Herein, we use citral as a model molecule to understand reactant-products-solvent competitive adsorption effects. A detailed study of such effects in hexane and ethanol is presented. These solvents were selected due to their dissimilarities in reactivity and selectivity and served as models for the range of results observed. Useful insights on the role of solvent determining the reactivity of citral and selectivity towards different reaction pathways will be provided. Adsorption studies – liquid isotherms, TEOM and DRIFTS – as well as ATR-IR studies on solvent-reactant interactions were performed to determine the extent of such interactions and unravel the role of solvent in the kinetics observed. Other effects, such as the initial reactant concentration, as well as the influence of support were studied. The aim of this work is to study the effect of solvent in a complex reaction network to understand the role of liquid-liquid interactions and catalyst-liquid interactions in the rate of reaction, selectivity and catalyst deactivation.

8.1 Experimental materials and methods

In this section, a review of the materials, including the procedure regarding the modification of the catalyst, is summarised in section 8.1.1, while complementary hydrogenation reactions are presented in section 8.1.2. The different characterisation techniques employed in order to gain an understanding on the effect of solvent in this study are presented in section 8.1.3.

8.1.1 Materials

5 wt% Pt/SiO_2 was provided by Johnson Matthey and was used as received. Textural properties and metal dispersion were presented in section 7.1.1. Details on reaction species used in this chapter, solvents and gases have also been provided in section 7.1.1.

8.1.1.1 Modification of the support: silylation

The hydrophilic-hydrophobic character of the support and the interactions of the catalyst with solvent and reaction species were investigated by means of sylilation of the SiO_2 support. Additional hydrogenation studies on such modified catalyst provided complementary information to understand the origins of the observed solvent effect. Approximately 1 g of the 5% Pt/SiO_2 catalyst was treated with triethoxyoctylsilane (Sigma Aldrich, > 97.5%)

following previous procedures (Blitz *et al.*, 1988; Weber *et al.*, 2010) to functionalise hydroxyl groups on the surface. The catalyst was mixed with 440 mg of the silane in 25 ml of toluene for 2 h under sonication at 323 K. The resulting sample was filtered, washed three times with toluene and dried in a vacuum oven (Fistreem Gallenkamp) at 393 K for 4 h. Silylation of the silica was confirmed *via* DRIFTS measurements. BET surface area was 317 $m^2\ g^{-1}$ and BJH pore volume was 1.3 $cm^3\ g^{-1}$ with 13 nm pore diameter.

8.1.2 Reaction studies

Hydrogenation of citral was performed in a 300 ml pressurised reactor (details have been presented in section 7.1.2.1). In order to study the effects of surface modification and initial citral concentration, the following reactions in hexane and ethanol were carried out: i) silylated catalyst with citral concentration of $c_0 = 0.13$ M; ii) standard 5% Pt/SiO_2 catalyst with an initial citral concentration of $c_0 = 0.33$ M maintaining the same reactant to catalyst ratio. The temperature was set to 373 K and the total pressure was maintained at 10 bar(g).

8.1.3 Characterisation techniques

8.1.3.1 Infrared spectroscopy

In-situ DRIFTS measurements on the adsorption of citral solutions (0.13 M) in ethanol and hexane were carried out at 373 K on pre-reduced 5% Pt/SiO_2 catalyst in a reaction chamber (Praying Mantis, Harrick) on a Nicolet 380 Avatar FTIR (Thermo Scientific). Reduction was carried out at 403 K for 1 h, with 40 $cm^3\ min^{-1}$ H_2 flow. Injection of citral solutions was carried out using a high-pressure liquid pump (LC-10AD VP, Shimadzu). A continuous flow of 0.08 $cm^3\ min^{-1}$ of the solution was injected into the reaction chamber, in addition to 40 $cm^3\ min^{-1}$ H_2 flow. Inlet and outlet lines were pre-heated to 393 K to maintain the flow compositions, vaporise the liquids and avoid the accumulation of any excess citral. After 6 h, the inlet flow was switched to He for 5 h to determine the remaining species present. Additionally, the adsorption of pure solvents at 293 K on the catalyst was monitored after injection of 5 μL of the liquid, following same pre-treatment conditions. A spectral resolution of 4 cm^{-1} was achieved with a DTGS-KBr detector; 256 scans were acquired. KBr was used as the spectral background.

Attenuated Total Reflectance Infrared (ATR-IR) measurements of citral-solvent binary liquid mixtures were conducted using a single reflection Smart Golden Gate accessory (Golden Gate, Specac) fitted with ZnSe lenses. Spectra were recorded in the range 4000 – 600 cm^{-1}

with a resolution of 1 cm^{-1}. The clean crystal was used as a reference spectrum. Binary mixtures of citral in methanol, ethanol, 2-propanol, 1-pentanol and acetone of 5, 10, 15 and 20% mol citral were measured in all cases. In addition, solutions with higher citral concentration were also studied for a subset of solvents. Spectra were compared with those of the pure liquids.

8.1.3.2 Adsorption isotherms

Adsorption isotherms were obtained using the batch adsorption technique or static method (Alwary *et al.*, 2011; Derylo-Marczewska *et al.*, 2011; Remy *et al.*, 2011) at four different temperatures: 298 K, 323 K, 348 K and 373 K. Citral solutions in hexane and ethanol were prepared. A series of 5 ml thread capped vials (Soham Scientific), each containing 2 ml of the prepared solution of different adsorbate concentrations, were prepared. Thus, 25 – 300 mg of pre-reduced 5% Pt/SiO_2 catalyst were added to 0.1 – 20 mM solutions. 50 mM and 100 mM hexane-citral mixtures were also prepared. Solutions were placed in an oven (T6060, Thermo Scientific) and kept for 12 h at the desired temperature, after which the solution was separated from the catalyst under centrifugation (minor S, MSE). The amount adsorbed was calculated by the different concentrations of citral present in solution before and after adsorption, measured *via* GC (6890, Hewlett-Packard; same conditions as per hydrogenation analysis).

8.1.3.3 TEOM

Mass uptake data were recorded using a Tapered Element Oscillating Microbalance (TEOM) (Rupprecht & Patashnick, R&P). Process conditions and data storage were controlled using Labview software. Mass data were acquired every 0.1 s. Results are shown at 10 s intervals, unless desorption dynamics are analysed, in which case the resolution is 1 s. Adsorption of citral and main intermediates of reaction, citronellal, citronellol, and an equimolar mixture of geraniol and nerol, was carried out at 373 K on pre-reduced 5% Pt/SiO_2 catalyst. Approximately 15 mg of 5% Pt/SiO_2 catalyst were pre-heated to 423 K in 50 $cm^3\ min^{-1}$ of H_2 for 1 h. Helium was used both as carrier gas for the adsorbates and purge gas for the TEOM at a flow rate of 50 $cm^3\ min^{-1}$. The adsorbate was placed in a saturator at 353 K, equivalent to vapour pressures of 3.9, 10.4, 3.1 and 2.6 mbar of citral, citronellal, citronellol and geraniol, respectively (Perry and Green, 1999). All stainless steel lines were heated to 423 K to prevent condensation. Pulse adsorption experiments were performed *via* a pneumatic actuated six-way valve (Valco Instruments). The amount of vapourised adsorbate as well as effluent

after adsorption were monitored *via* GC (6890 Hewlett Packard, splitless mode). Blank measurements were performed using sand (Sigma Aldrich). However, data were not subtracted from the samples, as negligible signal change occurred.

8.1.3.4 Temperature Programmed Studies (TPD/TPO)

Approximately 50 mg of spent catalyst were added into the microreactor described in section 2.2.1.2. Desorption of physisorbed species was achieved with a flow of He at 40 cm^3 min^{-1} for 1 h at 373 K. The samples were heated from 373 K to 1073 K with a ramp rate of 10 K min^{-1} at a flow rate of 40 cm^3 min^{-1} (He was used for TPD experiments, while 5% vol. O_2 in He was used during TPO experiments). An SEM detector was used to record the spectra of the desorbed species, set for m/z = 2 to 100. Particular attention was given to m/z = 28 for CO, m/z = 44 for CO_2, and m/z = 18 for water. m/z = 32 was followed to detect possible oxygenate species during TPD, and O_2 consumption during TPO. The solvents used, hexane and ethanol, were also detected during TPD, following m/z = 31 and 57 for ethanol and hexane, respectively.

8.2 Results

Citral hydrogenation rates and selectivities on 5% Pt/SiO_2 were obtained for a range of solvents, and the results were presented in **Tables 7.1** and **7.2**. These results showed the ability to tailor selectivity, among others, by careful solvent selection. In order to exploit these findings, it was necessary to understand the origin of such effects. In section 8.2.1, liquid-liquid interactions were considered. Interactions between citral and the solvent were studied using ATR-IR. Catalyst-liquid interactions will also play a significant role in the results observed. For example, competitive adsorption could play a role in determining the overall kinetics. Liquid adsorption isotherms, TEOM and DRIFTS were used in section 8.2.2 to elucidate the influence of such interactions with the catalyst. Moreover, in section 8.2.3, modifications of initial reactant concentration and silylation of the catalyst were conducted to investigate the dependence of such factors in the role of solvent.

8.2.1 Liquid-liquid interactions

As noted in the hydrogenation results, notable differences were observed in the selectivity towards geraniol and nerol with alcohols when compared to other solvents, especially at 298 K. In order to understand the origin of solvent effects, a study on the interactions taking place on the liquid phase was performed. IR spectroscopy was used in citral-solvent binary

mixtures to show if there were any interactions present that would enhance alcohol formation. Solvents examined included those where strong interaction with the reactant would be likely. A series of alcohol solvents as well as acetone were studied.

ATR-IR spectroscopy experiments were conducted on increasing citral concentration binary citral-solvent mixtures. Previous studies have looked at liquid-liquid interactions using novel methods (Li *et al.*, 2014), but also employing infrared-based techniques (Wan *et al.*, 2014; Ahmed *et al.*, 2012; Burikov *et al.*, 2012; Unger *et al.*, 2011; Hu *et al.*, 2010; Max *et al.*, 2002). **Figures 8.1** and **8.2** show the results on the ATR spectra for acetone-citral, methanol-citral, ethanol-citral and 2-propanol-citral binary mixtures. Changes in the IR bands indicative of interactions between solvent and citral functional groups – double-bond or aldehyde – in these binary systems were studied. As observed in **Figure 8.1A**, **8.1B** and **8.1C**, increasing the concentration of citral in alcohols resulted in a blue shift of the *ν*(OH), in the range 3310 cm^{-1} – 3330 cm^{-1}, to higher wavenumbers. This broad band corresponded to hydrogen-bonded hydroxyls from the solvent. A weak shift in the *ν*(C-O) band of methanol and ethanol in binary mixtures was also observed in **Figure 8.2**. Two bands were observed in ethanol in this region, as reported previously (Ahmed *et al.*, 2012). A red shift from 1023 cm^{-1} in pure methanol to 1026 cm^{-1} in 20% mol citral-methanol was noted. In contrast, a weaker red shift was observed in ethanol, from 1045 cm^{-1} in pure ethanol to 1047 cm^{-1} in 10% citral-ethanol to 1046 cm^{-1} in 20% citral-ethanol mixtures. Examination of the *ν*(C=O) band of citral at 1673 cm^{-1} revealed a second red shifted peak towards 1661 – 1665 cm^{-1} in all citral-alcohol mixtures (**Figure 8.1D** and **8.1E**). In comparison, the spectra of citral-acetone mixtures in **Figure 8.1F** showed no alteration of the conjugated C=O band at 1673 cm^{-1}, showing that these interactions were exclusive to polar protic solvents. Finally, bands at 2750 and 2715 cm^{-1}, corresponding to *ν*(C-H) at the aldehyde carbon appeared already at concentrations as low as 10% mol citral in acetone, whereas those bands were not visible until 50% mol citral in 2-propanol or 30% mol citral in 1-pentanol (not shown).

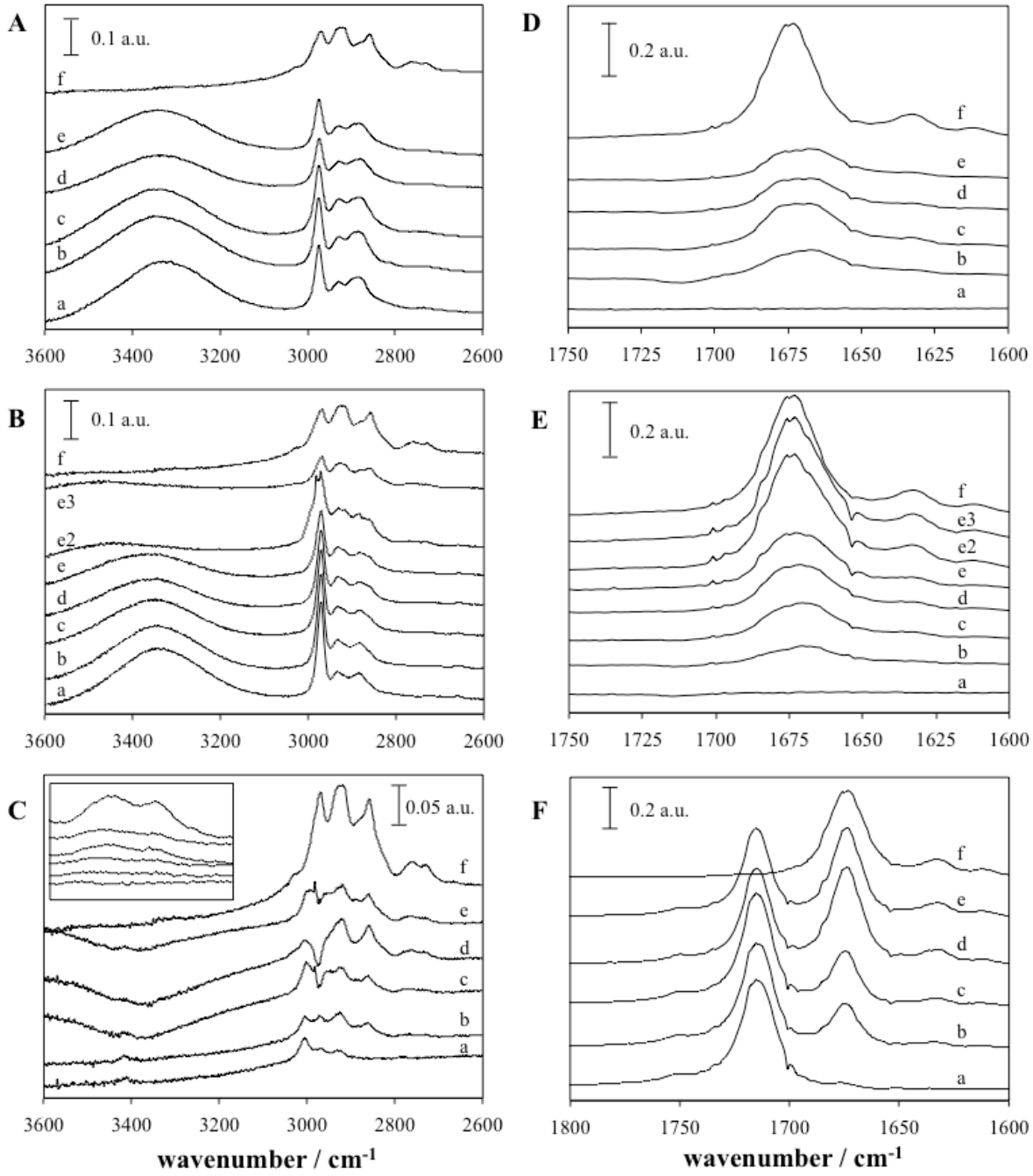

Figure 8.1. ATR-IR results on bulk citral-solvent binary mixtures in the regions 3600 – 2600 cm^{-1} (left), and 1800 – 1600 cm^{-1} (right). Citral / ethanol (A and D), citral / 2-propanol (B and E), and citral / acetone (C and F) binaries are shown. Concentration of citral increases on each figure from a) (solvent only) to f) (citral only) in the order: b) 5% mol, c) 10% mol, d) 15% mol, e) 20% mol, e2) 50% mol, e3) 70% mol. Inset in C shows the region 2800 – 2670 cm^{-1} for acetone.

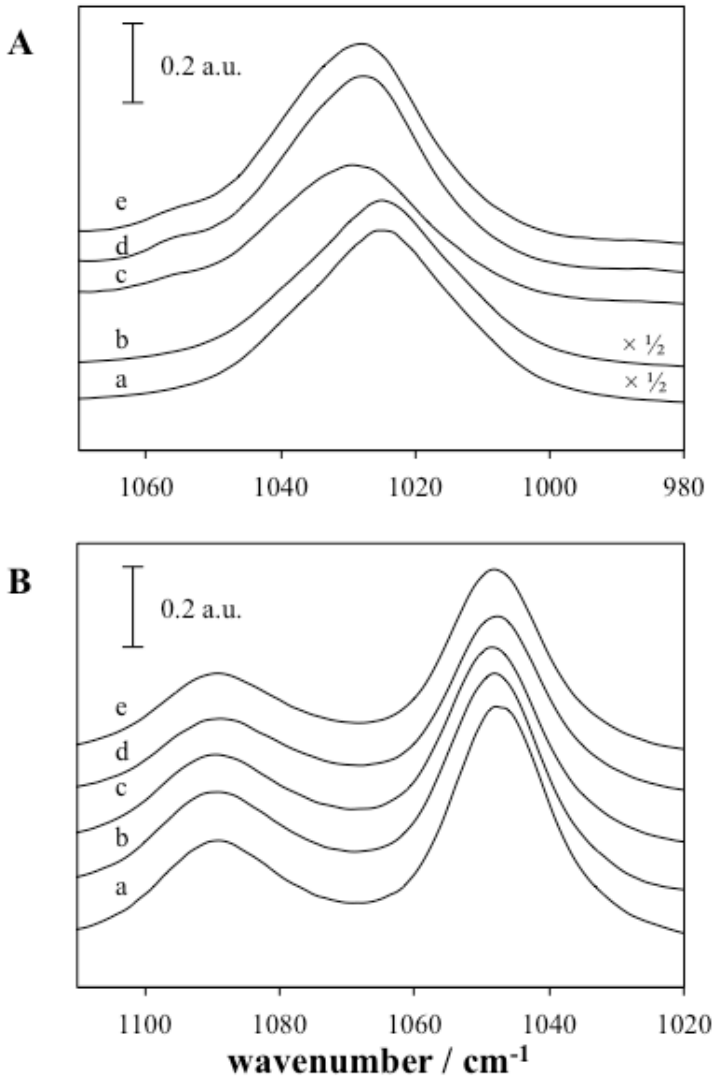

Figure 8.2. ATR-IR results on bulk citral-solvent binary mixtures in the region 1120 – 980 cm^{-1}. Citral-methanol (A), and citral-ethanol (B) binaries are shown. Concentration of citral increases on each figure following: a) 0% mol citral (solvent only), b) 5% mol, c) 10% mol, d) 15% mol, to e) 20% mol citral.

A number of studies of liquid mixtures have observed similar shifts in the bands described earlier. The blue shift of the *v*(OH) has been previously attributed to a significant weakening in the hydrogen bonds present in the mixture (Unger *et al.*, 2011; Burikov *et al.*, 2012). In agreement with those studies, it can be inferred that weaker interactions between citral-alcohol as compared to those in pure alcohol-alcohol systems were present. In addition, *v*(C-O) shifts were reported in a previous study in ethanol-water and methanol-water mixtures (Ahmed *et al.*, 2012) as a probe of hydrogen bonding. In their study, Ahmed *et al.* (2012) observed a blue shift in *v*(C-O) for the alcohol, possibly due to the net donation of water and

the acceptor character of the alcohol in those hydrogen bonds. In contrast, in this work, a red shift was observed for this band, in line with an expected donating contribution of the alcohols toward the conjugated carbonyl bond of citral. Thus, the presence of two bands corresponding to *v*(C=O) confirmed the acceptor character of the carbonyl bond. This observation has been previously noted in other carbonyl systems mixed with alcohol solvents (Liu *et al.*, 2007). In their work, the band appearing at lower frequency was ascribed to hydrogen bonding of free alcohol molecules with the carbonyl group. These results, in line with the behaviour of the *v*(C-H) at the aldehyde carbon in alcohol solvents *vs*. acetone confirmed a strong interaction with alcohols. Therefore, the presence of hydrogen bond interactions between the aldehyde group of citral and alcohol solvents was demonstrated, and it was stronger for shorter alcohol chains. These results were a strong indication of the effect of alcohol solvents in citral hydrogenation.

8.2.2 Interactions with the catalyst

In this section, a series of adsorption measurements were performed to determine the influence that catalyst-solvent-reactant interactions presented on the overall kinetics. Adsorption isotherms of citral in hexane and ethanol on 5% Pt/SiO_2 served to determine strength of interaction of citral on the catalyst as a function of solvent. In order to determine the influence of product adsorption in the overall catalyst performance, the adsorption of citral, citronellal, citronellol, geraniol and nerol was studied with the TEOM. Solvent adsorption on the catalyst was studied with DRIFTS. Complementary measurements using DRIFTS were performed on the adsorption of citral with and without solvent. In summary, the adsorption strength of citral and main intermediates of reaction on Pt/SiO_2 was measured in the presence of hexane and ethanol. Solvent adsorption measurements of hexane and ethanol with DRIFTS, and the influence of citral adsorption in both solvents provided information on the strength of solvent adsorption. Additionally, TPD and TPO measurements determined the remaining species adsorbed after reaction, in order to obtain a complete picture of the species strongly interacting with the catalyst. Overall, the various catalyst-adsorbate interactions were considered.

8.2.2.1 Liquid adsorption isotherms

The adsorption of citral on 5% Pt/SiO_2 catalysts was studied in the presence of hexane and ethanol. **Figure 8.3** presents the results on the uptake of citral on 5% Pt/SiO_2 in hexane and ethanol, respectively. Adsorption isotherms were obtained at 298, 323, 348 and 373 K, except for citral in hexane, where values at 373 K could not be obtained due to high reactivity of the adsorbate to C_{10} acyclic fragments. The experimental results were fitted to two adsorption isotherms, the Langmuir equation (equation 1.6), and the Langmuir-Freundlich equation (Sips, 1948), expressed as follows:

$$v = \frac{v_{sat}\left(k_{LF}c_e\right)^{n_{LF}}}{1+\left(k_{LF}c_e\right)^{n_{LF}}}. \qquad (8.1)$$

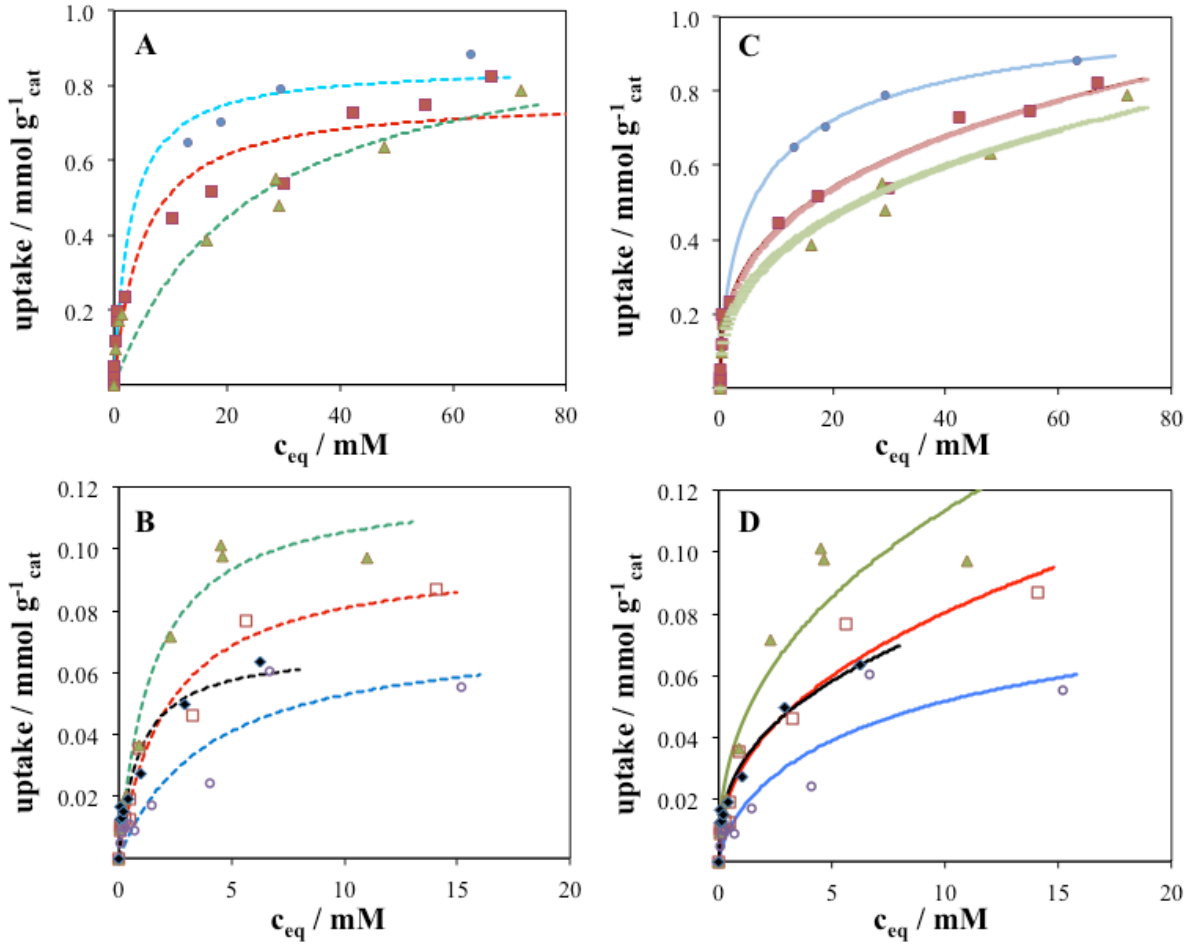

Figure 8.3. Adsorption isotherms for citral solutions in hexane (A and C) and ethanol (B and D), respectively, on pre-reduced 5% Pt/SiO_2 catalysts at 298 K (blue circle), 323 K (red square), 348 K (green triangle) and 373 K (black diamond). The dashed lines represent the Langmuir isotherm fit and the continuous lines the Langmuir-Freundlich fit to the experimental results.

Similarly to the Tóth equation (equation 1.7), v_{sat} is the saturation capacity, k_{LF} is the affinity or equilibrium constant and n_{LF} is the heterogeneity parameter (Haghseresht and Lu, 1998). Both the Langmuir isotherm equation (Almarri *et al.*, 2009; Haji and Erkey, 2003; Koizumi and Yoshitake, 2013; Samiey and Toosi, 2010; Somasundaram *et al.*, 2013; Wang *et al.*, 2013) and the Langmuir-Freundlich equation (Likozar *et al.*, 2012; Mohamed *et al.*, 2011; Wang *et al.*, 2012) have been previously used on adsorption of dissolved molecules with various functional groups in aqueous solvents on porous materials, hence the applicability in this system.

Adsorption of citral on the catalyst varied significantly with temperature and solvent, as seen in **Figure 8.3**. Comparing solvents, higher citral uptake values were observed in hexane as compared to ethanol at all temperatures. For the same citral concentration, uptake values decreased with increasing temperature in hexane, while they showed a maximum with temperature in ethanol. **Tables 8.1** and **8.2** show the fitted parameters for both the Langmuir and Langmuir-Freundlich equations, respectively. As seen in **Figure 8.3**, some of the fits fail to describe the final plateau or the initial uptake of the isotherm. However, the fits follow the overall trends with temperature and solvent, relevant for this study. Saturation capacity values varied significantly between both models, consistent with the observations of Choudary *et al.* (2002). The heterogeneity parameter n_{LF} showed values between 0.37 – 0.71, indicative of a strong heterogeneous material and the presence of lateral interactions. The dependence of n_{LF} with temperature was in agreement with previous descriptions in literature (Do, 1998). Considering the simplest model, v_{sat} values were in the range 0.77 – 0.99 mmol g^{-1}_{cat} in hexane. Simultaneously, there was a reduction in the affinity constant. Results in ethanol showed a maximum value of v_{sat} at 343 K, coinciding with a steady increase of the affinity constant k_L with increasing temperature. The enthalpies of adsorption at zero coverage were calculated applying the Van't Hoff equation (Ayanda *et al.*, 2013; Subra *et al.*, 1998). These values represent the adsorption of citral with the strongest sites of the catalyst. The calculation used the Henry constant of the linear adsorption regime (Rouquerol *et al.*, 1999), as described in section 4.3.2.1, hence only applicable with the Langmuir isotherm. Enthalpies of -34 ± 8 kJ mol^{-1} in hexane *vs.* 18 ± 5 kJ mol^{-1} in ethanol were obtained. Therefore, adsorption of citral was an exothermic process in hexane, while slightly endothermic in ethanol. Positive adsorption enthalpies have been reported previously, as a result of an endothermic process (Chen, 2010; Li *et al.*, 2005; McKay *et al.*, 1982). As can be seen, results indicated a favourable adsorption of citral on the catalyst in hexane. An indication of

an activated adsorption process was observed in ethanol, probably due to competitive adsorption caused by the presence of the alcohol.

Table 8.1. Langmuir isotherm constants for the adsorption of citral in the presence of a solvent on pre-reduced 5% Pt/SiO_2 catalyst.

solvent	T / K	v_{sat} / mmol g^{-1}_{cat}	k_L / mM^{-1}	R^2
hexane	298	0.86 ± 0.02	0.4 ± 0.1	0.991
	323	0.77 ± 0.03	0.2 ± 0.2	0.94
	348	0.99 ± 0.09	0.04 ± 0.06	0.90
ethanol	298	0.07 ± 0.01	0.3 ± 0.2	0.86
	323	0.10 ± 0.01	0.5 ± 0.2	0.95
	348	0.12 ± 0.01	0.7 ± 0.2	0.97
	373	0.07 ± 0.01	1.1 ± 0.5	0.89

Table 8.2. Langmuir-Freundlich isotherm constants for the adsorption of citral in the presence of a solvent on pre-reduced 5% Pt/SiO_2 catalyst.

solvent	T / K	v_{sat} / mmol g^{-1}_{cat}	$k_{LF} \times 10^2$ / mM^{-n}	n_{LF} / -	R^2
hexane	298	1.10 ± 0.04	13 ± 1	0.67 ± 0.02	0.9996
	323	6.0 ± 0.2	(10 ± 1) $\times 10^{-3}$	0.37 ± 0.01	0.990
	348	10.2 ± 0.4	(2.1 ± 0.2) $\times 10^{-3}$	0.39 ± 0.01	0.98
ethanol	298	0.11 ± 0.01	9 ± 2	0.71 ± 0.03	0.87
	323	1.9 ± 0.1	(8 ± 2) $\times 10^{-3}$	0.44 ± 0.02	0.95
	348	4.3 ± 0.3	(1.9 ± 0.4) $\times 10^{-3}$	0.42 ± 0.02	0.91
	373	2.4 ± 0.2	(1.6 ± 0.3) $\times 10^{-3}$	0.39 ± 0.02	0.97

8.2.2.2 TEOM and DRIFTS

Competitive adsorption between different reaction species as well as with the reactant and the solvent were also evaluated. Flow experiments comparing the adsorption of intermediates, as well as solvent interactions at reaction conditions were studied using TEOM and DRIFTS. Gas adsorption measurements of citral, citronellal, citronellol, and an equimolar mixture of geraniol and nerol were measured using TEOM and are shown in **Figure 8.4A**. As can be seen, all species showed similar uptake values, with citronellol and the unsaturated alcohols presenting higher saturation values, 880 μmol g^{-1}, as compared to citronellal and citral, 760 μmol g^{-1}. In addition to steady-state measurements, the time-resolved nature of the measurement allowed for the extraction of dynamic data. The following ratio was used for comparison of desorption dynamics:

$$normalised\ desorption\ uptake = \frac{M(t) - M_{eq}}{M_{sat} - M_{eq}} \quad (8.2)$$

where $M(t)$ denotes the recorded mass uptake at any point, M_{eq} is the mass uptake of adsorbate at equilibrium and M_{sat} is the saturated mass uptake of adsorbate during the injection pulse. In line with convention (Zhu *et al.*, 2004), only desorption data are considered for this analysis, as the dynamics of desorption are slower ($k_{ads} >> k_{des}$, in general) and can describe processes more accurately than adsorption data. Looking at the transient regime after the second pulse, shown in **Figure 8.4B**, citral and citronellal showed a faster desorption rate as compared to the unsaturated alcohols, geraniol, nerol and citronellol. Saturation values after desorption were also similar in all cases, indicating no major difference between the reaction species. Thus, 115 μmol g^{-1} of citral and 130 μmol g^{-1} of citronellol remained adsorbed after desorption. These values corresponded to 20% and 28% monolayer (ML) coverages, respectively, assuming an excluded area of 0.86 nm^2 of the adsorbents. In summary, TEOM results showed similar uptake values for citral and main intermediates of reaction in the absence of solvent. Inferior desorption rates for unsaturated alcohols might be indicative of a preferred interaction with the catalyst surface. Such information will be re-examined in section 8.3.2.1 and in chapter 9.

DRIFTS measurements were carried out on citral adsorption and reaction in the presence of hexane and ethanol to determine the extent of solvent-catalyst and reactant-catalyst interactions. **Figure 8.5A** (a-e) shows the subtracted spectra of a catalyst exposed i) to pure citral (a), and ii) reaction mixtures of citral-hexane (d-e) and citral-ethanol (b-c) in H_2. The spectra of ii) with both solvents revealed a number of similarities. The negative band at 3731 cm^{-1} and the appearance of a broad band at 3300 – 3200 cm^{-1} indicated the disappearance of the silanol OH and the presence of H-bond interactions between citral and SiO_2, in agreement with the assignment of Waghray and Blackmond (1993). In addition, $\nu(CH_3)$ and $\nu(CH_2)$ bands were present at 2987 cm^{-1}, 2925 cm^{-1} and 2873 cm^{-1} in hexane, and at 2962 cm^{-1}, 2921 cm^{-1}, and 2892 cm^{-1} in ethanol, characteristic of the solvents (Ahmed *et al.*, 2012; Max and Chapados, 2007). Such solvent peaks were superimposed to the bands associated to citral. Spectra for ii) recorded after 5 h of purging (c, e), showed new $\nu(CH_3)$ and $\nu(CH_2)$ bands at 2987 cm^{-1}, 2917 cm^{-1}, and 2856 cm^{-1}, matching those of citral. The presence of the citral bands after the disappearance of the solvent bands was indicative of the stronger interaction of citral in both systems. A shoulder around 3015 cm^{-1}, assigned to

v(=CH), in agreement with Dandekar and Vannice (1999) and Shahid and Sheppard (1994), and a band at 2720 cm^{-1}, assigned to *v*(C-H) of the aldehyde carbon, following assignment of Nishiyama *et al.* (1999) and Williams and Fleming (1997) were indicative of adsorbed citral. Moreover, *v*(C=O) bands at 1660 cm^{-1} and 1646 cm^{-1} indicated the interaction of the carbonyl with the catalyst, as previously reported by Burgener *et al.* (2004) and Coloma *et al.* (2000). These bands were tentatively assigned to interaction with the support and metal, respectively. Hence, solvent was observed to influence the extent of adsorption of citral, and when removed, citral adsorption was favoured.

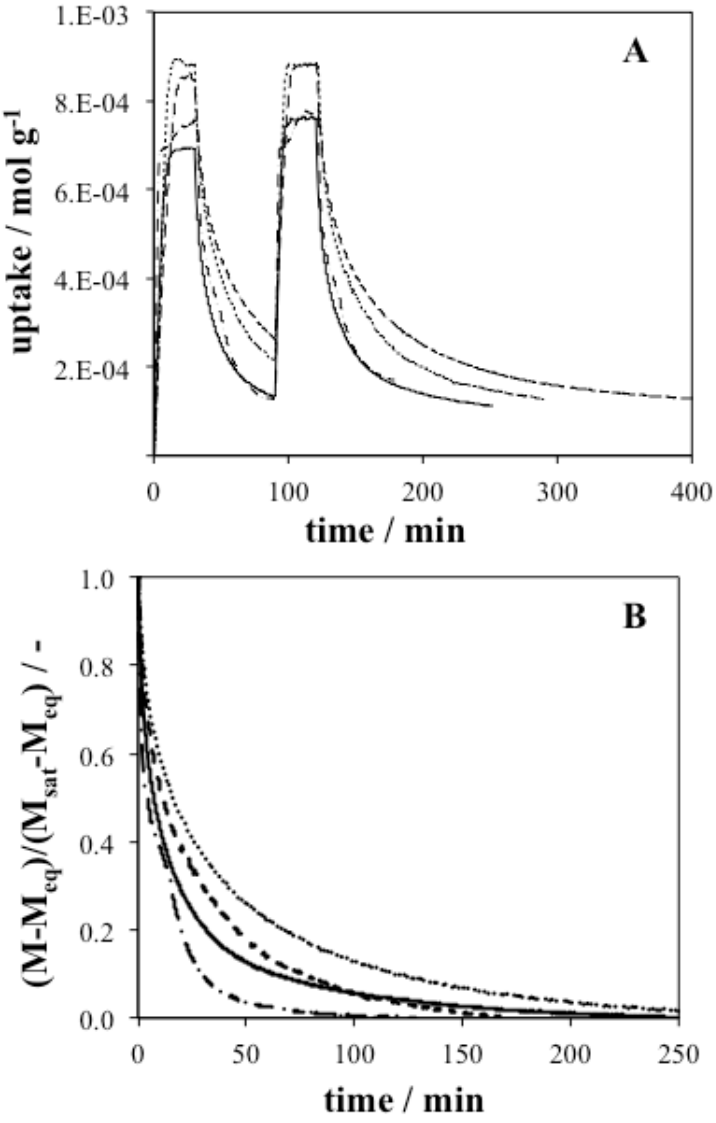

Figure 8.4. (A) Mass uptake during the adsorption of citral (-), citronellal (-.-), citronellol (--) and an equimolar mixture of geraniol and nerol (…) at 373 K on pre-reduced 5 % Pt/SiO_2 catalyst. Two 30 min pulses were injected followed by 60 min desorption time. (B) Mass uptake during the desorption after the last injection pulse of citral, citronellal, citronellol and an equimolar mixture of geraniol and nerol.

Formation of other species was also noted. Bands at 2046 cm^{-1} and 1841 cm^{-1} on ii) (b-e) indicated the presence of on-top and bridged CO adsorbed on Pt, respectively. The appearance of CO on the catalyst in α,β-unsaturated carbonyl molecules has been previously described as cause of catalyst deactivation (Burgener *et al.*, 2004; Englisch *et al.*, 1997a, Dandekar and Vannice, 1999; Waghray and Blackmond, 1993). *v*(C=O) bands at 1734 cm^{-1} have been reported for adsorbed citronellal or dihydrocitronellal. A small shoulder at 1595 – 1589 cm^{-1}, assigned to *v*(C=C) interacting with the metal, indicated dehydrogenated carbon residues were formed, in connection with previous work (Shahid and Sheppard, 1994). A band at 1438 cm^{-1}, present in both purged catalysts, was previously assigned to CH_3 deformations of hydrocarbons perturbed by hydrogen bonding with the support (Dandekar and Vannice, 1999). A broad band at 1259 cm^{-1}, present in catalyst used with ethanol, was attributed to long organic species or oxygenates. Such assignment was in line with results from previous studies (Englisch *et al.*, 1997a; Dandekar and Vannice, 1999), and also related to the proximity of *v*(C-C) and *v*(C-O) bands (Williams and Fleming, 1997). In addition a wide band at 1070 – 1010 cm^{-1}, present in ethanol, was attributed in this work to *v*(C-O) from the solvent, citral and acetals of citral, in agreement with spectra for pure species (SDBS, 1997). In summary, by-products from the hydrogenation of citral were formed in the presence of H_2.

Finally, pure solvent adsorption was also studied with DRIFTS. **Figure 8.5B** shows DRIFTS spectra for the adsorption of hexane and ethanol on 5% Pt/SiO_2. Spectra after injection and with remaining fraction adsorbed after adsorption-desorption are shown. Characteristic bands for ethanol and hexane, assigned previously, can be observed. Thus, *v*(CH_3) and *v*(CH_2) for both solvents, and *v*(OH) for ethanol are observed. As can be seen, no hexane remained adsorbed at room temperature, while ethanol bands were still present. These results indicated the difference in adsorption strength of both solvents. Overall, results from the adsorption-desorption of pure solvent, and of citral-solvent binary mixtures might indicate competitive adsorption between solvent and citral.

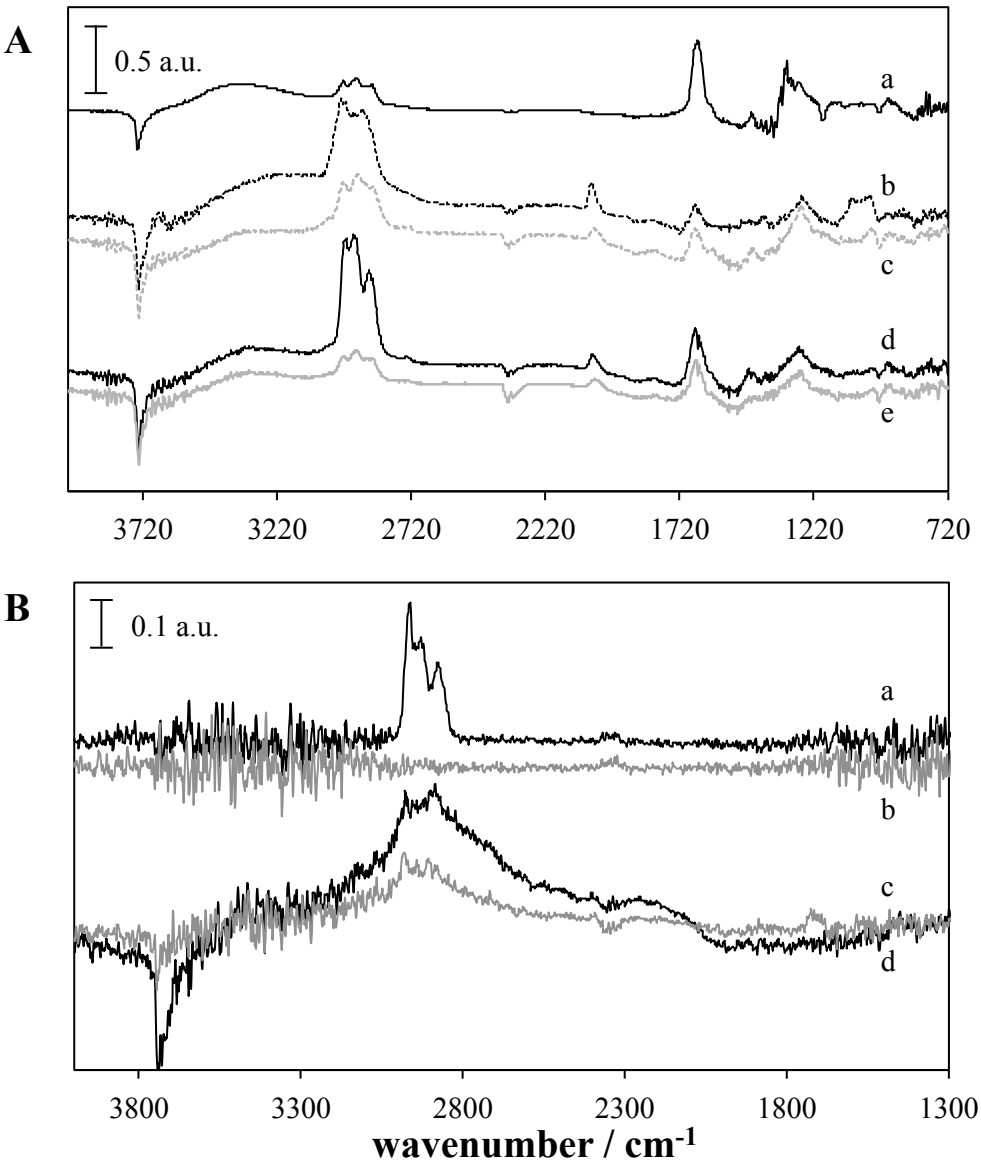

Figure 8.5. (A) DRIFTS subtracted spectra of the adsorption of citral at 373 K on pre-reduced 5% Pt/SiO_2 catalyst as individual species (a) or as 0.13 M citral in the presence of hexane (b and c), or ethanol (d and e) in H_2, respectively (black), and after 5 h He purge (grey). Pre-reduced catalyst spectrum was used for subtraction in both cases. (B) DRIFTS subtracted spectra of the adsorption of hexane (a and b) and ethanol (c and d) at 293 K on pre-reduced 5% Pt/SiO_2 catalyst as individual species (black), and after He purge (grey).

8.2.2.3 Temperature-programmed techniques: TPD/TPO

Temperature-programmed techniques were employed to study the species remaining on the surface of the catalyst. The amount of species desorbing, provided by TPD/TPO, and dependent on solvent used, related with the relative solvent-product strength of adsorption.

Additionally, information on the type of species observed would indicate the influence of solvent on deactivation.

TPD and TPO experiments were performed on spent catalysts used in reactions in hexane and ethanol at 298 and 373 K. TPD experiments revealed the presence of carbonaceous species desorbing at temperatures of 660 – 820 K. **Figure 8.6A** shows the desorption of fragments with $m/z = 28$. Desorption temperatures on Pt/SiO_2 were slightly higher to those reported on Ni/Al_2O_3 catalyst (Canning *et al.*, 2006). The amounts desorbed corresponded to low coverages on the catalyst (< 5%). m/z = 15, 27, 39, 41, 42 and 55 (this last one only present in hexane), were identified in the desorption peaks. These ions corresponded to fragments CH_3^+, $C_2H_2^+$, $C_3H_3^+$, $C_3H_5^+$, $C_3H_6^+$ and $C_4H_7^+$, respectively. Hence, alkyl groups were present on the catalyst most probably from carbonaceous deposits, also seen in DRIFTS (section 8.2.2.2). Desorption of oxygenates at those temperatures was not confirmed, although phenolic groups have been reported to desorb at temperatures > 873 K at m/z = 28, and alkoxy groups or weakly bound carbonyl groups at temperature > 950 K (Figueiredo *et al.*, 1999).

Figure 8.6B shows the TPO results of the desorbed CO and CO_2 (added for simplicity) evolved from the spent catalysts. As can be seen, two different desorption events appeared on the TPO: a very intense peak – accompanied by a shoulder for spent catalyst used at 298 K – at temperatures < 530 K, and a broader, less intense peak at temperatures > 630 K. The temperature and intensity of those peaks varied with solvent and reaction temperature. Thus, maximum desorption temperatures at 444 K and 485 K, were obtained on spent catalyst from reaction at 298 K in hexane. As comparison, the same peaks appeared at 471 K and 493 K in ethanol. The intermediate peak can be related with desorption of strongly adsorbed reaction molecules, *i.e.*, citral dimer in ethanol. Catalysts from reaction at 373 K presented desorption temperatures at 462 K in hexane *vs*. 438 K in ethanol. Only hexane presented significant peaks at temperatures > 630 K, at about 673 K, probably related with carbonaceous deposits. Comparing results, higher desorption temperatures were observed in catalyst used with ethanol at 298 K, while the opposite was true for catalysts with hexane.

In summary, the presence of by-products of reaction indicated that deactivation occurred by means of catalyst poisoning. Further to this, solvent was observed to play a major role on the adsorption of CO, influencing conversion.

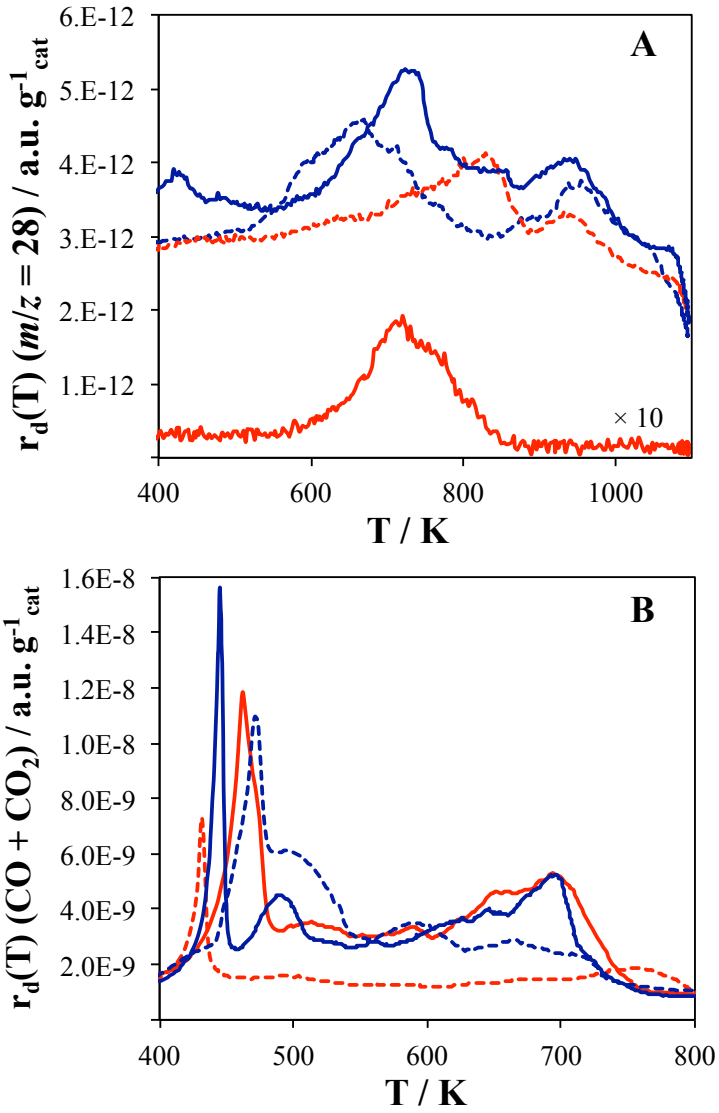

Figure 8.6. (A) TPD and (B) TPO of the spent 5%Pt/SiO_2 catalyst during the hydrogenation of citral at 298 K (blue) and 373 K (red) in hexane (bold) and ethanol (dashed). m/z = 28 was assigned to CO and m/z = 44 to CO_2 in TPO and TPD experiments.

8.2.3 Dependence of solvent effects with other parameters

In this section, results from extended studies on the hydrogenation of citral in hexane and ethanol are shown. The effects of initial citral concentration as well as of silylation of the support were studied. Competitive adsorption between citral and solvent was studied at a higher citral concentration, to complement the adsorption isotherm results. In addition, the hydrophobic-hydrophilic character of the surface and the impact it could present on relative solvent and catalyst adsorption was explored. Hence, the dependence of solvent effects in other relevant conditions was highlighted in these reactions, employed as indirect

characterisation methods. This subset of experiments was performed at 373 K, as stronger deactivation at 298 K would have reduce conversion and limit selectivity analysis.

8.2.3.1 Initial citral concentration

To study the effect of initial citral concentration, an additional composition of $c_0 = 0.33$ M was compared with the standard initial concentration, $c_0 = 0.13$ M, used in the experiments reported in section 8.2.1. **Table 8.3** and **Figure 8.7** show the hydrogenation rate as well as product selectivity in hexane and ethanol for initial citral concentrations of $c_0 = 0.33$ M in comparison with results at $c_0 = 0.13$ M. Initial citral concentration had a major impact on the initial reaction rates in hexane, with a decrease of almost two orders of magnitude, from 0.0115 s^{-1} to 0.0003 s^{-1}. In contrast, reaction in ethanol showed almost no variation. Reaction rates after 24 h showed a reduction related to deactivation, confirming the initial rate differences were linked to citral concentration. In terms of selectivity, unsaturated alcohols increased dramatically in hexane at low conversions, from 30% with $c_0 = 0.13$ M, to 75% with $c_0 = 0.33$ M. These values were in line with a decay in the selectivity towards the hydrogenation of the C=C conjugated bond. Results in ethanol at $c_0 = 0.33$ M showed a higher selectivity towards the formation of citral acetals, following Le Châtelier's principle. The relative hydrogenation of C=C bond *vs.* the C=O bond remained similar in ethanol, 33% and 67%, respectively with $c_0 = 0.13$ M *vs.* 39% and 61% with $c_0 = 0.33$ M. However, results at 70% conversion showed 65% of unsaturated alcohols at $c_0 = 0.33$ M *vs.* 83% at $c_0 = 0.13$ M. This reduction in selectivity coincided with the formation of product acetals (11.4%), mostly derived from dihydrocitronellal. These results indicated that increasing the concentration of reactant had important implications in the reaction rates and the final product distribution of the reaction, and such effects depended strongly on the solvent used.

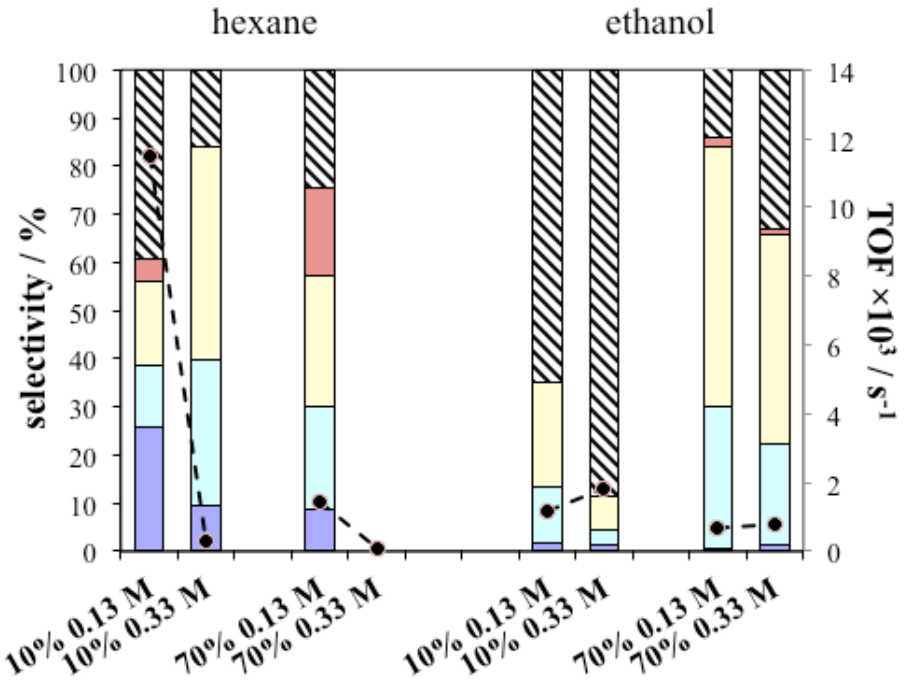

Figure 8.7. Selectivity (bars, left): product distributions of citral hydrogenation with initial concentrations of 0.13 M and 0.33 M, at 10 % and 70 % conversion; and initial rates, and rates after 24 h, in TOF, (dots, right) at 373 K on 5% Pt/SiO_2 catalyst, with hexane and ethanol, respectively. The lines connecting the TOF data points are a guide to the eye to indicate the change in reaction rate with citral initial concentration. Reaction conditions: 0.3 g 5% Pt/SiO_2, 150 cm^3 solvent, 10 bar(g). The legend of the different species is the same as shown in **Figure 7.4**.

8.2.3.2 Surface modification

Silylation of the support was carried out according to the method described in section 8.1.3.5. Silylation has previously been used to study the importance of support in hydrogenation catalysis (Kung *et al.*, 1974; Koopman *et al.*, 1981). The hydrophilic-hydrophobic character of the surface and the interactions with solvent and reactant were investigated to provide additional information to understand the origins of the observed solvent effect. Characterisation of the silylated 5% Pt/SiO_2 (Si-syl) catalyst revealed a more hydrophobic surface. **Figure 8.8** shows the DRIFTS spectra of Si-syl catalyst. A reduction in the ν(OH) bands at 3500 – 3000 cm^{-1} and δ(OH) band at 1621 cm^{-1}, assigned to hydrogen bonded water (Velázquez *et al.*, 2003), showed the loss of hydrophilic groups on the surface. Additionally, the decay in the band at 1342 cm^{-1}, related to surface OH groups, confirmed the hydrophobic character of Si-syl. Additionally, the $\nu(CH_3)$ and $\nu(CH_2)$ peaks at 2962 cm^{-1}, 2929 cm^{-1}, 2859 cm^{-1} and 2821 cm^{-1} indicated the presence of silanol groups attached to the surface, in agreement with findings from Blitz *et al.* (1988).

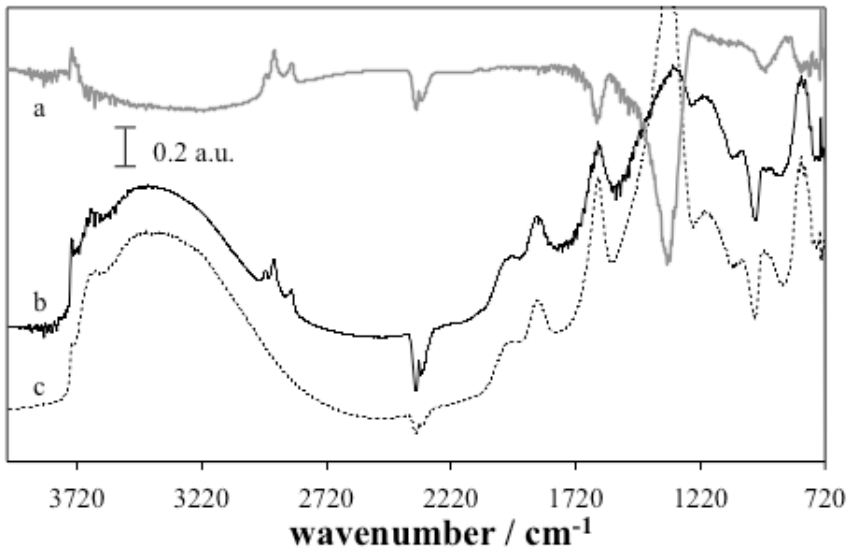

Figure 8.8. DRIFTS spectra of fresh 5% Pt/SiO_2 catalyst (b), after silylation process (c) and subtracted spectrum (a).

Reaction was performed using the silylated catalyst and compared to that of the standard catalyst. As seen in **Figure 8.9** and **Table 8.3**, initial hydrogenation rates were similar in ethanol on both catalysts. However, reaction in hexane showed a significant drop in the initial rates of over an order of magnitude, from 0.0115 s^{-1} on SiOH to 0.0011 s^{-1} on Si-syl. Reaction rates after 24 h showed a significant decay from initial rates in both cases. An increased selectivity was observed at 10% conversion towards geraniol and nerol in hexane, with 61% on Si-syl *vs.* 30% on 5% Pt/SiO_2. A slight reduction in the selectivity towards C=O hydrogenation, determined by the formation of acetals of citral was observed in ethanol. Interestingly, similar C=C *vs.* C=O bond hydrogenation patterns were observed in hexane and ethanol on Si-syl at high conversion. Hydrogenation of citral C=C bond to form citronellal, its acetals, and isopulegol, was 10.6% selective in hexane *vs.* 10.7% in ethanol, while the hydrogenation of the C=O bond was 75.5% selective in hexane and 71.1% in ethanol. The subtle differences depended on the formation of acetals in ethanol, not possible in hexane. In summary, geraniol and nerol were the major products in hexane on Si-syl, while in ethanol similar values were observed between Si-syl and 5% Pt/SiO_2. The silylation of the catalyst resulted in significant changes when hexane was used as solvent.

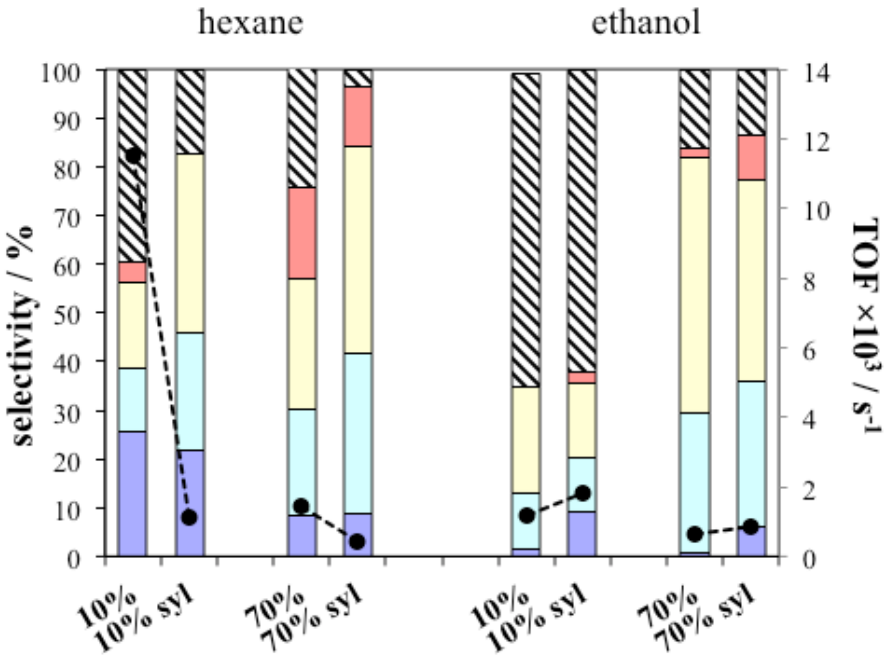

Figure 8.9. Selectivity (bars, left): product distributions of citral hydrogenation, at 10 % and 70 % conversion; and initial rates and rates after 24 h, in TOF, (dots, right) at 373 K on 5% Pt/SiO_2 and silylated 5% Pt/SiO_2 catalyst, with hexane and ethanol, respectively. The lines connecting the TOF data points are a guide to the eye to indicate the change in reaction rate with surface treatment. Reaction conditions: 0.3 g 5% Pt/SiO_2, 150 cm^3 solvent, 10 bar(g), c_0 = 0.13 M. The legend of the different species is the same as shown in **Figure 7.4**.

8.3 Discussion

The effect of solvent on reaction rates, selectivity, and deactivation was presented in section 7.3. These findings are linked in this section with the underpinning effects of solvent explained in terms of molecular interactions. The effect of the solvent with reaction species (liquid-liquid interactions) is discussed in section 8.3.1, and interactions of solvent and reactant with the catalyst (solid-liquid interactions), are reviewed in section 8.3.2. The results from the adsorption measurements performed – liquid isotherms, TEOM, ATR – as well as complementary studies on the effect of concentration and support silylation in hexane and ethanol are employed.

Table 8.3. Reaction rates and product distribution during the hydrogenation of citral on silylated catalyst or at higher initial concentration. Reaction conditions: 150 cm^3 solvent, 10 bar(g), 373 K. For abbreviations of the reaction species, refer to **Scheme 6.1**.

solvent	TOF[a] $\times 10^3$/ s^{-1}	citronellal	nerol	geraniol	isopulegols	citronellol	37OH	ENOLS	DHCAL	citral acetal	prod acetal	fragments
hexane[b]	0.3[a]	9.4	30	45	9.7	-	-	-	1.6	-	-	4.6
hexane[c]	1.1[a]	22	24	37	17	-	-	-	-	-	-	-
ethanol[b]	1.8[a]	1.2	3.3	6.8	0.6	-	-	-	0.7	81	4.9	1.5
ethanol[c]	1.8	9.0	11	15.2	7.3	2.1	-	-	-	49	6.4	-

solvent	TOF[d] $\times 10^3$/ s^{-1}	citronellal	nerol	geraniol	isopulegols	citronellol	37OH	ENOLS	DHCAL	citral acetal	prod acetal	fragments
hexane[b,e]	0.07	-	-	-	-	-	-	-	-	-	-	-
hexane[c]	0.32	8.6	33	42	2.0	12	0.7	0.5	-	-	-	0.2
ethanol[b]	0.80	1.2	21	44	5.7	1.1	1.3	-	0.6	8.8	11	5.5
ethanol[c]	0.86	6.1	30	41	1.4	9.2	1.0	0.5	-	7.5	-	-

a: TOF values calculated for initial 60 min of reaction; b: reaction carried out at initial citral concentration c_0 = 0.33 M; c: reaction performed in silylated 5% Pt/SiO_2 ; d: TOF values calculated for 24 h of reaction; e: reaction did not proceed to 70% conversion.

8.3.1 Catalyst-liquid interactions

Solvent affected the adsorption strength and geometry of adsorption of citral with the catalyst. Modified adsorption of reactant and products and direct competitive adsorption between solvent and reaction species were observed. Distinctively, competitive adsorption between solvent and reactant impacted reaction rates. The strong adsorption of the reactant with the surface or the strong interaction of the solvent with the reactant, have been described as crucial to determine reactivity (Mäki-Arvela *et al.*, 2005). As temperature increased, such interactions played less of an important role, clearly manifested in the differences in the hydrogenation of citral in diethyl ether and DCM between 298 and 373 K.

Citral liquid adsorption isotherms in hexane and ethanol, in combination with citral adsorption dynamics from TEOM, confirmed the differences in adsorption strength of citral with the catalyst. TEOM experiments recorded an equilibrium adsorption uptake of 0.7 mmol g^{-1} at 373 K, a coverage of 165% ML assuming a flat interaction with the surface, at a vapour pressure equivalent to a concentration of 0.13 mM in the absence of solvent. Hence, citral would inherently cover the surface of the catalyst. Liquid isotherm results in hexane showed a citral coverage of 0.70 mmol g^{-1} at a concentration of 18.8 mM at 298 K while 0.38 mmol g^{-1} where adsorbed at 16.3 mM and 348 K. The presence of hexane limited the adsorption of citral, being lower at higher temperature. Results in ethanol showed lower uptake values. Uptake values in ethanol did not exceed 0.11 mmol g^{-1} of citral in the range studied, reaching a plateau above citral concentrations of 15 mM. Therefore, the presence of ethanol had a more dramatic effect in the adsorption of citral. Citral enthalpies of adsorption at zero coverage were -34 kJ mol^{-1} in hexane *vs*. 18 kJ mol^{-1} in ethanol, indicating the opposite behaviour between the two reaction systems. Rate and selectivity results from the modification of initial citral concentration correlated with preferential citral adsorption in hexane, as shown by liquid isotherms. The reduction in the hydrogenation rates was directly caused by the increased adsorption of citral. At those concentrations, high coverages would be expected, due to the limited effect of ethanol. Moreover, selectivity changes were clearly observed when concentration was modified. The modification of adsorption modes with increased concentration has been previously reported in cinnamaldehyde hydrogenation (Breen *et al.*, 2004). Higher uptakes would modify the geometry of adsorption of citral, favouring C=O hydrogenation. Such modification in the geometry of adsorption will be explained in more detail in chapter 9. Opposite to hexane, results in ethanol showed no effect on rates for citral concentration, in line with the limited adsorption observed in liquid

isotherms. The role of solvent on the adsorption of citral limited site accessibility, explaining the significant differences in rate and selectivity during hydrogenation.

Modification of the surface by means of silylation of the support also revealed the extent of solvent interactions with the catalyst in reactivity and selectivity trends. Previous studies have shown that hydrophobicity plays an important role in driving adsorption processes (Derylo-Marczewska *et al.*, 2011; Koopman *et al.*, 1981). The modification of the support, from a hydrophilic hydroxyl surface to a surface coated with alkyl groups showed similar rate and selectivity effects in hexane to increasing initial citral concentration. A preferential citral adsorption would limit the hydrogenation and modify the geometry of adsorption, as discussed. These results are in line with findings from Chaouati *et al.* (2013) that observed an increased phenol uptake from aqueous solution on zeolite Y after silylation. In a similar fashion, the interaction of the solvent with the catalyst explained the limited hydrogenation in decalin at 373 K, by means of catalyst blockage. The differences between hexane and decalin resembled those observed between *n*-heptane and *n*-hexadecane (Birdi, 1984). In that study, *n*-hexadecane was believed to interact in a "solid-state" fashion with graphon, as opposite to a more liquid-like interaction of *n*-heptane. Such observation would relate with the limited hydrogenation in decalin when compared with hexane or other non-polar solvents at 373 K, where adsorption should be playing less of an important role. Results remained almost unaffected in ethanol in line with limited reactant adsorption, favoured in this case by the interplay of support-solvent interactions. The relative adsorption of solvent as a function of surface hydrophobicity was previously observed in cyclohexane/water mixtures in the selective hydrogenation of cyclohexene/cyclohexanone mixtures (Kung *et al.*, 1974; Koopman *et al.*, 1981). Additionally, solvent-reactant interactions were still important in ethanol (as will be discussed in section 8.3.2). The type of support strongly affected solvent-reactant competitive adsorption, as observed in this study on the hydrogenation of citral. Nevertheless, this behaviour could help understanding other reaction systems in the literature. Thus, while a reduction in the hydrogenation rates was reported on Ru/C with non-polar solvents (Wan *et al.* 2014), polar solvents were considered to interact strongly with Pt/Al_2O_3, in line with hydrophilic-hydrophobic effects.

Additionally, solvents with donating ability, such as acetone, THF or diethyl ether, were believed to interact strongly on Ru/Al_2O_3 (Takagi *et al.*, 1999). These observations were also in line with the absence of hydrogenation in DCM and diethyl ether at 298 K (**Table 7.1**). In this case, a clear competitive solvent-reactant adsorption process occurred. The solvent

already favoured a clear competitive adsorption process. Previously, benzene and acetonitrile adsorption hindered acetophenone reaction *via* blockage of the active sites, as measured by Bertero *et al.* (2011) using calorimetry. Thus, competitive adsorption between solvent and reactant limited citral adsorption and modified conversion. Within this group of solvents, cyclohexane was noted to also affect conversion at low temperature. However, as previously reported in section 7.3.2.1, cyclohexane was hypothesised to modify selectivity towards unsaturated alcohols, geraniol and nerol, at 298 K. Product blockage of unsaturated alcohols explained such low conversion, described *vide infra*.

TEOM experiments of citral, citronellal, citronellol, geraniol and nerol adsorption showed all reaction species would interact strongly with the surface in the absence of solvent, with slower desorption dynamics in citronellol and the equimolar geraniol:nerol mixture, as seen in **Figure 8.4**. Hence, solvent presented a key role in product desorption. Product desorption was confirmed *via* TPD/TPO results. The presence of excess reactant, products or other carbonaceous deposits adsorbed on the spent Pt/SiO_2 catalyst was noted. Previously, product blockage was observed during citral hydrogenation in hexane (Singh *et al.*, 2000) or by the formation of by-products, such as dehydration products and acetals (Kun *et al.*, 2001). The strong influence of solvent on product blockage was shown in 2-octanol oxidation (Mounzer *et al.*, 2010). Therefore, selectivity and deactivation were strongly affected by the solvent used. Additional information on the influence of solvent in product adsorption is presented in chapter 9. The increased selectivity towards geraniol and nerol observed in cyclohexane was in line with a simultaneous reduction in conversion, as compared to other non-polar solvents. The hindered desorption of products would limit conversion. In contrast, hydrogenation in cyclohexanol at 313 K (results not shown) showed high conversions with the formation of citronellal. The alcohol functionality in the product seemed to affect desorption, and limit the extent of citral hydrogenation. These effects were also observed in hexane when the catalyst was silylated, affecting the adsorption-desorption behaviour of products. This is consistent with the results of Ojeda *et al.* (2006). Their study reported that water adsorption was impeded on silylated Co/SiO_2 catalyst, while adsorption of carbon deposits was similar in silylated and non-silylated Co supported catalysts. TPD and TPO on spent catalyst provided information on deactivation, related to the fraction of CO adsorption. Solvent influenced product and by-product desorption, modifying conversion and selectivity.

Finally, the formation of other species and the effect of solvent on desorption of by-products was also relevant to determine deactivation. Deactivation was previously explained *via* CO

adsorption-desorption processes (Englisch *et al.*, 1997b; Mäki-Arvela *et al.*, 2006; Mukherjee and Vannice, 2006). *In-situ* DRIFTS and post-reaction TPD/TPO in hexane and ethanol indicated CO was adsorbed on Pt/SiO_2. The appearance of on-top and bridged adsorbed CO (Kinne *et al.*, 2002) at 373 K in DRIFTS was in agreement with previous studies in citral (Burgener *et al.*, 2004), prenal (Waghray and Blackmond, 1993) and crotonaldehyde (Dankenar and Vannice, 1999; Englisch *et al.*, 1997a). Additionally, TPD and TPO results revealed significant amounts of CO present in all catalysts except in which reaction was carried out in hexane at 373 K. Calculations from TPD desorption peaks for m/z = 28 (**Figure 8.6A**), assuming 2:1 on-top to bridge CO adsorption on Pt (Mieher *et al.*, 1989; Schweizer *et al.*, 1989), revealed CO coverages on surface Pt of 46% and 7% on catalyst used in hexane, and 73% and 65% on catalyst used in ethanol at 298 and 373 K, respectively. These results in hexane were in agreement with Singh and Vannice (2000), where CO could desorb at higher temperatures, allowing the reaction to progress at 373 K. As observed, solvent influenced the extent of CO adsorption and desorption from the surface, affecting deactivation.

In summary, the influence of solvent in the adsorption strength of citral modified the reaction rates observed. A modification in the adsorption geometry with solvent also explained the differences in selectivity. Additionally, hydrophilic-hydrophobic interactions played an important role in solvent and reactant competitive adsorption with the catalyst. Solvent also played a key role in deactivation and surface poisoning, by modifying reactivity and strength of adsorption of the different reaction species present on the surface.

8.3.2 Liquid-liquid interactions: solvent-reactant interactions

Interactions between solvent and reaction species were also observed. Polar aprotic solvents and polar protic solvents are believed to increase the solvation of the reactant, with H-bonding being the major mode of interaction in polar protic solvents (Bertero *et al.*, 2011; Hájek *et al.*, 2004). ATR-IR results in **Figures 8.1** and **8.2** confirmed H-bond interactions were present in various alcohols. Additionally, limited adsorption of citral in ethanol was observed in liquid isotherms, with a positive value of the enthalpy of adsorption at zero coverage. The solvation of citral in ethanol, and reactant-solvent interactions could explain this limited adsorption. Similar studies have also shown the influence of such interactions in a series of model oxygenates (Wan *et al.*, 2014) and in 2-butanone, where DFT simulations were also employed (Akpa *et al.*, 2012). Hence, the use of polar solvents in reactions with a

reactant presenting a polar functionality, *e.g.* citral, was shown to modify adsorption by means of solvation.

ATR-IR spectra revealed a preferential interaction of short chain alcohols with the carbonyl group in citral, as described in section 8.2.1. In the reaction, a selective hydrogenation process towards unsaturated alcohols was enhanced by the presence of short chain polar protic solvents at 298 K, simultaneously with relative citral isomer hydrogenation and geraniol to nerol formation. Akpa *et al.* (2012) showed the stabilising effect that water, and to a lower extent 2-propanol, exerted on the hydroxy intermediate towards the hydrogenation of the C=O bond (Sinha and Neurock, 2012). These solvents reduced the energy of the carbonyl transition state towards the formation of the alcohol. This stabilising effect was also shown in the hydrogenation of ketones in a series of alcohols (Wan *et al.*, 2014). In addition to alcohols, the formation of acetals in ethanol and, to a lower extent in 2-propanol, as well as the formation of ether in acetone rendered the formation of water. Although no relation has been established between C=O preferential hydrogenation and acetal formation in crotonaldehyde in water-ethanol mixtures on Pt/SiO_2 catalyst (Englisch *et al.*, 1997b), a co-operative effect of water cannot be discarded. Thus, selective hydrogenation of *p*-chloronitrobenzene on a series of SiO_2 supported catalysts revealed an enhancement in the rate of reduction by the addition of water (Ning *et al.*, 2007). Also, a cooperation between water and surface hydroxyls was observed during the hydrogenation of citral on Ru/AlO(OH) (Jiang *et al.*, 2012). These phenomena were in agreement with the hydroxy intermediate stabilisation described by Akpa *et al.* (2012). The interactions between short chain alcohols and citral, with the likely enhanced stabilisation of water, contributed towards a preferential C=O hydrogenation.

8.4 Conclusions

The hydrogenation of citral was selected as a model molecule to understand the role of solvent in reaction rates and selectivities based on differences in liquid-liquid and catalyst-liquid interactions. The strong variations in reaction rates and selectivities reported in chapter 7 were related with the strength of interaction of citral with the catalyst, as well as the degree of solvation, especially at 298 K. TEOM mass uptake values compared with liquid isotherm results showed that solvent reduced the adsorption capacity of citral, particularly in ethanol, related with the rate differences observed. DRIFTS results on the adsorption of solvent also confirmed such trends. Solvent-reactant competitive adsorption determined the

absence of reaction in diethyl ether and DCM at 298 K, as well as the effect of higher citral concentrations or the type of support in reaction rates. Similarly, deactivation of the catalyst was attributed to product and by-product desorption, facilitated by solvent, as observed in reaction in cyclohexane *vs.* cyclohexanol or TPD and TPO results with CO and hydrocarbon desorption. Selectivity trends were related to liquid-liquid interactions in polar protic solvents, especially at 298 K. Competitive adsorption influencing the geometry of adsorption of citral was also believed to affect C=O selective hydrogenation. These findings helped explain some of the disparity from data in the literature. ATR-IR measurements indicated solvent-citral interactions were solely present in polar-protic solvents in line with higher yields of geraniol and nerol. Adsorption geometry influenced by catalyst-liquid interactions, and liquid-liquid interactions in non-polar solvents impacted selectivity towards formation of unsaturated alcohols geraniol and nerol. The complex reaction network of citral served as an exemplary system for other reactions of multifunctional molecules important in the energy and fine chemical sectors. We believe the information provided in this work represents a coherent approach on solvent interactions to study catalytic reactions. Increasing reaction rates, improving selectivity and reducing deactivation can be exploited in terms of liquid-liquid and catalyst-liquid interactions in complex multifunctional molecules.

References

Ahmed, M.K., Ali, S., Wojcik, E. (2012) The C-O stretching infrared band as a probe of hydrogen bonding in ethanol-water and methanol-water mixtures. *Spectrosc. Lett.*, 45, 420 – 423.

Akpa, B.S., D'Agostino, D., Gladden, L.F., Hindle, K., Manyar, H., McGregor, J., Li, R., Neurock, M., Sinha, N., Stitt, E.H., Weber, D., Zeitler, J.A., Rooney, D.W. (2012) Solvent effects in the hydrogenation of 2-butanone. *J. Catal.*, 289, 30 – 41.

Almarri, M., Xiaoliang, M., Song, C. (2009) Role of surface xygen-containing functional groups in liquid-phase adsorption of nitrogen compounds on carbon-based adsorbents. *Energ. Fuel.*, 26, 470 – 478.

Alwary, L.; Gafar, M.; Rumie, A. (2011) Liquid phase adsorption of phenol and chloroform by activated charcoal. *Chem. Eng. Technol.*, 34, 1883 – 1890.

Ayanda, O.S., Fatoki, O.S., Adekola, F.A., Ximba, B.J. (2013) Removal of tributyltin from shipyard process wastewater by fly ash, activated carbon and fly ash/activated carbon composite: adsorption models and kinetics. *J. Chem. Technol. Biotechnol.*, 88, 2201 – 2208.

Bertero, N.M., Trasarti, A.F., Apesteguía, C.R. and Marchi, A.J. (2011) Solvent effect in the liquid-phase hydrogenation of acetophenone over Ni/SiO_2: a comprehensive study of the phenomenon. *Appl. Catal. A-Gen.*, 394, 228 – 238.

Birdi, K.S. (1984) Enthalpy of adsorption on solids from solution. In: Myers, A.L., Belfort, G. *Fundamentals of adsorption: proceedings of the Engineering Foundation conference at Schloss Elmau, Bavaria, West Germany, May 6-11, 1983*, The foundation, New York.

Blitz, J.P., Murthy, R.S.S., Leyden, D.E. (1988) Studies of silylation of Cab-O-Sil with methoxymethylsilanes by Diffuse Reflectance FTIR Spectroscopy. *J. Colloid Interf. Sci.*, 121, 63 -69.

Breen, J.P., Burch, R., Gómez-López, J., Griffin, K., Hayes, M. (2004) Steric effects in the selective hydrogenation of cinnamaldehyde to cinnamyl alcohol using an Ir/C catalyst. *Appl. Catal. A-Gen.*, 268, 267 – 274.

Burgener, M., Wirz, R., Mallat, T., Baiker, A. (2004) Nature of catalyst deactivation during citral hydrogenation: a catalytic and ATR-IR study. *J. Catal.*, 228, 152 – 161.

Burikov, S.A., Dolenko, T.A., Kurchatov, I.S., Patsaeva, S.V., Starokurov, Y.V. (2012) Computer analysis of vibrational spectra of aqueous ethanol solutions. *Izv. Vuz. Fiz.*, 55, 383 – 388.

Canning, A.S., Jackson, S.D., Mitchell, S. (2006) Identification, by selective poisoning, of active sites on Ni/Al_2O_3 for hydrogenation and isomerisation of *cis*-2-pentenitrile. *Catal. Today*, 114, 373 – 376.

Chaouati, N., Soualah, A., Chater, M. (2013) Adsorption of phenol from aqueous solution onto zeolites Y modified by sylilation. *C. R. Chimie*, 16, 222 – 228.

Choudary, N.V., Kumar, P., Bhat, T.S.G., Cho, S.H., Han, S.S., Kim, J.N. (2002) Adsorption of light hydrocarbon gases on alkene-selective adsorbent. *Ind. Eng. Chem. Res.*, 41, 2728 – 2734.

Chen, Q. (2010) Study on the adsorption of lanthanum (III) from aqueous solution by bamboo charcoal. *J. Rare Earth.*, 28, 125 – 131.

Coloma, F., Llorca, J., Homs, F., Ramírez de la Piscina, P., Rodríguez-Reinoso, F., Sepúlveda-Escrivano, A. (2000) Crotonaldehyde hydrogenation over alumina- and silica-supported Pt-Sn catalysts of different composition. *In situ* DRIFTS study. *Phys. Chem. Chem. Phys.*, 2, 3063 – 3069.

Dandekar, A., Vannice, M.A. (1999) Crotonaldehyde hydrogenation on Pt/TiO_2 and Ni/TiO_2 SMSI catalysts. *J. Catal.*, 183, 344 – 354.

Derylo-Marczewska, A., Buczek, B., Swiatkowski, A. (2011) Effect of oxygen surface groups on adsorption of benzene derivatives from aqueous solution onto active carbon samples. *Appl. Surf. Sci.*, 257, 9466 – 9472.

Do, D.D. (1998) *Adsorption analysis: equilibria and kinetics*. Imperial College Press, London, pp. 49 – 70.

Englisch, M., Jentys, A., Lercher, J.A. (1997a) Structure sensitivity of the hydrogenation of crotonaldehyde over Pt/SiO_2 and Pt/TiO_2. *J. Catal.*, 166, 25 – 35.

Englisch, M., Ranade, V.S., Lercher, J.A. (1997b) Liquid phase hydrogenation of crotonaldehyde over Pt/SiO_2 catalysts. *Appl. Catal. A-Gen.*, 163, 111 – 122.

Figueiredo, J.L., Pereira, M.F.R., Freitas, M.M.A., Órfão, J.J.M. (1999) Modification of the surface chemistry of activated carbons. *Carbon*, 37, 1379 – 1389.

Haghseresht, F., Lu, G.Q. (1998) Adsorption characteristics of phenolic compounds onto coal-reject-derived adsorbents. *Energ. Fuel.*, 12, 1100 – 1107.

Hájek, J., Kumar, N., Mäki-Arvela, P., Salmi, T. and Murzin, D.Y. (2004) Selective hydrogenation of cinnamaldehyde over Ru/Y zeolite. *J. Mol. Catal. A-Chem.*, 217, 145 – 154.

Haji, S., Erkey, C. (2003) Removal of dibenzothiophene from model diesel by adsorption on carbon aerogels for fuel cell applications. *Ind. Eng. Chem. Res.*, 42, 6933 – 6937.

Hu, N., Wu, D., Cross, K., Burikov, S., Dolenko, T., Patsaeva, S., Schaefer, D.W. (2010) Structurability: a collective measure of the structural differences in vodkas. *J. Agric. Food Chem.*, 58, 7394 – 7401.

Jiang, H-J., Jian, H-B., Zhu, D-M., Zheng, X-L., Fu, H-Y., Chen, H., Li, R-X. (2012) Cooperation between the surface hydroxyl groups of the support and organic additives in the highly selective hydrogenation of citral. *Appl. Catal. A-Gen.*, 445 – 446, 351 – 358.

Kinne, M., Fuhrmann, T., Whelan, C.M., Zhu, J.F., Pantförder, J., Probst, M., Held, G., Denecke, R., Steinrück, H-P. (2002) Kinetic parameters of CO adsorbed on Pt(111) studied by *in situ* high resolution x-ray photoelectron spectroscopy. *J. Chem. Phys.*, 117, 10852.

Koizumi, T., Yoshitate, H. (2013) Adsorption of iso- and terephtalaldehydes on 3-aminopropyl-functionalized SBA-15 with various loadings. *Bull. Chem. Soc. Jpn.*, 86, 657 – 662.

Koopman, P.G.J., Buurmans, H.M.A., Kieboom, A.P.G., van Bekkum, H. (1981) Solvent-reactant-support interactions in liquid phase hydrogenation. *Recl. Trav. Chim. Pays-Bas*, 100, 156 – 161.

Kun, I, Szöllösi, G., Bartók, M. (2001) Crotonaldehyde hydrogenation over clay-supported platinum catalysts. *J. Mol. Catal. A-Chem.*, 169, 235 – 246.

Kung, H.H., Brookes, B.I., Burwell, R.L. (1974) Effect of silylation upon the hydrogenating activity of supported platinum catalysts. *J. Phys. Chem.*, 78, 875 – 878.

Li, Y-H., Di, Z., Ding, J., Wu, D., Luan, Z., Zhu, Y. (2005) Adsorption thermodynamic, kinetic and desorption studies of Pb^{2+} on carbon nanotubes. *Water Res.*, 39, 605 – 609.

Li, R., D'Agostino, C., McGregor, J., Mantle, M.D., Zeitler, J.A., Gladden, L.F. (2014) Mesoscopic structuring and dynamics of alcohol/water solutions probed by terahertz time-domain spectroscopy and pulsed field gradient nuclear magnetic resonance*., J. Phys. Chem. B.*, 118, 10156 – 10166.

Likozar, B., Senica, D., Pavko, A. (2012) Equilibrium and kinetics of vancomycin adsorption on polymeric adsorbent. *AIChE Journal*, 58, 99 – 106.

Liu, Q., Cong, C., Zhang, H. (2007) Investigation on infrared spectra of androsterone in single solvents. *Spectrochim. Acta A*, 68, 1269 – 1273.

Mäki-Arvela, P., Hájek, J., Salmi, T., Murzin, D.Y. (2005) Chemoselective hydrogenation of carbonyl compounds over heterogeneous catalysts. *Appl. Catal. A-Gen.*, 292, 1 -49.

Mäki-Arvela, P, Kumar, N., Eränen, K., Salmi, T., Murzin, D.Y. (2006) Inverse temperatura dependence due to catalyst deactivation in liquid-phase citral hydrogenation over Pt/Al_2O_3. *Chem. Eng. J.*, 122, 127 – 134

Max, J-J., Chapados, C. (2007) Infrared spectroscopy of acetone-hexane liquid mixtures. *J. Chem. Phys.*, 126, 154511.

Max, J-J., Daneault, S., Chapados, C. (2002) 1-propanol hydrate by IR spectroscopy. *Can. J. Chem.*, 80, 113 – 123.

McKay, G., Blair, H.S., Gardner, J.R., Adsorption of dyes on chitin. I. Equilibrium studies. *J. Appl. Polym. Sci.*, 27, 3043 – 3057.

Mieher, W.D., Whitman, L.J., Ho, W. (1989) A time resolved electron energy loss spectroscopy study of CO on Pt(111): adsorption sites occupations versus coverage and temperature. *J. Chem. Phys.*, 91, 3228 – 3239.

Mohamed, E.F., Andriantsiferana, C., Willhelm, A.M., Delmas, H. (2011) Competitive adsorption of phenolic compounds from aqueous solution using sludge-based activated carbon. *Environ. Technol.*, 32, 1325 – 1336.

Mounzer, H.N., Wood, J., Stitt, E.H. (2010) Heterogeneous oxidation of 2-octanol on 5 wt%Pt – 1 wt%Bi/Carbon catalyst. *Chem. Eng. Sci.*, 65, 179 – 185.

Mukherjee, S., Vannice, M.A. (2006) Solvent effects in liquid-phase reactions I. Activiy and selectivity during citral hydrogenation on Pt/SiO_2 and evaluation of mass transfer effects. *J. Catal.* 243, 108 – 130.

Ning, J., Xu, J., Liu, J., Miao, H., Ma, H., Chen, C., Li, X., Zhou, L., Yu, W. (2007) A remarkable promoting effect of water addition on selective hydrogenation of p-chloronitrobenzene in ethanol. *Catal. Commun.*, 8, 1763 – 1766.

Nishiyama, S., Hara, T., Tsuruya, S., Masai, M. (1999) Infrared spectroscopy study of aldehydes adsorbed on Rh-Sn bimetallic systems: selective activation of aldehydes by tin. *J. Phys. Chem. B*, 103, 4431 – 4439.

Ojeda, M., Pérez-Alonso, F.J., Terreros, P., Rojas, S., Herranz, T., Granados, M.L., Fierro, J.L.G. (2006) Silylation of a Co/SiO_2 catalyst. Characterization and exploitation of the CO hydrogenation reaction. *Langmuir*, 22, 3131 – 3137.

Perry, R.H., Green, D.W. (1999) *Perry's Chemical Engineers' Handbook*. McGraw-Hill, pp. 121 – 130.

Remy, T.; Remi, J.C.S.; Singh, R.; Webley, P.A.; Baron, G.V.; Denayer, J.F.M. (2011) Adsorption and separation of C1 – C8 alcohols on SAPO-34. *J. Phys. Chem. C*, 115, 8117 – 8125.

Rouquerol, F, Rouquerol, J., Sing, K. (1999) *Adsorption by powders and porous solids.* Academic Press, London, pp. 51 – 92.

Samiey, B., Toosi, A.R. (2010) Adsorption of malachite on silica gel: effects of NaCl, pH and 2-propanol. *J. Hazard. Mater.*, 184, 739 – 745.

Schweizer, E., Persson, B.N.J., Tüshaus, M., Hoge, D., Bradshaw, A.M. (1989) The potential energy surface, vibrational phase relaxation and the order-disorder transition in the adsorption system Pt{111}-CO. *Surf. Sci.*, 213, 49 – 89.

SDBS (1997) *Spectral database of organic compounds* [Online] Available from: http://sdbs.db.aist.go.jp [Accessed October 2014]

Shahid, G., Sheppard, N. (1994) IR spectra and the structures of the chemisorbed species resulting from the adsorption of the linear butenes on a Pt/SiO_2 catalyst. *J. Chem. Soc. Faraday Trans.*, 90, 507 – 511.

Singh, U.K., Sysak, M.N., Vannice, M.A. (2000) Liquid-phase hydrogenation of citral over Pt/SiO_2 catalysts. II. Hydrogenation of reaction intermediate compounds. *J. Catal.*, 191, 181 – 191.

Singh, U.K., Vannice, M.A. (2000) Liquid-phase hydrogenation of citral over Pt/SiO_2 catalysts. I. Temperature effects on activity and selectivity. *J. Catal.*, 191, 165 – 180.

Sinha, N.K., Neurock, M. (2008) A first principles analysis of the hydrogenation of $C_1 – C_4$ aldehydes and ketones over Ru(0001). *J. Catal.*, 295, 31 – 44.

Sips, R. (1948) On the structure of a catalyst surface. *J. Chem. Phys.*, 16, 490 – 495.

Somasundaram, S., Sekar, K., Gupta, V.K., Ganesan, S. (2013) Synthesis and characterisation of mesoporous activated carbon from rice husk for adsorption of glycine from alcohol-aqueous mixture. *J. Mol. Liq.*, 177, 416 – 425.

Subra, P., Vega-Bancel, A., Reverchon, E. (1998) Breakthough curves and adsorption isotherms of terpene mixtures in supercritical carbon dioxide. *J. Supercrit. Fluids*, 12, 43 – 57.

Takagi, H., Isoda, T., Kusakabe, K., Morooka, S. (1999) Effects of solvents on the hydrogenation of mono-aromatic compounds using noble-metal catalysts. *Energ. Fuel.*, 13, 1191 – 1196.

Unger, M., Harnacke, B., Noda, I., Siesler, H.W. (2011) Solvent interactions in methanol/N,N-dimethylamide binary systems studied by Fourier Transform Infrared Attenuated Total Reflection (FT-IR/ATR) and Two-Dimensional Correlation Spectroscopy (2D-COS). *Appl. Spectrosc.*, 65, 892 – 900.

Velázquez, G., Herrera-Gómez, A., Martín-Polo (2003) Identification of bound water through infrared spectroscopy in methylcellulose. *J. Food Eng.*, 59, 79 – 84.

Waghray, A., Blackmond, D.G. (1993) Infrared spectroscopic studies of the adsorption and reaction of 3-methyl-2-butenal over alkali-promoted Ru/SiO_2 catalysts. *J. Phys. Chem.*, 97, 6002 – 6006.

Wan, H., Vitter, A., Chaudhari, B.V., Subramaniam, B. (2014) Kinetic investigations of unusual solvent effects during Ru/C catalyzed hydrogenation of model oxygenates. *J. Catal.*, 309, 174 – 184.

Wang, L., Sun, B., Yang, F.H., Yang, R.T. (2012) Effects of aromatics on desulfurization of liquid fuel by π-complexation and carbon adsorbents. *Chem. Eng. Sci.*, 73, 208 – 217.

Wang, W., Zheng, B., Deng, Z., Feng, Z., Fu, L. (2013) Kinetics and equilibria for adsorption of poly(vinyl alcohol) from aqueous solution onto natural bentonite. *Chem. Eng. J.*, 214, 343 – 354.

Weber, D., Sederman, A.J., Mantle, M.D., Mitchell, J., Gladden, L.F. (2010) Surface diffusion in porous catalysts. *Phys. Chem. Chem. Phys.*, 12, 2619 – 2624.

Williams, D.H., Fleming, I. (1997) *Spectroscopic methods in organic chemistry.* McGraw-Hill, Cambridge, pp. 32 – 62.

Zhu, W., Kapteijn, F., Groen, J. C., Linders, M. J. G., Moulijn, J. A. (2004) Adsorption of butane isomers and SF_6 on Kureha activated carbon: II. kinetics. *Langmuir*, 20, 1704 – 1710.

Chapter 9:

Application of NMR relaxometry to solvent effects in citral hydrogenation

9 Application of NMR relaxometry to solvent effects in citral hydrogenation

The effect of solvent in the hydrogenation of citral was studied, and reactivity and selectivity differences observed in chapter 7 were related to liquid-liquid and catalyst-liquid interactions in chapter 8. In this chapter, NMR relaxometry techniques will be used to probe the influence of adsorbate-adsorbent interactions during the hydrogenation of citral. NMR relaxometry techniques have been shown in chapters 4 and 5 to provide catalytically relevant information on adsorption, and will be used here in a particular reaction system. Hence, the hydrogenation of citral and main reaction intermediates, citronellal, unsaturated alcohols geraniol and nerol, and citronellol, in two different solvents, hexane and ethanol, has been examined. These solvents were selected following the reasons mentioned in chapter 8 – opposite reactivity and selectivity behaviour, and model for the set of solvents studied in chapter 7. Reaction rates for citral as well as selectivity trends at low and high conversion have been evaluated. Additionally, hydrogenation of the main intermediates of reaction, citronellal, geraniol and nerol, and citronellol was studied in hexane and ethanol. The product distribution observed in those cases was used to understand the preferential citral reaction pathways in both solvents. ^{13}C T_1 NMR relaxometry has been used to determine the geometry of citral upon adsorption in the presence of hexane and ethanol. ^{1}H 2D T_1-T_2 relaxometry correlations have been employed to determine the role of competitive adsorption of the main reaction intermediates, citronellal, unsaturated alcohols geraniol and nerol, and citronellol, as a function of solvent used. In particular, the reaction data for the hydrogenations performed in either hexane or ethanol are reported in section 9.2.1. It was observed that quite different selectivities were obtained for the two solvents. Given these data, hypotheses regarding the origin of the selectivity are given and tested using relaxometry in section 9.2.2. Discussion on the implication of these results is presented in section 9.3.

9.1 Experimental materials and methods

9.1.1 Materials

5 wt% Pt/SiO_2 (Johnson Matthey) was used as received. Textural properties and metal dispersion were presented in section 7.1.1. Citral (63%:34% E/Z mixture, 95%, Sigma Aldrich), unsaturated alcohols, geraniol (97%, Alfa Aesar) and nerol (97%, Alfa Aesar), citronellal (+/−, 96%, Alfa Aesar), and citronellol (95%, Alfa Aesar) were used as received for catalytic reactions. Hexane (≈ 95%, Fisher), ethanol (99%, Fisher), ethanol-d_6 (99.5%

atom D, Aldrich), H_2 (99.993%, Air Liquide), and N_2 (99.998%, Air Liquide) were used without further purification.

9.1.2 Hydrogenation reactions

Hydrogenation of citral and the main reaction intermediates, citronellal, unsaturated alcohols geraniol and nerol as 1:1 mol:mol geraniol:nerol mixtures (UALC), and citronellol, was performed in the reactor setup described in section 7.1.2. Details in preparation procedures, including catalyst pre-treatment, and sample analysis were shown in section 7.1.2.3. Hydrogenations of citral and intermediates were conducted at 373 K, $c_0 = 0.13$ M and total pressure of 10 bar(g).

Mass balances during the reaction were kept at 95% ± 5%.

9.1.3 NMR experiments

^{13}C T_1 NMR relaxation time analysis was performed for citral-hexane and citral-ethanol binaries adsorbed on 5% Pt/SiO_2 to obtain information on the adsorption geometry of citral. Two-dimensional ^1H T_1-T_2 correlation experiments were performed for the following binaries: citral-hexane, citral-ethanol, citral-ethanol-d_6, citronellal-hexane, citronellal-ethanol-d_6, UALC-hexane, UALC-ethanol-d_6, citronellol-hexane and citronellol-ethanol-d_6. Complementary citronellal-ethanol, UALC-ethanol, and citronellol-ethanol experiments were performed for comparative purposes. UALC mixtures with solvent were 1:1 mol:mol in geraniol:nerol in all NMR relaxometry experiments. Fully deuterated ethanol was used in ^1H T_1-T_2 experiments to unambiguously identify the signal from the citral reaction species. These experiments measured the relative adsorption strength of the given reaction species on 5% $PtSiO_2$ in the presence of the solvent. 20% vol. citral-solvent mixtures (6% mol citral-ethanol and 9.1% mol citral-hexane) and 10% mol intermediate-solvent mixtures were prepared to resemble reaction conditions and provide sufficient NMR signal. In all cases, the catalyst was pressed into 5 mm pellets, crushed and pre-reduced in a tubular furnace (Carbolite) at 423 K for 1 h under flowing H_2. The catalyst was then cooled down under N_2 and immerged immediately after in the prepared solutions. Samples were soaked in solutions for 12 h before NMR measurements were performed, as described in section 5.1.5. Previous ^{13}C T_1 NMR experiments shown in chapters 4 and 5 used submonolayer coverages. In this study, since the same catalyst is used in all experiments, a direct comparison can be established. Theoretical implications and comparison with T_1/T_2 analysis was described in detail in section 2.2.2.2.3. In addition, T_1 measurements are not

affected by internal gradient effects (Mitchell *et al.*, 2010), which represent an advantage on heterogeneous catalysts such as that employed in this study. The fast diffusion limit between the bulk liquid and surface is assumed, implying T_1 decay values are directly influenced by the surface interaction (Liu *et al*., 1991).

The NMR experiments were performed on a Bruker wide bore DMX 300 spectrometer operating at ^{13}C and ^{1}H frequencies of 75.46 and 300.23 MHz, respectively. ^{13}C T_1 relaxometry experiments were conducted using the inversion-recovery pulse sequence (**Figure 2.17**). In order to ensure all ^{13}C nuclei in the NMR spectrum were close to the resonance condition, three separate sets of ^{13}C spectra were acquired for each sample to capture the relevant chemical shift regions of citral. Thus, aliphatic carbons (δ: 15 – 45 ppm), olefinic carbons (δ: 120 – 135 ppm) and aldehyde and β carbon (δ: 160 – 195 ppm), respectively, were considered independently. The duration of the ^{13}C 90° pulses was calibrated as 21 μs at a power level of -6 dB. A recycle time of 20 s, approximately five times of ^{13}C T_1, was used. To achieve satisfactory signal-to-noise, 8 scans were averaged in the case of bulk liquid and 256 scans for adsorbed citral mixtures on 5% Pt/SiO_2. The time domain data were Fourier transformed with an exponential line broadening of 30 Hz. For 2D ^{1}H T_1-T_2 correlation studies both 90º and 180º pulses were calibrated for each sample. The 16 recovery delays varied logarithmically from t_R = 10 ms to 5 s. In the CPMG echo train, the intensities of n = 1024 echoes were acquired in a single shot with an echo spacing of t_E = 500 μs. Additionally, deconvolution of a reduced number of ^{1}H pulse-acquire spectra was done. The corresponding fit to each spectrum was calculated using Origin 8.6. Lorentzian curves were fitted to each relevant resonance present in each spectrum. Due to the effects of line broadening of the spectral resonances of the hydrocarbon upon adsorption, line fitting was performed by using a single-fitted lineshape to represent specific groups of similar δ-values.

9.2 Results

9.2.1 Hydrogenation

General trends on the hydrogenation of citral with different solvents were presented in section 7.2. In this case, a detailed analysis of reaction rates and product distribution for the hydrogenation of citral in hexane and ethanol at 373 K is presented. Selectivity values were shown in **Table 7.2**. However, a detailed analysis of citral hydrogenation products will link

with results on the hydrogenation of reaction intermediates, as well as NMR relaxometry results.

9.2.1.1 Hydrogenation of citral

Table 9.1 shows turnover frequency (TOF) values for the hydrogenation of citral on 5% Pt/SiO_2 with hexane and ethanol at 373 K and 10 bar(g) during the initial hydrogenation stages and after 24 h of reaction. In this work, citral hydrogenation rates were higher in the case of hexane, 11.5×10^{-3} s^{-1}, as compared to ethanol, 1.2×10^{-3} s^{-1}, with over an order of magnitude difference. As a comparison, a similar hydrogenation rate of 0.017 s^{-1} was observed by Singh and Vannice (2000) for the hydrogenation of 1.0 M of citral with hexane at 373 K and 20 atm H_2 on 1.44% Pt/SiO_2. In the present work, reaction rate values after 24 h indicated a drop in activity in the presence of both solvents, in agreement with previous observations reported by Mukherjee and Vannice (2006). This decay in activity was more significant in the case of hexane, almost an order of magnitude difference, from 0.012 s^{-1} to 0.001 s^{-1}, as compared to ethanol, where this decay represented less than half the initial rate, from 0.001 s^{-1} to 0.0007 s^{-1}. These results were in agreement with the observed citral conversion values after 24 h of 65% with hexane *vs.* 40% with ethanol. The progress of the reaction was monitored until no more significant activity was detected: a complete conversion of citral was observed with hexane with subsequent hydrogenation of reaction intermediates to citronellol and 3,7-dimethyl-1-octanol. However, no complete citral hydrogenation was observed when ethanol was used. Previous studies, where hexane and ethanol were used as solvents in the hydrogenation of 1 M citral at 373 K and 20 bar(g) over Pt/SiO_2 showed similar reaction rates (Mukherjee and Vannice, 2006), although very different metal dispersion was reported. Initial citral concentration (Reyes *et al.*, 2003) as well as metal dispersion (Zgolicz *et al.*, 2012) have been previously shown to have a significant impact in reactivity.

Table 9.1. Summary of reaction rates for the hydrogenation of citral with hexane and ethanol. Reaction conditions: 0.3 g 5% Pt/SiO_2, 150 cm^3 solvent, 373 K, 10 bar(g), c_0 = 0.13 M.

	initial[a] TOF $\times 10^3$/ s^{-1}	**TOF after 24 h $\times 10^3$/ s^{-1}**	**end conversion**
hexane	11.5	1.4	100%[b]
ethanol	1.2	0.7	95%

[a]Considered as the first 60 min in the reaction; [b]Intermediates are also hydrogenated

The complete product distribution of the hydrogenation of citral at 373 K and 10 bar(g) at low (10%) and high (70%) conversion was shown in **Tables 7.1** and **7.2**. **Figure 9.1** displays the product distribution towards main reaction intermediates in both hexane and ethanol. Looking at the results at 10% conversion with hexane, citronellal (26%), nerol (13%) and geraniol (17%) were formed during the initial stages. Further reaction products, such as isopulegol, were also formed (23%). The presence of secondary reactions, such as cyclisation, has been previously reported (Ekou *et al.*, 2012). Subsequent hydrogenation products from citronellal and geraniol and nerol, such as citronellol (4.5%) and 3,7-dimethyl-2-octen-1-ol (12%), were also formed. In ethanol, hydrogenation of citral mainly formed geraniol (22%) and nerol (11.6%); only minor amounts of citronellal (1.7%) were formed. Side reactions other than hydrogenation occurred to a great extent, leading to the formation of diethyl acetals of citral (49%) and citronellal (15%). Similar behaviour has been reported when low chain alcohols are used as solvents in the hydrogenation of α,β-unsaturated aldehydes (Barrales and Viveros, 2013; Mäki-Arvela *et al.*, 2002; Hájek *et al.*, 2004; Englisch *et al.*, 1997b). These studies have also indicated that the acidity of the catalyst, in the Si-OH moieties on silica, was responsible for these side reactions. C_9 - C_{10} decarbonylation fragments were detected in both solvents, with selectivities of 3.8% and 0.8% in hexane and ethanol, respectively.

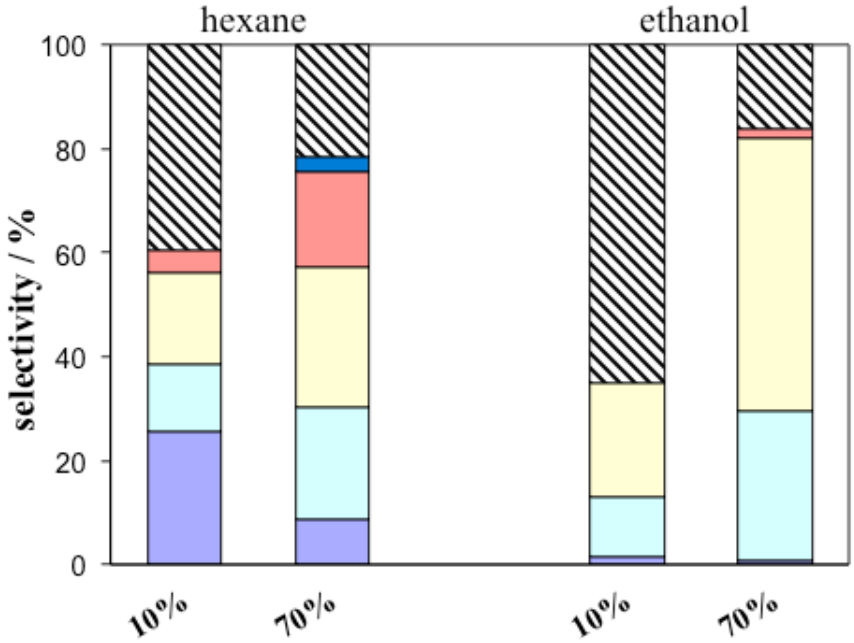

Figure 9.1. Selectivity: product distribution of citral hydrogenation with hexane and ethanol at 10% and 70% conversion. Reaction conditions: 0.3 g 5% Pt/SiO_2, 150 cm^3 solvent, 373 K, 10 bar(g), c_0 = 0.13 M. Citronellal (dark blue), nerol (light blue), geraniol (yellow), citronellol (dark red), 37OH (navy) and others (dashed black), are shown.

Product distribution at 70% conversion showed a shift in major products formed and increasing selectivity differences between solvents. With hexane, geraniol (27%) and nerol (22%) were the most abundant products, as compared to citronellal (8.5%). Selectivity to subsequent hydrogenated products increased: isopulegol (9.9%) hydrogenated to menthols (2%); citronellal, geraniol and nerol hydrogenated to citronellol (19%), which was reduced to 3,7-dimethyl-1-octanol (2.8%). In ethanol, a significant depletion of the diethyl acetals "pool" (14%) led to reduction of citral towards unsaturated alcohols geraniol and nerol. Nerol (30%) and geraniol (54%) were the dominant products formed, while citronellal (0.7%) was not the preferred pathway. Subsequent hydrogenation of geraniol, nerol and citronellal was very limited, with the formation of citronellol (2.8%). This significant reduction in the proportion of acetals was explained considering an aldehyde-diethyl acetal equilibrium. Previous studies have reported the reversibility of acetalysation in citral (Mäki-Arvela *et al.*, 2002) and crotonaldehyde (Englisch *et al.*, 1997b). The hydrogenation of isolated C=C in citral towards 3,7-dimethyl-2-octenal isomers (ENALS) and 3,7-dimethyl-2-octen-1-ol alcohols (ENOLS) was only observed in hexane. As mentioned in chapter 7, the formation of these species is usually not favoured (Mäki-Arvela *et al.*, 2004; Mukherjee and Vannice, 2006; Zgolicz *et al.*, 2012). With respect to the formation of decarbonylated fragments, similar selectivity of 3.6% at 70% conversion (3.8% at 10% conversion) was observed in hexane, and an increase to 2.5% from 0.8% was recorded in ethanol.

9.2.1.2 Hydrogenation of main reaction intermediates

In order to gain an understanding of the origin of the significant selectivity variations, hydrogenation of citronellal, 1:1 mol:mol geraniol:nerol mixtures (UALC), and citronellol were performed with hexane and ethanol. **Figure 9.2** shows the product distribution of these reactions and compares them with those of the hydrogenation of citral. **Table 9.2** shows the product distribution during the hydrogenation of citral and main intermediates of reaction, citronellal, UALC, and citronellol at 373 K. At 95%, hydrogenation of citral showed a significant increase in the formation of citronellol in hexane (31%), being the most abundant single species present. These selectivity results contrasted with values observed in **Figure 9.1** at 70% conversion. In ethanol, an increase in the selectivity towards geraniol (59%) and nerol (32%) was observed. Regarding hydrogenation of reaction intermediates, a substantial variation in product distribution was observed depending on the solvent used. Thus, reaction of citronellal in hexane produced mostly citronellol (89%) and small amounts of 3,7-dimethyl-1-octanol (9.0%) at 90% conversion. By contrast, at the same conversion,

cyclisation to isopulegol (15%) and subsequent hydrogenation to menthols (42%) was mostly detected in ethanol. Diethyl acetals of citronellal (4.9%) and of dihydrocitronellal (5.3%), citronellol (9.9%), and 3,7-dimethyl-1-octanol (15%), were also formed in ethanol. It is noteworthy that decarbonylated fragments were absent in the presence of hexane during hydrogenation of citronellal, but significant amounts were formed with ethanol (7.6%). Product distribution during hydrogenation of UALC was compared at lower conversion values (45 – 48%) due to the lower reactivity of UALC observed. Mostly citronellol (81%) and 3,7-dimethyl-1-octanol (9.1%) were formed in hexane. Conversely, only 2.3% citronellol was formed in the presence of ethanol and 1.4% of 3,7-dimethyl-1-octanol. This dramatic selectivity difference in ethanol was caused by a rapid formation of $C_9 - C_{10}$ decarbonylated and hydrodeoxygenated species (28%), as well as ethers of geraniol and nerol (45%) and citronellal (14%). Fragments were also formed in hexane, but to a lesser extent (6.9%). Hence, isomerisation of geraniol and nerol to citronellal occurred to a certain extent in ethanol, in agreement with previous reports on Pt/SiO_2 in 2-pentanol (Mäki-Arvela *et al.*, 2004), although the reverse reaction was not observed. Finally, hydrogenation of citronellol was only observed in the presence of hexane, forming 3,7-dimethyl-1-octanol (98%). The low reactivity of citronellol has been previously reported (Singh *et al.*, 2000). The unsaturated alcohols geraniol and nerol, as well as citronellol, presented a much lower reactivity towards hydrogenation as compared to citronellal. This observation was more pronounced when ethanol was used as solvent.

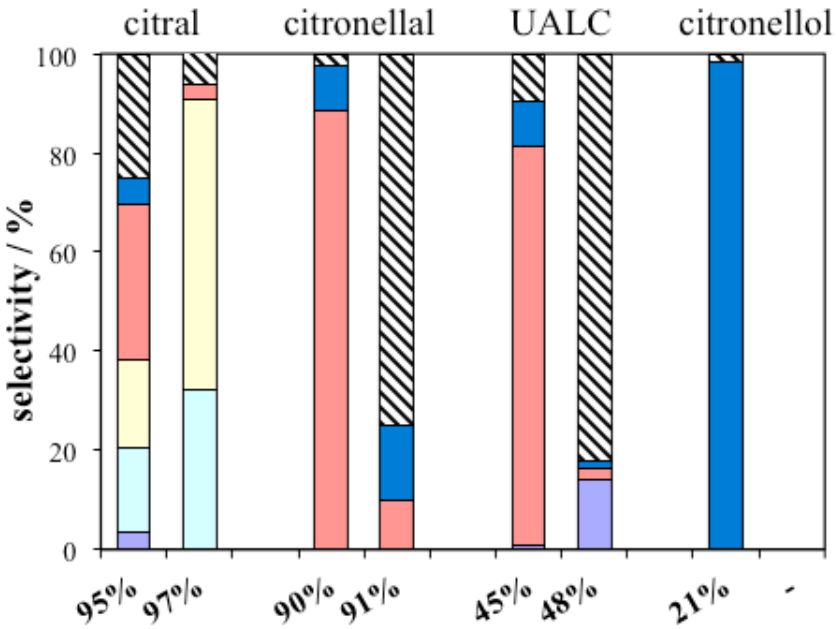

Figure 9.2. Selectivity: product distribution of the hydrogenation of citral and main intermediates of reaction with hexane (left) and ethanol (right), respectively. Results are shown at similar conversion values in all cases except citronellol, where no reaction was observed in ethanol. Reaction conditions: 0.3 g 5% Pt/SiO_2, 150 cm^3 solvent, 373 K, 10 bar(g), c_0 = 0.13 M. For legend details, refer to caption in **Figure 9.1**. For UALC hydrogenation in ethanol, UALC ethers were added into product acetals, and citronellal acetals were included into citronellal, as it was only present as citronellal diethyl acetals.

Table 9.2. Product distribution during the hydrogenation of citral and main intermediates of reaction, citronellal, unsaturated alcohols geraniol and nerol (UALC), and citronellol at 373 K. For each reaction species, the upper row shows results in hexane, and the lower row in ethanol. Reaction conditions: 0.3 g 5% Pt/SiO_2, 150 cm^3 solvent, 10 bar(g), c_0 = 0.13 M. For abbreviations of the reaction species, refer to **Scheme 6.1**.

reaction species	x_A[a] / %	CAL	nerol	geraniol	IP	IPH	COL	37OH	ENALS	ENOLS	DHCAL	citral acetal	prod acetal	fragm.
citral	95	3.5	17	18	12	4.3	31	5.4	1.2	3.3	0.5	-	-	3.4
	97	-	32	59	-	-	3.0	-	-	-	0.4	2.8	0.6	2.6
citronellal	90	-	-	-	0.9	0.9	89	9.0	-	-	0.7	-	-	-
	91	-	-	-	15	42	9.9	15	-	-	5.3	-	4.9	7.6
UALC	45	0.9	-	-	-	-	81	9.1	-	2.5	-	-	-	6.9
	48	14	-	-	-	0.5	2.3	1.4	1.1	3.5	0.9	3.8	45[b]	28
citronellol	21	-	-	-	-	-	-	98	-	-	-	-	-	1.7
	-[c]	-	-	-	-	-	-	-	-	-	-	-	-	-

a: Conversion values at which product distribution is shown; b: grouped as product acetals, they represent ethyl ethers of geraniol and nerol; c: citronellol did not react in ethanol.

9.2.2 NMR Relaxometry results

Understanding the composition of species present at the surface of the catalyst and the extent of adsorbate-adsorbent interactions is fundamental in order to understand the reaction mechanisms taking place. Selectivities at low conversion and initial hydrogenation rates were examined considering the relative strength of interaction and adsorbate geometry of citral in the presence of hexane and ethanol solvents. ^{13}C T_1 NMR relaxometry experiments of citral-hexane and citral-ethanol binaries were performed to determine the geometric configuration of citral on 5% Pt/SiO_2. 2D ^{1}H T_1-T_2 correlation experiments of the same systems were used to determine the relative strength of interaction of citral in the presence of two solvents (D'Agostino *et al.*, 2014). Selectivities at high conversion were related to the relative adsorption strength of the main intermediates of reaction, citronellal, geraniol, nerol, and citronellol, when in hexane and ethanol. To determine the relative adsorption strength of those molecules, 2D ^{1}H T_1-T_2 correlation experiments of citronellal-hexane, UALC-hexane, citronellol-hexane as well as citronellal-ethanol-d_6, UALC-ethanol-d_6 and citronellol-ethanol-d_6, were used to determine the relative strength of interaction of the main reaction species involved in the presence of two solvents. As mentioned in section 9.1.3, both deuterated and non-deuterated ethanol was used in the 2D experiments.

9.2.2.1 Adsorption of citral in hexane and ethanol

To determine the effect of solvent on the preferential C=O bond *vs.* C=C bond adsorption, as well as on the differences in the reaction rates observed, NMR relaxometry experiments were performed. ^{13}C T_1 NMR relaxometry was used to study the individual carbon atom interactions of citral, while 2D ^{1}H T_1-T_2 correlation experiments determined the interactions citral-catalyst in each solvent. **Figure 9.3** shows the ^{13}C NMR spectrum of 20% vol. citral in ethanol adsorbed on 5% Pt/SiO_2. **Figure 9.4** shows the $T_{1,ads}/T_{1,bulk}$ values of individual citral carbon atoms from the ^{13}C T_1 relaxometry experiments on 5% Pt/SiO_2 in the presence of hexane and ethanol. Only backbone carbons are shown for clarity, numbered following IUPAC rules. Carbons were identified in each spectrum according to their chemical shift and a single exponential curve was fitted for each resonance. Since the citral mixture was 63:34 E:Z, assignment of peaks was performed for the E-isomer, geranial, for C4, all other backbone carbons being unaffected by chemical shift stereoselectivity. Note that with this technique $T_{1,ads}/T_{1,bulk}$ of oxygen cannot be measured. As can be observed, the $T_{1,ads}/T_{1,bulk}$ values were lower in the case of hexane as compared to ethanol, particularly in the case of

unsaturated carbons, C2 - C3 (α,β), C6 – C7, and aldehydic carbon, C1, indicating a stronger interaction with the surface. Also, five citral carbon atoms in ethanol presented a value of $T_{1,ads}/T_{1,bulk} > 1$, indicating a disruptive effect of ethanol on citral-catalyst interactions. When looking specifically at the functional groups involved in the hydrogenation of citral, C1 had a $T_{1,ads}/T_{1,bulk} = 0.23$ in hexane, as compared with $T_{1,ads}/T_{1,bulk} = 0.75$ when in ethanol; the α,β-unsaturation showed $T_{1,ads}/T_{1,bulk} = 0.29$ for C2 and $T_{1,ads}/T_{1,bulk} = 0.17$ for C3 in hexane, as compared to $T_{1,ads}/T_{1,bulk} = 1.31$ for C2 and $T_{1,ads}/T_{1,bulk} = 0.69$ for C3 in ethanol. These values showed a relative weaker interaction strength of citral on 5% Pt/SiO_2 in ethanol, especially noticeable in the case of C2, part of the double bond. The presence of relatively low concentrations of citral diethyl acetal was not detected, indicated by the absence of peaks at ≈ 100 ppm (acetal carbon) and ≈ 62 ppm (ethylic carbon).

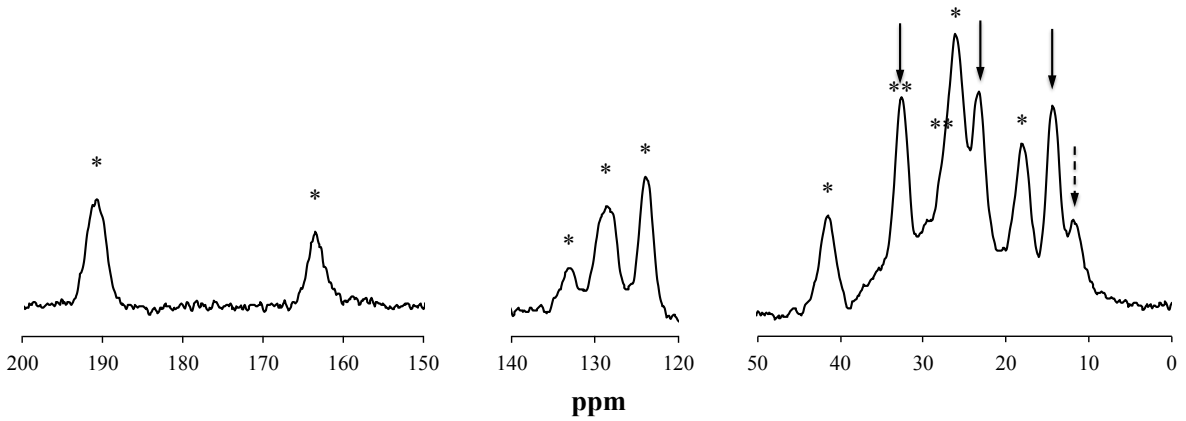

Figure 9.3. ^{13}C NMR spectra for the adsorption of 20% vol. citral (63%:34% E/Z mixture) in ethanol on 5% Pt/SiO_2 catalyst pre-treated at 423 K. Peaks marked with an asterisk (*) correspond with both citral isomers, while those marked with a double asterisk (**) correspond solely to Z-citral. Peaks marked with arrows correspond to hexane isomers (discontinuous arrow was representative of 3-methylpentane).

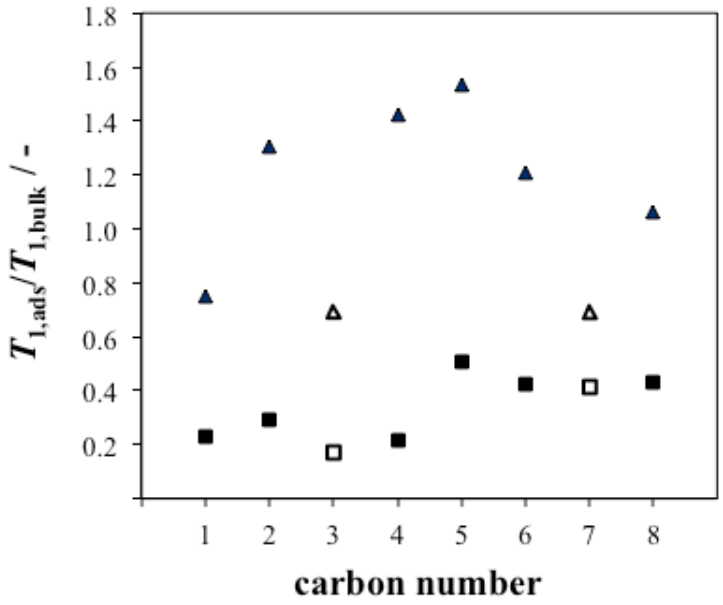

Figure 9.4. ^{13}C T_1 NMR relaxometry results for the adsorption of citral in the presence of solvent on 5% Pt/SiO_2 catalyst. Ratio of surface to bulk relaxation times $T_{1,ads}/T_{1,bulk}$ for individual carbon atoms in citral backbone in the presence of hexane (square) and in the presence of ethanol (triangle). Citral C3 and C7 (hollow) are bound to methyl groups, not shown. In both relaxometry experiments, relative errors of ± 5% in the calculation of $T_{1,ads}$ were observed, while errors of ± 5% in the calculation of $T_{1,bulk}$ were obtained. Hence, the errors were lower than the significant, and error bars are not shown.

Figure 9.5 shows the ^1H 2D T_1-T_2 correlation plots of citral in the presence of solvent on 5% Pt/SiO_2 catalyst. The T_1/T_2 values are indicated with a solid diagonal line on each plot passing through the maximum intensity of the relevant peak (citral or solvent), as described in section 5.2.5. From the T_1/T_2 ratios it is possible to infer the relative strengths of surface interaction of citral in the presence of hexane and ethanol. A value $T_1/T_2 = 54$ was reported for citral in the presence of hexane, while the solvent itself showed a value $T_1/T_2 = 21$. A value $T_1/T_2 = 37$ was recorded for citral in the presence of ethanol-d_6. **Table 9.3** shows the individual T_1 and T_2 values of citral and ethanol adsorbed on 5% Pt/SiO_2 as pure components. As noted, comparison with pure component values showed a significant drop in T_1/T_2 values. Spectral information also revealed a preferential adsorption of citral in hexane as compared to the prepared solution concentrations. **Figure 9.6** shows the spectra for three different systems: i) citral-hexane, ii) citral-ethanol and iii) citral-ethanol-d_6. Results from peak fitting revealed that the citral:solvent molar ratios were 1:2 in hexane *vs.* 1:7 in ethanol. Citral-ethanol-d_6 results from the fitting confirmed no alcohol was observed. These results indicated that citral interacted with the 5% Pt/SiO_2 surface more strongly in the presence of hexane, as compared to ethanol, in agreement with ^{13}C T_1 NMR results, *vide supra*.

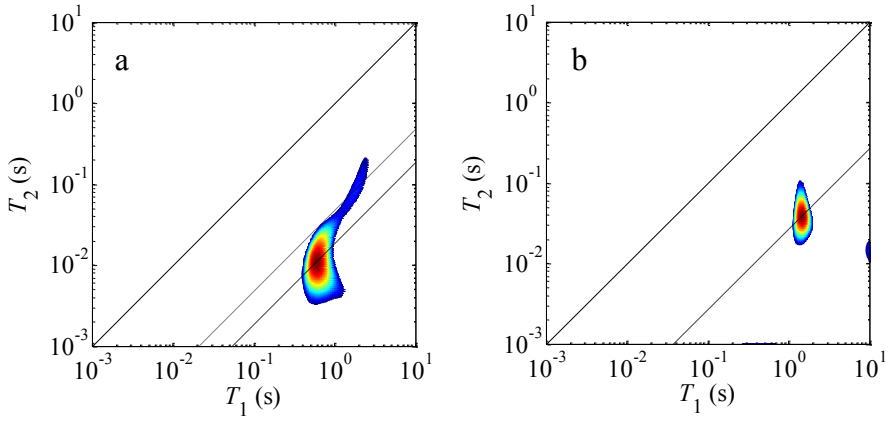

Figure 9.5. ^{1}H 2D T_1-T_2 correlation plots for the adsorption of citral on 5% Pt/SiO_2: (a) in the presence of hexane and (b) in the presence of ethanol-d_6. The solid diagonal lines represent $T_1 = T_2$. The dashed diagonal lines (citral) indicate (a) $T_1 = 54\ (\pm\ 6)\ T_2$ and (b) $T_1 = 37\ (\pm\ 2)\ T_2$, while the dotted diagonal line (a) indicates $T_1 = 21\ (\pm\ 2)\ T_2$.

Table 9.3. Summary of the T_1, T_2 and T_1/T_2 values observed in ^{1}H 2D T_1-T_2 relaxometry correlations for single component species adsorbed on 5% Pt/SiO_2.

	T_1 / s	T_2 / ms	T_1/T_2 / -
citral	0.699	10.8	65 ± 6
ethanol	0.989	18.2	54 ± 3

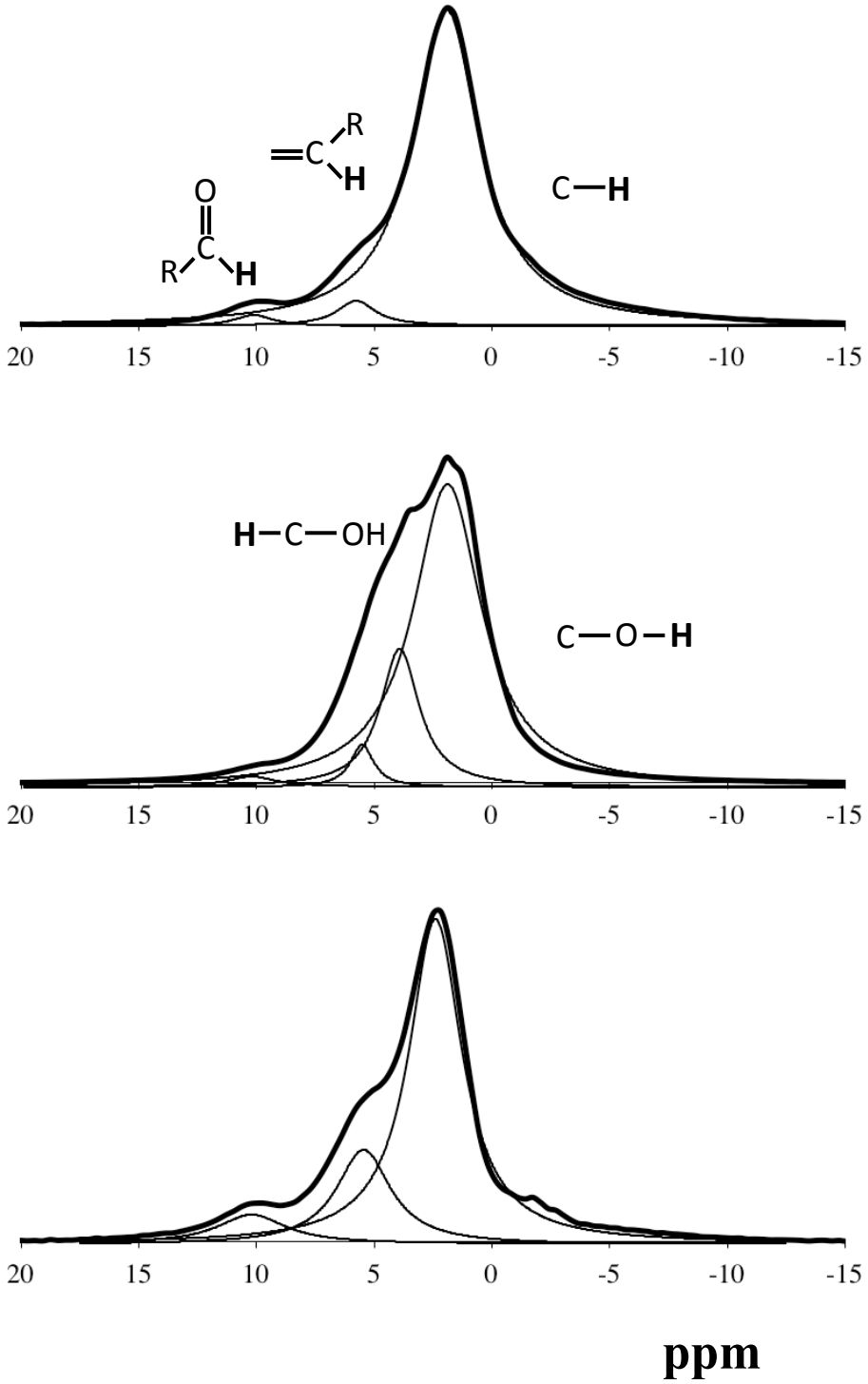

Figure 9.6. ^{1}H NMR spectra for the adsorption of (a) citral-hexane, (b) citral-ethanol, (c) citral-ethanol-d_6 on 5% Pt/SiO_2. Lorentz fitted curves for resonances corresponding to groups of ^{1}H of each molecule present in the mixture are shown under each spectrum. Specific groups of similar δ-values for citral-hexane are shown in (a), while additional groups corresponding to ethanol are shown in (b).

9.2.2.2 Adsorption of citronellal, geraniol and nerol (UALC), and citronellol

To gain an understanding of the effect that adsorbate-adsorbent interactions of main reaction intermediates might play on the selectivity of citral, NMR relaxometry results were performed for solvent-intermediate binary mixtures. **Figures 9.7** and **9.8** show the ^{1}H 2D T_1-T_2 correlation plots of the main reaction intermediates, citronellal, UALC, and citronellol, on 5% Pt/SiO_2 catalyst in the presence of hexane and ethanol(d_6), respectively. As can be seen, values of $T_1/T_2 = 29$ for citronellal, $T_1/T_2 = 38$ for UALC, and $T_1/T_2 = 68$ for citronellol were obtained in hexane. Values of hexane in these binary mixtures were also obtained with the aid of 1D relaxometry experiments. Spectrally resolved T_1 and T_2 values for hexane and reaction species were obtained. These values were contrasted with those observed in the 2D experiments. With this method, each peak in the 2D plots was assigned to hexane or a reaction species. For hexane, values of $T_1/T_2 = 8$ were obtained in citronellal and citronellol, while $T_1/T_2 = 37$ was seen in UALC. Also, a preferential adsorption of the reaction species was observed in this case in the spectra (results not shown). In ethanol-d_6, $T_1/T_2 = 25$ for citronellal, $T_1/T_2 = 32$ for UALC, and $T_1/T_2 = 28$ for citronellol were seen. The T_1/T_2 ratio assigned to citronellol showed a very significant difference, with $T_1/T_2 = 68$ in hexane and $T_1/T_2 = 28$ in ethanol. In all cases, the relative strength of interaction of these intermediates with the catalyst was lower when ethanol was present. In order to determine the effect of ethanol, binaries with non-deuterated solvent were also studied. **Figure 9.9** shows the T_1/T_2 results of the experiments performed in non-deuterated ethanol, and the T_1 and T_2 values are summarised in **Table 9.4**. As can be seen, the T_1/T_2 values were similar across experiments in non-deuterated samples. Analysis of the 1D chemical shift resolved relaxometry experiments in each case (results not shown) revealed that ethanol was the species being probed in non-deuterated samples. This is in agreement with the identical values observed in most of the binaries in ethanol. Hence, results in ethanol were interpreted considering both sets of experiments.

Overall, these results indicated that the solvent was strongly influencing the relative adsorption strength of citral and the main intermediates of the reaction. Accordingly, the relative interaction strength in hexane was citronellol > citral > UALC > citronellal, whereas when mixed with ethanol (according to deuterated experiments) the relative interaction strength followed citral > UALC > citronellol > citronellal.

Table 9.4. Summary of the T_1, T_2 and T_1/T_2 values observed in ^{1}H 2D T_1-T_2 relaxometry correlations for the citral reaction species-solvents mixtures adsorbed on 5% Pt/SiO_2.

	ethanol			ethanol-d_6		
	T_1 / s	T_2 / ms	T_1/T_2 / -	T_1 / s	T_2 / ms	T_1/T_2 / -
citral	0.719	21.8	33 ± 2	1.432	38.7	37 ± 2
citronellal	0.425	14.5	29 ± 2	1.035	42.5	25 ± 3
UALC	0.466	14.2	33 ± 2	1.190	37.0	32 ± 2
citronellol	0.567	17.2	33 ± 3	0.985	35.2	28 ± 2

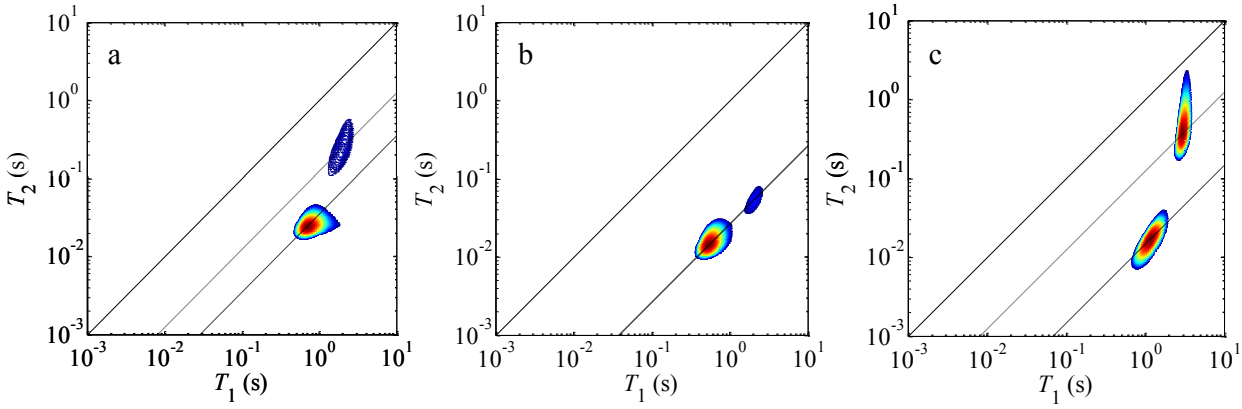

Figure 9.7. ^{1}H 2D T_1-T_2 correlation plots for the adsorption of (a) citronellal-hexane, (b) UALC-hexane and (c) citronellol-hexane on 5% Pt/SiO_2. The solid diagonal lines represent $T_1 = T_2$. The dashed diagonal lines (reaction intermediates) indicate (a) $T_1 = 29\ (\pm 3)\ T_2$, (b) $T_1 = 38\ (\pm 3)\ T_2$ and (c) $T_1 = 68\ (\pm 9)\ T_2$. The dotted diagonal lines (solvent) indicate (a) $T_1 = 8\ (\pm 1)\ T_2$, (b) $T_1 = 37\ (\pm 4)\ T_2$ and (c) $T_1 = 8\ (\pm 1)\ T_2$.

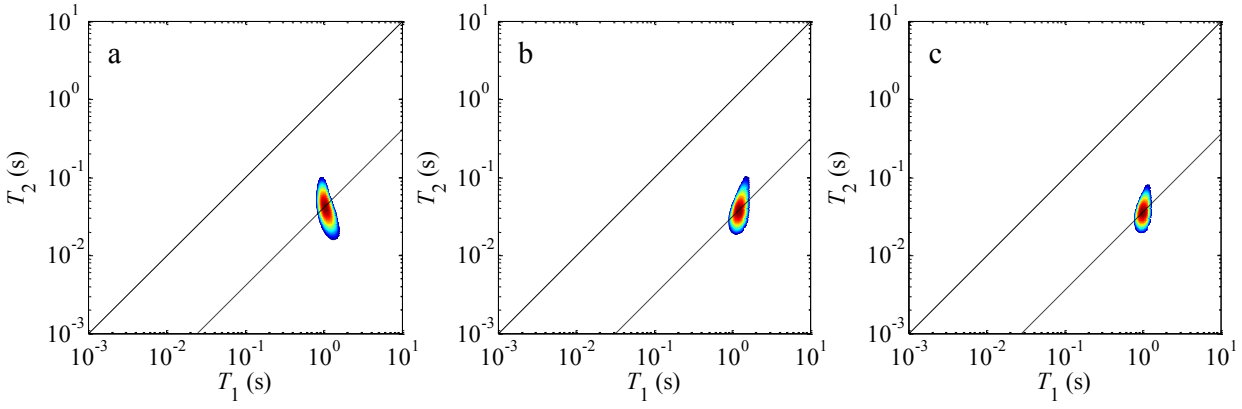

Figure 9.8. ^{1}H 2D T_1-T_2 correlation plots for the adsorption of (a) citronellal-ethanol-d_6, (b) UALC-ethanol-d_6 and (c) citronellol-ethanol-d_6 on 5% Pt/SiO_2. The solid diagonal lines represent $T_1 = T_2$. The dashed diagonal lines (reaction intermediates) indicate (a) $T_1 = 25\ (\pm 3)\ T_2$, (b) $T_1 = 32\ (\pm 2)\ T_2$ and (c) $T_1 = 28\ (\pm 2)\ T_2$.

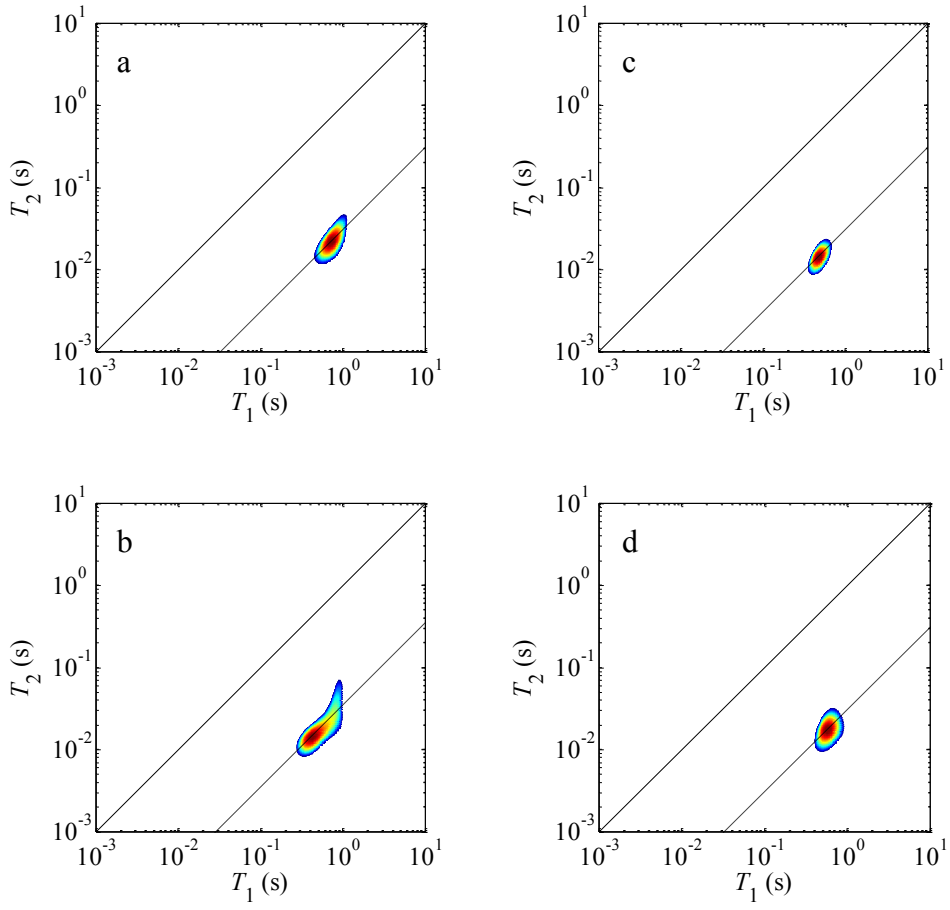

Figure 9.9. ^{1}H 2D T_1-T_2 correlation plots for the adsorption of (a) citral-ethanol, (b) citronellal-ethanol, (c) UALC-ethanol and (d) citronellol-ethanol on 5% Pt/SiO_2. The solid diagonal lines represent $T_1 = T_2$. The dashed diagonal lines (reaction intermediates) indicate (a) $T_1 = 33\ (\pm 2)\ T_2$, (b) $T_1 = 29\ (\pm 2)\ T_2$, (c) $T_1 = 33\ (\pm 2)\ T_2$ and (d) $T_1 = 33\ (\pm 3)\ T_2$.

9.3 Discussion

As was observed, the hydrogenation of citral in hexane and ethanol resulted in different product distributions. Selectivity towards desired unsaturated alcohols geraniol and nerol was higher in the presence of ethanol. These results are explained through preferential adsorption and differences in adsorbate-adsorbent interactions on each solvent by means of NMR relaxometry. Comparison with results in chapter 8 is presented in section 9.3.3.

While other effects, such as the type of promoters, deactivation mechanism, solvent polarity, etc. have been extensively discussed, there have not been significant investigations into the influence of solvent on adsorption (Mounzer *et al.*, 2010) or into competitive adsorption mechanisms. Solvent effects were addressed in prevention of side reactions (Mäki-Arvela *et al.*, 2002), or selective hydrogenation between conjugated *vs.* isolated double-bond

functionality (Chatterjee et al., 2004). Previous selectivity studies have addressed the effect of solvent in similar reaction systems, such as crotonaldehyde (Englisch *et al.*, 1997a, 1997b) or cinnamaldehyde (Hájek *et al.*, 2004; Ide *et al.*, 2012). In the former case, alcohol solvents rendered a higher selectivity towards geraniol and nerol as compared to non-polar solvents; however, a direct comparison cannot be established, as water was added in the reaction to demonstrate a rate enhancement. In the latter, although an attempt was made to describe the interactions present, some uncertainties still remained comparing different solvent types. Competitive hydrogenation caused by differences in competitive adsorption on metal surfaces has been proposed previously, as in the case of hydrogenation of benzene and toluene (Minot and Gallezot, 1990). The effect of competitive adsorption and the role played by intermediates was also discussed in the hydrogenation of α,β-unsaturated aldehydes on Pt and Pd model surfaces (Delbecq and Sautet, 1995). In this section, the selectivity in the hydrogenation of citral was studied in conjunction with NMR relaxometry experiments to determine the extent of adsorbate-adsorbent interactions of citral and main reaction intermediates, as well as the effect of solvent on the adsorption of such species. A comparison with results from the range of techniques employed in chapter 8 is summarised in section 9.3.3.

9.3.1 Selectivity during initial hydrogenation stages

Product distribution at low conversions in the hydrogenation of citral with hexane and ethanol, has shown a significant difference in selectivity to C=C and C=O hydrogenation. Considering only the major primary hydrogenation products, **Figure 9.10** shows the selectivity towards α,β-double-bond hydrogenation, C=C, *vs.* C=O hydrogenation in citral at 10% conversion. Thus, selectivity towards citronellal, citronellal diethyl acetal and isopulegols, is compared with selectivity to unsaturated alcohols geraniol and nerol, and 3,7-dimethyl-2-octen-1-ol. As can be seen, primary C=C hydrogenation in hexane represented 53% of the total products formed (28% of citronellal and 25% of isopulegols). The remaining 47% consisted in C=O hydrogenation towards geraniol (19%) and nerol (14%) and 3,7-dimethyl-2-octen-1-ol (14%). Citronellol was formed (< 4% of all products) but was not attributed to either hydrogenation pathway, as it could have proceeded from both. Preferential C=C primary hydrogenation in ethanol corresponded to < 33% of the total products at 10% conversion (3.4% citronellal and 29.3% citronellal diethyl acetal). Preferential hydrogenation of C=O represented 67% of the product distribution, entirely

towards geraniol (23%) and nerol (44%). As can be seen, a clear preferential hydrogenation of the C=O bond *vs.* the C=C bond was observed in the case of ethanol. This observation was also compared considering the TOF for the formation of geraniol + nerol and citronellal during the initial reaction stages (< 30 min), representing < 5% conversion. In the case of hexane, the sum of the initial hydrogenation rates of citronellal and isopulegols together was 6.8×10^{-3} s^{-1}, whereas the hydrogenation towards geraniol + nerol represented 4.5×10^{-3} s^{-1}. Adding both terms to obtain hydrogenation rate of C=C and C=O, a values of 11.3×10^{-3} s^{-1} was obtained. This result was almost equivalent to the initial citral hydrogenation rate of citral, with a value of 11.5×10^{-3} s^{-1} (**Table 9.1**). These values contrasted with the TOF in ethanol for the formation of geraniol + nerol, with $\approx 1.0 \times 10^{-3}$ s^{-1}, very similar to the value of 1.2×10^{-3} s^{-1} for citral reduction.

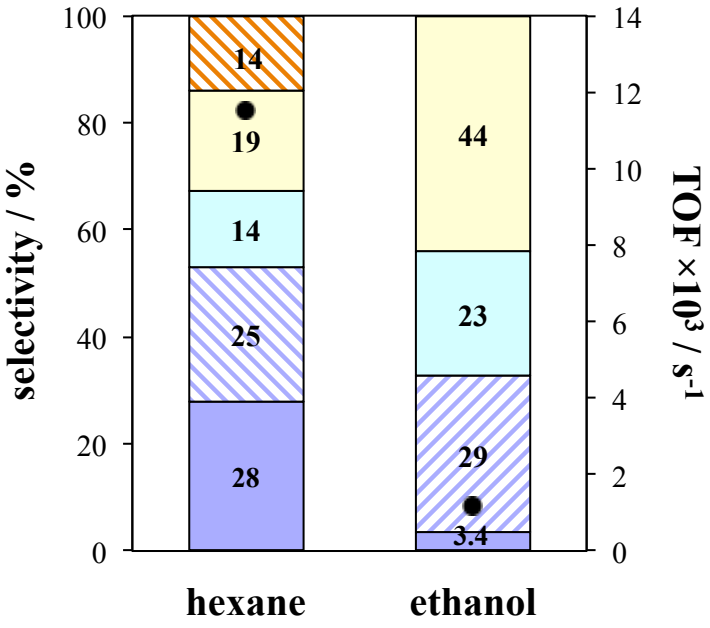

Figure 9.10. Selectivity (bars) and reaction rates (circles) of citral hydrogenation with hexane and ethanol. Product distribution towards primary hydrogenation species of citral at 10%. Reaction conditions: 0.3 g 5% Pt/SiO_2, 150 cm^3 solvent, 373 K, 10 bar(g), $c_0 = 0.13$ M. The legend of the different species is the same as shown in **Figure 9.1** for bulk bars. Dashed bars correspond to products related to citronellal (blue) or UALC (in yellow). See text for details.

This preferential C=O hydrogenation was observed previously in other studies, whereby the hydrogenation of citral in cyclohexane and 2-pentanol over Pt/Al_2O_3 resulted in selectivity towards geraniol + nerol of 15% and 31% on each solvent, respectively. (Mäki-Arvela *et al.*, 2006). Comparison with ethanol was performed in a similar study (Depboylu *et al.*, 2011), showing a higher geraniol + nerol selectivity of 39% in ethanol *vs.* 31% in 2-pentanol in the

hydrogenation of citral on 1% Pt/SiO_2. Hydrogenation of other α,β-unsaturated aldehydes, such as cinnamaldehyde (Shirai *et al.*, 2001) or crotonaldehyde (Englisch *et al.*, 1997a, 1997b) on Pt catalysts have reported similar trends, with higher selectivity towards C=O hydrogenation in the presence of alcohols as opposed to non-polar solvents. Selectivity towards unsaturated alcohols geraniol and nerol was influenced by solvent type in the hydrogenation of cinnamaldehyde with the following trend: methanol > ethanol > 2 propanol > cyclohexane. The use of chloroform and cyclohexane resulted in low conversions and in a low yield to the unsaturated alcohol crotylalcohol, 5% and 10% selectivity, respectively, as compared to 20% selectivity when ethanol was used. It is worth mentioning that actual selectivity values cannot be compared as selectivity towards C=C and C=O hydrogenation has been previously shown to be strongly dependent on the degree of substitution of the olefinic bond (Marinelli *et al.*, 1995).

Reaction rate, as well as product distribution results can also be understood from the NMR relaxometry data. ^{13}C T_1 NMR relaxometry, as well as ^{1}H 2D T_1-T_2 correlations showed a weaker interaction of citral on 5% Pt/SiO_2 when ethanol was present, in agreement with a lower reaction rate experimented by citral. Thus, values of $T_1/T_2 = 54$ and $T_1/T_2 = 37$ in the case of citral co-adsorbed with hexane and ethanol, respectively, showed that a weaker interaction of the reactant, led to a depletion in the reaction rates. These results are in agreement with previous work by D'Agostino *et al.* (2012). In that case, the presence of water on Au/TiO_2 showed a reduction in the reaction rates, and a significant depletion in the T_1/T_2 values. That result was associated with a reduced surface interaction of the reactant, 1,4-butanediol, in the presence of water. In terms of selectivity, a significant difference was observed in the general adsorption geometry of citral in the presence of hexane *vs.* ethanol. As can be seen in **Figure 9.5**, citral showed a stronger interaction of C1 to C4 as compared to the rest of the backbone chain, which arranged parallel to the Pt/SiO_2 surface. Comparing with the $T_{1,ads}/T_{1,bulk}$ maximum and minimum values of the solvent, hexane, $T_{1,ads}/T_{1,bulk} = 0.70$ and $T_{1,ads}/T_{1,bulk} = 0.35$, carbons C1 to C4 of citral presented a stronger interaction, as compared to the rest of the carbons. In the case of citral in the presence of ethanol, citral showed a stronger interaction of C1, C3 and C7, indicating a more complex arrangement with the Pt/SiO_2 surface. Comparing with the $T_{1,ads}/T_{1,bulk}$ values of the two carbons in ethanol, $T_{1,ads}/T_{1,bulk} = 0.60$ and $T_{1,ads}/T_{1,bulk} = 0.45$, all citral carbons presented a weaker interaction with the surface, with C1, C3 and C7 in line with ethanol values. These solvent-catalyst and reactant-catalyst interactions were in agreement with ^{1}H T_1/T_2 values

vide supra, particularly if considered with the solvent T_1/T_2 values. The $T_1/T_2 = 54$ for citral and $T_1/T_2 = 21$ for hexane reinforced the finding of a strong interaction of citral in that solvent. These results were also in line with a preferential citral adsorption observed in the NMR spectra. In ethanol, and using the results from deuterated and non-deuterated samples (**Table 9.4**), values of $T_1/T_2 = 37$ for citral and $T_1/T_2 = 33$ for ethanol were obtained. Clearly in ethanol, a much more similar interaction was observed between solvent and reactant.

If the reactive bonds are now considered, acknowledging it was not possible to determine the interaction strength of oxygen on 5% Pt/SiO_2 surface, a closer interaction of the α,β-double-bond was observed with hexane. Specifically, while a general weaker interaction is observed in C1, C2 and C3, the ratio $T_{1,ads}/T_{1,bulk}$ for C2 showed a significant change, from $T_{1,ads}/T_{1,bulk} = 0.29$ with hexane to $T_{1,ads}/T_{1,bulk} = 1.31$ in ethanol. These values suggested a preferential interaction of citral with ethanol, as compared to the 5% Pt/SiO_2 surface. Examining the variation of C1, C2 and C3 taking hexane as reference, it was observed a 3.3 fold increase in the $T_{1,ads}/T_{1,bulk}$ of C1 (from $T_{1,ads}/T_{1,bulk} = 0.29$ to $T_{1,ads}/T_{1,bulk} = 0.75$), a 4.5 fold increase for C2 and a 4.1 fold increase for C3. This comparison showed an enhanced weakening of the double-bond interaction as opposed to the carbonylic carbon. An examination of the values corresponding to each bond can be made. Comparing the average $T_{1,ads}/T_{1,bulk}$ of C2-C3 *vs.* C1, it is observed that a value of $T_{1,ads}/T_{1,bulk} = 0.23$ was observed for C1 and for C2-C3 in hexane *vs.* $T_{1,ads}/T_{1,bulk} = 0.75$ for C1 and $T_{1,ads}/T_{1,bulk} = 1$ for C2-C3 in ethanol. Previous studies have simulated the adsorption configuration of complex α,β-unsaturated aldehydes on Pt metal surfaces (Delbecq and Sautet, 1995). In this publication, mainly three adsorption modes were described to occur: i) di-σ_{cc}, C=C bond adsorption; ii) di-σ_{co}, C=O group interaction only; and iii) η_4, with both C=O and C=C adsorption. It was shown that only the di-σ_{co} mode favoured the formation of unsaturated alcohols geraniol and nerol. Those findings were applied in the hydrogenation of crotonaldehyde (Englisch *et al.*, 1997b), where an increased particle size was related with predominant Pt(111) planes exposed and di-σ_{co} adsorption. Similarly, in the hydrogenation of citral (Siani *et al.*, 2009) the addition of Fe showed a decrease in the di-σ_{cc} adsorption mode on Pt, making the di-σ_{co} adsorption mode the predominant one. It can be observed that in this study, the use of ethanol led to the same effect, observed experimentally *via* NMR relaxometry results.

9.3.2 Selectivity at high conversions

As seen in **Figure 9.1**, multiple components were present in the reaction mixture at 70% conversion. All of those species could participate in subsequent hydrogenation reactions, as opposed to sequential reaction systems, where only some of the molecules would dominate the surface. Therefore, it would be expected that the overall product distribution and surface reaction be conditioned by the presence of these intermediates, and not only citral. A hypothesis on the reaction pathway has been previously discussed in terms of competitive adsorption between different reaction intermediates. For example, the desorption of products has been shown to strongly determine selectivity, such as in the hydrogenation of acrolein on Pt(111) (Loffreda *et al.*, 2006). Hydrogenation of the main reaction intermediates observed during the hydrogenation of citral, citronellal, UALC and citronellol, was studied to obtain information on these mechanisms. The effect that the solvent might play in the adsorption behaviour of multicomponent reaction mixtures was addressed. NMR relaxometry results were used to understand the role that main reaction intermediates could play on product distribution as a function of solvent used. Thus, the interaction strength and the extent of adsorbate-adsorbent interactions of citronellal, UALC, and citronellol with 5% Pt/SiO_2 was determined in the presence of hexane and ethanol.

9.3.2.1 Hexane as solvent

Previous hydrogenation data shown in **Figure 9.1**, indicated that citral was equally reacting *via* C=C and C=O, showing no preferential hydrogenation, although rates were slightly faster in the case of citronellal formation. Results in **Figure 9.2** showed that citronellal and UALC reacted mainly towards citronellol. Isomerisation between citronellal and unsaturated alcohols, geraniol and nerol, was reported previously not to occur on this catalyst in liquid-phase citral hydrogenation (Singh and Vannice, 2000; Singh *et al.*, 2000). Only a slight isomerisation of geraniol and nerol towards citronellal (~1%) was observed. These findings indicated that product distribution was based solely on selectivity hydrogenation of C=O or C=C bond. Citronellal hydrogenation showed high conversion and high selectivity towards citronellol, whereas UALC hydrogenation exhibited lower conversion, in agreement with previous results (Singh *et al.*, 2000). This dissimilarity in conversion might be due to the formation of relative high amounts of fragments (7.6%) only seen in UALC, but reported previously in this type of catalyst (Mäki-Arvela *et al.*, 2004). Furthermore, the T_1/T_2 values of hexane, T_1/T_2 = 8 in citronellal *vs.* T_1/T_2 = 37 in UALC, suggested the presence of a

competitive adsorption-desorption process. In addition, citronellol hydrogenation reached only 20% conversion, towards the formation of 3,7-dimethyl-1-octanol, in agreement with previous reports (Singh and Vannice, 2000). These results from the hydrogenation of reaction intermediates could be interpreted considering that citronellol was preferentially adsorbing on the surface of the catalyst. Thus, citronellal, geraniol and nerol hydrogenated towards the formation of citronellol. Citronellol depleted the formation of other partially hydrogenated products, isopulegols and menthols from citronellal and 3,7-dimethyl-2-octen-1-ol from geraniol and nerol. At the same time, the strong adsorption of citronellol would limit the reaction on the Pt catalyst, as observed. Interpretation of the ^{1}H 2D T_1-T_2 NMR relaxometry results showed that the relative strength of interaction for the species studied was citronellol > citral > UALC > citronellal. As expected, T_1/T_2 of the reaction intermediates in the presence of hexane indicated that citronellol would preferentially adsorb over other intermediate species.

Hence, the hydrogenation of citral in hexane presented the following aspects: at low conversion both C=C and C=O could hydrogenate, as shown by the configuration of citral from ^{13}C T_1 NMR relaxometry results. At such point, citral was the major species in solution, and its relative interaction strength with T_1/T_2 = 54, was greater than citronellal, with T_1/T_2 = 29, and UALC, with T_1/T_2 = 38. As citral showed a stronger interaction, it continued hydrogenating and a net accumulation of citronellal and UALC was observed. Also, citronellal and UALC hydrogenation was observed. Reduction of citronellal progressed towards the formation of citronellol and cyclisation products. The formation of isopulegols has been previously shown to be favoured in apolar solvents (Iosif *et al.*, 2004; Mäki-Arvela *et al.*, 2002). Hydrogenation of UALC generated 3,7-dimethyl-2-octen-1-ol as well as citronellol. At high conversion, most of the citral was displaced by citronellol, controlling the reaction of other intermediates and determining subsequent hydrogenation.

9.3.2.2 Ethanol as solvent

Hydrogenation of citral in ethanol, showed a very different product distribution as compared to reduction in hexane, as shown in **Figure 9.1**. Preferential C=O bond hydrogenation vs. C=C bond reduction was shown. The accumulation of geraniol, nerol and citronellal diethyl acetal was observed at high conversion. Formation of citronellol or other reduced products was negligible. This behaviour is typical from a product competitive adsorption mechanism, preventing subsequent hydrogenation (Loffreda *et al.*, 2006). These results initially would

suggest that one of the species present could preferentially block the reaction, still allowing citral preferential adsorption. In this case, the reaction of intermediate species rendered useful information to clarify this aspect.

Hydrogenation of citronellal in ethanol revealed complete conversion could be obtained on 5% Pt/SiO_2. Selectivity results showed preferential cyclisation to isopulegols (15%) and subsequent hydrogenation to menthols (42%). Formation of citronellal diethyl acetals (4.9%) was noted, as well as dihydrocitronellal diethyl acetal (5.3%). Direct hydrogenation of the C=O bond towards citronellol (10%) and 3,7-dimethyl-1-octanol (15%) formation represented only a small fraction of the total products observed. In addition, the presence of some decarbonylation fragments was noted (7.6%). The predominant formation of cyclic products revealed that the catalyst used presented some acidity, as indicated by previous reports on the synthesis of menthols from citronellal (Trasarti *et al.*, 2007; Chuah *et al.*, 2001). More interesting was the extent of side reactions in ethanol, as compared to hexane. Previous studies have suggested that cyclisation reactions would be reduced by the formation of acetals (Gallezot and Richard, 1998; Mäki-Arvela *et al.*, 2002), something not observed in this case. Hydrogenation of UALC showed predominantly the formation of ethers of geraniol and nerol (45%), not related to the hydrogenation of the α,β double-bond. In addition, an increasing yield towards fragment products was observed, with 27.9% selectivity. The low proportion of citronellol (2.3%) and 3,7-dimethyl-1-octanol (1.4%) showed that UALC did not hydrogenate further, suggesting a possible blockage of the surface. Reactivity of geraniol and nerol towards other species was previously suggested as a deactivation mechanism of the catalyst *via* CO adsorption (Singh and Vannice, 2000). Surprisingly, citronellol did not show any reactivity in ethanol. These results indicated that the formation of 3,7-dimethyl-1-octanol in the hydrogenation of citronellal proceeded *via* hydrogenation of dihydrocitronellal and its acetal.

As was observed, reaction of citronellal and UALC intermediates was dominated by side reactions, while no reaction was observed with citronellol. The overall lack of direct hydrogenation activity of reaction intermediates suggested Pt sites were not crucial in this system. Therefore, a complex mechanism not only based on product adsorption would be expected. Analysis of both solvent and reaction intermediate data revealed an interesting phenomena (**Table 9.4**). Citral presented a $T_1/T_2 = 37$, citronellal $T_1/T_2 = 25$, UALC $T_1/T_2 = 32$ and citronellol $T_1/T_2 = 28$ in ethanol-d_6. Ethanol T_1/T_2 values of 32.5, 29, 33 and 33 were observed in the presence of citral, citronellal, UALC and citronellol, respectively.

Ethanol showed the same value across systems, except with citronellal. Comparing the solvent *vs*. reaction species T_1/T_2, the hydrogenation of citral was explained by preferential adsorption, which in fact also explained the inertness of citronellol in ethanol. UALC and ethanol showed very similar T_1/T_2 values, indicating a weak adsorption with the surface. Citronellal results indicated that no favourable interaction with the surface would occur, as the T_1/T_2 value in ethanol was higher. However, as mentioned, side reactions towards cyclic products were observed, which do not require the interaction with metal sites. The use of bifunctional catalysts has been design as a means to improve cyclisation of citronellal to isopulegols (Trasarti *et al.*, 2007). Acid sites in these catalysts allowed for cyclisation to occur while metal sites favoured hydrogenation to citronellal and menthol. Overall, these results would explain the formation of cyclic products from hydrogenation of citronellal, but not from citral, as the adsorption of citral would control the active reaction pathways.

In summary, the preferential adsorption of citral explained the reactivity observed. The interaction of the reaction intermediates and ethanol explained the product distribution observed. In addition, the presence of such similar T_1/T_2 values between ethanol and all reaction intermediate species indicated the presence of solvent-reactant interactions in this system. The result is consistent with the presence of hydrogen bonding between alcohol molecules. Recalling ^{13}C T_1 NMR relaxometry results, similar interactions were observed on citral double-bonds (C2-C3 and C6-C7), with $T_{1,ads}/T_{1,bulk} > 1$ for C2 and C6. These values indicated, as mentioned in section 4.1, the presence of strong solvent interactions with citral. The effect of alcohols on selectivity during hydrogenation of citral has been shown previously (Mäki-Arvela *et al.*, 2002), while the interaction of alcohols with reaction species has been studied on other carbonyl molecules (Akpa *et al.*, 2012). NMR relaxometry results have shown the interplay between surface, reactive molecules and solvent interactions, and the impact on the different reaction pathways.

9.3.3 Comparison: NMR relaxometry *vs*. other characterisation measurements

Liquid isotherms, TEOM, DRIFTS and ATR measurements, as well as complementary studies on the effect of concentration and support silylation in hexane and ethanol are compared with reaction of main intermediates as well as NMR relaxometry results. Three main points are considered: i) the strength and geometry of adsorption of citral, ii) product as well as solvent competitive adsorption, and iii) liquid-liquid interactions with solvent.

Both ^{13}C T_1 and 2D ^{1}H T_1-T_2 NMR relaxometry results clearly showed a much stronger adsorption of citral in hexane as compared to adsorption in the presence of ethanol. Previous adsorption isotherm studies (section 8.2.2.1) showed that citral adsorbed more strongly in hexane *vs*. ethanol across all temperatures. Additionally, DRIFTS results on the adsorption of solvent (section 8.2.2.2) were indicative of the stronger interaction of ethanol and the reduced strength of adsorption of citral. ^{1}H T_1/T_2 results on the adsorption of ethanol in single-component and binaries also indicated limited citral adsorption and solvent interactions with the catalyst. For example, reaction rate results in the silylated catalyst (section 8.2.3.2) indicated that any competition in the adsorption of citral due to hexane was affected by hydrophobic interactions with the support. Similarly, the increased concentration of citral showed the effect of preferential adsorption in hexane. In line with solvent interactions, the absence of hydrogenation in DCM and diethyl ether was considered a strong indication of solvent adsorption. In terms of selectivity, the geometry of interaction of citral on 5% Pt/SiO_2 was observed to modify the pathway towards C=C *vs*. C=O hydrogenation. ^{13}C T_1 NMR relaxometry results showed that for the same initial citral concentration ($c_0 = 0.13$ M), the use of hexane *vs*. ethanol resulted in a different reaction rate and product distribution. Non-NMR adsorption techniques did not provide information on the adsorption geometry of citral. However, the product distribution in hexane with $c_0 = 0.33$ M was indicative of a modification in the adsorption mode of citral (section 8.2.3.1). The modification of adsorption modes with increased concentration has been previously reported in cinnamaldehyde hydrogenation (Breen *et al.*, 2004).

Hydrogenation results and ^{1}H T_1/T_2 measurements showed product adsorption-desorption was strongly dependent on solvent type. Particularly, reaction in hexane was driven at high conversion by citronellol adsorption, while citronellal, geraniol and nerol did not show such adsorption behaviour. In contrast, TEOM results (section 8.2.2.2) showed similar adsorption of all reaction intermediates in the absence of solvent. Reaction studies with different solvents at 298 K showed the effect of product adsorption, particularly in cyclohexane. The hindered desorption of products limited conversion. Again, it is noteworthy the indirect detection of such product desorption. TPD and TPO studies (section 8.2.2.3) also related product desorption with deactivation as a function of solvent type, in particular with hexane and ethanol. Such information indicated the relevance, validity and versatility of NMR relaxometry measurements.

Interactions between solvent and reaction species were measured with IR. As noted in ATR measurements (section 8.2.1), the interaction of citral was noted in alcohol solvents, in particular with the aldehyde group, as contrasted with results in acetone. Thus, selectivity results in alcohols were also related with liquid-liquid interactions. Here, ^{1}H T_1/T_2 NMR relaxometry results in deuterated and non-deuterated binary mixtures revealed the similar interactions of ethanol and reaction intermediates with the surface. Those results were indicative of interactions in the liquid phase, as also observed with the ^{13}C $T_{1,ads}/T_{1,bulk}$ values of citral in ethanol (section 9.3.1). Complementary, results of the reaction of main intermediates, citronellal, citronellol and UALC, in ethanol showed the limited hydrogenation of intermediates and the marked importance of side reactions. Overall, these results were indicative of limited catalyst-surface interactions and the presence of strong liquid-liquid interactions.

As can be seen, NMR relaxometry results were complementary to adsorption techniques employed in chapter 8, and in line with reaction rate results, as well as information on catalyst-liquid interactions and liquid-liquid interactions.

9.4 Conclusions

NMR relaxometry has been used for the first time to understand the effect of solvent in the selective hydrogenation of α,β-unsaturated aldehydes, and the hydrogenation of thermodynamically less reactive C=O bond. Reaction rates and selectivities have been obtained for the hydrogenation of citral on 5% Pt/SiO_2 at 373 K using hexane and ethanol as solvents. Differences in the preferential hydrogenation of C=O *vs.* C=C bond as a function of solvent used have been observed, consistent with previous literature. Hydrogenation of the main reaction intermediates at the same conditions was used to obtain information on the preferred hydrogenation pathways of citral. A competitive adsorption mechanism was postulated based on differences in the selectivity from the hydrogenation of intermediates. ^{13}C T_1 NMR and ^{1}H 2D T_1-T_2 correlation experiments have been used to obtain adsorption geometry and relative strength of interaction of citral in the presence of hexane and ethanol, and relative strength of interaction of main reaction intermediates, citronellal, 1:1 mol:mol geraniol:nerol mixtures (UALC), and citronellol. ^{13}C T_1 relaxometry has shown that the interaction of the conjugated carbon-carbon double bond in citral was weaker in the presence of ethanol than in hexane, explaining the initial reaction selectivity towards primary hydrogenation products. ^{1}H 2D T_1-T_2 relaxometry has revealed that citronellol showed the

strongest surface interaction in the presence of hexane; while competitive adsorption of ethanol with reaction intermediates determined the selectivity and reaction pathways active in that solvent. The effect of the strongest adsorbed species correlated well with the observed conversion and selectivity for citral and the main intermediates of reaction. Additionally, a comparison of the conclusions from NMR relaxometry and the characterisation techniques from chapter 8 was established. This work represents a valuable approach towards a rational selection of solvent, where a prior understanding on adsorbate-adsorbent interactions in complex reaction systems can reduce the number of reaction studies.

References

Akpa, B.S., D'Agostino, D., Gladden, L.F., Hindle, K., Manyar, H., McGregor, J., Li, R., Neurock, M., Sinha, N., Stitt, E.H., Weber, D., Zeitler, J.A., Rooney, D.W. (2012) Solvent effects in the hydrogenation of 2-butanone. *J. Catal.*, 289, 30 – 41.

Barrales, C.A., Viveros, T. Synthesis of menthol from citral over mechanical mixtures of Ni/SiO_2 and sulfated zirconia. *Proceedings of the 23rd North American Catalysis Meeting (NAM), June 2-7, 2013, Louisville, Kentucky*

Breen, J.P., Burch, R., Gómez-López, J., Griffin, K., Hayes, M. (2004) Steric effects in the selective hydrogenation of cinnamaldehyde to cinnamyl alcohol using an Ir/C catalyst. *Appl. Catal. A-Gen.*, 268, 267 – 274.

Chatterjee, A., Chatterjee, M., Ikushima, Y., Mizukami, F. (2004) The role of solvent on selective hydrogenation of conjugated and isolated C=C of citral (3,7-dimethyl-2,6-octadienal) – a self consistent reaction field study. *Chem. Phys. Let.*, 395, 143 – 149.

Chuah, G.K., Liu, S.H., Jaenicke, S., Harrison, L.J. (2001) Cyclisation of citronellal to isopulegol catalysed by hydrous zirconia and other solid acids. *J. Catal.*, 200, 352 – 359.

D'Agostino, C., Brett, G.L., Miedziak, P.J., Knight, D.W., Hutchings, G.J., Gladden, L.F., Mantle, M.D. (2012) Understanding the solvent effect on the catalytic oxidation of 1,4-butanediol in methanol over Au/TiO2 catalyst: NMR diffusion and relaxation studies. *Chem. Eur. J.*, 18, 14426 – 14433.

D'Agostino, C., Mitchell, J., Mantle, M.D., Gladden, L.F. (2014) Interpretation of NMR relaxometry as a tool for characterising the adsorption strength of liquids inside porous materials. *Chem. Eur. J.*, 20, 1309 – 1315.

Delbecq, F., Sautet, P. (1995) Competitive C=C and C=O adsorption of α,β unsaturated aldehydes on Pt and Pd surfaces in relation with the selectivity of hydrogenation reactions: a theoretical approach. J. Catal., 152, 217 – 236.

Depboylu, C.O., Yilmaz, S., Akkurt, S. (2011) Effects of catalyst precursor type and preparation conditions, and solvent type on activity and selectivity of Pt/SiO_2 catalyst in citral hydrogenation. *Int. J. Chem. React. Eng.*, 9, A27.

Ekou, T., Flura, A., Ekou, L., Especel, C., Royer, S. (2012) Selective hydrogenation of citral to unsaturated alcohols over mesoporous $Pt/Ti\text{-}Al_2O_3$ catalyst. Effect of the reduction temperature and of the Ge addition. *J. Mol. Catal. A-Chem.*, 353, 148 – 155.

Englisch, M., Ranade, V.S, Lercher, J.A. (1997b) Liquid-phase hydrogenation of crotonaldehyde over Pt/SiO_2 catalysts. *Appl. Catal. A-Gen.*, 163, 111 – 122.

Englisch, M., Jentys, A., Lercher, J.A. (1997a) Structure sensitivity of the hydrogenation of crotonaldehyde over Pt/SiO_2 and Pt/TiO_2. *J. Catal.*, 166, 25 – 35.

Gallezot, P., Richard, D. (1998) Selective hydrogenation of α,β-unsaturated aldehydes. *Catal. Rev.-Sci. Eng.*, 40, 81 – 126.

Hájek, J., Kumar, N., Mäki-Arvela, P., Salmi, T. and Murzin, D.Y. (2004) Selective hydrogenation of cinnamaldehyde over Ru/Y zeolite. *J. Mol. Catal. A-Chem.*, 217, 145 – 154.

Ide, M.S., Hao, B., Neeurock, M., Davis, R.J. (2012) Mechanistic insights on the hydrogenation of α,β-unsaturated ketones and aldehydes to unsaturated alcohols over metal catalysts. *ACS Catal.*, 2, 671 – 683.

Iosif, F., Coman, S., Pârvulescu, V., Grange, P., Delsarte, S., de Vos, D., Jacobs, P. (2004) Ir-beta zeolite as a heterogeneous catalyst for the one-pot transformation of citronellal to menthol. *Chem. Commun.*, 1292 – 1293.

Liu, G., Li, Y., Jonas, J. (1991) Confined geometry effects on reorientational dynamics of molecular liquids in porous silica glasses. *J. Chem. Phys.*, 95, 6892 – 6901.

Loffreda, D., Delbecq, F., Vigné, F., Sautet, P. (2006) Chemo-regioselectivity in heterogeneous catalysis: competitive routes for C=O and C=C hydrogenations from a theoretical approach. *J. Am. Chem. Soc.*, 128, 1316 – 1323.

Mäki-Arvela, P., Tiainen, L-P., Neyestanaki, A.K., Sjöholm, R., Rantakyla, T-K., Laine, E., Salmi, T., Murzin, D.Y. (2002) Liquid phase hydrogenation of citral: suppression of side reactions. *Appl. Catal. A-Gen*., 237, 181 – 200.

Mäki-Arvela, P., Kumar, N., Paseka, I., Salmi, T., Murzin, D.Y. (2004) Support effects in nerol hydrogenation over Pt/SiO_2, Pt/H-Y and Pt/H-MCM-41 catalysts. *Catal. Lett.*, 98, 173 - 179.

Mäki-Arvela, P, Kumar, N., Eränen, K., salmi, T., Murzin, D.Y. (2006) Inverse temperatura dependence due to catalyst deactivation in liquid-phase citral hydrogenation over Pt/Al2O3. *Chem. Eng. J.*, 122, 127 – 134.

Marinelli, T.B.L.W., Nabuurs, S., Ponec, V. (1995) Activity and selectivity in the reactions of substituted α,β-unsaturated aldehydes. *J. Catal.*, 151, 431 – 438.

Minot, C., Gallezot, P. (1990) Competitive hydrogenation of benzene and toluene: theoretical study of their adsorption on ruthenium, rhodium and palladium. *J. Catal.*, 123, 341 – 348.

Mitchell, J., Chandrasekera, T.C., Johns, M.L., Gladden, L.F. (2010) Nuclear magnetic resonance relaxation and diffusion in the presence of internal gradients: the effect of magnetic field strength. *Phys. Rev. E*, 81, 026101.

Mounzer, H.N., Wood, J., Stitt, E.H. (2010) Heterogeneous oxidation of 2-octanol on 5 wt%Pt-1 wt%Bi/Carbon catalyst. *Chem. Eng. Sci.*, 65, 179 – 185.

Mukherjee, S., Vannice, M.A. (2006) Solvent effects in liquid-phase reactions I. Activiy and selectivity during citral hydrogenation on Pt/SiO_2 and evaluation of mass transfer effects. *J. Catal.* 243, 108 – 130.

Reyes, P., Rojas, H., Fierro, J.L.G. (2003) Kinetic study of liquid-phase hydrogenation of citral over Ir/TiO_2 catalysts. *Appl. Catal. A-Gen.*, 248, 59 – 65.

Shirai, M., Tanaka, T., Arai, M. (2001) selective hydrogenation of a,b-unsaturated aldehyde to unsaturated alcohols with supported platinum catalysts at high pressures of hydrogen. *J. Mol. Catal. A-Chem.*, 168, 99 – 103.

Siani, A., Alexeev, O.S., Lafaye, G., Amiridis, M.D. (2009) The effect of Fe on SiO_2-supported Pt catalysts: structure, chemisorptive and catalytic properties. *J. Catal.*, 266, 26 – 38.

Singh, U.K., Vannice, M.A. (2000) Liquid-phase hydrogenation of citral over Pt/SiO_2 catalysts. I. Temperature effects on activity and selectivity. *J. Catal.*, 191, 165 – 180.

Singh, U.K., Sysak, M.N., Vannice, M.A. (2000) Liquid-phase hydrogenation of citral over Pt/SiO_2 catalysts. II. Hydrogenation of reaction intermediate compounds. *J. Catal.*, 191, 181 – 191.

Trasarti, A.F., Marchi, A.J., Apesteguía, C.R. (2007) Design of catalyst systems for the one-pot systhesis of menthols from citral. *J. Catal.*, 247, 155 – 165.

Zgolicz, P.D., Stassi, J.P., Yañez, M.J., Scelza, O.A., de Miguel, S.R. (2012) Influence of the support and the preparation methods on the performance in citral hydrogenation of Pt based catalysts supported on carbon nanotubes. *J. Catal.*, 290, 37 – 54.

Chapter 10:

Conclusions and future work

10 Conclusions and future work

In this chapter, section 10.1 presents the conclusions of the work presented in chapters 3 to 5 and 7 to 9. Recommendations for future work are provided in section 10.2.

10.1 Conclusions

Chapters 4 and 5 provided information on the adsorption of a series of unsaturated hydrocarbons on γ- and θ-Al_2O_3, while chapters 7 to 9 presented results on the selective hydrogenation of citral. Section 10.1.1 reviews the studies of adsorption on aluminas, while the work related to the selective hydrogenation of citral is reviewed in section 10.1.2.

10.1.1 Adsorption of unsaturated hydrocarbons

Knowledge of adsorbate geometry and interaction strength is of importance in chemical sensors and heterogeneous catalysis where the interaction of adsorbates with active surface sites influences performance.

The adsorption of a series of C_5 and C_6 hydrocarbons on γ- and θ-Al_2O_3 was studied with various characterisation techniques. IR spectroscopy, volumetric adsorption isotherms, dynamic adsorption isotherms recording using a TEOM, temperature-programmed desorption (TPD) as well as ^{13}C T_1 NMR and ^{1}H 2D T_1-T_2 relaxometry methods were employed. Energies of adsorption as a function of coverage were obtained *via* adsorption isotherms and particular surface-adsorbate interactions were characterised using IR spectroscopy. IR showed a weak adsorption on the aluminas *via* the unsaturated bond bonded weakly to OH groups on the surface of porous alumina. Heats of adsorption were obtained for each hydrocarbon for coverages > 5 – 10% ML, evidence of the effect of the dependence of adsorption with coverage, adsorption sites and the presence of lateral interactions. 1-pentyne showed the strongest interaction with θ-Al_2O_3 (94 kJ mol^{-1}), followed by the acyclic olefins (54 - 34 kJ mol^{-1}) and cyclohexene with the weakest adsorption (11 kJ mol^{-1}). Information was extracted on the preferential triple bond interaction, as well as the relative linear *vs.* cyclic olefin adsorption. Additionally, the relative position of the double-bond in acyclic olefins, 54 kJ mol^{-1} for *trans*-2-pentene *vs*. 34 kJ mol^{-1} for *cis*-2-pentene, showed preferential adsorption behaviour. In contrast to the adsorption isotherm results, desorption energies obtained from TPD were significantly higher than adsorption energies. Energies of desorption were in the range 85 – 130 kJ mol^{-1} for initial surface coverages in the range 1-5%

ML. E_{max} values obtained from the TPD curves were insensitive to the molecule adsorbed. Reactivity of the aluminas was captured with TPD and was found to be weakly dependent on the adsorbate.

Comparisons were also made of a number of adsorption techniques. A comparison between dynamic – TEOM – and batch isotherms revealed similar uptake values for both adsorption methods. The results suggest that TEOM is also sensitive to any reactions occurring on the surface. A stronger interaction was observed on θ-Al_2O_3 as compared to γ-Al_2O_3 as noted by TEOM, IR and 2D ^{1}H T_1-T_2 NMR relaxometry results. Additional information was obtained on the effect of adsorption with pre-treatment temperature. Pre-treatment temperature of the alumina exposed stronger acid sites, as noted with TEOM and 2D ^{1}H T_1-T_2 and ^{13}C T_1 NMR relaxometry results. Furthermore, the presence of adsorbate-adsorbate interactions was identified in the adsorbed hydrocarbons. Hence, weak adsorption of the hydrocarbons on the aluminas was predominantly observed with IR, TEOM and volumetric isotherms. In contrast, high desorption energies, > 80 kJ mol^{-1}, were obtained with TPD. Two different energetic regimes were found for the adsorption of C_5 and C_6 unsaturated hydrocarbons on aluminas. Pyridine adsorption showed the presence of Lewis acid sites and a weak coordination with OH groups. It is proposed that the two interaction energies are associated with weak Brønsted and strong Lewis acid sites, respectively. The relative number of strong Lewis sites increases when higher pre-treatment temperatures are used. These results demonstrate the importance of using multiple techniques to gain a detailed description of the molecular processes occurring at the surface.

The application of chemical shift resolved ^{13}C NMR T_1 relaxometry for the characterisation of adsorbate interactions with alumina surfaces was also reported. Studies of adsorption as a function of surface coverage demonstrated the average interaction strength was greater at lower surface coverage, indicating molecules adsorb preferentially on the strongest adsorption sites. Similarly, the temperature of adsorption showed similar effects. More importantly, information on atom-specific adsorbate-adsorbent interaction strengths and the molecular conformations of the adsorbates was inferred with the use of ^{13}C NMR relaxometry. In addition, co-adsorption measurements showed the change in adsorption strength of 1-pentene when in the presence of a second molecule. Important implications of these results were discussed, such as the influence of coke, CO or alkyne adsorption on the relative strength of adsorption of olefins. The results on adsorption of 1-pentene showed that

^{13}C T_1 NMR relaxometry is a useful tool to determine interactions in catalytically-relevant surfaces. More generally, a comparison between NMR relaxometry results with information obtained from the rest of the adsorption techniques for the adsorption of unsaturated hydrocarbons on γ- and θ-Al_2O_3 was made. While ^{13}C T_1 NMR relaxometry was sensitive to the particular molecule adsorbed, its coverage and adsorption geometry, the T_1/T_2 values obtained from ^{1}H 2D T_1-T_2 showed a good correlation with the 1 % strongest adsorption sites probed. A good agreement between conventional characterisation techniques and NMR relaxometry methods was found. Recommendations on the different techniques to be used in future adsorption experiments were made.

10.1.2 Hydrogenation of citral

Insights from the adsorption of unsaturated hydrocarbons on aluminas were applied to understand why particular reaction pathways were followed in a catalytic reaction. A range of adsorption measurements was employed to obtain relevant information on adsorbate-adsorbent interactions. The hydrogenation of citral on 5% Pt/SiO_2 was studied in a range of solvents to provide information on solvent effects in reaction rates and selectivities. An understanding of the role of solvent in reaction rates and selectivities was obtained, based on differences in liquid-liquid and catalyst-liquid interactions as determined by the characterisation techniques discussed in section 10.1.1.

The selective hydrogenation of citral was studied on 5% Pt/SiO_2 at two different temperatures 298 K and 373 K and c_0 = 0.13 M. Polar protic solvents, ethanol, 2-propanol and 2-pentanol; polar aprotic solvents, diethyl ether, DCM and acetone; and non-polar solvents, hexane, cyclohexane and decalin, were used. Results showed that solvent polarity influenced reaction rates and selectivities in the hydrogenation of citral. However, H_2 solubility alone in the different solvents was not able to explain hydrogenation rates. Higher rates were observed in non-polar solvents at 298 K, while polar protic solvents showed lower initial hydrogenation rates. In contrast, polar protic solvents showed higher yields of geraniol and nerol. Diethyl ether and DCM inhibited reaction completely at 298 K. Reaction temperatures also had a strong influence on citral hydrogenation. Increasing the temperature to 373 K decreased initial reaction rates, affecting predominantly reactions occurring in non-polar solvents, while it also reduced deactivation. Selectivity towards unsaturated alcohols geraniol and nerol, increased with temperature predominantly in non-polar solvents, while it remained similar in polar protic solvents. Deactivation of the catalyst was observed to occur in all solvents, and

was considered to be strongly affected by by-product adsorption and decarbonylation. Deactivation was more pronounced at 298 K, with higher conversions observed at 373 K. Side reactions were also observed. Overall, cyclisation and decarbonylation were favoured in non-polar solvents, while acetals were reversibly formed in polar protic solvents. Finally, the hydrogenation of citral in DCM resulted in cyclisation reactions that led to the formation of cyclic hydrogenated dehydrated products, such as limonenes and menthanes.

The strong variations in reaction rates and selectivities reported were related to the strength of interaction of citral with the catalyst, as well as the degree of solvation, especially at 298 K. TEOM mass uptake values and liquid isotherm results showed that solvent reduced the adsorption capacity of citral, particularly in ethanol, and this caused a reduced rate of reaction. DRIFTS results on the adsorption of solvent also confirmed such trends. Solvent-reactant competitive adsorption determined the absence of reaction in diethyl ether and DCM at 298 K, as well as the effect of higher citral concentrations or the type of support on reaction rates. Similarly, deactivation of the catalyst was attributed to product and by-product retention on the surface, facilitated by solvent. This was demonstrated comparing citral conversion using cyclohexane *vs.* cyclohexanol as solvents, or comparing CO and hydrocarbon desorption from TPD and TPO from hydrogenation in hexane *vs.* ethanol. Selectivity trends were related to liquid-liquid interactions in polar protic solvents, especially at 298 K. ATR-IR measurements indicated solvent-citral interactions were solely present in polar-protic solvents in line with higher yields of geraniol and nerol.

Reaction rates and selectivities obtained on 5% Pt/SiO_2 at 373 K using hexane and ethanol as solvents, were also used as a characterisation method. Hydrogenation of citral, with $c_0 = 0.33$ M and with a silylated catalyst, was performed to determine the effect of initial citral concentration and surface hydrophobicity, respectively. Hydrogenation of the main reaction intermediates, citronellal, citronellol, and geraniol and nerol, at 373 K and $c_0 = 0.13$ M was used to obtain information on the preferred hydrogenation pathways of citral. Additionally, NMR relaxometry was used for the first time to understand the effect of solvent in the selective hydrogenation of α,β-unsaturated aldehydes, and the hydrogenation of the thermodynamically less reactive C=O bond. ^{13}C T_1 NMR and ^{1}H 2D T_1-T_2 correlation experiments were used to obtain adsorption geometry and relative strength of interaction of citral in the presence of hexane and ethanol, and relative strength of interaction of main reaction intermediates. ^{13}C T_1 relaxometry showed that the interaction of the conjugated

carbon-carbon double bond in citral was weaker in the presence of ethanol than in hexane, explaining the initial reaction selectivity towards primary hydrogenation products. Competitive adsorption influencing the geometry of adsorption of citral was determined to affect C=O selective hydrogenation. These findings helped explain some of the disparity from data in the literature. Adsorption geometry influenced by catalyst-liquid interactions, and liquid-liquid interactions in non-polar solvents impacted selectivity towards formation of unsaturated alcohols geraniol and nerol. ^{1}H 2D T_1-T_2 relaxometry revealed that citronellol showed the strongest surface interaction in the presence of hexane; while competitive adsorption of ethanol with reaction intermediates determined the selectivity and reaction pathways active in that solvent.

The information provided in this work represents a coherent approach to study the effect of solvent interactions on the rate and selectivity of catalytic reactions. This work suggests that liquid-liquid and catalyst-liquid interactions in complex multifunctional molecules can be exploited to increase reaction rates, improve selectivity and reduce deactivation.

10.2 Future work

Recommendations on future experiments are described in this section. Section 10.2.1 presents suggestions for the unsaturated hydrocarbon systems adsorbed on γ- and θ-Al_2O_3, while section 10.2.2 describes work on the citral hydrogenation system, both in terms of reaction and characterisation methods.

10.2.1 Adsorption of unsaturated hydrocarbons

The study performed on the adsorption of hydrocarbons could be extended in many ways. Work performed on 1-pentene has focused on support materials, γ- and θ-Al_2O_3. As noted, the interaction of the alkene with the alumina occurred on acid sites. Hence, it would be possible to compare the adsorption of 1-pentene on weaker acidic surfaces, such as SiO_2, with adsorption on stronger acidic surfaces, such as ZrO_2 or zeolites like H-ZSM-5 or SAPO-34. The effect of acid site energies, or acid site distributions can be examined on single component adsorption and co-adsorption. Furthermore, It would be interesting to perform adsorption studies in industrially used supported-metal catalysts for isomerization or hydrogenation, such as 1% Pd/θ-Al_2O_3 (Komhom et al., 2008). The resulting analysis would show the impact on the strength of interaction of 1-pentene on γ- and θ-Al_2O_3 compared with a metal-supported catalyst. Additionally, a possible hypothesis on the modes of interaction of

1-pentene with the metal, enhanced reactivity, as well as binding energies and sites of the metal with the support could be analysed.

The adsorption of C_5 and C_6 unsaturated hydrocarbons represented an extension to single-component adsorption studies performed on 1-pentene. A range of techniques was employed to help determine the type of adsorption taking place on the aluminas, and to probe the information obtained by the different adsorption techniques. Herein, it would be possible to include complementary measurements. For example, calorimetric methods with the addition of pulsed adsorption (Siril and Brown, 2006) could provide coverage-dependent enthalpies of adsorption of the alkenes on both aluminas. These data would enable a comparison between the volumetric method and calorimetry measurements in this system. These data will also provide a comparison between direct and indirect energy measurements. Furthermore, energies of interaction could be determined with the use of simulations. Density functional theory (DFT) has been used successfully in the study of adsorption and catalytic processes (Flaherty *et al.*, 2014). A correlation between theoretical predictions on adsorption energies on different sites and the NMR relaxation time analysis data would demonstrate the applicability of these measurements. In addition, it would provide information on the specific surface acid sites, Brønsted or Lewis, contributing to the overall relaxation determined by each method.

10.2.2 Selective hydrogenation of citral

10.2.2.1 Reaction studies

The results reported in the selective hydrogenation of citral can be extended in a number of ways. It would be possible to add further reaction temperatures or citral initial concentrations. The addition of other solvents representative of different functional groups is suggested. Moreover, variants of the solvents presented here are recommended so as to complete trends on a particular functional group or structure.

Further to additions on the previously presented results, other aspects can be considered. The effect of metal dispersion and particle size are relevant in the hydrogenation of α,β-unsaturated aldehydes, as observed in the liquid-phase hydrogenation of crotonaldehyde (Englisch *et al.*, 1997). The catalyst used presented a metal dispersion of about 10%, and a Pt particle size of 18 nm. As such, it would be interesting to perform hydrogenation experiments on a well-dispersed Pt catalyst on a range of solvents. Previous studies have implemented a

kinetic model to help understand the progress of the reaction and add complementary information (Singh and Vannice, 2000). Herein, the development of a kinetic model could confirm the results observed with the different adsorption techniques in terms of preferential adsorption, competitive adsorption or catalyst blockage. Additionally, a simple kinetic model would include the effect of adsorption of main intermediates of reaction. Thus, the parameters of the model for the hydrogenation of citral in a series of solvents at two different temperatures on 5% Pt/SiO_2, could present systematic results and extend the understanding of this and similar reaction systems. Furthermore, the effect of bimetallics in the enhanced selectivity towards unsaturated alcohols is well known (Especel *et al.*, 2014). Several hypotheses have been postulated on the different modes of adsorption of α,β-unsaturated carbonyls on bimetallic catalysts. Hence, it would be interesting to determine the effect of a second metal on the strength and geometry of adsorption of citral, and when relevant on the main reaction intermediates.

10.2.2.2 Characterisation methods

In terms of characterisation techniques to determine adsorption, including NMR relaxometry measurements, it would be interesting to complement the measurements performed. Thus, variable temperature adsorption isotherms for diethyl ether or DCM could complement measurements of competitive adsorption processes in the presence of solvent. Additionally, measurements on the adsorption of the main intermediates of reaction in cyclohexane would complete the information on catalyst poisoning by product blockage. The use of NMR relaxometry measurements in the study conducted in hexane and ethanol has provided valuable information on reaction rates and selectivities in those solvents. Hence, an extension of those techniques applied to the other solvents, in addition to variable temperature adsorption isotherms, could provide useful information on adsorbate-adsorbent interactions. Consequently, a systematic study on the effect of the functional groups of the solvents on the adsorption of citral and main intermediates of reaction could be obtained. Thus, results could provide a complete matrix on solvent effects in terms of catalyst-liquid and liquid-liquid interactions for the different reaction species and solvent functional groups.

As was observed, the use of 2D ^{1}H T_1-T_2 relaxometry correlations supported by 1D chemical shift resolved relaxometry results, was able to provide information on solvents as well as citral reaction species. The development of 2D ^{13}C T_1-T_2 relaxometry correlations, in conjunction with the use of 1D ^{13}C chemical shift resolved relaxometry results, could provide

a well-resolved relaxometry map for binary mixtures. Thus, relaxometry results on the adsorption of different reaction species in a range of solvents could provide information on the interaction of different molecular functional groups with the catalyst. Such information on the interaction of functional groups of both solvent and reaction species would complement results on the adsorption strength of each species. For example, information on the interaction of functional groups with the catalyst would be relevant in alcohol mixtures. ATR-IR results showed the presence of liquid-liquid interactions. NMR relaxometry results would inform on the weaker interaction of alcohol functional groups with the surface.

It might be interesting to study diffusion within the pores in order to gain a better understanding on the effect of co-adsorbates. The effects of desorption and diffusion of co-reactants, solvents, poisoning agents, products, etc. is of great interest in multiphase reaction systems. Pulsed Field Gradient NMR (PFG-NMR) methods are an established tool to probe the behaviour of liquid molecules held within a porous matrix (Mantle et al., 2010). These results would help to understand if solvents play a role in the diffusion of reactants within the pores and/or have an influence in transport properties. This insight would further develop a picture of catalytic processes, focusing not only on the active centre of the catalyst, but also assisting in the transport of reactants and products on the porous network.

In the long term, it would be ideal to apply these techniques under actual reaction conditions. It would be interesting to perform NMR experiments to study adsorption while reaction is occurring in a catalytic system. Previous reaction studies have been performed in trickle-bed-reactors, where chemical information, velocity maps and conversion were obtained via Magnetic Resonance Imaging (MRI) (Gladden et al., 2010). It would be crucial to extend the use of NMR relaxometry measurements to real catalytic conditions. Challenges of high temperature and pressure, or the presence of gas-phase reactants and products, with the subsequent loss in NMR signal, need to be considered. However, *operando* conditions have already been employed in spectroscopic studies in the oligomerisation of ethylene (Roberts *et al.*, 2013). The addition of NMR relaxometry and diffusometry measurements could provide very useful information on the citral reaction system. The compilation of catalytic data under *operando* conditions – including conversion and selectivity – as well as the characterisation of the reaction species – adsorption strength and geometry of interaction of adsorbates, and diffusion – would ultimately help design better catalysts and catalytic processes.

References

Englisch, M., Ranade, V.S, Lercher, J.A. (1997) Liquid-phase hydrogenation of crotonaldehyde over Pt/SiO_2 catalysts. *Appl. Catal. A-Gen.*, 163, 111 – 122.

Especel, C., Duprez, D., Epron, F. (2014) Bimetallic catalysts for hydrogenation in liquid phase. *C. R. Chimie*, 17, 790 – 800.

Flaherty, D.W., Hibbitts, D.D., Gürbüz, E.I., Iglesia, E. (2014) Theoretical and kinetic assessment of the mechanism of ethane hydrogenolysis on metal surfaces saturated with chemisorbed hydrogen. *J. Catal.*, 311, 350 – 356.

Komhom, S., Mekasuwandumrong, O., Praserthdam, P., Panpranot, J. (2008). Improvement of Pd/Al_2O_3 catalyst performance in selective acetylene hydrogenation using mixed phases Al_2O_3 support. *Catal. Commun.*, 10, 86 – 91.

Gladden, L.F., Abegão, F.J.R., Dunckley, C.P., Holland, D.J., Sankey, M.H., Sederman, A.J. (2010). MRI: Operando measurements of temperature, hydrodynamics and local reaction rate in a heterogeneous catalytic reactor. *Catal. Today*, 155, 157 – 163.

Mantle, M.D., Enache, D.I., Nowicka, E., Davies, S.P., Edwards, J.K., D'Agostino, C., Mascarenhas, D.P., Durham, L., Sankar, M., Knight, D.W., Gladden, L.F., Taylor, S.H. and Hutchings, G.J. (2011). Pulsed-Field Gradient NMR spectroscopic studies of alcohols in supported gold catalysts. *J. Phys Chem. C*, 115, 1073 – 1079.

Roberts, S.T, Renshaw, M.P., Lutecki, M., McGregor, J., Sederman, A., Mantle, M.D., Gladden, L.F. (2013) *Operando* magnetic resonance: monitoring the evolution of conversion and product distribution during the heterogeneous catalytic ethane oligomerisation reaction. *Chem. Commun.*, 49, 10519 – 10521.

Singh, U.K., Vannice, M.A. (2000) Liquid-phase hydrogenation of citral over Pt/SiO_2 catalysts. I. Temperature effects on activity and selectivity. *J. Catal.*, 191, 165 – 180.

Siril, P.F., Brown, D.R. (2006) Acid site accessibility in sulfonated polystyrene acid catalysts: calorimetric study of NH_3 adsorption from flowing gas stream. *J. Mol. Catal. A-Chem.*, 252, 125 – 131.